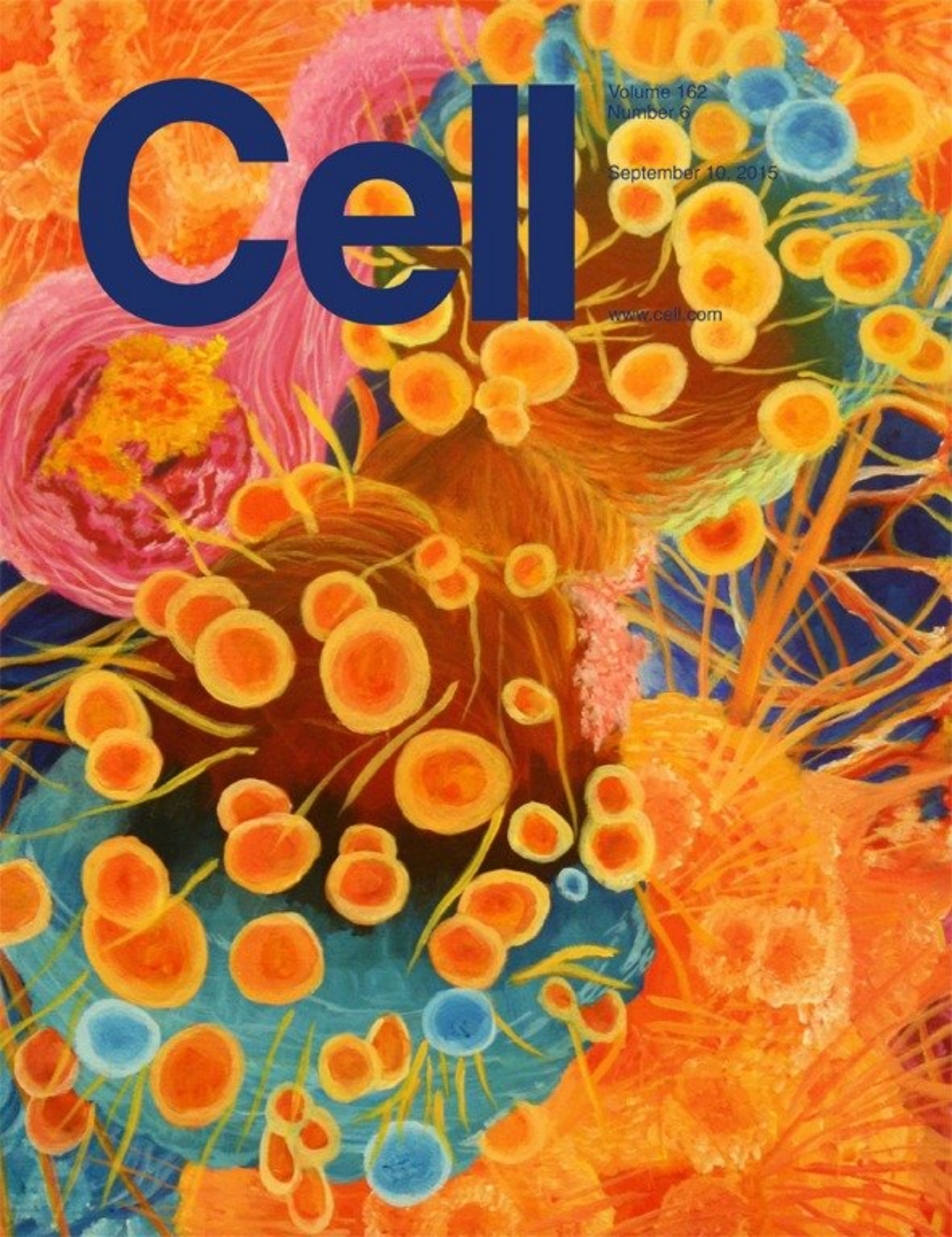


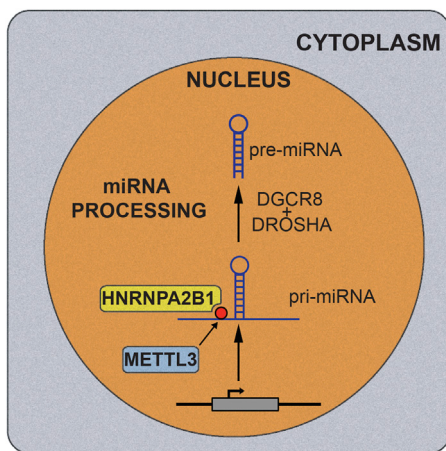
Cell

Volume 162
Number 6

September 10, 2015

www.cell.com





m6A Licensing miRNA Processing

ALARCON ET AL., PAGE 1299

The RNA binding protein HNRNPA2B1 is a nuclear reader of the m6A mark that recruits and positions a subset of precursor miRNAs in the Microprocessor complex, facilitating miRNAs maturation.

Tumor Sweet-Talk Exhausts T Cells

HO ET AL., PAGE 1217

CHANG ET AL., PAGE 1229

High rates of tumor cell glycolysis suppress intratumor T cell function by depriving T cells of glucose and the downstream metabolite phosphoenolpyruvate (PEP), which is necessary for maximal signaling in T cells. Metabolic re-wiring of T cells to generate PEP in glucose-poor conditions improves their anti-tumor responses and checkpoint blockade therapy can correct this resource imbalance.

Deadly Signal for Tumor Growth

KLEFFEL ET AL., PAGE 1242

PD-1/PD-L1 signaling has a cell-intrinsic function in certain types of mouse and human tumors, boosting cancer growth and promoting tumorigenesis, suggesting that immunotherapy with PD-1 blockers may have an effect in tumor growth that is separate from their effect in the immune response.

COX-ing Tumor Eradication

ZELENAY ET AL., PAGE 1257

Cyclooxygenase inhibitors drive tumor eradication through a synergy with checkpoint blockade immunotherapy by blunting prostaglandin E2-driven tumor growth.

A Changing Landscape of Resistant Tumors

HUGO ET AL., PAGE 1271

Acquisition of resistance to targeted therapies in melanoma is associated with highly recurrent non-genomic alterations as well as changes in the immune landscape of the tumor that in turn may decrease the response to rescue immunotherapy with anti-PD1/PD-L1.

Reverse the Curse

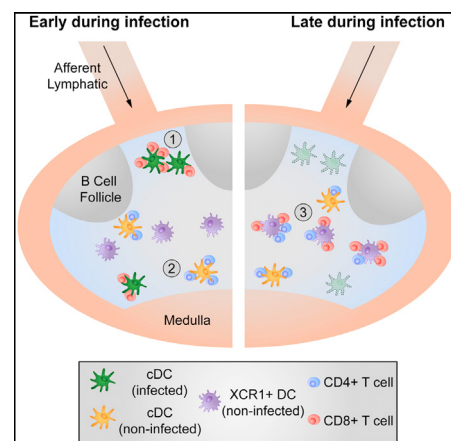
WALLACE ET AL., PAGE 1286

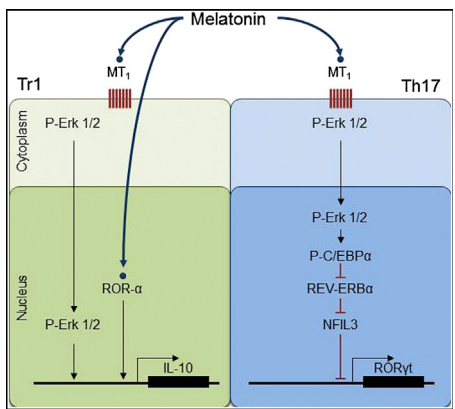
Instead of being irreparably misfolded and destined for degradation, aggregates of endogenous proteins triggered by heat stress in yeast can maintain activity and re-solubilize, suggesting an adaptive strategy underlying aggregation.

DC Conductor for T Cell Orchestra

EICKHOFF ET AL., PAGE 1322

During a viral infection, CD4+ and CD8+ T lymphocyte activation occurs initially through distinct spatial events but later a specific subset of dendritic cells orchestrates their communication to maximize immune defenses through CD8+ T cell expansion and memory function.





Seasonal (Auto)Immunity

FAREZ ET AL., PAGE 1338

Melatonin affects the differentiation and function of effector and regulatory T cells in vitro and in vivo, acting as an environmental cue that contributes to the seasonality of multiple sclerosis relapses, and a potential target for therapeutic intervention in immune-mediated diseases.

Random Encounters, Meaningful Outcomes

AVRAHAM ET AL., PAGE 1309

Functional heterogeneity in the response of host cells to infection is driven by cell-to-cell transcriptional variation in the population of infecting pathogens.

Green Stress Relief

ENDLER ET AL., PAGE 1353

Two enzymes involved in cellulose synthesis counter salt-induced cellular stress by directly altering microtubule dynamics and organization, providing insights into how plants combat environmental insults to sustain biomass.

Wasting Management

MURPHY ET AL., PAGE 1365

Antibodies against the receptor Fn14 prevent tumor-induced cachexia and extend lifespan by inhibiting weight loss and inflammation, while having only moderate effects on tumor growth.

Force on a Leash

ZHANG ET AL., PAGE 1391

The N-terminal ankyrin repeats of the mechanotransduction channel NOMPC tether the channel to microtubules so that force exerted through cell deformation gates the channel and activates touch-sensitive neurons.

Mindful Eating

STECULORUM ET AL., PAGE 1404

Increases in circulating uridine levels promote food intake in obese mice through a hypothalamic purogenic signaling pathway.

Vigor Trigger

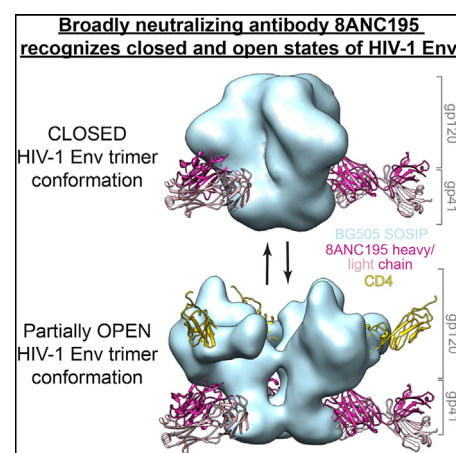
PANIGRAHI ET AL., PAGE 1418

Movement vigor, reduced in Parkinson's disease, is regulated by dopamine-dependent activity in the striatum.

Pushing the Envelope for HIV Treatment

SCHARF ET AL., PAGE 1379

Structural analysis of a broadly neutralizing HIV-1 antibody uncovers a previously unseen conformation of the envelope, marking a new site of virus vulnerability.



Making a Difference in Pain

Sexual dimorphism can be seen at many levels across the animal kingdom. In humans, it is still surrounded by much controversy and myth. While many sex-specific differences are remarkably obvious, others are subtle, complex, or even puzzling. Psychological and socio-cultural factors can also play a role by heavily influencing the perception of these differences. Take pain, for instance.

The old tale that women can handle pain better than men, perhaps because they endure labor pain, is far from being backed up by science. In fact, numerous studies have reported a higher prevalence of chronic pain and greater pain sensitivity among women as compared to men ([Mogil, 2012](#)). It is likely that there is a psychological component to this differential pain behavior, perhaps related to gender role expectations and to the fact that women seem to be more likely to seek health care than men. While these reports convincingly show that women are more sensitive to pain overall, the greatest scientific challenge is to untangle and decode the various elements implicated in pain behavior and the biological mechanisms underlying the differences between sexes. This endeavor is further complicated by the female hormonal cycle, which certainly impacts pain sensitivity. It is therefore somewhat intuitive to think about a common pain circuit between sexes that would be further modulated by circulating hormones. Indeed, this has been the pervasive view in the pain research community.

The recent discovery that pain hypersensitivity in female and male mice depends on different types of immune cells challenges this notion and offers new insights as to why men and women respond differently to pain ([Sorge et al., 2015](#)). The jumping off point for this study was the finding that inflammatory and neuropathic pain in male, but not female, mice depended on the Toll-like receptor 4 (TLR4) ([Sorge et al., 2011](#)). The team led by Jeffrey Mogil and Michael Salter now reports that the cell type where this receptor is expressed, the microglia, does not appear to be involved in neuropathic pain processing in female mice. Rather, females preferentially use an alternative pathway dependent on resident T-lymphocytes. In this study, when male mice were administered microglial inhibitors following nerve injury, their pain sensitivity was significantly reduced, while no improvement was seen in female mice ([Sorge et al., 2015](#)). As microglia have been regarded as promising targets to treat pain, these findings carry far-reaching clinical implications for pain management and analgesic drug development. Like all exciting discoveries, this study raises more questions than it answers—the most obvious being how these sex differences relate to disease and whether they can help explain why pain-related and auto-immune disorders, many of which involve T cell hyperactivity, are more prevalent in women ([Mogil, 2012](#)). A large-scale gene regulatory study led by the laboratory of Howard Chang shed some light on this conundrum ([Qu et al., 2015](#)). Here, the authors mapped open chromatin sites in human immune T cells, isolated from standard blood draws to generate a high-reso-



Image from iStock.com/Palto.

lution regulome in a snapshot in time within a single individual. Gender was by far the most significant source of T cell chromatin variability; hundreds of target genes were found to be differentially regulated between male and female T cells, including many autosomal genes associated with immune function and autoimmune diseases.

Taken together, these two studies indicate a broader than anticipated, and far more intricate, repertoire of immune-related sex differences. Historically, medical research has been conducted predominantly on males, and many studies still fail to appreciate the importance of sexual dimorphism both in experimental design and data interpretation. A painful, but valuable, lesson from this recent string of discoveries is that equal representation of both sexes in pain research, or in any biological discipline for that matter, is of utmost importance and that research performed mostly on males cannot be applied to both sexes in a clinical setting.

With the growing appreciation that sex differences in medicine are extensive, there's now little doubt that men and women may require different strategies for the treatment of pain and other conditions. As personalized medicine takes political and scientific spotlight, hopefully sex and gender-based medicine will follow.

REFERENCES

- Mogil, J.S. (2012). *Nat. Rev. Neurosci.* 13, 859–866.
- Qu, K., Zaba, L.C., Giresi, P.G., Li, R., Longmire, M., Kim, Y.H., Greenleaf, W.J., and Chang, H.Y. (2015). *Cell Syst.* 1, 51–61.
- Sorge, R.E., LaCroix-Fralish, M.L., Tuttle, A.H., Sotocinal, S.G., Austin, J.S., Ritchie, J., Chanda, M.L., Graham, A.C., Topham, L., Beggs, S., et al. (2011). *J. Neurosci.* 31, 15450–15454.
- Sorge, R.E., Mapplebeck, J.C., Rosen, S., Beggs, S., Taves, S., Alexander, J.K., Martin, L.J., Austin, J.S., Sotocinal, S.G., Chen, D., et al. (2015). *Nat. Neurosci.* 18, 1081–1083.

Marta Koch

Chris Marshall (1949–2015)

Chris Marshall, who died on August 8 at age 66, was a world-renowned cell biologist best known for his pioneering contributions to oncogene research and to cell signaling via GTPases, especially to our understanding of tumor cell signaling through the Ras-Raf-Mek-Erk pathway. He spent the whole of his independent research career at the Chester Beatty Laboratories of the Institute of Cancer Research (ICR) in London, where he was Professor of Cell Biology and Head of the Division of Cancer Biology. Not long after his arrival at ICR in 1980, he established a close and superbly successful research partnership with Alan Hall, who predeceased him by three months (*Cell* 161, pp. 1239–1240, 2015). It is poignant that Chris, who spoke so eloquently at Alan's funeral, was to follow so soon and that he succumbed to colon cancer, one of the tumors that most frequently carries *RAS* mutations. The international cancer research community keenly feels the dual loss of Chris and Alan.

Christopher John Marshall was born in Birmingham on January 19, 1949 to James and Lillian Marshall and later lived in Coventry, where he attended King Henry VIII School. His father was a works manager for Massey-Ferguson, the tractor manufacturers, and there was not a strong science tradition in his family. He won a scholarship to Churchill College, Cambridge to study natural sciences, specializing in genetics. As a graduate student, he joined Henry Harris's laboratory at the Sir William Dunn School of Pathology in Oxford, where he gained his DPhil in 1973. His doctoral studies concerned somatic cell genetics of hybrids between human and murine cells after Harris and Watkins developed an efficient method of cell fusion using inactivated Sendai virus. He used species-specific chromosome banding to examine chromosome segregation and studied the control of expression of ribosomal RNA in heterokaryons. His experience of somatic cell genetics served him well when he joined Sammy Franks' experimental pathology laboratory at the Imperial Cancer Research Fund Laboratories (now part of the Francis Crick Institute) and became interested in sup-

pression of the malignant phenotype in normal-tumor cell hybrids and in markers of neoplastic transformation in human carcinomas. He continued this interest in tumor suppression during a second post-doctoral position with Ruth Sager at the Dana-Farber Cancer Center at Harvard Medical School.

Chris Marshall's illustrious career took off in 1980, when he joined the ICR to establish his own team. With the grant that he won from the Cancer Research Campaign, now part of Cancer Research UK (CRUK), he planned to continue studies of tumor suppression, which was still a nascent field. However, he soon joined forces with Alan Hall in Robin Weiss's laboratory to study oncogenes instead. Alan introduced the relatively new recombinant DNA techniques to the ICR, and the two of them embarked on a project searching for human oncogenes by DNA transfection into murine NIH 3T3 cells. This technique had recently been shown to work for murine tumors, and it was the natural next step to apply it to human tumors. Marshall and Hall tried DNA transfer from many human neoplastic cell lines without success and were on the point of abandoning the project when they obtained transformed cells using DNA from two human sarcoma cell lines. They successfully cloned the human gene responsible for cell transformation to reveal a novel member of the *RAS* oncogene family, *NRAS*. *HRAS* and *KRAS* were originally identified as retroviral onco-

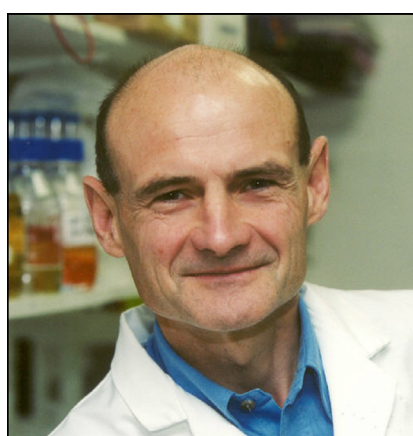
genes, but *NRAS* had not previously been characterized. The breakthrough exemplified two facets of Chris's aptitude for discovery: boldness to pursue a new avenue distinct from the original purpose of his research grant and perseverance.

The discovery of *NRAS* led to Chris's long-standing interest in cell signaling through the activation of small GTPases. About 12% of human tumors bear mutations in one of the three *RAS* genes that lead to constitutive signaling. Marshall and Hall made leading contributions to elucidating how Ras proteins transmit signals from the cell membrane through many steps to the nucleus. They played a major role in unraveling the signaling cascade that leads to cell proliferation via the Map-kinase pathway, and Chris's team showed that the p21 Ras protein must become farnesylated and thereby associate with membranes to function in the signaling pathway. They elucidated how Ras activates Raf, which acts on Mek and in turn activates Map-kinase, and showed that mutated *NRAS* results in overstimulation of this pathway.

Some years later, Chris employed his deep insight into the pathway to contribute to the first success of the Wellcome Trust Sanger Institute's Cancer Genome Project, in which Mike Stratton and his colleagues showed that the majority of melanomas tested carried a mutation in *BRAF*. Together with Richard Marais, he explored the biological consequences of the mutation and he returned to the bench to use his skills at transfection to demonstrate that the V600E mutant of *BRAF* is a transforming oncogene.

Chris was no ivory tower scientist. He adhered to Sydney Brenner's dictum that there is no real distinction between basic and applied research—only between good and mediocre research. He clearly saw the potential of exploiting the new knowledge of signal transduction for drug discovery. It was a source of great pleasure to him that four new classes of drug that target the pathway he did so much to elucidate have entered the clinic and that two of them are in widespread use.

During the past decade, Chris became interested in tumor cell motility and metastasis, and he extended his research into signaling pathways downstream of other GTPases such as Rac and Rho. He



Chris Marshall

showed that these pathways control two alternate modes of cell movement, which differ in their requirement for extracellular proteolysis, and demonstrated the key role of the Rho effector kinase Rock. Ever alert to the translational agenda, one of his most recent papers reports that Rock inhibitors block melanoma cell motility, invasion, and metastasis in an animal model.

Tackling difficult problems came naturally to Chris, provided that they were potentially soluble. He exhibited great energy in both professional and recreational life, approaching science and cycling with equal enthusiasm. Vigorous scientific discussion with colleagues did not end upon leaving the lab for the day but often continued in neighboring pubs. During his 35 years at ICR, Chris took on many roles, most notably that of Director of Research. His forceful championing of the translational agenda and his insistence that such work could, and should, be of the highest quality was of great importance to the success of the ICR and its partner, the Royal Marsden Hospital. He was mentor to numerous young

scientists who went on to successful research careers elsewhere, including Karen Vousden, Director of the CRUK Beatson Institute for Cancer Research in Glasgow, and Richard Marais, Director of the CRUK Manchester Institute, to name but two.

In contrast to enjoying the respect that he received from his scientific and academic peers, Chris did not regard himself as a pillar of the British "establishment." When he joined the ranks of worthy people with an entry in *Who's Who*, he gave his "club" as Norwood Paragon Cycling, and it seems to us that that summed him up nicely.

Chris held his opinions strongly and could at times appear acerbic, yet he was a kind, loyal, and helpful colleague. He sat on various national and international panels with distinction. He was elected a member of the European Molecular Biology Organization in 1993, a Fellow of the Royal Society in 1995, and in 1998 was awarded its Buchanan Medal. He was a founding member of the Academy of Medical Sciences. This year he received the Centenary Award of

the Biochemical Society, having previously been awarded its Novartis Prize. Throughout most of his career, Chris was supported by Cancer Research UK and its precursor organizations; he held the coveted Gibb Fellowship and recently won its Lifetime Achievement Award. For the past three years, Chris chaired CRUK's Science Funding Committee. Not least, Chris served continuously for 23 years on the editorial board of *Cell*!

Chris is survived by Lesley, his wife, and by Vivien, his first wife with whom he had three children. He delighted in his four grandchildren and the time they were able to spend together.

Peter W.J. Rigby^{1,*}
and Robin A. Weiss^{2,*}

¹Division of Cancer Biology, Chester Beatty Laboratories, Institute of Cancer Research, Fulham Road, London, SW3 6JB, UK

²Division of Infection and Immunity, University College London, Gower Street, London, WC1E 6BT, UK

*Correspondence: peter.ribgy@icr.ac.uk (P.W.J.R.), r.weiss@ucl.ac.uk (R.A.W.)
<http://dx.doi.org/10.1016/j.cell.2015.08.050>

A Well-Hung Horse: Sired by Knowledge and Imagination

Joseph L. Goldstein^{1,*}

¹Chair, Lasker Awards Jury

*Correspondence: joe.goldstein@utsouthwestern.edu

<http://dx.doi.org/10.1016/j.cell.2015.08.039>

For more than a century, historians of science have been spinning a philosophical roulette wheel, pondering which is more important in the creative process: imagination or knowledge. The most original scientists (and artists) in our day discover newness by blending existing knowledge with imaginative thinking.

Knowledge versus Imagination

The opening salvo in the imagination versus knowledge debate goes back to the Dutch chemist Jacobus van't Hoff, who was awarded the first Nobel Prize in Chemistry in 1901. van't Hoff is credited with two original achievements. The first is his proposal that atoms in a molecule are arranged in a three-dimensional space—a hypothesis that led to the discovery of the asymmetrical carbon atom and to the founding of a new field of physical chemistry. And the second is that the speed of a chemical reaction is related to temperature and the concentration of components in the reaction. Thus, two fundamental concepts—molecular shape and reaction kinetics—originated with this one individual.

van't Hoff believed that the key to scientific creativity was not facts and knowledge, but imagination. Imagination, in his view, is the essential building block of scientific inquiry. In 1878, van't Hoff assembled his ideas into an essay entitled *Imagination in Science*, in which he pointed out that many of the world's most original scientists like Newton, Galileo, Davy, and Boyle possessed life-long strange imaginings and superstitions that influenced their approach to science (Springer, 1967). Most creative scientists, according to van't Hoff, were a bit "crazy"—with "crazy" being shorthand for bold thinking and being free to try new things that less-creative colleagues would deem ridiculous.

Although van't Hoff was the first to emphasize the value of imagination in science, it was Einstein who put imagination on the philosophical map. In a 1929 interview in *The Saturday Evening Post*,

a journalist asked Einstein "How do you account for your discoveries? Through intuition or inspiration?" Einstein replied, "Both. I'm enough of an artist to draw freely on my imagination, which I think is more important than knowledge." He explained that knowledge is limited to what we already know and understand, while imagination leads to all there ever will be to know and understand (Viereck, 1929).

Einstein and van't Hoff were exceptional rarefied thinkers who viewed imagination and knowledge as horses of a different color. To them, imagination was the domain of scientists and artists; knowledge was for curators and accountants. In Einstein's universe, there was neither space nor time for the most imaginative of accountants—even those who could cook the books and never get caught.

In the real world of today, the most creative scientists possess a special knack for asking the right question, framed in the context of existing knowledge, which is then used as a stepping stone to imaginative thinking. A wonderful example of the creative blending of knowledge and imagination is illustrated by a portrait in Room 34 of the National Gallery in London. Room 34 contains famous 18th century British society portraits by Thomas Gainsborough and Joshua Reynolds, who painted their aristocratic subjects on a grand scale in the European manner. But the portrait that I will tell you about is not one of a famous English nobleman; rather, it's a horse of a different color; in fact, it's actually a portrait of a horse—a real Arabian horse named *Whistlejacket*, the star racehorse of his day in 18th century England (Figure 1, left). *Whistlejacket* was named

after a popular cocktail containing gin and molasses that was golden colored like *Whistlejacket*'s flanks.

Whistlejacket: A Historic Painting by George Stubbs

The oil-on-canvas painting of *Whistlejacket* was completed in 1762 by the British artist George Stubbs (1724–1806) (Warner and Blake, 2004). There are 2,300 paintings in the National Gallery's collection, which includes famous works by Caravaggio, Rembrandt, Rubens, Velasquez, Van Gogh, and Cezanne. In terms of viewer popularity and museum shop sales, *Whistlejacket* is the National Gallery's equivalent of The Louvre's *Mona Lisa*. The National's museum shop sells 32 different *Whistlejacket*-designed items, including the usual postcards, posters, scarfs, umbrellas, etc. But one of these items is unique for a museum shop—a bottle of Sloe Gin, a modern-day recreation of the 18th century *Whistlejacket* cocktail containing 27% alcohol (www.nationalgallery.org.uk).

Whistlejacket is monumental in size—9.5 feet by 8 feet—the size of an actual horse. *Whistlejacket* occupies pride of place in its location in the National Gallery (Longmuir, 1997). It is hung at one end of the Gallery's long main corridor in such a way that the museum-goer sees an enormous horse through multiple glass doorways as he or she wanders through ten intervening rooms that connect one end of the Gallery to the other (Figure 1, right). The painting is a true traffic-stopper and a powerful magnet, attracting and pulling people to it from remote parts of the museum. As a museum curator might say, *Whistlejacket* is a well-hung horse!



Figure 1. A Well-Hung Horse

(Left) *Whistlejacket* by George Stubbs, 1762. Oil on canvas. 9.5 × 8 ft. The painting hangs in London's National Gallery at one end of the museum's long main corridor and can be seen through ten intervening rooms that connect one end of the museum to the other. (Upper-right) *Whistlejacket* is seen through the door in Room 35 that leads directly to Room 34, where *Whistlejacket* hangs. (Lower-right) *Whistlejacket* is seen through the door in Room 9, which is located at the opposite end of the museum's long corridor from Room 34. <http://nationalgallery.org.uk/visiting/virtualtour/>.

So what makes *Whistlejacket* such a remarkable painting? The answer lies in the creativity of George Stubbs, whose deep knowledge of the anatomy of horses stimulated his imagination in a unique way. Stubbs began his career as a scientist, studying human anatomy at a medical school where he also taught himself to draw and paint. His first job in 1750 was to illustrate an anatomy book on human fetal development. He then switched his anatomical interests from humans to horses.

The Anatomy of a Horse: A Scientific Masterpiece by George Stubbs

For the next two years, Stubbs carried out grueling dissections and experiments on dead horses. To familiarize himself with the animal's anatomy and physiology, he suspended the dead horses from his stable roof, stripped away their muscles, injected their veins with wax, and positioned them in various poses so that he could make meticulous drawings and engravings (Rott, 2012).

Stubbs' studies of equine musculature and skeletal structure were published in 1766 in a graphic masterpiece, *The Anatomy of the Horse* (McCunn and Ottaway, 1976). The horse is presented in 36 large plates and 18 tables, with depictions of the skeleton alone, all of the muscle layers, and the ligaments, nerves, veins, glands, and cartilage. Stubbs' equine drawings are memorable for their life-like quality and exceptional anatomical precision—on par with Leonardo da Vinci's anatomical drawings of the human body. Stubbs' reputation as an expert on horses attracted the attention of the landed gentry whose passion in 18th century England was horse breeding and racing. Members of the Jockey Club of London commissioned him to paint portraits of their favorite horses.

Stubbs' portrait of *Whistlejacket* is a milestone in art history, making a radical break with convention and representing a prime example of the blending of knowledge with imagination. This was the first time that an animal was painted on a

scale reserved for a king. Unlike previous paintings involving horses, *Whistlejacket* is depicted alone with no people, no landscape, no battlefields, no saddles, no bridles, no whips—just one horse that is free to gallop in empty space with no noisy distractions. The only areas in the canvas where space is suggested are the two small shadows cast by the rear hooves. Stubbs' innovative use of empty space as a background focuses our attention on the subject's individuality—his flying mane, his shiny golden flanks, his taut muscles, and his terrified eye looking at us. Why is *Whistlejacket* so terrified?

When the portrait was nearly finished, an extraordinary event occurred. After Stubbs had removed the canvas from the easel and placed it against the stable wall, the portrait was glimpsed by the real *Whistlejacket*. The real *Whistlejacket* so believed that he was confronting a raging stallion that he began "to stare and look wildly at the picture, endeavoring to get at it to fight and kick it." This must surely have been the moment when Stubbs realized that he had created a masterpiece of realism—one that was recognized by his living subject (Warner and Blake, 2004; Longmuir, 1997).

Although George Stubbs painted *Whistlejacket* 250 years ago, he and his work are a reminder of a famous line by William Faulkner: "The past is never dead. It is not even past." Stubbs' passion for horses influenced all subsequent painters of horses, including Delacroix, Gericault, Degas, and Picasso. According to the art critic Robert Hughes (1984), *Whistlejacket* prefigured Picasso's famous horse in *Guernica*, the horse that thrusts "its outraged neck toward the indifferent sky of the 20th century."

Gift Horse: A Contemporary Sculpture Inspired by Whistlejacket

The most recent reminder of George Stubbs' past is a contemporary sculpture of a strutting horse that was recently installed on top of the Fourth Plinth in London's Trafalgar Square, situated just in front of The National Gallery where *Whistlejacket* hangs (Figure 2, top). The new equine sculpture was created by Hans Haacke, a 78-year-old German-born artist who has lived in the United

States for the last 50 years ([London Gov. UK, 2015](#)). Haacke is one of the fathers of Conceptual Art whose followers make minimalist sculptures from industrial materials and found objects. Lately, Haacke has led a new art movement called Institutional Critique in which artists use their art to draw attention to hidden connections between politics, business, and established organizations such as museums and churches ([Grasskamp, 2004](#)).

Haacke's new bronze sculpture is 15-feet tall, twice the size of a real horse, and weighs 4,000 pounds ([Figure 2](#), middle). It is attracting wide public attention not because it is a horse of enormous size but because it is a skeletal sculpture of a horse. The sculpture was inspired by George Stubbs' *Whistlejacket* painting and is based on one of the skeletal drawings in Stubbs' classic book *The Anatomy of the Horse* ([Figure 2](#), bottom). Haacke titled his bronze skeleton *Gift Horse*. Apropos of its name, one of the skeleton's front legs is wrapped with a large ribbon tied in a pretty bow like on a present ([Figure 2](#), middle). The ribbon displays a ticker-tape transmitting live electronic data from the London Stock Exchange. Why would Haacke decorate a dead horse from the 18th century with live stock quotes from the 21st century?

The answer lies in Haacke's knowledge of the historical background of Trafalgar Square combined with his imagination in using art as a platform to comment on established institutions. The Square's name commemorates the 1805 Battle of Trafalgar, the spectacular British naval victory over France dur-

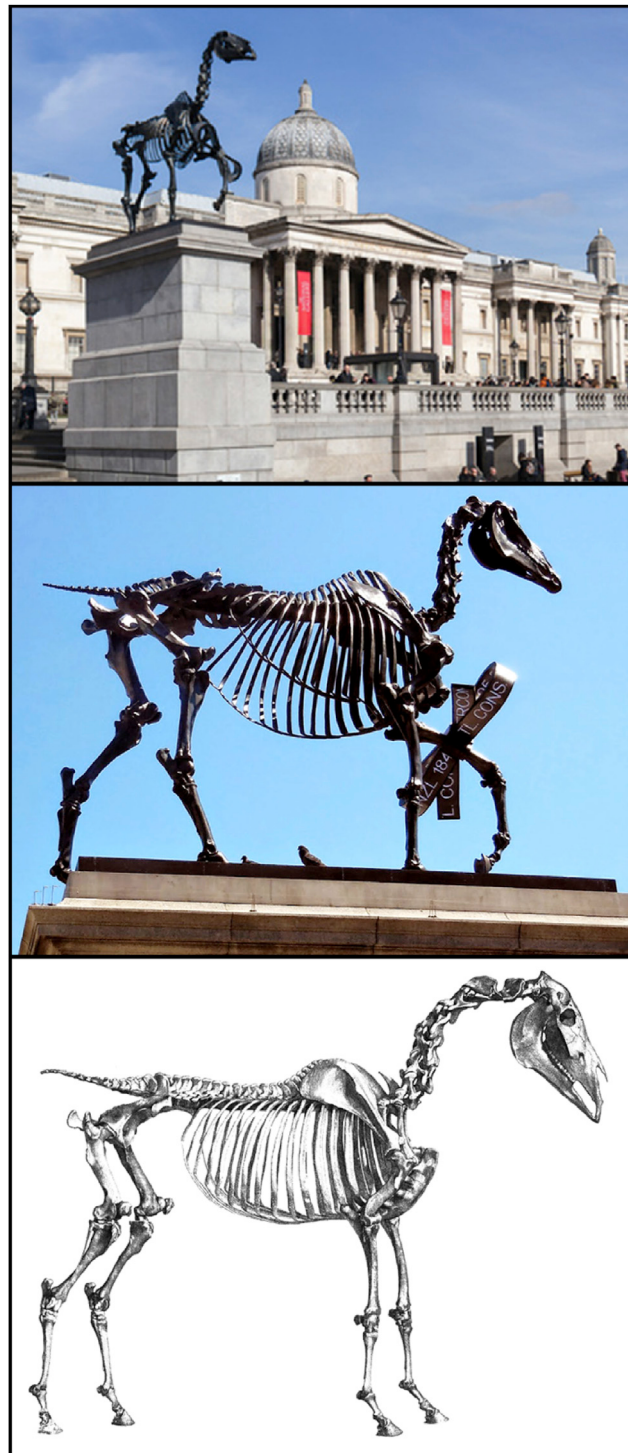


Figure 2. Haacke's Contemporary Bronze Sculpture Is Inspired by Stubb's Anatomical Horse

(Top) View of the north side of Trafalgar Square, showing the Fourth Plinth and the National Gallery from left to right. (Middle) Hans Haacke, *Gift Horse*, 2015. Bronze. Height, 15 ft. Exhibited on the Fourth Plinth at Trafalgar Square, London, 2015–2017. The tied ribbon bow on the right front leg of the horse skeleton displays a ticker-tape transmitting live electronic data from the London Stock Exchange. (Bottom) George Stubbs, *First Skeleton Table*, 1766. Copper plate drawing ([McCunn and Ottawa, 1976](#)).

ing the Napoleonic Wars ([Hood, 2005](#)). At the center of the Square stands a tall column on top of which sits a statue of Lord Horatio Nelson, England's greatest naval hero, who was killed at Trafalgar. Surrounding the Nelson Column are four large stone pedestals, which the British call the Four Plinths. Three of the four plinths carry equestrian sculptures of kings or military heroes.

The Fourth Plinth, erected in 1841, was intended to display a statue of King George IV on horseback, but the cost was so exorbitant that it was never completed, and it remained bare for 150 years until the British government decided to use it as a public platform for displaying a contemporary sculpture that could be viewed by the 40,000 people who visit Trafalgar Square each day. Every 1 to 2 years, 100 leading artists from around the world are invited to enter a competition. Since 1999, ten artists have been selected to showcase their artwork on the Fourth Plinth.

Combining Knowledge and Imagination to Create *Gift Horse*

Hans Haacke's *Gift Horse* is arguably the most deeply researched of all the sculptures to have appeared on the Fourth Plinth. As already mentioned, it is steeped in art history, reaching back to the anatomical work of George Stubbs. There is also the historical connection to the British and their passionate love for horses, which raises the question as to why Haacke would sculpt the skeleton of a horse rather than the real thing. I think he is teasing the British, reminding them of the precariousness of their Empire and of their poor financial situation 150 years ago, which left

the Fourth Plinth empty and bare. And now Haacke, a German-American, has come to the rescue—not with a sculpture of a real horse, but with the bare bones of King George's horse.

In addition to the historical references, there is a political bite to *Gift Horse*. The ticker-tape on the skeleton's leg is a reminder that money is the power that drives both the good and the bad in the world and the dynamic behind modern-day income inequality. Then there is the provocative title of *Gift Horse*. It is almost certainly an allusion to the Greeks' Trojan Horse that led to the saying "Beware of Greeks bearing gifts." Is Haacke telling us to "Beware of brokers bearing hot tips"?

George Stubbs and Hans Haacke produced their art in two different centuries. Yet, they achieved greatness by a similar route: both used existing knowledge as a stepping stone to imagination. Stubbs' knowledge of the anatomy and physiology of horses stimulated him to unite science and art in creative ways that resulted in his becoming one of our great portrait painters. Haacke's knowledge of complex contemporary social and financial systems stimulated him to expose in original ways those things in the world that need to be brought to public attention.

2015 Lasker Awards: A Marriage of Knowledge and Imagination

Like Stubbs and Haacke, the 2015 Lasker Awardees possess an intuitive talent for creating something new by blending knowledge with imagination. This special knack for newness allowed them to make discoveries that opened new fields of biomedical science. In much the way that Stubbs redefined portraiture by imaginative choice of subject matter and innovative elimination of background noise, this year's medical research laureates have produced original portraiture that explicitly and distinctly illustrates how our cells respond to DNA damage and how our immune system deploys a powerful strategy to fight cancer.

Basic Award

The Lasker Basic Research Award honors two scientists, Evelyn M. Witkin (Rutgers

University) and Stephen J. Elledge (Brigham and Women's Hospital), for discoveries concerning the DNA damage response—a mechanism that protects the genomes of all living organisms. The maintenance of genome integrity is a daunting task, owing to the constant assault on DNA by external agents (e.g., chemicals, radiation, UV light, etc.) and errors occurring during normal DNA replication. Witkin's groundbreaking research in the 1960s on UV radiation in bacteria led to the identification of the SOS response, a global response in which DNA damage leads to the expression of diverse gene products that not only enhance DNA repair and cell survival, but also increase mutagenesis and genetic variability. The mechanism mediating the bacterial SOS response involves the activation of about 30 unlinked but coordinately regulated genes, each controlled by a bacterial operon involving the same repressor (LexA) and inducer (RecA).

In the late 1980's, 25 years after Witkin's classic work in bacteria, Elledge began his studies of the DNA damage response in more complex organisms, working first in yeast and subsequently in mammalian cells. He discovered that eukaryotic cells sense and respond to DNA damage by a fundamentally different mechanism than bacterial cells even though the two systems share the same overarching theme. The eukaryotic mechanism is mediated by a signaling system involving a protein kinase cascade that senses damaged DNA. Once activated, the kinases produce multiple cellular responses, including changes in cell-cycle control, DNA repair, apoptosis, autophagy, and telomere maintenance as well as pathways involving RNA processing and modulation of energy metabolism. Human mutations in key components of this signaling cascade, such as those disrupting the function of ATM kinase, cause genome instability and cancer, as occur in patients with Ataxia Telangiectasia.

Clinical Award

The Lasker~DeBakey Clinical Research Award honors the scientist James P. Allison (University of Texas MD Anderson

Cancer Center), who pioneered a monoclonal antibody approach that unleashes the immune system to treat cancer, as first exemplified by the clinical success of CTLA-4 antibody therapy for metastatic melanoma. Allison's discovery of immune checkpoint blockade has now been extended to other T cell inhibiting pathways (e.g., anti-PD-1) for treatment of not only melanoma, but of other malignancies, including lung cancer.

Public Service Award

In much the same way that Haacke's knowledge of complex contemporary social and financial systems stimulated him to expose those things in the world that need to be brought to attention, this year's Lasker~Bloomberg Public Service Award honors Médecins Sans Frontières, an organization renowned for its bold and innovative responses to leadership in health emergencies, as recently exemplified by its frontline response to last year's Ebola crisis.

For a more detailed account of this year's Lasker awardees, please refer to the Lasker website at www.laskerfoundation.org and to the articles in this issue of *Cell*.

REFERENCES

- Grasskamp, W. (2004). *Hans Haacke* (Phaidon Press).
- Hood, J. (2005). *Trafalgar Square* (Sterling Publications).
- Hughes, R. (1984). George Stubbs: a vision of four-legged order. *Time*, November 19, 1984.
- London Gov UK. (2015). Gift Horse on Fourth Plinth. <https://www.london.gov.uk/priorities/arts-culture/fourth-plinth/2014-2015-commissions>.
- Longmuir, E. (1997). *The National Gallery Companion Guide* (National Gallery Company, Limited).
- McCunn, J.C., and Ottaway, C.W. (1976). *The Anatomy of the Horse* by George Stubbs (Dover Publications, Inc.).
- Rott H.W., ed. (2012). *George Stubbs: Science into Art* (Prestel Verlag).
- Springer G.F., ed. (1967). *J.H. van't Hoff's 1878 Imagination in Science* (Springer-Verlag).
- Viereck, G.S. (1929). What life means to Einstein. *The Saturday Evening Post*, October 26, 1929.
- Warner, M., and Blake, R. (2004). *Stubbs & the Horse* (Yale University Press).

Deciphering the DNA Damage Response

James E. Haber^{1,*}

¹Department of Biology and Rosenstiel Basic Medical Sciences Research Center, Brandeis University, Waltham, MA 02454, USA

*Correspondence: haber@brandeis.edu

<http://dx.doi.org/10.1016/j.cell.2015.08.034>

This year's Albert Lasker Basic Medical Research Award honors Evelyn Witkin and Stephen J. Elledge, two pioneers in elucidating the DNA damage response, whose contributions span more than 40 years.

Bacterial or human cells devote significant resources to maintain the integrity of their genomes. Among the most severe challenges are sources of DNA damage such as ultraviolet (UV) light and other chemical agents that alter DNA bases. Crosslinking of DNA bases creates blocks to normal DNA replication that must be removed or bypassed. Genome integrity is also assaulted by ionizing radiation and other clastogens that cause double-strand breaks that must be rejoined, either by nonhomologous end-joining or by homologous recombination. For repair to be successful, it must be completed before the cell divides; incompletely replicated chromosomes become trapped, while acentric broken chromosome segments get lost or mis-segregated. Failures of the DNA damage response are a common cause of cancer in humans. To assure that repair is accomplished before cell division, cells have evolved complex surveillance mechanisms to identify DNA damage, to impose checkpoints that arrest cell division until repair is completed, and to assure that an appropriate DNA repair response is launched. This year's Lasker prize honors two visionary scientists whose experiments and revolutionary insights set the stage for our present understanding of these critical processes.

Evelyn Witkin's contributions to the field of DNA repair began with her first publication, in 1946, identifying a mutant *E. coli* strain that is resistant to both UV light and X-rays. She noted that this strain does not show the usual delay in cell division or the filamentous elongation before cell division that is normally seen in wild-type strains. Subsequently, she noted many similarities between UV-induced filament formation and the UV-induced activation of the dormant phage λ . After moving from Cold Spring Harbor

Laboratory to the State University of New York Downstate Medical Center, Witkin pursued these ideas while also providing key insights into the process of UV-induced mutagenesis, identifying a "dark repair" process in addition to the photo-reversal of pyrimidine dimers and suggesting the existence of error-prone DNA polymerases.

In her seminal paper (Witkin, 1967), Evelyn Witkin invoked the ideas recently proposed by Jacob and Monod of a repressor that inhibits both UV-induced phenomena and that itself would be inactivated by UV irradiation. By this time, it was already known that phage λ itself has a repressor that is inactivated by UV light. Witkin proposed that the presence of UV photodimers triggers the inactivation of a common repressor that would then allow the expression of genes, which in turn would promote both the arrest of cell division and the induction of the

phage. Subsequently, Miro Radman, a postdoctoral fellow in Paris, circulated a letter in 1971 to leading scientists in the field, proposing the concept of a general "SOS response." Radman's ideas were not formally published and widely available until 1975, but Witkin quickly embraced this idea. She summarized the rapidly growing body of knowledge in a comprehensive review on "Ultraviolet mutagenesis and inducible DNA repair in *Escherichia coli*" (Witkin, 1976).

Soon after Witkin advanced her hypothesis, several labs identified key elements of this regulation. Activation of phage λ and inhibition of cell division depend on the recombination protein RecA. Witkin herself, now at Rutgers University, showed that UV-induced mutagenesis depends on an apparently UV-induced error-prone form of DNA replication controlled by LexA (Witkin and George, 1973), which proved to be the repressor of many SOS genes. The induction of phage λ depends on the proteolytic cleavage of the λ repressor, a process involving RecA. Initially RecA was thought to be a protease as well as the central recombination protein, but subsequent work has shown that RecA, which forms a filament on single-stranded DNA that is created at stalled replication forks (i.e., after UV irradiation) or on the resected single-stranded ends of X-ray broken DNA ends, acts as an allosteric effector to promote the autocleavage of both LexA and the λ repressor.

In the more than 40 years since Witkin's hypothesis began to take molecular shape, the SOS response has emerged as a much more complex network of responses to DNA damage. Nearly 70 genes have been identified that either regulate LexA response or are regulated directly by LexA and are induced by



Witkin and Elledge at Graham Walker's induction into the National Academy of Sciences in 2013. Photo credit: Gordon Walker.

DNA damage. These genes have been identified by reporter gene fusions to various promoters and subsequently by gene expression profiling or by bioinformatics approaches using the consensus SOS repressor sequence. Among the processes controlled by SOS are cell division, nucleotide excision repair, DNA repair by recombination, and translesion DNA polymerases. Witkin's decisive role in understanding the bacterial DNA damage response has been recognized by many awards, most notably the National Medal of Science in 2004.

One particular LexA-regulated "bypass" DNA polymerase, encoded by the UmuDC operon, provides the link between Evelyn Witkin and Stephen Elledge. Witkin had generously supported the research of young researchers such as Graham Walker (in his case, Witkin carried a sensitive UV dose meter from Paris to Cambridge, MA, so that Walker could carry out his experiments). Elledge and Walker (Elledge and Walker, 1983) cloned the UmuC and UmuD open reading frames. UmuD is cleaved in a RecA-dependent fashion to a smaller, active form called UmuD'. Witkin herself showed that there is a third key RecA-mediated activity, independent of the operon's induction by LexA or the cleavage of UmuD.

In Walker's lab, Elledge first displayed his remarkable facility in creating novel genetic screens and molecular tools for the analysis of complex regulation, inventing phasmid vectors for the complementation of *E. coli* mutants. Indeed, throughout his career, Elledge has invented remarkable research tools and genetic screens, most recently a powerful new method for profiling human populations with a drop of blood, using a synthetic human virome to detect anti-viral antibodies.

After earning his Ph.D., Elledge moved to Ron Davis' lab at Stanford for his post-doctoral work, making the transition from prokaryotes to the emerging eukaryotic model system, budding yeast. Elledge's initial goal was to use phage-expression techniques to screen for yeast's RecA on the assumption that an anti-RecA antibody would find the gene. Instead, he accidentally pulled out the gene encoding the small subunit of ribonucleotide reductase, Rnr2 (Elledge and Davis, 1987). (It would take another 5 years

before yeast's Rad51 protein would be shown to be similar to RecA.) Elledge demonstrated that *RNR2* mRNA is strongly induced by DNA damage and realized that this might be a tool through which he could interrogate the regulatory pathway responsible for RNR2's induction.

Elledge's characterization of *RNR2* regulation quickly established that it does not fit the paradigm of the *E. coli* response: its expression is still induced by UV in the absence of protein synthesis. A 42-bp regulatory region would confer damage inducibility to a reporter gene but does not share sequence similarity with the LexA binding site. Importantly, a protein kinase, Dun1, was found to be a key regulator of RNR gene expression after blocking DNA replication (Zhou and Elledge, 1993). Dun1 itself is activated for autophosphorylation in response to DNA damage. This finding established that DNA damage is indeed transduced by signal transduction, through a protein kinase, and was the first demonstration of what is now called the DNA damage response (DDR) pathway.

The concept of a DNA-damage-dependent cell-cycle delay in eukaryotes was intuited by Tobey (Tobey, 1975) studying drug and UV-sensitive mutants in fission yeast, and the concept of a DNA damage checkpoint was first articulated by Weinert and Hartwell (Weinert and Hartwell, 1988), who demonstrated that mutants in the *RAD9* gene, while proficient for repair of X-ray induced lesions, are X-ray sensitive because they fail to arrest prior to mitosis and thus give cells sufficient time to repair lesions before chromosome segregation. Several additional mutations, including mutants in *MEC1* (mitotic entry checkpoint) and *RAD53* (originally identified as an X-ray sensitive mutation), had been identified by Weinert et al. (Weinert et al., 1994), but the biochemical activities of these gene products were unknown. Elledge's lab contemporaneously identified S-phase arrest-defective (*sad*) mutants, including an allele of *RAD53* and an allele of *MEC1*, which later proved to be yeast's homolog of the ATR kinase (Allen et al., 1994). Allen et al. showed first that Rad53 is itself a protein kinase. Second, Rad53's kinase activity is required for the activation of Dun1, and Dun1 remains unphosphorylated in the *rad53*

mutant. Third, Rad53 is involved in the control of three distinct checkpoints: a pause in G1 after DNA damage, the failure to induce RNR genes in response to a replication block, and a failure to delay mitosis in the face of unrepaired DNA damage. At this point, it became clear that the response to DNA damage in eukaryotes was not going to be similar to the regulation of the LexA repressor. The studies of eukaryotic regulation "implicate protein phosphorylation in the cellular response to DNA damage and replication blocks" (Allen et al., 1994).

Indeed, the notion of a cascade of phosphorylation signals, and the counteracting dephosphorylations that must help terminate the checkpoint response, is the primary theme of eukaryotic cell-cycle regulation in response to DNA damage. On top of this scheme is another feature especially of higher eukaryotes, the self-destruction of cells with DNA damage by apoptosis, mediated principally through the p53 gene.

When Elledge set up his own lab at Baylor College of Medicine in 1989, he soon began to work on mammalian cells as well as yeast, embracing questions of the role of cyclin-dependent kinases in cell-cycle control. The yeast work quickly informed recent discoveries in the DNA damage response in mammalian cells. Soon thereafter, Elledge's lab showed that Mec1 and another kinase Tel1 phosphorylate and regulate Rad53 (Sanchez et al., 1996) and later that Tel1 phosphorylates yet another protein kinase Chk1. In collaboration with Errol Friedberg's lab, they established that Mec1 is a homolog of the mammalian ATM gene, whose mutant cells show many defects in response to DNA damage. In fact, Mec1 later proved to be the homolog of another PI3K-like kinase, ATR, while Tel1 is the closer homolog to the ATM-related ATR gene. As the work progressed, it became evident that the PI3K-like kinases Mec1 and Tel1 sat atop a protein kinase cascade whose immediate downstream targets include Rad53 and Chk1 (Matsuoka et al., 1998). In a flurry of other papers, the Elledge lab demonstrated the parallels between the Mec1/Tel1 regulation of Rad53 and Chk1 with the mammalian ATM/ATR control of Chk1 and Rad53's mammalian homolog, Chk2, respectively (Liu et al., 2000; Matsuoka et al., 1998;

Sanchez et al., 1999). The link between ATR and cell-cycle control became stronger when Elledge's lab, in collaboration with Helen Piwnica-Worms, demonstrated that Chk1 phosphorylates the key Cdk2 regulator, Cdc25 phosphatase (Sanchez et al., 1997), and later, with Elledge's long-time collaborator Wade Harper, showed that this phosphorylation triggers the degradation of Cdc25 and imposes cell-cycle arrest (Jin et al., 2003). Of course, while celebrating Stephen Elledge, it is important to remember that there were many important contributions by other labs as these ideas blossomed. To cite only a few, Yosef Shiloh's group first cloned and sequenced ATM; Michael Kastan demonstrated a key control by ATM of p53; Antony Carr and Karlene Cimprich characterized ATR; and Paul Russell and Paul Nurse outlined the phosphoregulation of the Cdk2 kinase.

The outlines of the full DDR are still being inked in. After moving to Harvard Medical School, Elledge's lab continued to enlarge the domain of DDR responses. A phosphoproteomic screen identified more than 700 *in vivo* substrates of ATM and ATR, implicating ATM/ATR control of processes as diverse as kinetochore

function, regulation of the cytoskeleton, control of ubiquitylation, and protein degradation by both the proteasome and autophagy. Most recently, his lab has carried out an analysis of proteins recruited to DNA-damaged chromatin and a quantitative "atlas" of ubiquitylation and acetylation associated with the DDR. In addition, Elledge's masterful reviews have guided the field. Stephen Elledge's insights into the eukaryotic DNA damage response have led to many awards, most recently the Rosenstiel Award and the Canada Gairdner Award in 2013.

Both bacteria and eukaryotes exhibit a complex DDR, but this is one of those fascinating instances in which there has been little evolutionary conservation of the mechanisms to achieve a common goal. Our present understanding of these processes owes much to Evelyn Witkin and Stephen Elledge, the two winners of this year's Albert Lasker Award in Basic Medical Research.

REFERENCES

- Allen, J.B., Zhou, Z., Siede, W., Friedberg, E.C., and Elledge, S.J. (1994). *Genes Dev.* 8, 2401–2415.
- Elledge, S.J., and Davis, R.W. (1987). *Mol. Cell. Biol.* 7, 2783–2793.
- Elledge, S.J., and Walker, G.C. (1983). *J. Mol. Biol.* 164, 175–192.
- Jin, J., Shirogane, T., Xu, L., Nalepa, G., Qin, J., Elledge, S.J., and Harper, J.W. (2003). *Genes Dev.* 17, 3062–3074.
- Liu, Q., Guntuku, S., Cui, X.S., Matsuoka, S., Cortez, D., Tamai, K., Luo, G., Carattini-Rivera, S., DeMayo, F., Bradley, A., et al. (2000). *Genes Dev.* 14, 1448–1459.
- Matsuoka, S., Huang, M., and Elledge, S.J. (1998). *Science* 282, 1893–1897.
- Sanchez, Y., Desany, B.A., Jones, W.J., Liu, Q., Wang, B., and Elledge, S.J. (1996). *Science* 271, 357–360.
- Sanchez, Y., Wong, C., Thoma, R.S., Richman, R., Wu, Z., Piwnica-Worms, H., and Elledge, S.J. (1997). *Science* 277, 1497–1501.
- Sanchez, Y., Bachant, J., Wang, H., Hu, F., Liu, D., Tetzlaff, M., and Elledge, S.J. (1999). *Science* 286, 1166–1171.
- Tobey, R.A. (1975). *Nature* 254, 245–247.
- Weinert, T.A., and Hartwell, L.H. (1988). *Science* 241, 317–322.
- Weinert, T.A., Kiser, G.L., and Hartwell, L.H. (1994). *Genes Dev.* 8, 652–665.
- Witkin, E.M. (1967). *Proc. Natl. Acad. Sci. USA* 57, 1275–1279.
- Witkin, E.M. (1976). *Bacteriol. Rev.* 40, 869–907.
- Witkin, E.M., and George, D.L. (1973). *Genetics* 73 (Suppl 73), 73, 91–10.
- Zhou, Z., and Elledge, S.J. (1993). *Cell* 75, 1119–1127.

Releasing the Brakes on Cancer Immunotherapy

Dan R. Littman^{1,2,*}

¹Molecular Pathogenesis Program, The Kimmel Center for Biology and Medicine of the Skirball Institute, New York University School of Medicine, New York, NY 10016, USA

²The Howard Hughes Medical Institute

*Correspondence: dan.littman@med.nyu.edu
<http://dx.doi.org/10.1016/j.cell.2015.08.038>

This year's Lasker~DeBakey Clinical Research Award goes to James Allison for discovering that antibody blockade of the T cell molecule CTLA-4 unleashes the body's immune response against malignant tumors. This has led to development of multiple "immune checkpoint therapies" that are prolonging and saving the lives of thousands of cancer patients.

Most advances in cancer therapy have come incrementally and have often been limited to individual types of malignancies. Early approaches that focused on surgical intervention were then supplemented or replaced by radiation therapy and, subsequently, chemotherapy during the last century. With the elucidation of signaling pathways that are dysregulated in cancers, "targeted therapies," most notably protein kinase inhibitors, were successfully adopted during the past two decades. However, despite these advances, durable responses to therapy for most metastatic or inoperable malignancies remain rare.

For this reason, it has long been the dream of physicians to be able to harness the body's own immune defenses to eliminate neoplastic cells, much as they eliminate invading pathogens. Even before the components making up the immune system were known, physicians noted patients whose solid tumors regressed and even disappeared after they suffered skin infections such as erysipelas, typically caused by Streptococci. In famous experiments in the late 19th century, William Coley injected bacterial extracts into multiple patients suffering from bone or soft tissue sarcomas and over several decades reported responses or complete remissions in a substantial fraction of them. Unfortunately, Coley never conducted controlled trials, and those who succeeded him were unable to garner the needed support to continue testing the "Coley toxins," particularly with the enthusiasm for radiotherapy and chemotherapy at that time.

Only a few immunologists continued to work on cancer therapies after the

mid-1950's. Even so, there were some notable successes, such as the anti-tumor response elicited by local injection of the BCG mycobacterium in bladder cancers and the sporadic successes of IL-2 therapy in melanoma and renal cancer patients. With the spectacular advances in our understanding of T cell immunity and antigen presentation over the past 30 years came the possibility that tumor vaccines could be engineered to elicit protective or therapeutic responses. Yet widespread skepticism remained within the oncology and immunology communities as to whether the body's immune responses could be mobilized to selectively kill tumor cells. Only a few brave souls dared to enter the field of tumor immunology, particularly during a period when most advances in immunology were being made at the level of molecular and cell mechanisms.

It is fair to say that the attitude of physicians and scientists alike toward cancer immunotherapy has changed dramatically during the past 5 years. The stunning successes in treating cancers with anti-CTLA-4 and anti-PD1 "immune checkpoint therapies" have spawned newfound optimism that targeting of additional immune pathways and optimization of drug regimens will be effective in numerous cancers and in larger proportions of patients. It is rare that such a sea change can be traced to any one individual, but the advent of checkpoint therapy would have been highly unlikely without the efforts of James Allison, the recipient of this year's Lasker~DeBakey Clinical Research Award.

Allison's critical insight built upon the recent elucidation of how T lymphocytes

become activated and target cells for killing. He recognized that a recently discovered cell surface receptor called CTLA-4, which turns on after T cell activation to help shut off the response and prevent excessive inflammation, could be targeted therapeutically to potentiate the cytolytic activity of tumor-infiltrating T cells. His studies confirmed that tumor-targeting T cells are not uncommon but are often disabled in tumors and hence need to be mobilized to become effective fighters against cancerous tissues.

Allison performed the seminal experiments showing that CTLA-4 blockade unleashes the body's immune response against multiple poorly immunogenic tumors and then embarked on a relentless campaign to find clinical partners who would translate the therapeutic approach to cancer patients. He had to overcome the profound skepticism among physicians that had developed over many decades, and it is a testament to his single-minded zeal that we are celebrating the dawn of a new age in cancer therapies. While this prize has been awarded for a discovery that has resulted in immense clinical benefit, it is based on work deeply rooted in basic science research, much by Allison himself, and is a showcase for the indispensability of animal research in advancing human health. Many individuals have contributed to our understanding of how T cells are activated, but Jim Allison saw the potential of targeting CTLA-4 to treat cancer, helped forge the needed collaboration with an industry partner, and advocated passionately and ultimately successfully for translation to patients. The clinical studies themselves required courage on

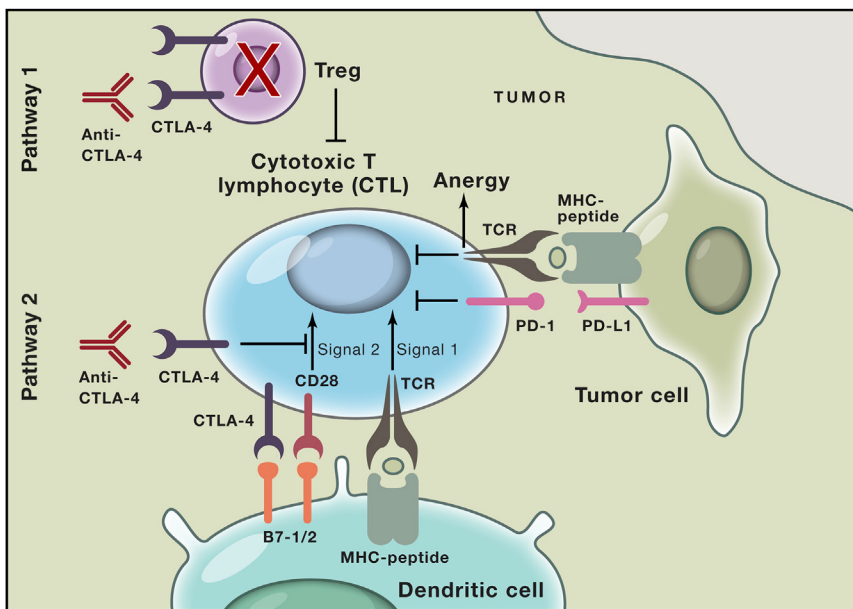


Figure 1. Activation of Anti-Tumor Cytotoxic T Cells by Blockade of CTLA-4

Proposed mechanisms for the activity of anti-CTLA-4 antibody in releasing inhibition of tumor cell killing by CD8⁺ T cells. (Pathway 1) Indirect mechanism through inhibition of regulatory T cell (Treg) accumulation in tumors, which requires binding of antibody to Fc receptor on innate immune cells and is mediated by antibody-dependent cellular cytotoxicity. (Pathway 2) Direct activity on cytotoxic T lymphocytes through inhibition of CTLA-4 interaction with B7-1 and B7-2 on antigen-presenting dendritic cells, thereby increasing CD28 co-stimulatory activity and/or reducing CTLA-4 inhibitory signaling. Note that tumor peptide antigen is cross-presented to CTL by dendritic cells, and direct interaction of T cells with tumor cells may result in anergy through the T cell receptor (TCR).

the part of companies and clinical oncologists, who ventured into uncharted territory by developing new criteria to evaluate responses to the therapy.

Laying the Groundwork

The discovery of CTLA-4 as a therapeutic target in cancer hinged on earlier work that identified T cell surface molecules and their cognate ligands that cooperate with the antigen receptor signaling machinery. The discovery of the T cell antigen receptor (TCR) in the early 1980's, an endeavor to which Allison contributed by identifying a clonally restricted heterodimer in a T cell lymphoma, launched efforts toward understanding how antigen recognition results in T cell activation. It was soon discovered that antibody stimulation of the TCR or its associated signaling machinery, the CD3 complex, was sufficient to activate immortalized cell lines in which much of the early biochemical work on signal transduction was carried out. However, proliferation of primary T cells required a second signal distinct from that transmitted through

TCR/CD3. In their influential "two-signal hypothesis" in 1970, Bretcher and Cohn had postulated that activation of antibody production by B lymphocytes requires signaling through both the membrane-bound antigen receptor and an accessory receptor and that cells receiving the antigenic signal alone would be rendered un-responsive or tolerant.

Ron Schwartz and his colleagues found that such a mechanism indeed operates in T lymphocyte activation. Pulsing antigen-presenting cells (APCs) with peptide antigen resulted in IL-2 production and proliferation of T cells bearing receptors specific for that peptide bound to major histocompatibility complex (MHC) molecules. By contrast, exposing antigen-specific T cells to MHC/antigen in lipid bilayers or in chemically fixed APCs induced T cell paralysis, such that they failed to proliferate upon subsequent exposure to unfixed cells (Jenkins and Schwartz, 1987). This phenomenon, known as anergy, could be overcome if non-antigen-pulsed APCs, even of mismatched MHC, were included in addition

to the chemically modified APCs. These experiments were the first to provide convincing evidence that full T cell activation requires engagement of both TCR and a second non-antigen-specific "co-stimulatory" pathway, activated by a ligand on a heterologous cell. These results attracted considerable attention, as they validated the "two-signal" hypothesis and also suggested a mechanism for tolerance to self-antigen when recognized by T cells in the absence of co-stimulation.

The Schwartz studies sparked concerted efforts to identify the co-stimulatory molecule. These culminated in studies by Marc Jenkins using human cells (Jenkins et al., 1991) and by Allison using mouse models (Harding et al., 1992), reporting that an immunoglobulin superfamily member, CD28, had the properties that would be expected of the co-stimulatory molecule. Specifically, crosslinked monoclonal antibodies against CD28 rescued IL-2 production and T cell proliferation when antigen was presented on fixed APCs, whereas monovalent antibodies (Fab) against CD28 rendered the T cells anergic after antigen presentation by unfixed APCs. Shortly thereafter, B7-1 (CD80) and B7-2 (CD86) were discovered to be CD28 ligands expressed by APCs; blocking antibodies against B7-1 inhibited T cell stimulation by antigen-pulsed APCs (Figure 1). Together, these results presented a pleasing explanation for co-stimulation. However, this was not the end of the story.

CTLA-4 Puts the Brakes on the T Cell Response

During the 1980's, new technologies for gene cloning, including subtractive hybridization and gene transfer, enabled identification of the genes encoding the TCR subunits and multiple other lymphocyte surface glycoproteins. Among these was CTLA-4, cloned by Pierre Golstein from a subtractive cDNA library produced from a CD8 lineage T cell clone. CTLA-4 is an immunoglobulin superfamily member whose locus is closely linked to that of CD28 and whose protein sequence bears substantial homology to CD28, particularly in its extracellular domain. Whereas CD28 is expressed constitutively at the surface of T cells, CTLA-4 expression

and translocation to the cell surface are induced only after activation of T cells.

These findings set in motion a number of efforts to manipulate CTLA-4 and thereby regulate T cell function. Peter Linsley, Jeffrey Ledbetter, and colleagues at Bristol-Myers Squibb (BMS) generated a CTLA-4-Ig fusion protein and showed that it bound to both B7-1 and B7-2 with substantially greater affinity than CD28 and was able to block T cell responses to allogeneic cells. Jeff Bluestone's group additionally showed that CTLA-4-Ig was effective when administered to mice, blocking allograft rejection, and he subsequently championed its utility for autoimmune disease therapy. These and other studies led BMS to develop CTLA-4-Ig as Otreos, which is used clinically to treat rheumatoid arthritis.

CTLA-4 was initially proposed to serve as a co-stimulatory molecule, much like CD28, since an anti-CTLA-4 antibody further enhanced the anti-CD28-mediated proliferative effect. However, Bluestone and colleagues, followed soon thereafter by Allison, found that, unlike anti-CD28 Fabs, anti-CTLA-4 monovalent Fab fragments actually enhanced T cell responses to allogeneic cells, while optimal crosslinking with full-length anti-CTLA-4 antibodies inhibited responses to anti-CD3/CD28. Both groups concluded that CTLA-4 expressed in activated T cells interacts with B7 ligands to compete for CD28 binding and also transduces a negative signal that inhibits IL-2 production and T cell proliferation, thus preventing over-activation of the immune system (Krummel and Allison, 1995; Walunas et al., 1994) (Figure 1). This conclusion was reinforced by the dramatic phenotype of *Ctla4* knockout mice. Unlike CD28-deficient mice, which have relatively subtle defects in their peripheral T cells, CTLA-4-deficient mice developed lethal lymphoproliferation within their first weeks of life, confirming that CTLA-4 has a key role in restraining T cell immune responses.

Targeting CTLA-4 in Cancer

Immunologists have long tried to develop therapeutic vaccines to target tumor-specific antigens, but this endeavor has been largely unsuccessful; even in mouse models, most tumors elicit only weak and ineffective immune responses. Although

tumor antigens can be presented to T cells by dendritic cells with co-stimulatory capacity (a phenomenon known as cross-priming), this process is inefficient and may even be thwarted by pre-emptive induction of anergy when infiltrating cytotoxic T cells interact with tumor cells directly and receive only the TCR signal (Figure 1). The discovery of the CD28-B7 co-stimulation axis raised the prospect that providing co-stimulatory capacity to tumors, which typically lack expression of B7-1 and B7-2, would enhance their immunogenicity and make them more susceptible to immune attack. Indeed, experiments by Lindsey and Allison showed that transfection of multiple types of tumor cells with B7-1 resulted in CD8 T cell-mediated elimination of the tumors after their implantation in mice. Remarkably, exposure of animals to B7-expressing tumors protected them from challenge with the same tumor lacking the co-stimulatory ligand. Enhanced co-stimulation could thus augment durable specific anti-tumor T cell responses.

These results, coupled with the new insights into the role of CTLA-4 as an inhibitory molecule, led Allison to hypothesize that blocking CTLA-4's interaction with B7-1 or B7-2 might release the "brake" on the CD8 T cell response, resulting in tumor killing. Consistent with this hypothesis, a pivotal paper by Leach, Krummel, and Allison, published in 1996, showed that anti-CTLA-4 administration resulted in dramatic reduction in the growth of some implanted tumors, even when these antibodies were administered after the tumors had expanded to a substantial size (Leach et al., 1996). Moreover, anti-CTLA-4-induced rejection of the tumor resulted in immunological memory, leading to long-lived immunity to secondary tumor challenge.

The precise mechanism by which anti-CTLA-4 antibody enhances killing of tumor cells and elicits a durable cytotoxic T cell response is not yet fully defined (Figure 1). Although the antibody interferes with the "braking" function of CTLA-4 in cytotoxic T cells, there is evidence that it also depletes intratumoral regulatory T cells, thus releasing inhibition of tumor-killing CD8⁺ T cells (Selby et al., 2013). However CTLA-4 blockade operates, Allison's 1996 paper and several follow-up studies made it clear that it

could be effective for killing many different types of tumors, alone or more often in combination with other therapies. For example, Allison and his colleagues demonstrated that CTLA-4 blockade, which they named "immune checkpoint therapy," was rendered more effective in animal models of a variety of tumors when combined with delivery of cytokines, with vaccination using irradiated tumor cells, or with chemotherapy or radiation therapy, which can result in stronger cross-priming of T cells by tumor antigens presented on tumor-resident myeloid cells. Together, these preclinical studies convinced Allison that antibody targeting of human CTLA-4 could be effective in the treatment of patients, and he set out to bring this approach into the clinic.

The Winding Path to the Success of Ipilimumab

The successful treatment of multiple mouse tumors with anti-CTLA-4 impressed immunologists, but the perceived failure of many earlier immune-based therapies created a very high bar for advancing immune checkpoint therapy to the clinic. Allison waged a campaign to convince funding agencies and pharmaceutical companies to move forward with clinical trials. Alan Korman, an immunologist at Nexstar Pharmaceuticals, a biotechnology company in Colorado, began working on an anti-human CTLA-4 antibody after hearing from Allison about the exciting results in mouse tumor models, and Nexstar licensed the CTLA-4 blockade technology from UC Berkeley in 1998. They then sub-licensed the technology to Medarex, a biotechnology company that had recently acquired GenPharm, a company led by Nils Lonberg specializing in producing human monoclonal antibodies in genetically manipulated mice.

Korman soon moved to Medarex, and he and Lonberg set to work developing fully human antibodies specific for human CTLA-4. One of these antibodies, MDX-010, was chosen for further development and was shown to be effective in macaques, potentiating antibody responses to immunogens and displaying no apparent autoimmune manifestations in that species (Keler et al., 2003). In 2000, Medarex began phase 1 studies with

Allison and clinical investigators at the University of California, San Francisco, evaluating patients with hormone-refractory prostate cancer and metastatic melanoma. Two out of 17 melanoma patients exhibited durable responses, and the therapy was well tolerated, which encouraged further studies at the National Cancer Institute, led by Steven Rosenberg, administering MDX-010 (later named Ipilimumab) to advanced melanoma patients, who also received a melanoma antigen vaccine. Immune cells infiltrated the tumors, and cancer regression was observed in 10%–20% of patients in small cohorts. However, there were severe inflammatory manifestations, including colitis, hepatitis, and hypophysitis, which required steroid therapy.

In 2004, Medarex initiated a collaboration with BMS to expand anti-CTLA-4 clinical trials, but the early optimism for the promise of the therapy was mixed with fear that the FDA would stop the trials due to the adverse side effects and its unclear efficacy. At that time, the response of solid tumors to any therapy was based on criteria developed during the era of chemotherapy, which focused on reduction in tumor size within a limited period of time post-administration. Accordingly, increases in tumor size or the appearance of new lesions during initial trials of anti-CTLA-4 were interpreted to indicate progressive disease and treatment failure. Nevertheless, some astute clinicians noted that many patients classified as having progressive disease went on to have favorable long-term outcomes. During 2004 and 2005, clinical workshops were convened to discuss how to classify treatment failures versus efficacy in patients receiving immune therapy. One of the conclusions of these discussions was that “responses to immune therapies may occur after conventional progressive disease” (Hoos et al., 2007). The Medarex/BMS clinical team and their academic collaborators, led by Jedd Wolchok, Axel Hoos, Steven O’Day, and Stephen Hodi, published an influential paper in which WHO criteria for assessment of clinical efficacy were reconfigured as immune-related response criteria (irRC) (Wolchok et al., 2009). By that time, however, Pfizer, which had also initiated an anti-CTLA-4 clinical program with their antibody, Tremelimumab, had already

dropped out after perceived failure of a phase 3 trial. To their credit, the Medarex-BMS team persevered in the face of this challenge, particularly after the FDA refused to approve Ipilimumab following a dose-ranging trial that had questionable efficacy and after BMS acquired Medarex in 2009.

The turning point came with a phase 3 trial comparing Ipilimumab to a melanoma peptide vaccine in metastatic melanoma patients who had the HLA A0201 allele (Hodi et al., 2010). Key to the success of the study was the decision to evaluate overall survival rather than response rate, and in the large study, Ipilimumab monotherapy resulted in more than 20% long-term survival. Significantly, among those who survived 24 months, there were very few relapses (Hodi et al., 2010), and we now know based on 10 years of follow-up data that about 20% of metastatic melanoma patients are cured with this single agent—a remarkable outcome considering that almost all of those patients would have died with conventional therapy within 1–2 years. The success of this trial led the FDA to finally approve Ipilimumab for the treatment of metastatic melanoma in 2011.

Targeting of PD-1 and PD-L1

At around the time when Ipilimumab was being considered for FDA approval, renewed excitement about immune checkpoint therapy came from clinical studies targeting a second immune inhibitory molecule, PD-1. PD-1 was discovered by Tasuku Honjo in 1992 in a screen for genes expressed during programmed cell death of a T cell hybridoma (Ishida et al., 1992). PD-1 disruption in mice resulted in inflammatory disease, including a lupus-like syndrome and cardiomyopathy. Although PD-1 is expressed more widely than CTLA-4, its major activity is thought to be in T cells, where it is upregulated during immune responses and transmits inhibitory signals upon interaction with its ligands, PD-L1 and PD-L2. Unlike CTLA-4, which functions mainly during primary immune responses, PD-1 signaling results in “exhaustion” of activated T cells, an anergic-like state that is thought to be due to a shift in the utilization of metabolic substrates (Pauken and Wherry, 2015). Antibody blockade of PD-1 was shown to enhance anti-tumor

and anti-viral responses in animal models, suggesting that this could be another immune checkpoint target for cancer.

The Medarex scientists began a program to develop anti-human PD-1 antibodies in the early 2000’s (Wang et al., 2014). This program followed closely on the heels of CTLA-4, and early clinical trials showed promising results in metastatic melanoma, non-small-cell lung cancer (NSCLC), and renal cell carcinoma, with much milder adverse effects than CTLA-4 blockade (Topalian et al., 2012). Schering Plough also acquired an anti-PD1 antibody developed by Organon, and this was introduced into the clinic as Pembrolizumab, after the company was acquired by Merck, and was approved by the FDA for treating advanced melanoma in 2014. The BMS drug, Nivolumab, was approved very shortly thereafter.

Future Prospects for Immune Checkpoint Therapy

Even though the initial CTLA-4 data were eventually accepted by immunologists and medical oncologists, this acceptance was grudging, because melanoma was thought to be an “immunologically responsive” tumor; indeed, melanomas occasionally regress by themselves. The finding that anti-PD-1 had activity against NSCLC was a dramatic refutation of this notion and sparked the enthusiasm seen today for immune therapy. During the past 2–3 years, outcomes of clinical trials with Ipilimumab and the PD-1 or PD-L1 inhibitors, alone or in combination, have dominated the news coming out of clinical oncology meetings. Combination therapy blocking both checkpoint pathways has been particularly effective, with response rates in advanced melanoma of over 80%.

The biopharmaceutical industry has embraced immunotherapy with unbridled enthusiasm, and acquisitions and licensing deals for new approaches are in the news almost every week. New checkpoint targets, including negative regulators of both adaptive and innate immune cells, are being actively investigated, as are combination therapies with cytokines, co-stimulatory molecules, antigen vaccines, and small-molecule modulators of signaling pathways and enzymes. The control of many cancers

will likely require combining immune therapies with targeted therapies, conventional chemotherapy, and radiation therapy to maximize efficacy and limit toxicity.

There are obviously many questions that remain to be answered, including why only certain tumors are effectively targeted by immune checkpoint therapy and why some patients but not others respond to the therapy. Answers to these and other questions will require sequencing of tumor genomes to elucidate the role of mutations and neo-antigens, combined with sophisticated monitoring of the immune cells and the microenvironments within different types of tumors.

James Allison appreciated early on the importance of immune monitoring in patients receiving immune checkpoint therapy. Indeed, in order to be closer to the patients, their invaluable tumor-derived biological specimens, and the clinicians providing treatment, he moved his laboratory from the University of California at Berkeley to the Memorial Sloan Kettering Cancer Center in 2004 and, subsequently, to the MD Anderson Cancer Center. This year's well-deserved Lasker Prize recognizes the impact of Allison's vision on

the many thousands of cancer patients already benefitting from the clinical development of immune checkpoint inhibitors. The change in attitude of clinical oncologists and immunologists toward the place of immune modulation in combatting cancer guarantees that there will be many exciting advances in immune-based therapies in the years ahead.

ACKNOWLEDGMENTS

I thank Ben Neel for his helpful suggestions with the manuscript.

REFERENCES

- Harding, F.A., McArthur, J.G., Gross, J.A., Raulet, D.H., and Allison, J.P. (1992). *Nature* **356**, 607–609.
- Hodi, F.S., O'Day, S.J., McDermott, D.F., Weber, R.W., Sosman, J.A., Haanen, J.B., Gonzalez, R., Robert, C., Schadendorf, D., Hassel, J.C., et al. (2010). *N. Engl. J. Med.* **363**, 711–723.
- Hoos, A., Parmiani, G., Hege, K., Sznol, M., Loibner, H., Eggemont, A., Urba, W., Blumenstein, B., Sacks, N., Keilholz, U., and Nichol, G.; Cancer Vaccine Clinical Trial Working Group (2007). *J. Immunother.* **30**, 1–15.
- Ishida, Y., Agata, Y., Shibahara, K., and Honjo, T. (1992). *EMBO J.* **11**, 3887–3895.
- Jenkins, M.K., and Schwartz, R.H. (1987). *J. Exp. Med.* **165**, 302–319.
- Jenkins, M.K., Taylor, P.S., Norton, S.D., and Urdahl, K.B. (1991). *J. Immunol.* **147**, 2461–2466.
- Keler, T., Halk, E., Vitale, L., O'Neill, T., Blanset, D., Lee, S., Srinivasan, M., Graziano, R.F., Davis, T., Lonberg, N., and Korman, A. (2003). *J. Immunol.* **171**, 6251–6259.
- Krummel, M.F., and Allison, J.P. (1995). *J. Exp. Med.* **182**, 459–465.
- Leach, D.R., Krummel, M.F., and Allison, J.P. (1996). *Science* **271**, 1734–1736.
- Pauken, K.E., and Wherry, E.J. (2015). *Trends Immunol.* **36**, 265–276.
- Selby, M.J., Engelhardt, J.J., Quigley, M., Henning, K.A., Chen, T., Srinivasan, M., and Korman, A.J. (2013). *Cancer Immunol. Res.* **1**, 32–42.
- Topalian, S.L., Hodi, F.S., Brahmer, J.R., Gettinger, S.N., Smith, D.C., McDermott, D.F., Powdery, J.D., Carvajal, R.D., Sosman, J.A., Atkins, M.B., et al. (2012). *N. Engl. J. Med.* **366**, 2443–2454.
- Walunas, T.L., Lenschow, D.J., Bakker, C.Y., Linsley, P.S., Freeman, G.J., Green, J.M., Thompson, C.B., and Bluestone, J.A. (1994). *Immunity* **1**, 405–413.
- Wang, C., Thudium, K.B., Han, M., Wang, X.T., Huang, H., Feingersh, D., Garcia, C., Wu, Y., Kuhne, M., Srinivasan, M., et al. (2014). *Cancer Immunol. Res.* **2**, 846–856.
- Wolchok, J.D., Hoos, A., O'Day, S., Weber, J.S., Hamid, O., Lebbe, C., Maio, M., Binder, M., Bohnsack, O., Nichol, G., et al. (2009). *Clin. Cancer Res.* **15**, 7412–7420.



Beginner's Luck

Evelyn Witkin

On June 5, 1944, I discovered a radiation-resistant mutant of *E. coli* in my first experiment at the Cold Spring Harbor laboratories. That's where the new field of bacterial genetics was germinating. I was a Columbia University graduate student, there to learn how to handle *E. coli* so I could do my doctoral research with bacteria.

I had planned to study the mechanism of induced mutation in *Drosophila*. Then, in 1943, Luria and Delbrück established that bacteria have genes like other organisms. I was so excited about the great potential value of bacteria for research in genetics that my advisor, Theodosius Dobzhansky, suggested that I switch from *Drosophila* to *E. coli* and that I spend the following summer at Cold Spring Harbor, tooling up for the change.

I found an impressive group of scientists gathered at Cold Spring Harbor that summer. There was talk everywhere—at meals, at the beach, in the labs—of the new work on bacteriophage and bacteria and of its potential impact in genetics. Looking back, I think I may have been sensing the early stirrings of the coming revolution in molecular biology.

On my first day there, Dr. Milislav Demerec, director of the laboratories, handed me a culture of *E. coli* and pointed me toward a germicidal ultraviolet (UV) lamp, saying "Go, induce mutations."

My mutant, which could tolerate 100 times more UV or X-rays than its parent strain, created something of a stir among the scientists at Cold Spring Harbor. Salvador Luria, Max Delbrück, and Barbara McClintock, among others I had been thrilled to meet that summer, seemed genuinely interested in it. Soon, with the approval of my advisor, it became the subject of my Ph.D. dissertation.

It turned out that the mutant was no more resistant to UV than most wild-type strains of *E. coli* such as K-12. What was remarkable was the extreme UV sensitivity of the parent strain, the wild-type strain B, which happened to be used at Cold Spring Harbor.

Why was the B strain so sensitive to radiation? The answer became evident when I exposed B bacteria to UV at a dose that killed 99% of them, spread them on agar, and examined them periodically under a microscope. By three hours of incubation, every cell had grown, without dividing, to form a snake-like filament 50–100 times normal length and then stopped growing and died. Filamentous growth was lethal.



At the same UV dose, the mutant cells grew and divided like the unirradiated controls, forming microcolonies of 50–100 cells in 3 hr. UV caused an irreversible arrest of cell division in the B strain, but not in the mutant, which I named strain B/r.

It was Barbara McClintock who had advised me, early and often, to study my bacteria under the microscope, the better to develop a kind of cross-species empathy, "a feeling for the organism," as an aid to intuition. It was good advice.

Evelyn Witkin in her laboratory at the Waksman Institute at Rutgers University in 1981. Looking on are her graduate students Owen McCall (left) and Howard Lieberman (right).

After receiving my Ph.D. from Columbia in 1947, I began my forty-five year investigation of the mechanism of UV mutagenesis. But I never lost my fascination with filamentous growth, and I managed to steal hours at the microscope, on and off over several years, to watch the UV-sensitive bacteria grow and die virtually before my eyes. I began to form an image in my mind, hazy at first, then quite vivid, of what could be happening inside those cells between UV irradiation and death by filamentation.

I noticed that, at a low UV dose that allowed about 50% survival, all the irradiated bacteria began to grow as filaments. About half of them grew into full-length filaments and never recovered cell division ability. The other half, however, started, between two and three hours, to pinch off cells of normal length at one end of the filament before it quite reached full length. By three hours, a small microcolony with a long tail appeared at that location.



After exposure to a very low sublethal UV dose, most of the bacteria showed no sign of filamentous growth by three hours, having formed microcolonies like those seen in the unirradiated controls. However, when examined earlier, between one and two hours, a few bacteria (perhaps 5%–10%) had a short tail attached to a growing microcolony, as if they had started to grow as incipient filaments, but had recovered cell division activity quite early.



The duration of cell division arrest in strain B after UV was clearly dose dependent. Gradually, I came to “see,” in the YouTube of my imagination, a scenario that could account for all of these observations. It went like this:

1. UV irradiation triggers synthesis of a cell division inhibitor.
2. The number of molecules of inhibitor synthesized is UV dose dependent, increasing with increasing dose.
3. When a cell grows to twice its length, a septation site, where cell division normally occurs, forms on the membrane at the midpoint of the elongated cell.
4. Cell division cannot occur if the septation site is bound by an inhibitor molecule.
5. Lethal filamentous growth appears when inhibitor molecules are abundant enough to bind all successive septation sites that form in three hours.
6. Cell division resumes at one end of the growing filament after all inhibitor molecules have been bound to septation sites and are effectively titrated out. Cell division resumes at the next septation site to be formed.

This was the 1940s, before Watson and Crick and before Monod and Jacob. Fast forward to 1967, when I noticed a number of striking similarities between λ prophage induction and filamentous growth in UV-irradiated *E. coli* B. Luria had just shown that λ repressor is destroyed in the course of prophage induction. I proposed that a bacterial gene encoding a cell division inhibitor, and possibly other bacterial genes, might be controlled by repressors similar enough to λ repressor to respond to the same induction signal.

I believe that linking prophage induction and filamentous growth as UV co-inducible was a step toward my recognition of *E. coli*'s SOS response, with Miroslav Radman, about five years later. The SOS response now comprises over forty DNA damage-inducible genes, all sharing a common

“It was Barbara McClintock who had advised me, early and often, to study my bacteria under the microscope, the better to develop a kind of cross-species empathy, ‘a feeling for the organism,’ as an aid to intuition. It was good advice.”



Evelyn Witkin and scientist Arnold Sparrow in Cold Spring Harbor in 1947.

repressor. Collectively, they promote the repair of genetic damage and the survival and reproduction of the damaged cell and of the population.

One of the SOS genes is *sfiA(sulA)*, which encodes a cell division inhibitor. My beginner's luck, the mutation in strain B/r, maps in *sfiA* and inactivates the inhibitor, increasing resistance to UV by preventing filamentous growth.

I have little doubt that my readiness to propose the co-inducibility of filamentous growth and λ prophage was subliminally informed by the hours I spent at the microscope twenty-some years earlier, mesmerized by watching the transformation of bacteria into snakes.



Accidents and Damage Control

Stephen J. Elledge

My work uncovering the eukaryotic DNA damage response pathway is a tale of serendipity and four amino acids. After graduate school at MIT, I joined Ron Davis's lab as a post-doc initially to work on plants but became interested in developing gene-targeting methods for mammals. I had reasoned, naively, that the protein responsible for homologous recombination in mammals would be related to the master regulator of recombination in bacteria, recA. RecA protein had the ability to initiate recombination in vitro on its own using ssDNA and ATP. Therefore, I decided to use the mammalian recA protein to coat ssDNA and inject the complex into cells where it would find its homologous sequence and initiate recombination. Voila, mission accomplished, right? The problem was that there was no mammalian recA gene or protein known. In fact, no yeast recA gene had even been identified yet, and it was quite possible that the recombinase in mammals was unrelated to recA.

This was more than a minor setback. I had to figure out a way around it and decided to see if yeast had a related protein to bacterial recA using antibodies to recA. Sure enough, budding yeast had a single band of molecular weight 44 kDa, just a little bigger than the bacterial protein. My strategy to isolate the gene was to use lambda gt11 cloning, a method to identify genes encoding proteins using antibody detection of proteins expressed in plaques. Using the antibodies to bacterial recA, I isolated the gene encoding the 44 kDa protein and showed that it encoded the protein I had observed. There was just the small matter of sequencing it to establish the degree of identity. This had to be done by hand in 1985. I finally got the sequence, and a friend of mine, Andy Buchman, offered to analyze the sequence for me, as he had expertise in computer analysis of sequences and access to what must have been a minuscule database of previously sequenced genes.

“I have good news and bad news...I identified your gene.’ And the bad news? ‘It is not recA.”

I went away for the weekend and came back and asked Andy if he had found anything. He said, with a bemused look on his face, “I have good news and bad news.” I said, “Give me the good news first.” He replied, “I identified your gene.” And the bad news? “It is not recA.” The gene I had cloned was the small subunit of ribonucleotide reductase, which I named *RNR2*, a gene involved in nucleotide metabolism.

I compared the sequences, and the only thing they had in common was that the last four amino acids were identical. I showed by deletion analysis that they indeed comprised the cross-reacting epitope. At this point, I was devastated. I definitely was going nowhere on this recombination idea, and nucleotide metabolism was last thing I wanted to work on. I thought, “This could only have been worse if I cloned a histone!” So I set the project aside and worked on some of my other projects.

However, things took an unexpected turn when David Stillman came through Stanford on the job circuit. I had a chance to talk with him and told him my story, and he said that ribonucleotide reductase was interesting because it was a tightly cell-cycle-regulated activity. That caught my attention. I started thinking about ribonucleotide reductase again and remembered an experiment I performed when I still thought the gene might be *recA*. I had done a Northern blot in the presence of a DNA damaging agent, 4-nitroquinoline-1-oxide, and the *RNR2* mRNA went up almost 20-fold like *recA*. This was an unusually strong effect. I began to examine what agents induced this gene and found that those that blocked DNA replication, like hydroxyurea and MMS, had by far the largest effects.

This got me thinking about how much cells must care about the capacity to synthesize DNA. I thought there must be a way to sense what is happening at stalled or damaged replication forks, perhaps through some signal that might be transduced to the promoter of *RNR2*, which could be a stepping stone into this pathway. And if this signal transduction pathway did indeed exist, it was

Steve Elledge in his lab at the Baylor College of Medicine, circa 1996.

likely to control much more than just *RNR2* gene expression. I published this work in 1987, noting that “it would be of great interest to investigate the signal responsible for the DNA damage inducibility of *RNR2*” and anticipated “that a detailed analysis of the *RNR2* promoter would allow us to identify the sequences involved in its complex regulation and through these, the genes responsible for that regulation.”

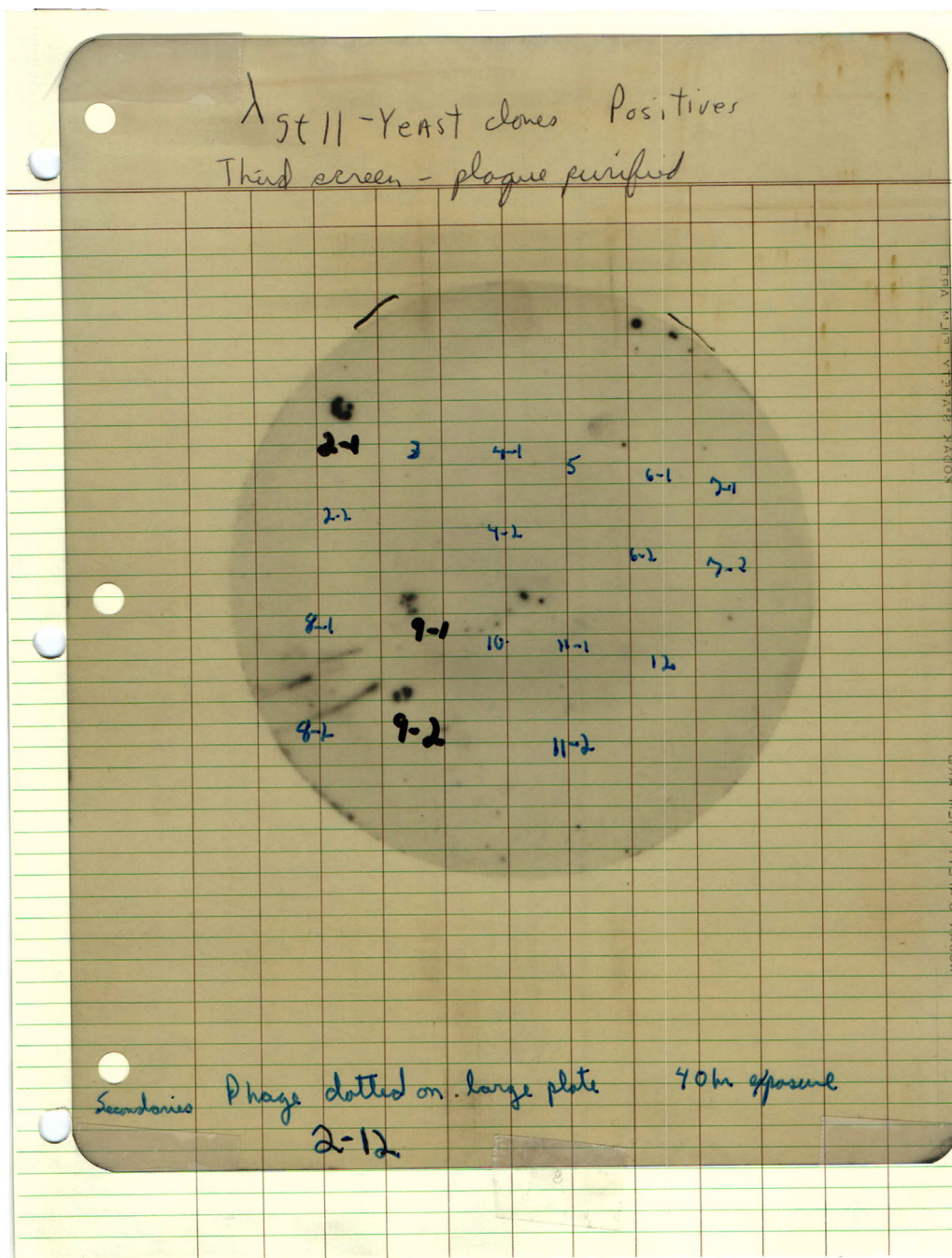
As it turned out, *RNR2* was in fact my entry point to the signal transduction pathway I had envisioned. Upon dissecting the *RNR2* promoter, I found that it was under active repression and identified enhancer elements that could confer inducibility on a heterologous promoter. In late 1987, I also isolated the genes that encoded the large subunit of ribonucleotide reductase using the human gene as a probe and found two genes, *RNR1*, which showed strong cell cycle regulated transcription, and *RNR3*, which was induced over 100-fold with replication stress!

A relationship between radiation-sensitive *RAD* mutants and defects in cell-cycle delays in response to DNA damage had been noted previously in 1976 in *S. pombe* by Nasim and colleagues and in mammalian cells by Painter and Young in 1980—who found that cells from patients with ataxia telangiectasia fail to slow S phase in the presence of DNA damage. In 1988, Weinert and Hartwell described another such mutant, this time in a budding yeast gene, *RAD9*, that also failed to arrest the cell cycle in response to DNA damage, and this was referred to as a cell-cycle checkpoint. With all this in mind, I began to wonder about connections between my pathway and *RAD* genes. However, I found that *RNR* transcription was still induced in *rad9* mutants when replication was stalled, so there was much more to be learned on these connections.

I started my own lab in the Biochemistry Department at the Baylor College of Medicine in 1989. There, I found a vibrant environment and began what would become a life-long collaboration with my fellow faculty member Wade Harper, studying the mammalian cell cycle and discovering Cdk inhibitors and the SCF ubiquitin ligases. My big early break in the *RNR* regulation project came when my first graduate student, Zheng Zhou, joined my lab. Zheng was a force of nature, and she set up a genetic selection for constitutive and uninducible *RNR* transcription (*CRT*) mutants. We found *RNR3* to be constitutively expressed in mutants in DNA polymerase alpha, providing a direct link to the replication fork, mutants in other components of nucleotide metabolism, and mutants in a transcriptional repressor complex whose DNA binding component encoded by *CRT1/RFX1* was later shown by a post-doctoral fellow Mingxia Huang to undergo inhibition in response to DNA damage, thereby establishing the mechanism of transcriptional induction. However, the DNA damage uninducible mutants (*DUN*) were the most revealing. One was found to be DNA polymerase II by my student Anthony Navas, providing yet another link to the fork. Another was found to be a protein kinase encoded by the DNA damage uninducible 1 gene, *DUN1*. *DUN1* was the most exciting because protein kinases are agents of signal transduction. However, it might have merely been constitutively required for some aspect of the pathway and might not actually transduce the signal. Fortunately, Zheng did the hard experiment and looked at the activity of Dun1 in vivo using metabolic labeling with ³²P-labeled organic phosphate and showed that Dun1 became highly auto-phosphorylated in response to DNA damage. This established that the presence of DNA damage was indeed transduced by signal transduction and was the first demonstration of what is now known as the DNA damage response pathway, the DDR.

Those early years in my lab witnessed a flurry of activity, with another student, Jim Allen, identifying the S phase arrest defective (*SAD*) genes that became known as *RAD53* and *MEC1*, alleles of which were also identified by Weinert and colleagues. Jim and Zheng showed that Rad53 was a protein kinase acting upstream of Dun1. This was the first step in identifying what we subsequently discovered to be a protein kinase cascade that activated Rad53 and Dun1 in response to agents that blocked replication. The work that followed in my lab identified further components of the pathway, with another student, Brian Desany, showing that the essential function of the *MEC1/RAD53* pathway was to regulate DNA synthesis, as even transient inhibition of DNA synthesis in hypomorphic mutants killed cells by preventing their ability to complete DNA replication. Meme Alcasabas in my lab then discovered *MRC1*, with Alex Osborn then showing that it traveled with the fork and was phosphorylated by Mec1 and that this phosphorylation was required for

“There was indeed a signal at the replication fork, just as I had imagined several years earlier.”



Plaque purification and screening of lambda gt11 clones probed with affinity purified anti-RecA antibodies. Lambda 2-1, 9-1, and 9-2 encode RNR2.

Rad53 activation. There was indeed a signal at the replication fork, just as I had imagined several years earlier.

By 1997, the field had grown tremendously, and many groups had made important contributions throughout, including the fission yeast geneticists Tony Carr, Paul Nurse, Nancy Walworth, and David Beach. They were approaching similar questions from the cell-cycle regulation perspective, which was much easier to study in *S. pombe* than in budding yeast due to its clear mitotic relationship to Cdc2 activation.

This field exploded again when we and others transitioned into mammals and found the overall outline of the pathway to be highly conserved but much more elaborate in humans. Elucidation of the human pathway allowed my post-docs Yolanda Sanchez, Shuhei Matsuoka, Dave Cortez, and Lee Zou to unravel the mechanism of how DNA damage and replication stress are sensed and transduced and revealed the true significance of this complex signal transduction pathway to cellular physiology. Important contributions were also made by the Abraham, Bartek, Carr, Chen, Cimprich, deLange, Dunphy, Gautier, Jackson, Kastan, Livingston, Lucas, Piwnica-Worms, Shiloh, and Yaffe labs and several others. These contributed to important connections being forged throughout the world to human physiology and disease, especially cancer, and drugs inhibiting the DDR kinase cascade are now being actively pursued as cancer therapies.

RecA has always played two roles in bacteria, recombination and control of the SOS DNA damage response. The ironic part of this long, strange trip is that it started out when I initially aimed to exploit the recombinational role of recA and instead discovered, quite accidentally, that eukaryotes have a completely different but analogous pathway to the SOS response, which is the other hat worn by recA.

Cell



Checkpoints

James P. Allison

I cup the harmonica and start playing with the rest of the band—The Checkpoints. The crowd gets on their feet, cheering and dancing to “King Bee.” It was the 2015 annual American Society of Clinical Oncology (ASCO) meeting. The Society for Immunotherapy of Cancer had organized for us to play one night at the House of Blues in Chicago. The place was packed. Immunologists, oncologists, radiologists, pathologists, journalists, and patients attended our gig. They were celebrating. Not just the skills of the band members—all cancer researchers—but the field of cancer immunotherapy and the amazing clinical successes that were just announced at that ASCO meeting.

The field of cancer immunotherapy certainly has had its ups and downs. The promise of being able to use the immune system to treat cancer has been around for many decades. Before being able to fulfill the promise, though, we had to understand the immune system.

“All of a sudden, I was totally hooked on understanding T cell activation.”

I was not trained as an immunologist. I was actually a biochemist. In my early years, while still a young assistant professor at the Smithville branch of MD Anderson Cancer Center, my friend and colleague, Ellen Ritchie, convinced me that I should pursue the holy grail of immunology, which, at the time, was identification of the T cell receptor. T cells are the soldiers of the immune system, but no one knew how they were turned on. Shortly after that, I attended a seminar by Irv Weissman, and it gave me an idea about how I may conduct an experiment to look for the T cell receptor. In 1982, I published a paper reporting what seemed to be the T cell antigen receptor protein. All of a sudden, I was totally hooked on understanding T cell activation.

By the mid-80s, I had moved to the University of California at Berkeley. Due to the work of Ron Schwartz, Marc Jenkins, and their colleagues at the NIAID, it was becoming clear that engagement of the T cell antigen receptor was by itself insufficient to generate T cell responses, and additional costimulatory signals were also required. Fiona Harding, in my lab, tackled this issue in collaboration with David Raulet and showed in 1992 that costimulatory signals mediated by the CD28 molecule were necessary and sufficient to allow full activation of virgin T cells.

However, there was yet another piece of the puzzle. CTLA-4, a gene induced in all T cells upon full activation, had been previously identified by Pierre Golstein and was highly homologous to CD28. Peter Linsley and his colleagues had found that the ligand for CD28 on antigen-presenting cells was the B7 molecule and went on to show that B7 was also a ligand for CTLA-4. The mystery now was what role this additional B7 counter-receptor was playing in T cell activation. Linsley’s data suggested that CTLA-4 was another costimulatory molecule, and its role was to sustain T cell activation and prolong T cell responses. On the flip side, Jeff Bluestone with his colleagues and my lab argued the opposite—that CTLA-4 was an inhibitory molecule that served to limit T cell responses. Max Krummel, at that time a grad student in my lab, published the critical in vitro studies showing that CTLA-4 opposed CD28 costimulation. The inhibitory nature of CTLA-4 was confirmed later when Tak Mak’s group, Arlene Sharpe’s lab, and the late Cynthia Chambers,

James P. Allison at his laboratory in Berkeley, circa 1995.



Sharon Belvin, now almost 10 years after receiving anti-CTLA-4 therapy, with her two children.

in our lab, showed that the genetic ablation of CTLA-4 in mice resulted in unrestrained proliferation of T cells and death.

It was about 10 years between our publications on the T cell receptor and CTLA-4. During that time, I thought of myself as a basic scientist trying to uncover the secrets of T cell regulation. I did not think of myself as a cancer researcher or translational scientist. However, I had always been interested in cancer, in part because I had lost my mother and two uncles, and later my brother, to cancer and had seen firsthand the ravages of radiation and chemotherapy. So I did what I think any basic scientist should do: occasionally stop and think about the implications of your fundamental findings for application to human disease. Meanwhile, I also started putting the pieces of the “T cell activation” puzzle together.

“So I did what I think any basic scientist should do: occasionally stop and think about the implications of your fundamental findings for application to human disease.”

It occurred to me that if T cells express CTLA-4 as an “off” signal every time they receive the “on” signals generated by T cell receptor and CD28, then the T cells would be limited in their ability to mediate anti-tumor responses. If only we could block the negative regulation by CTLA-4, then maybe T cell responses would be sustained long enough to eliminate cancer. Some of the implications of this strategy were very compelling. The first was that the therapy did not target the tumor cell but rather the patient’s immune system. Thus, CTLA-4 could be effective against any tumor that bore antigenic targets for T cells and might be a universal treatment of cancer. The second was a practical point: we would not need to know the exact antigenic targets for each individual tumor in order to try to obtain therapeutic vaccination. We would be unleashing, not harnessing, the immune system to attack cancer.

As an initial test of the hypothesis, we designed an experiment to treat tumor-bearing mice with an antibody that blocked CTLA-4. When Dana Leach, a postdoc in the lab who carried out the first experiments, showed me the initial data, I was shocked and surprised. The mice that were treated with anti-CTLA-4 rejected the tumors and lived normally while the untreated mice died. It was too

good to be true. I didn't believe the initial results. We repeated the experiment blinded during the Christmas holidays in 1994. Dana injected the mice with tumors and treated with antibodies and I did the tumor measurements not knowing which mice had received control or anti-CTLA-4 antibodies. For about 2 weeks, all of the tumors grew in all of the mice. I was disappointed but continued to record the results. Then, as if by magic, one group of mice started to show signs of tumor regression and then complete tumor rejection. We then treated many different tumor types. Anti-CTLA-4, as either monotherapy or in combination with agents such as vaccines or chemotherapy, led to improved anti-tumor responses and durable regression of a broad array of experimental tumors. While my group continued mouse studies and began to dissect the mechanisms of tumor rejection, my mind was elsewhere: I wanted desperately for CTLA-4 to be tested in clinical trials.

The road to convincing a company to develop a humanized anti-CTLA-4 antibody and test it in the clinic was filled with many bumps and colorful language along the way. Eventually, my friend Alan Korman at Medarex worked with me to develop a human version of anti-CTLA-4. Medarex made a fully human antibody and conducted the first clinical trial, and the rest, as they say, is history. Anti-CTLA-4 therapy led to durable tumor regression and improved overall survival in a subgroup of patients with late-stage melanoma. I still remember when it all dawned on me. I was at Memorial-Sloan Kettering Cancer Center in 2007 and Jedd Wolchok asked me to meet him in his clinic. He introduced me to Sharon Belvin, a lovely woman who had, in her mid-twenties, been diagnosed with metastatic, stage 4, melanoma. She failed other therapies and was given a few months to live before being enrolled in a clinical trial with anti-CTLA-4. I met her, her husband, and her parents on her one-year anniversary of having completed the treatment. Her disease had responded to the treatment and although she had not received any further treatment other than the 12-week course of anti-CTLA-4, she was considered in remission and possibly cured. She cried and I cried that day. Over the years, we have kept in touch, and she sent me photos of both of her two children.

I have had the pleasure of meeting many patients like Sharon over the years. As I am not a physician, these encounters have provided a real-life reminder of the potential impact of basic science in saving lives.

The antibody to CTLA-4, ipilimumab, has been approved by the Food and Drug Administration for the treatment of metastatic melanoma and is now a standard care for treatment of that disease. A recent retrospective study of about 5,000 patients treated with ipilimumab reported that about 22% of patients survived 10 years after a single round of treatment. While CTLA-4 was the first immune checkpoint to be identified, several others, each with their own mechanisms of action, are now known and at various stages of clinical development. The furthest along is PD-1, and antibodies targeting PD-1 have been approved by the FDA for the treatment of melanoma and lung cancer. The combination of antibodies to CTLA-4 and PD-1 elicits responses in about 50% of melanoma patients and has impact on several other types of cancer.

The new field of "Immune Checkpoint Therapy" has proudly taken its place as a pillar of cancer therapy. My goal now is to understand why some patients respond to treatment while others do not. To this end, I have partnered with a physician scientist, Padmanee Sharma, who conducts mechanism-based clinical trials to study immune responses in patients who receive the immune checkpoint agents. These studies have yielded promising new data, and I am truly optimistic that we can indeed apply immune checkpoint therapy, as monotherapy or in combination with other cancer treatments, to provide cures for patients with any type of cancer. The field of cancer immunotherapy looks brighter than ever, and I am honored to have played a part in it.

Nutrient Competition: A New Axis of Tumor Immunosuppression

Madhusudhanan Sukumar,¹ Rahul Roychoudhuri,¹ and Nicholas P. Restifo^{1,*}

¹Center for Cancer Research, National Cancer Institute (NCI), National Institutes of Health Bethesda, MD 20892, USA

*Correspondence: restifo@nih.gov

<http://dx.doi.org/10.1016/j.cell.2015.08.064>

It is thought that cancer cells engage in Warburg metabolism to meet intrinsic biosynthetic requirements of cell growth and proliferation. Papers by Chang et al. and Ho et al. show that Warburg metabolism enables tumor cells to restrict glucose availability to T cells, suppressing anti-tumor immunity.

In the presence of oxygen, most differentiated cells utilize mitochondrial oxidative phosphorylation to generate energy in the form of adenosine triphosphate (ATP) that can be used to sustain cellular processes. In the absence of oxygen, such cells revert to much less efficient glycolysis as a means of ATP production. Cancer cells often utilize glycolysis despite the presence of oxygen (aerobic glycolysis or the "Warburg effect") (Warburg, 1956). While less efficient at producing energy, it is thought that this form of metabolism supports the macromolecular requirements of cell growth and proliferation. Thus, the field has primarily focused on Warburg metabolism as an adaptation that confers intrinsic growth advantages to tumor cells themselves. However, cancer cells may consume nutrients, particularly glucose, in excess of their requirement to sustain proliferation and cell growth (Vander Heiden et al., 2009). This raises the possibility that nutrient consumption serves additional roles to meeting the intrinsic bioenergetic and biosynthetic requirements of cancer cells. In this issue of *Cell*, Ho et al. (2015) and Chang et al. (2015) show that Warburg metabolism provides tumor cells with a cell-extrinsic advantage, promoting depletion of extracellular glucose which renders tumor-infiltrating T cells dysfunctional.

In both studies, glycolysis within tumor cells is shown to cause depletion of extracellular glucose which restricts glucose availability to T cells. Decreased glucose availability causes suppression of glycolytic metabolism within T cells, and this is associated with decreased effector function (Figure 1,

left). Ho et al. identify a mechanism by which glucose metabolism directly controls effector function. The authors find that T cell receptor (TCR)-induced Ca^{2+} flux is markedly dependent upon extracellular glucose and glucose metabolism by T cells. Sarco/endoplasmic reticulum (ER) Ca^{2+} -ATPase (SERCA) is an ATP-dependent Ca^{2+} channel that pumps Ca^{2+} from the cytoplasm into the ER. Extracellular glucose is shown to promote accumulation of the glycolytic metabolite, phosphoenolpyruvate (PEP), which inhibits SERCA-dependent evacuation of Ca^{2+} from the cytosol into the ER, thereby increasing TCR-induced Ca^{2+} flux and effector function (Figure 1, right). This observation adds to a growing list of examples whereby metabolic processes directly control the outcome of T cell activation (Chang et al., 2013; MacLver et al., 2013).

That tumor cell glycolysis directly suppresses T cells raises the possibility that tumor metabolism can be therapeutically manipulated to improve immune function within tumors. Checkpoint blockade immunotherapy with anti-PD-L1 antibodies is thought to work by limiting inhibitory PD-1 signaling received by tumor-specific T cells (Keir et al., 2008). Chang et al. made the surprising observation that PD-1 ligand (PD-L1) expressed by tumor cells provides a constitutive "reverse signal" that promotes tumor cell glycolysis through activation of the AKT/mTOR pathway (Figure 1, left). Treatment of tumor cells with therapeutic anti-PD-L1 antibodies attenuates glycolysis by triggering PD-L1 endocytosis (Figure 1, right). Remarkably, two other check-

point-blockade antibodies, anti-PD-1 and anti-CTLA-4, are also shown to cause changes in extracellular glucose concentrations within tumors, though mechanisms for these observations are unclear. That PD-L1 expression causes constitutive activation of the Akt/mTOR pathway has important implications for understanding tumor cell biology and tumor-host interactions, and it will be important to characterize precise molecular mechanisms by which PD-L1 constitutively activates the Akt/mTOR pathway. Given that immune checkpoint blockade elicits durable clinical responses and improves survival in patients with certain metastatic cancers (Larkin et al., 2015; Topalian et al., 2012), it is relevant to measure the effect of checkpoint blockade antibodies on intratumoral nutrient availability and T cell metabolism in patients and correlate this with clinical outcomes. Further, it will be important to dissect the effects of checkpoint blockade on inhibitory T cell signaling versus tumor cell metabolism.

Instead of manipulating tumor cell metabolism, Ho et al. suggest an alternate approach to improve T cell function by mimicking nutrient availability within transferred T cells during adoptive cell therapy (ACT). Phosphoenolpyruvate Carboxykinase (PCK1) converts oxaloacetate into PEP. By overexpressing Pck1 in transferred T cells, Ho et al. are able to artificially increase PEP levels, restoring TCR-induced Ca^{2+} flux and anti-tumor T cell function despite the presence of low environmental glucose levels within tumors. Intriguingly, blocking glucose

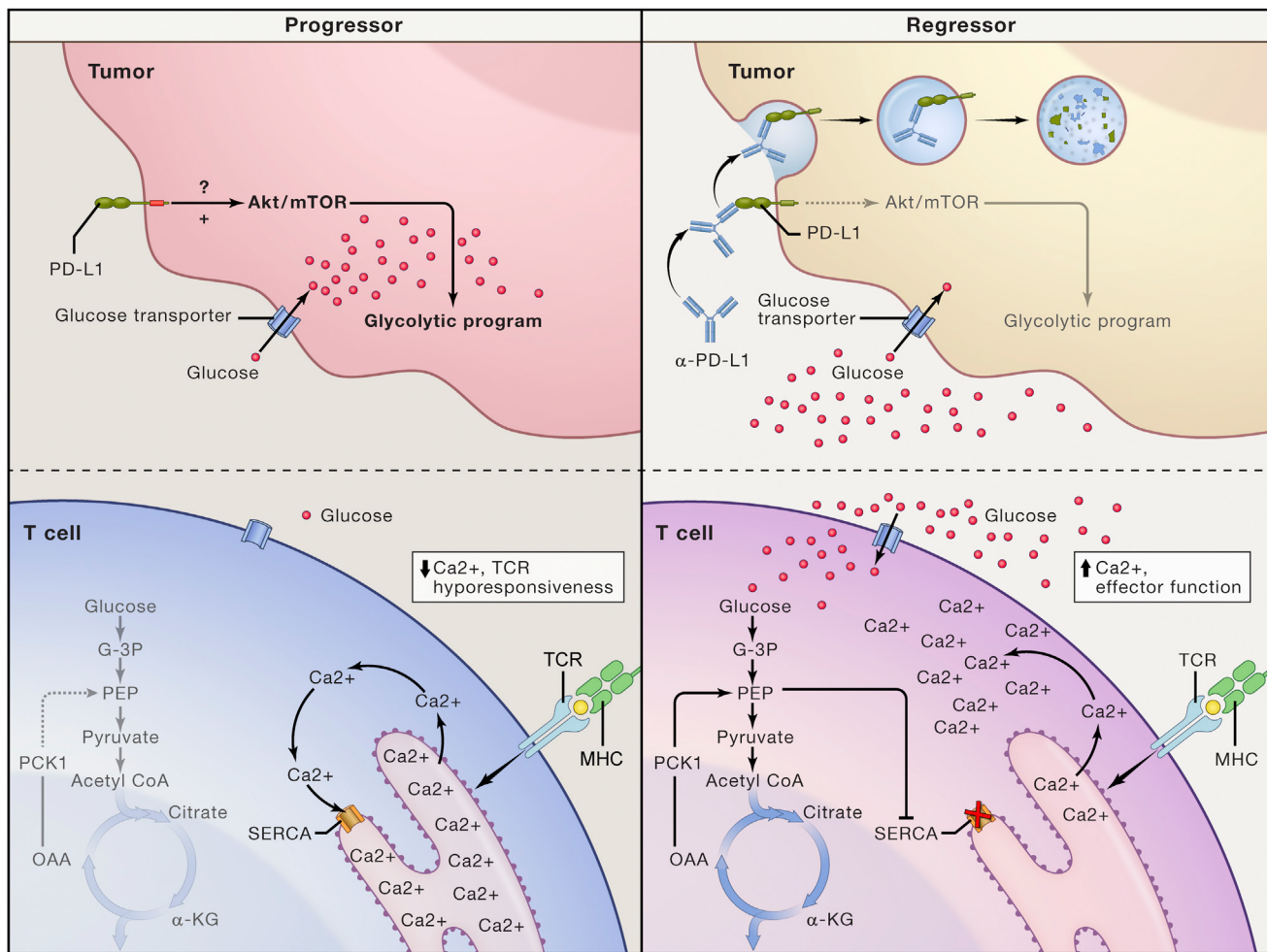


Figure 1. Nutrient Competition between Tumor Cells and T Cells Controls Immune Function within Tumors

Schematic depicting glucose metabolism and cellular signaling in highly glycolytic progressor tumors and regressor tumors undergoing therapy. In the progressor tumor (left), constitutive activation of the Akt/mTOR pathway by PD-L1 expressed on tumor cells causes high levels of tumor cell glycolysis and absorption of extracellular glucose. Decreased extracellular glucose levels causes impaired glycolysis in T cells, wherein depletion of the glycolytic metabolite PEP causes unrestrained SERCA activity, sequestration of cytoplasmic Ca^{2+} into the ER and impairment of TCR-induced Ca^{2+} flux and effector function. In the regressor tumor (right), therapeutic anti-PD-L1 antibodies bind to PD-L1 causing its endocytosis and inactivation. Loss of constitutive PD-L1 signaling leads to decreased activation of the Akt-mTOR pathway decreased tumor cell glycolysis and increased extracellular glucose concentrations. Increased extracellular glucose drives T cell glycolysis, replenishing PEP levels, inhibiting SERCA-dependent sequestration of cytoplasmic Ca^{2+} and promoting TCR-induced Ca^{2+} flux and anti-tumor effector functions. Alternatively, constitutive overexpression of PCK1 in adoptively transferred T cells increases availability of PEP leading to inhibition of SERCA, increased anti-tumor effector function and tumor regression.

metabolism during expansion of T cells for adoptive immunotherapy withholds effector differentiation and promotes differentiation of memory cells which mediate superior tumor clearance (Sukumar et al., 2013). These findings provide striking examples of how modulating T cell metabolism can improve the outcome of adoptive cell therapy for cancer.

Taken together, the two new studies provide compelling evidence that cancer cells subvert the metabolic charac-

teristics of the tumor microenvironment to shape immune responses within tumors. The results also provide an explanation of how nutrient consumption in excess of the bioenergetic and biosynthetic requirements may benefit cancer cells. As Warburg's original observation is revisited in ever new reincarnations, it remains to be seen whether insights from the field of immunometabolism will change the game at this new front in our war against cancer.

REFERENCES

- Chang, C.H., Curtis, J.D., Maggi, L.B., Jr., Faubert, B., Villarino, A.V., O'Sullivan, D., Huang, S.C., van der Windt, G.J., Blagih, J., Qiu, J., et al. (2013). *Cell* 153, 1239–1251.
- Chang, C.-H., Qiu, J., O'Sullivan, D., Buck, M.D., Noguchi, T., Curtis, J.D., Chen, Q., Gindin, M., Guabin, M.W., and van der Windt, G.J.W. (2015). *Cell* 162, this issue, 1229–1241.
- Ho, P.-C., Bihuniak, J.D., Macintyre, A.N., Staron, M., Liu, X., Amezquita, R., Tsui, Y.-C., Cui, G., Micevic, G., Perales, J.C., et al. (2015). *Cell* 162, this issue, 1217–1228.

Keir, M.E., Butte, M.J., Freeman, G.J., and Sharpe, A.H. (2008). *Annu. Rev. Immunol.* 26, 677–704.

Larkin, J., Chiarion-Sileni, V., Gonzalez, R., Grob, J.J., Cowey, C.L., Lao, C.D., Schadendorf, D., Dummer, R., Smylie, M., Rutkowski, P., et al. (2015). *N. Engl. J. Med.* 373, 23–34.

MacLver, N.J., Michalek, R.D., and Rathmell, J.C. (2013). *Annu. Rev. Immunol.* 31, 259–283.

Sukumar, M., Liu, J., Ji, Y., Subramanian, M., Crompton, J.G., Yu, Z., Roychoudhuri, R., Palmer, D.C., Muranski, P., Karoly, E.D., et al. (2013). *J. Clin. Invest.* 123, 4479–4488.

Topalian, S.L., Hodi, F.S., Brahmer, J.R., Gettlinger, S.N., Smith, D.C., McDermott, D.F., Powd-

erly, J.D., Carvajal, R.D., Sosman, J.A., Atkins, M.B., et al. (2012). *N. Engl. J. Med.* 366, 2443–2454.

Vander Heiden, M.G., Cantley, L.C., and Thompson, C.B. (2009). *Science* 324, 1029–1033.

Warburg, O. (1956). *Science* 123, 309–314.

Single-Cell Analysis: The Differences That Kill

Savaş Tay^{1,2,*}

¹Department of Biosystems Science and Engineering, ETH Zurich, Basel 4058, Switzerland

²Institute for Molecular Engineering, University of Chicago, Chicago 60637, USA

*Correspondence: tays@uchicago.edu

<http://dx.doi.org/10.1016/j.cell.2015.08.053>

Using single-cell RNA sequencing, Avraham et al. investigate how variability in macrophage response to infection is controlled by variability within the pathogen population. They find that heterogeneous expression of the *Salmonella* virulence factor PhoP and subsequent cell-wall modifications lead to the bimodal induction of the interferon-response in infected macrophages.

What exactly happens when pathogens penetrate the outer defenses of tissues and start infecting various cells? Since the dawn of modern biology, the battle between pathogens and immune cells has been a central focus, and thanks to powerful new methods that analyze individual cells, we are taking a fresh look at our understanding of infection and immunity. Unlike what traditional population-averaged analyses show, the outcome of pathogen exposure is vastly more complex at the individual-cell level. For example, some host cells completely avoid infection and survive. Other cells become infected and die, survive with the presence of bacteria inside them, or completely clear the pathogens and function normally afterward. The intricate workings of the molecular pathways determining infection and immunity are largely unclear. In this issue of *Cell*, Hung and colleagues take a new look at this fundamental problem using single-cell analysis and ask whether variability in infection outcomes can be explained by the variability among individual bacteria (Avraham et al., 2015). This is a unique approach as compared to most work in the newly emerging field of single-cell

immunology. In explaining heterogeneous infection outcomes, the field tends to focus on the state of the host and environment (Snijder et al., 2009), rather than pre-existing variability in the pathogen.

Hung's team focus on the infection of macrophages—first responders of the innate immune system—with *Salmonella typhimurium*, a pathogen that causes typhoid fever and food poisoning in humans. Despite a century of antibiotic treatment and improved hygiene, basic pathogens such as *Salmonella* remain a major health problem, especially in the developing world. Even the developed world is at risk from these basic infections, as evidenced by thousands of *salmonella* infections every year in the USA alone and the recent *E. coli* outbreak in Germany that killed 50 people over the course of a few weeks.

Salmonella typhimurium has specialized molecular tools to avoid, resist, and even hijack the mammalian immune system. Macrophages recognize these pathogen-associated factors and mount transcriptional programs to change their physiology and clear the pathogen. Individual *Salmonella* cells can vary in the manner they express virulence factors,

Can the variability in infection outcomes be explained by the variability within the pathogen population? And if so, what virulence factors control this variability? To answer these questions, Avraham et al. first use fluorescent single-cell microscopy to distinguish various infection outcomes: When mixed with *salmonella*, the macrophages could remain uninfected, or become infected with either live or dead bacteria inside. They isolate these single macrophages and use state-of-the-art RNA sequencing (RNA-seq) to determine their transcriptional state by measuring the expression of 535 immune response genes. These genes cluster into distinct groups; however, one cluster shows much higher expression variability between individual cells. These variable genes were related to innate immune recognition of the bacterial virulence factors, including bacterial cell-wall components like lipopolysaccharide (LPS), hinting that the LPS/TLR4 signaling pathway underlies phenotype variability. In particular, Type 1 interferon (IFN) response exhibit bimodal expression in host macrophages, with roughly one third of cells expressing IFN genes at high levels, and the rest at low levels

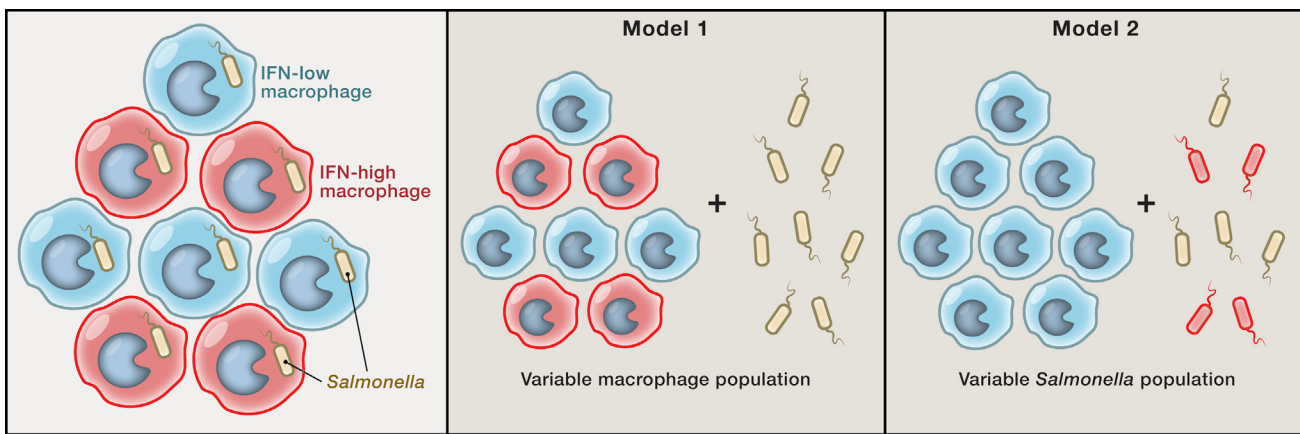


Figure 1. Infection Variability in Macrophages

When infected with single *Salmonella* cells, the macrophage population exhibits heterogeneous infection outcomes, with cells expressing either high (red) or low (blue) levels of *interferon (IFN)* genes. Avraham et al. (2015) show that the macrophage IFN expression variability is not due to variability in the macrophage population as shown in model 1, but is due to the variability in the infecting *Salmonella* cells as described by model 2.

(Figure 1A). The type 1 IFN response leads to secretion of a range of signaling molecules and regulation of cell fate decisions. Bimodality in IFN expression can indicate an underlying stochastic element controlling the IFN pathway (Tay et al., 2010). Intrigued with this bimodal expression pattern, the researchers narrow their focus onto the IFN response genes to uncover the molecular mechanisms driving infection variability.

Using a clever combination of fluorescent reporters, single-cell microscopy and single-cell RNA-seq, the authors ultimately identify the *Salmonella* virulence factor PhoP as underlying the variability in the macrophage infection outcome. Macrophages with high expression of PhoP response genes are also enriched for a Type 1 IFN response. Analysis with mutant strains shows that *Salmonella* expressing PhoP modify the cell-wall component LPS, allowing them to better induce the potentially lethal IFN response in the macrophages they infect. Finally, the researchers perform two conclusive *in vivo* experiments: They first inject mice with LPS extracted from either PhoP⁻ or PhoP⁺ bacteria, and observe the same correspondence between Type 1 IFN in macrophages from these mice. To further test the functional relevance of their findings, they use a mouse model of septic shock—which produces a cytokine storm leading to infection-related deaths—and again inject mice with modified or unmodified LPS. As expected, the PhoP-modi-

fied LPS confers a higher mortality rate in mice, and this effect can be reversed by co-administering a drug (BX795) inhibiting the Type1 IFN response.

What does this all mean? At the fundamental level, we now know that the heterogeneity in pathogen population can control the variability in host immune response (Figure 1). Understanding how pathogenic factors control infection outcomes can lead to better treatment options. Avraham et al. nicely adds to studies on the functional roles of “biological noise,” by considering not only the diversity on the host side but also the pathogen side (Snijder et al., 2009; Tay et al., 2010; Snijder and Pelkmans, 2011; Kellogg and Tay, 2015). Of course, the host factors are still involved in the final outcome, and it remains possible that other macrophage-related factors, such as their signaling history, also contribute to the observed phenotypes.

From the perspective of the pathogen, *Salmonella* seems to be using a bet-hedging strategy by diversifying the composition of their cell-wall, as if to wear different battle dress uniforms, to either camouflage themselves from the immune system or to directly attack it. Bet hedging is well studied in systems biology (Veenking et al., 2008), and these results constitute a medically relevant example of this interesting phenomenon.

At the molecular level, bimodal expression of *IFN* genes is another example of a digital signaling event (Tay et al.,

2010), where a binary switch controlling PhoP expression in *Salmonella* leads to a bimodal gene expression in macrophages. It would be interesting to find out what this switch is and how it could be manipulated with drugs.

A limitation of snapshot measurements like RNA-seq, however, is that they do not account for the dynamical changes in single cells. This can lead to misleading results if care is not taken: grouping expression levels in unsynchronized cells can be skewed by dynamically changing expression levels, especially for genes that are not at the steady state (and often, immune genes are not at steady state when induced with pathogen signals) (Tay et al., 2010; Kellogg and Tay, 2015). On the other hand, there are not many ways to measure gene dynamics except for live-cell microscopy with the few fluorescent reporters currently available to us. Nevertheless, there are known “master regulators,” transcription factors like NF- κ B, IRF3, and AP-1 that control the expression of genes studied here, and incorporating time-lapse microscopy by tagging these proteins in live cells could reveal more information on pathogen-host interactions (Tay et al., 2010; Kellogg and Tay, 2015; Selimkhanov et al., 2014). This kind of work would also benefit from new microfluidic and optogenetic methods, allowing better control of cell-cell interactions and creating more precise and realistic conditions *in vitro* (Kellogg et al., 2014; Frank and Tay, 2015; Toettcher et al., 2013). These tools would

be particularly useful in isolating the effects of paracrine and autocrine signals and in more precisely controlling the dosing and timing of pathogen inputs.

This work demonstrates the power of high-content single-cell techniques like RNA-seq in understanding pathogen-host interactions, but there is much left to do, both on the technical and biology sides. The researchers collected a very rich dataset on macrophage transcription and highlight the PhoPQ-IFN link, but there could be more to discover in this treasure chest of functional single-cell data.

REFERENCES

- Avraham, R., Haseley, N., Brown, D., Penaranda, C., Humberto, B.J., Trombetta, J.J., Sajita, R., Shalek, A.K., Ramnik, X., Regev, A., and Hung, D.T. (2015). *Cell* 162, this issue, 1309–1321.
- Frank, T., and Tay, S. (2015). *Lab Chip* 15, 2192–2200.
- Kellogg, R.A., and Tay, S. (2015). *Cell* 160, 381–392.
- Kellogg, R.A., Gómez-Sjöberg, R., Leyrat, A.A., and Tay, S. (2014). *Nat. Protoc.* 9, 1713–1726.
- Selimkhanov, J., Taylor, B., Yao, J., Pilko, A., Albeck, J., Hoffmann, A., Tsirring, L., and Wollman, R. (2014). *Science* 346, 1370–1373.
- Snijder, B., and Pelkmans, L. (2011). *Nat. Rev. Mol. Cell Biol.* 12, 119–125.
- Snijder, B., Sacher, R., Rämö, P., Damm, E.M., Liberali, P., and Pelkmans, L. (2009). *Nature* 461, 520–523.
- Tay, S., Hughey, J.J., Lee, T.K., Lipniacki, T., Quake, S.R., and Covert, M.W. (2010). *Nature* 466, 267–271.
- Toettcher, J.E., Weiner, O.D., and Lim, W.A. (2013). *Cell* 155, 1422–1434.
- Veenings, J.W., Smits, W.K., and Kuipers, O.P. (2008). *Annu. Rev. Microbiol.* 62, 193–210.

Helping the Help for CD8+ T Cell Responses

Sebastian Amigorena^{1,*}

¹INSERM U932, Institute Curie, 26 rue d'Ulm, 75248 Paris Cedex 05, France

*Correspondence: sebastian.amigorena@curie.fr

<http://dx.doi.org/10.1016/j.cell.2015.08.051>

Eickhoff et al. and Hor et al. use time-lapse intravital microscopy to show an unexpected choreography of CD4+ and CD8+ T cells “dancing” between different dendritic cell sub-populations during priming of cytotoxic immune responses to viruses.

The idea that clonal selection is at the basis of adaptive immune responses was first proposed in the Fifties by Nils Jerne and Sir Macfarlane Burnet. It was not, however, until the end of the Nineties that the field accepted that dendritic cells (DCs), first identified in 1973 by Ralph Steinman, are the antigen-presenting cells that support clonal selection and initiate adaptive immune responses in lymph nodes. The first visual *in situ* dynamic evidence of early interactions between naïve T lymphocytes and DCs came in the early 2000s when two-photon intravital imaging methods were developed in immunology (reviewed in Pittet and Mempel, 2008). These early studies revealed a high degree of unexpected complexity in these interactions. First, clonal selection occurs within a complex tissue environment and within specific regions of lymphoid tissue. Second, the encounter of an antigen-presenting cell and a T cell specific for that particular antigen is a rare, non-random event. Dendritic cells

accumulate in certain regions of lymph nodes and T cells migrate along preferential tracks, guided by combinations of chemokines. Third, the interactions between T cells and DCs have a specific controlled duration, which is critical for clonal expansion and T cell differentiation into effector and memory cells.

A key critical level in the initiation of immune responses, however, had not yet been addressed: DCs are a heterogeneous cell population that includes multiple cell subtypes with different functions. DCs fall into two main lineages (sometimes referred to as CD103+ and CD11b+ lineages), each including lymphoid tissue resident and migratory cells (Merad et al., 2013). One of the lineages (CD103+, CD8aa+, and XCR1+) specializes in the induction of CD8+ T cell responses and the presentation of internalized antigens on class I MHC molecules (cross-presentation) and will be referred to as XCR1+ DCs. The other subtype is more heterogeneous. CD11b+

DCs present internalized antigens on preferentially class II MHC molecules and induce CD4+ T cell and B cell responses (Merad et al., 2013). The current view of DC biology therefore underlines a repartition of antigen presentation to CD4+ and CD8+ T cells between DC subpopulations.

On the other hand, effective anti-viral cytotoxic immune responses by CD8+ T cells are strictly dependent on CD4+ T cells. In the absence of CD4+ T cells, CD8+ T cell responses are weak and lack long-lasting memory protection (Janssen et al., 2003; Shadlock and Shen, 2003). Different models have been proposed to account for these observations. The first proposed that CD4+ T cell help requires direct interactions between the three cell types (CD4+, CD8+ T cells, and DCs) (Ridge et al., 1998). The likelihood of this three-way cell interaction was questionable, and subsequent studies showed that the three cell types do not need to interact

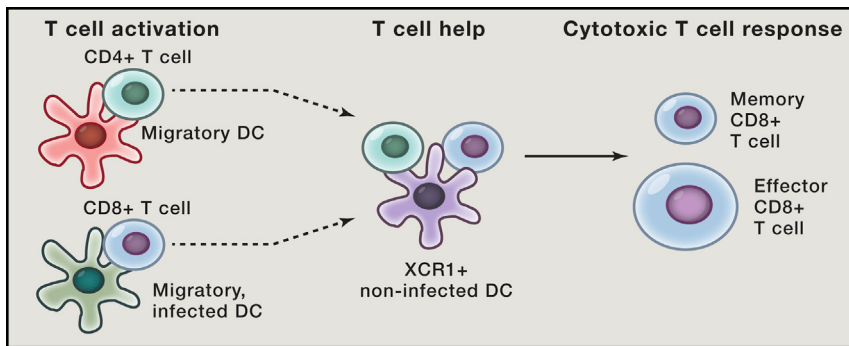


Figure 1. XCR1+ DC Platforms for T Cell Help during the Initiation of Anti-viral Immune Responses

Both CD4+ and CD8+ T cells are initially activated by distinct DCs in different anatomical sites of lymphoid organs. Activated T cells migrate to T cell zones and interact simultaneously in clusters containing the three-cell type. These three-cell interactions are indispensable for effector and memory anti-viral CD8+ T cell responses.

simultaneously. CD4+ cells deliver to DCs a “licensing” signal (through CD40-CD40L interactions) that activates DCs and permits the effective induction of CD8+ T cell responses (Schoenberger et al., 1998). This last model of T cell help does not predict simultaneous interactions between the three cell types.

Two studies now published in *Cell* (Eickhoff et al., 2015) and *Immunity* (Hor et al., 2015) investigate the nature of the cell-cell interactions that occur during the initiation of cytotoxic CD8+ T cell responses using intravital imaging in different viral infection models. Eickhoff et al. (2015) show that, early after infection by ovalbumin or LCMV glycoprotein expressing Vaccinia virus (MVA), CD8+ T cells are found within a series of dynamic clusters around infected DCs. These clusters, as well as initial priming of antigen-specific CD8+ T cells, do not require macrophages or resident XCR1+ DCs but another population of unidentified, MVA-OVA-infected DCs. When OVA-specific CD4+ T cells are also present, they form separate clusters, which do not contain CD8+ T cells and are found in the white pulp, whereas the CD8+ clusters are present in the marginal zone. CD8+ and CD4+ T cell initial priming therefore occurs in different anatomical localizations and on different individual DCs.

The study by Hor et al. (2015) makes a similar initial observation using a model of cutaneous HSV-1 infection in which HSV-1-specific CD4+ T cells expand earlier than CD8+ T cells. They

also show that early CD4+ T cell clusters in skin-draining lymph nodes are found in the medullary, the subcapsular sinus, and the B cell follicles rather than in the T cell zones. Using dynamic intravital imaging, they show that the early CD4+ cell clusters do not contain HSV-1-specific CD8+ T cells. Early CD8+ T cell clusters form around migratory skin DCs and not lymph node resident DCs. Therefore, like in the case of Vaccinia virus, after infection by HSV-1, the early priming of CD4+ and CD8+ T cells is physically segregated and seems to occur on distinct DC populations.

How then is CD4+ T cell help delivered to CD8+ T cells? The licensing model would have predicted that the DCs that had interacted with CD4+ T cells (the migratory ones in the case of HSV-1 and a CD11b+ population in the case of MVA) would then interact with CD8+ T cells to deliver the T cell help. This is not what was observed. In contrast, both studies show that, after infection (~40 hr in both the HSV-1 and the MVA models), dynamic clusters contain both CD4+ and CD8+ antigen-specific T cells. Eickhoff et al. (2015) show that these late “mix” clusters are present in the peripheral paracortex of the spleen. Hor et al. (2015) show that these clusters exclude migratory tissue-derived DCs and that the mix clusters form around XCR1+ DCs, suggesting that XCR1+ DCs present antigen on both class I and II MHC molecules. In the HSV-1 model, the same group showed previously that

the activation of CD8+ T cells is not induced by infected migratory DCs, but rather by cross-presentation after antigen transfer to resident DCs (Allan et al., 2006). Eickhoff et al. (2015) go one-step further using XCR1-DTR mice, in which DTX injection results in the specific depletion of XCR1+ resident DCs. Depletion of XCR1+ DCs caused loss of the mix CD4+/CD8+ T cell clusters, but not of single CD4+ or CD8+ T cell clusters, suggesting again that initial activation of both CD4+ and CD8+ T cells occurs on XCR1-negative DCs (migratory DCs for CD4+ T cells, in the case of HSV-1, and probably other populations of resident DCs in the case of MVA). The results from both studies indicate that XCR1+ DCs represent a “platform” for dynamic interactions between CD4+ and CD8+ T cells.

The final set of experiments in Eickhoff et al. (2015) addresses the physiological relevance of XCR1+ DCs for T cell help to cytotoxic effector and memory responses. They show that depletion of XCR1+ DCs deprives CD8+ T cells from CD4+ T cell help. These “helpless” CD8+ T cells display reduced expansion and differentiation after Vaccumia virus infection, and memory cytotoxic responses are compromised. Importantly, Eickhoff et al. (2015) show that selective KO of class II MHC molecules on XCR1+ DCs is sufficient to reproduce the phenotype, suggesting that antigen presentation to CD4+ T cells is required.

These studies make a critical contribution to our understanding of the initiation of cytotoxic immune responses to virus. They show that the initial priming of CD8+ T and CD4+ T cells occurs on different DC populations and that a secondary three-cell relationship is orchestrated by XCR1+ DCs (Figure 1). These XCR1+ DCs are not directly infected and must present viral antigens on both class I and II MHC molecules. They are absolutely required for effective cytotoxic primary and memory T cell responses. Previous studies showed that XCR1+ DCs are the most efficient antigen cross-presenting DCs (Merad et al., 2013). Their role as “platforms” for delivering CD4+ T cell help suggests that cross-presentation is not their only critical contribution to the initiation of cytotoxic immune responses. The production

of IL12, which is far higher in XCR1+ DCs than in other DC types, may also be important. It is also likely that XCR1+ DCs express a unique set of chemokines and chemokine receptors, maybe including XCR1 itself, that determines their function. It will be important to investigate how this new model for T cell help applies to other CD8+ T cell responses, including anti-tumor responses.

A key step for future research will certainly be to unravel the role of DC subpopulations during the initiation of immune responses in humans. Both T cell and DC lineage organizations are conserved between human and mice. However, in both cases, the functions of the subsets seem to have evolved differently. CD4+ human T cells are often cytotoxic, and it is still unclear if the human

lineage homologs of XCR1+ DCs, which express BDCA3+ and CD141+, cross-present antigens more efficiently than other DC subsets. In addition, the production of IL-12 is clearly not restricted to the human CD141+ DCs. Determining which human DC, if any, functions as a “T cell help platform” will certainly be a major challenge in the next years and an essential step toward designing effective CD8+ T cell vaccines.

REFERENCES

- Allan, R.S., Waithman, J., Bedoui, S., Jones, C.M., Villadangos, J.A., Zhan, Y., Lew, A.M., Shortman, K., Heath, W.R., and Carbone, F.R. (2006). *Immunity* 25, 153–162.
- Eickhoff, S., Brewitz, A., Gerner, M.Y., Klauschen, F., Komander, K., Hemmi, H., Garbi, N., Kaihso, T., Germain, R.N., and Kastenmüller, W. (2015). *Cell* 162, this issue, 1322–1337.
- Hor, J.L., Whitney, P.G., Zaid, A., Brooks, A.G., Heath, W.R., and Mueller, S.N. (2015). *Immunity*. Published online August 18, 2015. <http://dx.doi.org/10.1016/j.immuni.2015.07.020>.
- Janssen, E.M., Lemmens, E.E., Wolfe, T., Christen, U., von Herrath, M.G., and Schoenberger, S.P. (2003). *Nature* 421, 852–856.
- Merad, M., Sathe, P., Hefti, J., Miller, J., and Mortha, A. (2013). *Annu. Rev. Immunol.* 31, 563–604.
- Pittet, M.J., and Mempel, T.R. (2008). *Immunol. Rev.* 221, 107–129.
- Ridge, J.P., Di Rosa, F., and Matzinger, P. (1998). *Nature* 393, 474–478.
- Schoenberger, S.P., Toes, R.E., van der Voort, E.I., Offringa, R., and Melief, C.J. (1998). *Nature* 393, 480–483.
- Shedlock, D.J., and Shen, H. (2003). *Science* 300, 337–339.

Melatonin Lulling Th17 Cells to Sleep

Jacob S. Lee^{1,*} and Daniel J. Cua^{1,*}

¹IMR Pathway Biology, Merck Research Laboratory, 901 California Avenue, Palo Alto, CA 94304, USA

*Correspondence: jacob.lee@merck.com (J.S.L.), daniel.cua@merck.com (D.J.C.)

<http://dx.doi.org/10.1016/j.cell.2015.08.054>

In this issue, Farez et al. report that the circadian hormone melatonin, whose levels vary with seasonal changes in night length, shifts the immune response toward an anti-inflammatory state that may explain the seasonal variability of multiple sclerosis disease activity.

An imbalance between the inflammatory and regulatory responses of the immune system can lead to chronic immune cell activation and autoimmunity. Mounting evidence implicates the Th17 subset of T helper cells, characterized by the production of the proinflammatory cytokine interleukin-17 (IL-17), with playing a central role in autoimmune diseases, including multiple sclerosis (MS), rheumatoid arthritis (RA), psoriasis, and inflammatory bowel disease (IBD) (Gaffen et al., 2014). Predominantly located at barrier tissues that interface with the external world, Th17 cells maintain a high degree of flexibility to respond rapidly to constant fluctuations in environmental conditions and stimuli. The

mechanisms that allow the adaptation of Th17 cells to the ever-changing environment include the ability to respond to changing nutrient status through the aryl hydrocarbon receptor (AHR) (Quintana et al., 2008), to oxygen sensing pathways including HIF1 α (Dang et al., 2011), and to changes in osmotic pressure through serum/glucocorticoid regulated kinase 1 (SGK1) (Wu et al., 2013). In this issue of *Cell*, Farez et al. (2015) uncover another environmental cue—seasonal changes in daylight—that modulates the development of pathogenic Th17 cells. The daylight effect is mediated by the hormone melatonin, produced by the pineal gland and involved in the regulation of the circa-

dian rhythm (Brzezinski, 1997). Melatonin inhibits the development of proinflammatory Th17 cells and shifts the balance of the immune response toward immunosuppression.

It has been known for some time that the latitudinal gradient—the greater the distance from the equator—correlates with increasing occurrence of multiple sclerosis (Alonso and Hernán, 2008). One of the phenomena linked to latitude is seasonal variation in exposure to UV radiation. There are convincing epidemiological data supporting the role of UV radiation-dependent vitamin D in reducing the disease course of MS (Munger et al., 2004). Yet, this correlation does not explain the increase in MS

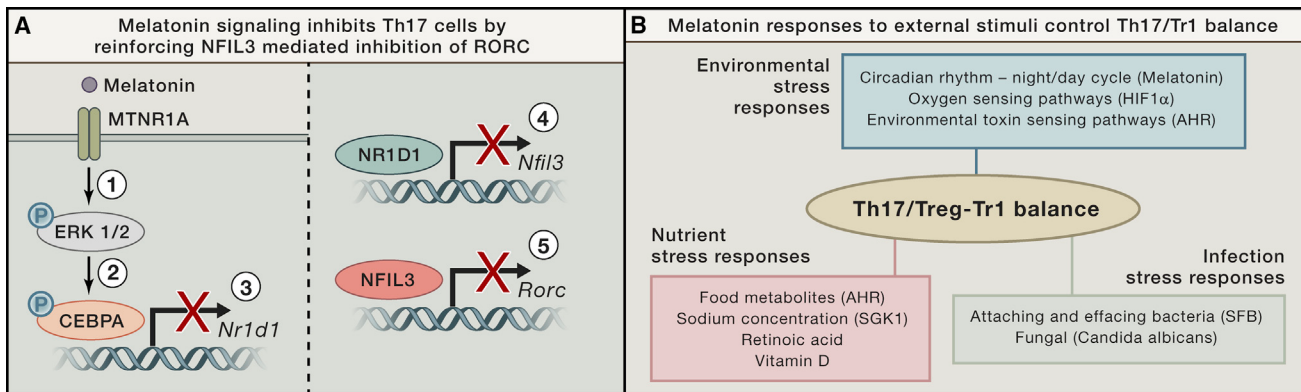


Figure 1. Melatonin Shifts the Balance from Th17 to Tr1

(A) Depicted is a schematic of the melatonin signaling pathway resulting in the inhibition of *Rorc*. (1) Melatonin signals through the melatonin receptor MTNR1A and results in ERK 1/2 phosphorylation. (2) Phosphorylated ERK 1/2 activates the transcription factor C/EBP α . (3) and represses the expression of *Nr1d1* (REV-ERB α). (4) NR1D1 represses the transcription of *Nfil3*, which is a (5) repressor of *Rorc*. Thus, melatonin signaling releases the inhibition of *Nfil3* by NR1D1 and results in the suppression of *Rorc*.

(B) A representation of various environmental cues regulating the balance between proinflammatory Th17 cells and immunosuppressive Treg/Tr1 cells.

relapse rates during spring and summer months, when UV rays are most abundant. In order to understand the environmental factors impacting the seasonal pattern of MS relapses, Farez et al. (2015) hypothesize that melatonin production, which also follows seasonal variation, may be involved in MS disease. Following up on a cohort of MS patients, the authors identify a negative correlation between clinical relapse and melatonin levels, with the highest levels of melatonin and the lowest exacerbation rate during the winter months. Indeed, serum from relapsing-remitting MS patients shows a negative correlation between the levels of melatonin and the proinflammatory cytokine IL-17 and a positive correlation with the anti-inflammatory cytokine IL-10. In vitro, the addition of melatonin suppresses the polarization of human T helper cells into the Th17 lineage, resulting in diminished expression of the Th17 master transcription regulator *RORC* and production of IL-17. In addition to its negative impact on Th17 differentiation, melatonin also enhances the polarization of type 1 regulatory cells (Tr1), which can suppress immune responses through the production of IL-10. Through a series of carefully designed experiments with mice genetically deficient in different components along the melatonin signaling pathway, the authors find that melatonin-dependent reinforcement of NFIL3, a negative regulator of *Rorc*, suppresses the development of

Th17 cell in murine cells, while activation of ROR α boosts the Tr1 cell fate.

Melatonin signals through the membrane melatonin receptor (MTNR1A) that is expressed on a variety of cell types, including T cells. Both melatonin and the small molecule agomelatine, a MTNR1A agonist, repress the differentiation of murine Th17 cells in vitro, resulting in the suppression of key Th17 signature genes, *Rorc*, *Il17*, and *Il23r*. Importantly, T cells from MTNR1A KO mice are resistant to the suppressive impact of melatonin in Th17 cell differentiation, arguing that the membrane melatonin receptor is critical to mediate the effects of melatonin in Th17 cell polarization. What is the molecular mechanism of melatonin-dependent inhibition of Th17 cells? The key to answering this question is based on a previous report (Yu et al., 2013) demonstrating an important contribution of REV-ERB α , a transcriptional repressor with key regulatory functions in the control of the circadian cycle, in promoting Th17 cell development, thus linking the circadian clock with Th17 cell development. Here is where the story gets complicated. Melatonin increases the activation of Erk 1/2 which in turn leads to an increase in the phosphorylation of the transcription factor C/EBP α . C/EBP α binds to the promoter of *Nr1d1* (REV-ERB α) and acts as a negative regulator. Confirming the regulatory function of REV-ERB α in *Nfil3*, melatonin suppression of *Nr1d1* expression results in increased NFIL3 binding

to the *Rorc* promoter, leading to reduced expression of *Rorc* (Figure 1A). In a complementary set of experiments, the authors find that melatonin signaling also enhances in vitro Tr1 cell polarization, increases IL-10 production, and boosts the suppressive ability of these cells. Melatonin increases binding of ROR α to the *Il10* promoter, which synergizes with AHR and c-Maf to enhance *Il10* expression. Taken together, melatonin shifts the balance from pathogenic Th17 cells to favor the immunosuppressive Tr1 cells. Importantly, administration of melatonin in a mouse model of MS leads to amelioration of disease. Melatonin reduces the frequency of Th17 cells infiltrating the central nervous system, particularly the pathogenic IL-17-IFN γ and IL-17-GMCSF double-positive cells, while concomitantly increasing IL-10 producing immunosuppressive Tr1 cells in the mouse model.

Over the past 50 years, there has been a steady rise in the incidence of autoimmune diseases such as MS, RA, psoriasis, and IBD, particularly in developed countries. Recent studies have uncovered many environmental stress factors associated with the modern life contributing to the development of inflammatory disorders (Figure 1B). One example is the “high-salt” Western diet, where SGK1 on Th17 cells play a role in exacerbating T cell inflammatory mechanisms (Wu et al., 2013). It is tempting to speculate whether the invention of artificial

lights—which facilitates chronic circadian disruptions—could have contributed to an imbalance between the inflammatory and regulatory responses of the immune system, leading to immune dysregulation. The current study establishes a clear link between melatonin, a hormone involved in the regulation of the circadian rhythm, and the inhibition of proinflammatory Th17 cells, thereby shifting the balance of the immune response toward immunosuppression. These findings support the immunosuppressive properties of melatonin, as well as define the melatonin-NFIL3-ROR γ t pathway as a potential therapeutic target for the treatment of MS.

ACKNOWLEDGMENTS

J.S.L. and D.J.C. are employed by Merck & Co.

REFERENCES

- Alonso, A., and Hernán, M.A. (2008). *Neurology* 71, 129–135.
- Brzezinski, A. (1997). *N. Engl. J. Med.* 336, 186–195.
- Dang, E.V., Barbi, J., Yang, H.Y., Jinaseya, D., Yu, H., Zheng, Y., Bordman, Z., Fu, J., Kim, Y., Yen, H.R., et al. (2011). *Cell* 146, 772–784.
- Farez, M.F., Mascanfroni, I.D., Méndez-Huergo, S.P., Yeste, A., Murugaiyan, G., Garo, L.P., Balbuena Aguirre, M.E., Patel, B., Ysraelit, M.C., Zhu, C., et al. (2015). *Cell* 162, this issue, 1338–1352.
- Gaffen, S.L., Jain, R., Garg, A.V., and Cua, D.J. (2014). *Nat. Rev. Immunol.* 14, 585–600.
- Munger, K.L., Zhang, S.M., O'Reilly, E., Hernán, M.A., Olek, M.J., Willett, W.C., and Ascherio, A. (2004). *Neurology* 62, 60–65.
- Quintana, F.J., Basso, A.S., Iglesias, A.H., Korn, T., Farez, M.F., Bettelli, E., Caccamo, M., Oukka, M., and Weiner, H.L. (2008). *Nature* 453, 65–71.
- Wu, C., Yosef, N., Thalhamer, T., Zhu, C., Xiao, S., Kishi, Y., and Kuchroo, V.K. (2013). *Nature* 496, 513–517.
- Yu, X., Rollins, D., Ruhn, K.A., Stubblefield, J.J., Green, C.B., Kashiwada, M., Rothman, P.B., Takahashi, J.S., and Hooper, L.V. (2013). *Science* 342, 727–730.

The Touching Tail of a Mechanotransduction Channel

Zachary A. Knecht,^{1,2} Rachelle Gaudet,³ and Paul A. Garrity^{1,2,*}

¹National Center for Behavioral Genomics

²Volen Center for Complex Systems, Department of Biology

Brandeis University, Waltham, MA 02458, USA

³Department of Molecular and Cellular Biology, Harvard University, Cambridge, MA 02138, USA

*Correspondence: pgarrity@brandeis.edu

<http://dx.doi.org/10.1016/j.cell.2015.08.049>

In mechanotransduction, sensory receptors convert force into electrical signals to mediate such diverse functions as touch, pain, and hearing. In this issue of *Cell*, Zhang et al. present evidence that the fly NompC channel senses mechanical stimuli using its N-terminal tail as a tether between the cell membrane and microtubules.

As far back as Aristotle, the sense of touch was valued, along with hearing, sight, smell, and taste, as one of the “five outward wits” central to the human experience. It is now clear that “touch” is not merely a core aspect of perception but represents a highly specialized, diverse, and complex series of sensory systems. Mechanosensation plays an important role not just in feeling objects and textures but also in eliciting pain or pleasure, detecting sounds, and sensing balance and the position of our own bodies. In this issue of *Cell*, Zhang et al. (2015) explore the molecular mechanisms of mechanosensory transduction, a process in which molecules in cell membranes convert mechanical forces

into electrical signals (Zhang et al., 2015). They present a strong case that the *Drosophila* NompC ion channel senses mechanical stimuli using its N-terminal tail as a tether between the cell membrane and the microtubules of the cytoskeleton (Figure 1).

Although numerous mechanosensing ion channels have been identified, the mechanisms by which force-to-signal conversions occur remain unclear in many cases (Anishkin et al., 2014). The rapid activation kinetics of mechanosensing channels, seemingly too rapid for second messenger generation, suggests they are gated directly by mechanical forces acting on the plasma membrane. Two non-exclusive models for

force-activation of channels have been proposed. In the membrane force model, pressure on the plasma membrane alters its shape and/or surface area, causing opening of the embedded protein channel. On the other hand, the tether model posits that molecular tethers convey force between the channel and the cytoskeleton or extracellular milieu. Although several examples of membrane force-activated channels exist, notably the bacterial MscL channel, there has been no direct molecular evidence supporting a tether model (Anishkin et al., 2014).

Zhang et al. (2015) focus on the *Drosophila* Transient Receptor Potential (TRP) channel NompC. Cation channels of the TRP family have long been

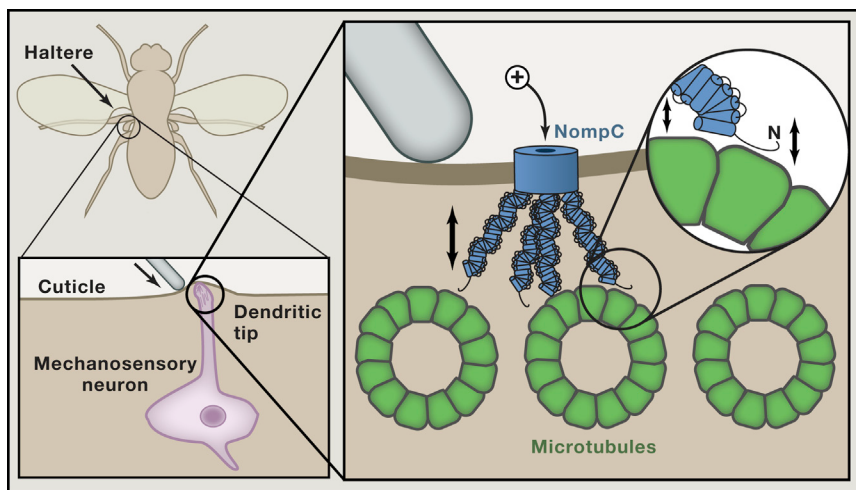


Figure 1. Model for Tethered Gating of the NompC Mechanotransduction Channel

Left: the NompC cation channel is present at the dendritic tips of mechanosensory neurons in the fly halteres, where it converts forces transmitted through the deformation of the overlying cuticle into neuronal depolarization. Right: the NompC tetramer (blue) sits in the plasma membrane, with its cytoplasmic N-terminal AR-containing tails represented as coils of helices (right). The ARs form molecular tethers to microtubules (green), helping convey force (represented here as membrane deformation) to the channel region.

associated with the transduction of sensory stimuli ranging from photons to chemicals. NompC was initially identified in a genetic screen for uncoordinated and touch-insensitive fly larvae and was the first TRP channel clearly linked to mechanotransduction (Walker et al., 2000). A hallmark of NompC is that its N-terminal tail contains a large number of ankyrin repeats (ARs), which are important for its function (Cheng et al., 2010). Long AR chains typically assume a coil-like structure and have been postulated to represent the sought-after gating spring component of a tethered mechanosensor (Howard and Bechstedt, 2004). With 29 ARs, NompC has the largest number of ARs of all known TRPs. Although mammals lack NompC orthologs, NompC functions as a mechanosensor for proprioception, light touch, and hearing in *Drosophila* (Cheng et al., 2010; Effertz et al., 2012; Yan et al., 2013), as well as mechanosensation in *C. elegans* (Kang et al., 2010), and it serves as a useful model for studying mechanotransduction.

To examine the molecular mechanisms by which NompC responds to force, Zhang et al. (2015) focus on this long tail of ARs and first test whether the tail is indeed cytoplasmic, a prerequisite for tethering to the cytoskeleton. They found that antibodies specific to either the

NompC N or C terminus labeled only permeabilized cells, whereas an antibody against a transmembrane loop region labeled non-permeabilized cells. Thus, NompC is localized at the plasma membrane and the ARs are indeed intracellular, a topology that could permit an interaction with the cytoskeleton.

Next, the authors generated truncated NompC channels with altered numbers and arrangements of ARs to determine their functional importance. None of the channels with partial or complete deletions of the ARs could function as force sensors; however, the channel did function as a mechanosensor when the AR tail was duplicated. This suggested that the full complement of ARs was required for mechanotransduction. This finding was confirmed *in vivo*—of the mutant channels tested, only the channel with the duplicated AR tail restored gentle touch to touch-sensitive neurons in the larval body wall and rescued behavioral responses to touch stimuli.

Having established that the ARs are required for NompC function, Zhang et al. (2015) searched for a connection between the AR region and the cytoskeleton, as might be expected of a tether and gating spring mechanism. The distal tips of mechanoreceptors located in the *Drosophila* halteres (a pair of

modified hindwings involved in steering) have highly organized, filamentous structures, termed membrane-microtubule connectors (MMCs), speculated to represent the tethering of NompC to the microtubule network (Liang et al., 2013). Zhang and colleagues test this hypothesis, finding that MMCs are absent in *nompC*⁷ null mutants, restored by WT, and elongated when the AR domain is duplicated. Using co-sedimentation experiments, they also demonstrate that NompC associates with microtubules. Microtubule disassembly using pharmacological agents also eliminated mechanogating of NompC. These results indicate that NompC associates with the microtubule cytoskeleton through its ARs and that both the ARs and microtubules are required for the channel's function as a mechanosensor. At the molecular level, follow-up questions to this work include which NompC ARs mediate the interaction and the structure of the NompC AR tail/microtubule interface.

While these observations indicate that the interaction of the NompC N terminus with microtubules is required for mechanogating of the channel, Zhang and colleagues go one step further and demonstrate that this region of NompC can confer mechanosensitivity upon another ion channel. They create a chimera that fuses the NompC N-terminal region (which includes the 29 ARs) to the structurally similar but mechanically insensitive Kv1.2 voltage-gated potassium channel. Expression of this chimeric channel allowed the authors to evoke mechanically activated currents in heterologous *Drosophila* S2 cells, whereas expression of WT Kv1.2 conferred no mechanical response. Importantly, this response was dependent on the integrity of microtubules in those cells, consistent with the association of the AR tether to the microtubule cytoskeleton endowing responsiveness to mechanical stimuli. It will be intriguing to ask to what extent such a chimeric channel supports function in the fly or whether *in vivo* function requires additional interactions mediated by other regions of the intact NompC channel.

The structure and gating of mechanically activated channels have been the subject of much speculation. This study is pioneering for presenting strong

evidence for a cytoskeleton-tethered gating spring mechanism, supporting the viability of a tethered channel model. In a broader sense, this work affirms, in conjunction with examples of membrane-force gated channels, that mechanical stimuli can be transduced in multiple ways. Thus, the work by [Zhang et al. \(2015\)](#) significantly enhances our understanding of mechanotransduction, raising new questions and presenting new research directions. For instance, as a TRP channel, NompC is a putative tetramer—does it require all four AR tails to provide multiple attachments to microtubules? Is the NompC/microtubule complex subject to post-translational modifications that alter its force-response properties and regulate its mechanosen-sitivity? Might other proteins or co-factors associate with the complex to regulate its

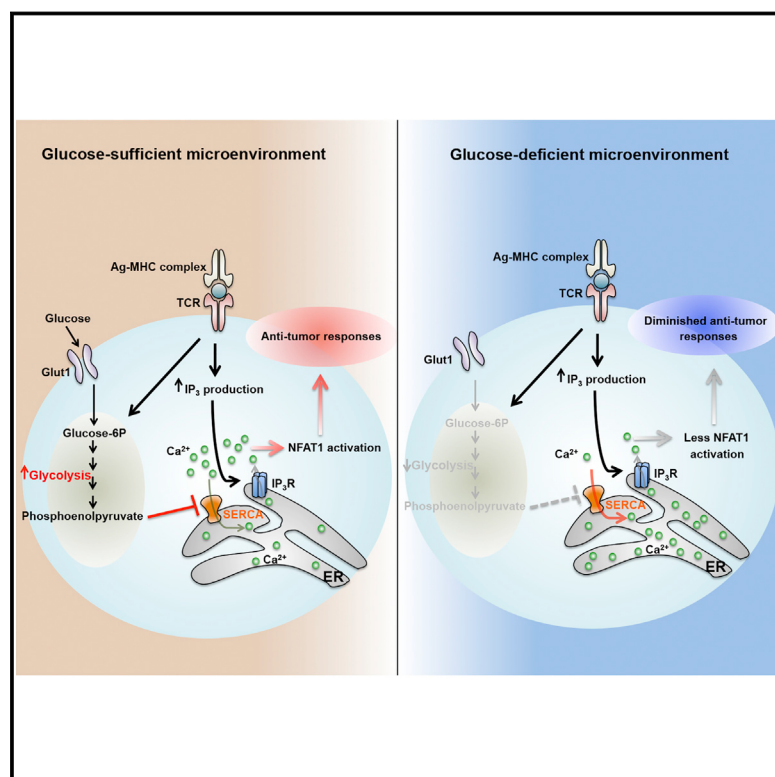
function? In its native context, NompC-mediated mechanotransduction is likely also influenced by additional factors, including other membrane-bound proteins like NompA, which is ideally positioned to help transfer force by providing an anchor to the extracellular matrix ([Chung et al., 2001](#)). More generally, this study paves the way for understanding how different varieties of mechanorecep-tors specialize for different functions and how their use is modulated across cell types to respond to the diverse mechanical stimuli an animal encounters.

REFERENCES

- [Anishkin, A., Loukin, S.H., Teng, J., and Kung, C. \(2014\). Proc. Natl. Acad. Sci. USA 111, 7898–7905.](#)
- [Cheng, L.E., Song, W., Looger, L.L., Jan, L.Y., and Jan, Y.N. \(2010\). Neuron 67, 373–380.](#)
- [Chung, Y.D., Zhu, J., Han, Y., and Kernan, M.J. \(2001\). Neuron 29, 415–428.](#)
- [Effertz, T., Nadrowski, B., Piepenbrock, D., Albert, J.T., and Göpfert, M.C. \(2012\). Nat. Neurosci. 15, 1198–1200.](#)
- [Howard, J., and Bechstedt, S. \(2004\). Curr. Biol. 14, R224–R226.](#)
- [Kang, L., Gao, J., Schafer, W.R., Xie, Z., and Xu, X.Z. \(2010\). Neuron 67, 381–391.](#)
- [Liang, X., Madrid, J., Gärtner, R., Verbavatz, J.M., Schiklenk, C., Wilsch-Bräuninger, M., Bogdanova, A., Stenger, F., Voigt, A., and Howard, J. \(2013\). Curr. Biol. 23, 755–763.](#)
- [Walker, R.G., Willingham, A.T., and Zuker, C.S. \(2000\). Science 287, 2229–2234.](#)
- [Yan, Z., Zhang, W., He, Y., Gorczyca, D., Xiang, Y., Cheng, L.E., Meltzer, S., Jan, L.Y., and Jan, Y.N. \(2013\). Nature 493, 221–225.](#)
- [Zhang, W., Cheng, L.E., Kittelmann, M., Li, J., Petkovic, M., Cheng, T., Jin, P., Guo, Z., Göpfert, M.C., Jan, L.Y., et al. \(2015\). Cell 162, this issue, 1391–1403.](#)

Phosphoenolpyruvate Is a Metabolic Checkpoint of Anti-tumor T Cell Responses

Graphical Abstract



Authors

Ping-Chih Ho, Jessica Dauz Bihuniak, Andrew N. Macintyre, ..., Marcus W. Bosenberg, Jeffrey C. Rathmell, Susan M. Kaech

Correspondence

ping-chih.ho@unil.ch (P.-C.H.), susan.kaech@yale.edu (S.M.K.)

In Brief

High rates of tumor cell glycolysis suppress intratumoral T cell function by depriving T cells of glucose and the downstream metabolite phosphoenolpyruvate (PEP), which is necessary for maximal Ca²⁺-NFAT signaling in T cells. Metabolic rewiring of T cells to generate PEP in glucose-poor conditions improves their anti-tumor responses.

Highlights

- Glucose deprivation suppresses anti-tumor T cell effector functions
- Glycolytic metabolite PEP sustains Ca²⁺ and NFAT signaling by blocking SERCA
- Ca²⁺ signaling is an integrator of glycolytic activity and TCR signaling
- T cell metabolic reprogramming enhances anti-tumor effector functions

Phosphoenolpyruvate Is a Metabolic Checkpoint of Anti-tumor T Cell Responses

Ping-Chih Ho,^{1,*} Jessica Dauz Bihuniak,² Andrew N. Macintyre,³ Matthew Staron,¹ Xiaojing Liu,⁴ Robert Amezquita,^{1,5} Yao-Chen Tsui,^{1,6} Guoliang Cui,¹ Goran Micevic,⁷ Jose C. Perales,⁸ Steven H. Kleinstein,⁵ E. Dale Abel,⁹ Karl L. Insogna,² Stefan Feske,¹⁰ Jason W. Locasale,⁴ Marcus W. Bosenberg,^{5,7} Jeffrey C. Rathmell,³ and Susan M. Kaech^{1,6,*}

¹Department of Immunobiology, Yale University School of Medicine, New Haven, CT 06519, USA

²Department of Internal Medicine, Yale University School of Medicine, New Haven, CT 06519, USA

³Department of Pharmacology and Cancer Biology, Immunology, Duke Molecular Physiology Institute, Duke University, Durham, NC 27710, USA

⁴Division of Nutritional Sciences, Cornell University, Ithaca, NY 14853, USA

⁵Department of Pathology, Yale University School of Medicine, New Haven, CT 06519, USA

⁶Howard Hughes Medical Institute, Chevy Chase, MD 20815, USA

⁷Department of Dermatology, Yale University School of Medicine, New Haven, CT 06519, USA

⁸Biophysics Unit, Department of Physiological Sciences II, IDIBELL-University of Barcelona, Fexia Llarga s/n 08907, Spain

⁹Fraternal Order of Eagles Diabetes Research Center, Division of Endocrinology and Metabolism, Department of Medicine, Carver College of Medicine University of Iowa, Iowa City, IA 52242, USA

¹⁰Department of Pathology, New York University Langone Medical Center, New York, NY 10016, USA

*Correspondence: ping-chih.ho@unil.ch (P.-C.H.), susan.kaech@yale.edu (S.M.K.)

<http://dx.doi.org/10.1016/j.cell.2015.08.012>

SUMMARY

Activated T cells engage aerobic glycolysis and anabolic metabolism for growth, proliferation, and effector functions. We propose that a glucose-poor tumor microenvironment limits aerobic glycolysis in tumor-infiltrating T cells, which suppresses tumoricidal effector functions. We discovered a new role for the glycolytic metabolite phosphoenolpyruvate (PEP) in sustaining T cell receptor-mediated Ca^{2+} -NFAT signaling and effector functions by repressing sarco/ER Ca^{2+} -ATPase (SERCA) activity. Tumor-specific CD4 and CD8 T cells could be metabolically reprogrammed by increasing PEP production through overexpression of phosphoenolpyruvate carboxykinase 1 (PCK1), which bolstered effector functions. Moreover, PCK1-overexpressing T cells restricted tumor growth and prolonged the survival of melanoma-bearing mice. This study uncovers new metabolic checkpoints for T cell activity and demonstrates that metabolic reprogramming of tumor-reactive T cells can enhance anti-tumor T cell responses, illuminating new forms of immunotherapy.

INTRODUCTION

Host immunity provides wide spectrum protection that serves to eradicate cancerous cells in addition to infectious pathogens. Multiple types of immune cells are involved in tumor immunosurveillance and of particular importance are the tumor-infiltrating lymphocytes (TILs) (i.e., T cells) (Braumüller et al., 2013; Shiao et al., 2011). In most established tumors, however, the tumoricidal effector functions of TILs such as IFN γ production and cyto-

toxicity are restricted by multiple environmental factors. This includes the accumulation of immunoregulatory cells such as regulatory CD4+ T cells (Tregs), myeloid derived suppressor cells (MDSCs) and tolerogenic antigen-presenting cells (APCs) (Mellman et al., 2011; Shiao et al., 2011). Additionally, alterations in the availability of nutrients (e.g., lactate and tryptophan-related metabolites such as kynurene) in the tumor microenvironment can limit TIL activity (Yang et al., 2013). Another prominent feature of TILs is the increased expression of inhibitory checkpoint receptors (e.g., programmed cell death protein 1 [PD-1], lymphocyte-activation gene 3 [Lag3], and cytotoxic T-lymphocyte-associated protein 4 [CTLA-4]) that desensitizes T cell receptor (TCR) signaling and contributes to their functional impairment (Baitsch et al., 2012). T cells displaying such properties are commonly referred to as “functionally exhausted” (Wherry, 2011). These discoveries have led to the development of cancer immunotherapies that reawaken exhausted TILs by blocking inhibitory checkpoint receptors such as PD-1 or CTLA-4 or targeting other immunoregulatory cells. Adoptive cell therapy (ACT) of tumor-specific T cells is another promising form of anti-cancer immunotherapy that increases the repertoire of cytotoxic T cells to eradicate established tumors. ACT has the added benefit of permitting genetic modifications of TILs to express proteins that could aide in tumor destruction (Maude et al., 2014). These breakthroughs demonstrate that tumor immunotherapy holds great promise (Callahan et al., 2010; Wolchok et al., 2013), but also present us with challenges to devise additional treatment options in conjunction with those currently available to further increase patient objective responses. To meet these challenges, we must gain a clearer understanding of what causes T cell exhaustion in tumors, and we hypothesize that the metabolic states of the TILs and tumor cells, as well as other cell types in the tumor microenvironment, are principal components of this process.

Deregulated anabolic metabolism and increased rates of aerobic glycolysis (i.e., the Warburg effect), glutaminolysis and fatty acid synthesis are cardinal features of most tumor cells that fuels their growth and proliferation (Hanahan and Weinberg, 2011; Ward and Thompson, 2012). Interestingly, activated T lymphocytes undergo a metabolic switch similar to cancer cells and upregulate aerobic glycolysis and glutaminolysis to permit proliferation and differentiation into specialized effector T cells. Given their similarities in metabolic profiles and nutrient requirements, it is possible that the abnormally high metabolic rates and consumption of nutrients by tumor cells competes with neighboring T cells, which leads to T cell metabolic exhaustion that underlies their functional exhaustion. Supporting this notion, reports have shown that the concentration of extracellular glucose are lower in tumors compared to healthy tissues (Gullino et al., 1964). Thus, limited glucose availability could be an environmental restriction that promotes T cell exhaustion, and if true, it is important to learn how this affects T cell receptor (TCR) signaling and effector functions in tumors. Perhaps, new therapies directed at reprogramming T cell metabolism could be developed to enhance their functional fitness in the tumor microenvironment.

TCR stimulation activates numerous key signaling pathways that coordinately induce anabolic metabolism, aerobic glycolysis, and effector T cell proliferation and differentiation (Smith-Garvin et al., 2009). Increased aerobic glycolysis is essential for the production of biosynthetic precursors that fuel effector T cell proliferation and production of effector molecules like IFN γ , IL-2, and IL-17 and Granzyme B in T cells (Cham et al., 2008; Chang et al., 2013; Finlay et al., 2012; Michalek et al., 2011). Activation of PI3K, Akt, and mTOR triggers the switch to anabolic metabolism by inducing transcription factors such as Myc and hypoxia-inducible factor 1 (HIF1) (MacIver et al., 2013; Wang et al., 2011a). T cells rendered functionally anergic that are unable to activate Ca $^{2+}$ and nuclear factor of activated T cells (NFAT) signaling show diminished rates of aerobic glycolysis and anabolic metabolism following stimulation (Srinivasan and Frauwirth, 2007; Zheng et al., 2009). Similarly, CD8 T cells with increased PD-1 expression fail to fully activate mTOR or aerobic glycolysis following TCR stimulation and conversely, those with hyper-HIF1 α activity and aerobic glycolysis are refractory to functional exhaustion (Doedens et al., 2013; Parry et al., 2005; Staron et al., 2014). The glycolytic enzymes may also serve direct roles in regulating effector functions in T cells because recent work showed that when glycolytic rates are low, the glyceraldehyde phosphate dehydrogenase (GAPDH) binds to and suppresses Ifng mRNA translation in T cells (Chang et al., 2013; Gubser et al., 2013). These findings demonstrate strong interconnections between T cell metabolism and effector functions but little remains known about how metabolic pathways or their metabolites fine-tune T cell activity.

In this study, we found that intratumoral CD4 T cells displayed signs of glucose deprivation and diminished anti-tumor effector functions, suggesting that a glucose-poor tumor microenvironment might contribute to TIL exhaustion. Furthermore, increased expression of hexokinase 2 (HK2) in tumor cells allowed for more efficient evasion of CD4 T cell-mediated immune surveillance indicating that a metabolic competition could exist between TILs and tumor cells. Linking glucose-deprivation to T cell func-

tion, we also discovered that insufficiency of the glycolytic metabolite phosphoenolpyruvate (PEP) led to defects in Ca $^{2+}$ -NFAT signaling and T cell activation by increasing SERCA-mediated Ca $^{2+}$ re-uptake. Most importantly, we provided proof-of-concept evidence that metabolic reprogramming of T cells to increase PEP production could be a promising strategy to elevate T cell mediated anti-tumor immune responses and improve the effects of adoptive T cell transfer immunotherapy.

RESULTS

Glucose Limitation Suppresses Anti-tumor Effector Functions of Intratumoral TH1 CD4 T Cells while Stimulating TGF β Production

To investigate whether limited glucose availability within the tumor microenvironment suppressed aerobic glycolysis and hence, effector functions in TILs, we first compared the concentration of glucose in the interstitial fluid of the spleen, blood, and tumors from melanoma-bearing Tyr-creERT2/BrafV600E/Pten-*lox* (Braf/Pten) mice (Dankort et al., 2009) (Figure 1A) and B16 melanoma-bearing mice (data not shown). As reported in other solid tumors (Gullino et al., 1964), the glucose level of the tumor interstitial fluid (~0.6 mM) was approximately ten times lower than that of the spleen and blood (~9 mM). Additionally, intratumoral CD44hi CD25lo CD4+ T cells (i.e., activated non-Treg CD4+ T cells) failed to take-up glucose as efficiently as their counterparts in the spleen based on intracellular staining with the fluorescent glucose analog 2-NBDG (Figure 1B). We further assessed 2NDBG-uptake in tumor infiltrating non-Treg CD4+ T cells, Tregs, tumor-associated macrophages (TAMs), and MDSCs. This showed that non-Treg CD4+ T cells take-up marginally less 2NDBG than TAMs, but not MDSCs. Unexpectedly, the intratumoral and splenic Tregs demonstrated higher 2NDBG uptake compared to the other cell populations (Figure S1A). Furthermore, co-culturing TH1 CD4+ T cells with Braf/Pten melanoma cells demonstrated that the presence of tumor cells could reduce glucose uptake by TH1 cells (Figure 1C), suggesting that tumor cells may directly restrict glucose availability for TILs. As there is no facile way to directly and specifically measure rates of glycolysis in TILs *in vivo* or *in situ*, we attempted to determine if intratumoral CD4+ T cells express genes induced by glucose deprivation. We identified a “glucose-deprivation transcriptional signature” in CD4+ T cells by comparing the differentially expressed genes of activated TH1 cells cultured in high (10 mM) or low (0.1 mM) glucose concentrations using RNA-sequencing and microarrays (Figure S1B), and observed that intratumoral CD4+ T cells expressed higher levels of the glucose-deprived signature genes than CD4+ T cells in the draining lymph nodes (dLNs) (Figure 1D). This result suggested that some portion of the CD4+ TILs experienced glucose-deprivation within the tumor microenvironment *in vivo*.

Next, we stimulated functional TH1 CD4+ T cells (isolated from lymphocytic choriomeningitis virus (LCMV)-infected animals) in different concentrations of glucose (ranging from 0.1–10 mM) to directly interrogate the effects of glucose deprivation on production of CD40 ligand (CD40L) and IFN γ —two factors critical for maintaining an immunostimulatory microenvironment in the Braf/Pten melanomas (Ho et al., 2014). This showed that

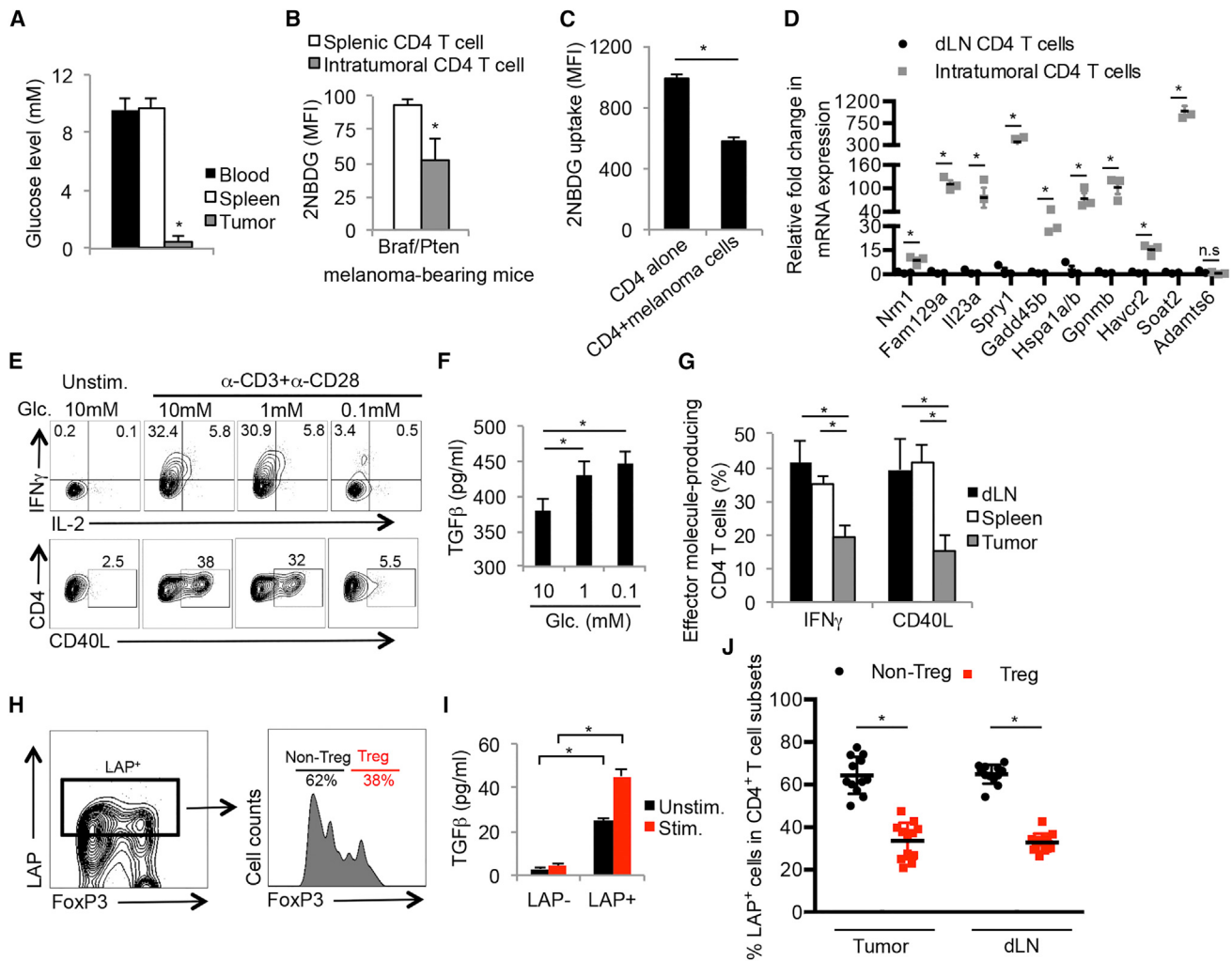


Figure 1. Tumor Microenvironment Deprives Glucose to Infiltrating CD4⁺ T Cells

(A) Bar graphs show the glucose concentration in blood and interstitial fluid of tumors and spleens from Braf/Pten melanoma-bearing mice.

(B and C) Glucose uptake in splenic and intratumoral CD44⁺/CD25^{lo} and CD44⁺/CD25^{hi} CD4⁺ T cells (B) or in T_H1 cells cultured with or without Braf/Pten melanoma cells (C) was determined using fluorescent 2-NBDG and measured by flow cytometry.

(D) The expression of glucose-deprived signature genes in CD4⁺ T cells isolated from melanomas and draining lymph nodes (dLNs) was determined by qRT-PCR.

(E and F) T_H1 CD4⁺ T cells derived from LCMV Armstrong-infected mice were stimulated by anti-CD3/anti-CD28 mAbs in vitro in the indicated glucose concentrations for 5 hr. The expression of IFN γ , IL-2, and CD40L was analyzed by flow cytometry (E), and production of TGF β was determined by ELISA (F).

(G) The production of CD40L and IFN γ in CD4⁺ T cells isolated from the dLN, spleen, or tumors in Braf/Pten mice was analyzed by flow cytometry.

(H) LAP surface expression was compared between activated FoxP3⁺ (T_{reg}) and FoxP3⁻ (non-T_{reg}) CD4⁺ T cells within melanomas using flow cytometry.

(I) Validation of LAP staining as a surrogate for TGF β secreting capability was performed by stimulating purified intratumoral LAP⁺ and LAP⁻ CD44⁺ CD4⁺ T cells with or without anti-CD3/anti-CD28 mAbs for 16 hr and measuring the amount of TGF β in culture supernatants by ELISA.

(J) The frequency of LAP⁺ FoxP3⁺ (T_{reg}) and FoxP3⁻ (non-T_{reg}) CD4⁺ T cells within melanomas or dLNs was assessed using flow cytometry.

Data shown are cumulative of two (A and B, D, H, I) ($n = 3\text{--}6$ mice/group/experiment) and three (G and J) independent experiments ($n = 3\text{--}4$ mice/group/experiment) or representative of three (C, E and F) independent experiments ($n = 3\text{--}5$ group). Data are expressed as mean \pm SD and (C) is presented as mean \pm SEM. * $p < 0.05$ by unpaired Student's t test.

these effector functions were suppressed by limited amounts of glucose (Figure 1E). Conversely, glucose deprivation augmented TGF β production in activated CD4⁺ T cells (Figure 1F), suggesting that glucose deprivation can cause CD4⁺ T cells to switch from immuno-supportive to immuno-suppressive states. Importantly, the CD4⁺ T cells isolated directly ex vivo from melanomas displayed similar functional attributes to the in vitro glucose-deprived TH1 cells. For example, the percentage of CD44hi

CD25^{lo} (non-T_{reg}) CD4⁺ T cells that produced IFN γ or CD40L in the tumors was ~50% lower than that in the spleen or dLN (Figure 1G). Additionally, the expression of the TGF β latency associated peptide (LAP), a surrogate marker for cells competent to produce TGF β , was examined on the CD4⁺ T cells (Figures 1H–J), and this showed that a greater proportion of non-T_{reg} CD4⁺ T cells expressed elevated LAP compared to the FoxP3⁺ Tregs in both the tumors and dLNs (Figure 1J).

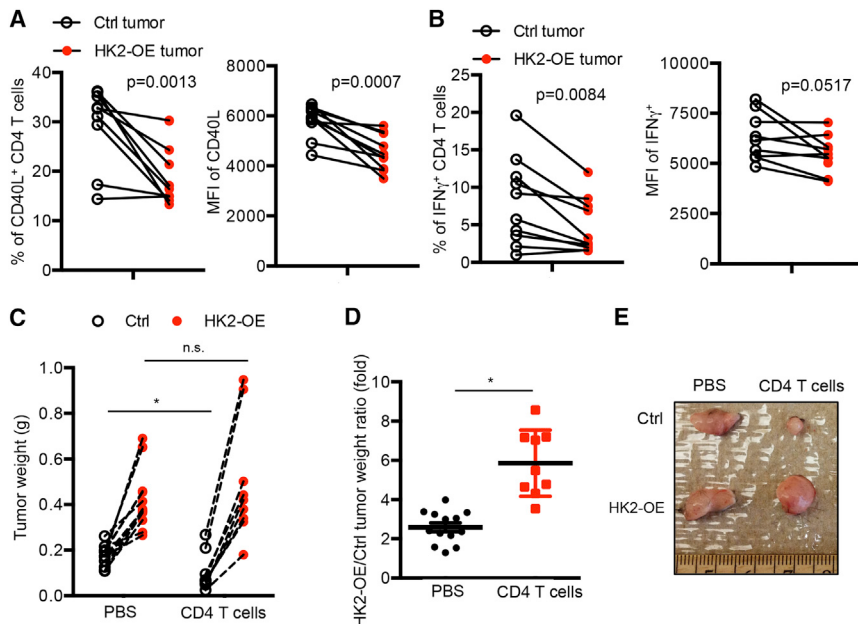


Figure 2. HK2 Overexpression in Melanoma Cells Suppresses CD4⁺ T Cell-Mediated Anti-tumor Responses

(A and B) Control (Ctrl) or HK2-OE Braf/Pten tumors were engrafted into the right and left flanks of C57BL/6 mice. Fourteen days later, the CD4⁺ TILs were isolated, stimulated *in vitro* by anti-CD3/anti-CD28 mAbs for 5 hr and analyzed for CD40L and IFN γ expression by flow cytometry. Left: percentage of CD40L⁺ (A) or IFN γ ⁺ (B); right: mean fluorescence intensity (MFI) of the indicated proteins. (C–E) Ctrl or HK2-OE Braf/Pten tumors were engrafted into the right and left flanks of Rag1-KO mice that were either injected with PBS or reconstituted with CD4⁺ T cells and 14 days later the weight (C and D) and size (E) of tumors was assessed. (C and D) Graphs show tumor weights of the contralateral pairs of ctrl and HK2-OE melanomas collected from same mouse expressed as actual weights (C) or as a ratio (D). Data shown are cumulative of three (A and B) independent experiments ($n = 3\text{--}4$ mice/group) or four (C and D) independent experiments ($n = 2\text{--}4$ mice/group). Data are expressed as mean \pm SD and * $p < 0.05$ by unpaired Student's *t* test.

Collectively, these data demonstrate that CD4⁺ TILs display genetic and functional features associated with glucose-deprivation and suggest that competition between tumor cells and TILs for glucose in the tumor microenvironment could contribute to an immunosuppressive environment.

Increased Rates of Aerobic Glycolysis in Melanoma Cells Suppress CD4⁺ T Cell-Mediated Immunosurveillance

Increased rates of aerobic glycolysis and expression of glycolytic enzymes (e.g., hexokinase 2 [Hk2]) are common hallmarks of cancer cells (Hanahan and Weinberg, 2011), and this may lead to glucose-deprivation and T cell dysfunction in tumors as suggested by the data above. To investigate this hypothesis further, we analyzed the expression of effector T cell genes (e.g., *Ifng* and *Cd40lg*) and markers of glycolysis (e.g., *Hk2*) mRNA within the tumors of 384 melanoma patients (data obtained from The Cancer Genome Atlas [TCGA]) (Cerami et al., 2012; Gao et al., 2013). Interestingly, this showed that the amount of *Cd40lg* and *Ifng* mRNA inversely correlated with *Hk2* mRNA (Figure S2A). To more directly test if the glycolytic rates of tumor cells affect tumor immunosurveillance by CD4⁺ T cells, we established stable clones of the Braf/Pten melanoma cell line (YUMM1.7) that expressed either a control vector or one overexpressing Hk2 (HK2-OE). As expected, HK2-OE tumor cells had higher rates of aerobic glycolysis than the control cells based on extracellular acidification rates (ECAR) using the Seahorse Extracellular Flux Analyzer (Figure S2B) and HK2-OE tumor cells more efficiently suppressed glucose uptake of TH1 CD4⁺ T cells in the co-culture assay (Figure S2C). Then we engrafted control and HK2-OE melanoma cell lines into the left and right flanks, respectively, of wild-type C57BL/6 mice. Two weeks later, the production of CD40L and IFN γ by CD4⁺ TILs re-stimulated directly *ex vivo* was assessed and compared to CD4⁺

T cells isolated from the control melanomas, those isolated from HK2-OE tumors had lower production of CD40L and IFN γ (Figures 2A and 2B and S2D). This result demonstrated that T cell effector functions could be affected by the rates of tumor cell aerobic glycolysis. Next, we compared the growth rates of control and HK2-OE melanoma cell lines engrafted into the left and right flanks, respectively, of Rag1-KO mice that were either reconstituted with CD4⁺ T cells or not. In accord with higher rates of aerobic glycolysis, the HK2-OE melanomas grew faster compared to the control tumors in both groups of mice (Figure 2C). However, the presence of CD4⁺ T cells potently suppressed the growth of control melanoma cells, but had little effect on the HK2-OE melanoma cells (Figures 2C–2E). Taken together, these results support the intriguing model that tumor cells with increased rates of aerobic glycolysis are better able to evade anti-tumor CD4⁺ T cell responses.

Glucose Deprivation Suppresses TCR-Dependent Activation of Ca²⁺ and NFAT Signaling

To better understand how glucose deprivation alters TH1 cell functions, we examined how glycolysis affects TCR signaling after TCR stimulation using several approaches. First, we observed that the induction of the immediate early gene Nur77 (as measured using a Nur77-eGFP reporter that reads out TCR signaling in a Ca²⁺-dependent manner; Moran et al., 2011) was suppressed in glucose-poor conditions or in the presence of 2-DG (Figure 3A). In contrast, the amount of phosphorylated ERK1/2 (pERK1/2) or AKT (pAKTS473 and pAKTT308) was minimally affected following activation of TH1 CD4⁺ T cells in glucose-deprived conditions (Figure S3). The defect in Nur77 induction prompted us to more closely monitor cytoplasmic calcium flux using the ratiometric Ca²⁺-sensitive dyes (Fluo-4 and Fura-Red) and flow cytometry, and this revealed that glucose deprivation profoundly repressed TCR-induced Ca²⁺

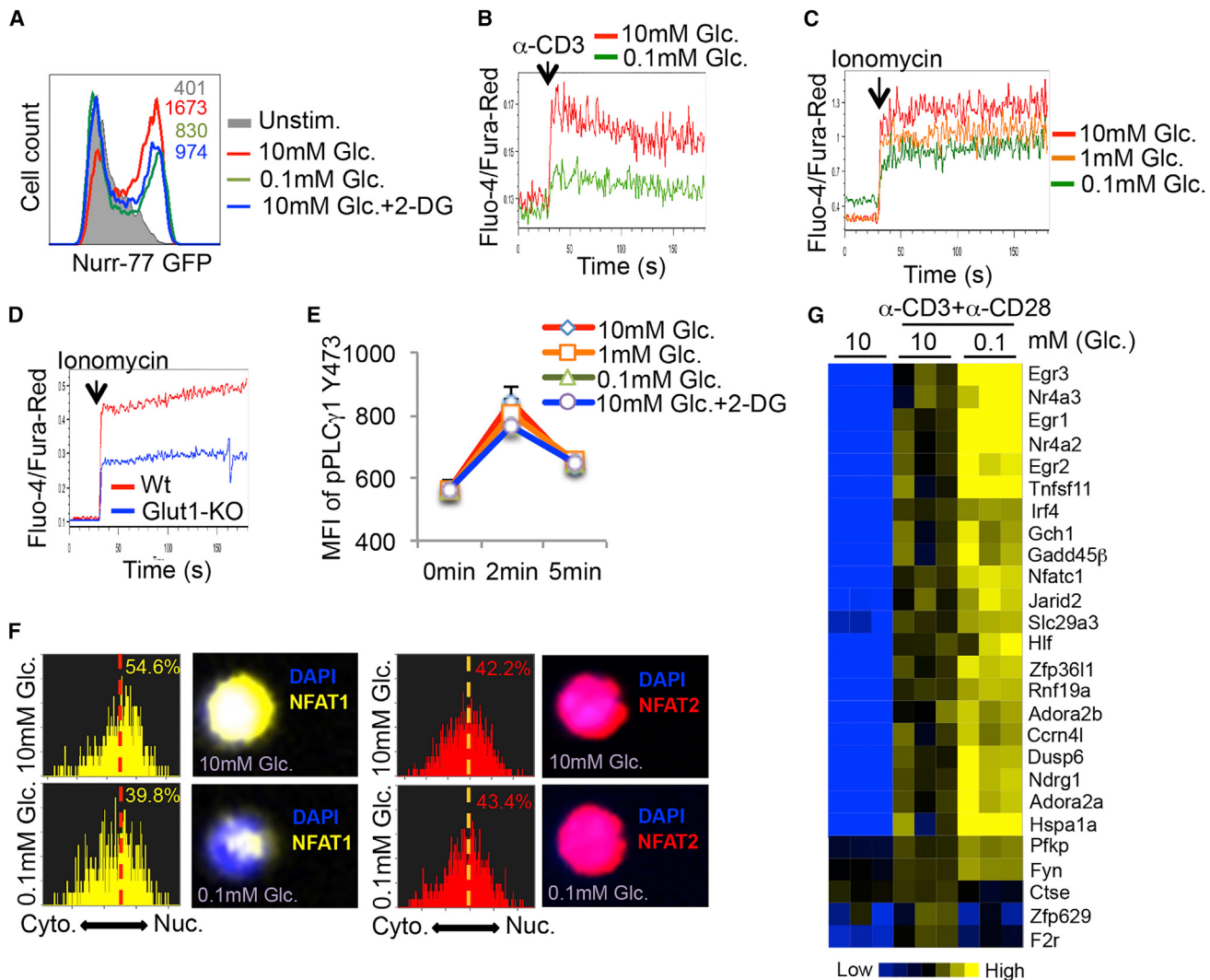


Figure 3. Glycolysis Modulates the Ca^{2+} -NFAT1 Signaling Pathway in CD4+ T Cells

(A) Naive CD4+ T cells from Nurr-77-eGFP mice were left unstimulated or stimulated with anti-CD3/anti-CD28 mAbs for 5 hr in the indicated conditions and GFP fluorescence was measured by flow cytometry. Glc.: glucose; 2-DG: 2-deoxy-D-glucose.

(B and C) Intracellular Ca^{2+} levels were measured in Fluo-4- and Fura-Red-labeled TH1 CD4+ T cells cultured in 10 mM glucose or 0.1 mM glucose before and after activation with anti-CD3 crosslinking antibodies (B) or ionomycin (C). The ratio of Fluo-4 and Fura-Red fluorescence was measured using flow cytometry.

(D) Intracellular Ca^{2+} levels were measured as above in naive CD4+ T cells isolated from wild-type (Wt) or GLUT-1-knockout (Glut1-KO) mice.

(E) T_H1 CD4+ T cells were stimulated with anti-CD3/anti-CD28 in the indicated conditions and amounts of phospho-PLC γ 1 were measured by flow cytometry.

(F) T_H1 cells were stimulated with ionomycin in medium containing 10 mM or 0.1 mM glucose for 10 min and the cytoplasmic versus nuclear distribution of NFAT1 and NFAT2 was determined by Amnis Imagestream. Representative histograms and images show the similarity profiles of NFAT1 (yellow, left) or NFAT2 (red, right) with DAPI staining to measure nuclear localization. The percentage of T cells with nuclear NFAT1 or NFAT2 is shown.

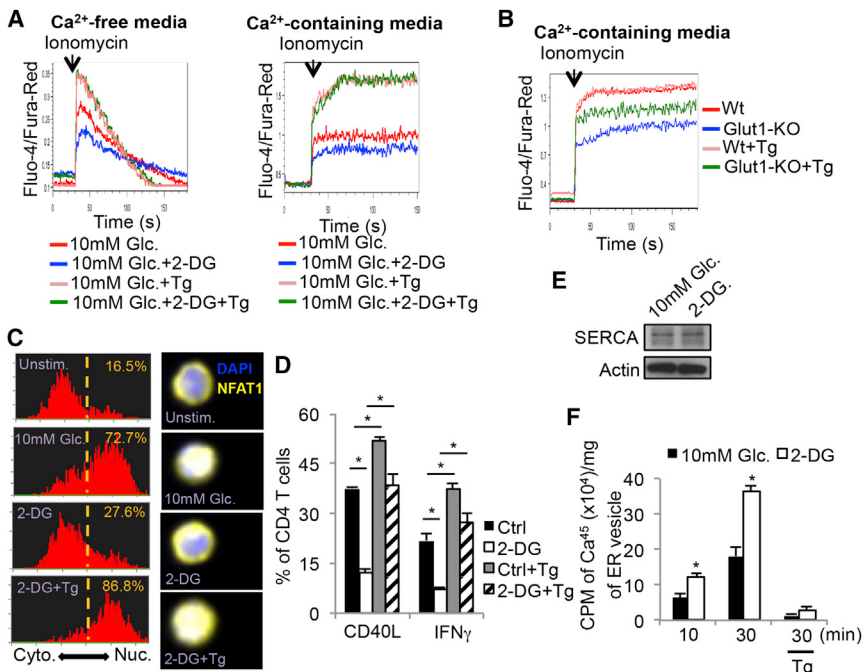
(G) Heat map shows normalized expression of select genes associated with T cell energy (Safford et al., 2005) in T_H1 cells stimulated for 5 hr with anti-CD3/anti-CD28 mAbs in glucose-sufficient (10 mM) or glucose-deficient (0.1 mM) conditions.

Data shown are representative of two (D and E) and three (A–C, F) independent experiments or cumulative of three (G) independent experiments ($n = 2$ mice/group).

flux in activated TH1 cells (Figure 3B). Moreover, reducing aerobic glycolysis in activated TH1 cells by glucose deprivation or deletion of the glucose transporter 1 (Macintyre et al., 2014) also suppressed ionomycin-induced cytosolic Ca^{2+} accumulation (Figures 3C and 3D). This latter result indicated that the defect in Ca^{2+} flux could be IP3-independent because ionomycin triggers Ca^{2+} efflux from the ER in an IP3-independent manner.

In agreement, glucose deprivation did not affect TCR-induced phosphorylation of PLC γ -1 in TH1 cells (Figure 3E). Altogether, these results suggested that glucose-deprivation dampened the magnitude of TCR-induced Ca^{2+} flux, and consequently CD4+ T cell effector functions.

Interestingly, anergic T cells, which have similar functional defects to those observed with glucose-deprivation, also



(F) Ca^{2+} -uptake using radiolabeled 45CaCl_2 was measured in ER microsomal fractions isolated from Jurkat T cells treated with or without 2-DG for 10 or 30 min. Data shown are representative of two (E and F) and three (A and B, C-E) independent experiments ($n = 3/\text{group}$ in D and F). Data are expressed as mean \pm SD and $*p < 0.05$ by unpaired Student's t test.

display defects in Ca^{2+} signaling (Schwartz, 2003). Other work has shown that the reduced Ca^{2+} signaling in anergic CD8 T cells impairs the nuclear localization of NFAT1, but not that of NFAT2, indicating differential sensitivity to cytoplasmic Ca^{2+} levels between these two transcription factors (Srinivasan and Frauwrith, 2007). These phenotypes prompted us to examine the cellular distribution of NFAT1 and 2 and expression of anergy-associated genes in glucose-deprived TH1 cells (Safford et al., 2005). In agreement with the prior study (Srinivasan and Frauwrith, 2007), nuclear translocation of NFAT1, but not NFAT2, was severely compromised in glucose-deprived TH1 cells (Figure 3F). Importantly, 5 hr of glucose deprivation led to increased expression of several “anergy” signature genes, including *Egr2*, *Egr3*, *Irf4*, *Hspa1a*, *Gadd45b*, and *Nfatc1* as previously described (Figure 3G, note the augmented expression of some of these genes in TILs in Figure 1D) (Safford et al., 2005). Collectively, these results identified that glycolysis is critical for sustaining high amounts of Ca^{2+} -NFAT signaling in TH1 cells and that glucose-deprivation results in CD4 T cell dysfunction and expression of anergy-associated genes.

Glycolysis Modulates SERCA-Mediated ER Calcium Uptake Activity

Stimulation of the TCR initially triggers Ca^{2+} efflux from the ER, which subsequently induces extracellular Ca^{2+} import via the calcium-release-activated calcium (CRAC) channel (Feske et al., 2012). To distinguish ER Ca^{2+} efflux from extracellular Ca^{2+} influx, we stimulated CD4+ T cells in the presence or absence of 2-DG with ionomycin in Ca^{2+} -free or Ca^{2+} -containing

Figure 4. Glycolysis Sustains Cytoplasmic Ca^{2+} Accumulation via Modulation of SERCA-Mediated Calcium Reuptake

(A) Intracellular calcium levels were measured in Fluo-4- and Fura-Red-labeled CD4+ T cells cultured in Ca^{2+} -free (left) or Ca^{2+} -containing media (right) in 10 mM glucose or 2-DG with or without thapsigargin (Tg).

(B) Intracellular Ca^{2+} levels were measured as above in naive CD4+ T cells isolated from wild-type (Wt) or GLUT1-knockout (Glut1-KO) mice and cultured in Ca^{2+} -containing media with or without Tg.

(C) Naive CD4+ T cells were left unstimulated or stimulated with ionomycin in the presence of 10 mM glucose, 2-DG or 2-DG plus Tg for 10 min and the cytoplasmic versus nuclear distribution of NFAT1 was determined by Amnis Imagestream. Representative histograms (left) and images (right) show the similarity profiles of NFAT1/DAPI staining to measure NFAT1 nuclear localization. The frequency of T cells with nuclear NFAT1 is shown. (D) Control or 2-DG treated TH1 cells were stimulated with anti-CD3/anti-CD28 mAbs for 5 hr in the absence or presence of Tg. The expression of CD40L and IFN γ was analyzed by flow cytometry. (E) Western blots showing the amount of SERCA protein in Jurkat T cells treated with or without 2-DG for 30 min.

media and found that 2-DG treatment diminished ionomycin-induced cytosolic accumulation in either condition (Figure 4A, compare red and blue lines in left and right). This suggested that glycolysis is important for maintenance of cytosolic Ca^{2+} levels to support T cell activation. Several Ca^{2+} channels expressed on the plasma membrane (plasma membrane Ca^{2+} ATPase: PMCA), mitochondrial membrane (mitochondrial Ca^{2+} uniporter: MCU), and ER membrane (SERCA) could lower cytosolic Ca^{2+} levels, so we next tested if blocking these Ca^{2+} channels could restore Ca^{2+} flux in glucose-deprived T cells. In contrast to blocking PMCA and MCU channels, treatment with the SERCA inhibitor thapsigargin (Tg) increased Ca^{2+} flux in 2-DG treated or Glut1-KO CD4+ T cells (compare blue and green lines, Figures 4A and 4B and Figure S4). This result suggested that glucose-deprived T cells have increased SERCA activity that suppressed maximal Ca^{2+} flux. Importantly, Tg treatment also restored nuclear translocation of NFAT1 (Figure 4C) as well as IFN γ and CD40L production (Figure 4D) in 2-DG treated TH1 cells. Western blotting of Jurkat T cells showed that 2-DG treatment did not affect the overall amounts of SERCA compared to control cells (Figure 4E), suggesting that the increase in ER Ca^{2+} re-uptake stemmed from increased SERCA activity. Indeed, measurement of radio-labeled Ca^{2+} uptake in ER vesicles isolated from Jurkat T cells revealed that 2-DG treatment increased SERCA-dependent Ca^{2+} uptake by ~2-fold compared to the control cells (Figure 4F). Taken together, these findings strongly indicate that glycolysis suppresses SERCA activity and consequently, glucose deprivation leads to defective Ca^{2+} -NFAT signaling and effector functions in glucose-deprived T cells.

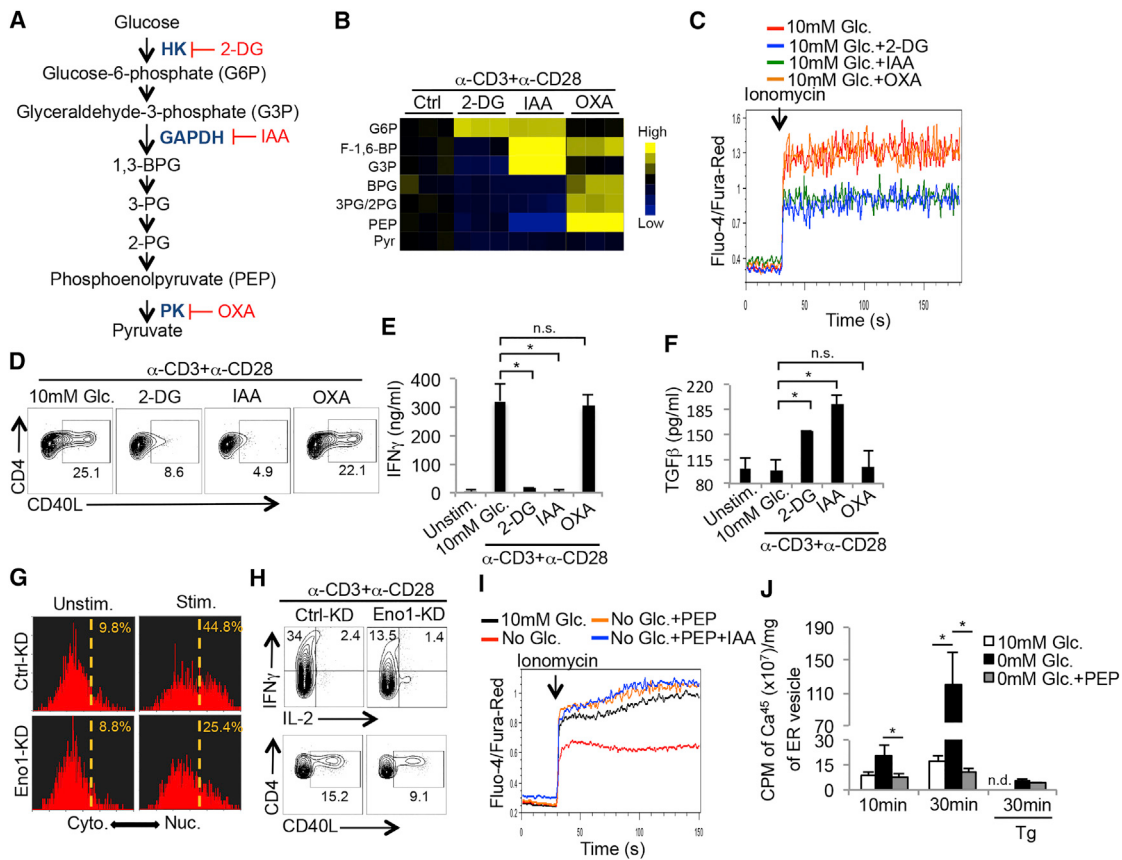


Figure 5. PEP Suppresses SERCA-Mediated ER Calcium Reuptake

(A) Illustration of the glycolysis pathway and the targets of the indicated glycolytic inhibitors. 2-DG: 2-deoxyglucose; IAA: iodoacetate; OXA: oxalate.

(B) Heat map shows the normalized concentrations of the indicated glycolytic metabolites in CD4+ T cells stimulated with anti-CD3/anti-CD28 mAbs for 1 hr in the absence or presence of the glycolytic inhibitors described in (A) as measured by LC-QE-MS.

(C) Intracellular Ca $^{2+}$ levels were measured in Fluo-4- and Fura-Red-labeled T_H1 cells treated with indicated glycolytic inhibitors before and after activation with ionomycin.

(D–F) T_H1 cells were left alone or stimulated with anti-CD3/anti-CD28 mAbs for 5 hr in 10 mM glucose in the absence or presence of indicated glycolytic inhibitors and the expression of CD40L (D), IFN γ (E) and TGF β (Φ) was measured by flow cytometry (D) or ELISA (E and F).

(G and H) CD4+ T cells were transduced with empty vector control retroviruses (RV, Ctrl-KD) or those expressing enolase-1 shRNAi (eno1-KD). RV-infected T cells were left alone or stimulated with ionomycin for 10 min and the cytoplasmic versus nuclear distribution of NFAT1 was determined by Amnis Imagestream as described in Figure 3F (G), or alternatively were stimulated with anti-CD3/anti-CD28 mAbs in vitro in the presence of 10 mM glucose for 5 hr and the expression of IFN γ , IL-2 and CD40L was analyzed by flow cytometry (H).

(I) Intracellular Ca $^{2+}$ levels in CD4+ T cells that were partially permeabilized and recovered in the absence or presence of PEP were measured as in (C) in the absence or presence of glycolytic inhibitor IAA.

(J) Ca $^{2+}$ -uptake assay as described in Figure 4F was performed on ER microsomal fractions isolated from Jurkat T cells cultured in the presence or absence of glucose or exogenous PEP. The addition of Tg served as a specificity control for SERCA-dependent activity.

Data shown are representative of two (H and J) and three (C and D, G and I) independent experiments or cumulative of three (B, E and F) independent experiments. Data are expressed as mean \pm SD and *p < 0.05 by unpaired Student's t test.

The Glycolytic Metabolite Phosphoenolpyruvate Regulates Ca $^{2+}$ -NFAT Signaling in TH1 CD4+ T Cells by Inhibiting SERCA Activity

To determine which steps of glycolysis regulate cytosolic Ca $^{2+}$ accumulation and T cell effector functions, TH1 cells were treated with 2-DG, iodoacetate (IAA) and oxalate (OXA), to inhibit hexokinase (HK), glyceraldehyde phosphate dehydrogenase (GAPDH), and pyruvate kinase (PK), respectively, at doses that showed comparable inhibition of lactate production (Figure 5A and data not shown). The glycolytic metabolites

were examined by high-resolution liquid-chromatography Q-exactive mass spectrometry (LC-QE-MS) in the CD4+ T cells stimulated in the absence or presence of the inhibitors and as expected, the levels of 3- and 2-phosphoglycerate (3-PG/2-PG), and phosphoenolpyruvate (PEP) were suppressed by 2-DG and IAA, but promoted by OXA (Figures 5B and S5A). Interestingly, 2-DG and IAA, but not OXA, suppressed TH1 cell Ca $^{2+}$ flux after ionomycin stimulation (Figure 5C) and CD40L and IFN γ production after TCR stimulation (Figures 5D and 5E). Likewise 2-DG and IAA, but not OXA, augmented TGF β production

(Figure 5F). These results suggested that a metabolite produced downstream of GAPDH and upstream of PK fine-tunes Ca^{2+} signaling and TH1 effector functions.

We hypothesized that such a metabolite may be PEP because of the above inhibitor studies and because TCR activation increases expression of the less-active M2 isoform of pyruvate kinase (PKM2) (Wang et al., 2011a), which allows the accumulation of several metabolic intermediates, including PEP, in proliferating cells (Vander Heiden et al., 2010). To more rigorously confirm the role of PEP in regulating the Ca^{2+} -NFAT pathway, we knocked down enolase 1 (Eno-1), the glycolytic enzyme that converts 2-PG into PEP (Figure S5B), and analyzed NFAT1 nuclear translocation and expression of IFN γ and CD40L in activated CD4+ T cells. This showed that NFAT1 nuclear translocation and the production of IFN γ and CD40L (Figures 5G and 5H) were impaired by Eno-1 knock down. Additionally, treating TH1 CD4+ T cells with PKM2 activator DASS, which will decrease intracellular PEP levels (data not shown) (Anastasiou et al., 2012), similarly suppressed the production of IFN γ and CD40L (Figure S5C). Finally, supplementation of PEP (1 $\mu\text{g}/\text{ml}$), but not fosfomycin (a structurally related analog), to glucose-deprived CD4+ T cells restored Ca^{2+} flux in the presence of IAA (Figures 5I and S5D). Together these experiments narrowing in on the enzymes regulating PEP metabolism in cells, demonstrate that the accumulation of PEP is critical for sustaining Ca^{2+} -NFAT signaling.

To directly test if PEP can inhibit SERCA-mediated calcium uptake, we repeated the ER Ca^{2+} uptake assay by isolating ER vesicles from Jurkat T cells cultured in the presence or absence of glucose. This showed that glucose deprivation promoted ER Ca^{2+} uptake ability; however, PEP supplementation to the ER vesicle fraction significantly suppressed ER Ca^{2+} uptake indicating that PEP can inhibit SERCA activity (Figure 5J). Given that oxidation of SERCA on cysteine residues (e.g., Cys674 and Cys675) reduces SERCA activity (Sharov et al., 2006), we then examined whether glucose deprivation in T cells affects the redox state of SERCA using fluorescent thiol probes that measure the abundance of reduced cysteine residues on proteins. Jurkat T cells were cultured in glucose-replete or -deplete conditions, and ER vesicles were isolated and labeled with fluorescent probes that covalently bind to free thiols. SERCA was then immunoprecipitated from the ER vesicles and the amount of sample fluorescence measured indicated the abundance of reduced cysteines in SERCA. ER vesicles from glucose-deprived cells treated with H_2O_2 or β -mercaptoethanol (β -ME) served as positive controls for maximal cysteine oxidation and reduction, respectively. These experiments showed that compared to cells cultured in glucose-replete medium, glucose-deprivation increased the abundance of free thiols on SERCA, indicative of a more reduced state (Figure S5E). The addition of PEP, but not fosfomycin, to the ER vesicles decreased thiol abundance on SERCA similar to the amounts observed with H_2O_2 (Figure S5E). This result suggests that PEP likely impairs SERCA activity by promoting cysteine oxidation. To further explore this possibility, we found that treating glucose-deprived CD4+ T cells with H_2O_2 , which suppresses SERCA activity via cysteine oxidation (Qin et al., 2013), could restore their ability to flux Ca^{2+} (Figure S5F). Collectively, these results identify a previously uncharacterized role for the metab-

olite PEP in controlling Ca^{2+} signaling through inhibition, and likely the oxidation, of SERCA in T cells. These findings elucidate a nutrient-sensing mechanism by which T cells integrate their functional states with their metabolic states.

Metabolic Reprogramming of TILs Boosts Tumoricidal Activities in the Glucose-Deprived Tumor Microenvironment

The above findings support a model whereby the hyper-anabolic metabolic states of tumor cells reduce the availability of nutrients, such as glucose, and prevent TILs from sustaining Ca^{2+} -NFAT signaling and effector functions, in part, from PEP insufficiency. If so, it may be possible to metabolically reprogram anti-tumor T cells to increase their fitness and function in the tumor microenvironment. Because the data indicated that PEP was a critical metabolite controlling T cells function, we speculated that overexpression of phosphoenolpyruvate carboxykinase 1 (PCK1), which converts oxaloacetate (OAA) into PEP, could bolster the tumoricidal activity of TILs (Figure 6A). To examine this hypothesis, PCK1 (PCK1-OE) was overexpressed in Trp-1 CD4+ T cells specific for the melanoma antigen gp75/tyrosinase-related protein 1 (TRP-1), and this demonstrated that PCK1-OE specifically boosted PEP levels in T cells cultured in glucose-poor conditions (Figure 6B, compare blue and green bars), but had little effect on the amount of PEP above and beyond that normally found in T cells cultured in glucose-rich conditions. In contrast to control cells, PCK1-overexpression also reversed the effects of glucose-deprivation on Ca^{2+} flux and NFAT1 nuclear localization in CD4+ T cells (Figures 6C and 6D). It is important to note that the effects of glucose deprivation and PCK1-OE on CD8 T cell Ca^{2+} flux and effector functions were very similar to those observed in CD4 T cells. For example, blocking PEP accumulation via glycolytic inhibitors or PKM2 activators also diminished CD8+ T cell IFN γ production (Figures S6A and S6B). Additionally, PCK1-overexpression restored Ca^{2+} flux in glucose-deprived CD8+ T cells (Figure S6C). Thus, PCK1-OE lessened the dependence of both CD4 and CD8 T cells on glucose for Ca^{2+} -NFAT1 signaling in glucose-poor conditions.

Next, we examined whether PCK1-OE could enhance the anti-tumor responses of tumor-infiltrating Trp-1 CD4+ T cells. To this end, PCK1-OE or control Trp-1 CD4+ T cells were adoptively transferred into mice that contained engrafted B16 melanomas. Strikingly, PCK-OE increased Trp-1 CD4+ T cell production of IFN γ and CD40L over that of control cells in the tumors, but not in the spleen or draining lymph nodes where glucose is more abundant (Figure 6E). Additionally, relatively higher amounts of costimulatory ligand (CD86) and MHC class I and II expression were observed on TAMs in mice that received PCK1-OE Trp-1 CD4+ T cells compared to those that received control cells (Figure 6F), suggesting that restored effector functions by PCK1-OE Trp-1 CD4+ T cells promoted the maturation of TAMs. Most importantly, transfer of PCK1-OE Trp-1 CD4+ T cells suppressed melanoma growth (Figure 6G) and prolonged the survival of B16 melanoma-bearing mice (Figure 6H) compared to the control T cells. Of note, a similar suppression in tumor growth was observed in separate experiments when PCK1 was overexpressed in Pmel CD8+ T cells, specific for the melanoma antigen gp100 (Figures S6D and S6E). Taken

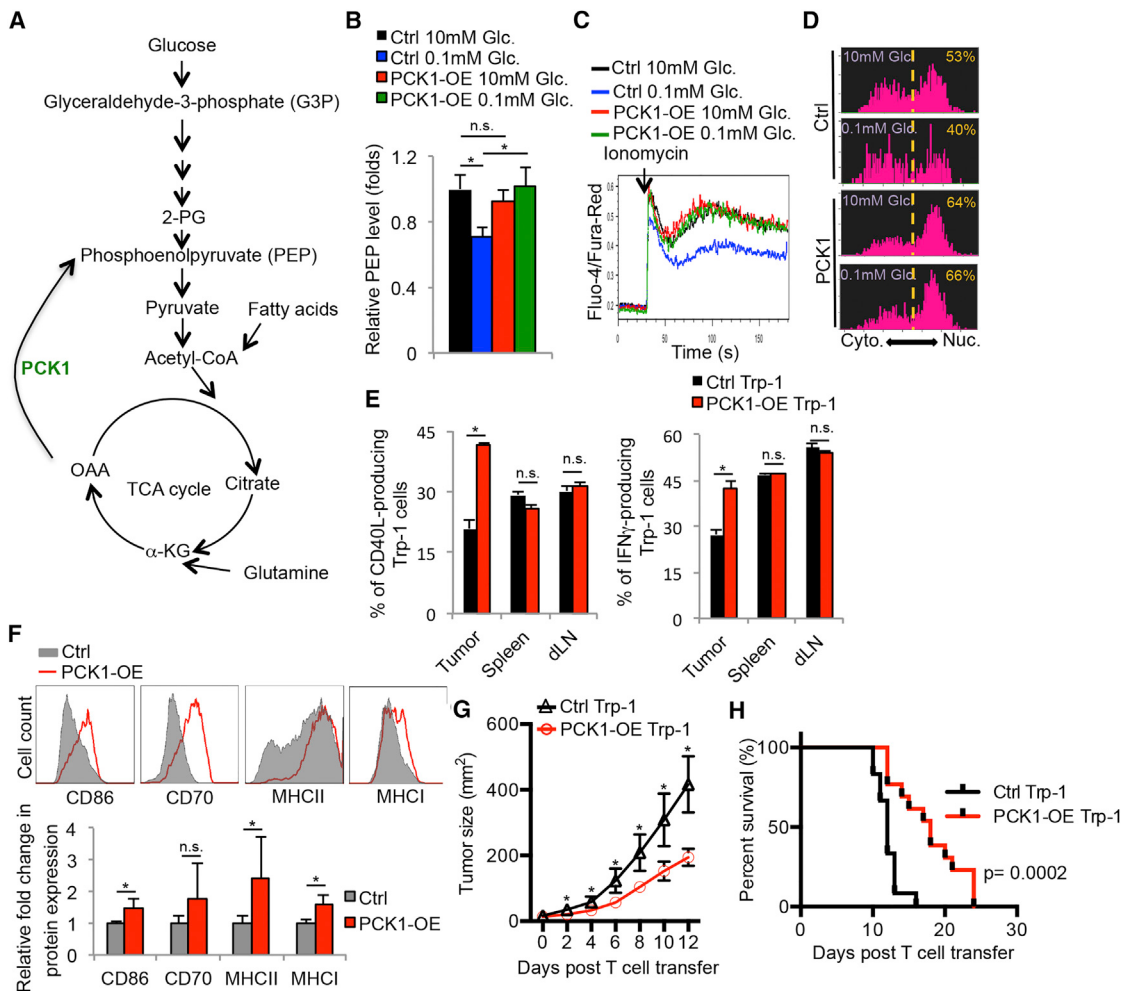


Figure 6. Overexpression of Phosphoenolpyruvate Carboxykinase 1 Boosts Ca²⁺-NFAT Signaling and Tumoricidal Activities of Tumor-Specific CD4+ T Cells

(A) Illustration of the metabolic function of PCK1 in converting OAA to PEP.

(B–D) CD4+ T cells were transduced with control (Ctrl) or PCK-1 overexpressing (PCK1-OE) RVs. (B) Intracellular PEP levels were measured after culturing the RV-transduced cells for 1 hr in the indicated conditions using a fluorescence-based assay. (C) Intracellular Ca²⁺ levels were measured in the transduced CD4+ T cells cultured in 10 mM or 0.1 mM glucose before and after activation with ionomycin.

(D) The cytoplasmic versus nuclear distribution of NFAT1 was determined in the RV-transduced CD4+ T cells stimulated with ionomycin in 10 mM glucose or 0.1 mM glucose for 10 min by Amnis Imagestream as described in Figure 5G.

(E–H) Melanoma-specific Trp-1⁺ CD4+ T cells transduced with Ctrl or PCK-1-OE RVs were adoptively transferred into B16 melanoma-bearing mice. (E and F) Three days later, the donor Trp-1⁺ CD4+ T cells (E) or TAMs (F) were isolated from the indicated tissues and analyzed for expression of the indicated proteins by flow cytometry. Rates of tumor growth (G) and animal survival (H) were determined over time.

Data shown are representative of two (D) and three (C) independent experiments or cumulative of two (F) (n = 2–3 mice/group/experiment), three (B, E) (n = 2–3 mice/group/experiment), and four (G and H) independent experiments (n = 3–4 mice/group/experiment). Data are expressed as mean ± SD (B and F) or mean ± SEM (E) and *p < 0.05 by unpaired Student's t test.

together, our results provide strong evidence that metabolic reprogramming of both CD4 and CD8 T cells is a promising strategy to boost effector functions of tumor-specific T cells in nutrient stressed conditions.

DISCUSSION

It is well appreciated that deregulated metabolism drives tumor cell growth, but it is underappreciated how this affects

the metabolic or functional states of cells that infiltrate tumors (Pearce et al., 2013). Do cancer cells play a “metabolic tug-of-war” with immune cells in tumors? Our work suggests they may because tumors with elevated rates of glycolytic activity were better able to elude T cell immunosurveillance. Further, TILs displayed signs of glucose deprivation, including impaired production of IFN γ and CD40L, but increased expression of TGF β and genes associated with T cell anergy. This led to the discovery that glycolysis controls T cell Ca²⁺-NFAT

signaling and effector functions via the glycolytic metabolite PEP. Importantly, manipulation of this pathway by metabolically reprogramming TILs to increase PEP production yielded stronger anti-tumor responses. This work reveals that a glucose-poor tumor microenvironment can impose immunosuppressive properties on TILs and provides critical proof-of-concept evidence that metabolic reprogramming of tumor-specific T cells can be an adjunct form of immunotherapy.

In addition to other well-known immunosuppressive factors, our work indicates that glucose deprivation is another critical environmental restriction in solid tumors that restrains the tumocidal functions of infiltrating tumor-specific CD4+ T cells. Support for this model also stems from studies showing that tumor-specific T cells regain effector function after being cultured *in vitro* for a short period of time (6–24 hr) in nutrient replete conditions (Wang et al., 2011b). Targeted inhibition of oncogenes, such as BrafV600E and KrasG12D, can stimulate T cell infiltration and production of IFN γ in tumors, and it is possible that these effects stem from their suppression of tumor cell aerobic glycolysis (Ho et al., 2014; Ying et al., 2012). However, further *in vivo* analyses are required to determine if tumor cells restrict glucose to infiltrating T cells through their own glycolytic activities and if this contributes to an immunosuppressive tumor microenvironment. Given that PD-1 signaling suppresses Akt-mTOR pathway and aerobic glycolysis (Parry et al., 2005; Staron et al., 2014), the therapeutic effects of anti-PD-1 immunotherapy will most certainly rely on TILs re-engaging aerobic glycolysis to regain proliferation and function. Indeed, rapamycin treatment abrogated the therapeutic effects of anti-PDL1 blockade on exhausted CD8 T cells during chronic viral infection (Staron et al., 2014). That both tumor cells and activated T cells share similar requirements for anabolic metabolism raises important considerations for designing drug treatments that combine metabolically targeted therapies with immunotherapy. For example, drugs that suppress tumor cell glycolysis may have poor efficacy long-term because of their unintended effects on TIL function. Therefore, as new treatments are tested, the effects of anti-cancer drugs on the metabolism and function of tumor infiltrating immune cells should be considered and examined.

It is clear that certain metabolic pathways serve as “metabolic checkpoints” to control T cell activation and function, but mechanistically how this occurs is not well understood. Our study uncovers a mechanism through which the glycolytic intermediate PEP regulates the amplitude of Ca²⁺ flux and NFAT activation to fine-tune T cell effector function. Although PEP could inhibit SERCA activity and increase its oxidative state, the precise molecular mechanism(s) by which this occurs remains unknown. Possibly PEP directly conjugates to or oxidizes cysteine residues on SERCA or alternatively PEP could serve as a high-energy phosphate donor to phosphorylate SERCA or other proteins that inhibit its activity (Vander Heiden et al., 2010). Future biochemical studies are needed to precisely characterize which residues in SERCA, if any, are modified by PEP.

Metabolic flexibility allows activated T cells to adapt to changes in glucose availability by utilizing alternative substrates

for energy production (Blagih et al., 2015; Frauwirth et al., 2002). Possibly, TILs become dependent on other carbon sources, such as lactic acid and free fatty acids (FFAs) abundant in the tumor microenvironment, and this not only changes the metabolic activities of TILs, but also their effector functions. Indeed, it is interesting to consider which carbon sources are used by the PCK-1 overexpressing T cells to manufacture PEP when glucose-deprived; our preliminary studies *in vitro* suggest that both lactic acid and FFAs may be involved (data not shown). Future in-depth metabolite profiling of TILs will help to characterize the nutrients they consume and the metabolic pathways they exercise *in vivo*, through which, one may develop more robust methods to harness anti-tumor T cell responses via metabolic manipulation.

Overall, our findings describe a metabolic checkpoint for T cell activity in tumors in which a glycolytic metabolite, PEP, serves as an intracellular sensor for glucose availability in the environment to regulate T cell activation and production of effector molecules. Together with another recent discovery identifying a secondary role for GAPDH in inhibiting IFN γ mRNA translation in T cells (Chang et al., 2013), these finding demonstrate that both metabolites and metabolic enzymes have adopted additional roles as metabolic checkpoint regulators to control specialized functions in T cells. From a therapeutic standpoint, better delineation of the metabolic pathways or enzymes differentially utilized by cancer cells and cancer-specific T cells could reveal vulnerable drug-targets in cancer cells. Additionally, rewiring the metabolic activity of TILs, as demonstrated herein and elsewhere (Doedens et al., 2013), could pose a new strategy for enhancing the potency and durability of ACT.

EXPERIMENTAL PROCEDURES

Mice, Tumor Engraftment, and Tumor Induction

The inducible mouse model of melanoma was previously described (Dankort et al., 2009) and Trp-1 TCR transgenic mice were purchased from Jackson Laboratory (Bar Harbor, ME). For melanoma cell engraftment, 2x105 B16 or Braf/Pten melanoma cells were suspended in 50 μ l of PBS and then injected subcutaneously into wild-type C57BL/6 mice (Jackson Laboratory). All mouse experiments were performed according to the approved procedures of the Yale Institutional Animal Care and Use Committee.

ER Vesicle Isolation and Calcium Uptake Assay

Jurkat cells were cultured in glucose-free RPMI with 10% dialyzed FBS in the indicated conditions for 30 min. ER microsomal fractions were then isolated as previously described (Ho et al., 2011). ER vesicles were then analyzed by a calcium uptake assay with 45CaCl₂ as the tracer of calcium uptake, as previously described (Borge and Wolf, 2003). For analysis of the effect of PEP on ER calcium uptake, the calcium uptake assay was performed in the presence of 6 μ M PEP.

Fluorescence Labeling of SERCA Thiol Groups

ER microsomal fractions were then isolated from Jurkat cells cultured in glucose-free RPMI with 10% dialyzed FBS in 10 mM glucose or 0.1 mM glucose for 30 min. Two hundred micrograms of ER microsomal fraction was re-suspended in 20 mM sodium phosphate (pH7.4) buffer and then incubated with control vehicle, 1 μ g/ml PEP, 1 μ g/ml phosphomycin, 5 mM H₂O₂ or 1 mM β -mercaptoethanol for 10 min at 37°C. 200 nM Thiol-fluorescent probe IV (EMD Millipore, Billerica, MA) in the presence of 1% SDS for 30 min at 37°C. Then the reaction mixture was subjected for immunoprecipitation of SERCA or control IgG. The fluorescence intensity of the immunoprecipitates was then determined.

Statistical Analysis

Results were presented as mean \pm SD or mean \pm SEM and statistical significance was examined by an unpaired Student's t test. p value < 0.05 was considered as statistically significant.

ACCESSION NUMBERS

The accession number for the RNA-seq data reported in this paper is SRA: SRP058700.

SUPPLEMENTAL INFORMATION

Supplemental Information includes Supplemental Experimental Procedures and six figures and can be found with this article online at <http://dx.doi.org/10.1016/j.cell.2015.08.012>.

AUTHOR CONTRIBUTIONS

P-C.H., S.M.K., J.D.B., K.L.I., and A.N.M. designed the research. P-C.H., J.D.B., A.N.M., X.L., M.S., Y-C.T., G.C., R.A. G.M., M.W.B. and S.H.K. performed the experiments and bioinformatics analyses. J.C.P. and E.D.A. provided critical reagents. P-C.H., J.W.L., J.C.R., S. F., and S.M.K. analyzed the results. P-C.H. and S.M.K. wrote the manuscript.

ACKNOWLEDGMENTS

This study was supported in part by the Yale Cancer Center, Yale SPORE in Skin Cancer (5 P50 CA121974, R. Halaban, PI), Wade F.B. Thompson/Cancer Research Institute-CLIP grant, Howard Hughes Medical Institute, Melanoma Research Alliance (S.M.K.), Melanoma Research Foundation (M.W.B.), National Cancer Center (P-C.H.), CCFA award (284879, A.N.M.), Alliance for Lupus Research (J.C.R.) and NIH grants R37AI066232 and R01AI074699 to S.M.K., R01HL108006 to J.C.R., R00CA168997 and R01AI110613 to J.W.L.

Received: February 11, 2015

Revised: June 3, 2015

Accepted: July 21, 2015

Published: August 27, 2015

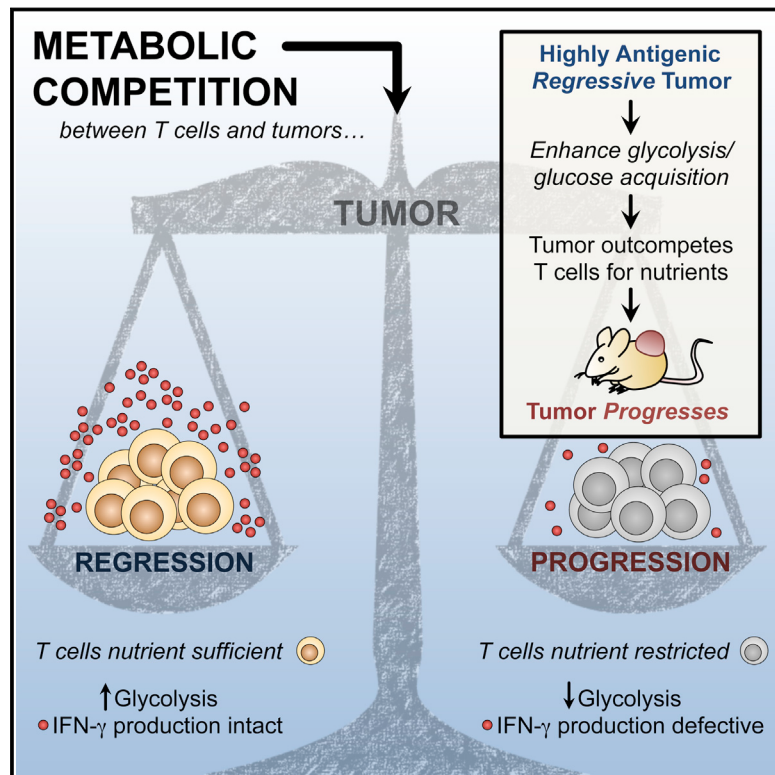
REFERENCES

- Anastasiou, D., Yu, Y., Israelsen, W.J., Jiang, J.K., Boxer, M.B., Hong, B.S., Tempel, W., Dimov, S., Shen, M., Jha, A., et al. (2012). Pyruvate kinase M2 activators promote tetramer formation and suppress tumorigenesis. *Nat. Chem. Biol.* 8, 839–847.
- Baitsch, L., Fuertes-Marraco, S.A., Legat, A., Meyer, C., and Speiser, D.E. (2012). The three main stumbling blocks for anticancer T cells. *Trends Immunol.* 33, 364–372.
- Blagih, J., Coulombe, F., Vincent, E.E., Dupuy, F., Galicia-Vázquez, G., Yurchenko, E., Raissi, T.C., van der Windt, G.J., Viollet, B., Pearce, E.L., et al. (2015). The energy sensor AMPK regulates T cell metabolic adaptation and effector responses in vivo. *Immunity* 42, 41–54.
- Borge, P.D., Jr., and Wolf, B.A. (2003). Insulin receptor substrate 1 regulation of sarco-endoplasmic reticulum calcium ATPase 3 in insulin-secreting beta-cells. *J. Biol. Chem.* 278, 11359–11368.
- Braumüller, H., Wieder, T., Brenner, E., Aßmann, S., Hahn, M., Alkhaled, M., Schilbach, K., Essmann, F., Kneilling, M., Griessinger, C., et al. (2013). T-helper-1-cell cytokines drive cancer into senescence. *Nature* 494, 361–365.
- Callahan, M.K., Wolchok, J.D., and Allison, J.P. (2010). Anti-CTLA-4 antibody therapy: immune monitoring during clinical development of a novel immunotherapy. *Semin. Oncol.* 37, 473–484.
- Cerami, E., Gao, J., Dogrusoz, U., Gross, B.E., Sumer, S.O., Aksoy, B.A., Jacobsen, A., Byrne, C.J., Heuer, M.L., Larsson, E., et al. (2012). The cBio cancer genomics portal: an open platform for exploring multidimensional cancer genomics data. *Cancer Discov.* 2, 401–404.
- Cham, C.M., Driessens, G., O'Keefe, J.P., and Gajewski, T.F. (2008). Glucose deprivation inhibits multiple key gene expression events and effector functions in CD8+ T cells. *Eur. J. Immunol.* 38, 2438–2450.
- Chang, C.H., Curtis, J.D., Maggi, L.B., Jr., Faubert, B., Villarino, A.V., O'Sullivan, D., Huang, S.C., van der Windt, G.J., Blagih, J., Qiu, J., et al. (2013). Post-transcriptional control of T cell effector function by aerobic glycolysis. *Cell* 153, 1239–1251.
- Dankort, D., Curley, D.P., Cartlidge, R.A., Nelson, B., Karnezis, A.N., Damsky, W.E., Jr., You, M.J., DePinho, R.A., McMahon, M., and Bosenberg, M. (2009). Braf(V600E) cooperates with Pten loss to induce metastatic melanoma. *Nat. Genet.* 41, 544–552.
- Doedens, A.L., Phan, A.T., Stradner, M.H., Fujimoto, J.K., Nguyen, J.V., Yang, E., Johnson, R.S., and Goldrath, A.W. (2013). Hypoxia-inducible factors enhance the effector responses of CD8(+) T cells to persistent antigen. *Nat. Immunol.* 14, 1173–1182.
- Feske, S., Skolnik, E.Y., and Prakriya, M. (2012). Ion channels and transporters in lymphocyte function and immunity. *Nat. Rev. Immunol.* 12, 532–547.
- Finlay, D.K., Rosenzweig, E., Sinclair, L.V., Feijoo-Carnero, C., Hukelmann, J.L., Rolf, J., Panteleyev, A.A., Okkenhaug, K., and Cantrell, D.A. (2012). PDK1 regulation of mTOR and hypoxia-inducible factor 1 integrate metabolism and migration of CD8+ T cells. *J. Exp. Med.* 209, 2441–2453.
- Frauwirth, K.A., Riley, J.L., Harris, M.H., Parry, R.V., Rathmell, J.C., Plas, D.R., Elstrom, R.L., June, C.H., and Thompson, C.B. (2002). The CD28 signaling pathway regulates glucose metabolism. *Immunity* 16, 769–777.
- Gao, J., Aksoy, B.A., Dogrusoz, U., Dresdner, G., Gross, B., Sumer, S.O., Sun, Y., Jacobsen, A., Sinha, R., Larsson, E., et al. (2013). Integrative analysis of complex cancer genomics and clinical profiles using the cBioPortal. *Sci. Signal.* 6, pl1.
- Gubser, P.M., Bantug, G.R., Razik, L., Fischer, M., Dimeloe, S., Hoenger, G., Durovic, B., Jauch, A., and Hess, C. (2013). Rapid effector function of memory CD8+ T cells requires an immediate-early glycolytic switch. *Nat. Immunol.* 14, 1064–1072.
- Gullino, P.M., Clark, S.H., and Grantham, F.H. (1964). The Interstitial Fluid of Solid Tumors. *Cancer Res.* 24, 780–794.
- Hanahan, D., and Weinberg, R.A. (2011). Hallmarks of cancer: the next generation. *Cell* 144, 646–674.
- Ho, P.C., Chuang, Y.S., Hung, C.H., and Wei, L.N. (2011). Cytoplasmic receptor-interacting protein 140 (RIP140) interacts with perilipin to regulate lipolysis. *Cell. Signal.* 23, 1396–1403.
- Ho, P.C., Meeth, K.M., Tsui, Y.C., Srivastava, B., Bosenberg, M.W., and Kaech, S.M. (2014). Immune-based antitumor effects of BRAF inhibitors rely on signaling by CD40L and IFN γ . *Cancer Res.* 74, 3205–3217.
- Macintyre, A.N., Gerriets, V.A., Nichols, A.G., Michalek, R.D., Rudolph, M.C., Deoliveira, D., Anderson, S.M., Abel, E.D., Chen, B.J., Hale, L.P., and Rathmell, J.C. (2014). The glucose transporter Glut1 is selectively essential for CD4 T cell activation and effector function. *Cell Metab.* 20, 61–72.
- Maclver, N.J., Michalek, R.D., and Rathmell, J.C. (2013). Metabolic regulation of T lymphocytes. *Annu. Rev. Immunol.* 31, 259–283.
- Maude, S.L., Frey, N., Shaw, P.A., Aplenc, R., Barrett, D.M., Bunin, N.J., Chew, A., Gonzalez, V.E., Zheng, Z., Lacey, S.F., et al. (2014). Chimeric antigen receptor T cells for sustained remissions in leukemia. *N. Engl. J. Med.* 371, 1507–1517.
- Mellman, I., Coukos, G., and Dranoff, G. (2011). Cancer immunotherapy comes of age. *Nature* 480, 480–489.
- Michalek, R.D., Gerriets, V.A., Jacobs, S.R., Macintyre, A.N., Maclver, N.J., Mason, E.F., Sullivan, S.A., Nichols, A.G., and Rathmell, J.C. (2011). Cutting edge: distinct glycolytic and lipid oxidative metabolic programs are essential for effector and regulatory CD4+ T cell subsets. *J. Immunol.* 186, 3299–3303.
- Moran, A.E., Holzapfel, K.L., Xing, Y., Cunningham, N.R., Maltzman, J.S., Punt, J., and Hogquist, K.A. (2011). T cell receptor signal strength in Treg and iNKT cell development demonstrated by a novel fluorescent reporter mouse. *J. Exp. Med.* 208, 1279–1289.

- Parry, R.V., Chemnitz, J.M., Frauwirth, K.A., Lanfranco, A.R., Braunstein, I., Kobayashi, S.V., Linsley, P.S., Thompson, C.B., and Riley, J.L. (2005). CTLA-4 and PD-1 receptors inhibit T-cell activation by distinct mechanisms. *Mol. Cell. Biol.* 25, 9543–9553.
- Pearce, E.L., Poffenberger, M.C., Chang, C.H., and Jones, R.G. (2013). Fueling immunity: insights into metabolism and lymphocyte function. *Science* 342, 1242454.
- Qin, F., Siwik, D.A., Lancel, S., Zhang, J., Kuster, G.M., Luptak, I., Wang, L., Tong, X., Kang, Y.J., Cohen, R.A., and Colucci, W.S. (2013). Hydrogen peroxide-mediated SERCA cysteine 674 oxidation contributes to impaired cardiac myocyte relaxation in senescent mouse heart. *J. Am. Heart Assoc.* 2, e000184.
- Safford, M., Collins, S., Lutz, M.A., Allen, A., Huang, C.T., Kowalski, J., Blackford, A., Horton, M.R., Drake, C., Schwartz, R.H., and Powell, J.D. (2005). Egr-2 and Egr-3 are negative regulators of T cell activation. *Nat. Immunol.* 6, 472–480.
- Schwartz, R.H. (2003). T cell anergy. *Annu. Rev. Immunol.* 21, 305–334.
- Sharov, V.S., Dremina, E.S., Galeva, N.A., Williams, T.D., and Schöneich, C. (2006). Quantitative mapping of oxidation-sensitive cysteine residues in SERCA in vivo and in vitro by HPLC-electrospray-tandem MS: selective protein oxidation during biological aging. *Biochem. J.* 394, 605–615.
- Shiao, S.L., Ganeshan, A.P., Rugo, H.S., and Coussens, L.M. (2011). Immune microenvironments in solid tumors: new targets for therapy. *Genes Dev.* 25, 2559–2572.
- Smith-Garvin, J.E., Koretzky, G.A., and Jordan, M.S. (2009). T cell activation. *Annu. Rev. Immunol.* 27, 591–619.
- Srinivasan, M., and Frauwirth, K.A. (2007). Reciprocal NFAT1 and NFAT2 nuclear localization in CD8+ anergic T cells is regulated by suboptimal calcium signaling. *J. Immunol.* 179, 3734–3741.
- Staron, M.M., Gray, S.M., Marshall, H.D., Parish, I.A., Chen, J.H., Perry, C.J., Cui, G., Li, M.O., and Kaech, S.M. (2014). The transcription factor FoxO1 sustains expression of the inhibitory receptor PD-1 and survival of antiviral CD8(+) T cells during chronic infection. *Immunity* 41, 802–814.
- Vander Heiden, M.G., Locasale, J.W., Swanson, K.D., Sharfi, H., Heffron, G.J., Amador-Noguez, D., Christofk, H.R., Wagner, G., Rabinowitz, J.D., Asara, J.M., and Cantley, L.C. (2010). Evidence for an alternative glycolytic pathway in rapidly proliferating cells. *Science* 329, 1492–1499.
- Wang, R., Dillon, C.P., Shi, L.Z., Milasta, S., Carter, R., Finkelstein, D., McCormick, L.L., Fitzgerald, P., Chi, H., Munger, J., and Green, D.R. (2011a). The transcription factor Myc controls metabolic reprogramming upon T lymphocyte activation. *Immunity* 35, 871–882.
- Wang, S.F., Fouquet, S., Chapon, M., Salmon, H., Regnier, F., Labroquère, K., Badoual, C., Damotte, D., Validire, P., Maubec, E., et al. (2011b). Early T cell signalling is reversibly altered in PD-1+ T lymphocytes infiltrating human tumors. *PLoS ONE* 6, e17621.
- Ward, P.S., and Thompson, C.B. (2012). Metabolic reprogramming: a cancer hallmark even warburg did not anticipate. *Cancer Cell* 21, 297–308.
- Wherry, E.J. (2011). T cell exhaustion. *Nat. Immunol.* 12, 492–499.
- Wolchok, J.D., Kluger, H., Callahan, M.K., Postow, M.A., Rizvi, N.A., Lesokhin, A.M., Segal, N.H., Ariyan, C.E., Gordon, R.A., Reed, K., et al. (2013). Nivolumab plus ipilimumab in advanced melanoma. *N. Engl. J. Med.* 369, 122–133.
- Yang, M., Soga, T., and Pollard, P.J. (2013). Oncometabolites: linking altered metabolism with cancer. *J. Clin. Invest.* 123, 3652–3658.
- Ying, H., Kimmelman, A.C., Lyssiotis, C.A., Hua, S., Chu, G.C., Fletcher-Sanikone, E., Locasale, J.W., Son, J., Zhang, H., Coloff, J.L., et al. (2012). Oncogenic Kras maintains pancreatic tumors through regulation of anabolic glucose metabolism. *Cell* 149, 656–670.
- Zheng, Y., Delgoffe, G.M., Meyer, C.F., Chan, W., and Powell, J.D. (2009). Anergic T cells are metabolically anergic. *J. Immunol.* 183, 6095–6101.

Metabolic Competition in the Tumor Microenvironment Is a Driver of Cancer Progression

Graphical Abstract



Authors

Chih-Hao Chang, Jing Qiu, David O'Sullivan, ..., Robert D. Schreiber, Edward J. Pearce, Erika L. Pearce

Correspondence

pearce@ie-freiburg.mpg.de

In Brief

Glucose consumption by antigenic tumors can metabolically restrict T cells, directly dampening their effector function and allowing tumor progression. Checkpoint blockade therapy may correct this resource imbalance through a direct effect in the tumor cells.

Highlights

- Tumor cells and TILs compete for glucose within the tumor niche
- Metabolic competition can drive cancer progression
- Checkpoint blockade antibodies alter the metabolic balance in a tumor
- PD-L1 promotes Akt/mTOR activation and glycolysis in tumor cells

Metabolic Competition in the Tumor Microenvironment Is a Driver of Cancer Progression

Chih-Hao Chang,^{1,2} Jing Qiu,^{1,2,4} David O'Sullivan,^{1,4} Michael D. Buck,^{1,4} Takuro Noguchi,¹ Jonathan D. Curtis,^{1,4} Qiongyu Chen,¹ Mariel Gindin,¹ Matthew M. Gubin,¹ Gerritje J.W. van der Windt,^{1,3} Elena Tomic,¹ Robert D. Schreiber,¹ Edward J. Pearce,¹ and Erika L. Pearce^{1,4,*}

¹Department of Pathology and Immunology, Washington University School of Medicine, St. Louis, MO, 63110, USA

²Co-first author

³Present Address: Academic Medical Center, 1105 AZ Amsterdam, Netherlands

⁴Present Address: Max Planck Institute of Immunobiology and Epigenetics, Freiburg 79108, Germany

*Correspondence: pearce@ie-freiburg.mpg.de

<http://dx.doi.org/10.1016/j.cell.2015.08.016>

SUMMARY

Failure of T cells to protect against cancer is thought to result from lack of antigen recognition, chronic activation, and/or suppression by other cells. Using a mouse sarcoma model, we show that glucose consumption by tumors metabolically restricts T cells, leading to their dampened mTOR activity, glycolytic capacity, and IFN- γ production, thereby allowing tumor progression. We show that enhancing glycolysis in an antigenic “regressor” tumor is sufficient to override the protective ability of T cells to control tumor growth. We also show that checkpoint blockade antibodies against CTLA-4, PD-1, and PD-L1, which are used clinically, restore glucose in tumor microenvironment, permitting T cell glycolysis and IFN- γ production. Furthermore, we found that blocking PD-L1 directly on tumors dampens glycolysis by inhibiting mTOR activity and decreasing expression of glycolysis enzymes, reflecting a role for PD-L1 in tumor glucose utilization. Our results establish that tumor-imposed metabolic restrictions can mediate T cell hyporesponsiveness during cancer.

INTRODUCTION

Establishing why some cancers progress while others do not is a longstanding challenge in immunology. Destruction of strongly immunogenic tumors is a critical part of the antitumor immune response. However, cancers that express weakly immunogenic antigens evade killing and this can be a primary mechanism of tumor progression (Vesely and Schreiber, 2013). Tumors are also known to escape immunity via T cell dysfunction or hyporesponsiveness. Anergy, exhaustion, and senescence, have all been described in T cells from cancer patients (Crespo et al., 2013; Wherry, 2011)—and chronic TCR stimulation, lack of costimulation, and active suppression by other cells are implicated in T cell dysfunction. However, whether other mechanisms exist, or precisely how T cell hyporesponsiveness in tumors is established, remains unclear.

Nutrient competition between cells can influence cell growth, survival, and function. A fierce competition likely exists between cells in the tumor microenvironment, as demand for resources in this niche is high. Metabolic interplay between tumors and immune cells has been demonstrated. Tumor cells can express indoleamine 2,3-dioxygenase, an enzyme that depletes tryptophan and inhibits T cell proliferation (Munn and Mellor, 2013; Munn et al., 1999). Tumor-derived lactate can also suppress T cell function by blocking lactate export (Fischer et al., 2007), which disrupts their ability to maintain aerobic glycolysis. Aerobic glycolysis is required for optimal T cell effector function (Cham et al., 2008), but not for activation, proliferation, or survival (Chang et al., 2013). We previously found that in vitro, tumor cells outcompete T cells for glucose, and this lack of glucose directly impedes cytokine production that can be critical for tumor clearance. Since many tumors have high rates of glycolysis (Gatenby and Gillies, 2004; Warburg, 1956), we hypothesized that tumor-infiltrating CD8 $^{+}$ T lymphocytes (TILs) could experience a loss of function, due to altered metabolism resulting from tumor-imposed glucose restriction. We sought to establish whether glucose competition in the tumor microenvironment, in its own right, could determine cancer progression by regulating the “nutrient-fed” state of TILs, and thus their functionality.

RESULTS

Tumors Glucose-Restrict T Cells, Altering Their Metabolism and Function

We used an established mouse model of regressing and progressing tumors (Gubin et al., 2014; Matsushita et al., 2012). D42m1-T2 (R tumor) is a regressor clone of the d42m1 sarcoma that expresses the major rejection antigen mutant spectrin- β 2. After transplantation into mice, tumor rejection occurs at ~day 12 in a manner that depends on IFN- γ production from TILs (Matsushita et al., 2012). D42m1-T3 (P tumor) is a progressor clone of d42m1 that lacks this rejection antigen and grows progressively after transplantation (Figure 1A). We cultured R or P tumors with activated C3 T cells, which recognize mutant spectrin- β 2 (Matsushita et al., 2012) and measured IFN- γ production. We predicted that regardless of glucose competition, C3 T cells cultured with R tumor cells might produce more IFN- γ , since they would be stimulated by antigen on the R tumor cells, while

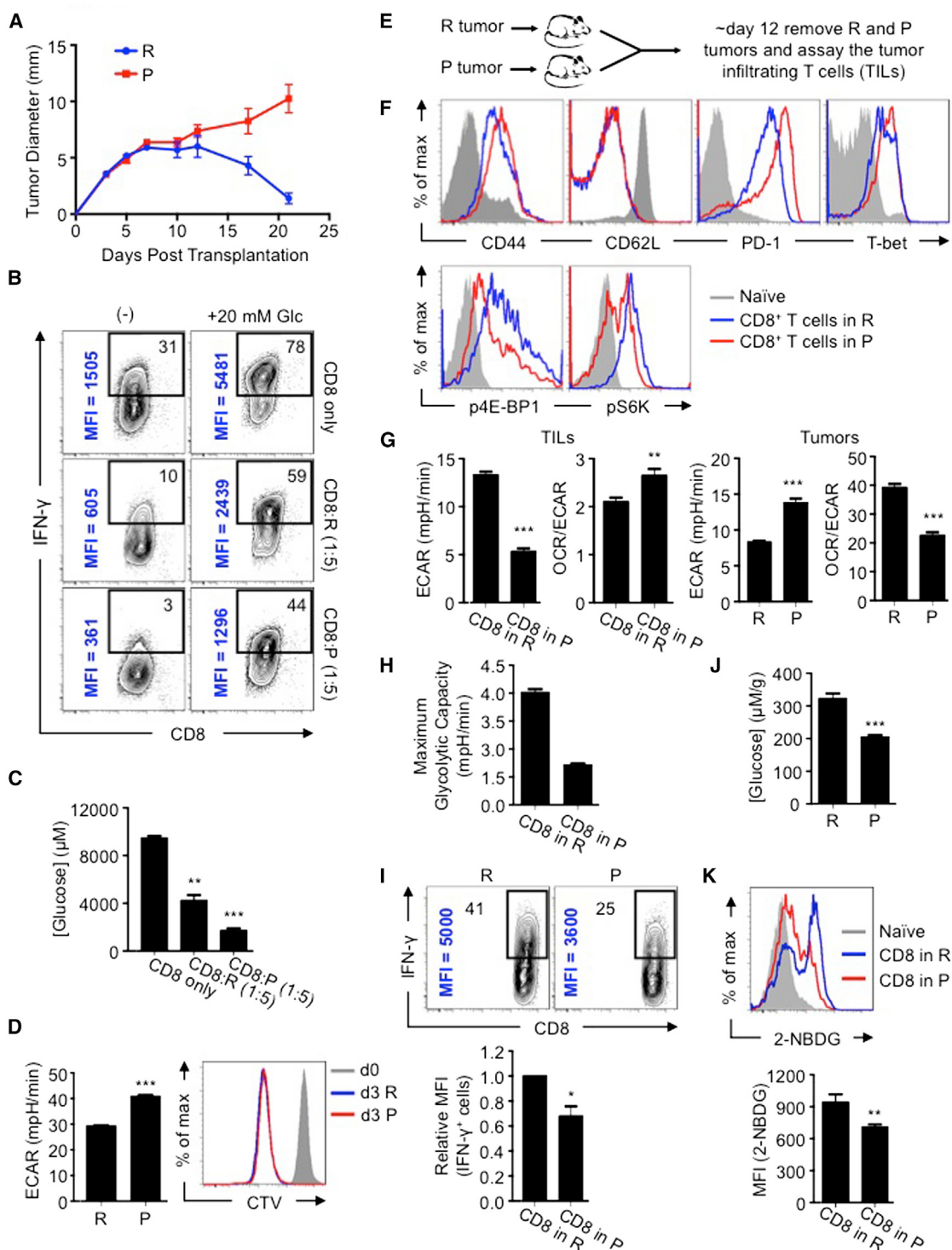


Figure 1. Tumor-Mediated Glucose Restriction Alters T cell Metabolism and Dampens Their Ability to Produce Cytokine

(A) 1×10^6 d42m1 derived R or P tumor cells were injected s.c. into 129S6 mice ($n = 5$). Tumor size is shown as average of two perpendicular diameters \pm SEM from 10 mice of 2 independent experiments.

(B) Activated C3 T cells were cultured alone, or with 1:5 P or R cells for 24h, then PMA/ionomycin stimulated \pm 20 mM additional glucose (Glc) for 5h and IFN- γ measured by FACS. % of IFN- γ $^{+}$ T cells (top right) and mean fluorescence intensity (MFI) (vertical); representative of ≥ 2 independent experiments.

(C) Glucose concentrations in cultures (B) before stimulation; represent ≥ 2 independent experiments, shown as mean \pm SEM, ** $p = 0.0087$, *** $p = 0.0011$.

(legend continued on next page)

C3 T cells cultured alone, or with P tumor cells, would make less as they would receive no additional stimulation. However, C3 T cells cultured alone produced more IFN- γ than when cultured with R tumor cells, and C3 T cells cultured with P tumor cells made the least (Figure 1B). Similar results in IFN- γ production were observed when tumors were cultured with activated polyclonal T cells (data not shown). Furthermore, IFN- γ production correlated to the amount of glucose that remained in the media after co-culture (Figure 1C). We added glucose to the co-cultures and IFN- γ production significantly increased (Figure 1B), indicating that glucose utilization, and thus competition for this sugar, was directly regulating T cell effector function. We confirmed that the extracellular acidification rate (ECAR) (Nicholls et al., 2010), an indicator of aerobic glycolysis, the process where glucose is converted to lactate in the presence of oxygen, was higher in the P than the R tumor (Figure 1D, left), supporting that the P tumor consumes more glucose (Figure 1C). Although the ECAR of these tumors differed, their rates of proliferation *in vitro* were similar (Figure 1D, right), demonstrating that glycolysis is not directly coupled to proliferation in these cells. To further explore glucose competition, we impaired R tumor glycolysis with an inhibitor of mechanistic target of rapamycin (mTOR) (Kim et al., 2002; Laplante and Sabatini, 2012), or promoted glycolysis with the Akt activator 4-hydroxytamoxifen (4-HT) (Doughty et al., 2006; Kohn et al., 1998) (Figure S1A). We cultured tumor cells with activated OT-I T cells, which recognize Ova peptide and cannot mediate an antigen-specific response against this tumor, allowing us to assess cytokine responses independently of antigen-specific stimulation. Upon PMA/ionomycin stimulation, T cells cultured with rapamycin-pretreated R tumor cells produced more IFN- γ than those with untreated tumor cells (Figure S1B), while T cells cultured with 4-HT-pretreated R tumor cells produced less IFN- γ (Figure S1C). Adding glucose enhanced IFN- γ production in a dose dependent manner (Figure S1C), indicating that tumor and T cells competed for glucose.

Although R and P tumors differ in antigenicity, tumor-specific T cells infiltrate both tumors (Gubin et al., 2014; Matsushita et al., 2012). TILs in the R and P tumors were activated and expressed T-bet (Figures 1E and 1F, top), suggesting that TILs from either tumor were transcriptionally competent to produce IFN- γ (Anichini et al., 2010; Parish and Kaech, 2009). However, as has been shown (Gubin et al., 2014), TILs in the P tumors were PD-1^{hi}, consistent with hyporesponsiveness (Ahmadzadeh et al., 2009; Baitsch et al., 2011). Grossly, the immune cell infiltrates were similar in R and P tumors, although the relative fre-

quency of T regulatory (Treg) cells and the balance of M1 versus M2 macrophages differed (Figures S1D–S1F). These results suggested that while activated TILs infiltrate both tumors, TILs in the P tumor might be hyporesponsive.

We wondered whether higher glycolysis in P tumors limited glucose in the microenvironment and contributed to TIL hyporesponsiveness. mTOR is an environmental sensor, and mTOR pathway signals decrease when nutrients are restricted (Gate-ny and Gillies, 2004; Kim et al., 2002). We reasoned that mTOR activity would directly reflect TIL nutrient status. P-TILs had decreased 4E-BP1 and S6 kinase phosphorylation compared to R-TILs (Figure 1F, bottom). These data support the view that P tumors, which consume more glucose (Figure 1C) and display higher ECAR (Figure 1D, left), and thus have a higher glycolytic rate, impose a more severe glucose restriction on TILs than R tumors.

While many signals exist in tumors that dampen T cells (Francisco et al., 2010; Keir et al., 2008; Simpson et al., 2013), we focused on whether metabolic competition in tumors is a fundamental force that drives immune cell dysfunction. ECAR of P-TILs was lower than R-TILs (Figure 1G, left), indicating less aerobic glycolysis. Unlike R-TILs, P-TILs did not robustly augment glycolysis when respiration was blocked (Figure 1H). Ex vivo P tumor cells also exhibited higher ECAR than R tumor cells (Figure 1G, right), which was inversely proportional to the metabolism of TILs isolated from that tumor (Figure 1G, left), suggesting a metabolic interplay between tumors and TILs. After re-stimulation, P-TILs produced less IFN- γ than R-TILs (Figure 1I) and glucose concentration in the P tumor milieu was lower (Figure 1J). These data link elevated ECAR of P tumors with lower available glucose in the tumor microenvironment. To directly address whether P-TILs are glucose-restricted, we injected the fluorescent glucose analog 2-NBDG and tracked its uptake by TILs. P-TILs acquired less 2-NBDG than R-TILs (Figure 1K), which is consistent with their reduced ECAR (Figure 1G, left). Taken together, these results suggest that TILs are glucose-restricted in the P tumor and that this could account for their impaired glycolytic capacity and effector function.

Tumor-Imposed Nutrient Restrictions Can Lead to T Cell Hyporesponsiveness, Even When Tumors Are Highly Antigenic

Antigen-specific T cell responses are critical for tumor clearance (Baitsch et al., 2011; Matsushita et al., 2012) and mutant spectrin- β 2 expressed by R (but not P) tumors is an important target for tumor rejection (Matsushita et al., 2012). Given that the

(D) ECAR and R or P tumor proliferation. CellTrace Violet (CTV) labeled cells were measured for proliferation at day 0 and 3, representative of ≥ 3 independent experiments, ***p = 0.001.

(E) R or P tumors were injected s.c. into 129S6 mice and TILs isolated at ~day 12.

(F) CD44, CD62L, PD-1, T-bet, phosphorylated 4E-BP1 (p4E-BP1) and S6K (pS6K) expression in TILs by FACS, representative of ≥ 3 independent experiments.

(G) ECAR and OCR/ECAR of ex vivo tumor cells and TILs. OCR (O_2 consumption rate) is an indicator of OXPHOS. Data shown as mean \pm SEM from 3 independent experiments. **p = 0.003, ***p = 0.001.

(H) Maximum glycolytic capacity of TILs. Bar graph shown as mean \pm SEM, representative of 2 independent experiments.

(I) IFN- γ production in TILs measured 5h after PMA/ionomycin stimulation. Contour plots (above) and MFI of IFN- γ producing cells (below). Representative of ≥ 3 independent experiments.

(J) Glucose concentration in extracellular milieu of tumors, ***p = 0.0005. Data averaged from 5 mice.

(K) 2-NBDG was injected i.v. into tumor-bearing mice and tumors harvested 15 min later. Histogram (above) depicts TIL 2-NBDG uptake. Bar chart (below) shows mean MFI \pm SEM from 3 mice. **p = 0.0147. See also Figure S1.

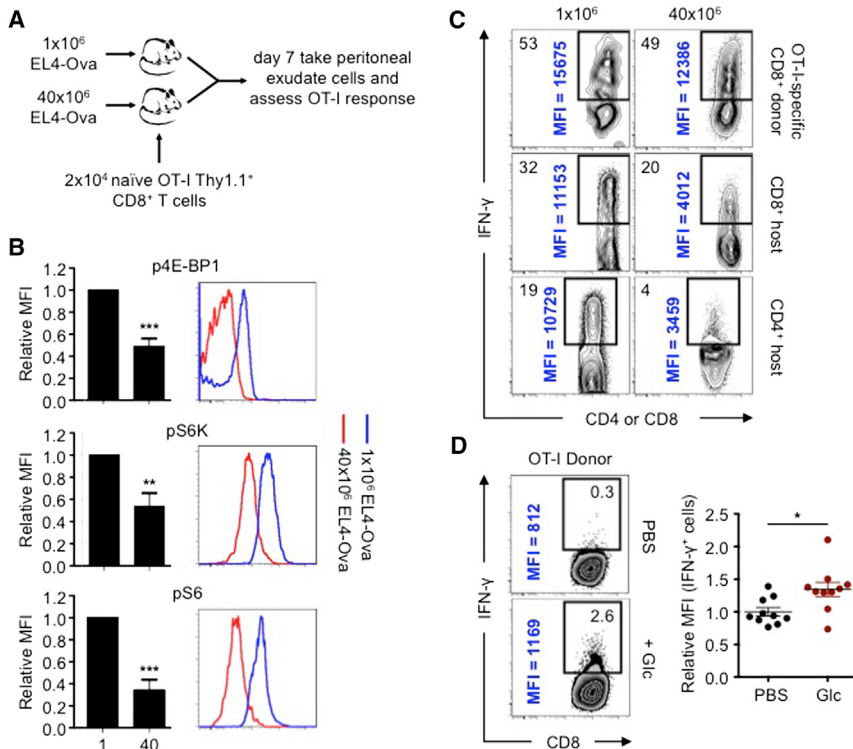


Figure 2. In Vivo Competition for Glucose Modulates mTOR Activity and Cytokine Production in Antigen-Specific T Cells

(A) 1×10^6 or 40×10^6 EL4-Ova cells were injected i.p. into C57BL/6 mice that received 2×10^4 naive OT-I Thy1.1⁺ T cells i.v. Cells in the peritoneal cavity were assessed at day 7. (B) Phosphorylated p4E-BP1 (p4E-BP1), S6K (pS6K), and S6 (pS6) of OT-I T cells assessed by FACS and relative MFI from mice transplanted with 1×10^6 EL4-Ova cells (1) or 40×10^6 EL4-Ova cells (40) normalized to MFI of T cells from mice injected with 1×10^6 EL4-Ova cells. Bar graphs shown as mean \pm SEM from 4 independent experiments. **p = 0.0085, ***p = 0.001.

(C) IFN- γ production by donor OT-I T cells and CD8⁺ and CD4⁺ host T cells 5h post-PMA/ionomycin restimulation; % of IFN- γ ⁺ T cells (top left) and MFI of IFN- γ ⁺ cells (vertical), representative of 2 independent experiments.

(D) Donor OT-I T cell in vivo IFN- γ production. Mice were injected i.p. with EL4-Ova cells and congenic naive OT-I T cells i.v. Mice were injected 7 days later i.p. with BFA and PBS or glucose, and again 2.5h later. Cells were harvested 5h after the first injection and analyzed by FACS. Dot plots show MFI of IFN- γ ⁺ cells relative to mice treated with PBS. Dots represent individual mice; horizontal bars indicate mean \pm SEM from 2 independent experiments. *p = 0.0142.

antigenicity of R and P tumors differs, we designed experiments to address how nutrient competition alone could affect TIL activity. We began by using EL4 tumors that express Ova (EL4-Ova) and OT-I T cells, allowing us to investigate the impact of nutrient limitation in T cells with defined antigen specificity. We enhanced nutrient restriction by increasing tumor cell number. We injected either 1×10^6 or 40×10^6 EL4-Ova cells intraperitoneally (i.p.) and then intravenously (i.v.) transferred 2×10^4 naive OT-I T cells into mice (Figure 2A). OT-I T cells infiltrated the peritoneal cavities of mice with high or low tumor burdens; however, they displayed lower mTOR activity in mice injected with 40×10^6 tumor cells (Figure 2B). Moreover, these cells produced less IFN- γ after restimulation, which was also apparent in endogenous T cells that had entered the peritoneal cavity as part of the antitumor response (Figure 2C). In attempt to transiently enhance glucose levels in mice that received OT-I T cells and 40×10^6 EL4-Ova cells, we injected a bolus of glucose or PBS 2.5 and 5 hr prior to assessing OT-I T cell IFN- γ production. We concurrently injected brefeldin A (BFA) into these mice to capture in situ IFN- γ production. The T cells in the glucose-injected mice produced more IFN- γ (Figure 2D). These data show that antigen-specific T cell effector function can be affected by tumor cell numbers and glucose concentrations in vivo, suggesting that tumor-imposed nutrient-restriction of T cells can contribute to hyporesponsiveness.

Nutrient Competition between Tumors and T Cells Can Regulate Cancer Progression

The experiments in Figure 2 show that T cell hyporesponsiveness developed despite the presence of more antigen, differing

from published data showing that increases in cell-free antigen concentrations promote T cell IFN- γ production (Constant et al., 1995). We reasoned that when antigen is sufficient, tumors might inhibit immunity through nutrient consumption, leaving TILs at a metabolic disadvantage. We aimed to alter tumor metabolism directly so that we could compare between groups using the same tumor with equal cell numbers, removing the confounding factor of differing antigenicity. Tumor cells cultured for extended periods of time in low glucose adapt by increasing respiration (Birsoy et al., 2014), indicating that modulating nutrients can alter metabolism. We cultured R tumor cells in high glucose (50 mM) and low serum (1% FCS) over several weeks to select R tumor cells with increased glycolysis (R-1%), while also culturing the original R tumor in control media (11 mM glucose, 10% FCS). When returned to control media, the R-1% tumor cells displayed enhanced ECAR and glucose uptake compared to the original R tumor cells, although not to the extent observed in P tumor cells (Figure 3A). We transplanted R-1% tumors into mice and 10 of 14 recipients developed either fully progressing tumors, or exhibited delayed regression (Figures 3B and S2A). At day 20, all 13 of the original R tumors had regressed, while only 4 of 14 R-1% tumors had fully regressed (Figures 3B and S2A). The progressing R-1% tumors still expressed mutant spectrin- β 2 (Figures 3C and S2B), indicating that gain of a “progressor” phenotype in R-1% tumors was not due to the loss of a dominant epitope recognized by TILs. Furthermore, R and R-1% tumor cells grow at the same rate both in vitro (Figure S2C), and in RAG^{-/-} mice, which lack B and T cells (Figure 3D). These data demonstrate that progression of R-1% tumors was not due to enhanced proliferation or a

tumor-intrinsic survival advantage, but rather due to tumor imposed impairment of the adaptive immune response.

While there could be differences in the R-1% tumors beyond glycolysis, we reasoned that they progressed due to their enhanced glucose uptake (Figure 3A, right). Therefore, we predicted that manipulating the glycolysis pathway directly should also turn the R tumor into a progressor tumor. Using a genetic gain-of-function approach, we transduced R tumors with retrovirus expressing c-Myc, a transcription factor that drives glycolysis (Gordan et al., 2007). c-Myc expressing R tumors (R-cMyc) displayed enhanced ECAR in vitro (Figure 3E), compared to R tumors expressing the empty vector (R-EV Ctrl). We also observed that the R-EV Ctrl tumors displayed higher ECAR than non-transduced R tumor cells. These data suggested that while the enhanced glycolysis of R-cMyc tumors should confer a progressor phenotype compared to non-transduced R tumors and R-EV Ctrl tumors, the R-EV Ctrl tumors could also conceivably exhibit some progression compared to non-transduced R tumors, due to their enhanced glycolysis. We transplanted R-cMyc tumors into mice and 22 of 30 mice (73%) had tumors ≥ 5 mm at day 21, while only 5 of 41 mice (12%) with R-EV Ctrl tumors had tumors larger than this size (Figures 3F, S2D). We speculated that the elevated ECAR in R-EV Ctrl tumors compared to non-transduced R tumors caused progression or delayed regression in a few mice when compared to non-transduced R tumors, which normally fully regress by day 21 (Figures 1A and 3B). Therefore, we compared between groups based on tumor size at day 21. Importantly, c-Myc expressing R tumors maintained expression of mutant spectrin- $\beta 2$ (Figures 3G and S2B). These data show that in spite of remaining antigenic, c-Myc expressing tumors became more glycolytic and gained a “progressor” phenotype.

Since c-Myc may drive programs beyond glycolysis, we more directly tested the role of glucose competition in antigenic tumor progression. We transduced R tumors with retrovirus expressing pyruvate dehydrogenase kinase 1 (PDK1), an enzyme that sits at a key bifurcation point between glycolysis and OXPHOS (Gerriets et al., 2015). We also transduced R tumor cells with the glucose transporter Glut1, and hexokinase II (HK2), the first enzyme in the glycolysis pathway. PDK1-, Glut1-, and HK2-expressing R tumors (R-PDK1, R-Glut1, and R-HK2) displayed higher ECAR compared to R-EV Ctrl cells, consistent with enhanced glycolysis (Figure 3E). When transplanted into mice, 16 of 25 R-PDK1 tumors (64%), 6 of 15 R-Glut1 tumors (40%), and 10 of 15 R-HK2 tumors (67%) were ≥ 5 mm at day 21, compared to only 5 of 41 R-EV Ctrl tumors (12%) (Figures 3F and S2D). All tumors expressed mutant spectrin- $\beta 2$ (Figures 3G and S2B). In addition, activated C3 T cells efficiently killed the R-1% and the transduced R tumors when in nutrient rich conditions in vitro, further confirming that these tumors remained fully antigenic (Figures S2E and S2F). Moreover, the transduced tumors cultured in vitro (Figure S2G), or in RAG $^{-/-}$ mice, grew at fairly similar rates (Figure S2H), indicating that the difference in progression between the tumors expressing glycolysis genes versus the EV Ctrl was not only due to differences in growth rates. We injected 2-NBDG into mice bearing transduced tumors. TILs in tumors expressing glycolysis genes acquired less glucose than TILs in tumors expressing the EV-Ctrl (Figure 3H). In co-culture, glycolysis gene transduced tumor cells dampened

OT-I T cell IFN- γ production more than the EV Ctrl transduced tumors, and the addition of glucose substantially increased IFN- γ production (Figure S2I). Together these results suggest that tumor cell metabolism can determine cancer progression by impairing antigen-specific immune responses.

Checkpoint Blockade Therapy Corrects Nutrient Restriction Experienced by T Cells in a Progressing Tumor

Checkpoint blockade therapy activates antitumor immunity by targeting proteins that inhibit T cells (Brahmer et al., 2012; Hamid et al., 2013; Hodi et al., 2010). This treatment can affect T cell proliferation (Spranger et al., 2014), function (Spranger et al., 2014; West et al., 2013), and glucose uptake (Parry et al., 2005), but the exact mechanisms of how these various treatments work remain unclear (Page et al., 2014). We reasoned that since these treatments are effective at inducing the regression of P tumors (Gubin et al., 2014), there should be an effect on tumor/TIL metabolism after treatment if our proposed model of metabolic competition in the tumor was correct. We transplanted P tumors into mice and treated with isotype control or CTLA-4, PD-1, or PD-L1 blockade antibodies at days 3, 6, and 9 after transplantation and assessed metabolic parameters and TIL function on day 12 (Figure 4A). Treatment with all blockade antibodies resulted in P tumor regression (Figure 4B) (Gubin et al., 2014) and the isotype had no effect on the outcome of P or R tumor growth (Figure 4B). We excised tumors on day 12 and measured glucose concentrations in the extracellular milieu. Tumors from blockade antibody-treated mice had more extracellular glucose (similar to that in R tumors) than isotype treated mice (Figure 4C). In addition, P-TILs from blockade antibody treated mice had enhanced ECAR compared to TILs from isotype treated mice (Figure 4D), correlating glucose availability in the tumor with glycolysis in TILs. Phosphorylation of mTOR targets in P-TILs was restored to a level similar to that in R-TILs (Figure 4E). Finally, the increased glucose in the tumor, and the greater ECAR observed in TILs, correlated with increased IFN- γ production by the TILs after therapy (Figure 4F). Our data indicate that blockade therapy corrects the tumor-induced glucose restriction experienced by TILs and restores their glycolytic capacity and hence their effector function.

Changes in glucose availability might also be reflected in changes in TIL OXPHOS. By plotting OCR versus ECAR, we established a baseline for metabolic fitness of TILs from R versus P tumors; this measurement emphasized that R-TILs have higher OXPHOS and glycolysis compared to P-TILs (Figure 4G). CTLA-4 and PD-1 antibodies increased ECAR and OCR in P-TILs to levels equal or above those observed in R-TILs, indicating that these treatments enhanced the overall metabolic fitness of the TILs. PD-L1 antibodies, however, primarily promoted aerobic glycolysis, rather than OCR, in the TILs (Figure 4G).

In addition to augmenting the capacity of TILs to compete for glucose, blockade antibodies might increase the ability of TILs to compete for other substrates. We assessed the protein expression of glutamate dehydrogenase (Glud1), which catalyzes the oxidative deamination of glutamate to α -ketoglutarate, an important process for energy homeostasis in T cells (Wang et al., 2011). Glud1 expression was increased in P-TILs from mice

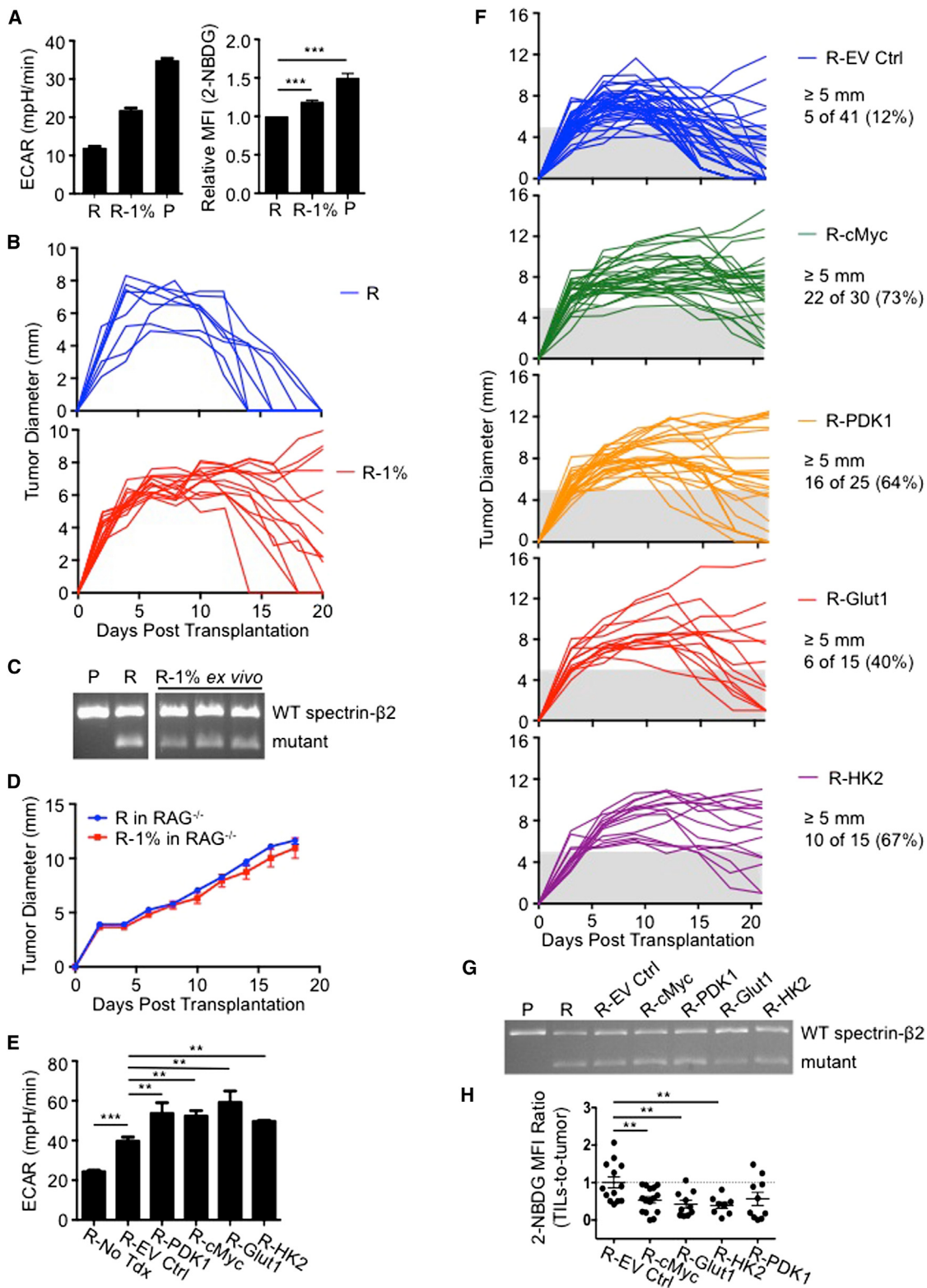


Figure 3. Enhancing Glycolytic Metabolism in Antigenic Tumors That Are Normally Rejected Promotes Tumor Progression

(A) R tumors were cultured in complete media (11 mM glucose and 10% FCS; R) or in high glucose/low FCS media (50 mM and 1% FCS; R-1%) > 3 weeks and ECAR measured (left). 2-NBDG uptake in tumor cells measured by FACS (right). Data are average of 3 independent experiments, with R and P group values also used in Figure 5B. 2-NBDG MFI is normalized to R tumor MFI. ECAR data are representative of 3 independent experiments, ***p = 0.001.

(legend continued on next page)

treated with PD-L1 antibodies (Figure S3A). These data suggest that, in addition to glucose, competition for amino acids, or even other nutrients and growth factors not examined here, may occur within tumors, and emphasize the fact that checkpoint blockade broadly increases the metabolic fitness of TILs, which may be central to the beneficial effects of these treatments in cancer therapy.

We speculated that the enhanced glucose in tumors of treated mice resulted from immune-mediated killing, which led to reduced tumor cell numbers and thus a reduction in glucose consumption. It is known that blocking inhibitory receptors enhances T cell activation (Francisco et al., 2010; Keir et al., 2008), which might reflect that these treatments allow T cells to better compete for nutrients like glucose, allowing a greater engagement of glycolysis by TILs. Consistent with this idea and published reports (Parry et al., 2005; Patsoukis et al., 2015; Pedicord et al., 2015; Staron et al., 2014), even treating *in vitro* activated T cells, which are already highly glycolytic, with PD-1 and CTLA-4 antibodies further slightly increased ECAR (Figures S3B and S3C).

PD-L1 Directly Regulates Tumor Metabolism

IFN- γ from T cells induces PD-L1 on tumors, and PD-L1 can allow the tumor to evade immune mediated attack by inhibiting T cell function through PD-1/PD-L1 interaction (Francisco et al., 2010; Keir et al., 2008). While there is a correlation between PD-L1 expression on melanomas and T cell infiltration (Quezada and Peggs, 2013), this is not the case for every cancer. Patients with glioblastoma often have high PD-L1 expression, but this does not correlate with levels of TILs observed in the tumors (Berghoff et al., 2014). Also, PD-L1 expression on neurons has been shown to, through an unknown, but immune-independent mechanism, kill glioblastoma cells (Liu et al., 2013), and PD-L1 on cancer cells mediated killing of T cells *in vitro*, which occurred independently of PD-1 (Dong et al., 2002). Recently, it has been found that PD-L1 is a direct target of HIF-1 α in myeloid-derived suppressor cells (MDSC). Blockade of PD-L1 under hypoxia enhanced MDSC-mediated T cell proliferation and function. We considered the possibility that PD-L1 has a function beyond negatively signaling to T cells via PD-1. We tested whether blocking PD-L1 on tumors directly altered tumor metabolism. P tumor cell ECAR, as well as glucose uptake, were reduced after *in vitro* treatment with PD-L1 antibodies (Figures 5A and 5B). R tumor cells, which display lower ECAR than P tumor cells, showed a smaller reduction in ECAR after treatment (Figure 5A). Antibodies against major histocompatibility complex-I, another surface protein, did not affect ECAR (Figure S4A). PD-L1 blockade also in-

hibited ECAR, to varying degrees, in B16 melanoma, MC38 colon carcinoma, L cells, and progressor clones derived from the d42m1 parent sarcoma (Figure S4B), suggesting a differential sensitivity to this treatment among tumors.

We treated P tumor cells with anti-PD-L1 and observed decreased phosphorylation of mTOR target proteins (Figures 5C and S4C), which correlated with reduced ECAR. Given that mTOR directly regulates mRNA translation and ribosome biogenesis (Laplante and Sabatini, 2012), we analyzed protein expression of several glycolysis enzymes after PD-L1 blockade. We also assessed Akt phosphorylation, since growth factors signal to mTOR via Akt. Expression of glycolysis enzymes and Akt phosphorylation were decreased after anti-PD-L1 treatment (Figures 5D and S4D). Consistent with the idea that mTOR affects glycolysis by regulating translation, we found no differences in transcript levels of key glycolysis genes following anti-PD-L1 treatment (Figure S4E). These data suggest that PD-L1 regulates the Akt/mTOR pathway, which results in decreased translation of glycolysis enzymes and thus dampened glycolysis.

We wanted to determine how PD-L1 blockade dampened mTOR signals in our *in vitro* system, which is devoid of T cell-expressed PD-1. We reasoned that PD-L1 antibodies might cause PD-L1 internalization and resultant cessation of downstream events. PD-L1 moved from the surface to the interior of the cell after treatment with anti-PD-L1 for 30 min at 37°C, indicating internalization (Figures 5E and S4F). These results suggest that surface expressed PD-L1 is important for Akt/mTOR signaling in tumors.

To confirm that PD-L1 regulates glycolysis, we transduced P tumors cells with a retrovirus expressing a short-hairpin (hp) RNA against PD-L1 (PD-L1 hp) to decrease PD-L1 expression. These tumor cells exhibited reduced ECAR, mTOR pathway and Akt activity, and glycolysis enzyme expression compared to cells with a control hairpin (Ctrl hp) (Figures 5F–5H and S4G). Also, P tumors expressed higher PD-L1 than R tumors (Figure 5I, upper), which correlated with greater ECAR (Figures 1D and 1G), glucose uptake (Figures 1B and 1J), and glycolysis. Along with decreased ECAR, PD-L1 shRNA decreased PD-L1 expression (Figure 5I, lower), but did not affect cell proliferation *in vitro* (Figure S4H), nor did it affect tumor growth when transplanted into RAG $^{−/−}$ mice (Figure S4I), suggesting that neither PD-L1, nor the glycolysis pathway, is necessarily coupled to tumor cell proliferation. To further verify that PD-L1 expression on tumors modulated glycolysis, we used retroviral transduction to generate R tumor clones that expressed different PD-L1 levels (high and low). High PD-L1 expressing R tumors had greater ECAR than low PD-L1 expressing tumors (Figure 5J). Together

(B) 129S6 mice were injected s.c. with 1×10^6 R or R-1% tumor cells. Tumor size is shown as average of two perpendicular diameters \pm SEM.

(C) Ex vivo R-1% ‘progressed’ tumors and cultured R and P tumor cell spectrin-β2 expression. Data presented from 3 individual ex vivo R-1% tumors.

(D) 1×10^6 R or R-1% tumor cells were injected s.c. into Rag $^{−/−}$ 129S6 mice and tumor growth monitored. Data (B and D) from 2 independent experiments.

(E) R tumor cells (R-No Tdx) were transduced with empty retroviral vector (R-EV Ctrl) or vectors expressing c-Myc (R-cMyc), PDK1 (R-PDK1), Glut1 (R-Glut1), or HK2 (R-HK2) and ECAR measured; represent ≥ 4 independent experiments. **p = 0.0012 for R-EV Ctrl versus R-cMyc, p = 0.0091 for R-EV Ctrl versus R-PDK1, p = 0.0026 for R-EV Ctrl versus R-Glut1, and p = 0.0196 for R-EV Ctrl versus R-HK2; ***p = 0.001 for R-No Tdx versus R-EV Ctrl.

(F) 2×10^6 transduced R tumor cells were injected s.c. into 129S6 mice and tumor growth monitored for 21 days, represent ≥ 3 independent experiments.

(G) Spectrin-β2 expression from transduced tumors.

(H) Mice bearing transduced tumors were injected i.v. with 2-NBDG on day 12 and acquisition by TILs and tumor cells measured by FACS. Data shown as MFI ratios of TILs-to-tumors normalized to R-EV Ctrl. Dots represent individual mice; horizontal bars indicate means \pm SEM of 3 independent experiments. **p = 0.009 for R-EV Ctrl versus R-cMyc, p = 0.0065 for R-EV Ctrl versus R-Glut1, and p = 0.0066 for R-EV Ctrl versus R-HK2. See also Figure S2.

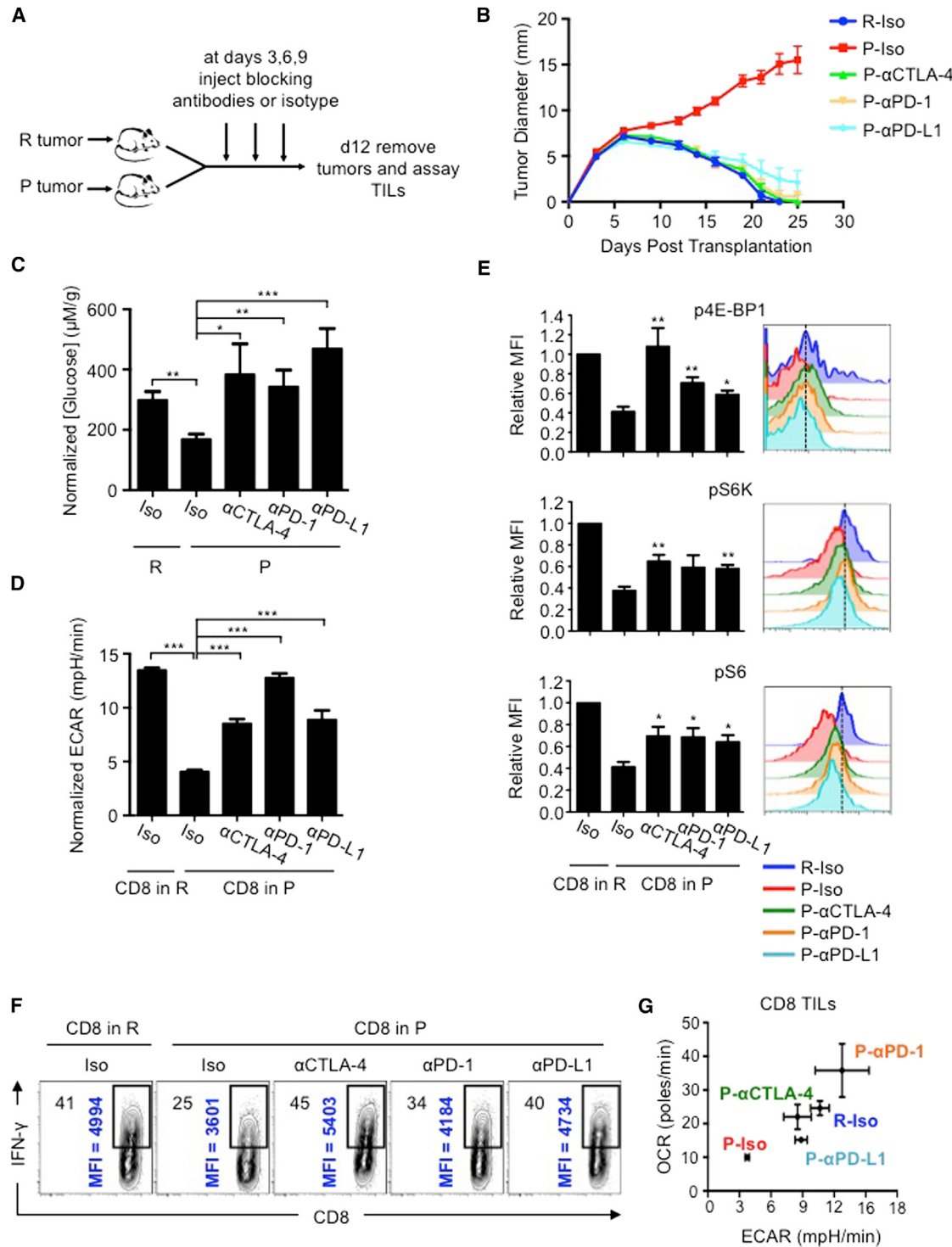


Figure 4. T Cells in Progressing Tumors Regain Glycolytic Capacity and Effector Function after Checkpoint Blockade Therapy

(A) 129S6 mice ($n = 6$ -8) were injected s.c. with R or P tumor cells and treated with anti-CTLA-4 ($\alpha\text{CTLA-4}$), anti-PD-1 ($\alpha\text{PD-1}$), anti-PD-L1 ($\alpha\text{PD-L1}$), or isotype control (Iso) antibody at days 3, 6 and 9 after tumor inoculation.

(B) Tumor size shown as average of two perpendicular diameters \pm SEM of ≥ 3 independent experiments.

(C-E) Glucose concentrations in the extracellular milieu of tumors measured at day 12 (C). Data normalized to R-Iso tumors and depict mean \pm SEM from 1-3 independent experiments. * $p = 0.0208$, ** $p = 0.0015$ (R versus P-Iso), ** $p = 0.0024$, *** $p = 0.001$. (D) TIL ECAR after checkpoint blockade. Data normalized to R-Iso tumors and depict mean \pm SEM from 3 independent experiments. *** $p < 0.001$. (E) Phosphorylation of 4E-BP1, S6 and S6K in TILs measured by FACS. Bar graphs

(legend continued on next page)

our data indicate that PD-L1 expression on tumor cells is directly associated with their glycolytic rate.

Our results suggest that PD-L1 is immunomodulatory, not only because it delivers a negative signal to T cells via PD-1 (Keir et al., 2008; Spranger et al., 2014), but also because it enhances tumor cell glycolysis and thus depletes glucose from immune cells in the tumor microenvironment. To further support the idea that PD-L1 can modulate tumor cell metabolism, independently of the adaptive immune system, we transplanted PD-L1 expressing tumors into RAG^{-/-} mice and treated with PD-L1 blockade or isotype antibodies. Glucose levels in the extracellular milieu of excised tumors isolated from mice that received anti-PD-L1 were higher compared to isotype treated mice (Figure 5K). Importantly, anti-PD-L1 treatment of PD-L1-expressing tumors in RAG^{-/-} mice had only a minor effect on reducing tumor size (data not shown), supporting that in immunocompetent mice, T cell mediated clearance of tumors is critical (Gubin et al., 2014; Matsushita et al., 2012). Our results show that expression of PD-L1 on the tumor cell surface maintains Akt/mTOR signaling, which in turn supports the translation of glycolysis enzymes and promotes this metabolic pathway. Our data further indicate that PD-L1 blockade therapy dampens glycolysis in tumors, leaving more available glucose in the extracellular tumor milieu.

DISCUSSION

Antigen recognition by T cells is critical for tumor clearance, and stronger antigens lead to stronger activation (Lanzavecchia and Sallusto, 2002; Rao et al., 2010) and a greater capacity to compete for nutrients. T cells must acquire adequate nutrients to engage the metabolism that supports their function. We (Chang et al., 2013; O'Sullivan and Pearce, 2015; Pearce et al., 2013), and others (Mellor and Munn, 2008; Mockler et al., 2014; Srivastava et al., 2010), have speculated that nutrient competition in the tumor microenvironment *in vivo* impacts T cell function. We show here that tumors can dampen TIL function by competing for glucose, despite the presence of robust tumor antigens recognized by T cells, demonstrating that metabolic competition, as a distinct mechanism, can lead to T cell hyporesponsiveness. Although we only directly address glucose in our study, this model of resource competition likely extends beyond glucose. Availability of amino acids, fatty acids, and other metabolites and the presence of growth factors, other cell types, and costimulatory signals that dictate whether T cells will express appropriate transporters to allow nutrient acquisition, will all influence T cell function in tumors. We focus on IFN- γ production from TILs; however, it is likely that a variety of effector functions, in many immune cell types, might be dampened in a glucose-depleted environment.

It makes sense that nutrient competition in a tumor shapes the ability of immune cells to perform in that environment. T cells are

primed in lymphoid tissues, which are likely nutrient-replete, and traffic to inflammatory sites where they must compete with other cells for resources. There they could experience nutrient deprivation that impairs their function, but not necessarily their survival, leading to hyporesponsiveness and cancer progression. It was shown that TILs specific for defined P tumor antigens infiltrate the P sarcoma prior to checkpoint blockade; however, these cells do not produce IFN- γ until after therapy (Gubin et al., 2014), suggesting that conditions in the microenvironment, even when antigen is recognized, can dampen T cell function. This view is consistent with the idea that T cell activation and costimulation remodel metabolism, endowing the cell with features that allow it to efficiently compete for nutrients, e.g., Glut1 expression (Jacobs et al., 2008). It is not coincidental that CD28 signaling—the very process that prevents T cell anergy—functions to increase glucose uptake (Frauwirth et al., 2002). Tregs and M2 macrophages, neither of which require aerobic glycolysis but instead use fatty acid oxidation (Huang et al., 2014; Michalek et al., 2011; Vats et al., 2006), may often appear in progressing tumors because they can likely survive in low glucose environments. This is also consistent with observations that M1 macrophages and effector T cells, both of which use glycolysis for function (Pearce et al., 2013), appear in regressing tumors, which might be relatively glucose-replete.

Our data suggest that glucose, which is stably regulated in metazoans, can become limiting for T cells in the tumor microenvironment. We demonstrate that differences in glucose acquisition between tumors do not necessarily relate to proliferation differences. It is intriguing to speculate that enhanced glucose acquisition, or even glycogen storage, is selected for in tumors (Favaro et al., 2012) to deprive T cells of glucose and thus reduce the effectiveness of the antitumor response. Our understanding of how competition for resources, including basic nutrients, is dynamically regulated in a particular niche and how this imposes functional changes in cells is only beginning to develop.

Aerobic glycolysis is required for T cells to attain full effector status, which is regulated by the bi-functional enzyme GAPDH (Chang et al., 2013). When glucose is present, GAPDH engages in its enzymatic function; when cells are glucose-restricted, GAPDH becomes available to bind the 3'UTR of IFN- γ mRNA, preventing its efficient translation. When T cells are glucose-restricted for shorter times, cytokine production can be rescued by reintroducing glucose, as GAPDH will re-engage in glycolysis. However, our preliminary observations indicate that if T cells experience prolonged nutrient deprivation, dampened cytokine production becomes relatively irreversible, leading to more permanent dysfunction that cannot be corrected through simple re-exposure to nutrients. Strategies to elevate glucose in an established tumor may not necessarily reverse TIL hyporesponsiveness. TILs might be unable to respond to glucose readily, for example, if they have not maintained Glut1 expression.

(left) shown as mean \pm SEM from 4 independent experiments and histograms (right) representative of 4 independent experiments. p4E-BP1: *p = 0.0249, **p = 0.0047 (α CTLA-4), **p = 0.0050 (α PD-1). pS6K: **p = 0.0024 (α CTLA-4), **p = 0.0025 (α PD-L1). pS6: *p = 0.0145 (α CTLA-4), *p = 0.015 (α PD-1), *p = 0.0134 (α PD-L1).

(F) IFN- γ production of TILs 5h after PMA/ionomycin restimulation. % of IFN- γ^+ cells (top left) and MFI of IFN- γ^+ cells (vertical); representative of 3 independent experiments.

(G) OCR versus ECAR (mean \pm SEM for both) of TILs after checkpoint blockade. Data from 3 independent experiments. See also Figure S3.

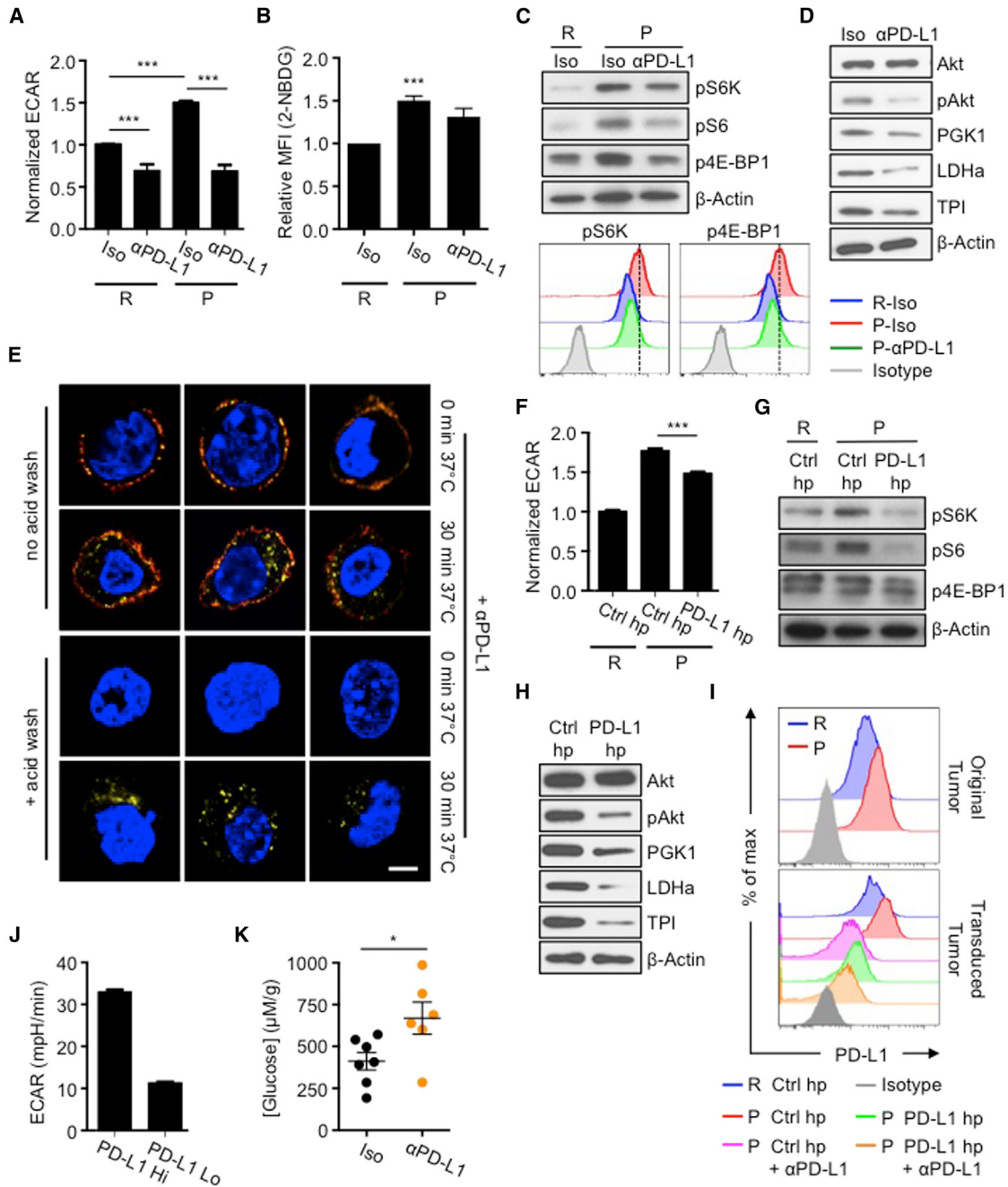


Figure 5. PD-L1 Promotes mTOR Activity and Glycolytic Metabolism in Tumor Cells

R or P tumor cells pre-treated with IFN- γ , followed by PD-L1 blockade (α PD-L1) or isotype control (Iso) antibodies. (A) ECAR post-treatment. Data from ≥ 5 independent experiments shown as relative ECAR normalized to R-Iso tumors. ***p = 0.0001.

(B) 2-NBDG uptake by tumor cells measured by FACS. Data from 3 independent experiments normalized to R tumor MFI values. ***p = 0.001. (C) p4E-BP1, pS6K and pS6 analyzed by western blot; representative of 3 independent experiments; representative histograms of p4E-BP1 and pS6K assessed by FACS.

(D) Akt, phosphorylated Akt (pAkt) and glycolytic enzymes PGK1, TPI, and LDHa examined by western blot; representative of 3 independent experiments.

(E) R tumor clones expressing high levels of PD-L1 were treated with anti-PD-L1 antibody (α PD-L1) for 15 min on ice, then kept on ice (0 min) or incubated at 37°C for 30 min (30 min) and washed in acidic solution to dissociate antibody from the cell surface (+ acid wash) or left untreated (no acid wash). After fixation, cells were incubated with anti-Rat IgG A488 (red) to detect α PD-L1 on the cell surface. After permeabilization, cells were incubated with anti-Rat IgG A647 (yellow) to detect surface expressed and internalized α PD-L1 and nuclear stained (blue). Cells imaged by confocal microscopy. Data representative of 4 independent experiments.

(F) ECAR of tumor cells transduced with *pd/l1* shRNA (PD-L1 hp) or control hp against luciferase (Ctrl hp). From 2 independent experiments represented as relative ECAR normalized to R Ctrl hp cells, ***p < 0.0001.

(G) p4E-BP1, pS6, and pS6K examined by western blot; representative of 3 independent experiments.

(legend continued on next page)

Also, if the metabolic balance between tumors and TILs is not perturbed in favor of the T cells prior to glucose exposure, the tumor will likely continue to outcompete the T cells, even when more available glucose is present (O'Sullivan and Pearce, 2015). Our current studies are aimed at understanding how metabolic restrictions in vivo can lead to long-term hyporesponsiveness in T cells.

We envisage that the various states of T cell hyporesponsiveness that have been described in cancer and infection may be induced by an initial metabolic restriction. This could manifest from a shortage of glucose, or from any signal, or lack of signal, to the T cell that abrogates its ability to acquire glucose. If this model were correct, then there might only be a narrow window of time during which T cells already present in a tumor could be targeted to regain function. Strategies that aim to deplete tumor-promoting immune cells in a tumor, coupled with those that promote glycolysis in newly infiltrating T cells, may be the most effective way to metabolically remodel the tumor microenvironment. This could explain why combining checkpoint blockade therapies that target CTLA-4, which depletes tumor Treg cells (Simpson et al., 2013), with those against PD-1, are particularly effective (Hamid et al., 2013; Wolchok et al., 2013).

Our data suggest that checkpoint blockade antibodies that affect glucose metabolism might be most effective against tumors with higher glycolytic rates. It is likely that tumors that rely more on OXPHOS and use diverse substrates for fuel might not starve the microenvironment of glucose and thus would be less affected by these therapies. These results could explain why these therapies do not work for some patients. We are investigating whether the glycolytic rate of a tumor could be used as a prognostic tool to determine the efficacy of these treatments.

Our finding that PD-L1 regulates tumor metabolism was serendipitous. Although PD-L1 is known to inhibit T cells via PD-1, it has remained unclear whether it serves additional biological advantages for tumors (Carlsson and Issazadeh-Navikas, 2014). Consistent with our findings that PD-L1 has T cell independent function, it has been shown that neurons can inhibit astrocytoma cell proliferation (Hatten and Shelanski, 1988) and that killing of murine glioblastoma cells is dependent on expression and activity of PD-L1 on neurons (Issazadeh-Navikas, 2013; Kingwell, 2013). The precise mechanism by which these events occur is unknown; however, PD-L1 might confer higher glycolysis to one cell type, e.g., neurons, which allowed them to deplete glucose from, and subsequently lead to the dampened survival of another cell type, e.g., cancer cells.

The 30 amino acid cytoplasmic tail of PD-L1 is highly conserved, which suggests functional significance (Francisco

et al., 2010; Keir et al., 2008). Our data show that PD-L1 shRNA-mediated knockdown phenocopies our results with PD-L1 blockade antibody, which decreases expression of surface PD-L1 via receptor internalization. Experiments are underway to identify how surface PD-L1 signals to Akt and mTOR, and which proteins might be involved in this process. It is conceivable that the cytoplasmic tail of PD-L1 is posttranslationally modified to facilitate its interaction with other proteins that relay information to mTOR. Likewise, it is also possible that PD-L1 sits in a cell membrane domain that promotes its association with other signaling proteins. This would not necessarily be dependent on any signaling capacity inherent to the cytoplasmic domain, but rather accessory proteins could signal to mTOR. We envisage that if PD-L1 is not expressed at the surface, its association with other proteins in the membrane is destabilized, and signaling to mTOR is blunted. More work is required to determine exactly how PD-L1 signals.

In summary, we have shown that glucose competition between tumors and T cells can directly influence cancer progression and have discovered an unexpected role for PD-L1 in regulating tumor cell metabolism. New efforts to target cancer should incorporate the idea that metabolic competition occurs in tumors and this can influence tumor progression. Future therapies may consider combining treatments that dampen tumor metabolism with those that enhance TIL nutrient acquisition in order to promote optimal antitumor immunity.

EXPERIMENTAL PROCEDURES

Mice and Tumor Transplantation

129S6 mice from Taconic Farms and C57BL/6 mice from The Jackson Laboratory were used for all experiments. Unless otherwise indicated, 1–2 × 10⁶ R or P tumor cells were injected subcutaneously (s.c.) into the right flank of mice. Sarcoma tumors were excised from mice at ~12 days (d10–d13) post-transplantation. Isolated tumors were chopped and digested in type IA collagenase and DNase I at 37°C.

In Vivo Checkpoint Blockade Treatment

Tumor bearing mice were injected i.p. with 200 µg of αCTLA4 (9H10) or αPD-1 (RMP1-14) or αPD-L1 (10F.9G2) or with isotype control antibodies on days 3, 6, and 9 after tumor transplantation.

Metabolism Assay

OCR and ECAR were analyzed on a XF96 Extracellular Flux Analyzer (Seahorse Bioscience). Cells were plated in nonbuffered RPMI 1640 media with 25 mM glucose. Measurements were obtained under basal conditions and after the addition of 1 µM oligomycin (maximum glycolytic capacity).

Transduction

Tumor cells were transduced with GFP-reporting virus expressing shRNA against luciferase (Ctrl hp) or shRNA against CD274 (PD-L1 hp) in media containing 8 µg/ml Polybrene (Sigma) and 20 mM HEPES (Hyclone) for 5 hr,

(H) Western blot of Akt, pAkt, PGK1, LDHa, and TPI; representative of 3 independent experiments.

(I) PD-L1 expression on IFN-γ pre-treated R or P tumor cells (top) or on PD-L1 hp or Ctrl hp transduced tumor cells treated with anti-PD-L1 (bottom).

(J) ECAR of R tumors expressing high (Hi) and low (Lo) levels of surface PD-L1 after transduction with PD-L1 expressing retrovirus, represented as mean ± SEM of 2 independent experiments.

(K) Rag^{-/-} mice were injected s.c. with 2 × 10⁶ R-PD-L1 expressing tumor cells, followed by treatment with PD-L1 antibodies (αPD-L1) at days 2, 5, 8 and 11 after transplantation. Extracellular glucose was measured at day 12. Dots represent individual mice; horizontal bars indicate means ± SEM from 2 independent experiments. *p = 0.0319. Figures 5D, H, and Figures S4D, G contain separate blots from equally loaded lanes due to similar sizes of glycolysis enzymes that necessitated separate probing. See also Figure S4.

followed by additional transduction with the same virus overnight. Transduced tumor cells were sorted by GFP expression. R tumor cells were transduced with retrovirus expressing c-Myc, PDK1, Glut1, or HK2, or with empty vector.

Glucose Assay

Glucose concentrations in the supernatant were measured by the Glucose Assay Kit (Eton Bioscience). For ex vivo glucose levels, harvested tumors were weighed and minced in fixed amounts of PBS. Glucose concentration was quantified in accordance with the weight of tumors and the volume of collected supernatant, and normalized with glucose concentrations in R tumors.

Statistical Analysis

Comparisons for two groups were calculated by using an unpaired, two-tailed Student's t test. Comparisons for more than two groups were calculated using 1-way ANOVA followed by Bonferroni's multiple comparison tests.

SUPPLEMENTAL INFORMATION

Supplemental Information includes Supplemental Experimental Procedures and four figures and can be found with this article online at <http://dx.doi.org/10.1016/j.cell.2015.08.016>.

AUTHOR CONTRIBUTIONS

C.-H.C., J.Q., D.O., M.D.B., T.N., G.J.W.v.d.W., R.D.S., E.J.P., and E.L.P. designed the research. C.-H.C., J.Q., D.O., M.D.B., T.N., J.D.C., M.G., Q.C., M.M.G., E.T. and E.L.P. performed experiments and analyzed data. C.-H.C., J.Q., D.O., M.D.B., R.D.S., E.J.P., and E.L.P. prepared manuscript.

ACKNOWLEDGMENTS

We thank A. Shaw, C. Hsieh, H. Christofk, J. Cyster, Y. Feng, B. Edelson, J. Lin, J. Hu, H. Yu, M. Colonna, A. Fuchs, G. Randolph, and L. Huang. This work was supported by grants from the NIH (CA181125, AI091965 to E.L.P.; CA43059, CA141541 to R.D.S.; CA164062, AI032573 to E.J.P.), The Burroughs Wellcome Fund Investigator in the Pathogenesis of Infectious Disease (E.L.P.), CRI, WWWWW Foundation, and BMS (R.D.S.), Irvington Fellowship (M.M.G.), Netherlands Organisation for Scientific Research (G.J.W.v.d.W.), and NSF Graduate Research Fellowship DGE-1143954 (M.D.B.). Robert Schreiber is a cofounder of Igenica Biotherapeutics, and is a senior advisor to Jounce Therapeutics.

Received: February 23, 2015

Revised: May 27, 2015

Accepted: July 16, 2015

Published: August 27, 2015

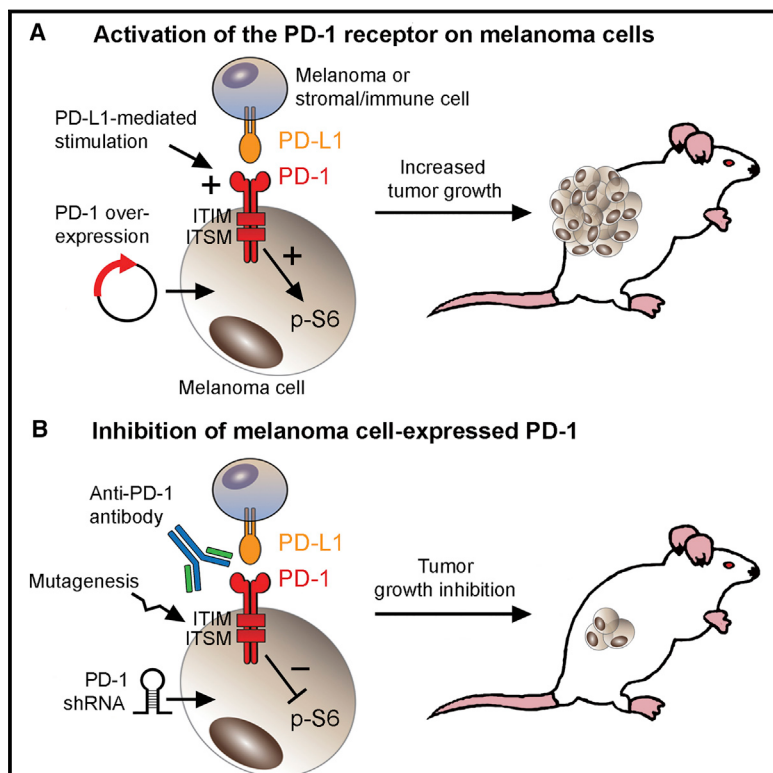
REFERENCES

- Ahmazadeh, M., Johnson, L.A., Heemskerk, B., Wunderlich, J.R., Dudley, M.E., White, D.E., and Rosenberg, S.A. (2009). Tumor antigen-specific CD8 T cells infiltrating the tumor express high levels of PD-1 and are functionally impaired. *Blood* **114**, 1537–1544.
- Anichini, A., Molla, A., Vegetti, C., Bersani, I., Zappasodi, R., Arienti, F., Ravagnani, F., Maurichi, A., Patuzzo, R., Santinami, M., et al. (2010). Tumor-reactive CD8+ early effector T cells identified at tumor site in primary and metastatic melanoma. *Cancer Res.* **70**, 8378–8387.
- Baitsch, L., Baumgaertner, P., Devèvre, E., Raghav, S.K., Legat, A., Barba, L., Wieckowski, S., Bouzourene, H., Deplancke, B., Romero, P., et al. (2011). Exhaustion of tumor-specific CD8+ T cells in metastases from melanoma patients. *J. Clin. Invest.* **121**, 2350–2360.
- Berghoff, A.S., Kiesel, B., Widhalm, G., Rajky, O., Ricken, G., Wohrer, A., Dieckmann, K., Filipits, M., Brandstetter, A., Weller, M., et al. (2014). Programmed death ligand 1 expression and tumor-infiltrating lymphocytes in glioblastoma. *Neuro-oncol.* **17**, 1064–1075.
- Birsoy, K., Possemato, R., Lorbeer, F.K., Bayraktar, E.C., Thiru, P., Yucel, B., Wang, T., Chen, W.W., Clish, C.B., and Sabatini, D.M. (2014). Metabolic determinants of cancer cell sensitivity to glucose limitation and biguanides. *Nature* **508**, 108–112.
- Brahmer, J.R., Tykodi, S.S., Chow, L.Q., Hwu, W.J., Topalian, S.L., Hwu, P., Drake, C.G., Camacho, L.H., Kauh, J., Odunsi, K., et al. (2012). Safety and activity of anti-PD-L1 antibody in patients with advanced cancer. *N. Engl. J. Med.* **366**, 2455–2465.
- Carlsson, R., and Issazadeh-Navikas, S. (2014). PD-L1, Inflammation and Glioblastoma. *J. Immunol. Clin. Res.* **2**, 1013.
- Cham, C.M., Driessens, G., O'Keefe, J.P., and Gajewski, T.F. (2008). Glucose deprivation inhibits multiple key gene expression events and effector functions in CD8+ T cells. *Eur. J. Immunol.* **38**, 2438–2450.
- Chang, C.H., Curtis, J.D., Maggi, L.B., Jr., Faubert, B., Villarino, A.V., O'Sullivan, D., Huang, S.C., van der Windt, G.J., Blagih, J., Qiu, J., et al. (2013). Post-transcriptional control of T cell effector function by aerobic glycolysis. *Cell* **153**, 1239–1251.
- Constant, S., Pfeiffer, C., Woodard, A., Pasqualini, T., and Bottomly, K. (1995). Extent of T cell receptor ligation can determine the functional differentiation of naive CD4+ T cells. *J. Exp. Med.* **182**, 1591–1596.
- Crespo, J., Sun, H., Welling, T.H., Tian, Z., and Zou, W. (2013). T cell anergy, exhaustion, senescence, and stemness in the tumor microenvironment. *Curr. Opin. Immunol.* **25**, 214–221.
- Dong, H., Strome, S.E., Salomao, D.R., Tamura, H., Hirano, F., Flies, D.B., Roche, P.C., Lu, J., Zhu, G., Tamada, K., et al. (2002). Tumor-associated B7-H1 promotes T-cell apoptosis: a potential mechanism of immune evasion. *Nat. Med.* **8**, 793–800.
- Doughty, C.A., Bleiman, B.F., Wagner, D.J., Dufort, F.J., Mataraza, J.M., Roberts, M.F., and Chiles, T.C. (2006). Antigen receptor-mediated changes in glucose metabolism in B lymphocytes: role of phosphatidylinositol 3-kinase signaling in the glycolytic control of growth. *Blood* **107**, 4458–4465.
- Favarro, E., Bensaad, K., Chong, M.G., Tenant, D.A., Ferguson, D.J., Snell, C., Steers, G., Turley, H., Li, J.L., Günther, U.L., et al. (2012). Glucose utilization via glycogen phosphorylase sustains proliferation and prevents premature senescence in cancer cells. *Cell Metab.* **16**, 751–764.
- Fischer, K., Hoffmann, P., Voelkl, S., Meidenbauer, N., Ammer, J., Edinger, M., Gottfried, E., Schwarz, S., Rothe, G., Hoves, S., et al. (2007). Inhibitory effect of tumor cell-derived lactic acid on human T cells. *Blood* **109**, 3812–3819.
- Francisco, L.M., Sage, P.T., and Sharpe, A.H. (2010). The PD-1 pathway in tolerance and autoimmunity. *Immunol. Rev.* **236**, 219–242.
- Frauwirth, K.A., Riley, J.L., Harris, M.H., Parry, R.V., Rathmell, J.C., Plas, D.R., Elstrom, R.L., June, C.H., and Thompson, C.B. (2002). The CD28 signaling pathway regulates glucose metabolism. *Immunity* **16**, 769–777.
- Gatenby, R.A., and Gillies, R.J. (2004). Why do cancers have high aerobic glycolysis? *Nat. Rev. Cancer* **4**, 891–899.
- Gerriets, V.A., Kishton, R.J., Nichols, A.G., Macintyre, A.N., Inoue, M., Ilkayeva, O., Winter, P.S., Liu, X., Priyadarshini, B., Slawinska, M.E., et al. (2015). Metabolic programming and PDHK1 control CD4+ T cell subsets and inflammation. *J. Clin. Invest.* **125**, 194–207.
- Gordan, J.D., Thompson, C.B., and Simon, M.C. (2007). HIF and c-Myc: sibling rivals for control of cancer cell metabolism and proliferation. *Cancer Cell* **12**, 108–113.
- Gubin, M.M., Zhang, X., Schuster, H., Caron, E., Ward, J.P., Noguchi, T., Ivanova, Y., Hundal, J., Arthur, C.D., Krebber, W.J., et al. (2014). Checkpoint blockade cancer immunotherapy targets tumour-specific mutant antigens. *Nature* **515**, 577–581.
- Hamid, O., Robert, C., Daud, A., Hodi, F.S., Hwu, W.J., Kefford, R., Wolchok, J.D., Hersey, P., Joseph, R.W., Weber, J.S., et al. (2013). Safety and tumor responses with lambrolizumab (anti-PD-1) in melanoma. *N. Engl. J. Med.* **369**, 134–144.
- Hatten, M.E., and Shelanski, M.L. (1988). Mouse cerebellar granule neurons arrest the proliferation of human and rodent astrocytoma cells in vitro. *J. Neurosci.* **8**, 1447–1453.

- Hodi, F.S., O'Day, S.J., McDermott, D.F., Weber, R.W., Sosman, J.A., Haanen, J.B., Gonzalez, R., Robert, C., Schadendorf, D., Hassel, J.C., et al. (2010). Improved survival with ipilimumab in patients with metastatic melanoma. *N. Engl. J. Med.* 363, 711–723.
- Huang, S.C., Everts, B., Ivanova, Y., O'Sullivan, D., Nascimento, M., Smith, A.M., Beatty, W., Love-Gregory, L., Lam, W.Y., O'Neill, C.M., et al. (2014). Cell-intrinsic lysosomal lipolysis is essential for alternative activation of macrophages. *Nat. Immunol.* 15, 846–855.
- Issazadeh-Navikas, S. (2013). Alerting the immune system via stromal cells is central to the prevention of tumor growth. *Oncolmumonology* 2, e27091.
- Jacobs, S.R., Herman, C.E., Maciver, N.J., Wofford, J.A., Wieman, H.L., Hammen, J.J., and Rathmell, J.C. (2008). Glucose uptake is limiting in T cell activation and requires CD28-mediated Akt-dependent and independent pathways. *J. Immunol.* 180, 4476–4486.
- Keir, M.E., Butte, M.J., Freeman, G.J., and Sharpe, A.H. (2008). PD-1 and its ligands in tolerance and immunity. *Annu. Rev. Immunol.* 26, 677–704.
- Kim, D.H., Sarbassov, D.D., Ali, S.M., King, J.E., Latek, R.R., Erdjument-Bromage, H., Tempst, P., and Sabatini, D.M. (2002). mTOR interacts with raptor to form a nutrient-sensitive complex that signals to the cell growth machinery. *Cell* 110, 163–175.
- Kingwell, K. (2013). Neuro-oncology: Glioblastoma prognosis linked to neuronal PD-L1 expression in tumour-adjacent tissue. *Nat. Rev. Neurol.* 9, 602–603.
- Kohn, A.D., Barthel, A., Kovacina, K.S., Boge, A., Wallach, B., Summers, S.A., Birnbaum, M.J., Scott, P.H., Lawrence, J.C., Jr., and Roth, R.A. (1998). Construction and characterization of a conditionally active version of the serine/threonine kinase Akt. *J. Biol. Chem.* 273, 11937–11943.
- Lanzavecchia, A., and Sallusto, F. (2002). Progressive differentiation and selection of the fittest in the immune response. *Nat. Rev. Immunol.* 2, 982–987.
- Laplante, M., and Sabatini, D.M. (2012). mTOR signaling in growth control and disease. *Cell* 149, 274–293.
- Liu, Y., Carlsson, R., Ambjörn, M., Hasan, M., Badn, W., Darabi, A., Siesjö, P., and Issazadeh-Navikas, S. (2013). PD-L1 expression by neurons nearby tumors indicates better prognosis in glioblastoma patients. *J. Neurosci.* 33, 14231–14245.
- Matsushita, H., Vesely, M.D., Koboldt, D.C., Rickert, C.G., Uppaluri, R., Magrini, V.J., Arthur, C.D., White, J.M., Chen, Y.S., Shea, L.K., et al. (2012). Cancer exome analysis reveals a T-cell-dependent mechanism of cancer immunoediting. *Nature* 482, 400–404.
- Mellor, A.L., and Munn, D.H. (2008). Creating immune privilege: active local suppression that benefits friends, but protects foes. *Nat. Rev. Immunol.* 8, 74–80.
- Michalek, R.D., Gerriets, V.A., Jacobs, S.R., Macintyre, A.N., MacIver, N.J., Mason, E.F., Sullivan, S.A., Nichols, A.G., and Rathmell, J.C. (2011). Cutting edge: distinct glycolytic and lipid oxidative metabolic programs are essential for effector and regulatory CD4+ T cell subsets. *J. Immunol.* 186, 3299–3303.
- Mockler, M.B., Conroy, M.J., and Lysaght, J. (2014). Targeting T cell immunometabolism for cancer immunotherapy: understanding the impact of the tumor microenvironment. *Front. Oncol.* 4, 107.
- Munn, D.H., and Mellor, A.L. (2013). Indoleamine 2,3 dioxygenase and metabolic control of immune responses. *Trends Immunol.* 34, 137–143.
- Munn, D.H., Shafizadeh, E., Attwood, J.T., Bondarev, I., Pashine, A., and Mellor, A.L. (1999). Inhibition of T cell proliferation by macrophage tryptophan catabolism. *J. Exp. Med.* 189, 1363–1372.
- Nicholls, D.G., Darley-Usmar, V.M., Wu, M., Jensen, P.B., Rogers, G.W., and Ferrick, D.A. (2010). Bioenergetic profile experiment using C2C12 myoblast cells. *J. Vis. Exp.* 46, 2511.
- O'Sullivan, D., and Pearce, E.L. (2015). Targeting T cell metabolism for therapy. *Trends Immunol.* 36, 71–80.
- Page, D.B., Postow, M.A., Callahan, M.K., Allison, J.P., and Wolchok, J.D. (2014). Immune modulation in cancer with antibodies. *Annu. Rev. Med.* 65, 185–202.
- Parish, I.A., and Kaech, S.M. (2009). Diversity in CD8(+) T cell differentiation. *Curr. Opin. Immunol.* 21, 291–297.
- Parry, R.V., Chemnitz, J.M., Frauwirth, K.A., Lanfranco, A.R., Braunstein, I., Kobayashi, S.V., Linsley, P.S., Thompson, C.B., and Riley, J.L. (2005). CTLA-4 and PD-1 receptors inhibit T-cell activation by distinct mechanisms. *Mol. Cell. Biol.* 25, 9543–9553.
- Patsoukis, N., Bardhan, K., Chatterjee, P., Sari, D., Liu, B., Bell, L.N., Karoly, E.D., Freeman, G.J., Petkova, V., Seth, P., et al. (2015). PD-1 alters T-cell metabolic reprogramming by inhibiting glycolysis and promoting lipolysis and fatty acid oxidation. *Nat. Commun.* 6, 6692.
- Pearce, E.L., Poffenberger, M.C., Chang, C.H., and Jones, R.G. (2013). Fueling immunity: insights into metabolism and lymphocyte function. *Science* 342, 1242454.
- Pedicord, V.A., Cross, J.R., Montalvo-Ortiz, W., Miller, M.L., and Allison, J.P. (2015). Friends not foes: CTLA-4 blockade and mTOR inhibition cooperate during CD8+ T cell priming to promote memory formation and metabolic readiness. *J. Immunol.* 194, 2089–2098.
- Quezada, S.A., and Peggs, K.S. (2013). Exploiting CTLA-4, PD-1 and PD-L1 to reactivate the host immune response against cancer. *Br. J. Cancer* 108, 1560–1565.
- Rao, R.R., Li, Q., and Shrikant, P.A. (2010). Fine-tuning CD8(+) T cell functional responses: mTOR acts as a rheostat for regulating CD8(+) T cell proliferation, survival and differentiation? *Cell Cycle* 9, 2996–3001.
- Simpson, T.R., Li, F., Montalvo-Ortiz, W., Sepulveda, M.A., Bergerhoff, K., Arce, F., Roddie, C., Henry, J.Y., Yagita, H., Wolchok, J.D., et al. (2013). Fc-dependent depletion of tumor-infiltrating regulatory T cells co-defines the efficacy of anti-CTLA-4 therapy against melanoma. *J. Exp. Med.* 210, 1695–1710.
- Spranger, S., Koblish, H.K., Horton, B., Scherle, P.A., Newton, R., and Gajewski, T.F. (2014). Mechanism of tumor rejection with doublets of CTLA-4, PD-1/PD-L1, or IDO blockade involves restored IL-2 production and proliferation of CD8(+) T cells directly within the tumor microenvironment. *J. Immunother. Cancer* 2, 3.
- Srivastava, M.K., Sinha, P., Clements, V.K., Rodriguez, P., and Ostrand-Rosenberg, S. (2010). Myeloid-derived suppressor cells inhibit T-cell activation by depleting cystine and cysteine. *Cancer Res.* 70, 68–77.
- Staron, M.M., Gray, S.M., Marshall, H.D., Parish, I.A., Chen, J.H., Perry, C.J., Cui, G., Li, M.O., and Kaech, S.M. (2014). The transcription factor FoxO1 sustains expression of the inhibitory receptor PD-1 and survival of antiviral CD8(+) T cells during chronic infection. *Immunity* 41, 802–814.
- Vats, D., Mukundan, L., Odegaard, J.I., Zhang, L., Smith, K.L., Morel, C.R., Wagner, R.A., Greaves, D.R., Murray, P.J., and Chawla, A. (2006). Oxidative metabolism and PGC-1beta attenuate macrophage-mediated inflammation. *Cell Metab.* 4, 13–24.
- Vesely, M.D., and Schreiber, R.D. (2013). Cancer immunoediting: antigens, mechanisms, and implications to cancer immunotherapy. *Ann. N Y Acad. Sci.* 1284, 1–5.
- Wang, R., Dillon, C.P., Shi, L.Z., Milasta, S., Carter, R., Finkelstein, D., McCormick, L.L., Fitzgerald, P., Chi, H., Munger, J., and Green, D.R. (2011). The transcription factor Myc controls metabolic reprogramming upon T lymphocyte activation. *Immunity* 35, 871–882.
- Warburg, O. (1956). On the origin of cancer cells. *Science* 123, 309–314.
- West, E.E., Jin, H.T., Rasheed, A.U., Penalosa-Macmaster, P., Ha, S.J., Tan, W.G., Youngblood, B., Freeman, G.J., Smith, K.A., and Ahmed, R. (2013). PD-L1 blockade synergizes with IL-2 therapy in reinvigorating exhausted T cells. *J. Clin. Invest.* 123, 2604–2615.
- Wherry, E.J. (2011). T cell exhaustion. *Nat. Immunol.* 12, 492–499.
- Wolchok, J.D., Kluger, H., Callahan, M.K., Postow, M.A., Rizvi, N.A., Lesokhin, A.M., Segal, N.H., Ariyan, C.E., Gordon, R.A., Reed, K., et al. (2013). Nivolumab plus ipilimumab in advanced melanoma. *N. Engl. J. Med.* 369, 122–133.

Melanoma Cell-Intrinsic PD-1 Receptor Functions Promote Tumor Growth

Graphical Abstract



Authors

Sonja Kleffel, Christian Posch,
Steven R. Barthel, ..., Arlene H. Sharpe,
Thomas S. Kupper, Tobias Schatton

Correspondence

tschatton@bwh.harvard.edu

In Brief

PD-1/PD-L1 signaling has cell-intrinsic functions in certain types of mouse and human tumors, boosting cancer growth and promoting tumorigenesis. This suggests that immunotherapy with PD-1 blockers may produce an effect on tumor growth that is separate from their effect on the immune response.

Highlights

- Human melanomas frequently contain PD-1-expressing cancer cell subpopulations
- Inhibition of melanoma-PD-1 reduces tumor growth, independently of adaptive immunity
- PD-1 overexpression and melanoma-PD-1:PD-L1 interactions promote tumor growth
- Activation of the melanoma-PD-1 receptor modulates downstream mTOR signaling

Melanoma Cell-Intrinsic PD-1 Receptor Functions Promote Tumor Growth

Sonja Kleffel,¹ Christian Posch,^{1,2} Steven R. Barthel,¹ Hansgeorg Mueller,^{1,3} Christoph Schlapbach,⁴ Emmanuella Guenova,⁵ Christopher P. Elco,^{1,6} Nayoung Lee,¹ Vikram R. Juneja,⁷ Qian Zhan,⁶ Christine G. Lian,⁶ Rahel Thomi,⁴ Wolfram Hoetzenegger,⁵ Antonio Cozzio,⁵ Reinhard Dummer,⁵ Martin C. Mihm, Jr.,¹ Keith T. Flaherty,⁸ Markus H. Frank,^{1,9,10} George F. Murphy,⁶ Arlene H. Sharpe,^{6,7,11} Thomas S. Kupper,¹ and Tobias Schatton^{1,9,*}

¹Harvard Skin Disease Research Center, Department of Dermatology, Brigham and Women's Hospital, Harvard Medical School, Boston, MA 02115, USA

²Department of Dermatology, The Rudolfstiftung Hospital, 1030 Vienna, Austria

³Department of Dermatology, Innsbruck Medical University, 6020 Innsbruck, Austria

⁴Department of Dermatology, University of Bern, 3010 Bern, Switzerland

⁵Department of Dermatology, University Hospital Zurich, 8091 Zurich, Switzerland

⁶Department of Pathology, Brigham and Women's Hospital, Harvard Medical School, Boston, MA 02115, USA

⁷Department of Microbiology and Immunobiology, Harvard Medical School, Boston, MA 02115, USA

⁸Division of Medical Oncology, Massachusetts General Hospital Cancer Center, Harvard Medical School, Boston, MA 02114, USA

⁹Department of Medicine, Children's Hospital Boston, Harvard Medical School, Boston, MA 02115, USA

¹⁰School of Medical Sciences, Edith Cowan University, Joondalup, WA 6027, Australia

¹¹Evergrande Center for Immunologic Diseases, Brigham and Women's Hospital, Harvard Medical School, Boston, MA 02115, USA

*Correspondence: tschatton@bwh.harvard.edu

<http://dx.doi.org/10.1016/j.cell.2015.08.052>

SUMMARY

Therapeutic antibodies targeting programmed cell death 1 (PD-1) activate tumor-specific immunity and have shown remarkable efficacy in the treatment of melanoma. Yet, little is known about tumor cell-intrinsic PD-1 pathway effects. Here, we show that murine and human melanomas contain PD-1-expressing cancer subpopulations and demonstrate that melanoma cell-intrinsic PD-1 promotes tumorigenesis, even in mice lacking adaptive immunity. PD-1 inhibition on melanoma cells by RNAi, blocking antibodies, or mutagenesis of melanoma-PD-1 signaling motifs suppresses tumor growth in immunocompetent, immunocompromised, and PD-1-deficient tumor graft recipient mice. Conversely, melanoma-specific PD-1 overexpression enhances tumorigenicity, as does engagement of melanoma-PD-1 by its ligand, PD-L1, whereas melanoma-PD-L1 inhibition or knockout of host-PD-L1 attenuate growth of PD-1-positive melanomas. Mechanistically, the melanoma-PD-1 receptor modulates downstream effectors of mTOR signaling. Our results identify melanoma cell-intrinsic functions of the PD-1:PD-L1 axis in tumor growth and suggest that blocking melanoma-PD-1 might contribute to the striking clinical efficacy of anti-PD-1 therapy.

INTRODUCTION

Immune checkpoints are crucial regulatory pathways that maintain immune homeostasis by modulating the amplitude and quality of several adaptive and innate effector mechanisms in

favor of immunogenic tolerance (Pardoll, 2012). Using various strategies, such as triggering functional exhaustion of tumor-reactive cytotoxic T-lymphocytes (CTLs), cancers exploit immune checkpoints to evade antitumor immunity. Programmed cell death 1 (PD-1) is a prominent checkpoint receptor that, upon engagement by its ligands, PD-L1 (also known as B7-H1) or PD-L2 (also known as B7-DC), dampens T effector functions by inhibiting signaling downstream of the T cell receptor (TCR) (Topalian et al., 2012a). Thus, expression of PD-1 ligands, and particularly PD-L1, in the tumor microenvironment (TME) protects cancers from immune-mediated rejection (Dong et al., 2002; Topalian et al., 2012a). Consequently, a number of antibody-based therapeutics targeting the PD-1:PD-L1 axis have entered clinical development or have been approved for melanoma therapy (Postow et al., 2015).

In phase I trials (Hamid et al., 2013; Herbst et al., 2014; Topalian et al., 2012b; Wolchok et al., 2013), PD-1 pathway blockade demonstrated unprecedented response rates and encouraging toxicity profiles in patients with advanced-stage cancers of various etiologies, including malignant melanoma. On the basis of recent phase III data demonstrating improved overall survival in melanoma patients receiving PD-1 inhibitors compared to those treated with chemotherapy, the FDA approved two anti-PD-1 antibodies, nivolumab and pembrolizumab, for the treatment of patients with advanced melanoma who are no longer responding to other drugs (Postow et al., 2015; Weber et al., 2015). PD-L1 expression by cancer cells and tumor-infiltrating lymphocytes (TILs) (Herbst et al., 2014; Topalian et al., 2012b; Tumeh et al., 2014), the presence of type 1 T-helper cell (Th1)-associated inflammatory mediators (Herbst et al., 2014; Tumeh et al., 2014), increased density and proliferation and decreased diversity in antigen specificity of CD8⁺ T cells (Tumeh et al., 2014), and the frequency of tumor-associated neo-antigens within the TME (Gubin et al., 2014; Rizvi et al., 2015; Yadav et al., 2014) are associated with clinical response

to PD-1 pathway interference. These findings established that optimal anti-PD-1 cancer therapeutic efficacy requires the activation and expansion of tumor-specific T cell immunity.

However, in addition to benefiting patients afflicted with immunogenic cancers, such as malignant melanoma (Hamid et al., 2013; Herbst et al., 2014; Topalian et al., 2012b; Wolchok et al., 2013), PD-1 pathway blockade has also yielded meaningful clinical activity in patients with lesser immunogenic cancers that have hitherto not typically responded to immunotherapy (Herbst et al., 2014; Topalian et al., 2012b). Moreover, patients with advanced melanoma refractory to treatment with ipilimumab, an FDA-approved antibody targeting the immune checkpoint protein, cytotoxic T-lymphocyte antigen (CTLA)-4, showed marked clinical response to anti-PD-1 therapy (Hamid et al., 2013; Weber et al., 2015; Wolchok et al., 2013). While the presence of neo-antigens and an immune-active TME are similarly associated with favorable outcome in melanoma patients treated with either PD-1- (Gubin et al., 2014; Rizvi et al., 2015; Yadav et al., 2014) or CTLA-4-directed checkpoint blockade (Snyder et al., 2014), current evidence suggests that PD-1 inhibitors produce greater anticancer activity and fewer immune-related adverse events than ipilimumab (Postow et al., 2015). Taken together, these observations raise the possibility that anti-PD-1 therapy, in addition to deregulating T-cell-specific immune checkpoint functions, may also inhibit complementary protumorigenic mechanisms, thereby contributing to its superior clinical efficacy compared to CTLA-4 blockade. Because PD-1 is not only expressed by immune cells, but also by melanoma subpopulations with enhanced tumorigenicity, even in highly immunocompromised tumor xenograft recipient mice (Schatton et al., 2010), we hypothesized that the growth-suppressive effects of PD-1 therapy might also partially result from the direct inhibition of this protein on melanoma cells.

Here, we report that established human and murine melanoma cell lines as well as clinical melanomas frequently contain PD-1-expressing cancer subpopulations and that enforced melanoma-PD-1 expression enhances melanoma growth, even in the absence of adaptive immunity. Conversely, antibody-mediated melanoma-PD-1 blockade and melanoma-specific PD-1 knockdown, as well as mutagenesis of melanoma-PD-1 signaling motifs inhibit tumor growth independently of adaptive immunity. Efficient melanoma-PD-1-driven tumorigenesis requires melanoma-PD-1 interactions with its predominant ligand, PD-L1, which activate effectors of the mTOR signaling pathway downstream of the melanoma-PD-1 receptor. Our results expand our current understanding of PD-1 pathway functions in melanoma and suggest that cancer cell-intrinsic PD-1 targeting might significantly contribute to the therapeutic efficacy of PD-1 antibodies, rendering PD-1 inhibition, in conjunction with its demonstrated effect on immune checkpoint blockade, superior to alternative therapies that target immune checkpoints alone.

RESULTS

Melanomas Frequently Contain PD-1-Expressing Cancer Subpopulations

We first examined PD-1 expression in a series of melanoma patient samples and established melanoma cell lines to further expand upon the potential clinical significance of our previous

demonstration that melanoma cells can express PD-1 (Schatton et al., 2010). Flow cytometric analysis of single-cell suspensions derived from clinical tumor specimens ($n = 8$ patients) revealed PD-1 surface protein expression by melanoma subpopulations negative for the pan-lymphocyte marker, CD45, and the endothelial marker, CD31, in 8/8 melanoma specimens examined, with tumor cell frequencies ranging from 3.5% to 16.5% (cell frequency $8.7\% \pm 1.5\%$, mean \pm SEM, Figure 1A and Figure S1A). Immunofluorescence double labeling of clinical melanoma biopsies ($n = 50$) for PD-1 and the melanoma antigen recognized by T cells (MART)-1 further confirmed PD-1 protein expression by subpopulations of MART-1⁺ melanoma cells that were cytologically distinct from CD45⁺ lymphocytes (Figure 1B), with $n = 22/36$ melanoma patients demonstrating melanoma-PD-1 positivity in at least one of their tumor lesions (Table S1).

Based on our intention to mechanistically dissect the role of melanoma-expressed PD-1 in experimental tumor growth, we next characterized PD-1 expression in established human and murine melanoma cell lines. RT-PCR amplification and sequencing of the full coding sequence (CDS) of the human PD-1 (*PDCD1*) gene revealed *PDCD1* mRNA expression (Figure 1C), and immunoblot analysis demonstrated PD-1 protein expression by human A375, C8161, and G3361 melanoma cells (Figure 1D). Flow cytometric analyses showed PD-1 surface protein expression by 8/8 melanoma lines tested, with PD-1⁺ tumor cell frequencies ranging from $11.3\% \pm 1.2\%$ to $29.5\% \pm 3.7\%$ (mean \pm SEM, Figure 1E), and revealed preferential PD-1 expression by melanoma cell subsets positive for the tumor-initiating cell determinant (Schatton et al., 2008), ABCB5 (Figures S2A–S2C), consistent with our previous demonstration of PD-1 expression by melanoma-initiating cells (Schatton et al., 2010). Human melanoma lines also demonstrated positivity for both PD-1 ligands, PD-L1 and PD-L2, ranging from $2.4\% \pm 0.1\%$ to $99.2\% \pm 0.1\%$ and $0.6\% \pm 0.1\%$ to $88.9\% \pm 2.6\%$ of cells (mean \pm SEM), respectively (Figure S1B), and PD-1 co-expression with its ligands (not shown). Murine B16-F0 and B16-F10 cultures also expressed both PD-1 (*Pdcd1*) mRNA, as determined by amplification and sequencing of the full *Pdcd1* CDS (Figure 1F), and PD-1 protein as determined by immunoblotting (Figure 1G). Flow cytometric analysis revealed PD-1 (cell frequency $9.4\% \pm 2.5\%$ and $6.6\% \pm 2.4\%$, mean \pm SEM, Figure 1H) and PD-L1 ($43.4\% \pm 9.4\%$ and $37.5\% \pm 2.3\%$), but not PD-L2 surface protein expression by B16-F0 and B16-F10 melanoma cells (Figure S1C). B16 melanoma grafts grown in non-obese diabetic severely combined immunodeficient (NOD/SCID) interleukin-2 receptor (IL-2R) γ -chain(−/−) null (NSG) mice lacking adaptive immunity also demonstrated PD-1 expression by MART-1⁺ melanoma cells (Figure 1I).

Melanoma-Expressed PD-1 Promotes Murine Tumor Growth

To functionally dissect the potential role of melanoma-expressed PD-1 in tumor growth, we generated stable *Pdcd1* knockdown (KD) and *Pdcd1*-overexpressing (OE) B16 melanoma lines. Transduction of B16-F0 and B16-F10 cells with two distinct short hairpin (sh) RNAs targeting *Pdcd1* inhibited murine PD-1 mRNA expression by $\geq 59\%$ and significantly blocked PD-1 protein expression compared to controls (Figure 2A), but did not

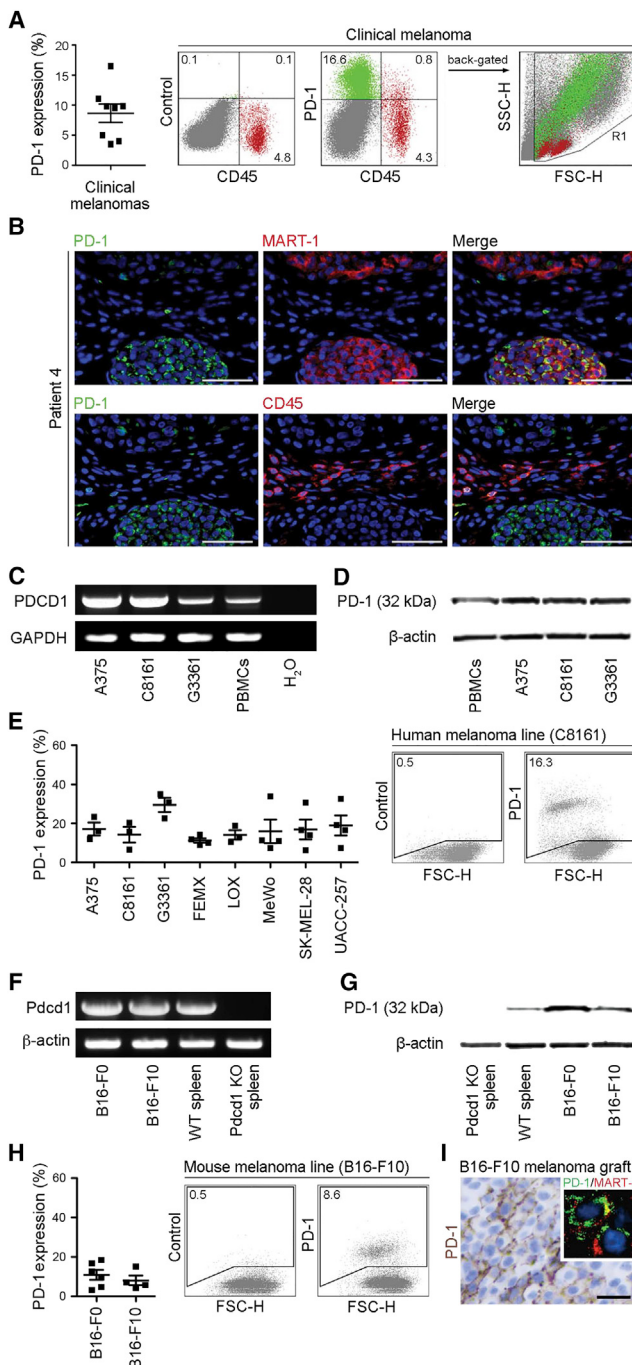


Figure 1. PD-1 Expression by Melanoma Cells

(A) Percentages (mean \pm SEM) (left) and representative flow cytometry plots (right) of PD-1 surface protein expression by clinical tumor biopsy-derived melanoma cells (green) from $n = 8$ distinct melanoma patients. These cells are negative for the CD45 lymphocyte common antigen (red) and the CD31 endothelial marker (see also Figure S1A).

(B) Representative immunofluorescence double staining of a clinical melanoma biopsy for co-expression of PD-1 (green) and MART-1 (red) or of PD-1 (green) and CD45 (red) on a serial tissue section. Nuclei were counterstained with DAPI (blue). Size bars, 100 μ m. Representative of $n = 22/36$ melanoma patients demonstrating melanoma-PD-1 positivity. A patient was considered

significantly alter expression of PD-L1 or PD-L2, respectively (not shown). Conversely, transduction of B16 cells with *Pdcld1*-encoding constructs resulted in upregulation of PD-1, both at the mRNA and protein level (Figure 2B). Melanoma-specific *Pdcld1*-KD resulted in decreased and *Pdcld1*-OE in increased B16-F0 and B16-F10 melanoma growth in immunocompetent C57BL/6 mice compared to that of vector controls (Figure 2C). *Pdcld1*-KD melanoma grafts demonstrated diminished (Figure S3A) and *Pdcld1*-OE melanomas significantly enhanced *Pdcld1* mRNA and PD-1 protein expression compared to control tumors at the experimental endpoint (Figure S3B). We next compared the tumorigenic ability of native PD-1 $^{+}$ versus PD-1 $^{-}$ -sorted B16-F0 and B16-F10 melanoma cells and found that PD-1 $^{+}$ subpopulations demonstrated significantly increased growth in C57BL/6 mice compared to PD-1 $^{-}$ cells (Figure S3C). Together, these findings identify melanoma-expressed PD-1 as a protumorigenic mechanism.

PD-1 expressed by cells of the adaptive immune system has been established as a modulator of tumor-specific immunity (Topalian et al., 2012a). To determine whether the observed tumor growth-accelerating effects of melanoma-expressed PD-1 depend on melanoma-PD-1:lymphocyte interactions, we compared the abilities of *Pdcld1*-KD and *Pdcld1*-OE versus control B16 melanomas to initiate tumor growth in immunocompromised, T-, and B-cell-deficient NSG mice. We found that *Pdcld1*-KD inhibited and *Pdcld1* overexpression increased tumorigenicity of B16-F0 and B16-F10 melanomas in NSG mice compared to controls (Figure 2D), suggesting lymphocyte-independent roles of melanoma-PD-1 in tumorigenesis. Significant *Pdcld1*-KD (Figure S4A) and overexpression (Figure S4B) in B16 melanoma grafts was confirmed after in vivo growth. Consistent with our findings using *Pdcld1*-overexpressing melanoma variants, we found that PD-1 $^{+}$ melanoma subpopulations purified from native B16-F0 and B16-F10 lines demonstrated increased tumorigenicity in NSG mice compared to PD-1 $^{-}$ cell isolates (Figure S4C).

We next examined whether melanoma-specific *Pdcld1* silencing or overexpression affects melanoma cell growth in vitro, in the complete absence of immune cells, using

melanoma-PD-1 positive if any tumor biopsy (total of $n = 50$) showed expression of PD-1 by MART-1 $^{+}$ and/or CD45 $^{-}$ cells. See also Table S1.

(C and D) RT-PCR expression analysis (C) of full-length PD-1 (*PDCD1*) mRNA and (D) immunoblot of PD-1 protein expression by human melanoma lines and PBMCs.

(E) Percentages (mean \pm SEM, left) and representative flow cytometry plots (right) of PD-1 surface protein expression by human melanoma lines ($n = 3$ –4 independent experiments, respectively).

(F and G) RT-PCR expression analysis (F) of full-length PD-1 (*Pdcld1*) mRNA and (G) immunoblot of PD-1 protein expression by murine B16-F0 and B16-F10 melanoma cells, wild-type (WT), and *Pdcld1* knockout (KO) C57BL/6-derived splenocytes.

(H) Percentages (mean \pm SEM, left) and representative flow cytometry plots (right) of PD-1 surface protein expression by B16 cells ($n = 4$ –6 independent experiments, respectively).

(I) Representative PD-1 immunohistochemistry and immunofluorescence double staining for co-expression of PD-1 (green) with MART-1 (red) (inset photomicrograph) of a B16-F10 melanoma graft grown in NSG mice (size bar, 50 μ m).

See also Figures S1 and S2, and Table S1.

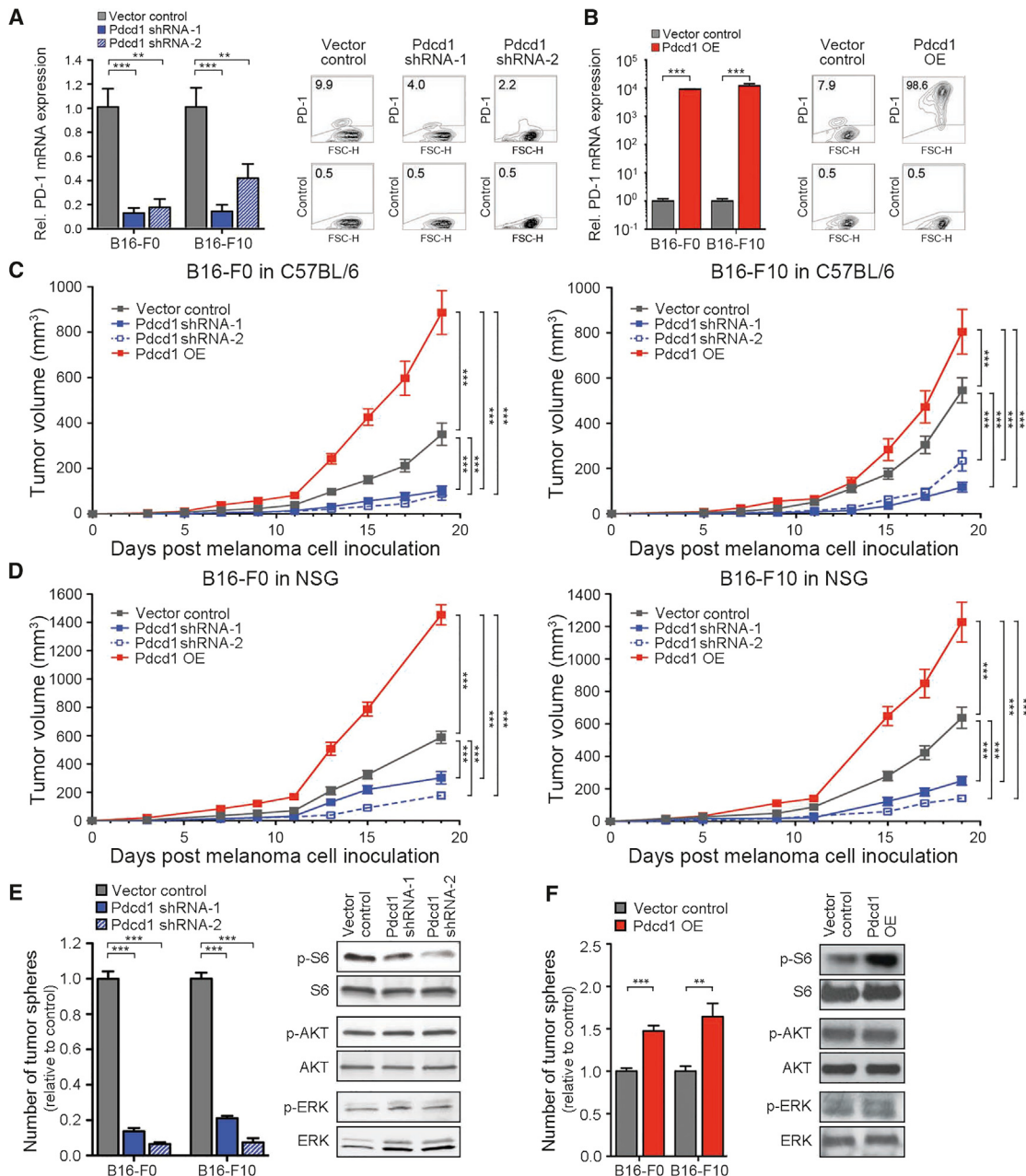


Figure 2. Melanoma-Expressed PD-1 Promotes Tumorigenicity in Murine Melanoma Models

(A and B) PD-1 mRNA and protein expression by *Pdcd1*-shRNA-1 and *Pdcd1*-shRNA-2 versus vector control (A) and by *Pdcd1*-overexpressing (OE) versus vector-control B16-F0 or B16-F10 melanoma cells (B). Representative flow cytometry plots show PD-1 expression in B16-F10 melanoma variants.

(C and D) Tumor growth kinetics (mean \pm SD) of *Pdcd1*-shRNA-1/-2 versus *Pdcd1*-OE versus vector control B16-F0 or B16-F10 melanomas in C57BL/6 mice ($n = 10\text{--}30$ each) (C) or NSG mice ($n = 10\text{--}20$ each) (D).

(E and F) Mean number of tumor spheres \pm SEM (left) and immunoblot analysis of phosphorylated (p) and total S6, AKT, and ERK (right) in *Pdcd1*-shRNA-1 and *Pdcd1*-shRNA-2 versus control (E) and *Pdcd1*-OE versus vector-control B16 melanoma variants (F). Results are representative of $n = 2\text{--}3$ independent experiments (** $p < 0.01$, *** $p < 0.001$).

See also Figures S3 and S4.

established culture system designed for the study of tumorigenic minority populations (Aceto et al., 2012; Civenni et al., 2011). Consistent with our in vivo findings, *Pdcd1*-KD impaired (Figure 2E) and *Pdcd1*-OE promoted in vitro three-dimensional

B16-F0 and B16-F10 culture growth compared to respective controls (Figure 2F). Because PD-1 receptor signaling in T cells modulates several downstream pathways (Riley, 2009) that also serve critical roles in melanomagenesis (Flaherty et al.,

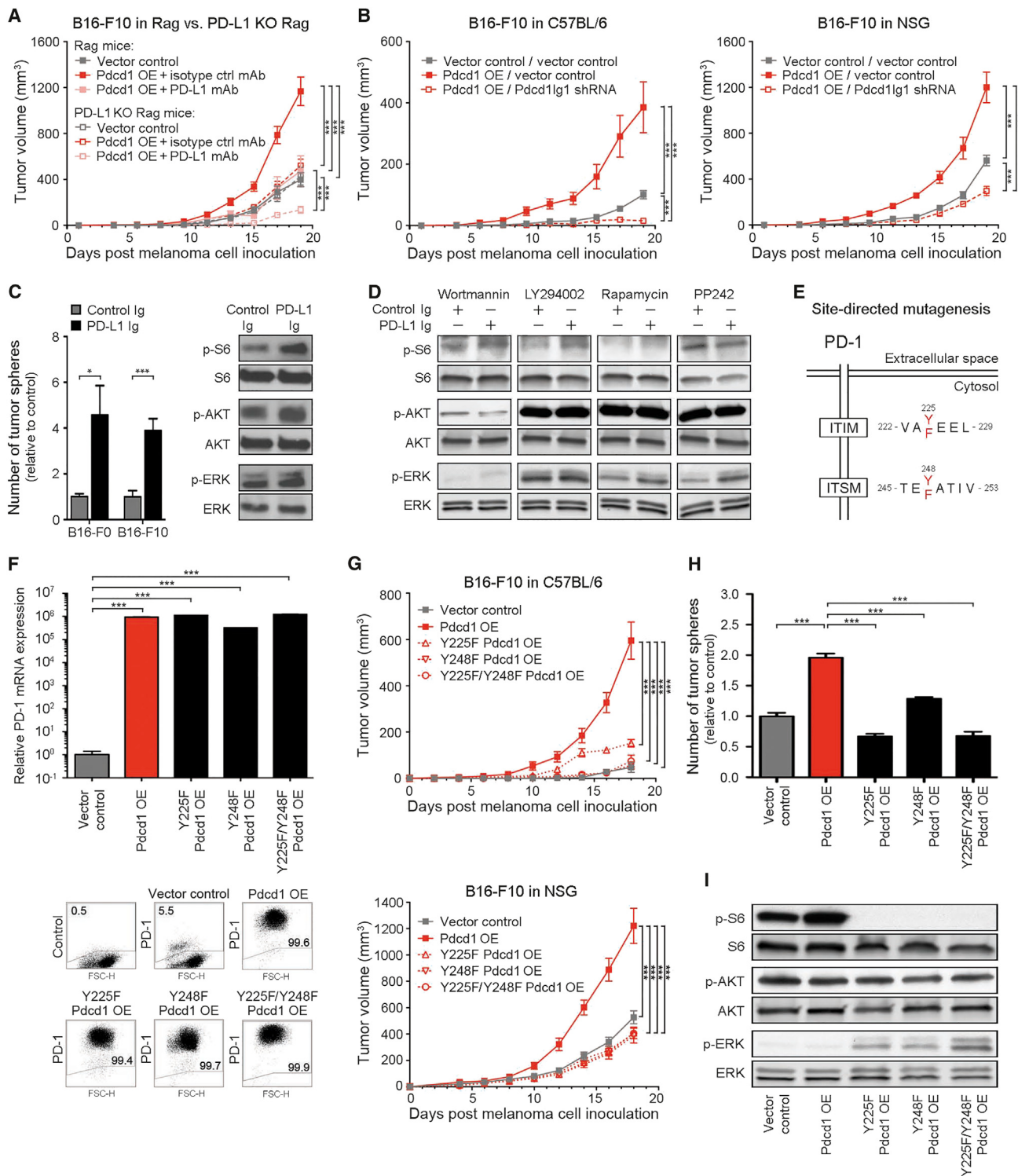


Figure 3. Tumor Cell-Intrinsic PD-1 Signaling Promotes Murine Melanoma Growth

(A) Growth kinetics (mean \pm SD) of *Pdcd1*-OE versus vector control B16-F10 melanomas in PD-L1(–/–) KO Rag(–/–) KO (n = 14 versus 20 versus 10) versus wild-type Rag(–/–) KO recipients (n = 14 versus 14 versus 8) treated with anti-PD-L1- versus isotype control monoclonal antibody (mAb).

(B) Growth kinetics (mean \pm SD) in C57BL/6 (left) and NSG mice (right) of *Pdcd1*-OE B16-F10 cells co-transduced with PD-L1 (*Cd274*, also known as *Pdcd1lg1*)-shRNA versus control-shRNA compared to vector controls (n = 10 each).

(legend continued on next page)

2012), such as MAPK/ERK, PI3K/AKT, and mTOR signaling, we next examined melanoma-*Pdcd1*-specific changes in phospho (p)-ERK1/2, p-AKT, and p-S6 ribosomal protein levels. *Pdcd1*-KD reduced (Figure 2E) and *Pdcd1*-OE increased phosphorylation of the mTOR effector molecule, S6, compared to control B16 melanoma cells (Figure 2F), indicating melanoma cell-intrinsic, PD-1-mediated induction of protumorigenic mTOR pathway activity. Together, these *in vitro* findings suggest lymphocyte-independent, cancer cell-intrinsic functions of melanoma-expressed PD-1 in tumor growth.

Melanoma-PD-1:PD-L1 Interactions Promote Murine Melanoma Growth

We next examined whether ligation of melanoma-PD-1 to its predominant ligand, PD-L1, is required for PD-1-driven tumorigenesis. To test whether melanoma-PD-1:host-PD-L1 interactions promote tumor growth in the absence of adaptive immunity, we grafted *Pdcd1*-OE versus control B16-F10 cells to wild-type Rag(−/−) versus PD-L1(−/−) KO Rag(−/−) mice (Francisco et al., 2009). We found that the growth of *Pdcd1*-OE melanomas was attenuated in PD-L1(−/−) KO Rag(−/−) compared to PD-L1(+/+) Rag(−/−) recipients (Figure S5A). To examine if PD-L1 expressed by melanoma cells (Figure S1) also contributes to melanoma-PD-1-dependent tumorigenesis, we treated PD-L1(−/−) KO Rag(−/−) versus wild-type Rag(−/−) mice grafted with *Pdcd1*-OE melanomas with a PD-L1 blocking antibody. We found that PD-L1 blockade inhibited *Pdcd1*-OE B16-F10 melanoma growth compared to isotype control antibody treatment in PD-L1(−/−) KO mice (Figure 3A). Additionally, PD-L1 antibody treatment resulted in significantly reduced tumor growth of *Pdcd1*-OE melanomas in PD-L1(−/−) KO Rag(−/−) compared to wild-type Rag(−/−) mice (Figure 3A). These findings suggest growth-accelerating functions not only of host-PD-L1:melanoma-PD-1, but also of melanoma-PD-L1:melanoma-PD-1 interactions.

To further demonstrate protumorigenic melanoma-PD-L1 effects in the absence of adaptive immunity, we generated PD-L1 gene (*Cd274*, also known as *Pdcd1lg1*)-KD B16-F10 melanoma cells (Figure S5B) and tested their ability to maintain culture growth and form tumors. Compared to vector controls, *Pdcd1lg1* silencing impaired three-dimensional B16 melanoma growth *in vitro* (Figure S5C) and *in vivo* tumorigenesis in both immunocompetent C57BL/6 and immunocompromised NSG mice (Figure S5D). Moreover, *Pdcd1lg1*-KD reversed the significant increase in tumorigenicity of *Pdcd1*-OE versus vector control B16-F10 melanoma cells in C57BL/6 and NSG mice (Figure 3B). To further demonstrate that PD-L1 interactions with melanoma-PD-1 promote melanoma growth, we treated native

B16-F0 and B16-F10 cultures with a recombinant PD-L1 Fc-fusion protein (PD-L1 Ig), known to elicit changes in PD-1 receptor signaling in T cells (Francisco et al., 2009). Compared to control Ig treatment, addition of PD-L1 Ig to B16 cultures significantly augmented three-dimensional growth and phosphorylation of S6 ribosomal protein (Figure 3C). Because both PI3K/AKT and mTOR signaling are known to feed into downstream S6 phosphorylation, we examined whether pharmacologic inhibition of either pathway can reverse the observed increase in p-S6 expression. We found that mTOR pathway blockade (via rapamycin or PP242) but not PI3K inhibition (via wortmannin or LY294002) suppressed the PD-L1 Ig-dependent phosphorylation of S6 in murine B16-F10 melanoma cells (Figure 3D). Together, these findings demonstrate that interactions between melanoma-expressed PD-1 with its ligand, PD-L1, promote tumor growth and activate mTOR signaling.

Tumor Cell-Intrinsic PD-1 Signaling Is Required for Efficient Murine Melanoma Growth

To determine whether melanoma cell-intrinsic PD-1 signaling is required for efficient tumor growth, we generated *Pdcd1*-OE B16 variants containing tyrosine to phenylalanine single-point mutations of two PD-1 signaling motifs, the immunoreceptor tyrosine-based inhibitory motif (ITIM, disrupted by Y225F mutation) and the immunoreceptor tyrosine-based switch motif (ITSM, disrupted by Y248F mutation), within the cytoplasmic tail of melanoma-PD-1 (Figure 3E). A construct containing point mutations of both tyrosines (Y225F/Y248F) was also created. In immune cells, ITIM and ITSM play pivotal roles in PD-1 signaling (Riley, 2009). Transduction of wild-type versus mutant *Pdcd1* constructs into B16-F0 or B16-F10 melanoma cells resulted in similarly high expression levels of PD-1 (Figure 3F and Figure S5E), permitting a direct comparison between wild-type *Pdcd1*-OE and each of the mutant variants. Strikingly, mutation of either one (Y225F or Y248F) or both (Y225F/Y248F) melanoma-PD-1 signaling motifs significantly abrogated the increased tumor growth observed in both C57BL/6 and NSG mice grafted with wild-type *Pdcd1*-OE versus vector-control B16 melanoma variants (Figure 3G and Figure S5F), suppressed three-dimensional tumor growth *in vitro* (Figure 3H and Figure S5G), and phosphorylation of S6 ribosomal protein (Figure 3I) compared to enforced expression of wild-type *Pdcd1*, respectively.

Melanoma Cell-Intrinsic PD-1 Enhances Human Tumor Xenograft Growth

We next analyzed the effects of melanoma-specific PD-1 knockdown versus PD-1 overexpression on human melanoma xenograft growth. Transduction of human A375, C8161, or G3361

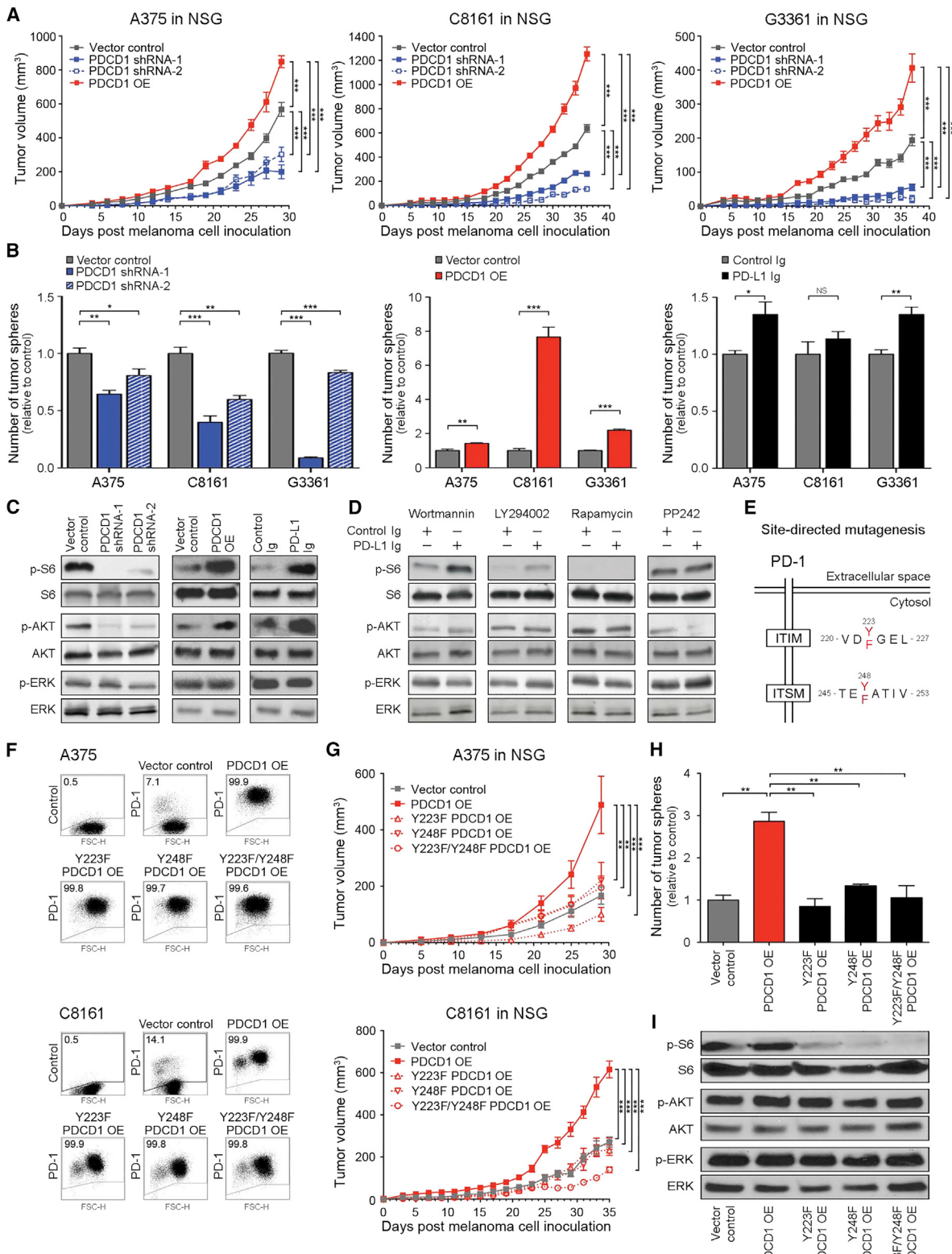
(C) Mean number of tumor spheres ± SEM (left), and immunoblot analysis of p- and total S6, AKT, and ERK in PD-L1 Ig versus control Ig-treated B16 cultures (right).

(D) Immunoblot analysis of p- and total S6, AKT, and ERK in PD-L1 Ig versus control Ig-treated B16-F10 melanoma cells cultured in the presence of the pharmacologic PI3K inhibitors, wortmannin or LY294002, or the mTOR pathway inhibitors, rapamycin or PP242.

(E) Schematic diagram illustrating the introduction of tyrosine to phenylalanine mutations to murine PD-1 signaling motifs via site-directed mutagenesis.

(F) Relative *Pdcd1* mRNA expression (top, mean ± SEM) and representative flow cytometry plots of PD-1 surface protein expression (bottom) by wild-type *Pdcd1*-OE versus Y225F-*Pdcd1*-OE, Y248F-*Pdcd1*-OE, Y225F/Y248F-*Pdcd1*-OE, and vector-control B16-F10 variants.

(G–I) Tumor growth kinetics (G) in C57BL/6 (top, n = 10–14 each) and NSG mice (bottom, n = 8–10 each), (H) mean number of tumor spheres ± SEM, and (I) immunoblot analysis of p- and total S6, AKT, and ERK in B16-F10 melanoma variants as in (F). Immunoblot results are representative of n = 2 independent experiments, respectively (*p < 0.05, **p < 0.01, ***p < 0.001). See also Figure S5.



(legend on next page)

melanoma cells with two distinct *PDCD1*-shRNAs significantly inhibited PD-1 mRNA expression and blocked PD-1 protein expression between 53%–75% (Figure S6A), and infection with *PDCD1*-OE constructs resulted in marked upregulation of PD-1, both at the mRNA and protein level (>90% positivity), respectively (Figure S6B). *PDCD1*-KD significantly inhibited and *PDCD1*-OE markedly increased human melanoma xenograft growth in NSG mice compared to vector-control-transduced A375, C8161, or G3361 tumors (Figure 4A). Preservation of *PDCD1* silencing and overexpression were confirmed for all melanoma xenografts at the experimental endpoint, respectively (Figures S6C and S6D). Moreover, PD-1⁺ cancer cell subsets purified from native C8161 cultures showed significantly increased tumorigenicity in NSG mice, compared to PD-1⁻ C8161 cells (Figure S6E). Consistent with our *in vivo* findings, *PDCD1*-KD impaired and *PDCD1*-OE promoted three-dimensional A375, C8161, and G3361 culture growth compared to controls (Figure 4B). Furthermore, relative to control Ig treatment, addition of human PD-L1 Ig augmented tumor sphere formation of A375 and G3361, but not C8161 melanoma cultures (Figure 4B), the latter of which express greater than 3-fold higher endogenous PD-L1 levels than A375 and G3361 cells (Figure S1B). Similar to our findings in murine B16 cells, human *PDCD1*-KD lines showed a reduction and *PDCD1*-OE and PD-L1 Ig-treated human G3361 melanoma cells an increase in p-S6 levels compared to respective controls (Figure 4C). Additionally, pharmacologic inhibition of mTOR but not PI3K signaling blocked the increase in p-S6 expression in PD-L1 Ig compared to control Ig-treated human G3361 melanoma cells (Figure 4D), indicating mTOR pathway dependence of S6 phosphorylation downstream of the melanoma-PD-1 receptor, consistent with our findings in murine B16 melanoma cells (Figure 3D).

Furthermore, generation of human *PDCD1*-OE ITIM (Y223F) and/or ITSM (Y248F) mutant A375 and C8161 cell lines (Figure 4E) with similarly high expression levels of human PD-1 (Figure 4F) revealed that mutation of either one (Y223F or Y248F) or both (Y223F/Y248F) signaling motifs within the melanoma-PD-1 cytoplasmic tail abrogated the increased tumor growth observed in mice grafted with wild-type *PDCD1*-OE versus vector-control A375 or C8161 variants (Figure 4G). Additionally, Y223F-, Y248F-, and Y223F/Y248F mutant *PDCD1*-OE C8161 melanoma cells demonstrated significantly impaired three-dimensional culture growth (Figure 4H) and reduced p-S6 levels compared

to wild-type *PDCD1*-OE C8161 cells (Figure 4I). Together, these findings identify PD-1 expressed by human melanoma cells as a lymphocyte-independent tumor growth-accelerating mechanism.

Antibody-Mediated Blockade of PD-1 on Melanoma Cells Inhibits Murine Melanoma Growth

We next examined whether antibody-mediated melanoma-PD-1 blockade significantly inhibits tumor growth, even in immunocompromised NSG hosts, as would be expected based upon the herein demonstrated melanoma cell-intrinsic, protumorigenic PD-1 receptor functions. First, administration of a PD-1 blocking antibody to immunocompetent, C57BL/6 recipients starting one day before inoculation with B16-F10 cells resulted in modest inhibition of melanoma growth between days 5 and 11 post inoculation ($p < 0.01$), but showed no significant differences in tumorigenicity compared to isotype control antibody-treatment at later time points (Figure 5A), consistent with previous studies (Peng et al., 2012; Woo et al., 2012). However, we found that antibody-mediated PD-1 blockade significantly ($p < 0.05$) inhibited B16-F10 melanoma growth in PD-1(−/−) KO C57BL/6 mice compared to controls, for the entire duration of the experiment (Figure 5B). Immunohistochemical examination of melanoma grafts harvested at the experimental endpoint revealed >5-fold increased binding ($p < 0.05$) of *in vivo*-administered anti-PD-1 antibody to B16 melanoma target tissue in PD-1(−/−) KO (Figure 5B) compared to wild-type C57BL/6 hosts (Figure 5A), supporting the notion of a more pronounced PD-1 antibody effect on melanoma cells in PD-1(−/−) KO mice. A >20% increase in PD-1 antibody titer in the serum of PD-1(−/−) KO versus PD-1(+/+) C57BL/6 hosts, as determined by rat-IgG2a-specific ELISA (Figure S7A), further indicated that increased PD-1 antibody availability might, at least in part, contribute to the growth-inhibitory effect of PD-1 blockade in PD-1(−/−) KO hosts. Anti-PD-1 antibody administration to NSG mice also significantly ($p < 0.001$) diminished B16-F10 melanoma growth compared to isotype control antibody treatment (Figure 5C). Interestingly, while compared to B16 melanoma grafts grown in C57BL/6 mice, B16 melanomas grafted to NSG mice tended to show increased anti-PD-1 antibody binding, antibody titers were not increased in NSG mouse serum (Figure S7A), suggesting strain-specific differences in PD-1 antibody kinetics. To control for the possibility that the observed growth-inhibitory

Figure 4. PD-1 Expression by Human Melanoma Cells Promotes Experimental Tumor Growth

- (A) Tumor growth kinetics (mean ± SD) of *PDCD1*-shRNA-1, *PDCD1*-shRNA-2, and *PDCD1*-OE versus vector control human A375 (left), C8161 (center), and G3361 melanoma cells (right) grafted to NSG mice ($n = 8$ –20 each).
 - (B) Mean number of tumor spheres ± SEM and (C) immunoblot analysis (G3361) of phosphorylated (p) and total ribosomal protein S6, AKT, and ERK in *PDCD1*-shRNA-1/-2 versus vector control, *PDCD1*-OE versus vector-control, and PD-L1 Ig- versus control Ig-treated human A375, C8161, and G3361 melanoma cultures.
 - (D) Immunoblot analysis of p- and total S6, AKT, and ERK in PD-L1 Ig versus control Ig-treated G3361 melanoma cells cultured in the presence of the pharmacologic PI3K inhibitors, wortmannin or LY294002, or the mTOR pathway inhibitors, rapamycin or PP242.
 - (E) Schematic diagram illustrating the introduction of tyrosine to phenylalanine mutations to human PD-1 signaling motifs via site-directed mutagenesis.
 - (F and G) Representative flow cytometry plots (F) of PD-1 surface protein expression and (G) tumor growth kinetics (mean ± SD) of *PDCD1*-OE versus Y223F-*PDCD1*-OE, Y248F-*PDCD1*-OE, Y223F/Y248F-*PDCD1*-OE, and vector-control human A375 (top, $n = 10$ –24) and C8161 melanomas (bottom, $n = 10$ –12) in NSG mice, respectively.
 - (H and I) Mean number of tumor spheres (H) ± SEM and (I) immunoblot analysis of p- and total S6, AKT, and ERK in C8161 melanoma variants as in (D). Immunoblot results are representative of $n = 2$ –3 independent experiments (* $p < 0.05$, ** $p < 0.01$, *** $p < 0.001$).
- See also Figure S6.

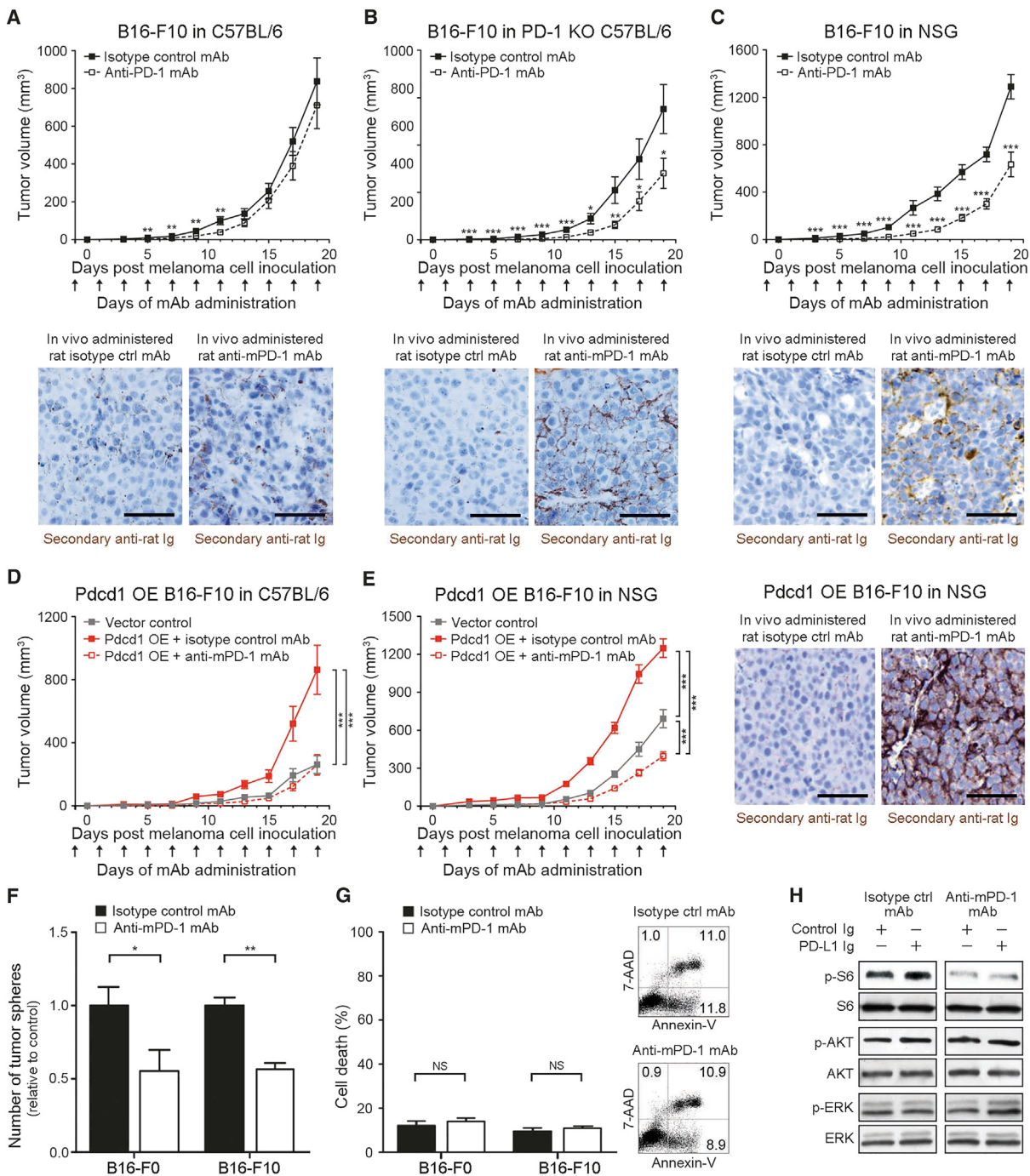


Figure 5. Anti-PD-1 Blocking Antibody Inhibits Murine Melanoma Growth in Immunocompetent, Immunocompromised and PD-1-Deficient Tumor Graft Recipient Mice

(A–E) Tumor growth kinetics (A) (mean \pm SD) of B16-F10 melanomas in wild-type C57BL/6 ($n = 32$ versus 34), (B) PD-1($-\/-$) knockout (KO) C57BL/6 ($n = 20$ versus 16), and (C) NSG ($n = 20$ versus 18), and of (D) *Pdcd1*-overexpressing (OE) versus vector control B16-F10 melanomas in C57BL/6 ($n = 10$ each) or (E) NSG mice ($n = 10$ each) treated with anti-PD-1- versus isotype control antibody. Representative immunohistochemical images illustrate binding of in vivo-administered rat anti-mouse PD-1 blocking but not isotype control antibody to the respective B16-F10 melanoma grafts (size bars, 50 μ m).

(F and G) Mean number of tumor spheres \pm SEM (F) and (G) flow cytometric assessment of cell death (percent AnnexinV $^+$ /7AAD $^+$ cells, mean \pm SEM (left) and representative flow cytometry plots (right) of anti-PD-1- versus isotype control mAb-treated murine B16-F0 and B16-F10 melanoma cultures.

(H) Immunoblot analysis (representative of $n = 2$ independent experiments) of phosphorylated (p) and total ribosomal protein S6, AKT, and ERK in B16 cultures concurrently treated with PD-L1 Ig versus control Ig and/or anti-PD-1- versus isotype control mAb (NS: not significant, * $p < 0.05$, ** $p < 0.01$, *** $p < 0.001$).

See also Figure S7.

effects might result from antibody-mediated blockade of PD-1-expressing innate immune cell subtypes present in NSG mice, we administered anti-PD-1 antibody to NK cell-, macrophage-, and neutrophil-depleted NSG recipients of B16-F10 melanoma cells (Figure S7B). We also generated NSG mice depleted of all three innate immune effector subsets. Anti-PD-1 antibody treatment inhibited B16 melanoma growth compared to isotype control antibody in all innate immune cell-depleted NSG hosts (Figure S7C).

To further confirm melanoma-specific PD-1 inhibition of the PD-1 blocking antibody, we administered anti-PD-1 antibody to C57BL/6 and NSG mice grafted with *Pdcd1*-OE versus vector control B16-F10 melanoma cells. Anti-PD-1 antibody treatment reversed the increase in tumor growth of isotype control-treated *Pdcd1*-OE compared to vector-control B16 melanomas in both C57BL/6 (Figure 5D) and NSG mice, concomitant with binding of in vivo-administered anti-PD-1 antibody to B16 melanomas (Figure 5E), thereby confirming recognition of melanoma-PD-1 by the PD-1 blocking antibody. Antibody-mediated PD-1 blockade also reduced three-dimensional B16-F0 and B16-F10 melanoma growth in vitro (Figure 5F), but did not induce significant cell death compared to isotype control antibody-treatment (Figure 5G). Moreover, treatment of B16 melanoma cultures with anti-PD-1 but not isotype control antibody inhibited phosphorylation of S6 ribosomal protein (Figure 5H). Together, these findings show that antibody-mediated PD-1 blockade directly on melanoma cells inhibits tumor cell-intrinsic, protumorigenic PD-1 functions, including in the absence of adaptive immunity.

Antibody-Mediated PD-1 Blockade Inhibits Human Melanoma Xenograft Growth in Immunodeficient Mice

We next examined whether antibody-mediated PD-1 blockade can also inhibit human melanoma growth in NSG mice. To assess the translational relevance of targeting melanoma cell-intrinsic PD-1 to impede tumor growth, we first administered anti-PD-1 antibody to NSG mice grafted with patient-derived melanoma cells. Consistent with our findings in murine B16 models (Figure 5C), in vivo anti-PD-1 antibody administration to NSG mice significantly inhibited mean tumor volumes of clinical melanoma xenografts derived from three distinct melanoma patients (Figure 6A). Anti-PD-1 antibody treatment also significantly inhibited the growth of human A375, C8161, and G3361 melanoma xenografts in NSG mice compared to that of the respective control antibody-treated melanomas (Figure 6B). Immunohistochemical analysis revealed binding of in vivo-administered anti-human PD-1 antibody to melanoma xenografts (Figure 6C). Administration of anti-PD-1 antibody to NSG mice also abrogated the increased melanoma xenograft growth of isotype control-treated human *PDCD1*-OE compared to vector-control C8161 xenografts (Figure 6D). Marked melanoma binding of in vivo-administered anti-PD-1 antibody to *PDCD1*-OE C8161 melanomas (Figure 6D) confirmed melanoma-PD-1 reactivity of the human anti-PD-1 blocking antibody. Compared to isotype control antibody-treatment, PD-1 blockade also decreased three-dimensional melanoma growth in vitro (Figure 6E), but did not significantly induce apoptosis in human A375, C8161, or G3361 melanoma cultures (Figure 6F). Finally, treatment of G3361 melanoma cells with anti-PD-1 but

not isotype control antibody inhibited PD-L1 Ig-dependent phosphorylation of S6 ribosomal protein (Figure 6G). Together, our findings in NSG mice indicate that anti-PD-1-mediated melanoma growth inhibition results from direct interference with melanoma-expressed PD-1 and is not necessarily dependent on adaptive immunity.

Melanoma Cell Expression of the PD-1 Effector Molecule, p-S6, Correlates with Response to PD-1 Therapy in Cancer Patients

To further assess the translational relevance of melanoma cell-intrinsic PD-1 receptor signaling, we performed p-S6 staining and quantitatively assessed melanoma-p-S6 positivity in pre-treatment versus post-treatment tumor biopsies obtained from $n = 11$ melanoma patients undergoing anti-PD-1 therapy. We found that melanoma biospecimens sampled post PD-1 therapy demonstrated significantly ($p = 0.005$) decreased p-S6 expression compared to patient-matched pre-treatment biopsies (Figure 7A), consistent with our findings in PD-1 antibody-treated melanoma cell lines (Figures 5H and 6G). Additionally, in a cohort of $n = 34$ melanoma patients where pre-treatment tumor tissue was available for analysis, we found that patients with high p-S6 expression (>25% of melanoma cells, Figure 7B) prior to treatment showed a >3-fold increase in progression-free survival (mean progression-free survival: 17.0 versus 4.5 months, $p = 0.001$, Figure 7C) and significantly ($p < 0.05$) enhanced overall survival (mean overall survival: 25.1 versus 13.0 months, Figure 7D) compared to melanoma patients with low p-S6 levels (<25% of melanoma cells, Figure 7B) in pre-treatment tumor biospecimens (Table S2). These findings suggest a relationship between p-S6 and response to PD-1 pathway blockade, thereby indicating the potential translational relevance of melanoma cell-intrinsic PD-1 receptor functions.

DISCUSSION

Our study provides several insights into PD-1 pathway functions in melanoma. First, we have conducted a comprehensive characterization of PD-1 transcript and protein expression by cancer cells in clinical tumor biopsies and established melanoma lines. Until now, PD-1 expression has been mainly reported in immune-competent cells of the hematopoietic lineage (Topalian et al., 2012a). We found that both melanoma cell lines and surgical specimens frequently harbor PD-1-expressing cancer cells. However, PD-1 is not uniformly present on all melanoma cells among heterogeneous tumor samples. Rather, it is restricted to small melanoma subpopulations that are nonetheless critically important for tumor growth, consistent with our previous findings demonstrating preferential PD-1 expression by melanoma-initiating cells (Schatton et al., 2010). In our current study, RT-PCR, immunoblot, and flow cytometric analyses revealed PD-1 on melanoma cells in all cell lines and clinical tumor samples examined. Furthermore, immunofluorescence double labeling similarly showed PD-1 expression by melanoma subpopulations in clinical biopsy specimens obtained from >60% of melanoma patients. Thus, using various independent methods, our work clearly establishes that melanomas frequently contain PD-1⁺ tumor cell fractions. Comparably, melanoma cell expression of the

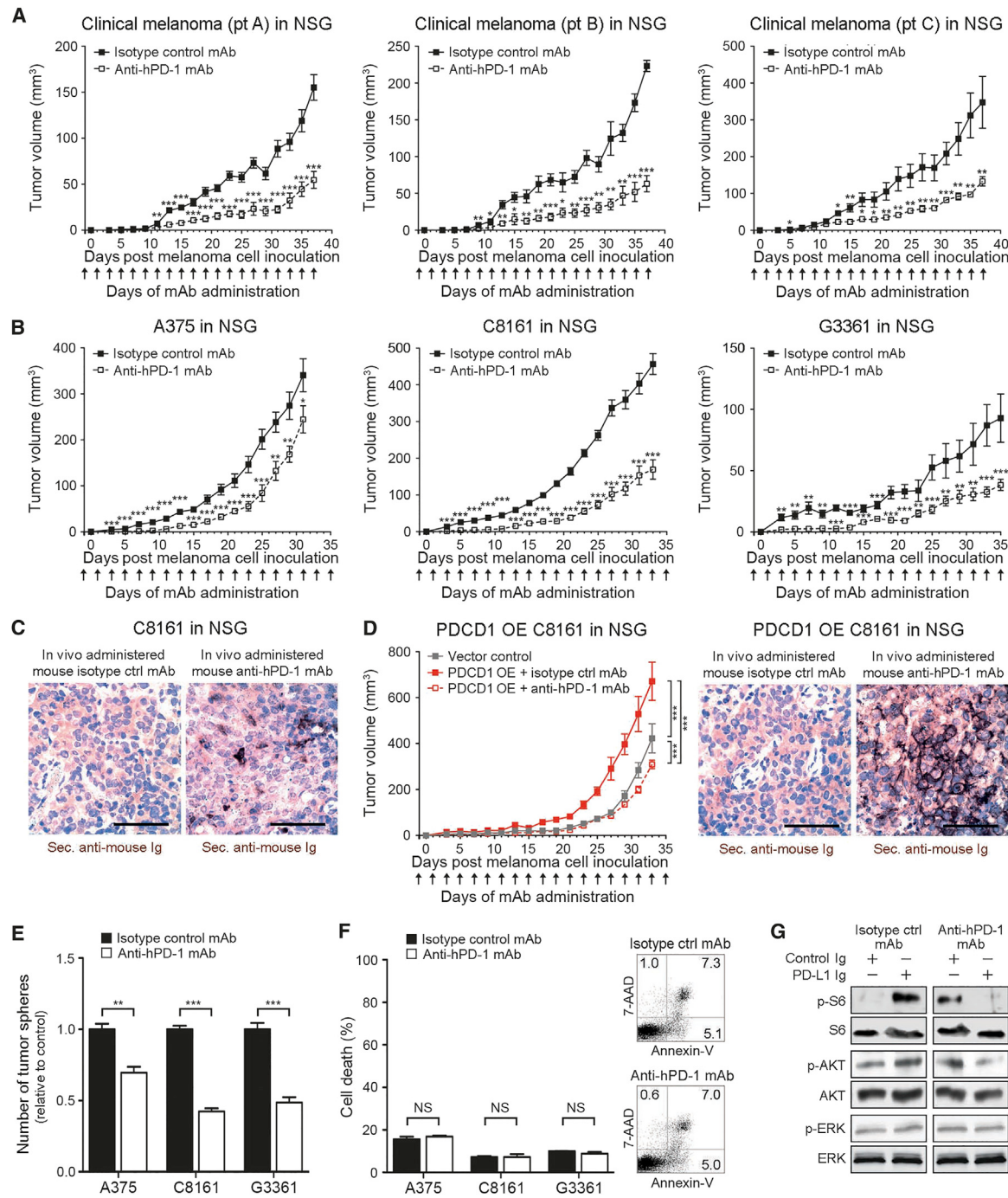


Figure 6. Anti-PD-1 Blocking Antibody Inhibits Human Melanoma Xenograft Growth in Immunocompromised Mice

(A) Kinetics (mean \pm SD) of clinical melanoma xenograft growth in NSG mice treated with anti-human PD-1 or isotype control antibody (patient A, n = 7 each; patient B, n = 5 versus 4; patient C: n = 10 each).

(B–D) Tumor growth kinetics (B) (mean \pm SD) and (C) representative secondary antibody staining (size bars, 50 μm) of mouse anti-human PD-1 versus isotype control antibody-treated human A375 (n = 14 each), C8161 (n = 14 each), or G3361 melanoma xenografts (n = 16 versus 12) or of (D) human *PDCD1*-OE versus vector control-transduced C8161 xenografts in NSG mice (n = 10 each). Immunohistochemical images illustrate binding of in vivo-administered mouse anti-human PD-1 blocking but not isotype control antibody to the respective human melanoma xenograft (size bars, 50 μm).

(E and F) Mean number of tumor spheres (E) \pm SEM and (F) flow cytometric assessment of cell death (percent AnnexinV⁺/7AAD⁺ cells, mean \pm SEM (left) and representative flow cytometry plots (right) of anti-PD-1- versus isotype control mAb-treated human A375, C8161, and G3361 melanoma cultures.

(H) Immunoblot analysis (representative of n = 3 independent experiments) of phosphorylated (p) and total ribosomal protein S6, AKT, and ERK in G3361 cultures concurrently treated with PD-L1 Ig versus control Ig and/or anti-PD-1- versus isotype control mAb (NS: not significant, *p < 0.05, **p < 0.01, ***p < 0.001).

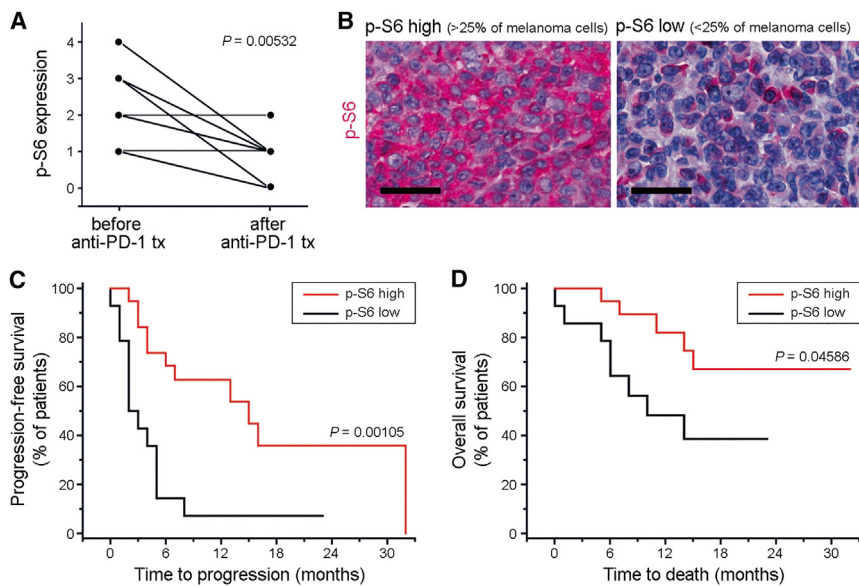


Figure 7. Analysis of p-S6 Expression in Tumor Biospecimens Obtained from Patients with Advanced-Stage Melanoma Undergoing anti-PD-1 Antibody Therapy

(A) Expression of phospho (p)-S6 ribosomal protein by melanoma cells in tumor biospecimens obtained from $n = 11$ patients with stage IV melanoma before treatment start compared to that in patient-matched progressive lesions sampled after initiation of anti-PD-1 antibody therapy. p-S6 expression by melanoma cells was determined by immunohistochemical analysis and graded by three independent investigators blinded to the study outcome on a scale of 0–4 (0: no p-S6 expression by melanoma cells; 1: p-S6 expression in 1%–25%; 2: 26%–50%; 3: 51%–75%; 4: >75% of melanoma cells).

(B) Representative p-S6 immunohistochemistry of tumor biospecimens obtained from melanoma patients before initiation with systemic anti-PD-1 antibody therapy showing low (<25%) versus high (>25%) melanoma cell expression of p-S6. Size bars, 50 μ m.

(C and D) Kaplan-Meier estimates (C) of progression-free survival and (D) of overall survival prob-

ability in stage IV melanoma patients ($n = 34$) demonstrating low (<25%, $n = 14$ patients) versus high melanoma cell-expression of p-S6 (>25%, $n = 20$ patients) in tumor biospecimens obtained before initiation of systemic anti-PD-1 antibody treatment.

See also Table S2.

PD-1 ligand, PD-L1, is often confined to small subsets of cancer cells within clinical tumor specimens (Herbst et al., 2014; Topalian et al., 2012b).

Second, this study demonstrates PD-1 receptor signaling in a non-immune cell type, i.e., melanoma cells. To date, PD-1 immunobiology has been mainly studied in T cells (Topalian et al., 2012a). Binding of T-cell-expressed PD-1 to its ligands mediates inhibitory signals that downmodulate T effector functions. For example, in the cancer context, PD-1 expression by tumor-reactive CTLs results in their exhaustion or functional impairment (Fourcade et al., 2010; Sakuishi et al., 2010), which represents a key mechanism underlying tumor immune evasion (Pardoll, 2012). Similar to the protumorigenic effects of T-cell-expressed PD-1, our findings establish PD-1 expressed by melanoma cells as a tumor-growth-promoting mechanism in multiple independent experimental in vitro and in vivo systems. However, while T cell-PD-1 promotes cancer progression by dampening anti-tumor immune responses, melanoma-PD-1 promotes tumor growth, even in the absence of a functional adaptive immune system.

Our results further indicate that efficient, PD-1-driven tumorigenesis requires melanoma-PD-1 interactions with host- and/or melanoma-expressed PD-L1, because both PD-L1-deficient and PD-L1 antibody-treated mice grafted with *Pdcd1*-OE melanomas demonstrate decreased tumor growth compared to respective controls. Additionally, PD-L1 (*Pdcd1lg1*) silencing reversed melanoma-PD-1-driven tumorigenesis and recombinant PD-L1 Ig treatment promoted melanoma spheroid growth. PD-L1 expression by melanoma cells has established roles in tumor immune evasion (Dong et al., 2002). Beyond promoting cancer progression by engaging with TIL-expressed PD-1, our study indicates that melanoma-expressed PD-L1 may also pro-

mote tumor growth via paracrine or autocrine interactions with the melanoma-PD-1 receptor.

In T cells, PD-1 engagement by its ligands modulates signaling networks downstream of the TCR, including mTOR and PI3K/AKT (Riley, 2009). Consistent with the interrelationship of PD-1 and PI3K/AKT/mTOR signaling in T cells, the important role of these pathways in melanoma proliferation (Flaherty et al., 2012), and the herein described protumorigenic effects of melanoma-PD-1, we found that *PDCD1*-KD, antibody-mediated PD-1 blockade, and mutagenesis of melanoma-PD-1 signaling motifs decreased, while *PDCD1*-OE and PD-L1 Ig-treatment increased phosphorylation of the mTOR effector molecule (Corcoran et al., 2013), ribosomal protein S6. Melanoma-PD-1-dependent S6 phosphorylation was reversed via pharmacologic inhibition of mTOR but not PI3K, suggesting that the PD-1 receptor on melanoma cells activates downstream mTOR signaling through a PI3K/AKT-independent pathway. However, whereas PD-1 activation augments p-S6 levels in melanoma cells and enhances tumor growth, it dampens mTOR signaling in T cells, leading to diminished proliferation (Riley, 2009). Because S6 phosphorylation represents a point of convergence that integrates multiple upstream signaling networks (Corcoran et al., 2013; Flaherty et al., 2012), it is possible that melanoma-PD-1 might also modulate several alternative signaling networks, in addition to the mTOR pathway.

PD-1 ligation in T-lymphocytes is known to recruit phosphatases SHP-1 and SHP-2 to its ITIM and ITSM cytosolic loci, which induces dephosphorylation of proximal TCR signaling intermediaries and subsequent suppression of several pathways downstream of the TCR, including mTOR (Riley, 2009). SHP-2 is also expressed by melanoma cells (Ostman et al., 2006) and tumor-initiating cell subsets in other cancers (Aceto et al.,

2012; Liu et al., 2011), paralleling our previous findings of preferential PD-1 expression by melanoma-initiating cells (Schattton et al., 2010). In cancer cells, SHP-2-dependent signaling promotes activation of protumorigenic pathways, including mTOR (Liu et al., 2011; Ostman et al., 2006). The divergent effects of PD-1 ligation on mTOR signaling in melanoma cells versus T cells are thus entirely consistent with the opposing, protumorigenic versus growth-inhibitory roles of SHP-2 in the respective tissues.

Finally, our work reveals that PD-1 pathway interference exerts tumor growth-inhibitory effects, not only in mice with fully intact immunity, but also in melanoma cultures devoid of immune cells and in severely immunocompromised, T cell-, B cell-, and innate-immune-cell-deficient hosts. Together, these results show that antibody-mediated blockade of PD-1 at the level of the melanoma cell inhibits tumor growth. Because PD-1 pathway inhibitors have produced unprecedented response rates in otherwise treatment-refractory patients with advanced cancers, including malignant melanoma (Hamid et al., 2013; Herbst et al., 2014; Topalian et al., 2012b; Weber et al., 2015; Wolchok et al., 2013), our findings are of potential translational importance. It has been well established that PD-1 blockade reverses cancer-antigen-specific T cell exhaustion, thereby restoring anti-tumor immunity (Fourcade et al., 2010; Sakuishi et al., 2010). Nevertheless, our data suggest that blockade of PD-1 directly on melanoma cells might represent an important additional, tumor cell-intrinsic mechanism that could contribute to the clinical effectiveness of PD-1 cancer therapy. In support of this possibility, our data obtained in a small cohort of patients with stage IV melanoma suggests that tumoral expression of the PD-1 receptor signaling mediator, p-S6, appears to correlate with response to anti-PD-1 antibodies. However, the possible utility of p-S6 as a potential biomarker of PD-1 inhibitor sensitivity will require independent validation in larger patient cohorts, including prospective cohort studies.

Consistent with our findings of protumorigenic effects of the melanoma-PD-1:PD-L1 axis, clinical trial data suggest a correlation between melanoma-PD-L1 and TIL-PD-L1 expression and objective response to PD-1 checkpoint blockade (Herbst et al., 2014; Topalian et al., 2012b; Tumeh et al., 2014). Interestingly, both elevated PD-L1 (Jiang et al., 2013) and p-S6 expression levels (Corcoran et al., 2013) have evolved as potential biomarkers of resistance to melanoma therapies targeting oncogenic BRAF mutations. Therefore, our data suggest that combination of therapies targeting the MAPK pathway (Flaherty et al., 2012) with PD-1 inhibitors may be effective, not only because they activate tumor-specific immunity while concurrently blocking the MAPK oncogenic pathway, but also because PD-1/PD-L1 blockade might additionally suppress mTOR-associated protumorigenic signals. Furthermore, in light of our findings, the superior clinical activity and safety profile of anti-PD-1 compared to anti-CTLA-4 therapy (Hamid et al., 2013; Pardoll, 2012; Postow et al., 2015; Weber et al., 2015) might, at least in part, relate to the fact that the latter merely interferes with T cell function, whereas PD-1 antibody treatment may also directly target other PD-1-expressing immune cell types (Topalian et al., 2012a) or the tumor itself, as suggested by our data. Finally, robust clinical response to anti-PD-1 therapy in patients

with cancers that have hitherto not typically responded to immunotherapy (Herbst et al., 2014; Topalian et al., 2012b) could at least be partially explained by direct PD-1 inhibition on tumor cells in the respective malignancies.

In summary, our findings identify PD-1 expressed by melanoma cells as a tumor growth receptor and molecular mediator of melanoma cell-intrinsic mTOR signaling, serving to promote tumorigenesis in addition to its protumorigenic role when expressed by immune cells. Recognition of melanoma-PD-1 receptor-driven tumorigenesis critically enhances our understanding of the mechanisms underlying melanoma progression and could contribute to the further refinement of PD-1-targeted therapies, for improved outcomes in patients with advanced stage cancer.

EXPERIMENTAL PROCEDURES

Melanoma Cell Lines, Culture Methods, and Clinical Specimens

Melanoma cell lines were cultured as described (Schattton et al., 2008). Human PBMCs were obtained from healthy volunteers and clinical tumor biospecimens were obtained from melanoma patients in accordance with protocols approved by the IRBs of Partners Health Care Management, the Dana-Farber Cancer Institute, the University of Zurich, Switzerland, and the University of Bern, Switzerland. Informed consent was obtained from all subjects and all studies were conducted in accordance with the Declaration of Helsinki. PD-1⁺ and PD-1⁻ melanoma subpopulations were generated as described (Schattton et al., 2008; Schattton et al., 2010).

RT-PCR, Real-Time qPCR, and Flow Cytometry

Full-length *PDCD1* was amplified and sequenced following reverse transcription of total mRNA using *PDCD1*-specific primer pairs. Relative *PDCD1*, *PDCD1LG1* (*CD274*), and *PDCD1LG2* (*CD273*) transcript levels were determined by real-time qRT-PCR and calculated using the $2^{(-\Delta\Delta Ct)}$ method (Schattton et al., 2008; Schattton et al., 2010). PD-1 surface protein expression by established melanoma lines and patient-derived melanoma single-cell suspensions was analyzed by flow cytometry (Schattton et al., 2008; Schattton et al., 2010).

Western Blot Analysis

Cells were lysed, total protein separated by SDS/PAGE and transferred to a PVDF membrane by electroblotting (Posch et al., 2013). Expression levels of human and murine PD-1 and of phosphorylated versus total ERK1/2, AKT, and S6 proteins were determined using enhanced chemiluminescence (Posch et al., 2013) or the Odyssey CLx imaging system (LI-COR Biosciences).

Immunohistochemistry and Immunofluorescence Staining

Immunofluorescence double labeling for PD-1, MART-1, and/or CD45, and immunohistochemical analysis of PD-1 expression in experimental tumors and of p-S6 expression in tumor biospecimens obtained from melanoma patients undergoing anti-PD-1 antibody therapy were carried out as described (Schattton et al., 2008; Schattton et al., 2010). p-S6 immunoreactivity by melanoma cells was graded by three independent investigators blinded to the study outcome on a scale of 0–4 (0: no p-S6 expression by melanoma cells; 1: p-S6 expression in 1%–25%; 2: 26%–50%; 3: 51%–75%; 4: >75% of melanoma cells).

Generation of Stable PD-1 or PD-L1 Knockdown and PD-1-Overexpressing Melanoma Cell Line Variants

Stable PD-1 or PD-L1 knockdown melanoma lines were generated using lentiviral transduction particles containing shRNAs against human *PDCD1*, murine *Pdcd1*, or murine *Pdcd1lg1* (*CD274*), and PD-1-overexpressing melanoma lines by infection with viral particles containing the full-length murine *Pdcd1* or human *PDCD1* CDS. *PDCD1*-OE melanoma variants containing tyrosine to phenylalanine single-point mutations within PD-1 signaling motifs were

generated by site-directed mutagenesis followed by enforced expression, as above.

Three-Dimensional Melanoma Culture

Melanoma tumor sphere cultures of native or melanoma-PD-1 variant lines were maintained, as described (Aceto et al., 2012; Civenni et al., 2011), in standard culture medium, as above, in the presence or absence of anti-PD-1 or isotype control mAb, recombinant PD-L1 Ig or control Ig.

Murine Melanoma Induction and Human Melanoma Xenotransplantation

C57BL/6, PD-1(−/−) KO C57BL/6, NSG, Rag(−/−), and PD-L1(−/−) KO Rag(−/−) mice (Francisco et al., 2009) were maintained and experiments performed in accordance with IACUC approved experimental protocols. For tumorigenicity studies, melanoma cells were injected subcutaneously into flanks of recipient mice (Schatton et al., 2008). For PD-1 and PD-L1 targeting experiments melanoma cells were grafted, mice intraperitoneally injected with anti-PD-1, anti-PD-L1, or isotype control mAbs (200 µg, respectively) every other day starting one day before melanoma inoculation and tumor formation/growth assessed as described (Schatton et al., 2008).

Statistical Analysis

Gene and protein expression levels, tumor spheroid, and in vivo melanoma growth were compared statistically using the unpaired Student's t test, the nonparametric Mann-Whitney test (comparison of two experimental groups) or repeated-measures two-way ANOVA followed by the Bonferroni correction (comparison of three or more experimental groups). Kaplan-Meier estimates and the log-rank test were used to analyze statistical differences in progression-free and overall survival between melanoma patients treated with anti-PD-1 antibody therapy, whose pre-treatment tumor biopsies showed low versus high melanoma cell expression of p-S6. Differences in p-S6 expression in patient-matched tumor biospecimens obtained before and after PD-1 therapy were statistically compared using the paired Student's t test. Data were tested for normal distribution using the D'Agostino and Pearson omnibus normality test. A two-sided value of $p < 0.05$ was considered statistically significant.

See also the [Supplemental Experimental Procedures](#).

SUPPLEMENTAL INFORMATION

Supplemental Information includes Supplemental Experimental Procedures, seven figures, and two tables and can be found with this article online at <http://dx.doi.org/10.1016/j.cell.2015.08.052>.

AUTHOR CONTRIBUTIONS

S.K. and T.S. planned the project. S.K., C.P., S.R.B., H.M., C.S., E.G., C.P.E., N.L., V.R.J., Q.Z., R.T., W.H., and T.S. carried out experimental work. S.K., C.P., S.R.B., H.M., C.S., E.G., C.P.E., N.L., V.R.J., Q.Z., W.H., A.C., R.D., M.C.M., K.T.F., M.H.F., G.F.M., A.H.S., T.S.K., and T.S. analyzed data. S.K. and T.S. wrote the paper. All authors discussed the results and commented on the manuscript.

ACKNOWLEDGMENTS

We thank M. Joubert, I. Portugal, C. Correia, and C. Lee for technical assistance. This work was supported by an Innovative Research Grant from the Melanoma International Foundation, a Fund to Sustain Research Excellence from the Brigham Research Institute, Brigham and Women's Hospital, Department of Dermatology funding for new investigators (to T.S.), a Swiss National Science Foundation grant PMDPP3_151326 (to E.G.), and NIH/NCI grants 1R01CA158467 (to M.H.F. and G.F.M.), and U54 CA163125 (to A.H.S.). T.S. is the recipient of a Research Career Development award from the Dermatology Foundation. C.P. and H.M. are recipients of a Klaus Wolff Fellowship by the Austrian Society of Dermatology and Venereology and received salary support from the Fondation René Touraine. C.P. was awarded a Melanoma

Research Scholar Award from the Outrun the Sun Melanoma Foundation. N.L. is the recipient of a Medical Student Grant from the American Skin Association. V.R.J. is supported by the Department of Defense through the National Defense Science and Engineering Graduate Fellowship (NDSEG) Program. The authors declare that there are no conflicts of interest.

Received: April 10, 2015

Revised: August 18, 2015

Accepted: August 25, 2015

Published: September 10, 2015

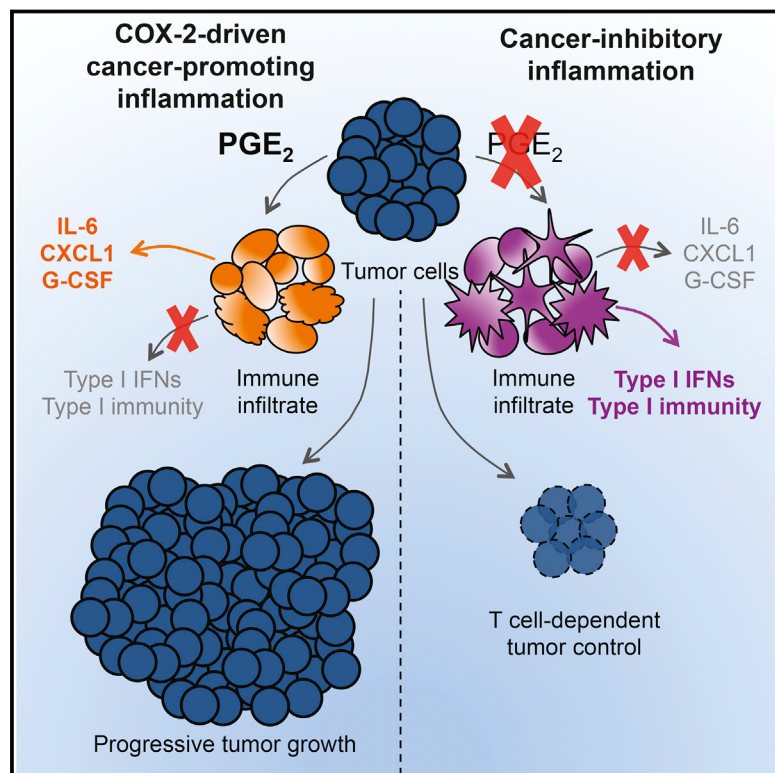
REFERENCES

- Aceto, N., Sausgruber, N., Brinkhaus, H., Gaidatzis, D., Martiny-Baron, G., Mazzarol, G., Confalonieri, S., Quarto, M., Hu, G., Balwierz, P.J., et al. (2012). Tyrosine phosphatase SHP2 promotes breast cancer progression and maintains tumor-initiating cells via activation of key transcription factors and a positive feedback signaling loop. *Nat. Med.* 18, 529–537.
- Civenni, G., Walter, A., Kobert, N., Mihic-Probst, D., Zipser, M., Belloni, B., Seifert, B., Moch, H., Dummer, R., van den Broek, M., and Sommer, L. (2011). Human CD271-positive melanoma stem cells associated with metastasis establish tumor heterogeneity and long-term growth. *Cancer Res.* 71, 3098–3109.
- Corcoran, R.B., Rothenberg, S.M., Hata, A.N., Faber, A.C., Piris, A., Nazarian, R.M., Brown, R.D., Godfrey, J.T., Winokur, D., Walsh, J., et al. (2013). TORC1 suppression predicts responsiveness to RAF and MEK inhibition in BRAF-mutant melanoma. *Sci. Transl. Med.* 5, 196ra98.
- Dong, H., Strome, S.E., Salomao, D.R., Tamura, H., Hirano, F., Flies, D.B., Roche, P.C., Lu, J., Zhu, G., Tamada, K., et al. (2002). Tumor-associated B7-H1 promotes T-cell apoptosis: a potential mechanism of immune evasion. *Nat. Med.* 8, 793–800.
- Flaherty, K.T., Hodi, F.S., and Fisher, D.E. (2012). From genes to drugs: targeted strategies for melanoma. *Nat. Rev. Cancer* 12, 349–361.
- Fourcade, J., Sun, Z., Benallaoua, M., Guillaume, P., Luescher, I.F., Sander, C., Kirkwood, J.M., Kuchroo, V., and Zarour, H.M. (2010). Upregulation of Tim-3 and PD-1 expression is associated with tumor antigen-specific CD8+ T cell dysfunction in melanoma patients. *J. Exp. Med.* 207, 2175–2186.
- Francisco, L.M., Salinas, V.H., Brown, K.E., Vanguri, V.K., Freeman, G.J., Kuchroo, V.K., and Sharpe, A.H. (2009). PD-L1 regulates the development, maintenance, and function of induced regulatory T cells. *J. Exp. Med.* 206, 3015–3029.
- Gubin, M.M., Zhang, X., Schuster, H., Caron, E., Ward, J.P., Noguchi, T., Ivanova, Y., Hundal, J., Arthur, C.D., Krebber, W.J., et al. (2014). Checkpoint blockade cancer immunotherapy targets tumour-specific mutant antigens. *Nature* 515, 577–581.
- Hamid, O., Robert, C., Daud, A., Hodi, F.S., Hwu, W.J., Kefford, R., Wolchok, J.D., Hersey, P., Joseph, R.W., Weber, J.S., et al. (2013). Safety and tumor responses with lambrolizumab (anti-PD-1) in melanoma. *N. Engl. J. Med.* 369, 134–144.
- Herbst, R.S., Soria, J.C., Kowanetz, M., Fine, G.D., Hamid, O., Gordon, M.S., Sosman, J.A., McDermott, D.F., Powderly, J.D., Gettinger, S.N., et al. (2014). Predictive correlates of response to the anti-PD-L1 antibody MPDL3280A in cancer patients. *Nature* 515, 563–567.
- Jiang, X., Zhou, J., Giobbie-Hurder, A., Wargo, J., and Hodi, F.S. (2013). The activation of MAPK in melanoma cells resistant to BRAF inhibition promotes PD-L1 expression that is reversible by MEK and PI3K inhibition. *Clin. Cancer Res.* 19, 598–609.
- Liu, K.W., Feng, H., Bachoo, R., Kazlauskas, A., Smith, E.M., Symes, K., Hamilton, R.L., Nagane, M., Nishikawa, R., Hu, B., and Cheng, S.Y. (2011). SHP-2/PTPN11 mediates gliomagenesis driven by PDGFRA and INK4A/ARF aberrations in mice and humans. *J. Clin. Invest.* 121, 905–917.
- Ostman, A., Hellberg, C., and Böhmer, F.D. (2006). Protein-tyrosine phosphatases and cancer. *Nat. Rev. Cancer* 6, 307–320.

- Pardoll, D.M. (2012). The blockade of immune checkpoints in cancer immunotherapy. *Nat. Rev. Cancer* 12, 252–264.
- Peng, W., Liu, C., Xu, C., Lou, Y., Chen, J., Yang, Y., Yagita, H., Overwijk, W.W., Lizée, G., Radvanyi, L., and Hwu, P. (2012). PD-1 blockade enhances T-cell migration to tumors by elevating IFN- γ inducible chemokines. *Cancer Res.* 72, 5209–5218.
- Posch, C., Moslehi, H., Feeney, L., Green, G.A., Ebaee, A., Feichtenschlager, V., Chong, K., Peng, L., Dimon, M.T., Phillips, T., et al. (2013). Combined targeting of MEK and PI3K/mTOR effector pathways is necessary to effectively inhibit NRAS mutant melanoma in vitro and in vivo. *Proc. Natl. Acad. Sci. USA* 110, 4015–4020.
- Postow, M.A., Callahan, M.K., and Wolchok, J.D. (2015). Immune Checkpoint Blockade in Cancer Therapy. *J. Clin. Oncol.* 33, 1974–1982.
- Riley, J.L. (2009). PD-1 signaling in primary T cells. *Immunol. Rev.* 229, 114–125.
- Rizvi, N.A., Hellmann, M.D., Snyder, A., Kvistborg, P., Makarov, V., Havel, J.J., Lee, W., Yuan, J., Wong, P., Ho, T.S., et al. (2015). Mutational landscape determines sensitivity to PD-1 blockade in non-small cell lung cancer. *Science* 348, 124–128.
- Sakuishi, K., Apetoh, L., Sullivan, J.M., Blazar, B.R., Kuchroo, V.K., and Anderson, A.C. (2010). Targeting Tim-3 and PD-1 pathways to reverse T cell exhaustion and restore anti-tumor immunity. *J. Exp. Med.* 207, 2187–2194.
- Schatton, T., Murphy, G.F., Frank, N.Y., Yamaura, K., Waaga-Gasser, A.M., Gasser, M., Zhan, Q., Jordan, S., Duncan, L.M., Weishaupt, C., et al. (2008). Identification of cells initiating human melanomas. *Nature* 451, 345–349.
- Schatton, T., Schütte, U., Frank, N.Y., Zhan, Q., Hoerning, A., Robles, S.C., Zhou, J., Hodi, F.S., Spagnoli, G.C., Murphy, G.F., and Frank, M.H. (2010). Modulation of T-cell activation by malignant melanoma initiating cells. *Cancer Res.* 70, 697–708.
- Snyder, A., Makarov, V., Merghoub, T., Yuan, J., Zaretsky, J.M., Desrichard, A., Walsh, L.A., Postow, M.A., Wong, P., Ho, T.S., et al. (2014). Genetic basis for clinical response to CTLA-4 blockade in melanoma. *N. Engl. J. Med.* 371, 2189–2199.
- Topalian, S.L., Drake, C.G., and Pardoll, D.M. (2012a). Targeting the PD-1/B7-H1(PD-L1) pathway to activate anti-tumor immunity. *Curr. Opin. Immunol.* 24, 207–212.
- Topalian, S.L., Hodi, F.S., Brahmer, J.R., Gettinger, S.N., Smith, D.C., McDermott, D.F., Powderly, J.D., Carvajal, R.D., Sosman, J.A., Atkins, M.B., et al. (2012b). Safety, activity, and immune correlates of anti-PD-1 antibody in cancer. *N. Engl. J. Med.* 366, 2443–2454.
- Tumeh, P.C., Harview, C.L., Yearley, J.H., Shintaku, I.P., Taylor, E.J., Robert, L., Chmielowski, B., Spasic, M., Henry, G., Ciobanu, V., et al. (2014). PD-1 blockade induces responses by inhibiting adaptive immune resistance. *Nature* 515, 568–571.
- Weber, J.S., D'Angelo, S.P., Minor, D., Hodi, F.S., Gutzmer, R., Neyns, B., Hoeller, C., Khushalani, N.I., Miller, W.H., Jr., Lao, C.D., et al. (2015). Nivolumab versus chemotherapy in patients with advanced melanoma who progressed after anti-CTLA-4 treatment: a randomised, controlled, open-label, phase 3 trial. *Lancet Oncol.* 16, 375–384.
- Wolchok, J.D., Kluger, H., Callahan, M.K., Postow, M.A., Rizvi, N.A., Lesokhin, A.M., Segal, N.H., Ariyan, C.E., Gordon, R.A., Reed, K., et al. (2013). Nivolumab plus ipilimumab in advanced melanoma. *N. Engl. J. Med.* 369, 122–133.
- Woo, S.R., Turnis, M.E., Goldberg, M.V., Bankoti, J., Selby, M., Nirschl, C.J., Bettini, M.L., Gravano, D.M., Vogel, P., Liu, C.L., et al. (2012). Immune inhibitory molecules LAG-3 and PD-1 synergistically regulate T-cell function to promote tumoral immune escape. *Cancer Res.* 72, 917–927.
- Yadav, M., Jhunjhunwala, S., Phung, Q.T., Lupardus, P., Tanguay, J., Bumbaca, S., Franci, C., Cheung, T.K., Fritzsche, J., Weinschenk, T., et al. (2014). Predicting immunogenic tumour mutations by combining mass spectrometry and exome sequencing. *Nature* 515, 572–576.

Cyclooxygenase-Dependent Tumor Growth through Evasion of Immunity

Graphical Abstract



Authors

Santiago Zelenay, Annemarthe G. van der Veen, Jan P. Böttcher, ..., Sergio A. Quezada, Erik Sahai, Caetano Reis e Sousa

Correspondence

santiago.zelenay@cruk.manchester.ac.uk (S.Z.), caetano@crick.ac.uk (C.R.S.)

In Brief

Cyclooxygenase-driven prostaglandin E2, produced by a variety of tumors, drives malignant growth through successful evasion of type I interferon and/or T-cell-dependent tumor elimination. A remarkable synergy between cyclooxygenase inhibitors and checkpoint blockade immunotherapy results in tumor eradication.

Highlights

- Cyclooxygenase in tumors induces PGE₂ that subverts myeloid cell function
- COX ablation in tumors enables immune control
- COX inhibition synergizes with checkpoint blockade therapy
- A COX inflammatory signature is conserved across mouse and human cancer biopsies

Cyclooxygenase-Dependent Tumor Growth through Evasion of Immunity

Santiago Zelenay,^{1,6,*} Annemarthe G. van der Veen,¹ Jan P. Böttcher,¹ Kathryn J. Snelgrove,¹ Neil Rogers,¹ Sophie E. Acton,¹ Probir Chakravarty,² Maria Romina Girotti,³ Richard Marais,³ Sergio A. Quezada,⁴ Erik Sahai,⁵ and Caetano Reis e Sousa^{1,*}

¹Immunobiology Laboratory, The Francis Crick Institute, Lincoln's Inn Fields Laboratory, 44 Lincoln's Inn Fields, London WC2A 3LY, UK

²Bioinformatics, The Francis Crick Institute, Lincoln's Inn Fields Laboratory, 44 Lincoln's Inn Fields, London WC2A 3LY, UK

³Molecular Oncology Group, Cancer Research UK Manchester Institute, The University of Manchester, Manchester M20 4BX, UK

⁴Cancer Immunology Unit, Research Department of Haematology, University College London Cancer Institute, London WC1E 6DD, UK

⁵Tumor Cell Biology Laboratory, The Francis Crick Institute, Lincoln's Inn Fields Laboratory, 44 Lincoln's Inn Fields, London WC2A 3LY, UK

⁶Present address: Cancer Inflammation and Immunity Group, Cancer Research UK Manchester Institute, The University of Manchester, Manchester M20 4BX, UK

*Correspondence: santiago.zelenay@cruk.manchester.ac.uk (S.Z.), caetano@crick.ac.uk (C.R.S.)

<http://dx.doi.org/10.1016/j.cell.2015.08.015>

SUMMARY

The mechanisms by which melanoma and other cancer cells evade anti-tumor immunity remain incompletely understood. Here, we show that the growth of tumors formed by mutant *Braf*^{V600E} mouse melanoma cells in an immunocompetent host requires their production of prostaglandin E2, which suppresses immunity and fuels tumor-promoting inflammation. Genetic ablation of cyclooxygenases (COX) or prostaglandin E synthases in *Braf*^{V600E} mouse melanoma cells, as well as in *Nras*^{G12D} melanoma or in breast or colorectal cancer cells, renders them susceptible to immune control and provokes a shift in the tumor inflammatory profile toward classic anti-cancer immune pathways. This mouse COX-dependent inflammatory signature is remarkably conserved in human cutaneous melanoma biopsies, arguing for COX activity as a driver of immune suppression across species. Pre-clinical data demonstrate that inhibition of COX synergizes with anti-PD-1 blockade in inducing eradication of tumors, implying that COX inhibitors could be useful adjuvants for immune-based therapies in cancer patients.

INTRODUCTION

Inflammation has emerged as a major factor promoting cancer development (Coussens et al., 2013; Grivennikov et al., 2010; Mantovani et al., 2008; Rakoff-Nahoum and Medzhitov, 2009). Tumor-promoting inflammation is characterized by the presence of sub-types of neutrophils, macrophages, dendritic cells (DCs), and T lymphocytes that support cancer progression (Balkwill et al., 2005; Coussens et al., 2013; Mantovani et al., 2008). Mediators secreted by these cells that directly or indirectly promote cancer cell growth include cytokines, chemokines, and growth factors, such as VEGF-A, CSFs, IL-1, IL-6, IL-8, or CXCL1 (Balkwill et al., 2005; Coussens et al., 2013). Yet inflammation can also

have cancer-inhibitory effects (Coussens et al., 2013; Mantovani et al., 2008), in part by favoring immune attack (Vesely et al., 2011). Indeed, in most mouse and human cancers, the presence of immune cells, such as cytotoxic T cells and DCs (in particular, the Batf3-dependent CD103⁺ sub-type), or of inflammatory mediators, such as type I interferons (IFNs), IFN- γ , and IL-12, is associated with good prognosis (Fridman et al., 2012; Gajewski et al., 2013; Vesely et al., 2011). Notably, several “immune checkpoint blockade” therapies aimed at unleashing the anti-cancer potential of tumor-specific T cells have recently shown great promise (Page et al., 2014; Sharma and Allison, 2015). These observations suggest that cancer cells do not pass unnoticed by the immune system but actively evade anti-tumor immunity.

In line with the above, tumors arising in immunosufficient hosts are commonly poorly immunogenic as a consequence of immunoediting (Schreiber et al., 2011). Reduced tumor immunogenicity can be a “recessive” consequence of downregulation of antigen-presenting MHC molecules or loss of antigens that serve as targets for T cell-mediated control (DuPage et al., 2012; Matsushita et al., 2012). Loss of immunogenicity can also be due to blockade of T cell access to tumor cell targets, recruitment of suppressive cells, and/or production of immunosuppressive factors (Joyce and Fearon, 2015). The latter can act in part by dampening production of type I interferons, IL-12, and other factors that are required for priming or restimulating anti-tumor T cells and for sustaining T cell-independent anti-tumor immunity (Dunn et al., 2005; Vesely et al., 2011). Unlike recessive mechanisms of immunoediting, immunosuppressive factors act in a dominant fashion and therefore offer a unique opportunity for immune therapy intervention so long as the antigenic determinants for tumor rejection have not been lost.

Inflammatory mediators can be produced by the stroma, by tumor-infiltrating leukocytes, or directly by the cancer cells themselves. Prominent among tumor-sustaining mediators is prostaglandin E2 (PGE₂), a prostanoid lipid associated with enhancement of cancer cell survival, growth, migration, invasion, angiogenesis, and immunosuppression (Wang and Dubois, 2010). Cyclooxygenase (COX)-1 and 2, enzymes critical for the production of PGE₂, are often overexpressed in colorectal, breast, stomach, lung, and pancreatic cancers (Dannenberg

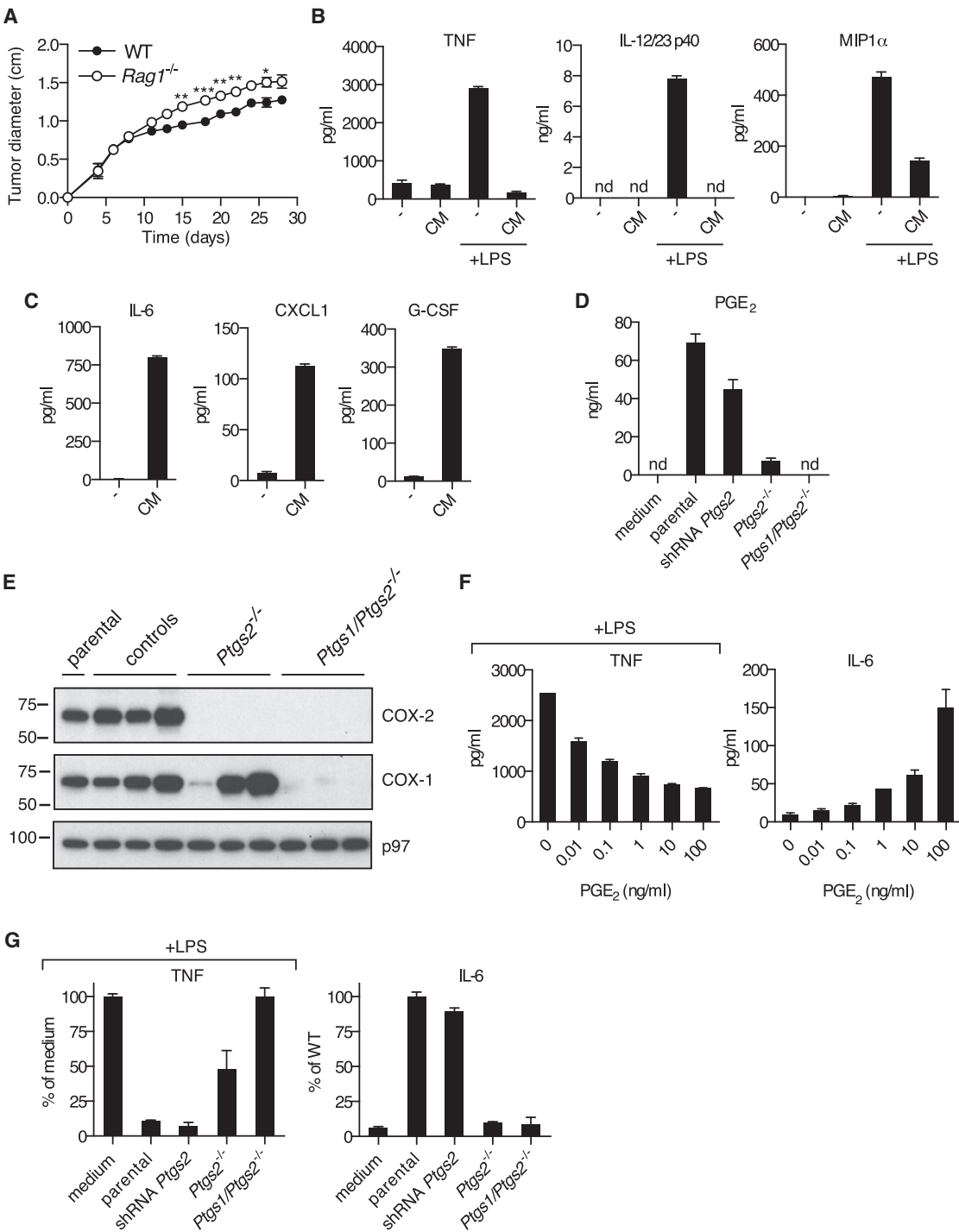


Figure 1. COX-1- and COX-2-Dependent Tumor-Derived Prostanoids Modulate Myeloid Cells

(A) Growth of $\text{Braf}^{\text{V600E}}$ cells following implantation into WT and $\text{Rag1}^{-/-}$ mice. Data are presented as average tumor diameters \pm SEM and are representative of three independent experiments with three to five mice per group. Tumor growth profiles were compared using two-way ANOVA. * $p < 0.05$, ** $p < 0.01$, *** $p < 0.001$.

(B and C) BMMCs were cultured in the presence or absence of CM from $\text{Braf}^{\text{V600E}}$ cells with or without LPS (100 ng/ml). The concentration of TNF, IL-12/23 p40, and MIP1 α (B) or IL-6, CXCL1, and G-CSF (C) in supernatants was determined after overnight culture.

(D) $\text{Braf}^{\text{V600E}}$ cells unmodified (parental), control, stably expressing a Ptgs2 -specific targeting shRNA construct, $\text{Ptgs2}^{-/-}$, or $\text{Ptgs1/Ptgs2}^{-/-}$ were cultured to confluence, and the concentration of PGE₂ in the supernatant was determined by ELISA.

(E) Immunoblot of COX-2 and COX-1 in parental $\text{Braf}^{\text{V600E}}$ cells and three independent control, $\text{Ptgs2}^{-/-}$, or $\text{Ptgs1/Ptgs2}^{-/-}$ clones generated by CRISPR/Cas9-mediated genome engineering using distinct sets of sgRNAs targeting different regions of the Ptgs1 and Ptgs2 loci. p97 served as a loading control.

(legend continued on next page)

and Subbaramiah, 2003; Wang and Dubois, 2010). Here, we identify tumor-derived COX activity in a mouse melanoma driven, as in human, by an oncogenic mutation in *Braf*, as the key suppressor of type I IFN- and T cell-mediated tumor elimination and the inducer of an inflammatory signature typically associated with cancer progression. COX-dependent immune evasion was also critical for tumor growth in other melanoma, colorectal, and breast cancer models. Notably, tumor immune escape could be reversed by a combination of immune checkpoint blockade and administration of COX inhibitors, suggesting that the latter may constitute useful additions to the arsenal of anti-cancer immunotherapies.

RESULTS

Braf^{V600E} Melanoma Cell Supernatants Have Immunomodulatory Effects on Myeloid Cells

In order to identify immune evasion mechanisms operative in melanoma, we used a transplantable tumor cell line established from a *Braf*^{+/+LSL-V600E;Tyr::CreERT2^{+/-};p16^{INK4a-/-} mouse (Dhommen et al., 2009) (henceforth, *Braf^{V600E}* cells). We reasoned that such cells, isolated from a genetically engineered cancer-prone mouse bearing an intact immune system, are likely to possess key attributes that allow them to escape immune control in the original host. Indeed, underscoring their poor immunogenicity, *Braf^{V600E}* melanoma cells formed progressively growing tumors upon implantation into wild-type (WT) mice, and this was only marginally enhanced in T- and B-cell-deficient *Rag1^{-/-}* mice (Figure 1A). We tested whether the poor immunogenicity of *Braf^{V600E}* cells could result from compromised or subverted activation of antigen-presenting cells, including dendritic cells (DCs) and monocyte-derived cells. We cultured mouse bone marrow-derived mononuclear cells (BMMCs), a mixed population of DCs and monocyte-derived macrophages (Heft et al., 2015), with conditioned medium (CM) from *Braf^{V600E}* cells in the presence or absence of a strong innate immune stimulus, lipopolysaccharide (LPS). Remarkably, LPS-induced production of TNF, IL-12/23p40, and MIP1 α by BMMCs was strongly inhibited by CM from *Braf^{V600E}* cells (Figure 1B). Moreover, addition of CM alone induced a distinct set of proinflammatory mediators, including IL-6, CXCL1, and G-CSF (Figure 1C). The latter, as well as IL-1 β , IL-10, and RANTES, were also induced by LPS, but CM, if anything, enhanced their accumulation (Figure S1A). Thus, tumor-derived secreted factors subvert the normal pattern of myeloid cell-driven inflammation.}

Cyclooxygenase-Dependent Prostanoids Account for the Immunomodulatory Effects of *Braf^{V600E}* Tumors on Myeloid Cells

Neither heat inactivation (to denature proteins) nor benzonase treatment (to degrade nucleic acids) impacted the ability of tu-

mor CM to promote IL-6 production or inhibit LPS-dependent induction of TNF by BMMCs (Figure S1B). We therefore investigated whether the immunomodulatory factor might be a lipid. The ability to inhibit IL-12 p40 production was reminiscent of the effects of the prostanoid PGE₂ (Kaliniski, 2012), which we found in high amounts in CM from *Braf^{V600E}* melanoma cells (Figure 1D). These cells also expressed cyclooxygenase (COX)-1 and -2, two enzymes critical for prostanoid synthesis (Figure 1E). Treatment with a *Braf* or a MEK inhibitor led to reduced COX-2 protein and PGE₂ secretion, indicating that COX-2 expression in *Braf^{V600E}* cells was dependent on active RAF/MEK signaling (Figure S2).

Addition of synthetic PGE₂ to BMMCs mimicked the effect of CM (Figure 1F). To assess the importance of COX-2-derived prostanoids, we targeted the *Ptgs2* gene (encoding COX-2) in *Braf^{V600E}* melanoma cells with several small hairpin RNAs (shRNAs). Although COX-2 expression was clearly diminished (Figure S3), the concentration of PGE₂ in CM from these cells was only modestly reduced and the modulatory effect of CM on BMMCs was unchanged (Figures 1D and 1G). As residual COX-2 expression could account for these observations, we resorted to CRISPR/Cas9 technology to generate *Ptgs2^{-/-}* (COX-2-deficient) *Braf^{V600E}* melanoma cells (Figure 1E). Production of PGE₂ by *Ptgs2^{-/-}* CRISPR-targeted clones was greatly decreased (Figure 1D), and their CM was no longer able to inhibit LPS-mediated TNF production or to induce IL-6 secretion by BMMCs (Figure 1G). These data demonstrate that COX-2 expression largely accounts for the myeloid cell modulatory properties of CM from *Braf^{V600E}* melanoma cells. Of note, in agreement with previous reports (Dannenberg and Subbaramiah, 2003), we found PGE₂ in CM from many, but not all, mouse cancer cell lines, including 4T1 breast cells, CT26 colorectal cells, a line derived from a *Nras^{G12D}*-driven melanoma-bearing mouse (Pedersen et al., 2013), and a methylcholanthrene-induced fibrosarcoma (Matsushita et al., 2012) (Figure S4).

COX Activity in *Braf^{V600E}* Cells Shifts the Inflammatory Profile at the Tumor Site

To test the effect of tumor-derived prostanoids in vivo, we inoculated WT mice with parental or *Ptgs2^{-/-}* *Braf^{V600E}* cells and assessed the expression of an array of inflammatory and immune mediators in whole-tumor biopsies of comparable size (Figure 2A), containing immune-infiltrating cells, at 4 days post-implantation. In agreement with the effects seen in vitro, loss of COX-2 expression by tumor cells led to a significant decrease in expression of IL-6 or CXCL1 in vivo (Figures 2B and 2C). In contrast, several mRNAs encoding known anti-tumor immune mediators or reflective of anti-tumor type I immunity, including IFN- γ , T-bet, CXCL10, and IL-12 (Vesely et al., 2011), were markedly increased in *Ptgs2^{-/-}* melanomas (Figures 2B and 2D).

(F) BMMCs were cultured in the presence of increasing amounts of synthetic PGE₂ plus or minus LPS (100 ng/ml). The concentration of TNF (+LPS) and IL-6 (no LPS) in the supernatant was determined after overnight culture.

(G) BMMCs were cultured as in (B) or (C) in presence of CM from the indicated *Braf^{V600E}* melanoma cell lines. The concentration of TNF after overnight culture is expressed relative to the concentration of TNF in the supernatant of BMMCs cultured in presence of LPS without any CM (% of medium). The concentration of IL-6 is expressed relative to the concentration of IL-6 in the supernatant of BMMCs cultured with CM from parental *Braf^{V600E}* cells (% of parental). nd, not detected. See also Figures S1, S2, S3, and S4.

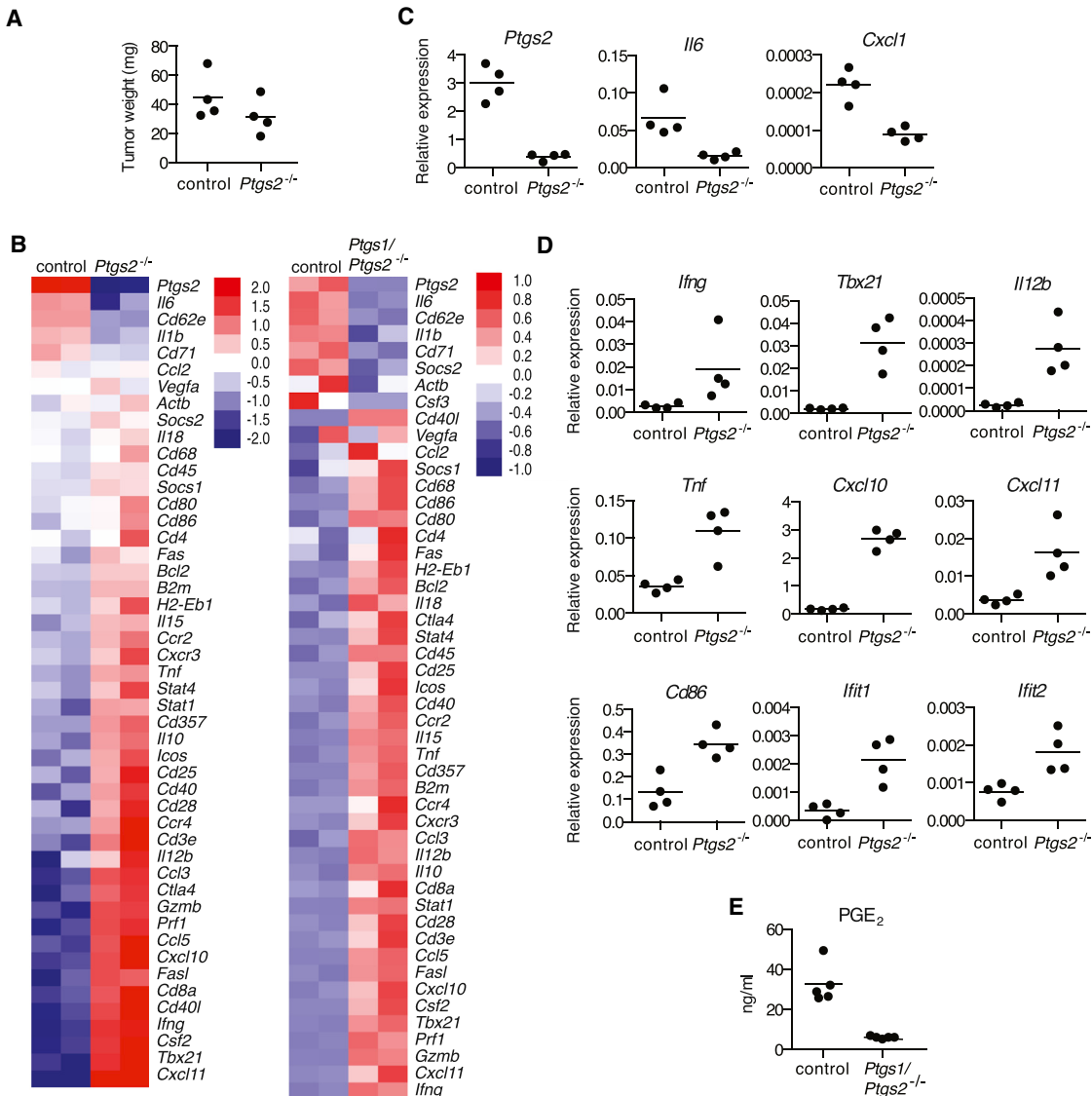


Figure 2. Genetic Ablation of COX in *Braf*^{V600E} Cells Shifts the Tumor Inflammatory Profile

(A–E) WT mice were inoculated with 10^6 control, *Ptgs2*^{-/-}, or *Ptgs1/Ptgs2*^{-/-} *Braf*^{V600E} cells. 4 days later, the expression of an array of immune-associated genes was determined by qPCR in whole-tumor homogenates.

(A) Tumor weight at the time of harvest is shown.

(B) Heatmaps for a selected list of genes show log₂ ΔCT values normalized to *hprt* of two biological replicates for each value. The genes are ordered from highest to lowest by fold change in control relative to *Ptgas2*^{-/-} or *Ptgas1/Ptgas2*^{-/-} samples.

(C and D) Relative expression of each gene normalized to *hprt*.

(E) Concentration of PGE₂ in lysates from 10⁵ total tumor cells. Each dot represents one independent tumor.

See also Figure S5

Likewise, mRNA levels of *Ifit1* and *Ifit2*, two type I IFN-stimulated genes (ISGs), were also elevated in *PtgS2*^{-/-} tumors (Figure 2D), indicative of enhanced type I interferon (IFN- α/β) signaling, which is central to immune-mediated tumor control (Gajewski et al., 2013; Vesely et al., 2011). We failed to detect a reduction in the expression of type 2 cytokines, such as IL-4, IL-5, or IL-13, or markers associated with M2 macrophage polarization, such as iNOS, arginase I, Gas-3, or E-cadherin (Figure S5; data not shown), despite the fact that they have been reported to

be induced by prostanoids within tumors (Wang and Dubois, 2010). Also, we did not detect decreased expression of IL-10 (Figure 2B), an anti-inflammatory cytokine that has been suggested to mediate many of the immunosuppressive effects of COX-2 (Kajlinski, 2012).

Even though COX-2 activity accounted for more than 90% of PGE₂ production by Braf^{V600E} cells, we still detected low levels of PGE₂ and some degree of BMMC modulatory activity in supernatants from *Ptg2s*^{-/-} cells, particularly from clones that

stochastically displayed higher COX-1 expression (Figures 1D and 1G; data not shown). To fully eliminate COX activity and avoid potential in vivo selection for cells that compensate for COX-2 deficiency by upregulating COX-1, we generated COX-1 and COX-2 doubly deficient *Braf^{V600E}* cells (*Ptgs1/Ptgs2^{-/-}* cells; Figure 1E). These cells fully lacked the ability to produce PGE₂ and did not modulate the activity of BMMCs in vitro (Figures 1D and 1G). Tumors formed by *Ptgs1/Ptgs2^{-/-}* cells displayed markedly reduced global PGE₂ levels, indicating a dominant role for tumor-derived over stroma-derived PGE₂ in vivo (Figure 2E). Importantly, as for *Ptgs2^{-/-}* singly deficient cells, a clear shift in the inflammatory profile toward increased expression of anti-tumor immune mediators was seen in tumors formed by *Ptgs1/Ptgs2^{-/-}* doubly deficient cells (Figure 2B). We conclude that *Braf^{V600E}* melanoma-derived prostanoids drive the expression of multiple tumor-promoting cytokines and growth factors in the local tumor microenvironment, while preventing type I immunity and other anti-tumor immune effector pathways, including those controlled by type I IFNs.

COX Expression in *Braf^{V600E}* Cells Prevents CD103⁺ DC Accumulation and Activation in Tumors

DCs, especially the Batf3-dependent sub-family characterized by CD8 α and/or CD103 expression, are essential for anti-cancer immune responses (Diamond et al., 2011; Fuentes et al., 2011; Hildner et al., 2008). We therefore assessed the impact of tumor-specific COX ablation on the prevalence and activation status of DCs at the tumor site, focusing on the CD103⁺ subset. Despite being only a minority of DCs, CD103⁺ DCs were selectively absent from COX-competent tumors (Figure 3A). Moreover, the fraction of intratumoral CD103⁺ DCs producing IL-12 p40 was higher in COX-deficient tumors (Figure 3B). Finally, CD103⁺ DCs, as well as CD103⁻ CD11b⁺ DCs, displayed higher levels of costimulatory molecules in tumors formed by *Ptgs1/Ptgs2^{-/-}* cells (Figure 3B). Thus, tumor-derived prostanoids impair accumulation of Batf3-dependent CD103⁺ DCs within tumors and suppress their activation, including IL-12-producing activity.

Genetic Ablation of COX in *Braf^{V600E}* Cells Permits Tumor Control by Innate and Adaptive Immune Mechanisms

Given the COX-dependent phenotypes described above, we sought to establish the contribution of COX to the ability of *Braf^{V600E}* melanoma cells to grow in immunocompetent mice. Notably, *Ptgs1/Ptgs2^{-/-}* cells formed spontaneously regressing tumors in WT mice in contrast to a COX-sufficient control clone which, despite having undergone the CRISPR/Cas9-mediated targeting procedure, retained COX-1 and COX-2 expression (Figure 1E) and grew similarly to the parental cells (Figure 4A). Importantly, *Ptgs1/Ptgs2^{-/-}* tumors were able to grow in *Rag1^{-/-}*, *Tap1^{-/-}*, and *Batf3^{-/-}* hosts (Figures 4A and 4B), indicating that prostanoid deficiency did not impair tumor formation in a cell-intrinsic fashion but rather acted to prevent CD8 α ⁺/CD103⁺ DC-dependent rejection mediated by CD8 α ⁺ T lymphocytes. Similar results were obtained using two other independent *Ptgs1/Ptgs2^{-/-}* clones generated using a different set of single-guide RNAs (sgRNAs) (Figures 1E and S6A). Thus, COX activity is

a key driver of adaptive immune escape by *Braf^{V600E}* melanoma cells.

Tumors formed by *Ptgs1/Ptgs2^{-/-}* *Braf^{V600E}* cells were noticeably smaller than their COX-sufficient counterparts even before adaptive immunity is expected to impact on tumor size (Figure 4A). As none of the *Ptgs1/Ptgs2^{-/-}* cell lines showed an obvious proliferative impairment in vitro (Figure S6B), we investigated whether a T and B lymphocyte-independent innate immune response was responsible. Given the COX-dependent inhibition of ISGs observed in the tumor microenvironment (see above), we examined the role of host type I IFN signaling in initial tumor growth control. We found that *Ptgs1/Ptgs2^{-/-}* tumors grew considerably faster in *Ifnar1^{-/-}* mice than in WT animals during the first 8 to 10 days post-inoculation, indistinguishably from tumors formed by parental COX-expressing *Braf^{V600E}* cells (Figure 4C). Of note, the growth of the latter was unaffected by IFNAR deficiency, consistent with the fact that they do not display an IFN signature (Figures 2B and 2D). These data indicate that an early type I IFN-dependent innate immune response restricts the growth of *Ptgs1/Ptgs2^{-/-}* cells.

Finally, we assessed the development of immunity following challenge with *Ptgs1/Ptgs2^{-/-}* tumors. Most mice that rejected *Ptgs1/Ptgs2^{-/-}* cells were resistant to a subsequent challenge with unmodified parental *Braf^{V600E}* melanoma cells (Figure 4D), implying the development of immunity to shared target antigens and excluding a scenario of cancer immune privilege driven locally by tumor-derived prostanoids.

An Essential Role for PGE₂ in *Braf^{V600E}*-Melanoma Immune Escape

COX-1 and COX-2 are essential for the production of multiple prostanoids, and COX deficiency can shunt arachidonic acid into different metabolic pathways (Ricciotti and FitzGerald, 2011). To evaluate the specific contribution of PGE₂, we generated *Braf^{V600E}* melanoma cells genetically deficient in microsomal prostaglandin E synthase (mPGES)-1 and -2 (referred to as *Pges^{-/-}* cells), two of the enzymes specifically required for the synthesis of PGE₂, but not other prostanoids. PGES-deficient melanoma cells phenocopied COX-deficient ones in that their CM lacked BMMC immunomodulatory activity (Figure 4E), and they were spontaneously rejected in immune competent recipients but grew progressively in T- and B-cell-deficient hosts (Figure 4F). Thus, these data indicate a major and non-redundant role for PGE₂ among prostanoids in the ability of *Braf^{V600E}* melanoma cells to avoid immune destruction.

COX-Dependent Immune Escape Is a Feature of Different Mouse Cancer Cells

To extend our findings, we examined the ability of COX to facilitate immune escape of other mouse cancers. A melanoma cell line driven by expression of *Nras^{G12D}* in melanocytes (Pedersen et al., 2013) also produced PGE₂ and formed tumors that were practically identical in *Rag*-sufficient and *Rag*-deficient mice (Figure 4G). In contrast, *Nras^{G12D}* melanoma cells rendered genetically deficient in COX-2 were spontaneously rejected in WT mice but grew like parental COX-2-competent tumors in *Rag1^{-/-}* hosts (Figure 4G). Mice that rejected *Ptgs2^{-/-}* tumors subsequently rejected parental COX-competent *Nras^{G12D}* melanoma

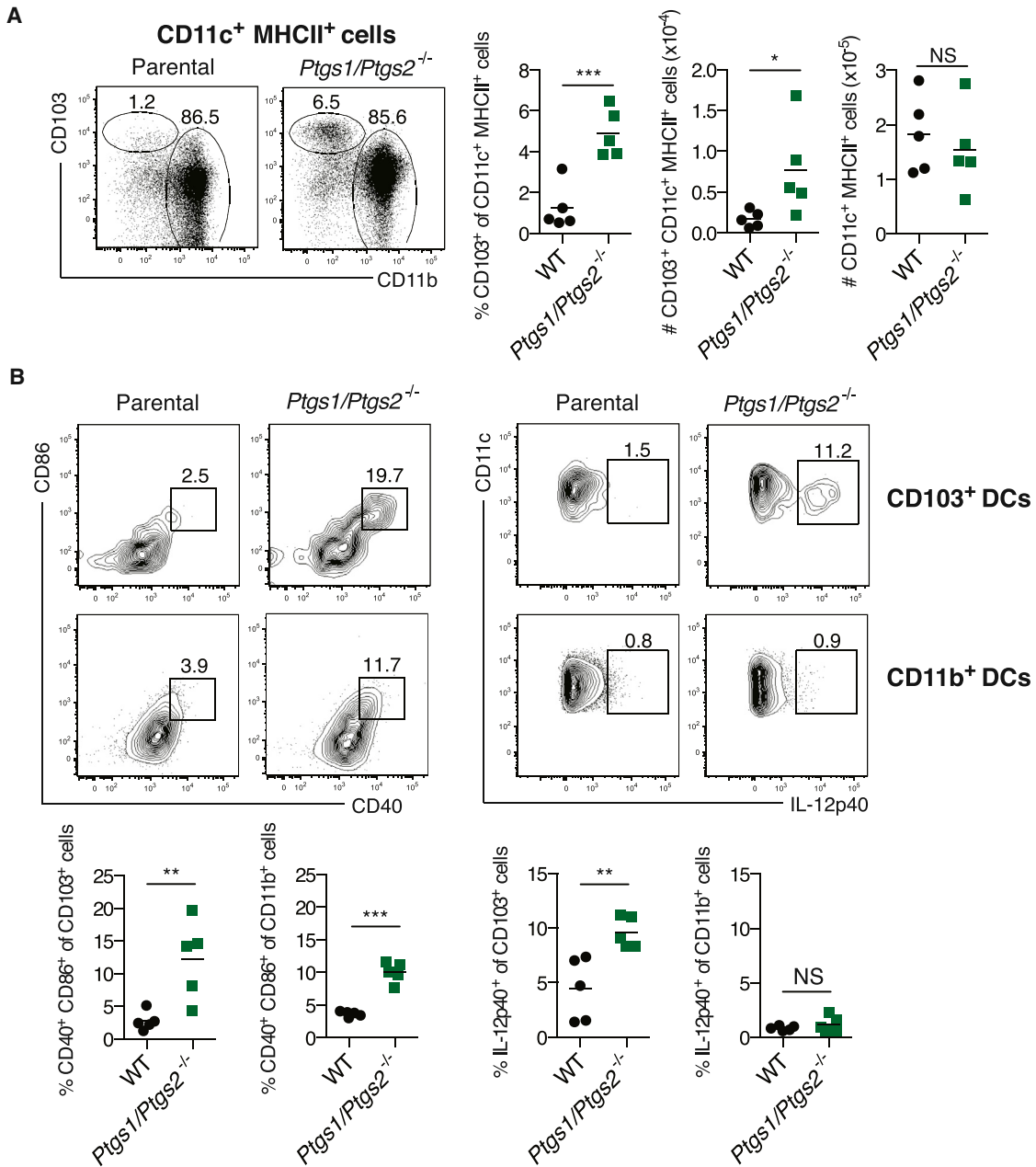


Figure 3. Tumor-Derived Prostanoids Prevent CD103⁺ DC Accumulation and Activation

(A and B) WT mice were inoculated with 10^6 parental or *Ptgs1/Ptgs2*^{-/-} *Braf*^{V600E} cells and tumor-infiltrating DCs were analyzed 4 days later. (A) Left: representative fluorescence-activated cell sorting (FACS) plots for CD103 versus CD11b within a CD11c⁺ MHCII⁺ DC gate. Right: percentage and number (#) of CD103⁺ CD11c⁺ MHCII⁺ or CD11b⁺ MHCII⁺ cells. (B) Upper: representative FACS plots for CD11c versus IL-12p40 or CD86 versus CD40 within a CD103⁺ or CD11b⁺ CD11c⁺ MHCII⁺ gate. Lower: percentage of IL-12p40⁺ or CD86⁺ CD40⁺ within CD103⁺ or CD11b⁺ CD11c⁺ MHCII⁺ cells. Each symbol in (A) and (B) represents an independent tumor. Samples were compared using two-tailed Student's t test. *p < 0.05, **p < 0.01, ***p < 0.001.

cells (Figure 4H), indicating the development of immunological memory and underscoring the presence of cryptic rejection antigens in parental Nras^{G12D} melanoma cells. In contrast to experiments with *Braf*^{V600E} cells, we did not find an obvious component of COX-dependent early innate immune control of Nras^{G12D} cells via type I IFN (data not shown).

To assess cancers other than melanoma and use mouse strains other than C57BL/6, we chose CT26 colorectal and 4T1 breast cancer cell lines that grow in BALB/c mice and also display constitutively active RAS/RAF/MEK/ERK signaling (Castle et al., 2014; Phan et al., 2013) and produce PGE₂ (Figures 5A and S4). Like the melanoma lines, these cancer cells exerted

immunomodulatory effects on BMMCs in vitro and grew identically in WT and T-cell-deficient nude mice (Figures 5A and 5B). In either case, genetic ablation of COX rendered the cells unable to produce PGE₂, abrogated their immunomodulatory effects on BMMCs, and allowed a marked degree of T-cell-dependent tumor growth control (Figures 5A and 5B). As for Braf^{V600E} cells, COX-deficiency was associated with a shift in the inflammatory profile at the tumor site, with reduced expression of tumor promoting factors, such as *Il6* or *Il1b* and increased levels of mediators associated with anti-tumor immune pathways (Figure 5C). Finally, mice that fully rejected COX-deficient CT26 or 4T1 tumors were immune to subsequent challenge with the respective COX-competent parental lines (data not shown). We conclude that prostanoid-dependent subversion of the inflammatory response and escape from anti-cancer immunity is a general feature of COX-expressing tumors.

COX Inhibitors Enhance the Efficacy of Immunotherapy with an Anti-PD-1 Blocking Antibody

Aspirin blocks both COX-1 and COX-2 and can be administered to mice in drinking water. However, this had no effect on the progression of implanted COX-competent Braf^{V600E} melanoma cells (Figures 6A–6C), perhaps because of incomplete inhibition of COX activity. However, even a modest degree of COX inhibition might help enhance the efficacy of immunotherapies, including those based on immune checkpoint blockade. Consistent with that notion, aspirin in the drinking water, in combination with treatment with anti-PD-1 monoclonal antibody, promoted much more rapid tumor regression and eradication of Braf^{V600E} melanoma cells than anti-PD-1 alone (Figures 6A and 6B). The potent synergy of the aspirin/anti-PD-1 combination was fully dependent on adaptive immunity as it was lost in *Rag1*^{-/-} mice (Figure 6B). It was also manifest in experiments using a larger inoculum of tumor cells, in which anti-PD-1 blockade alone had no effect (Figure 6C). Mice that fully eradicated COX-sufficient tumors upon treatment with aspirin + anti-PD-1 were immune to a subsequent challenge in the absence of further treatment (Figure 6D). Administration of celecoxib, a COX-2-specific inhibitor, also significantly synergized with anti-PD-1 treatment (Figure 6E), albeit to a lesser degree than aspirin, possibly due to suboptimal COX-2 inhibition and/or a potential contribution of COX-1-derived PGE₂. Finally, we addressed whether the synergy of the combination could be observed with tumors besides melanoma. Notably, treatment of mice bearing CT26 colorectal tumors with aspirin and anti-PD-1-induced tumor growth control and rapid and complete shrinkage in 30% of mice, whereas monotherapy showed little efficacy (Figure 6F). These experiments suggest that COX inhibitors could be useful additions to immune checkpoint blockade or conventional treatment of cancer patients so long as prostanoids also constitute a means of tumor immune escape in humans.

The COX-Dependent Inflammatory Signature Is Conserved in Human Cutaneous Melanoma Biopsies

To evaluate the latter, we asked whether evidence for COX-dependent immune modulation can be found in human melanomas. We correlated PTGS2 (encoding COX-2) mRNA expression levels in human melanoma biopsies containing tumor, as

well as stromal and infiltrating, cells with levels of mRNAs encoding various immune mediators, including those that we found to be controlled by COX-2 in the mouse models. Strikingly, mRNA expression levels for IL-6, G-CSF, CXCL1, and other known tumor-promoting inflammatory factors showed strong positive correlation with those of PTGS2 in samples from human cutaneous melanoma (Figures 7A and 7C). No correlation was observed between PTGS2 levels and levels of markers indicative of total leukocyte (CD45), regulatory T cell (FOXP3), or B cell (CD19 and CD20) presence (Figure 7B). In contrast, PTGS2 mRNA levels were inversely correlated with CD8A and CD8B transcript levels, a measure of the presence of CD8⁺ T cells in tumors associated with longer survival and favorable treatment outcome (Fridman et al., 2012; Gajewski et al., 2010). Similarly, expression of PTGS2 was inversely correlated with that of CXCL10 and CXCL9, chemokines associated with cytotoxic T cell recruitment (Fridman et al., 2012; Gajewski et al., 2010) (Figures 7A and 7D). We also found a significant and consistent negative association between PTGS2 expression and that of numerous ISGs (Figures 7A and 7E). Together, these data indicate a qualitative change in immune infiltrate composition that is driven by COX expression and shows remarkable parallels between mice and human.

DISCUSSION

The extent to which the immune system acts as a natural barrier to tumor progression has been the subject of long-standing debate (Hanahan and Weinberg, 2011). Data from both mouse and human cancers over the last two decades has lent support to the notion that neoplastic development is associated with an immunoediting process, whereby the immune system selects the outgrowth of less immunogenic tumor cells (Rooney et al., 2015; Schreiber et al., 2011; Vesely et al., 2011). The mechanisms underlying immunoediting are only beginning to be explored and include selection for tumor cells that lose dominant tumor rejection antigens (DuPage et al., 2012; Matsushita et al., 2012). Here, we uncover PGE₂-dependent suppression of myeloid cell activation as a potent additional mechanism of tumor immune escape. Our findings suggest that immunoediting can result in selection of tumors producing immunosuppressive factors, which block initial type I IFN-dependent innate immune cell activation and/or prevent subsequent T cell activity against tumor antigens. The latter indicates that edited tumor cells may continue to express relevant target antigens that can be functionally unmasked upon removal of tumor-derived suppressive factors that subvert myeloid cell, including DC, function. These findings have obvious therapeutic implications, as discussed below. In addition, they help to explain apparently contradictory earlier findings suggesting that genetically driven mouse cancers are not subject to immune surveillance (Willinsky and Blankenstein, 2005) by showing that production of suppressive factors by the tumor is in fact a feature of immunoediting. The low immunogenicity of tumors can therefore result from immune sculpting of their antigenic and/or immunostimulatory properties.

Our experiments rely partly on the ability to genetically engineer cancer cells using CRISPR/Cas9-mediated technology to assess the contribution of specific tumor pathways to immune

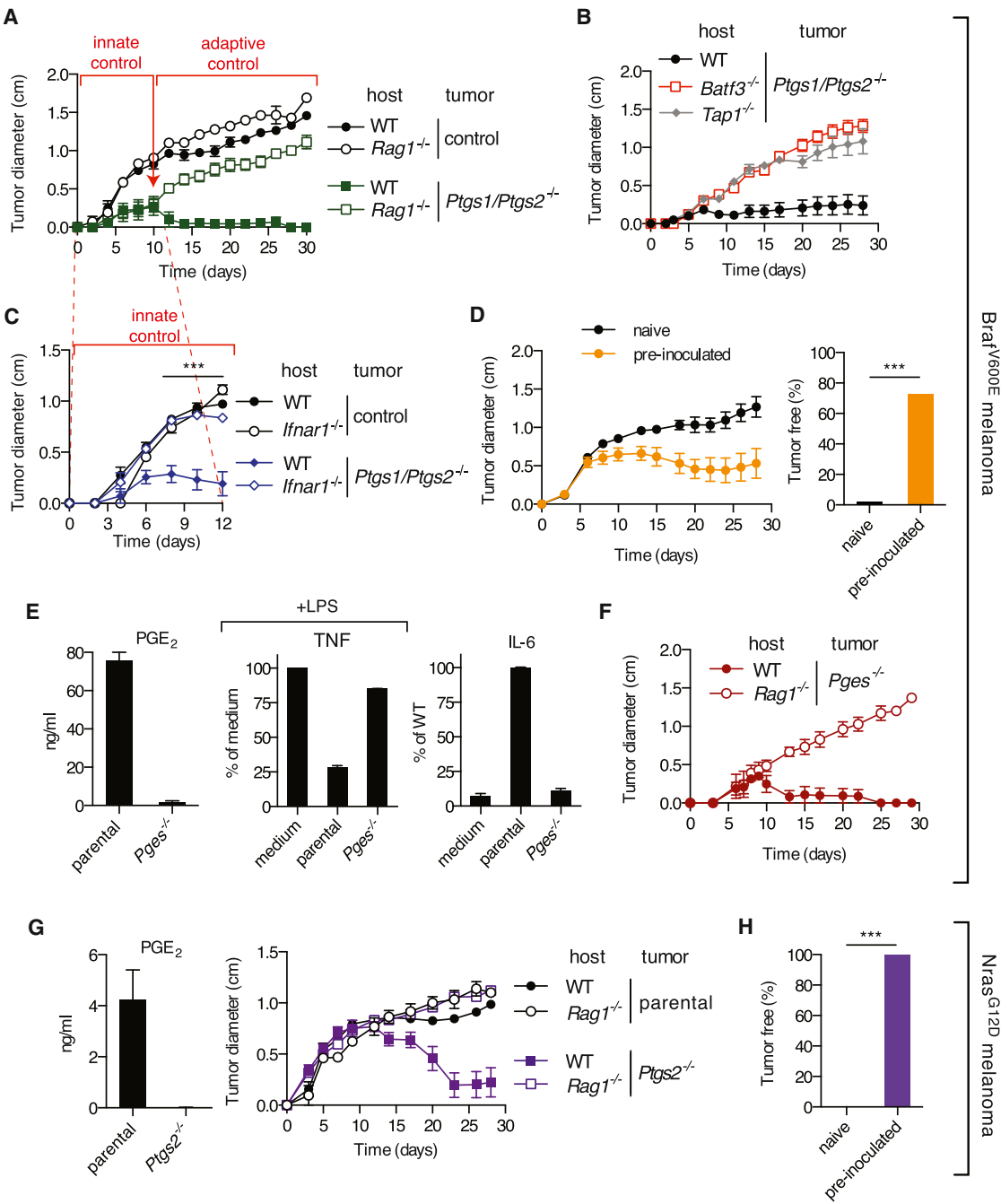


Figure 4. Genetic Ablation of COX in *Braf*^{V600E} or *Nras*^{G12D} Melanoma Cells Enables Immune-Dependent Tumor Eradication

(A–C) Growth of tumors formed following implantation of 10⁵ control or *Ptgs1/Ptgs2*^{-/-} *Braf*^{V600E} cells into WT C57BL/6 (A–C), *Rag1*^{-/-} (A), *Batf3*^{-/-}, *Tap1*^{-/-} (B), or *Ifnar1*^{-/-} (C) mice.

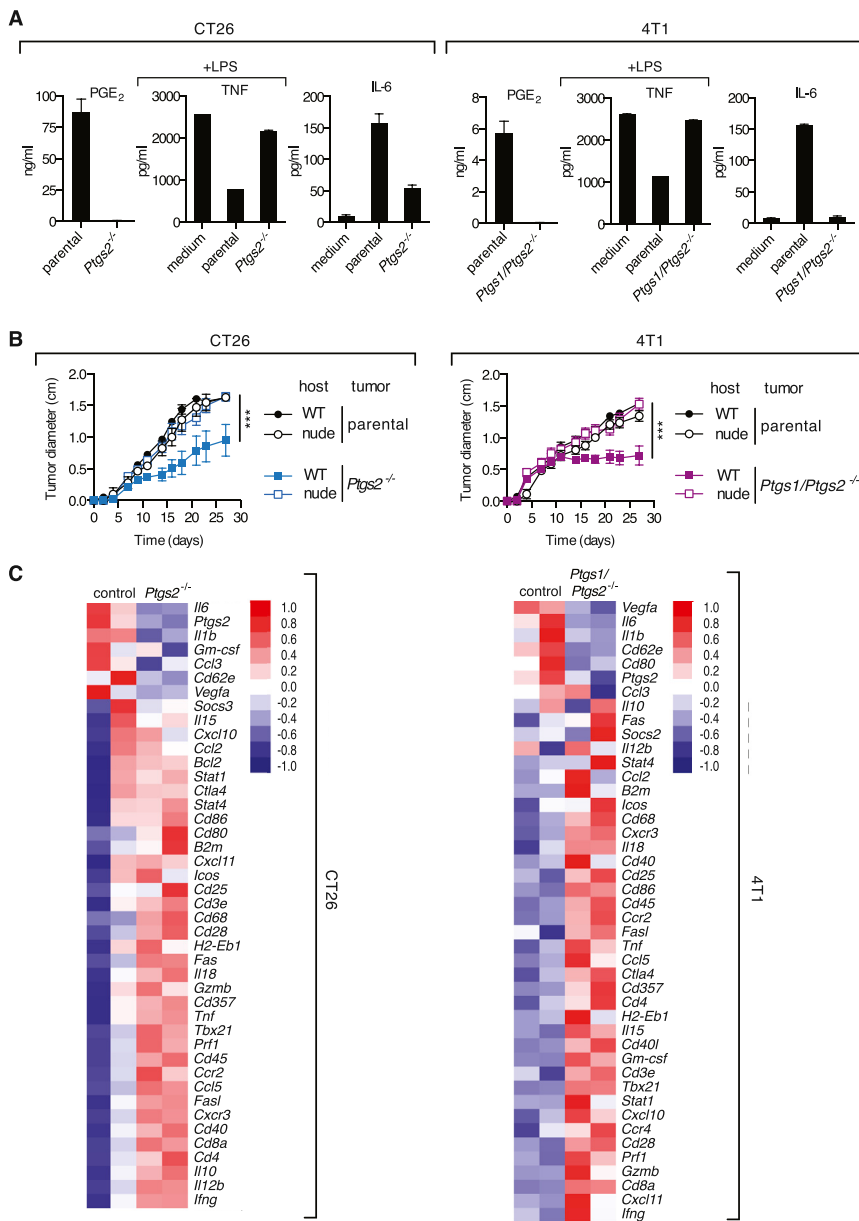
(D) Growth of parental *Braf*^{V600E} cells following implantation into naive WT C57BL/6 mice or mice that previously rejected *Ptgs1/Ptgs2*^{-/-} *Braf*^{V600E} tumors (pre-inoculated). Data are compiled from three independent experiments and presented as tumor growth profile (left) and as percentage of tumor-free mice at 6 weeks post-parental tumor inoculation (right).

(E) Concentration of PGE₂ in CM from confluent parental or *Pges*^{-/-} cell cultures or of TNF and IL-6 in the supernatant of an overnight culture of BMMCs cultured as in Figure 1 in presence of CM from the indicated cell line and expressed as in Figure 1G.

(F) Growth profile of tumors formed following implantation of 10⁵ parental or *Pges*^{-/-} *Braf*^{V600E} cells into WT or *Rag1*^{-/-} mice.

(G) Concentration of PGE₂ in CM from confluent cell cultures or growth profile of tumors formed following implantation of 10⁵ parental or *Ptgs2*^{-/-} *Nras*^{G12D} cells into WT or *Rag1*^{-/-} mice (right). (H) The percentage of tumor-free mice at 6 weeks post-implantation of parental *Nras*^{G12D} cells into naive WT C57BL/6 mice or

(legend continued on next page)



escape in the absence of alterations in the same pathways in host stroma. Off-target Cas9 nuclease activity can be a concern (e.g., Frock et al., 2015), but because we have used multiple sgRNAs to ablate *Ptges1*, *Ptges2*, and/or *Pges1/2* in four different cancer cell lines that, in all cases, become susceptible to immune-mediated control, we believe that on-target ablation of the ability of the tumor cells to produce PGE₂ accounts for our findings. Similarly, although the introduction of nucleotide insertions and/or deletions is inherent to the CRISPR

that tumor-derived prostanoids promote immune evasion merely by preventing tumor infiltration by lymphocytes or access of the latter to their targets (Joyce and Fearon, 2015). In such a scenario, COX-competent parental cells should create an immune-privileged site and form progressive tumors even when the host has previously rejected COX-deficient cells.

Antigen-presenting cells, in particular DCs, are greatly affected by tumor-derived PGE₂ and likely to be an important target of the lipid for tumor immune escape. While DCs have

Figure 5. COX Ablation in Colorectal or Breast Cancer Cells Promotes Cancer-Inhibiting Inflammation and T-Cell-Dependent Tumor Growth Control

(A) Concentration of PGE₂ in CM from confluent parental and COX-deficient CT26 and 4T1 cell cultures and of TNF and IL-6 in the supernatant of an overnight culture of BMMCs cultured as in Figure 1 in presence of the indicated cell line CM.

(B) Growth profile of tumors formed following implantation of 10⁵ parental or *Ptg_{s2}^{-/-}* CT26 colorectal or of parental or *Ptg_{s1}/Ptgs2^{-/-}* 4T1 breast cancer cells into WT Balb/c or nude mice. Data are presented as average tumor diameters ± SEM and are representative of at least three independent experiments with four to six mice per group. Tumor growth profiles were compared using two-way ANOVA. ***p < 0.001.

(C) WT Balb/c mice were inoculated with 10⁶ parental, *Ptg_{s2}^{-/-}* CT26 or *Ptg_{s1}/Ptgs2^{-/-}* 4T1 cells, and 4 days later the expression of an array of immune-associated genes was determined by qPCR in whole-tumor homogenates. Heatmaps for a selected list of genes show log₂ ΔCT values normalized to *hprt* of two biological replicates for each value. The genes are ordered from highest to lowest by fold change in parental relative to *Ptg_{s2}^{-/-}* or *Ptg_{s1}/Ptgs2^{-/-}* samples.

mice that previously rejected *Ptg_{s2}^{-/-}* Nras^{G12D} tumors (pre-inoculated). All growth profiles are presented as average tumor diameters ± SEM and are representative of at least two independent experiments with four to six mice per group. Tumor growth profiles were compared using two-way ANOVA and the percentage of tumor-free mice using Fisher's exact test. ***p < 0.001.

See also Figure S6.

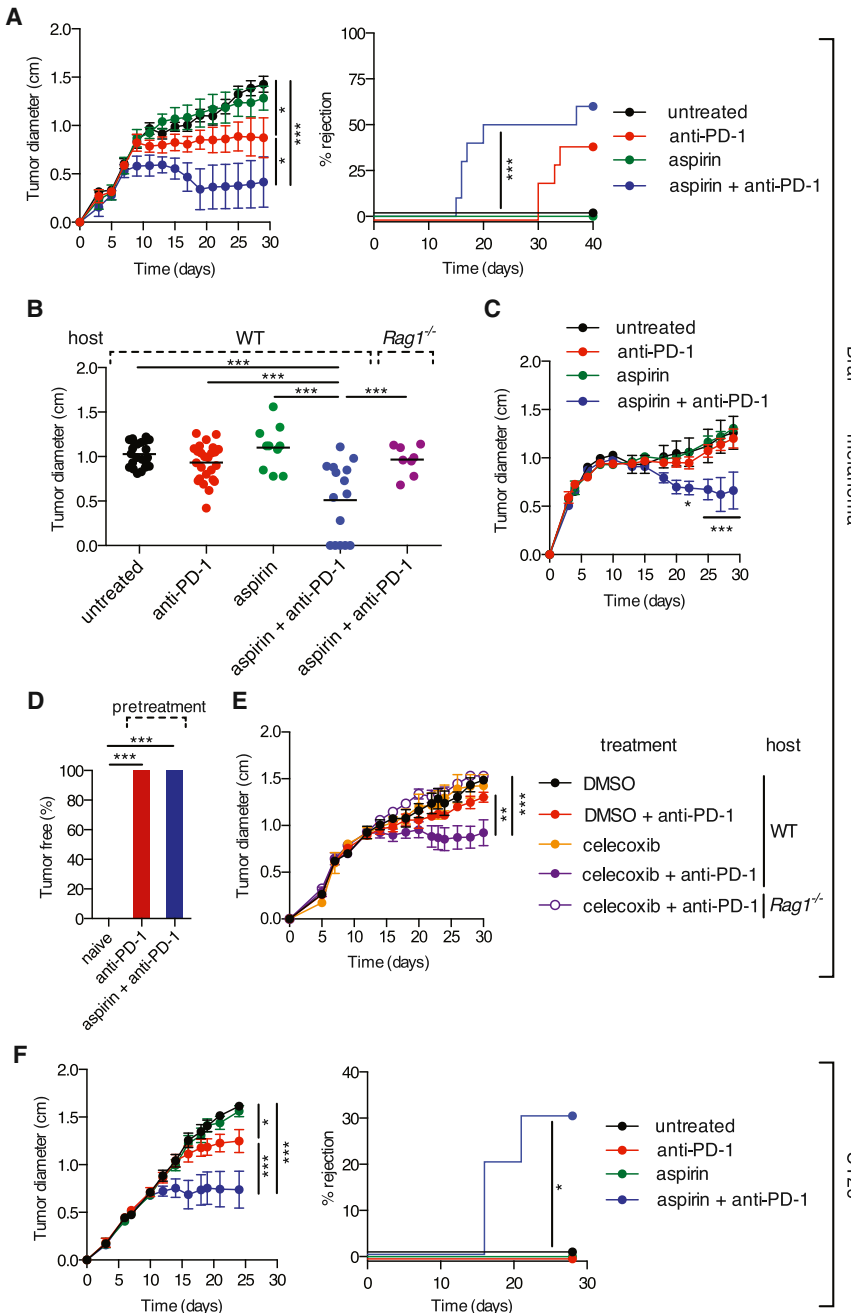


Figure 6. COX Inhibition Synergizes with Anti-PD-1 Blockade in Immune-Dependent Tumor Growth Control

(A) Left: growth of parental COX-competent tumors following implantation of 10^5 $Braf^{V600E}$ melanoma cells into C57BL/6 mice. Mice received aspirin in the drinking water and/or 200 μ g of anti-PD-1 monoclonal antibody i.p. every 3–4 days from day 3 to day 24. Right: the percentage of mice that fully rejected tumors over time is shown.

(B) Pooled tumor diameters at 19 days post-implantation of $Braf^{V600E}$ melanoma cells into WT or $Rag1^{-/-}$ mice treated as in (A). Each dot represents one independent tumor.

(C) As in (A) but using an inoculum of 10^6 melanoma cells.

(D) The percentage of tumor-free mice at 6 weeks post-implantation of parental $Braf^{V600E}$ cells into C57BL/6 mice that were untreated ($n = 15$) (naive) or that previously rejected $Braf^{V600E}$ cells following anti-PD-1 ($n = 6$) or aspirin + anti-PD-1 treatment ($n = 8$) (pre-treatment).

(E) As in (A) but C57BL/6 mice received celecoxib i.p. daily from day 0.

(F) As in (A) but Balb/c mice received 10^5 CT26 colorectal cells. Growth profiles are presented as average tumor diameters \pm SEM and are representative of at least two independent experiments with five mice per group.

Samples were compared using two-way ANOVA (A, C, E, and F), one-way ANOVA (B), Fisher's exact test (D), and log rank test (A and F). * $p < 0.05$, ** $p < 0.01$, *** $p < 0.001$.

been most prominently studied for their ability to prime anti-tumor T cells in lymph nodes, they are also emerging as key players at the tumor site. Recent studies have indicated that tumor accumulation of rare Batf3-dependent DCs bearing the CD103 marker is associated with good prognosis and immune-mediated control across mouse and human species (Broz et al., 2014; Ruffell et al., 2014). Batf3-dependent DCs appear to act by restimulating cytotoxic T lymphocyte (CTL) at the tumor site, in part by locally providing IL-12. Their dual activity in cross-priming anti-tumor CTL within lymph nodes and restimulating CTL within tumors probably contributes to the general

reports demonstrating an inhibitory role for PGE₂ on type I IFN production during infection with influenza or mycobacteria (Coulombe et al., 2014; Mayer-Barber et al., 2014). This may be especially relevant to melanoma where the expression of a type I IFN signature associates with spontaneous remissions (Wenzel et al., 2005) and increased relapse-free survival (Bald et al., 2014). Finally, tumor-derived prostanooids directly induce the production by myeloid cells of known cancer-promoting factors such as IL-6, CXCL1, and G-CSF, effectively shifting the tumor microenvironment from one favorable to tumor eradication to one that has pro-tumor activity.

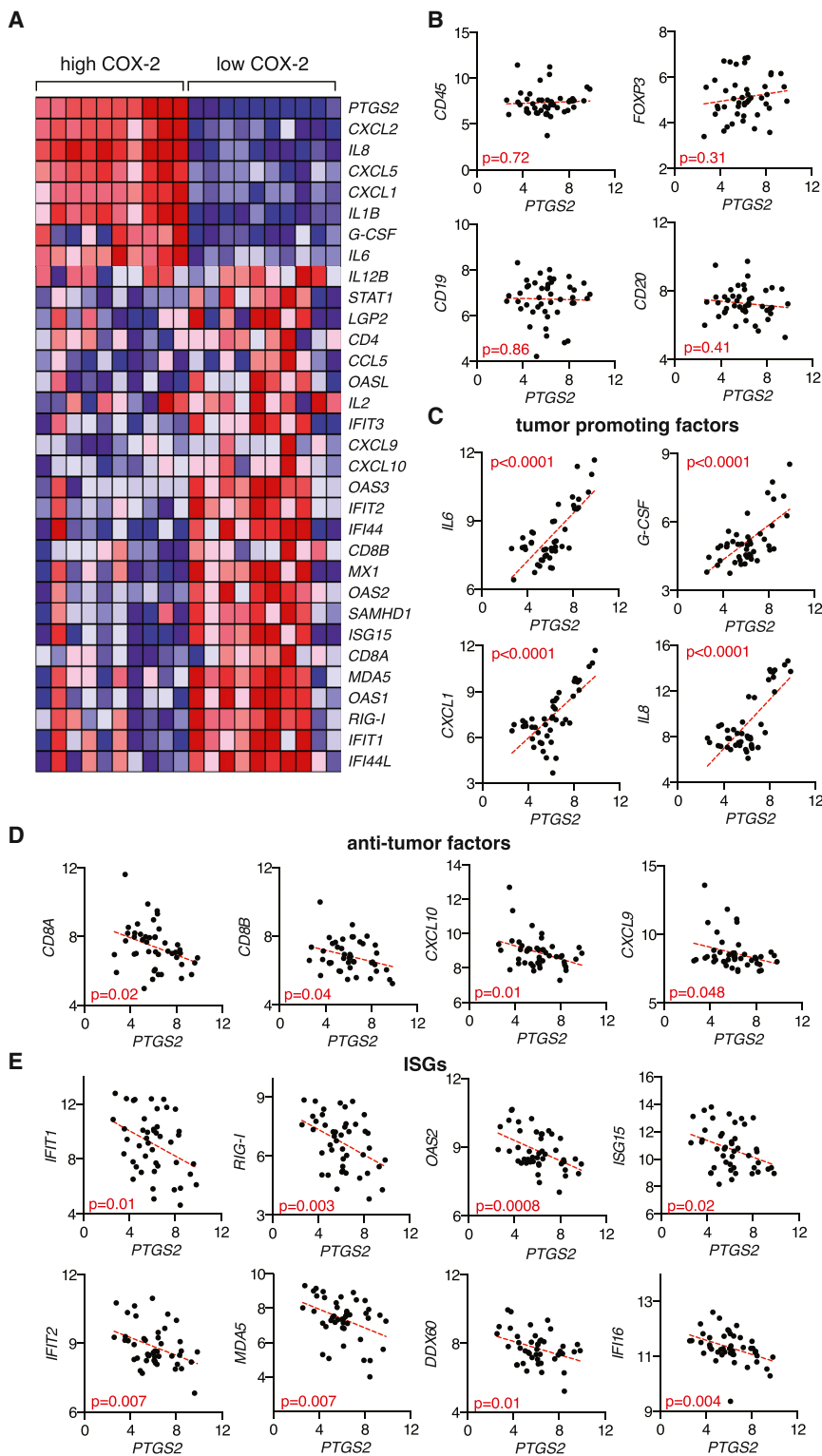


Figure 7. COX-2 Levels in Human Melanoma Biopsies Correlate Positively with Tumor-Promoting Factors and Negatively with Factors Associated with CTL Infiltration and Type I IFN Signaling

(A–E) Microarray expression data (Talantov et al., 2005) from human cutaneous melanoma biopsies containing tumor cells, stroma, and infiltrate were analyzed for the association of *PTGS2* expression with that of several immune-related genes.

(A) Heatmap for a selected list of genes showing log₂ expression signal for 20% of samples with highest (high COX-2) and lowest (low COX-2) *PTGS2* expression. Genes were clustered using a Euclidean distance matrix and average linkage clustering. Red indicates higher expression, and blue indicates low expression relative to the mean expression of the gene across all samples.

(B) Correlation data for *PTGS2* versus *CD45* (*PTPRC*), *FOXP3*, *CD19*, and *CD20* expression.

(C) Correlation data for *PTGS2* versus *IL-6*, *G-CSF* (*CSF3*), *CXCL1*, and *IL-8* expression.

(D) Correlation data for *PTGS2* versus *CD8A*, *CD8B*, *CXCL10*, and *CXCL9*.

(E) Correlation data for *PTGS2* versus the following ISGs: *IFI1*, *IFI2*, *RIG-I* (*DDX58*), *MDA5* (*IFIH1*), *OAS2*, *DDX60*, *ISG15*, and *IFI16*.

In (B)–(E), all cutaneous melanoma samples (*n* = 45) from the dataset (Talantov et al., 2005) were included in the analysis, with each dot representing one sample. The statistical significance of the correlation was determined using the Pearson's correlation coefficient. A linear regression-fitting curve is shown as a dotted red line.

unclear (Becker et al., 2009; Denkert et al., 2001; Goulet et al., 2003; Kuźnicki et al., 2006). Our analysis of a publicly available dataset of a cohort of human melanoma biopsies (Talantov et al., 2005) suggests that the natural variability in COX-2 expression levels within samples might be of functional relevance. Thus, samples with high COX-2 levels showed higher expression of numerous tumor-promoting factors, including those whose expression was directly controlled by COX in the mouse model. Likewise, COX-2^{low} melanomas showed a qualitative change in infiltrate composition, displaying increased expression of anti-tumor mediators and hallmarks of activation of the type I IFN system. Thus, our combined analysis of the mouse model and the human samples argues for COX activity as a common mechanism co-opted by cancer cells to promote immune escape across species.

Prostanoids have been implicated in carcinogenesis through enhancement of cancer cell survival, proliferation, invasion,

Interestingly, COX-2 is often overexpressed in several human cancers, including colorectal, breast, stomach, lung, and pancreatic tumors (Dannenberg and Subbaramaiah, 2003). Whether melanomas similarly express abnormal levels of COX-2 remains

and angiogenesis (Wang and Dubois, 2010). COX inhibitors were recently reported to enhance the efficacy of antiangiogenic therapy in pre-clinical models by inhibiting VEGF-independent PGE₂-induced tumor angiogenesis (Xu et al., 2014). As such, it is remarkable that COX-deficient cancer cells are able to grow indistinguishably from their COX-competent counterparts in immunodeficient mice. These results indicate that, at least for some tumors, the main role of cancer-cell-derived prostanoïd production is to promote immune evasion and that any effects on angiogenesis or tumor cell survival and proliferation are likely secondary to immune suppression or redundant with stroma-derived PGE₂. Notably, our findings that COX-2 expression depends on active RAF/MEK signaling suggests that reduced production of PGE₂ by melanoma cells may contribute to the immune-dependent anti-cancer activity elicited by BRAF inhibitors (Frederick et al., 2013; Knight et al., 2013). Nevertheless, COX-2 upregulation is likely to also be driven by MAPK-independent pathways, consistent with the presence of multiple regulatory elements in the *PTGS2* promoter.

We find a remarkable conservation between signatures of COX-dependent subversion of inflammation across mouse and human melanoma. We therefore propose that COX-2 levels and COX-dependent inflammatory mediators in human melanoma and other cancers might constitute useful biomarkers predictive of prognosis and treatment outcome, including in response to checkpoint blockade inhibitors, such as anti-CTLA4 and anti-PD-1/PD-L1. Finally, our data show that COX inhibitors act synergistically with anti-PD-1 mAb in pre-clinical models. We therefore speculate that COX inhibitors, reported to reduce the risk of several cancers, including colorectal (Rothwell et al., 2010), gastric (Tian et al., 2010), breast cancer (Gierach et al., 2008), and, even, melanoma (Gamba et al., 2013), might help unleash anti-cancer immunity and thereby constitute useful additions to the arsenal of conventional and immune-based cancer therapies, most notably those based on immune checkpoint blockade.

EXPERIMENTAL PROCEDURES

Mice

All animal experiments were performed in accordance with national and institutional guidelines for animal care and were approved by an institutional Animal Ethics Committee and by the Home Office, UK.

Cancer Cell Lines

Cells were cultured under standard conditions and were confirmed to be mycoplasma free. *Braf*^{V600E} and *Nras*^{G12D} melanoma cell lines were established from C57BL/6 *Braf*^{+/+LSL-V600E};Tyr::CreERT2^{+/-};p16^{Ink4a-/-} (Dhomen et al., 2009) and C57BL/6 *Nras*^{+/+LSL-G12D};Tyr::CreERT2^{+/-} (Pedersen et al., 2013) mice, respectively. CT26, 4T1, and EL4 cells were from ATCC. *Ptgs2*^{-/-}, *Ptgs1/Ptgs2*^{-/-}, and *Pges*^{-/-} cells were generated by CRISPR/Cas9-mediated genome engineering using the CRISPR design tool provided by the Zhang lab (<http://www.genome-engineering.org>). Correctly targeted clones were selected based on their inability to produce PGE₂, and genetic ablation of COX-1, COX-2, mPGES-1, and mPGES-2 was verified by sequencing.

Tumor Cell Injections

Tumor cells were harvested by trypsinization, washed three times with PBS, and injected subcutaneously into the right flank of recipient mice at 10⁵ to 10⁶ cells in 100 µl of endotoxin-free PBS. Tumor cells were >98% viable at the time of injection as determined by propidium iodide staining. Tumor size

was quantified as the mean of the longest diameter and its perpendicular. For COX inhibition *in vivo*, aspirin was administered in the drinking water at 600 µg/ml 1 to 3 days before injection of tumor cells and replaced every 3 days. Alternatively, mice received 200 µl of celecoxib (Sigma and LC Laboratories) intraperitoneally (i.p.) at 500 µg/ml (12.5% DMSO in PBS) daily from day 0. Anti-PD-1 monoclonal antibody (clone RMP1-14, BioXCell) was administered i.p. at 200 µg/mouse from day 3 post-tumor cell inoculation every 3 to 4 days for a maximum of six injections.

In Vitro Culture

Mouse BMMCs were generated using GM-CSF as described (Hefti et al., 2015). Cells were plated at 0.5- to 1 × 10⁶ cells/ml in 96-well plates at 37°C in absence or presence of 100 µl of conditioned medium from tumor cells plus or minus LPS (10 to 100 ng/ml) in a total volume of 200 µl. After overnight culture, cytokine and chemokine concentration in the supernatant was determined by ELISA or by cytometric bead array using standard procedures.

qPCR

Tumors were collected and homogenized, and total RNA was isolated with Trizol reagent (Invitrogen) and further purified on RNAeasy columns (QIAGEN). cDNA was synthesized using SuperScriptII reverse transcriptase (Invitrogen). Expression of an array of immune genes was performed using a TaqMan mouse immune array (v.2.1), following the manufacturer's instructions.

Human Microarray Dataset Analysis

Raw CEL files from the microarray dataset GSE3189 were downloaded from GEO (<http://www.ncbi.nlm.nih.gov>).

Statistics

Statistical significance was determined using an unpaired two-tailed Student's t test, one-way ANOVA, two-way ANOVA, Fisher's exact test, log rank test, and the Pearson correlation coefficient as indicated. A p value < 0.05 was considered significant (* p < 0.05; ** p < 0.01; *** p < 0.001).

SUPPLEMENTAL INFORMATION

Supplemental Information includes Supplemental Experimental Procedures and six figures and can be found with this article online at <http://dx.doi.org/10.1016/j.cell.2015.08.015>.

AUTHOR CONTRIBUTIONS

S.Z. conducted experiments with assistance from A.G.V., J.P.B., K.J.S., and S.E.A. P.C. and S.Z. carried out bioinformatic analysis. A.G.V. and S.Z. carried out cell engineering. N.R. managed mouse stocks. M.R.G. and R.M. provided key reagents. A.G.V., S.A.Q., and E.S. provided advice, analyzed data, and contributed to experimental design. S.Z. and C.R.S. designed the study, analyzed data, and wrote the manuscript.

ACKNOWLEDGMENTS

This work was funded by Cancer Research UK, The Francis Crick Institute, and a European Research Council Advanced Researcher Grant. A.G.V. was supported by an EMBO Long-Term Fellowship and a Rubicon Fellowship from the Netherlands Organization for Scientific Research. The authors are grateful to members of the Immunobiology Laboratory for assistance and helpful discussions.

Received: October 28, 2014

Revised: April 22, 2015

Accepted: July 16, 2015

Published: September 3, 2015

REFERENCES

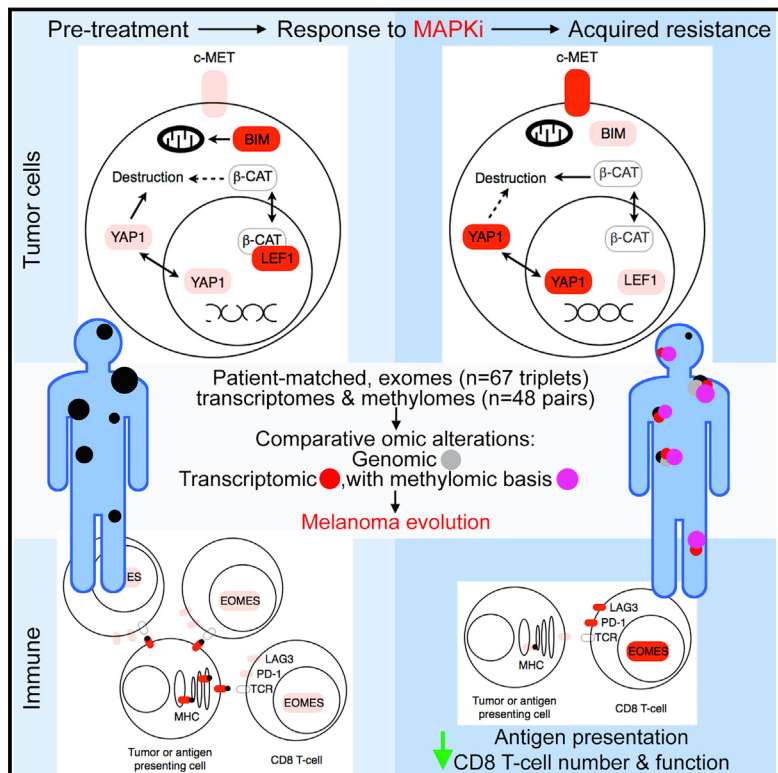
- Bald, T., Landsberg, J., Lopez-Ramos, D., Renn, M., Glodde, N., Jansen, P., Gaffal, E., Steitz, J., Tolba, R., Kalinke, U., et al. (2014). Immune cell-poor

- melanomas benefit from PD-1 blockade after targeted type I IFN activation. *Cancer Discov.* 4, 674–687.
- Balkwill, F., Charles, K.A., and Mantovani, A. (2005). Smoldering and polarized inflammation in the initiation and promotion of malignant disease. *Cancer Cell* 7, 211–217.
- Becker, M.R., Siegelin, M.D., Rempel, R., Enk, A.H., and Gaiser, T. (2009). COX-2 expression in malignant melanoma: a novel prognostic marker? *Melanoma Res.* 19, 8–16.
- Broz, M.L., Binnewies, M., Boldajipour, B., Nelson, A.E., Pollack, J.L., Erle, D.J., Barczak, A., Rosenblum, M.D., Daud, A., Barber, D.L., et al. (2014). Dissecting the tumor myeloid compartment reveals rare activating antigen-presenting cells critical for T cell immunity. *Cancer Cell* 26, 638–652.
- Castle, J.C., Loewer, M., Boegel, S., de Graaf, J., Bender, C., Tadmor, A.D., Boisguerin, V., Bukur, T., Sorn, P., Paret, C., et al. (2014). Immunomic, genomic and transcriptomic characterization of CT26 colorectal carcinoma. *BMC Genomics* 15, 190.
- Chen, J.H., Perry, C.J., Tsui, Y.-C., Staron, M.M., Parish, I.A., Dominguez, C.X., Rosenberg, D.W., and Kaech, S.M. (2015). Prostaglandin E2 and programmed cell death 1 signaling coordinately impair CTL function and survival during chronic viral infection. *Nat. Med.* 21, 327–334.
- Coulombe, F., Jaworska, J., Verway, M., Tzelepis, F., Massoud, A., Gillard, J., Wong, G., Kobinger, G., Xing, Z., Couture, C., et al. (2014). Targeted prostaglandin E2 inhibition enhances antiviral immunity through induction of type I interferon and apoptosis in macrophages. *Immunity* 40, 554–568.
- Coussens, L.M., Zitvogel, L., and Palucka, A.K. (2013). Neutralizing tumor-promoting chronic inflammation: a magic bullet? *Science* 339, 286–291.
- Dannenberg, A.J., and Subbaramaiah, K. (2003). Targeting cyclooxygenase-2 in human neoplasia: rationale and promise. *Cancer Cell* 4, 431–436.
- Denkert, C., Köbel, M., Berger, S., Siegert, A., Leclerc, A., Trefzer, U., and Hauptmann, S. (2001). Expression of cyclooxygenase 2 in human malignant melanoma. *Cancer Res.* 61, 303–308.
- Dhomen, N., Reis-Filho, J.S., da Rocha Dias, S., Hayward, R., Savage, K., Delmas, V., Larue, L., Pritchard, C., and Marais, R. (2009). Oncogenic Braf induces melanocyte senescence and melanoma in mice. *Cancer Cell* 15, 294–303.
- Diamond, M.S., Kinder, M., Matsushita, H., Mashayekhi, M., Dunn, G.P., Archambault, J.M., Lee, H., Arthur, C.D., White, J.M., Kalinke, U., et al. (2011). Type I interferon is selectively required by dendritic cells for immune rejection of tumors. *J. Exp. Med.* 208, 1989–2003.
- Dunn, G.P., Bruce, A.T., Sheehan, K.C.F., Shankaran, V., Uppaluri, R., Bui, J.D., Diamond, M.S., Koebel, C.M., Arthur, C., White, J.M., and Schreiber, R.D. (2005). A critical function for type I interferons in cancer immunoediting. *Nat. Immunol.* 6, 722–729.
- DuPage, M., Mazumdar, C., Schmidt, L.M., Cheung, A.F., and Jacks, T. (2012). Expression of tumour-specific antigens underlies cancer immunoediting. *Nature* 482, 405–409.
- Frederick, D.T., Piris, A., Coggill, A.P., Cooper, Z.A., Lezcano, C., Ferrone, C.R., Mitra, D., Boni, A., Newton, L.P., Liu, C., et al. (2013). BRAF inhibition is associated with enhanced melanoma antigen expression and a more favorable tumor microenvironment in patients with metastatic melanoma. *Clin. Cancer Res.* 19, 1225–1231.
- Fridman, W.-H., Pagès, F., Sautès-Fridman, C., and Galon, J. (2012). The immune contexture in human tumours: impact on clinical outcome. *Nat. Rev. Cancer* 12, 298–306.
- Frock, R.L., Hu, J., Meyers, R.M., Ho, Y.-J., Kii, E., and Alt, F.W. (2015). Genome-wide detection of DNA double-stranded breaks induced by engineered nucleases. *Nat. Biotechnol.* 33, 179–186.
- Fuertes, M.B., Kacha, A.K., Kline, J., Woo, S.-R., Kranz, D.M., Murphy, K.M., and Gajewski, T.F. (2011). Host type I IFN signals are required for antitumor CD8+ T cell responses through CD8alpha+ dendritic cells. *J. Exp. Med.* 208, 2005–2016.
- Gajewski, T.F., Louahed, J., and Brichard, V.G. (2010). Gene signature in melanoma associated with clinical activity: a potential clue to unlock cancer immunotherapy. *Cancer J.* 16, 399–403.
- Gajewski, T.F., Schreiber, H., and Fu, Y.-X. (2013). Innate and adaptive immune cells in the tumor microenvironment. *Nat. Immunol.* 14, 1014–1022.
- Gamba, C.A., Swetter, S.M., Stefanick, M.L., Kubo, J., Desai, M., Spaunhurst, K.M., Sinha, A.A., Asgari, M.M., Sturgeon, S., and Tang, J.Y. (2013). Aspirin is associated with lower melanoma risk among postmenopausal Caucasian women: the Women's Health Initiative. *Cancer* 119, 1562–1569.
- Gierach, G.L., Lacey, J.V., Jr., Schatzkin, A., Leitzmann, M.F., Richesson, D., Hollenbeck, A.R., and Brinton, L.A. (2008). Nonsteroidal anti-inflammatory drugs and breast cancer risk in the National Institutes of Health-AARP Diet and Health Study. *Breast Cancer Res.* 10, R38.
- Goulet, A.-C., Einsphar, J.G., Alberts, D.S., Beas, A., Burk, C., Bhattacharyya, A., Bangert, J., Harmon, J.M., Fujiwara, H., Koki, A., and Nelson, M.A. (2003). Analysis of cyclooxygenase 2 (COX-2) expression during malignant melanoma progression. *Cancer Biol. Ther.* 2, 713–718.
- Grivennikov, S.I., Greten, F.R., and Karin, M. (2010). Immunity, inflammation, and cancer. *Cell* 140, 883–899.
- Hanahan, D., and Weinberg, R.A. (2011). Hallmarks of cancer: the next generation. *Cell* 144, 646–674.
- Heft, J., Böttcher, J., Chakravarty, P., Zelenay, S., Huotari, J., Schraml, B.U., Goubau, D., and Reis e Sousa, C. (2015). GM-CSF mouse bone marrow cultures comprise a heterogeneous population of CD11c(+)MHCII(+) macrophages and dendritic cells. *Immunity* 42, 1197–1211.
- Hildner, K., Edelson, B.T., Purtha, W.E., Diamond, M., Matsushita, H., Kohyama, M., Calderon, B., Schraml, B.U., Unanue, E.R., Diamond, M.S., et al. (2008). Batf3 deficiency reveals a critical role for CD8alpha+ dendritic cells in cytotoxic T cell immunity. *Science* 322, 1097–1100.
- Joyce, J.A., and Fearon, D.T. (2015). T cell exclusion, immune privilege, and the tumor microenvironment. *Science* 348, 74–80.
- Kalinski, P. (2012). Regulation of immune responses by prostaglandin E2. *J. Immunol.* 188, 21–28.
- Knight, D.A., Ngiow, S.F., Li, M., Parmenter, T., Mok, S., Cass, A., Haynes, N.M., Kinross, K., Yagita, H., Koya, R.C., et al. (2013). Host immunity contributes to the anti-melanoma activity of BRAF inhibitors. *J. Clin. Invest.* 123, 1371–1381.
- Kuźnicki, L., Sarnecka, A., and Chwirot, B.W. (2006). Expression of cyclooxygenase-2 in benign naevi and during human cutaneous melanoma progression. *Melanoma Res.* 16, 29–36.
- Mantovani, A., Allavena, P., Sica, A., and Balkwill, F. (2008). Cancer-related inflammation. *Nature* 454, 436–444.
- Matsushita, H., Vesely, M.D., Koboldt, D.C., Rickert, C.G., Uppaluri, R., Magrini, V.J., Arthur, C.D., White, J.M., Chen, Y.-S., Shea, L.K., et al. (2012). Cancer exome analysis reveals a T-cell-dependent mechanism of cancer immunoediting. *Nature* 482, 400–404.
- Mayer-Barber, K.D., Andrade, B.B., Oland, S.D., Amaral, E.P., Barber, D.L., Gonzales, J., Derrick, S.C., Shi, R., Kumar, N.P., Wei, W., et al. (2014). Host-directed therapy of tuberculosis based on interleukin-1 and type I interferon crosstalk. *Nature* 511, 99–103.
- Page, D.B., Postow, M.A., Callahan, M.K., Allison, J.P., and Wolchok, J.D. (2014). Immune modulation in cancer with antibodies. *Annu. Rev. Med.* 65, 185–202.
- Pedersen, M., Küsters-Vandervelde, H.V.N., Viros, A., Groenen, P.J.T.A., Sanchez-Laorden, B., Gilhuis, J.H., van Engen-van Grunsven, I.A., Renier, W., Schieving, J., Niculescu-Duvaz, I., et al. (2013). Primary melanoma of the CNS in children is driven by congenital expression of oncogenic NRAS in melanocytes. *Cancer Discov.* 3, 458–469.
- Phan, V.T., Wu, X., Cheng, J.H., Sheng, R.X., Chung, A.S., Zhuang, G., Tran, C., Song, Q., Kowanetz, M., Sambrone, A., et al. (2013). Oncogenic RAS pathway activation promotes resistance to anti-VEGF therapy through G-CSF-induced neutrophil recruitment. *Proc. Natl. Acad. Sci. USA* 110, 6079–6084.
- Rakoff-Nahoum, S., and Medzhitov, R. (2009). Toll-like receptors and cancer. *Nat. Rev. Cancer* 9, 57–63.

- Ricciotti, E., and FitzGerald, G.A. (2011). Prostaglandins and inflammation. *Arterioscler. Thromb. Vasc. Biol.* 31, 986–1000.
- Rooney, M.S., Shukla, S.A., Wu, C.J., Getz, G., and Hacohen, N. (2015). Molecular and genetic properties of tumors associated with local immune cytolytic activity. *Cell* 160, 48–61.
- Rothwell, P.M., Wilson, M., Elwin, C.-E., Norrving, B., Algra, A., Warlow, C.P., and Meade, T.W. (2010). Long-term effect of aspirin on colorectal cancer incidence and mortality: 20-year follow-up of five randomised trials. *Lancet* 376, 1741–1750.
- Ruffell, B., Chang-Strachan, D., Chan, V., Rosenbusch, A., Ho, C.M.T., Pryer, N., Daniel, D., Hwang, E.S., Rugo, H.S., and Coussens, L.M. (2014). Macrophage IL-10 blocks CD8+ T cell-dependent responses to chemotherapy by suppressing IL-12 expression in intratumoral dendritic cells. *Cancer Cell* 26, 623–637.
- Schreiber, R.D., Old, L.J., and Smyth, M.J. (2011). Cancer immunoediting: integrating immunity's roles in cancer suppression and promotion. *Science* 331, 1565–1570.
- Sharma, P., and Allison, J.P. (2015). The future of immune checkpoint therapy. *Science* 348, 56–61.
- Talantov, D., Mazumder, A., Yu, J.X., Briggs, T., Jiang, Y., Backus, J., Atkins, D., and Wang, Y. (2005). Novel genes associated with malignant melanoma but not benign melanocytic lesions. *Clin. Cancer Res.* 11, 7234–7242.
- Tian, W., Zhao, Y., Liu, S., and Li, X. (2010). Meta-analysis on the relationship between nonsteroidal anti-inflammatory drug use and gastric cancer. *Eur. J. Cancer Prev.* 19, 288–298.
- Vesely, M.D., Kershaw, M.H., Schreiber, R.D., and Smyth, M.J. (2011). Natural innate and adaptive immunity to cancer. *Annu. Rev. Immunol.* 29, 235–271.
- Wang, D., and Dubois, R.N. (2010). Eicosanoids and cancer. *Nat. Rev. Cancer* 10, 181–193.
- Wenzel, J., Bekisch, B., Uerlich, M., Haller, O., Bieber, T., and Tüting, T. (2005). Type I interferon-associated recruitment of cytotoxic lymphocytes: a common mechanism in regressive melanocytic lesions. *Am. J. Clin. Pathol.* 124, 37–48.
- Willimsky, G., and Blankenstein, T. (2005). Sporadic immunogenic tumours avoid destruction by inducing T-cell tolerance. *Nature* 437, 141–146.
- Xu, L., Stevens, J., Hilton, M.B., Seaman, S., Conrads, T.P., Veenstra, T.D., Logsdon, D., Morris, H., Swing, D.A., Patel, N.L., et al. (2014). COX-2 inhibition potentiates antiangiogenic cancer therapy and prevents metastasis in preclinical models. *Sci. Transl. Med.* 6, 242ra84.

Non-genomic and Immune Evolution of Melanoma Acquiring MAPKi Resistance

Graphical Abstract



Highlights

- Non-genomic and immune alterations recur highly in acquired MAPKi-resistant melanoma
- Methylome/transcriptome-wide alterations occur in tumor cells and functional genes
- c-MET, LEF1, and YAP1 dysregulation reduces MAPK addiction and apoptotic sensitivity
- Resistant tumors recurrently lose CD8 T cell numbers/function and antigen presentation

Authors

Willy Hugo, Hubing Shi, Lu Sun, ...,
Jeffrey A. Sosman, Antoni Ribas,
Roger S. Lo

Correspondence

rlo@mednet.ucla.edu

In Brief

Resistance to targeted therapies in melanoma is associated with acquisition of highly recurrent non-genomic alterations as well as changes in the immune landscape of the tumor that may result in cross-resistance to salvage anti-PD-1/PD-L1 immunotherapy.

Accession Numbers

GSE65186

Non-genomic and Immune Evolution of Melanoma Acquiring MAPKi Resistance

Willy Hugo,^{1,6,10} Hubing Shi,^{1,6,10} Lu Sun,^{1,6,10} Marco Piva,^{1,6,10} Chunying Song,^{1,6} Xiangju Kong,^{1,6} Gatien Moriceau,^{1,6} Aayoung Hong,^{1,6} Kimberly B. Dahlman,^{7,9} Douglas B. Johnson,^{8,9} Jeffrey A. Sosman,^{8,9} Antoni Ribas,^{2,3,4,5,6} and Roger S. Lo^{1,2,5,6,*}

¹Division of Dermatology, Department of Medicine, University of California, Los Angeles, Los Angeles, CA 90095-1662, USA

²Department of Molecular and Medical Pharmacology, University of California, Los Angeles, Los Angeles, CA 90095-1662, USA

³Division of Hematology and Oncology, Department of Medicine, University of California, Los Angeles, Los Angeles, CA 90095-1662, USA

⁴Division of Surgical Oncology, Department of Surgery, University of California, Los Angeles, Los Angeles, CA 90095-1662, USA

⁵Jonsson Comprehensive Cancer Center, University of California, Los Angeles, Los Angeles, CA 90095-1662, USA

⁶David Geffen School of Medicine, University of California, Los Angeles, Los Angeles, CA 90095-1662, USA

⁷Department of Cancer Biology, Vanderbilt-Ingram Cancer Center, Nashville, TN 37232, USA

⁸Department of Medicine, Vanderbilt-Ingram Cancer Center, Nashville, TN 37232, USA

⁹Vanderbilt-Ingram Cancer Center, Nashville, TN 37232, USA

¹⁰Co-first author

*Correspondence: rlo@mednet.ucla.edu

<http://dx.doi.org/10.1016/j.cell.2015.07.061>

SUMMARY

Clinically acquired resistance to MAPK inhibitor (MAPKi) therapies for melanoma cannot be fully explained by genomic mechanisms and may be accompanied by co-evolution of intra-tumoral immunity. We sought to discover non-genomic mechanisms of acquired resistance and dynamic immune compositions by a comparative, transcriptomic-methylomic analysis of patient-matched melanoma tumors biopsied before therapy and during disease progression. Transcriptomic alterations across resistant tumors were highly recurrent, in contrast to mutations, and were frequently correlated with differential methylation of tumor cell-intrinsic CpG sites. We identified in the tumor cell compartment supra-physiologic c-MET up-expression, infra-physiologic LEF1 down-expression and YAP1 signature enrichment as drivers of acquired resistance. Importantly, high intra-tumoral cytolytic T cell inflammation prior to MAPKi therapy preceded CD8 T cell deficiency/exhaustion and loss of antigen presentation in half of disease-progressive melanomas, suggesting cross-resistance to salvage anti-PD-1/PD-L1 immunotherapy. Thus, melanoma acquires MAPKi resistance with highly dynamic and recurrent non-genomic alterations and co-evolving intra-tumoral immunity.

INTRODUCTION

Understanding how melanomas acquire resistance to BRAF inhibitors (BRAFi) via genetic alterations shown to reactivate

the MAPK pathway (Nazarian et al., 2010; Shi et al., 2012a, 2012b, 2014a, 2014b; Van Allen et al., 2014; Wagle et al., 2011) has guided the clinical development of BRAFi+MEKi combinatorial therapy. Despite superior clinical benefits, the double-drug approach commonly fails due to acquired resistance (Larkin et al., 2014; Long et al., 2014b) caused by a similar set of mutant genes responsible for acquired resistance to BRAFi monotherapy (Long et al., 2014a; Moriceau et al., 2015; Villanueva et al., 2013; Wagle et al., 2014). These shared mutations, which include V600E BRAF amplification and single nucleotide variants (SNVs) in NRAS, KRAS, MEK1/2, PTEN, CDKN2A, and DUSP4, indicate that the reservoir of genomic diversity strongly limits the long-term efficacy of dual (i.e., BRAFi+MEKi) or likely higher-order (i.e., BRAFi+MEKi+ERKi) MAPKi therapy.

In addition to harboring heterogeneous genetic alterations in the MAPK and PI3K-PTEN-AKT core pathways, melanomas at distinct sites with acquired BRAFi resistance in any given patient display extensively branched evolution (Shi et al., 2014a, 2014b). Furthermore, many on-treatment tumors re-grow without any clear genetic mechanism (Rizos et al., 2014; Shi et al., 2014b). These observations suggested that a diverse array of melanoma sub-clones, sometimes concurrent intra-tumorally, evolve to circumvent the “bottleneck” of BRAFi therapy (Shi et al., 2014b) and that exome-scale dissection of acquired MAPKi resistance falls short of fully explaining clinical resistance. Earlier (Johannessen et al., 2010; Nazarian et al., 2010) studies have pointed to transcriptome-based mechanisms of acquired BRAFi resistance. Given these leads, there is a clear need for comprehensive analyses of transcriptomic and epigenetic alterations underlying acquired MAPKi resistance in patient-derived melanoma samples. Identification of highly recurrent, non-genomic mechanisms may open the door to new combinatorial therapeutic strategies.

In the current therapeutic landscape, salvage therapies for patients with disease progression on MAPKi often involve immunotherapies, e.g., inhibitors of CTLA-4, PD-1 checkpoints, or

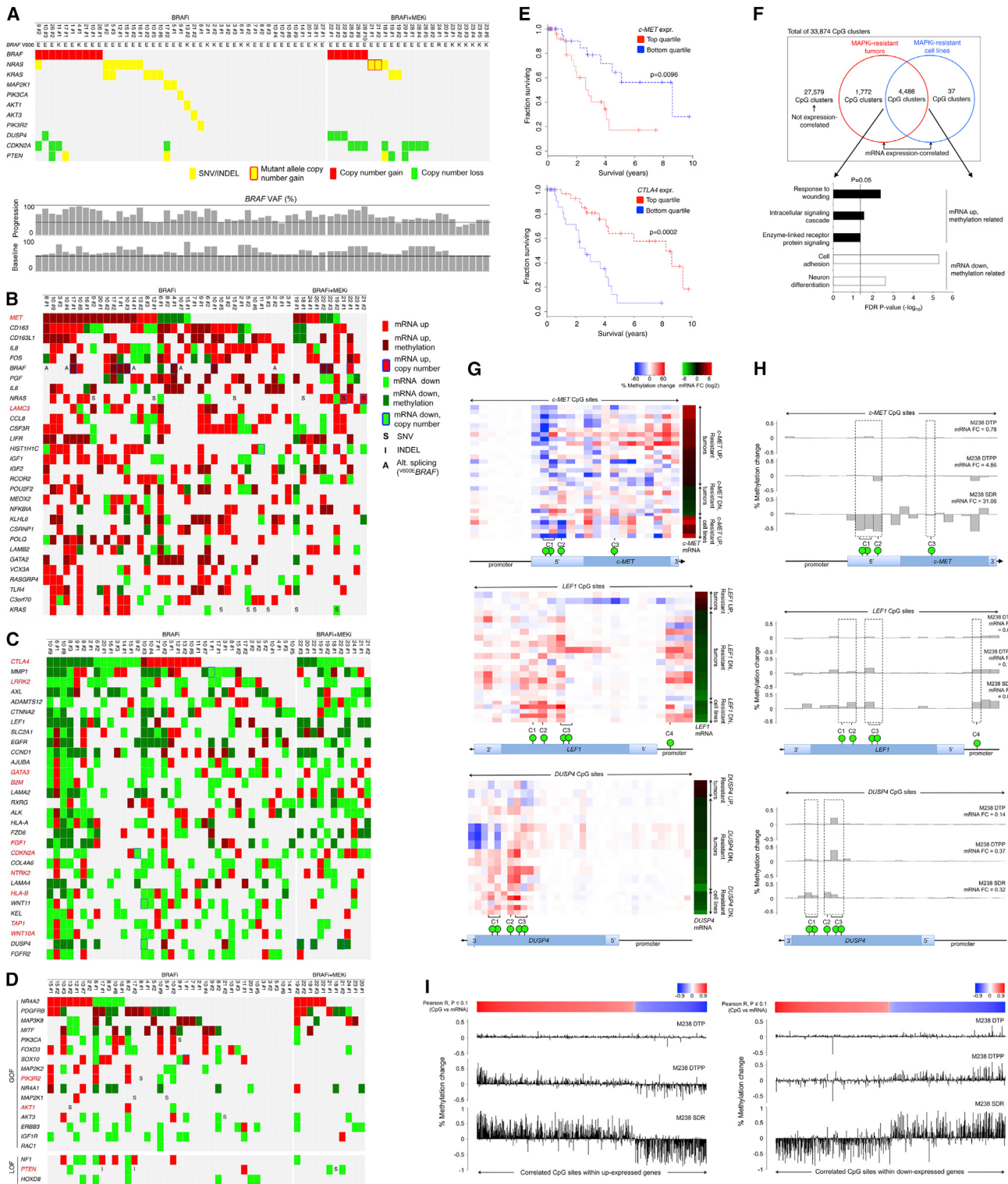


Figure 1. Landscape of Genomic, Transcriptomic, and Methylomic Alterations in Melanoma with Acquired MAPKi Resistance

Figure 1. Landscape of Genomic, Transcriptomic, and Methylyomic Alterations in Melanoma with Acquired MAPK Resistance

(A) Matrix of disease progressive melanomas ($n = 67$; indicated by patient and then tumor numbers) on BRAFi or BRAFi+MEKi therapies and of genes whose mutations cause acquired MAPK resistance. Bottom, *BRAF* variant allelic frequencies or VAFs (resulting in $V600E/K$) adjusted by estimated tumor purities.

(B and C) Tiling of top 30 recurrent GOF (B) or LOF (C) gene-based events among cancer/melanoma/immune genes across 48 disease-progressive $V600E$ -*BRAF* mutant melanoma samples relative to patient-matched baseline melanomas (left, BRAFi; right, BRAFi+MEKi). GOF or LOF events defined as GOF:LOF ratio ≥ 2 .

(legend continued on next page)

CSF1R on tumor-associated macrophages. But it is not known whether MAPKi-resistant melanomas are distinct in their immuno-phenotypes and susceptibilities to anti-CTLA-4 or -PD-1 therapies. In fact, studies are emerging which support immune microenvironment modulation by BRAFi as a contributor to in vivo anti-tumor effects. Thus, immune evasion may contribute to acquired MAPKi resistance (Ferrari de Andrade et al., 2014; Knight et al., 2013).

Hence, we sought a landscape perspective on the relative contributions of genomic and non-genomic mechanisms to acquired MAPKi resistance and co-evolutionary dynamics of the intra-tumoral immune microenvironment in patient-derived melanoma tissues.

RESULTS

Genetic Mechanisms of Acquired MAPKi Resistance in Melanoma

We analyzed whole-exome sequences (WESs) of serial tumor biopsies (baseline and acquired resistant tumors) and normal tissues from patients with advanced melanoma treated with MAPK inhibitor (MAPKi) regimens, which included single-drug (i.e., BRAFi) or double-drug (i.e., BRAFi+MEKi) therapies (Table S1A). When multiple disease-progressive or acquired MAPKi-resistant tumors were obtained from patients, they were compared to the same patient-matched baseline tumors. To assess the degree to which functionally validated genetic mechanisms account for clinically acquired MAPKi resistance, we visualized the recurrence of these mutations specific to or highly enriched in single-drug and double-drug disease-progressive (DP and DD-DP, respectively) melanomas ($n = 67$) relative to matched baseline tumors (Figure 1A). These functionally validated mutations (Moriceau et al., 2015; Shi et al., 2014b) included gain-of-function (GOF) events in $V600E/K$ BRAF, NRAS, KRAS, MEK1 or MAP2K1, PIK3CA, AKT1, AKT3 and loss-of-function (LOF) events in PIK3R2, DUSP4, CDKN2A, PTEN. The most recurrent resistance mutations were detected almost mutually exclusively in $V600E/K$ BRAF (copy-number gains in 15 of 67 or 22%) or RAS (single-nucleotide variants with or without copy-number gains in 17 of 67 or 25%). Less prevalent resistance mutations occurred at $\leq 9\%$ (in PTEN, DUSP4) or as

singleton events. Mutations in MITF, MEK2, RAC1, and NF1 were not specifically associated with resistant tumors. Importantly, 26 of 67 or 39% of resistant melanomas were not accounted for by any validated mutational mechanism.

Landscape of Transcriptomic Alterations in Acquired MAPKi Resistance

We profiled the temporal transcriptomic alterations in 48 DP or DD-DP compared with patient-matched baseline melanoma tissues (Table S1A) and integrated analysis (Figure S1A) of temporal transcriptomic with expressed exomic alterations to assess the combined recurrences of GOF and LOF gene-based events. We rank-ordered recurrences of resistance-specific alterations based on the number of resistant samples and (in cases of ties) of patients. The gene list included 855 cancer-, melanoma-, and MAPKi-resistance-, and immunotherapy-related genes (Table S1B). Importantly, among the top 30 GOF and LOF genes, transcriptomic alterations were generally more recurrent per gene and affected more genes than exomic alterations (Figures 1B, 1C, and S1B; Tables S1C and S1D). Notably, transcriptional up- or down-expression occurred recurrently and, respectively, in bona fide, mutated GOF (i.e., BRAF, NRAS, KRAS) and LOF (i.e., CDKN2A, DUSP4) resistance genes, with the transcriptomic events exceeding the mutational events in some cases (i.e., CDKN2A, DUSP4). Interestingly, $V600E/K$ BRAF was subject to not only mutational alterations (copy-number gain) (eight of 16) (Shi et al., 2012b) (Figures 1A and 1B), transcriptional up-expression (three of 16), and alternative splicing (five of 16) (Figure 1B), but also, in the absence of aforementioned mechanisms, mutant allele-selective expression (Figure S1B; Table S1E). In total, GOF events in BRAF occurred in 16 of 48 or 33% of resistant tumors. Similarly, NRAS and KRAS GOF events (26 of 48 or 54%) were a mixture of mRNA up-expression (16 of 26), mutational activation (11 of 26), and mutant allele-specific gene amplification (two of 26) (Moriceau et al., 2015). In contrast to BRAF where both genetic and non-genetic alterations affected the mutant gene selectively, up-expression of WT NRAS or KRAS was commonly detected in acquired MAPKi-resistant melanoma tumors and was capable of conferring MAPKi resistance to sensitive melanoma lines (Lidsky et al., 2014; Shi et al., 2014b) (Figure S1C). Also,

or LOF:GOF ratio ≥ 2 , respectively. SNV, expressed non-synonymous single-nucleotide variants; INDELs, expressed small insertion-deletions. Darker colors, differential mRNA expression significantly correlated with differential CpG cluster methylation. Splice variants based on RT-PCR detection reported for BRAF only. Genes in red, expression levels correlated with survival in the TCGA Melanoma data.

(D) Resistance driver genes proposed in the literature and their genetic and non-genetic alterations in acquired MAPKi-resistant samples. GOF and LOF assignment based on each gene's reported mechanism.

(E) Kaplan-Meier 10-year survival curves for c-MET and CTLA4 expression groups among TCGA patients with BRAF mutant melanoma ($n = 118$) and whose follow-up durations were within 10 years. p values, log-rank test.

(F) Numbers of mRNA expression-correlated CpG clusters in resistant melanoma tissues and/or cell lines. Annotated genes from the overlapping CpG clusters grouped by up- or down-expression and Gene Ontology term enrichments.

(G) Expression-correlated CpG clusters on c-MET, LEF1, and DUSP4. Green bubble, a CpG site with anti-correlated differential mRNA expression versus gDNA methylation. Heatmaps showing (left) percentage of methylation change at all profiled CpG sites (red, hyper-methylation; blue, hypo-methylation) across all resistant tumors and cell lines sorted by fold change (FC) of mRNA expression (right) of each gene (red, up-expression; green, down-expression).

(H) Methylation changes at profiled CpG sites (green bubbles, CpG sites nominated by aggregate tumor and cell line analysis as expression correlated) and mRNA expression fold changes (FC). Both percentages of methylation change and mRNA FC for each cell line sub-population were expressed relative to vehicle-treated M238.

(I) Methylation changes across all expression-correlated CpG sites (top heat scale, Pearson correlation R values) nominated by aggregate tumor and cell line analysis and located within up-(left) or down-(right) expressed genes in the SDR sub-population (versus vehicle-treated parental M238).

See also Table S1, Figure S1, and Data S1.

we observed statistically significant overlaps between genes that were recurrently mutated and recurrently differentially expressed (maximal recurrence capped at $n = 5$ resistance tumors; **Table S1F**). This association was particularly strong with recurrent copy-number alterations. Non-copy-number genetic alterations tended to be differentially expressed, although the statistical significance was weaker. Of interest, four genes were recurrently mutated in a GOF manner (excluding copy-number variances [CNVs]) in at least five resistant tumors. These genes were recurrently up-expressed and included *NRAS* and *KRAS*.

Most highly recurrent GOF events (**Figure 1B**; **Table S1C**) were purely transcriptomic and could involve either tumor cell-intrinsic or stromal differential gene expression. *c-MET* and *IL-8* (Sanchez-Laorden et al., 2014) were up-expressed, respectively, in 21 of 48 or 44% and 19 of 48 or 40% of resistant tumors. Furthermore, *c-FOS* and *MEOX2* encode tumor cell-intrinsic transcriptional factors implicated in MAPKi resistance (Johannessen et al., 2013). Other purely transcriptomic, highly recurrent GOF events involved the macrophage markers (*CD163* and *CD163L1*). Up-expression of other genes such as *CCL8* (critical for chemotaxis of monocytes, lymphocytes, and granulocytes), *CSF3R* (critical for granulocyte function), and *NFKBIA* suggested inflammatory tumor infiltration. Thus, highly recurrent and GOF transcriptomic events may reflect evolution in both the tumor cell and immune compartments of acquired MAPKi-resistant melanoma tissues.

The majority of highly recurrent LOF gene-based events (**Figure 1C**; **Table S1D**) arose from transcriptomic down-expressions. These involved a gene most commonly mutated in Parkinson's disease (*LRRK2*); an immune response modulation gene (*CTLA4*); antigen presentation genes (*B2M*, *HLA-A*, *HLA-B*, and *TAP1*); Wnt signaling genes (*LEF1*, *FZD6*, *WNT11*, and *WNT10A*); and RTK genes (*AXL*, *EGFR*, *ALK*, *NTRK2*, and *FGFR2*). *CTLA4* may be down-expressed in both the immune and tumor cell compartments, since in three melanoma expression data sets *CTLA4* expression, in contrast to *PDGDC1* (*PD-1*) expression, was less correlated with the expression of T cell genes *CD3*, *CD4*, or *CD8* (**Table S1G**). Also, we have observed *CTLA4* down-expression in several acquired MAPKi-resistant melanoma cell lines compared to their parental counterparts (data not shown). In the tumor cell compartment, *CTLA4* may be a direct therapeutic target of ipilimumab (Laurent et al., 2013). Moreover, the finding here of frequent *AXL* and *EGFR* down-expression in acquired MAPKi-resistant melanoma contrasted with previous cell line-based observations (Girotti et al., 2013; Müller et al., 2014). We therefore evaluated systematically the *in vivo* relevance of resistance mechanisms previously proposed based on functional studies in cell lines (**Figure 1D**). Despite the clear importance of *CRAF* as a convergent signaling node for various mechanisms of resistance (Moriceau et al., 2015; Nazarian et al., 2010; Shi et al., 2012b), *CRAF* (*RAF1*) itself was not subject to a single genetic or non-genetic alteration.

Beyond assessing recurrence as evidence of selection, we systematically gauged the impact of gene expression levels (top versus bottom quartiles) on TCGA melanoma patients' 10-year survival (significance cutoff, log-rank test $p \leq 0.05$). Importantly, *c-MET* and *CTLA4* were not only the most recurrently up- and down-expressed genes, respectively, among

resistant melanomas (**Figures 1B** and **1C**) but also genes whose expression levels portended survival significance (**Figure 1E**; **Table S1H**), even after adjusting for age, tumor ulceration, and stage (*c-MET*: Cox HR = 2.67 for the top quartile group, p value = 0.002, 95% CI, 1.4–5.0; *CTLA4*: Cox HR = 2.0 for the bottom quartile group, p value = 0.024, 95% CI, 1.1–3.8). In addition to assessing the survival impacts of gene expression levels, we validated our recurrent transcriptomic GOF and LOF events using a published microarray study of an independent set of tissues (Long et al., 2014a; Rizos et al., 2014). Again, *c-MET* was recurrently up-expressed in 8 of 35 (23%) MAPKi-resistant tumors from 7 of 26 (27%) patients (**Table S1I**); *CTLA4* was down-expressed in 9 of 35 (26%) MAPKi-resistant tumors from 7 of 26 (27%) patients (**Table S1J**).

A Common Methylomic Basis of Transcriptomic Alterations

An integrated transcriptome-methylome analysis (**Figures 1B** and **1C**) revealed a subset of recurrent differential mRNA expression events, including those affecting *c-MET*, *LEF1*, and *DUSP4*, as highly correlated with differential genomic DNA (gDNA) CpG methylation (**Table S1K**). Methylation levels at 6,295 of all 33,874 (18.6%) CpG clusters were significantly correlated with differential mRNA expression (**Figure 1F**; **Supplemental Experimental Procedures**). To estimate the scope of tumor cell-intrinsic events, we calculated the numbers of expression-correlated CpG clusters across MAPKi-resistant tumors ($n = 43$ pairs) and cell lines ($n = 5$ pairs) and found that 4,486 of 6,295 (71.2%) expression-correlated CpG clusters were found in both (**Figures 1F**; **Figure S1D**). We then performed Gene Ontology (GO) enrichment analysis of genes annotated to overlapping expression-correlated CpG clusters; these genes included *c-MET*, *LEF1*, and *DUSP4* (**Figure 1G**; **Table S1K**). Genes with methylation-correlated up-expression were enriched for wound healing and receptor-linked or intracellular signaling, whereas genes displaying methylation-correlated down-expression were enriched for cell adhesion and neuron differentiation (**Figure 1F**). In *c-MET*, three CpG clusters (C1–3) with differential methylation were negatively correlated with differential mRNA expression (**Figure 1G**). The extent and significance of these correlations compared favorably with those between mRNA levels of *c-MET* and its positive transcriptional factors (TFs) (**Figure S1E**). In nearly all (90%) pairwise comparisons of tumors and cell lines, differential *c-MET* mRNA expression could be accounted for by at least one differential CpG cluster methylation ($\Delta\beta \geq 10\%$ and FDR adjusted $p \leq 0.05$). In contrast, only 48% displayed a concordant differential expression pattern of at least one *c-MET* TF (**Figure S1F**). Similarly for *LEF1*, *DUSP4*, and *EPHA2*, differential methylation at specific CpG clusters negatively correlated with differential mRNA expression (**Figures 1G**, **S1G**, and **S1H**; **Table S1K**).

To corroborate expression-methylation correlations, we analyzed data from 335 TCGA melanoma samples. The Pearson correlation between the absolute methylation levels at C1 and normalized mRNA expression of *c-MET* was -0.48 ($p < 2.2 \times 10^{-16}$), while the correlation with *MITF* was 0.42 ($p = 2.2 \times 10^{-15}$). We also compared the top and bottom quartiles of methylation levels (β values) in the *c-MET* CpG clusters and their mRNA

expression levels. In particular, C1 CpG hypo-methylation associated strongly (Wilcoxon rank sum test $p < 2.2 \times 10^{-16}$) with high levels of *c-MET* mRNA expression (Figure S1I; C2 CpG cluster, not covered). Similar analysis for *LEF1* and *DUSP4* also supported expression-methylation correlations at specific CpG clusters (Figures S1J and S1K). Overall, among 7,769 individual expression-correlated CpG sites from 6,295 CpG clusters (Figure 1F), 4,086 CpG sites (53%) showed concordant differential mRNA expression and CpG site methylation (top versus bottom quartiles) among the TCGA melanoma tumors. Furthermore, we examined our tissue-derived data for phenotypes inferred from expression patterns of methylation-regulated genes such as *c-MET*, *LEF1*, and *DUSP4* (Table S1L). Genes whose differential expression positively correlated with that of *c-MET* were enriched in the GO term “pigmentation during development”; those negatively correlated for “cell adhesion” and “positive regulation of cell proliferation,” which suggested a motile phenotype (Data S1A and S1B). On the other hand, differential expression of *LEF1* and *DUSP4* correlated strongly with enrichment of a mutant *BRAF* signature (*LEF1*, Pearson $R = 0.62$ $p = 8.9 \times 10^{-6}$; *DUSP4*, Pearson $R = 0.60$ $p = 1.8 \times 10^{-5}$) (Data S1C and S1D), which associated *LEF1* and *DUSP4* down-expression with reduced MAPK addiction. Taken together, MAPK inhibition in *BRAF* mutant melanoma may lead to epigenetic transcriptomic alterations with functional consequences.

We then assessed whether BRAF inhibition in melanoma cell lines would lead to temporally incremental and correlated alterations between methylation and mRNA levels in *c-MET*, *LEF1*, *DUSP4*, and in general. Using two human *V600E**BRAF* melanoma cell lines, we profiled the methylomes and transcriptomes of vemurafenib (BRAFi)-selected sub-populations over time, including drug-tolerant persisters (DTPs) (days of treatment), drug-tolerant proliferating persisters (DTPPs) (weeks), and single-drug resistant (SDR) sub-lines (months to years) as described (Shi et al., 2014a). We observed in time-dependent BRAFi-selected sub-populations (relative to vehicle-treated cells) methylation decreases at *c-MET*'s nominated CpG clusters along with mRNA increases. In contrast, methylation at nominated CpG clusters in *LEF1* and *DUSP4* increased, while their mRNA levels decreased with BRAFi treatment duration (Figure 1H; Data S1E). We also examined the temporal methylation changes at all CpG sites within all genes displaying differential expression between vehicle-treated cells versus their isogenic SDR sub-lines. Importantly, the magnitudes of methylation changes were time dependent; the directions of methylation changes were concordant with the sites' correlation scores independently derived from the aggregate analysis of the tissue and cell line pairs (Figure 1I; Data S1F and S1G). Thus, BRAFi treatments of cell lines led to progressive methylation-expression changes akin to observations across MAPKi-sensitive versus resistant tumors.

Highly Recurrent *c-MET* Up-Expression Mediates MAPKi Resistance

Because acquired MAPKi-resistant melanomas displayed highly recurrent *c-MET* up-expression (Figure 1B), we compared the absolute *c-MET* expression levels in three resistant and one sensitive melanoma sub-groups: (1) *c-MET*-up-expression (*c-MET* UP), (2) no *c-MET* differential expression, (3) *c-MET*

down-expression, and (4) baseline (Figure 2A) and observed that *c-MET* UP resistant-melanomas in particular displayed supra-physiologic levels of *c-MET* transcripts compared to the sensitive, drug-naive melanomas in both our and the validation cohorts. Additionally, the overall *c-MET* expression levels across the spectrum of sensitive- and resistant-melanomas correlated with single-sample enrichments of *c-MET* signatures generated from the TCGA Melanoma data set (Figure 2B; Table S2). Genes up-expressed ($\log_2 FC \geq 2$, FDR adjusted Wilcoxon p value ≤ 0.05) in the top quartile of *c-MET* expression (versus the bottom quartile) defined the *c-MET*_UP signature, and genes up-expressed in the bottom quartile defined the *c-MET*_DOWN or DN signature. Importantly, *c-MET* up-expression in MAPKi-resistant melanomas generally concurred with positive enrichment of the *c-MET*_UP TCGA signatures (and down-expression with negative enrichment) (Figure 2C). By combining the transcriptomic analysis of RTK genes in both discovery and validation data sets ($n = 82$ differential expressions), we found that another RTK *EPHA2*, which like *c-MET* has been nominated as a cancer metastasis gene, was up-expressed ($n = 25$) in a largely mutually exclusive manner to *c-MET* up-expression ($n = 29$) (one-sided Fisher's exact test p value = 0.031; odds ratio 0.34) (Figure 2D). *EPHA2* up-expression among MAPKi-resistant melanomas also occurred in a supra-physiologic range (Figure S2A), and its top-quartile expression associated significantly with worse patient survival (Figure S2B). Using available patient-matched FFPE samples (Figure 2E), we detected relative *c-MET* protein up-expression in disease progressive tissue sections (Figure 2F) using a validated antibody (Figure S2C) and found *c-MET* up-expression in MAPKi resistance to be tumor cell-intrinsic.

We then assessed the functional role of tumor cell-intrinsic, supra-physiologic *c-MET* up-expression using two triplets of isogenic cell lines where the drug-resistant sub-lines were (1) derived from the M229 and SKMEL28 human *V600E**BRAF* melanoma cell lines by chronic BRAFi (vemurafenib) (single-drug resistance or SDR) or BRAFi (vemurafenib)+MEKi (selumetinib) (double-drug resistance or DDR) treatment (Figure 3A) and (2) shown to display dramatic mRNA and protein up-expression of *c-MET* compared to their parental cell lines. In stark contrast to acquired MAPKi-resistant cell lines driven by genetic mechanisms such as *NRAS* mutations, *V600E**BRAF* amplification, and/or *MEK1* mutations, acquired SDR or DDR sub-lines up-expressing *c-MET* was highly refractory to downstream MAPK suppression (Figure 3A). Despite this, stimulation of cells by HGF addition during the course of BRAFi (for parental and SDR cell lines) or BRAFi+MEKi (for DDR cell lines) treatment accelerated p-ERK recovery or reactivation only in resistant cell lines and in a manner reversible by co-treatment with an inhibitor of *c-MET*, crizotinib (Figure 3B). *c-MET* up-expression was accompanied by enhanced activation-associated phosphorylation (Y1234/1235) and p-AKT (T308, S473) induction, which could be augmented by HGF stimulation and repressed by crizotinib treatment (Figure 3C). These studies indicate that supra-physiologic *c-MET* up-expression in SDR and DDR sub-lines mediates MAPK-redundant survival signaling.

Importantly, HGF stimulation enhanced the clonogenic survival of M229 and SKMEL28 SDR and DDR sub-lines cultured with MAPK inhibitor(s) but not the parental cell lines (without

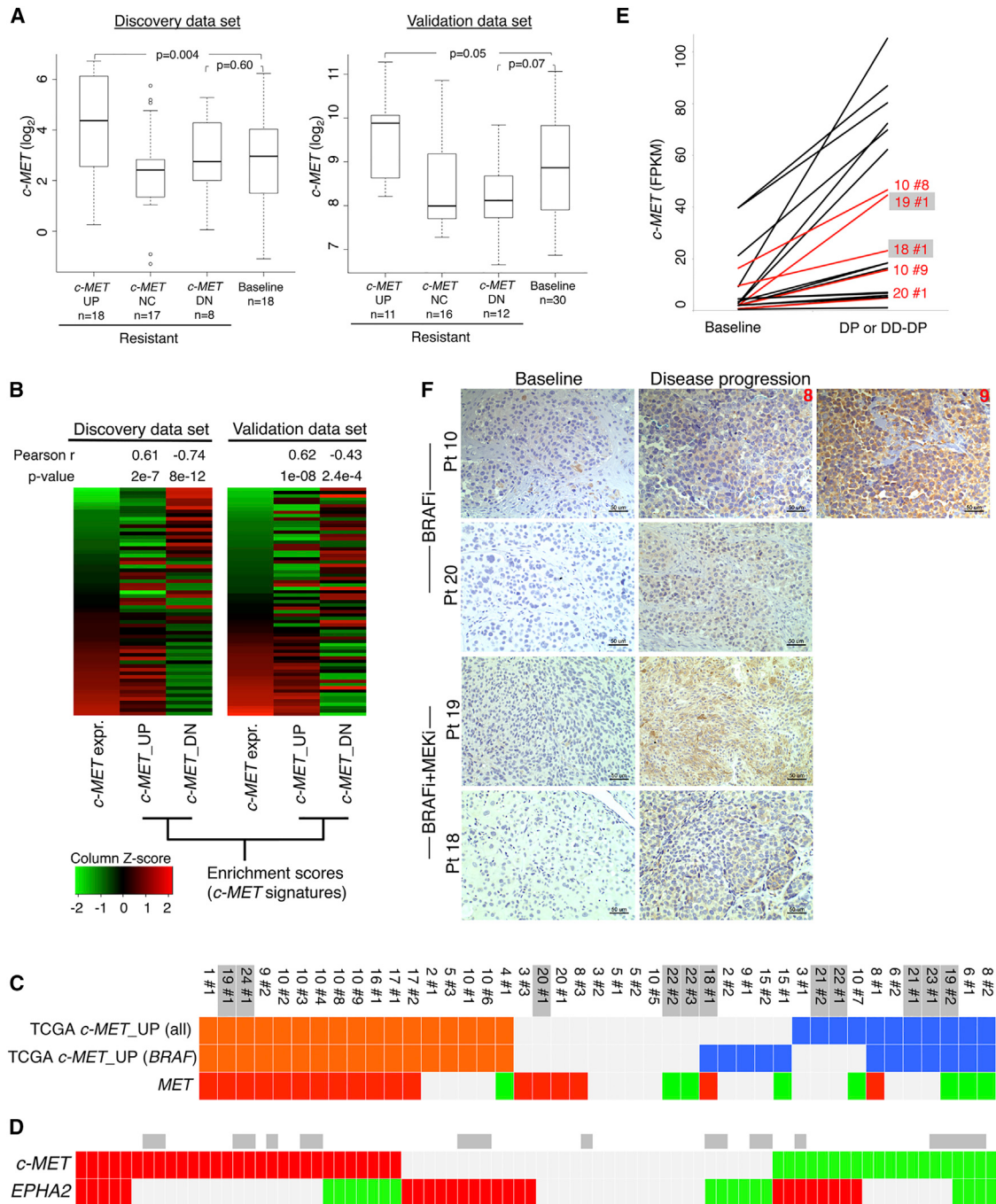


Figure 2. Recurrent c-MET Up-Expression in Disease Progressive Melanomas

(A) *c-MET* mRNA expression levels in distinct subsets of disease progressive sample. p values, Wilcoxon rank-sum test.

(B) Pearson correlation (p values, t test) of the *c-MET* mRNA expression levels in all baseline and disease progressive melanoma samples (discovery, n = 59; validation, n = 61) with enrichment scores of the TCGA melanoma-derived *c-MET* signatures.

(C and D) Tiling of *c-MET* signature enrichment (orange and blue, positive and negative enrichments) (C) and differential *c-MET* (C and D) and *EPHA2* (D) expression (red and green, up- and down-expression) across disease progressive melanomas (DD-DP samples, gray) (both discovery and validation cohorts, D). (E and F) Levels of *c-MET* mRNA (E) and protein (F) (for samples in red) in patient-matched pairs where resistance-associated *c-MET* mRNA up-expression was detected (ruler, 50 μ m).

See also Table S2 and Figure S2.

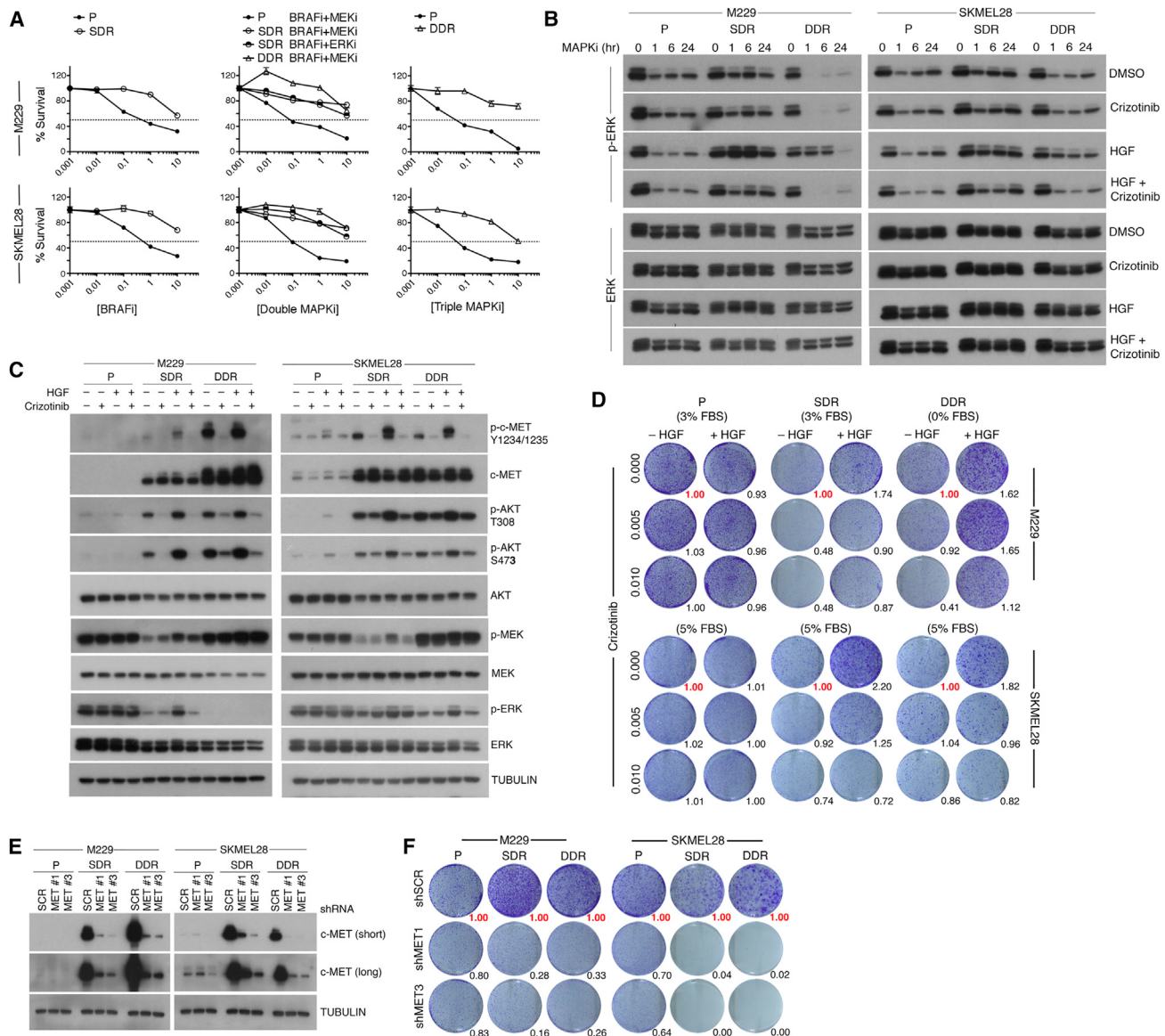


Figure 3. c-MET Up-Expression Drives Acquired MAPKi Resistance

(A) Three-day MTT survival assays of two isogenic melanoma triplets in response to single MAPKi (BRAFi), double MAPKi (as indicated), or triple MAPKi (BRAFi+MEKi+ERKi). BRAFi, vemurafenib; MEKi, selumetinib; ERKi, SCH772984 (all in μ M). Error bars, SEM, n = 5; normalized to DMSO vehicle as 100%.

(B) Western blot (WB) analysis of p-ERK recovery in both isogenic triplet cell lines in response to a single dose of 1 μ M BRAFi (P, SDR) or BRAFi+MEKi (DDR) under four conditions (DMSO/PBS, crizotinib (0.1 μ M)/PBS, DMSO/HGF (20 ng/ml), and HGF/crizotinib (μ M)). SDR and DDR sub-lines were first plated without MAPKi for 16 hr. Loading controls, ERK.

(C) WB levels of activation-associated phosphorylation and total levels of indicated proteins in response to vehicle, crizotinib, and/or HGF treatments (1 hr). TUBULIN, loading control. Only SDR and DDR lines were cultured with MAPKi.

(D) Long-term (10 days) clonogenic assay (P, no inhibitor; SDR, 1 μ M BRAFi; DDR, 1 μ M BRAFi+MEKi) \pm HGF and crizotinib (μ M). Growth quantifications are relative to cultures without HGF and crizotinib (in red).

(E) WB analysis of c-MET knockdown (short and long exposures).

(F) Long-term (10 days) clonogenic assay \pm c-MET knockdown. Growth quantifications relative to shScramble (shSCR) controls.

MAPKi) (Figure 3D), indicating that the growth-promoting effect of HGF depended on c-MET up-expression. Also, treatments with low concentrations of crizotinib reduced the clonogenic growth of SDR and DDR sub-lines, with or without HGF stimulation, but not the parental melanoma cell lines. Furthermore,

c-MET knockdown using two independent small hairpin RNA (shRNAs) (Figure 3E) preferentially reduced the clonogenic growth of resistant melanoma sub-lines (Figure 3F). Collectively, these data argue that melanoma cells can acquire MAPKi resistance via addiction to c-MET up-expression and hyper-activity.

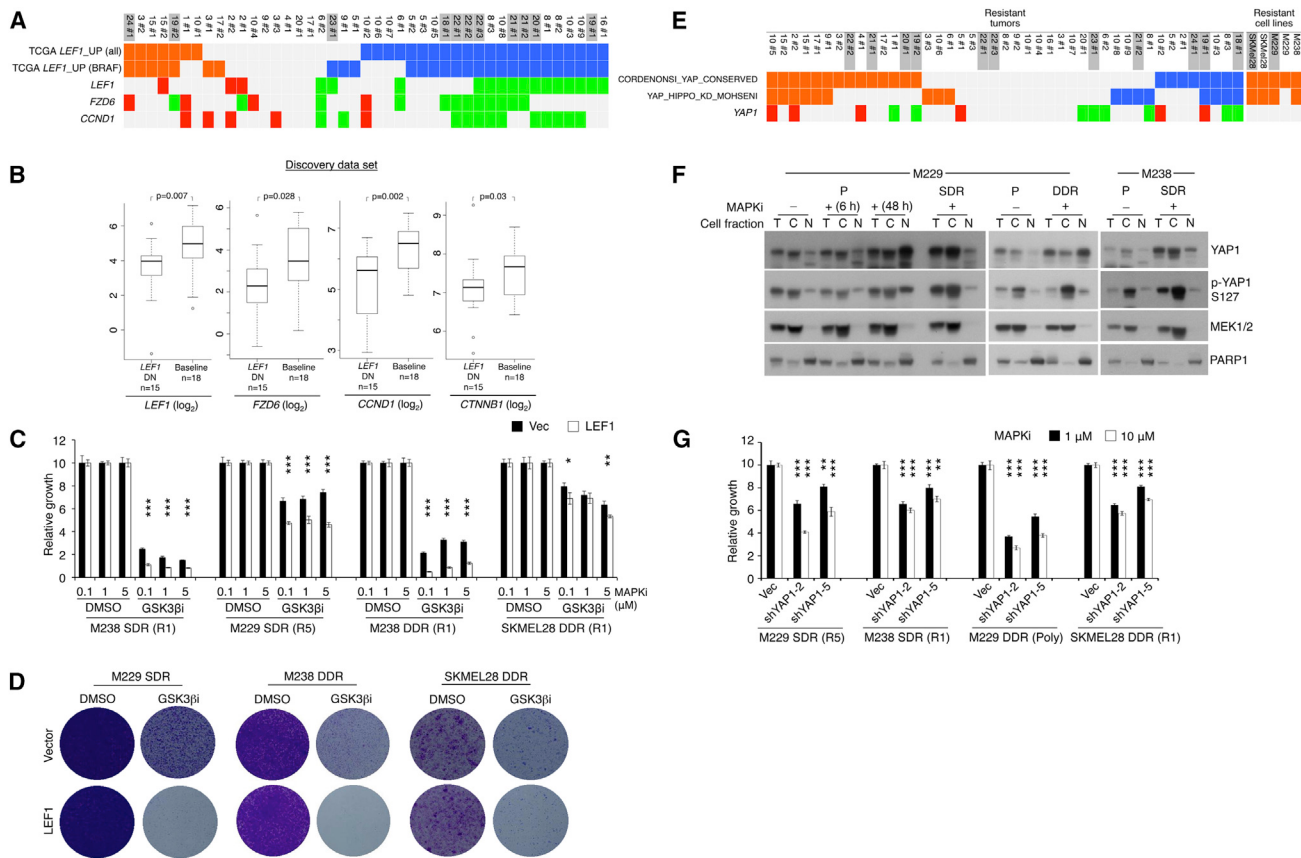


Figure 4. β -Catenin-LEF1 Up- and YAP1 Downregulation Sensitize Resistant Melanoma to MAPKi

- (A) Tiling of *LEF1_UP* gene signature enrichment and differential expression of *LEF1*, *FZD6*, and *CCND1* across disease progressive melanomas.
- (B) Indicated mRNA expression levels in *LEF1* down-expressed, MAPKi-resistant melanomas versus baseline melanomas. p values, Wilcoxon rank-sum test.
- (C) Three-day survival assays of resistant melanoma cell lines at varying [BRAFi] and [BRAFi+MEKi], \pm GSK3 β i (10 μ M CHIR99021) or LEF1 overexpression.
- (D) Clonogenic assays of resistant cell lines (cultured with 1 μ M MAPKi) \pm LEF1 overexpression, with DMSO (9 days) or GSK3 β i (10 μ M, 18 days).
- (E) As in (A) except signature enrichment and differential expression indicated for YAP1.
- (F) Western blot analysis of indicated parental (P) and isogenic resistant cell lines for levels of total and phospho-YAP1 and marker proteins in cytoplasmic (C) and nuclear (N) fractions (T, total lysate). MAPKi, 1 μ M.
- (G) Three-day survival assays of resistant melanoma cell lines at two indicated [BRAFi] or [BRAFi+MEKi], \pm YAP1 knockdown.

*p < 0.01, **p < 0.001, ***p < 0.0001, Student's t test p values, \pm LEF1 overexpression (C) or shVector versus shYAP1 (G) Error bars, SEM; n = 5 per group.

See also Figure S3 and Table S3.

Altered β -Catenin-LEF1 and YAP1 Signaling Reduces Apoptosis and Promotes MAPKi Resistance

Whereas supra-physiologic *c-MET* up-expression in resistant tumors correlated strongly with its down-methylation, *LEF1* down-expression correlated with its up-methylation (Figures 1C and 1G) and resulted in infra-physiologic expression levels (Figures 4A, 4B, and S3A). Moreover, *LEF1* (and its related pathway genes, *FZD6* and *CCND1*) down-expression concurred strongly with negative enrichment of TCGA melanoma *LEF1_UP* signatures (Figure 4A; Table S3), indicating downregulation of β -catenin-LEF1 transcriptional activity. Consistently, we detected robust *LEF1* protein down-expression in resistant tumors using a FFPE-validated antibody (Figures S3B and S3C). We also detected *LEF1* down-expression in a panel of SDR or DDR cell lines (versus parental cell lines) (Figure S3D). To understand whether

β -catenin-LEF1 signal downregulation promoted MAPKi resistance, we tested whether restoration of *LEF1* expression and/or β -catenin-LEF1 signaling in these MAPKi-resistant melanoma cell lines would re-sensitize them to MAPKi. GSK3 β inhibition using CHIR99021 strongly decreased p- β -catenin (Ser33/37 and Thr41) and increased total β -catenin levels in the parental cell lines (e.g., Figure S3E); these effects of GSK3 β inhibition were weaker in the SDR and DDR cell lines (Figure S3F), consistent with a compromised β -catenin-LEF1 pathway. Importantly, GSK3 β i strongly re-sensitized SDR and DDR melanoma cell lines to BRAFi and BRAFi+MEKi, respectively, and this re-sensitization to MAPKi was augmented by *LEF1* re-expression in short-term (Figure 4C) and long-term (Figure 4D) survival assays. Hence, recurrent β -catenin-LEF1 downregulation promotes MAPKi insensitivity.

Although analysis of recurrent, differential mRNA expression can uncover key transcriptome- and methylome-based resistance genes such as *c-MET* and *LEF1*, we asked whether gene signature-based analysis would identify resistance genes with post-transcriptional mechanism. One such candidate resistance gene, *YAP1*, was supported by recurrent signature enrichment without necessarily its mRNA up-expression in both MAPKi-resistant tumors and cell lines (Figure 4E). Importantly, western blot analysis showed that these acquired MAPKi-resistant cell lines harbored increased total levels of YAP1 and phospho-YAP1, in the cytoplasmic, nuclear or both compartments, compared with levels in the untreated parental cell lines (Figure 4F). In fact, BRAFi treatment of the M229 parental line led to an accumulation of YAP1 protein but not its mRNA level. Consistently, we showed, using a validated anti-YAP1 antibody (Figure S3G), that YAP1 protein was up-expressed in disease progressive melanoma tissues (despite the lack of *YAP1* mRNA up-expression) compared to their baseline tissues (Figure S3H). Notably, in SDR and DDR melanoma cell lines with positive enrichment of *YAP1* signatures, *YAP1* knockdown (Figure S3I) re-sensitized these resistant cell lines to BRAFi or BRAFi+MEKi (Figure 4G).

Given known intersections between the β -catenin-LEF1 and YAP1 signaling pathways in other biological contexts, we explored whether β -catenin-LEF1 downregulation and YAP1 up-regulation may co-regulate resistance. Inhibition of GSK3 β with overexpression of LEF1 in YAP1 signature-enriched, MAPKi-resistant cell lines strongly induced apoptosis, as measured by PARP1 cleavage (cPARP1) (Figure 5A), suggesting that β -catenin-LEF1 signaling promoted apoptotic sensitivity to MAPKi. Since BIM levels are known to modulate melanoma sensitivity to apoptotic induction, we tested whether GSK3 β treatment and restoration of LEF1 expression would promote the levels of the pro-apoptotic protein BIM. Indeed, this combination accelerated and/or augmented BIM accumulation in all acquired MAPKi-resistant cell lines tested (Figure 5B). Interestingly, while GSK3 β inhibition and YAP1 knockdown each induced apoptosis, they together induced greater apoptosis (Figure 5C) in association with BIM accumulation (Figure 5D). Consistently, GSK3 β inhibition with YAP1 knockdown resulted in the most extensive clonogenic growth suppression of acquired MAPKi-resistant melanoma cell lines (Figure 5E). Conversely, heterologous overexpression of YAP1, beyond the endogenously up-expressed levels in these resistant cell lines, reduced apoptosis and BIM induction by GSK3 β inhibition (Figures 5F and 5G). Accordingly, exogenous YAP1 overexpression strongly rescued MAPKi-resistant melanoma cells from clonogenic growth suppression elicited by GSK3 β inhibition (Figure 5H). Together, these results support the concept that β -catenin-LEF1 and YAP1 signaling antagonistically co-regulate the tumor cell-intrinsic, apoptotic threshold of melanoma to MAPKi.

Acquiring MAPKi Resistance Can Deplete and Exhaust Intra-tumoral CD8 T Cells

Among the most recurrent gene-based transcriptomic alterations in acquired MAPKi resistant melanomas were those related to tumor-associated immune cells or inflammatory states (Figures 1B and 1C). By quantifying changes in gene set enrich-

ment values between resistant versus matched baseline tumors, we found that the most highly recurrent net positive enrichments were in signatures related to NF- κ B signaling or inflammation (from C6 oncogenic signatures, Broad Institute), monocyte functions (C7 immune signatures), and additional immune and inflammation signatures related to, for instance, T cell function, serum response, and NF- κ B signaling (C2 chemical and genetic perturbation signatures) (Data S2A–S2C). In assessing a potential relationship between monocyte function and intra-tumoral inflammation, we found that the enrichments (positive or negative) of NF- κ B/inflammation and of monocyte activation signatures aligned correspondingly with each other (Figure 6A). Additionally, positive enrichment of NF- κ B or inflammation signatures related strongly to the up-expression of a panel of M2 macrophage markers, including those among the top GOF genes such as *CD163* and *CD163L1* (Figure 1B). Thus, changes in tumor-associated macrophages likely contributed to distinct inflammatory states in melanomas with acquired MAPKi resistance.

Given that tumor-associated M2 macrophages can antagonize the recruitment and effector functions of T cells, we analyzed the relationship between macrophage-associated inflammation with expression markers of T cell abundance/function. Interestingly, we found that a subset (group B, Figure 6A) among MAPKi-resistant melanomas with enhanced expression of macrophage-associated inflammation (groups A+B, Figure 6A) was strongly associated with reduced expression of T cell marker/function. *CSF1R* and *CD163* (M2 macrophage markers) expression levels displayed a highly positive correlation that was comparable to the correlation between *CD8A* and *CD8B* expression levels (Data S2D and S2E), indicating that the majority of *CSF1R* up-expression occurred in *CD163*-positive macrophage cells. Furthermore, negative enrichment of the NF- κ B signature in resistant tumors was significantly associated with expression loss of tumor-associated M2 macrophage markers, *CD163* or *CSF1R* (Figure 6B). The putative deficiency of tumor-associated M2 macrophages and a pauci-inflammatory tumor microenvironment marked a second subset of intra-tumoral T cell loss. Importantly, a similar pattern of immune re-composition was observed in the validation data set (Data S2F). Thus, the states of macrophage and T cell inflammation co-evolved with MAPKi resistance, suggesting the potential utility of *CSF1R* inhibitors.

We investigated further the dynamic loss of CD8 T cells in a significant subset of acquired MAPKi resistance. We observed: (1) a concurrent down-expression of *CD8A*, *CD8B*, *PDCD1* (*PD-1*), and *TNFRSF9* (4-1BB/*CD137*), where *PDCD1* (*PD-1*) and *TNFRSF9* (4-1BB/*CD137*) expression marks the melanoma tumor-reactive CD8 T cell population (Gros et al., 2014) (Table S4), and (2) a suppression of CD8 T cell numbers (reflected by the absolute *CD8A* expression values) to a level significantly below the baseline range, and (3) lower *CD8A* (italicized) expression values in association with down-enrichment of the NF- κ B signature (Figure 6C; Data S2G). We could directly visualize suppression of CD8 T cell numbers using anti-CD8 (along with differential levels of macrophages using anti-*CD163*) immunofluorescence of fixed tissues from tumor sections adjacent to those subjected to RNA sequencing (RNA-seq) (Figure 6D). Given

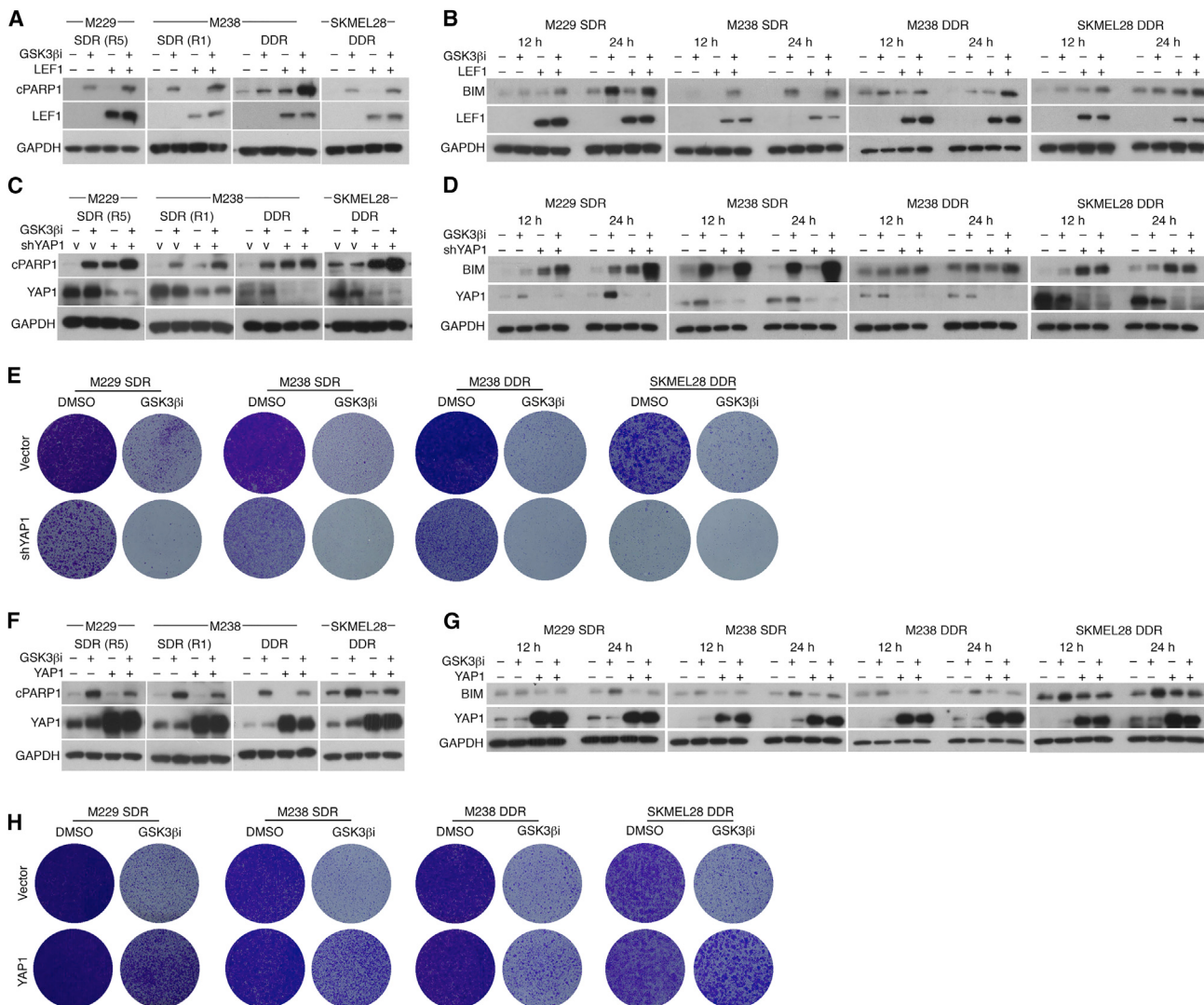


Figure 5. β -Catenin-LEF1 and YAP1 Co-regulate Apoptotic Sensitivity of Acquired MAPKi-Resistant Melanoma Cells

(A) Western blot (WB) analysis of indicated resistant melanoma cell lines (cultured with 1 μ M MAPKi) for levels of cleaved PARP1 (cPARP1), LEF1, and GAPDH (loading control). Cells were treated with DMSO or GSK3 β i (10 μ M CHIR99021), \pm LEF1 overexpression, for 1–2 days.

(B–D) As in (A), except cell lysates were collected at 12 and 24 hr and probed for BIM levels (B and D) or harbored shVector (V) or shYAP1 (C and D).

(E) Clonogenic assays of indicated resistant cell lines (cultured with 1 μ M MAPKi) treated with DMSO or GSK3 β i (10 μ M CHIR99021) for 14 days, \pm YAP1 knockdown.

(F and G) As in (A), except cells \pm YAP1 overexpression and WBs were probed for YAP1 and cPARP1 (F) or BIM (G).

(H) As in (E), except \pm YAP1 overexpression; all cultures for 14 days except M238 DDR cultures with GSK3 β i (22 days).

highly recurrent down-expression of antigen presentation genes (e.g., *B2M*, *HLA-A*, *HLA-B*, and *TAP1*) (Figure 1C), we analyzed the potential relationship in the dynamic expression of genes related to antigen presentation, dendritic cells, and CD8 T cells (Figure 6E). This revealed a consistent concurrence between levels of intra-tumoral antigen presentation and CD8 T cells' function in both the discovery and validation tissue cohorts, indicating that \sim 50% of all resistant melanoma displayed a relative loss of CD8 T cells and their function (Data S2H). This was not surprising considering a general and tight correlation between *CD8A* versus *TAP1* or *B2M* expression levels among all mel-

omas in our cohort (Figures 6F and 6G), in the validation cohort (Figure S4A), and in the TCGA melanoma cohort (Figure S4B). Importantly, the subgroups of resistant melanomas with *CD8A* down-expression or of all melanomas with the lowest quartile of *CD8A* expression displayed a high ratio of *EOMES/CD8A* expression (where *EOMES* is a transcription factor related to T cell exhaustion (Twyman-Saint Victor et al., 2015) (Figures 6H and S4C). Reduced intra-tumoral *CD8A* expression was associated with increased ratios of expression in a panel of CD8 T cell exhaustion genes to *CD8A* (Figure 6I), and the sub-group of resistant tumors with *CD8A* down-expression was

strongly associated with T cell exhaustion (Figure S4D). Moreover, expression levels of the CD8 T cell marker (*CD8A*), its functional feedback (*PDCD1/PD-1*, *CD274/PD-L1*) driven by IFN- γ , and its effector function (geometric average of *PRF1*, *GZMA* expressions defined as a cytolytic score (Rooney et al., 2015) were found to be clinically important, as they impacted patient survival in the TCGA melanoma data (Figure 6J). Lastly, the dynamic nature of intra-tumoral CD8 T cells before and during progression on MAPKi therapy was further underscored by an inverse relationship in the expression levels of these CD8 T cell marker/function genes at baseline and during disease progression (Figures 6K and S4E). In short, MAPKi resistance and CD8 T cell deficiency/exhaustion co-evolve frequently with downregulation of the antigen presentation machinery.

DISCUSSION

Unraveling the complexities of cancer genomics has relied heavily on the recurrence of genetic events as a sine qua non evidence for functional selection. However, when the evolution of melanoma treated with MAPK inhibitor(s) was actually sampled by serial biopsies, the genetic variants positively selected by the inhibitors were not highly recurrent and together could not explain clinical relapse comprehensively. Here, we showed that gene-and signature-based transcriptomic alterations in acquired MAPKi-resistant melanoma were highly recurrent. Transcriptomic alterations, unlike mutations, could not be attributed to tumor or stromal/immune cells without specific validations through histologic analysis of tissues and functional analysis of cell line models of acquired resistance. We highlighted specific genes (*c-MET*, *LEF1*, *YAP1*) and pathways subject to recurrent differential regulation in resistant tumor cells. That *c-MET* up- and *LEF1* down-expression cause acquired MAPKi resistance is reminiscent of findings that HGF stimulation and β -catenin activation can modulate innate BRAFi sensitivity (Biechele et al., 2012; Straussman et al., 2012). Thus, determinants of innate versus acquired MAPKi resistance may converge on pathways. This is further exemplified in studies showing PI3K-AKT activation in both early and late resistance (Obenauf et al., 2015; Shi et al., 2011, 2014a, 2014b). As YAP1 signal activation in resistant melanoma appeared post-transcriptional, its altered post-translational regulation requires additional studies. Overall, genetic and epigenetic mechanisms can account broadly for disease progression on MAPKi therapies and contribute extensively to intra-tumor/patient and inter-patient tumor heterogeneity (Figures 7A and 7B).

For some of the gene targets of transcriptomic and functional alterations identified in MAPKi resistance (e.g., *c-MET*, *TAP1*, *B2M*), their baseline expression ranges in the TCGA data were shown to impact patient survival. This point is of particular importance given the highly dynamic (i.e., out of range) up-expression (*c-MET*, *YAP1*, *EPHA2*; Paraiso et al., 2015) or down-expression (*LEF1*, *TAP1*, *B2M*, *CD8A*, *DUSP4*) events occurring with the evolution of MAPKi-resistant in melanoma (Figure 7C). It may not be surprising to find that the expression levels of genes reflective of CD8 T cell and antigen presentation abundance and function were linked to patient survival given the relatively high mutation/neoantigen load and immunogenicity of mel-

noma and the clinical efficacy of PD-1 targeting in melanoma. We also presented evidence that differential CpG methylation likely underlay dynamic expression of the tumor cell-intrinsic transcriptome during the evolution of MAPKi resistance. Broadly, the selection of distinct transcriptomic-methylomic state(s) imposed by MAPK-targeting likely impacts the panoply of melanoma phenotypes or “hallmarks” (Figure 7D).

Transcriptomic analysis of temporally paired tumor biopsies revealed highly recurrent evolutionary events in the immune compartment. That half of all melanoma with acquired MAPKi resistance displayed a profound CD8 T cell deficiency and exhaustion should bear on the selection of patients for salvage immunotherapies, specifically PD-1 inhibitors, and the clinical sequencing of immune checkpoint versus MAPK inhibitors. We showed that the expression levels of PD-1, T cell effector genes, and a marker of melanoma tumor-reactive CD8 T cells, *TNFRSF9* (4-1BB/CD137), tightly correlated with *CD8A* expression. Specifically, *CD8A* expression in disease progressive tumors can decrease with respect to not only the patient-matched baseline expression level but also the general baseline expression range (i.e., infra-physiologic). This distinctive expression pattern of *CD8A*, in both relative and absolute terms, denotes both CD8 T cell depletion and exhaustion. Finally, since high intra-tumoral CD8 T cell inflammation before therapy was correlated with a loss of intra-tumoral CD8 T cell inflammation at disease progression, studies are warranted to examine the functional contributions of immune evasion to acquired MAPKi resistance, as CD8 T cells may contribute to the anti-tumor response of BRAF inhibition in vivo (Knight et al., 2013; Mok et al., 2015).

To anticipate cancer evolution, the iterative process of understanding acquired resistance and informing next-generation therapies should incorporate analysis of both genomic and non-genomic selection, including tumor and host-immune co-evolution. The extent of non-genomic and immune evolution in acquired MAPKi resistance documented here mandates a comprehensive analysis of early tumor responses to therapies in order to understand the true influence of targeted therapies on cancer evolution.

EXPERIMENTAL PROCEDURES

Analyses of Tumor Specimens

Patient-matched normal tissues and melanoma tumors (pre-treatment, during disease progression) were obtained with the approval of institutional review boards (IRBs) and patients' consents. Ninety specimens were subjected to exome, transcriptome, and methylome profiling. WES and mRNA expression profiles were performed using pair-end sequencing with read length of 2 × 100 bps (Illumina HiSeq2000), except that microarray was used for tumors from patients 10–14, whereas data for patients 11–14 were taken from a published study (Long et al., 2014a; Rizos et al., 2014). Paired methylome profiles were generated from the Illumina Infinium Methyl450K array.

Bioinformatic Analysis

We re-analyzed WES data from previous studies (Moriceau et al., 2015; Shi et al., 2014b) and defined differential gene expression (DGE) events based on the RNA-seq (2-fold cutoff) as concordant DGE calls from at least two of three programs (Supplemental Experimental Procedures). Analysis of the microarray data (DGE cutoff at 1.5-fold) of patient 10 was performed using the Oligo R package and of the validation data set using the beadarray R package.

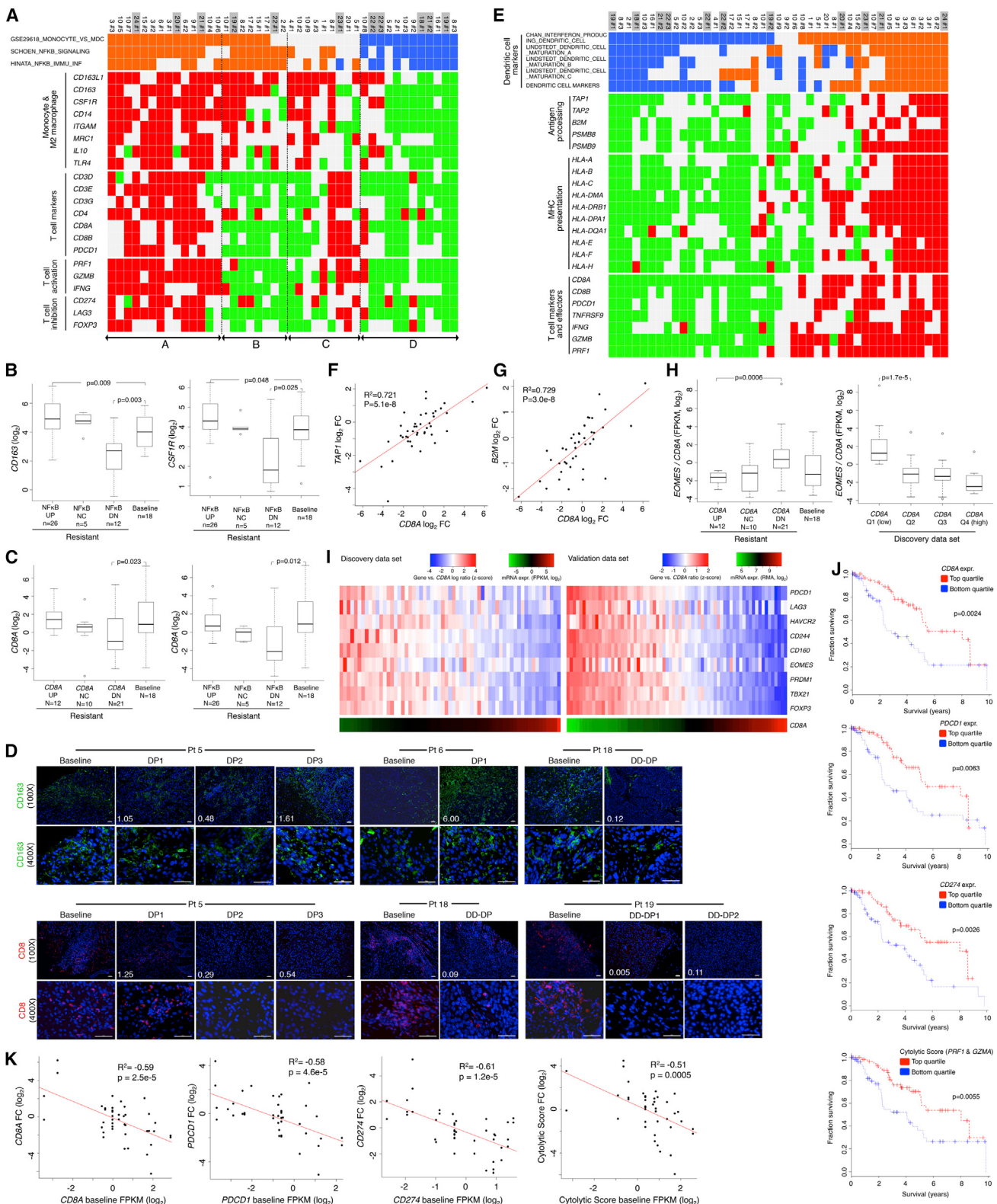
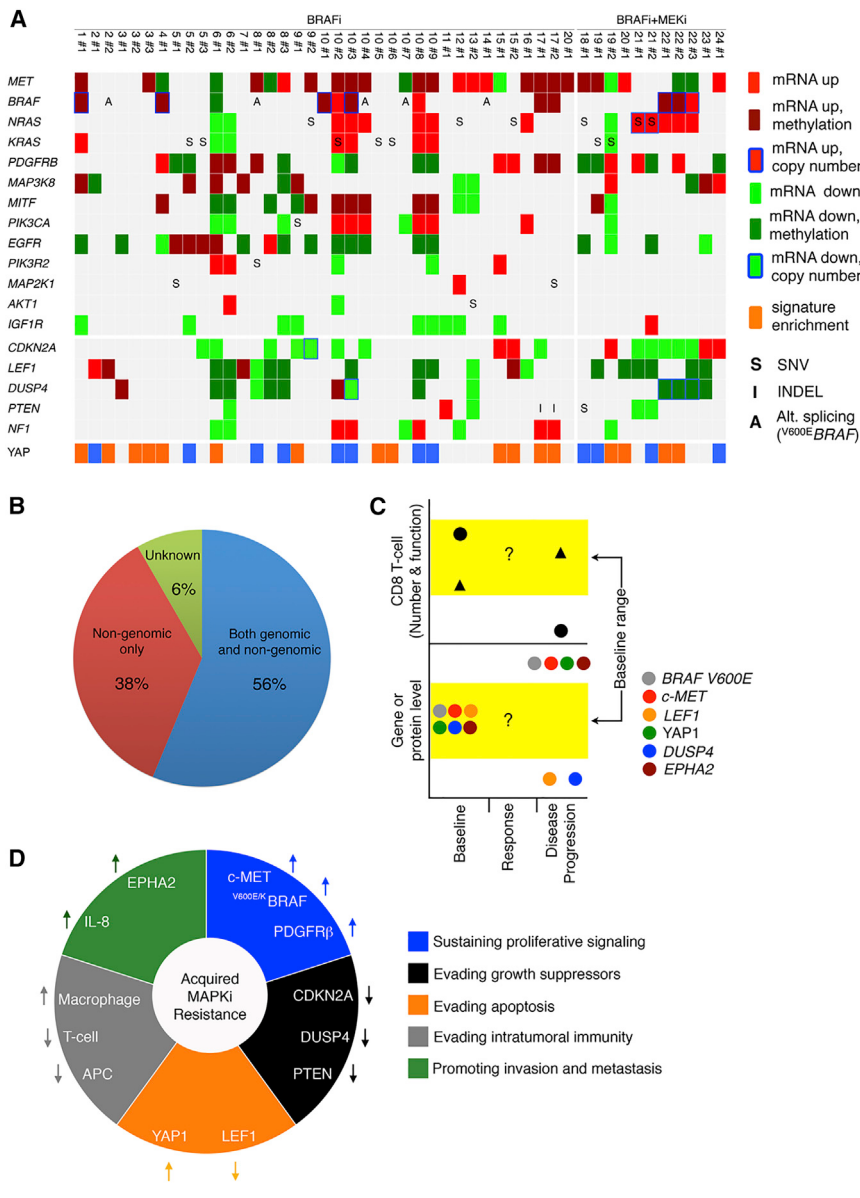


Figure 6. A Pro-tumorigenic Immune Microenvironment Co-evolves with MAPKi Resistance

(A) Tiling of differential gene signature enrichment (orange, positive; blue, negative) and expression (red, up; green, down) across disease progressive melanomas (DD-DP samples shaded gray).

(legend continued on next page)



For DGE of immune genes, we relaxed the cutoffs to 1.5-fold (RNA-seq) and 1.25-fold (microarray), as the immune compartments were smaller than the tumor cell compartments. In addition to DGE, for each baseline and DP or DD-DP sample, we tabulated the normalized gene expression levels, which were

Figure 7. Melanoma Evolution Driven by MAPK-Targeted Therapies

(A) Recurrence of alterations and heterogeneity of mechanisms across proposed resistance genes and across acquired resistant tumors grouped by patients.

(B) Scope of genomic and/or non-genomic acquired resistance mechanisms.

(C) Dynamic gene expression alterations during the evolution of acquired resistance. Black circle and triangle, distinct tumor subsets.

(D) Contributions of non-genomic alterations to cancer phenotypes of acquire MAPKi-resistant melanoma.

expressed in FPKM. Expressed SNVs or INDELS were defined by FPKM values ≥ 0.1 . CNV-related DGE events were defined as concurrent copy-number gain and RNA up-expression ($\log_2 FC \geq 1$ with q value ≤ 0.05) or copy-number loss and RNA down-expression ($\log_2 FC \leq -1$, q value ≤ 0.05). To analyze gene set enrichment of paired samples, we estimated the enrichment of a gene set based on the rank sum of fold changes of genes in the set compared to all fold changes in the sample (Wilcoxon rank-sum test; p value cut-off ≤ 0.05 ; median of up- or down-expression across all genes in the gene set $\geq 10\%$). For single-sample gene set enrichments, values were derived using the GSVA program. GO enrichments were computed using DAVID.

For each CpG site in the array, the methylation change was measured by the percentage methylation difference ($\Delta\beta$) between baseline and resistant samples. The p values for the change were corrected for multiple hypotheses testing with false discovery rates (FDR) q values ≤ 0.05 defining differential methylation. CpG clusters were defined as a set of consecutive CpG sites whose methylation changes correlated with their nearest target gene's mRNA expression changes across all resistant samples and cell lines. Those CpG sites with Pearson R correlation coefficient (adjusted) p value ≤ 0.1 were defined as expression-correlated, and their Pearson R coefficients were defined as correlation scores. For each sample, we identified all CpG clusters with significant differential methylation (q value ≤ 0.05 , $|\Delta\beta| \geq 10\%$) and significant DGE (q value ≤ 0.05 , $|\log_2 FC| \geq 1$) and assessed whether the direction of the changes of methylation and mRNA expression was consistent with the overall correlation between the CpG cluster and gene expression across all samples. Based on this, we nominated DGE events

(B and C) Boxplots of mRNA levels detected in baseline versus subsets of MAPK-resistant melanomas categorized by enrichment status of the SCHOEN_NFKB_SIGNALING signature (B and C) or differential CD8A expression status (C).

(D) Anti-CD8 and -CD163 immunofluorescence of formalin-fixed, patient-matched melanoma tissues (ruler, 50 μ m; white text, values of mRNA fold change). (E) Refer to (A).

(F and G) Correlations between mRNA levels of TAP1 (E) or B2M (F) versus CD8A.

(H) Boxplots of the ratio of EOMES/CD8A mRNA levels in baseline versus distinct subsets of MAPKi-resistant melanoma based on CD8A fold change (FC) status (left) and in each quartile of CD8A expression across all tumor samples (right).

(I) Heatmaps (left, discovery; right, validation) showing expression ratios of T cell exhaustion genes to CD8A. Bottom, absolute mRNA levels of CD8A.

(J) Ten-year survival of TCGA melanoma patients in the top and bottom quartile expression groups of indicated genes (p values, log-rank test).

(K) Pearson correlations between mRNA levels at baseline versus the FC from baseline to MAPKi-resistant melanomas.

p values by t test for Pearson correlations and by one-sided Wilcoxon rank-sum test for boxplots. FC cutoff at ≥ 1.5 . See also Figure S4, Table S4, and Data S2.

as driven by differential methylation at the expression-correlated CpG cluster(s).

Cell Culture, Inhibitors, and Constructs

Cell lines were maintained in DMEM with 10% heat-inactivated FBS, 2 mmol/l glutamine in a humidified 5% CO₂ incubator. Stocks and dilutions of crizotinib (Selleck Chemicals), PLX4032 (Plexxikon), AZD6244 (Selleck Chemicals), and CHIR99021 (Tocris Bioscience) were made in DMSO. HGF (Life Technologies) was suspended in PBS. MTT and clonogenic assays were performed and quantified as described (Moriceau et al., 2015). shc-METs were cloned using the pLL3.7-GFP vector (sequences available upon request); shYAP1s were purchased from Dharmacon (vector pLK0.1); and LEF1, YAP1, and NRAS WT or Q61R were constructed in pRRRLsin-cPPT-CMV-IRES-GFP and pLVX-Tight-puro lentiviral vectors.

Protein Detection

Cell lysates for western blots were made in RIPA buffer (Sigma) supplemented with protease (Roche) and phosphatase (Santa Cruz Biotechnology) inhibitor cocktails. We used the NE-PER Nuclear and Cytoplasmic extraction reagents (Pierce Biotechnology) for cellular fractionation. For immunohistochemistry (IHC), after deparaffinization and rehydration, tissue sections were antigen-retrieved at 95°C for 30 min. Immunostaining with anti-c-MET (Cell Signaling Technology) was performed using a streptavidin-biotin, horseradish peroxidase and DAB chromogen (Vector Laboratories). IHC with anti-YAP1 (Santa Cruz Biotechnology) and anti-LEF1 (Santa Cruz Biotechnology) was performed using alkaline phosphatase, vulcan fast red chromogen (Biocare Medical), and hematoxylin counterstain (Thermo Scientific). Immunostaining with anti-CD8 (Dako) and anti-CD163 (Abcam) was visualized by TRITC- and FITC-labeled secondary antibodies, respectively, and nuclei were counter-stained by DAPI.

ACCESSION NUMBERS

The accession number for the transcriptome and methylome data sets reported in this paper is GEO: GSE65186.

SUPPLEMENTAL INFORMATION

Supplemental Information includes Supplemental Experimental Procedures, four figures, four tables, and two data files and can be found with this article online at <http://dx.doi.org/10.1016/j.cell.2015.07.061>.

AUTHOR CONTRIBUTIONS

W.H., H.S., L.S., M.P., C.S., X.K., and R.S.L. designed and performed experiments and analyzed data. X.K., G.M. A.H., K.B.D., D.B.J., J.A.S. A.R., and R.S.L. provided reagents. All authors contributed to manuscript preparation. R.S.L. supervised the study. R.S.L. and W.H. wrote the paper.

ACKNOWLEDGMENTS

We are grateful to G. Bollag (Plexxikon Inc.) for providing PLX4032 and Donald Hucks for tissue processing. This work was funded by Burroughs Wellcome Fund (to R.S.L.), Stand Up To Cancer (to R.S.L.), Melanoma Research Alliance (to R.S.L.), the NIH (1R01CA176111 to R.S.L.; 1P01CA168585 to A.R. and R.S.L.; K12CA0906525 to D.B.J.), Wade F.B. Thompson/Cancer Research Institute CLIP Grant (to R.S.L.), the SWOG/Hope Foundation (to R.S.L. and A.R.), the Ressler Family Foundation (to R.S.L. and A.R.), the Ian Copeland Melanoma Fund (to R.S.L.), and the T.J. Martell Foundation and the Robert J. Kleberg, Jr. and Helen C. Kleberg Foundation (to K.B.D.).

Received: April 9, 2015

Revised: June 20, 2015

Accepted: July 31, 2015

Published: September 10, 2015

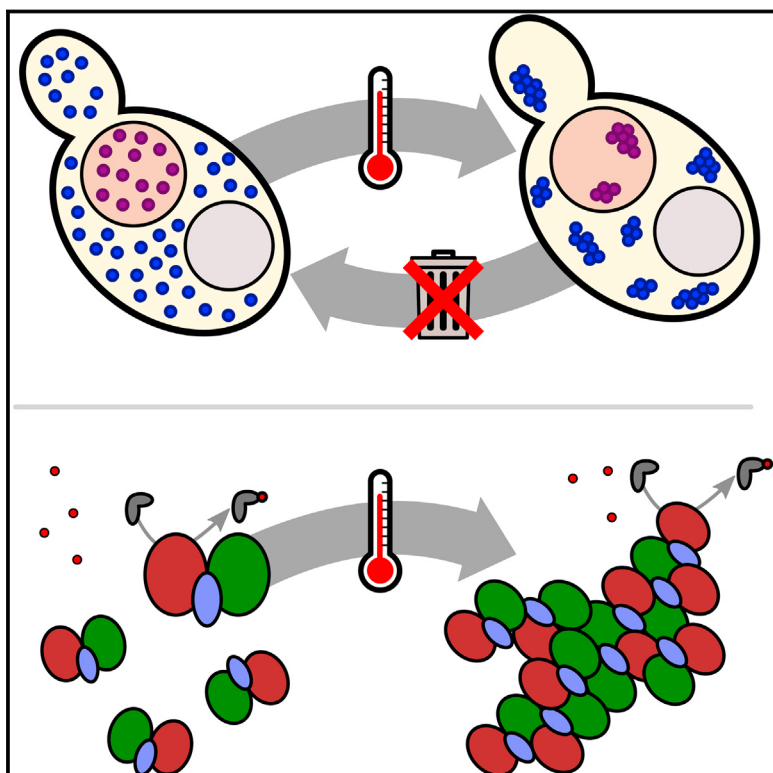
REFERENCES

- Biechele, T.L., Kulikauskas, R.M., Toroni, R.A., Lucero, O.M., Swift, R.D., James, R.G., Robin, N.C., Dawson, D.W., Moon, R.T., and Chien, A.J. (2012). Wnt/β-catenin signaling and AXIN1 regulate apoptosis triggered by inhibition of the mutant kinase BRAFV600E in human melanoma. *Sci. Signal.* 5, ra3.
- Ferrari de Andrade, L., Ngiow, S.F., Stannard, K., Rusakiewicz, S., Kalimuthu, M., Khanna, K.K., Tey, S.K., Takeda, K., Zitvogel, L., Martinet, L., and Smyth, M.J. (2014). Natural killer cells are essential for the ability of BRAF inhibitors to control BRAFV600E-mutant metastatic melanoma. *Cancer Res.* 74, 7298–7308.
- Girotti, M.R., Pedersen, M., Sanchez-Laorden, B., Viros, A., Turajlic, S., Niculescu-Duvaz, D., Zambon, A., Sinclair, J., Hayes, A., Gore, M., et al. (2013). Inhibiting EGF receptor or SRC family kinase signaling overcomes BRAF inhibitor resistance in melanoma. *Cancer Discov.* 3, 158–167.
- Gros, A., Robbins, P.F., Yao, X., Li, Y.F., Turcotte, S., Tran, E., Wunderlich, J.R., Mixon, A., Farid, S., Dudley, M.E., et al. (2014). PD-1 identifies the patient-specific CD8⁺ tumor-reactive repertoire infiltrating human tumors. *J. Clin. Invest.* 124, 2246–2259.
- Johannessen, C.M., Boehm, J.S., Kim, S.Y., Thomas, S.R., Wardwell, L., Johnson, L.A., Emery, C.M., Stransky, N., Cogdill, A.P., Barretina, J., et al. (2010). COT drives resistance to RAF inhibition through MAP kinase pathway reactivation. *Nature* 468, 968–972.
- Johannessen, C.M., Johnson, L.A., Piccioni, F., Townes, A., Frederick, D.T., Donahue, M.K., Narayan, R., Flaherty, K.T., Wargo, J.A., Root, D.E., and Garraway, L.A. (2013). A melanocyte lineage program confers resistance to MAP kinase pathway inhibition. *Nature* 504, 138–142.
- Knight, D.A., Ngiow, S.F., Li, M., Parmenter, T., Mok, S., Cass, A., Haynes, N.M., Kinross, K., Yagita, H., Koya, R.C., et al. (2013). Host immunity contributes to the anti-melanoma activity of BRAF inhibitors. *J. Clin. Invest.* 123, 1371–1381.
- Larkin, J., Ascierto, P.A., Dréno, B., Atkinson, V., Liszkay, G., Maio, M., Mandalà, M., Demidov, L., Stroyakovskiy, D., Thomas, L., et al. (2014). Combined vemurafenib and cobimetinib in BRAF-mutated melanoma. *N. Engl. J. Med.* 371, 1867–1876.
- Laurent, S., Queirolo, P., Boero, S., Salvi, S., Piccoli, P., Boccardo, S., Minghelli, S., Morabito, A., Fontana, V., Pietra, G., et al. (2013). The engagement of CTLA-4 on primary melanoma cell lines induces antibody-dependent cellular cytotoxicity and TNF-α production. *J. Transl. Med.* 11, 108.
- Lidsky, M., Antoun, G., Speicher, P., Adams, B., Turley, R., Augustine, C., Tyler, D., and Ali-Osman, F. (2014). Mitogen-activated protein kinase (MAPK) hyperactivation and enhanced NRAS expression drive acquired vemurafenib resistance in V600E BRAF melanoma cells. *J. Biol. Chem.* 289, 27714–27726.
- Long, G.V., Fung, C., Menzies, A.M., Pupo, G.M., Carlino, M.S., Hyman, J., Shahheydari, H., Tembe, V., Thompson, J.F., Saw, R.P., et al. (2014a). Increased MAPK reactivation in early resistance to dabrafenib/trametinib combination therapy of BRAF-mutant metastatic melanoma. *Nat. Commun.* 5, 5694.
- Long, G.V., Stroyakovskiy, D., Gogas, H., Levchenko, E., de Braud, F., Larkin, J., Garbe, C., Jouary, T., Hauschild, A., Grob, J.J., et al. (2014b). Combined BRAF and MEK inhibition versus BRAF inhibition alone in melanoma. *N. Engl. J. Med.* 371, 1877–1888.
- Mok, S., Tsoi, J., Koya, R.C., Hu-Lieskovan, S., West, B.L., Bollag, G., Graeber, T.G., and Ribas, A. (2015). Inhibition of colony stimulating factor-1 receptor improves antitumor efficacy of BRAF inhibition. *BMC Cancer* 15, 356.
- Moriceau, G., Hugo, W., Hong, A., Shi, H., Kong, X., Yu, C.C., Koya, R.C., Samatar, A.A., Khanlou, N., Braun, J., et al. (2015). Tunable-combinatorial mechanisms of acquired resistance limit the efficacy of BRAF/MEK cotargeting but result in melanoma drug addiction. *Cancer Cell* 27, 240–256.
- Müller, J., Krijgsman, O., Tsoi, J., Robert, L., Hugo, W., Song, C., Kong, X., Possik, P.A., Cornelissen-Stejger, P.D., Foppen, M.H., et al. (2014). Low MITF/AXL ratio predicts early resistance to multiple targeted drugs in melanoma. *Nat. Commun.* 5, 5712.

- Nazarian, R., Shi, H., Wang, Q., Kong, X., Koya, R.C., Lee, H., Chen, Z., Lee, M.K., Attar, N., Sazegar, H., et al. (2010). Melanomas acquire resistance to B-RAF(V600E) inhibition by RTK or N-RAS upregulation. *Nature* 468, 973–977.
- Obenauf, A.C., Zou, Y., Ji, A.L., Vanharanta, S., Shu, W., Shi, H., Kong, X., Bosenberg, M.C., Wiesner, T., Rosen, N., et al. (2015). Therapy-induced tumour secretomes promote resistance and tumour progression. *Nature* 520, 368–372.
- Paraiso, K.H., Das Thakur, M., Fang, B., Koomen, J.M., Fedorenko, I.V., John, J.K., Tsao, H., Flaherty, K.T., Sondak, V.K., Messina, J.L., et al. (2015). Ligand-independent EPHA2 signaling drives the adoption of a targeted therapy-mediated metastatic melanoma phenotype. *Cancer Discov.* 5, 264–273.
- Rizos, H., Menzies, A.M., Pupo, G.M., Carlino, M.S., Fung, C., Hyman, J., Haydu, L.E., Mijatov, B., Becker, T.M., Boyd, S.C., et al. (2014). BRAF inhibitor resistance mechanisms in metastatic melanoma: spectrum and clinical impact. *Clin. Cancer Res.* 20, 1965–1977.
- Rooney, M.S., Shukla, S.A., Wu, C.J., Getz, G., and Hacohen, N. (2015). Molecular and genetic properties of tumors associated with local immune cytolytic activity. *Cell* 160, 48–61.
- Sanchez-Laorden, B., Viros, A., Girotti, M.R., Pedersen, M., Saturno, G., Zamboon, A., Niculescu-Duva, D., Turajlic, S., Hayes, A., Gore, M., et al. (2014). BRAF inhibitors induce metastasis in RAS mutant or inhibitor-resistant melanoma cells by reactivating MEK and ERK signaling. *Sci. Signal.* 7, ra30.
- Shi, H., Kong, X., Ribas, A., and Lo, R.S. (2011). Combinatorial treatments that overcome PDGFR β -driven resistance of melanoma cells to V600EB-RAF inhibition. *Cancer Res.* 71, 5067–5074.
- Shi, H., Moriceau, G., Kong, X., Koya, R.C., Nazarian, R., Pupo, G.M., Bacchiocchi, A., Dahlman, K.B., Chmielowski, B., Sosman, J.A., et al. (2012a). Preexisting MEK1 exon 3 mutations in V600E/KBRAF melanomas do not confer resistance to BRAF inhibitors. *Cancer Discov.* 2, 414–424.
- Shi, H., Moriceau, G., Kong, X., Lee, M.K., Lee, H., Koya, R.C., Ng, C., Chodon, T., Scolyer, R.A., Dahlman, K.B., et al. (2012b). Melanoma whole-exome sequencing identifies (V600E)B-RAF amplification-mediated acquired B-RAF inhibitor resistance. *Nat. Commun.* 3, 724.
- Shi, H., Hong, A., Kong, X., Koya, R.C., Song, C., Moriceau, G., Hugo, W., Yu, C.C., Ng, C., Chodon, T., et al. (2014a). A novel AKT1 mutant amplifies an adaptive melanoma response to BRAF inhibition. *Cancer Discov.* 4, 69–79.
- Shi, H., Hugo, W., Kong, X., Hong, A., Koya, R.C., Moriceau, G., Chodon, T., Guo, R., Johnson, D.B., Dahlman, K.B., et al. (2014b). Acquired resistance and clonal evolution in melanoma during BRAF inhibitor therapy. *Cancer Discov.* 4, 80–93.
- Straussman, R., Morikawa, T., Shee, K., Barzily-Rokni, M., Qian, Z.R., Du, J., Davis, A., Mongare, M.M., Gould, J., Frederick, D.T., et al. (2012). Tumour micro-environment elicits innate resistance to RAF inhibitors through HGF secretion. *Nature* 487, 500–504.
- Twyman-Saint Victor, C., Rech, A.J., Maity, A., Rengan, R., Pauken, K.E., Stellekati, E., Benci, J.L., Xu, B., Dada, H., Odorizzi, P.M., et al. (2015). Radiation and dual checkpoint blockade activate non-redundant immune mechanisms in cancer. *Nature* 520, 373–377.
- Van Allen, E.M., Wagle, N., Sucker, A., Treacy, D.J., Johannessen, C.M., Goetz, E.M., Place, C.S., Taylor-Weiner, A., Whittaker, S., Kryukov, G.V., et al.; Dermatologic Cooperative Oncology Group of Germany (DeCOG) (2014). The genetic landscape of clinical resistance to RAF inhibition in metastatic melanoma. *Cancer Discov.* 4, 94–109.
- Villanueva, J., Infante, J.R., Krepler, C., Reyes-Uribe, P., Samanta, M., Chen, H.Y., Li, B., Swoboda, R.K., Wilson, M., Vultur, A., et al. (2013). Concurrent MEK2 mutation and BRAF amplification confer resistance to BRAF and MEK inhibitors in melanoma. *Cell Rep.* 4, 1090–1099.
- Wagle, N., Emery, C., Berger, M.F., Davis, M.J., Sawyer, A., Pochanard, P., Kehoe, S.M., Johannessen, C.M., Macconail, L.E., Hahn, W.C., et al. (2011). Dissecting therapeutic resistance to RAF inhibition in melanoma by tumor genomic profiling. *J. Clin. Oncol.* 29, 3085–3096.
- Wagle, N., Van Allen, E.M., Treacy, D.J., Frederick, D.T., Cooper, Z.A., Taylor-Weiner, A., Rosenberg, M., Goetz, E.M., Sullivan, R.J., Farlow, D.N., et al. (2014). MAP kinase pathway alterations in BRAF-mutant melanoma patients with acquired resistance to combined RAF/MEK inhibition. *Cancer Discov.* 4, 61–68.

Reversible, Specific, Active Aggregates of Endogenous Proteins Assemble upon Heat Stress

Graphical Abstract



Authors

Edward W.J. Wallace,
Jamie L. Kear-Scott,
Evgeny V. Pilipenko, ..., Tao Pan,
Bogdan A. Budnik, D. Allan Drummond

Correspondence

dadrummond@uchicago.edu

In Brief

The aggregates of endogenous proteins triggered by heat stress in yeast are reversible. Rather than representing irreparably misfolded proteins destined for degradation, they can maintain activity and re-solubilize, suggesting an adaptive strategy underlying aggregation.

Highlights

- Mass spectrometry quantifies aggregation of endogenous proteins during heat stress
- Aggregates form rapidly in specific subcellular compartments
- Endogenous protein aggregates are disassembled without degradation during recovery
- In vitro, a heat-aggregated enzyme complex retains activity and fidelity

Reversible, Specific, Active Aggregates of Endogenous Proteins Assemble upon Heat Stress

Edward W.J. Wallace,¹ Jamie L. Kear-Scott,¹ Evgeny V. Pilipenko,¹ Michael H. Schwartz,¹ Paweł R. Laskowski,¹ Alexandra E. Rojek,^{1,2} Christopher D. Katanski,¹ Joshua A. Riback,¹ Michael F. Dion,³ Alexander M. Franks,⁴ Edoardo M. Airolidi,^{3,4} Tao Pan,¹ Bogdan A. Budnik,³ and D. Allan Drummond^{1,*}

¹Department of Biochemistry and Molecular Biology, The University of Chicago, 929 East 57th Street, Chicago, IL 60637, USA

²Department of Molecular and Cellular Biology, Harvard University, Cambridge, MA 02138, USA

³FAS Center for Systems Biology, Harvard University, Cambridge, MA 02138, USA

⁴Department of Statistics, Harvard University, Cambridge, MA 02138, USA

*Correspondence: dadrummond@uchicago.edu

<http://dx.doi.org/10.1016/j.cell.2015.08.041>

SUMMARY

Heat causes protein misfolding and aggregation and, in eukaryotic cells, triggers aggregation of proteins and RNA into stress granules. We have carried out extensive proteomic studies to quantify heat-triggered aggregation and subsequent disaggregation in budding yeast, identifying >170 endogenous proteins aggregating within minutes of heat shock in multiple subcellular compartments. We demonstrate that these aggregated proteins are not misfolded and destined for degradation. Stable-isotope labeling reveals that even severely aggregated endogenous proteins are disaggregated without degradation during recovery from shock, contrasting with the rapid degradation observed for many exogenous thermolabile proteins. Although aggregation likely inactivates many cellular proteins, in the case of a heterotrimeric aminoacyl-tRNA synthetase complex, the aggregated proteins remain active with unaltered fidelity. We propose that most heat-induced aggregation of mature proteins reflects the operation of an adaptive, autoregulatory process of functionally significant aggregate assembly and disassembly that aids cellular adaptation to thermal stress.

INTRODUCTION

Following heat shock—a rapid increase in temperature to stressful but non-lethal levels—cells accumulate protein aggregates, decelerate protein synthesis, and mount a transcriptional program called the heat-shock response. Upregulated transcripts encode so-called heat-shock proteins, of which many are molecular chaperones. The standard interpretation of these events is that heat causes endogenous (species-native) proteins to misfold into aggregation-prone species whose toxicity is mitigated

and reversed by chaperones (Lindquist, 1986; Mogk et al., 1999; Vabulas et al., 2010; Verghese et al., 2012). Misfolding here refers to the deleterious loss of—or failure to attain—natively folded protein structure, sometimes by adopting stable non-native conformations.

Newly synthesized proteins are particularly susceptible to heat-induced misfolding and aggregation and appear to be the major triggers of the heat-shock response, as well as the main beneficiaries of its induction (Baler et al., 1992; Vabulas et al., 2010). In agreement, heat triggers rapid degradation of newly synthesized proteins, but not of bulk cellular protein (Medicherla and Goldberg, 2008).

Mature, folded proteins also aggregate in response to heat shock, forming protein/poly(A)⁺-RNA structures called heat-shock granules (HSGs). Discovered in plants (Nover et al., 1983), HSGs form upon robust heat shock in a range of eukaryotes, including budding yeast, trypanosome, insect, and mammalian cells (Grousl et al., 2009, 2013; Cherkasov et al., 2013; Farny et al., 2009). HSGs are functionally defined by their components, notably poly(A)-binding protein and eukaryotic initiation factor 4G; some components are common to RNA/protein granules formed during other stresses (Buchan et al., 2010, 2011; Kedersha and Anderson, 2002). The mechanism(s) of HSG formation remain unclear.

Many studies demonstrate aggregation and degradation of exogenous (heterologous or other non-species-native) proteins (Cherkasov et al., 2013; Heck et al., 2010; Fredrickson et al., 2013). Colocalization of exogenous aggregated proteins and HSGs has been interpreted as signaling the presence of endogenous misfolded proteins in HSGs (Cherkasov et al., 2013). However, the identities and folding states of HSG-associated proteins are largely unknown.

When cells return to lower temperatures, HSG dissolution is promoted by the disaggregase Hsp104 and the chaperone Hsp70 (Cherkasov et al., 2013), which also disaggregate misfolded proteins in vitro (Glover and Lindquist, 1998). It is unknown what fraction of disaggregated proteins are degraded *in vivo*, although evidence that stress granules are degraded by autophagy (Buchan et al., 2013) suggests that degradation might be the dominant fate of stress-induced aggregates.

Here, using the model eukaryote budding yeast (*Saccharomyces cerevisiae*), we report the results of experiments aimed at answering many of these fundamental questions. Which endogenous proteins aggregate during heat shock, and how do proteins differ in their propensity to aggregate? What is the relationship between protein aggregation and the formation of granules and other large subcellular foci? How does heat affect the function and fidelity of proteins determined to aggregate in response to heat shock *in vivo*? And what are the fates of endogenous aggregated proteins after heat shock?

RESULTS

Aggregation Profiling Identifies Many Thermally Sensitive Proteins

We quantified aggregation of proteins into high-molecular-weight particles by biochemical separation into supernatant and pellet fractions using ultracentrifugation, stable-isotope labeling, and liquid chromatography coupled to tandem mass spectrometry (LC-MS/MS) (Figure 1A). With these data, we estimated the proportion of each protein in the supernatant (pSup) using a statistical method that controls for differences in fraction mixing and inter-experiment variability (Experimental Procedures and Figure S1). Here and throughout, we refer to pelletable species of proteins that are soluble before heat shock as “aggregates,” without prejudging whether the particles result from misfolding, formation of protein/RNA granules, or other homogeneous or heterogeneous oligomerization processes.

We quantified protein aggregation in cells transferred from 30°C to 46°C for 2, 4, and 8 min and to 37°C and 42°C for 8 min (Figure 1 and Table S1). During these treatments, which are shorter than those typically used to study HSG formation (Grousl et al., 2009; Cherkasov et al., 2013; Supplemental Experimental Procedures), genes upregulated in the transcriptional heat-shock response show no significant change in protein levels (Figure S2A). By contrast, aggregation is rapid and widespread and increases with time and temperature (Figures 1B and 1C).

Heat Triggers Rapid and Specific Protein Aggregation

In the 46°C time course, 982 proteins are detected with at least two unique peptides at all time points (“well-detected,” 73% of the proteome by mass, 17% of verified open reading frames [Cherry et al., 2012]), upon which we focus. Most cellular proteins remain in the supernatant throughout (Figure 1B), and cytosolic and ribosomal proteins are the most enriched gene ontology (GO) terms describing these proteins (Figure S3). Proteins found in the pellet in all conditions are primarily membrane associated (Figure S3). Heat triggers the aggregation of a large group of proteins (177 well-detected proteins), classified by consistent and substantial movement from the supernatant in unheated cells to the pellet after a shift to 46°C (Table S3 and Experimental Procedures). Only four proteins moved from pellet to supernatant in the same interval (Table S4).

Of 18 HSG components identified in the literature (Table S2), we detected all but one (Ngr1). Twelve of these meet our criteria

for heat-triggered aggregation, including poly(A)-binding protein (Pab1), eIF4G/Tif4631, and eIF3, where our data show aggregation of all five stably complexed eIF3 subunits (Nip1/Rpg1/Prt1, reported previously [Grousl et al., 2009], and Tif34/Tif35 reported here) and eukaryotic release factors eRF1/Sup45 and eRF3/Sup35 (Figure S4A). Of the remaining five, Whi3 is not well detected but aggregates, and three proteins (Dhh1, eIF4G2/Tif4632, and small-subunit ribosomal protein Rps30A/B) do not clearly aggregate. The behavior of Rps30A/B is consistent with the lack of aggregation in 82 other well-detected ribosomal gene products from both subunits and with *in situ* hybridization against ribosomal RNA (Cherkasov et al., 2013). Our experimental conditions therefore allow us to quantify biochemically the aggregation of proteins reported to form HSGs by fluorescence microscopy.

In our data, 17 proteins aggregate more than any previously reported HSG component after 2 min heat shock at 46°C; we dub these “superaggregators” (Table S3 and Experimental Procedures). For example, the nuclear protein Ett1 plunges from a supernatant proportion of 0.93 to 0.15 after 2 min at 46°C, while the mRNA-binding protein Gbp2 drops from 0.8 to 0.25. In the same interval, HSG-forming proteins such as Pab1 and eIF3 remain mostly soluble (Figures 1C and S4). Notably, most superaggregators also show clear aggregation after 8 min at 37°C and 42°C (Figures 1C and 1D). At these temperatures and times, Pab1-marked HSGs do not form (Cherkasov et al., 2013).

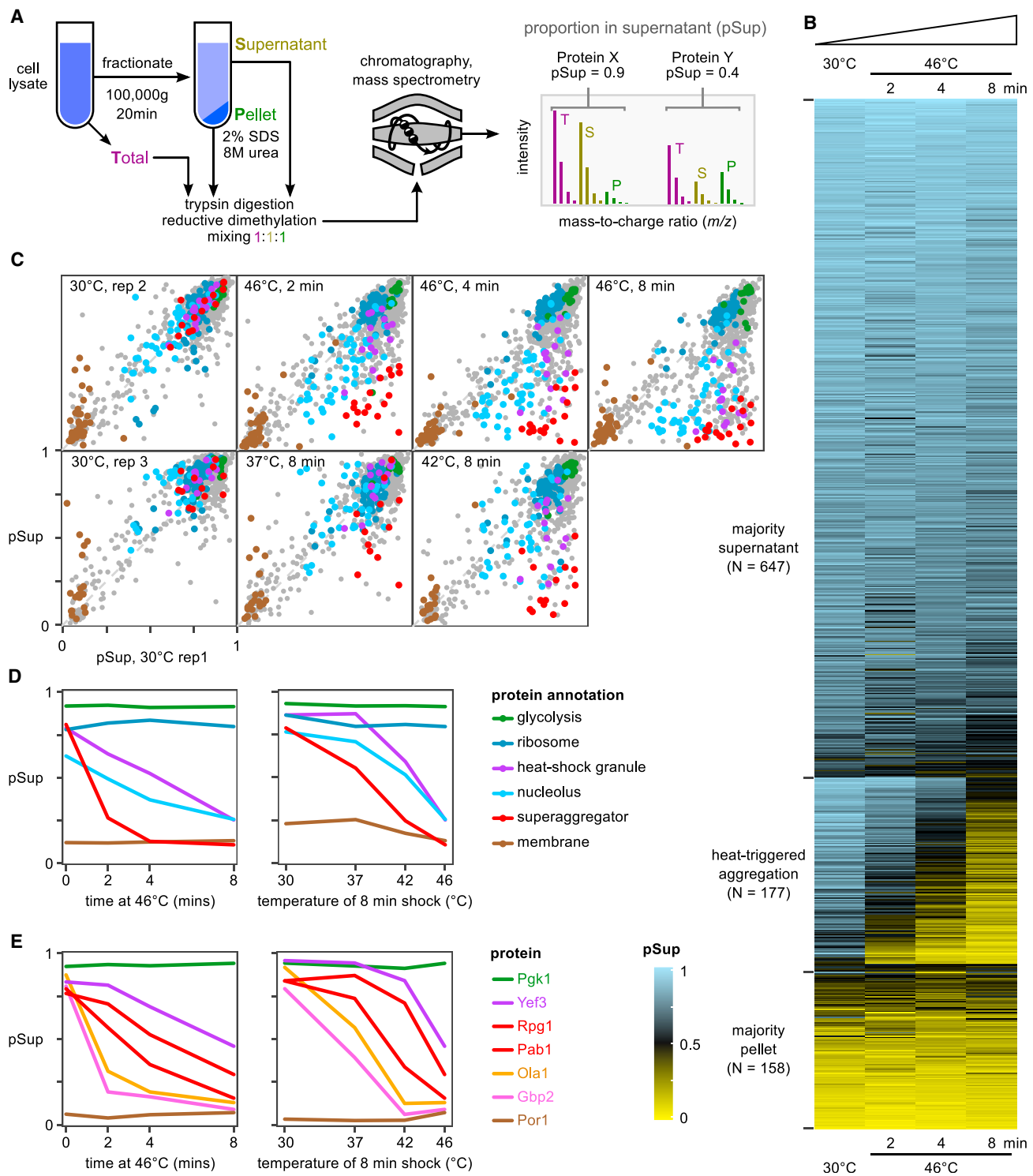
GO terms enriched in heat-aggregating proteins include the molecular functions RNA binding (exemplified by poly(A)-binding protein Pab1 along with Npl3, Pub1, and Gbp2) and RNA helicase activity (seven proteins, including Ded1 and Dbp2/3) (Figure S3). Enriched cellular components include cytosolic stress granules, polysomes, and notably the nucleolus (16 nucleolar proteins).

Six aminoacyl-tRNA-synthetases aggregate, including the yeast multisynthetase complex composed of methionyl- and glutamyl-tRNA synthetases Mes1 and Gus1 bound together by the aminoacylation cofactor Arc1. We return to this complex later.

Molecular chaperones, which colocalize with HSGs, largely remain soluble in our data, suggesting a biochemical distinction between aggregation and recruitment to aggregates. However, notable exceptions exist, including the ribosome-associated chaperone complex (RAC) discussed later. The small heat-shock proteins Hsp26 and Hsp42, despite poor detection in our dataset, partition into the pellet upon heat shock (Figure S4A).

Endogenous Proteins Aggregate in Distinct Compartments

To determine the subcellular location and morphology of aggregates for MS-identified aggregators, we imaged yeast strains engineered with fluorescent C-terminally tagged proteins at their native chromosomal loci. We tagged select proteins with mRuby2, a red fluorescent protein, and tagged the HSG marker Pab1 with Clover, a green fluorescent protein (Lam et al., 2012), mating these strains to form dual-tagged diploids (Figure 2A). Fusions of the non-aggregating glycolytic enzyme Pgk1 stay cytosolic and diffuse when heat shocked, and diploids bearing

**Figure 1. Proteome-wide Aggregation Profiling**

(A) Aggregation profiling by isotope labeling and mass spectrometry yields estimates of the proportion of each protein in the supernatant (pSup) before and after thermal stress.

(B) pSup values in the 46°C time course for all well-detected proteins show proteins consistently found in the supernatant (top), consistently found in the pellet (bottom), and transitioning from supernatant to pellet during the 8 min heat shock (middle, see text).

(legend continued on next page)

Pab1 tagged with both fluorophores (no untagged Pab1 present) form cytosolic foci containing both colored tags (Figure 2B), indicating that these fluorophores neither cause nor prevent aggregation.

Proteins detected to aggregate by mass spectrometry after an 8 min 46°C heat shock also form foci (Figures 2B and 2C). Mes1 and Gus1, components of the multisynthetase complex, form cytosolic foci colocalized with Pab1. Arc1, the third multisynthetase component, likewise forms fluorescent foci colocalized with Gus1 (Figure 2C). Ola1, a superaggregating cytosolic protein previously implicated in translation termination (Samanfar et al., 2014), also forms foci colocalized with Pab1. These four proteins are all thus bona fide heat-shock granule components.

Some heat-aggregating proteins form nuclear foci. Gbp2, a nuclear poly(A)-RNA-binding protein involved in nuclear-cytosolic mRNA transport, forms sub-nuclear granules during heat shock (Figure 2B). Fpr3, a nucleolar component adopting the diagnostic nucleolar crescent shape under non-shock conditions, becomes increasingly granular within the nucleolus during heat shock (Figure 2B). Ett1, a nuclear protein and the most rapidly aggregating protein detected by mass spectrometry, forms nuclear foci during heat shock (Figure 2B) which colocalized with Gar1, a nucleolar protein that shows no heat-triggered aggregation by MS (Figure S5A). These results suggest that Ett1 aggregates in or near the nucleolus upon heat shock, possibly consistent with localization to the intranuclear quality-control compartment (INQ) (Miller et al., 2015a). We often observe multiple Ett1 foci per cell (Figure S5C).

Translation Inhibition Impedes Granule Formation but Does Not Prevent Stress-Triggered Protein Aggregation

Our data indicate clear distinctions between the heat-triggered *in vivo* formation of fluorescent foci and of submicroscopic, biochemically detectable aggregates. After milder shocks, several proteins producing pelletable aggregates did not form foci, such as Ett1 (at 37°C) and Pab1 (at 42°C) (Figures S5B and S5C). Also, Hsp104 forms foci co-localized with Pab1 upon heat shock (Cherkasov et al., 2013) while remaining highly soluble (Figure S4A), showing its recruitment to, but not stable association with, substrates within heat-shock granules.

A series of studies has demonstrated the preferential retention of cytosolic heat-induced protein aggregates by mother cells during budding (Aguilaniu et al., 2003; Liu et al., 2010; Zhou et al., 2014); these cytosolic Hsp104 foci are heat-shock granules. Zhou et al. (2014) observe that Hsp104 focus formation during heat shock is blocked by the translation elongation inhibitor cycloheximide (CHX) and conclude that heat-induced aggregation requires active translation. By contrast, Jacobson et al. (2012) observe that CHX blocks Hsp104 foci during arsenite stress, but not during heat shock. We wondered whether

biochemical detection might shed useful light on the relationship between aggregation, heat-shock granules, and translation.

To study these phenomena, we treated cells with 100 µg/ml CHX for 5 min and then subjected them to either a 42°C heat shock for 30 min as in Zhou et al. (2014) or to a 46°C heat shock for 8 min. This dose of CHX attenuates formation of visible fluorescent foci by tagged Pab1 (Figures 3A and 3B). However, the cytosolic heat aggregators Yef3 and Ola1 still form some fluorescent foci in the presence of CHX (Figures 3A and 3B). Thus, translation inhibition attenuates the heat-triggered formation of foci for some, but not all, cytosolic proteins.

We also measured protein aggregation biochemically during identical heat shocks by analyzing 100,000 g pelleting particles. Pab1, Ssz1, and Yef3 all enter the 100,000 g pellet after a 46°C, 10 min heat shock, with reduced aggregation after a 42°C, 30 min shock. Surprisingly, biochemical aggregation was unaffected by CHX (Figure 3C).

The data are consistent with a model of multi-stage aggregation in which initial formation of biochemical aggregates is followed by CHX-sensitive collection of these aggregates into larger bodies visible as foci. To test this model, we progressively fractionated cell lysate first at 8,000 g × 3 min (pellet, P8, largest aggregates), then fractionated the supernatant at 20,000 g × 5 min (pellet, P20, smaller aggregates), and then fractionated the second supernatant at 100,000 g × 20 min (pellet, P100, smallest aggregates), collecting residual 100,000 g supernatant (S). Western blotting against native Pab1 showed that 75% of Pab1 remained in the supernatant from unshocked cells regardless of CHX treatment (Figures 3D and S6). In cells heat shocked for 8 min at 46°C, most Pab1 entered P8 and P100; treatment with CHX blocked formation of P8 particles and increased levels of P100 particles, as predicted (Figure 3D). Ssz1 shows the same pattern (Figure 3D), as does Yef3 (total protein gel, Figure S6).

These results support a CHX-blockable secondary assembly of aggregates into cytosolic foci, which does not affect heat-induced formation of smaller aggregates.

Translation-Related Proteins Aggregate in Coherent Groups

The heat-triggered aggregation of eIF3 and the multisynthetase complex prompted us to examine aggregation of other protein complexes involved in translation. Translation factors partition into heat aggregators and non-aggregators (Figure 4A). Assuming that aggregated translation factors are inactive, the observed aggregation of eIF2B, eIF4B/G, eEF3, or eRF1 would be individually sufficient to substantially reduce net protein synthesis (Firczuk et al., 2013).

Each stable protein complex falls into a single category: of the components of eukaryotic elongation factor 1 (eEF1), all elements of the stable subcomplex eEF1B heat aggregate, but

(C) Progressive protein aggregation quantified by proportion in the supernatant fraction (pSup) during a 46°C treatment compared to unshocked replicates (top) and with increasing 8 min shock temperature (bottom; see Table S1 for design). Protein annotations in C and D are the same; superaggregators (see text) include five nucleolar proteins.

(D) Behavior of proteins in various categories (cf. C) as a function of temperature, for 8 min, and time at 46°C.

(E) Individual proteins aggregate at different rates in response to heat; more are shown in Figure S4A. In D and E, 30°C rep 1 is shown in the time course plots, the same biological sample as the 46°C data; 30°C rep 3 is shown in the temperature course plots, the same biological sample as 37°C and 42°C, 8 min, data.

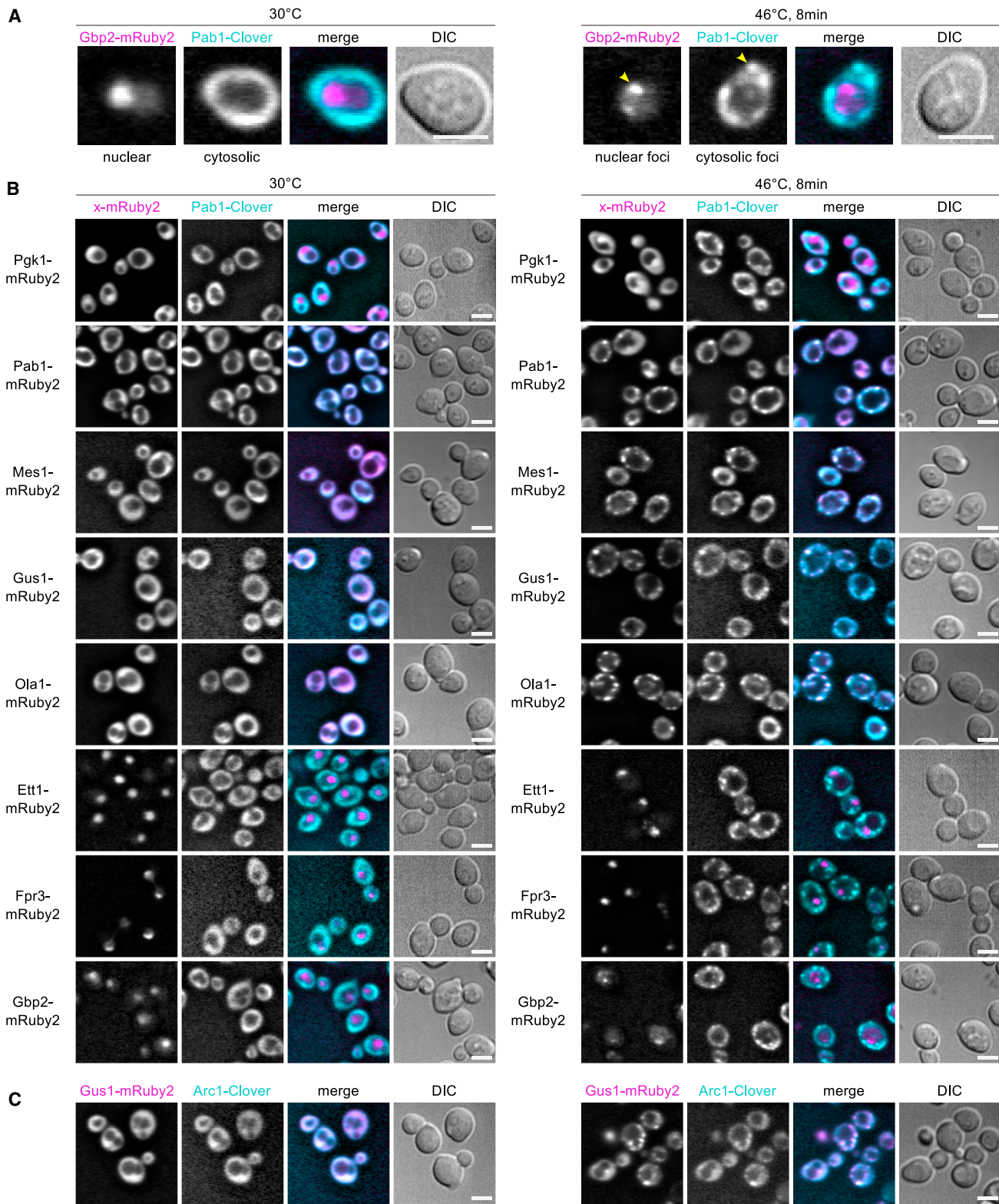


Figure 2. Live-Cell Microscopy Identifies Heat-Aggregating Proteins Forming Cytosolic or Nuclear Granules

Diploid strains containing the HSG component Pab1 tagged with the green fluorescent protein (FP) Clover (cyan in merged images) and test proteins tagged with the red FP mRuby2 (magenta in merge) were imaged at 30°C and after 8 min heat shock at 46°C. Scale bar, 5 μm.

(legend continued on next page)

Tef1/eEF1 α does not (Figure 4A). All components of eIF2 have similar high pSup across conditions, while all components of eIF3 heat aggregate with similar kinetics (Figure 4B). Aggregation of the multisynthetase complex is particularly synchronous (Figure 4B).

Complexes with shared interaction partners show distinct aggregation patterns: for example, the nascent-polypeptide-associated complex (NAC; Egd1/Egd2) and the ribosome-associated chaperone complex (RAC; Ssz1/Zuo1), along with Ssb1/2, bind the ribosome near the nascent peptide exit tunnel (Preissler and Deuerling, 2012). Both detected NAC components remain soluble across conditions, as do ribosomes; in contrast, RAC components aggregate swiftly and in lockstep (Figure 4C). More broadly, proteins associated in annotated complexes (Pu et al., 2009) have more similar pSup trajectories than expected by chance (Figure S7).

The Yeast Multisynthetase Complex Forms Active Heat-Triggered Aggregates In Vitro

The tight correlation of the three yeast multisynthetase components during heat-triggered aggregation (Figure 4) and their aggregation into the same subcellular location (Figure 2) prompted us to ask how heat affects this complex and its activity in isolation. The complex, dubbed AME, is a heterotrimer formed by the aminoacylation cofactor Arc1 (A), methionyl-tRNA synthetase Mes1 (M), and glutamyl-tRNA synthetase Gus1 (E), which interact through eukaryote-specific N-terminal domains in each protein (Frechin et al., 2014).

Recombinant reconstituted AME remains in the supernatant of a 100,000 g, 20 min spin but after a severe 46°C 15 min treatment aggregates completely into pelletable material and cannot be resolubilized by dilution and 1 hr incubation at 30°C with or without substrates (Figure 5A).

Gentler centrifugation revealed that AME pellets as a stoichiometric complex (Figure 5A) despite wide variation in the aggregation propensity of its constituents (Figure S7C). Severely heat-shocked AME retains substantial activity, all of which resides in the aggregated fraction, as indicated by absence of activity in the supernatant after centrifugation (Figure 5B). Similarly, the activity of heat-treated Mes1 is reduced >7-fold after spinning out aggregates (Figure 5B). Gus1's non-catalytic N-terminal domain proved necessary and sufficient for heat-induced Gus1 aggregation (Figure S7D).

We next assessed the fidelity of tRNA-Met aminoacylation by AME before and after heat shock using tRNA microarrays. Under conditions in which AME is fully aggregated (cf. Figure 5A), it retains fidelity indistinguishable from untreated AME or Mes1 (Figure 5C).

Bacterial inclusion bodies can contain active exogenous enzymes (Martínez-Alonso et al., 2009). Our results reveal heat-induced formation of endogenous, active, stoichiometric aggregates with normal fidelity. Here, reduced activity may indicate partial loss of function or reduced ability of large tRNA substrates to penetrate these in vitro aggregates.

Global Profiling of Disaggregation during Recovery Reveals Near-Complete Reversibility of Aggregation

Heat-shock granules slowly disappear after cells are returned to non-shock temperatures (Cherkasov et al., 2013; Parsell et al., 1994), yet it has remained unclear whether endogenous aggregate dispersion is due to disaggregation followed by degradation and resynthesis or due to disaggregation back into a stable soluble pool.

To measure disaggregation and new synthesis at the proteome scale without blocking synthesis or degradation, we performed a media-shift experiment (Figure 6A and Experimental Procedures) in which cells are grown on a first set of stable-isotope-labeled amino acids, shifted to media containing a second set of labels, then heat shocked at 42°C and allowed to recover for a defined time at 30°C. Upon collection, these cells are mixed with cells from an unshocked (30°C) reference sample grown on a third label. Supernatant fractions of these mixtures measured after 0, 20, and 60 min of recovery allowed us to observe the depletion of aggregating proteins from the supernatant after shock followed by their recovery in both the pre- and post-shock labels, indicating new synthesis, or only in the pre-shock label, indicating disaggregation.

Heat-insensitive proteins, such as the glycolytic enzyme Pfk1, show minimal change in pre-shock ratio in the supernatant, indicating no aggregation, and a slight increase in post-shock ratio, indicating low levels of new synthesis during recovery (Figure 6B). Heat-aggregating proteins have low pre-shock ratio immediately after shock, and their disaggregation is indicated by increase of the pre-shock ratio during recovery with only background-level changes in the post-shock ratio, as seen for the RNA helicase Ded1 (Figure 6B). Proteins synthesized in response to heat shock, such as the chaperone Hsp104, show an increase in both pre- and post-shock ratios, indicating new synthesis; increased signal in both channels reflects incorporation of imported post-shock amino acids and residual or recycled pre-shock amino acids (Figure 6B). Aggregated, degraded, and resynthesized proteins would show a low pre-shock ratio after shock and an increase in post-shock ratio; we do not observe this pattern.

A biological replicate with isotopic labels permuted shows the same behavior (Figure S2B). An additional time point 180 min post-shock, after a full cell doubling, shows that, as expected, the majority of the proteome incorporates the post-shock label (Figure S2C).

Proteins previously identified as superaggregators by MS aggregate aggressively at 42°C and disaggregate fully after 1 hr of recovery (Figures 6C and S4B). Complexes which aggregate coherently also disaggregate coherently, including the multisynthetase complex and the RAC (Figure 6C).

(A) Heat-induced nuclear and cytosolic aggregation of Gbp2-mRuby2 and Pab1-Clover, respectively.

(B) Non-aggregating Pfk1-mRuby2 remains diffuse during heat shock, while Pab1-Clover forms HSGs. Pab1-Clover and Pab1-mRuby2 form colocalized foci during heat shock. Fusions of MS-identified heat-aggregating proteins form foci that colocalize with Pab1 during heat shock (Mes1, Gus1, Ola1) or form sub-nuclear foci (Ett1, Fpr3, Gbp2).

(C) The aminoacylation cofactor in the multisynthetase complex, Arc1, forms heat-induced foci colocalized with Gus1.

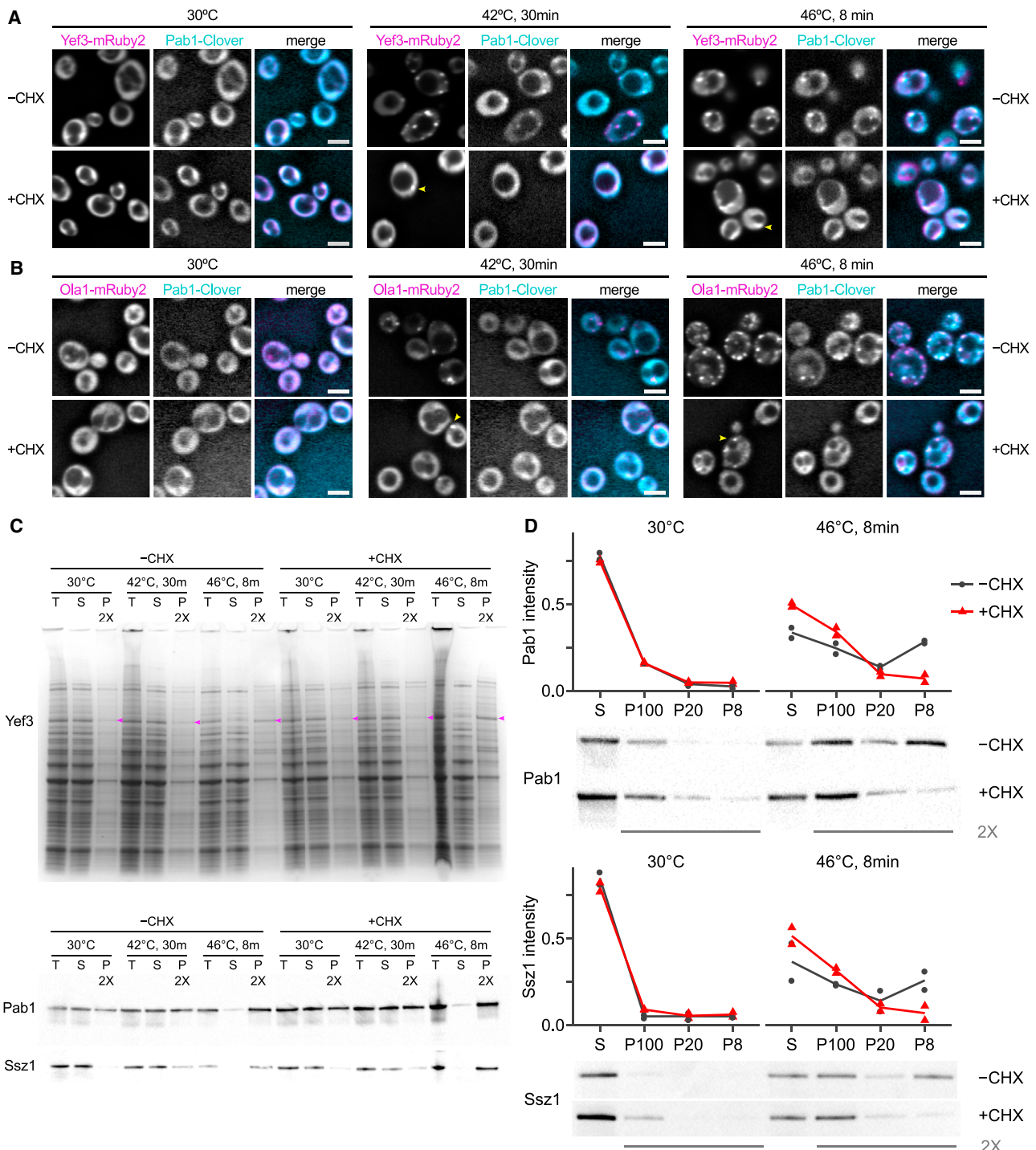


Figure 3. Heat-Triggered Protein Aggregation Does Not Require Ongoing Translation

(A) Cycloheximide (CHX; 100 µg/ml) blocks formation of heat-triggered cytosolic foci by fluorescently tagged Pab1 and attenuates formation of foci by Yef3. Scale bars, 5 µm; arrows indicate foci.

(B) Ola1 forms fluorescent foci in response to heat shock in the presence of CHX.

(C) Pab1, Ssz1, and Yef3 (arrows on gel) are found in the 100,000 g supernatant (S) in lysate from unshocked cells but enter the 100,000 g pellet (P) after heat shock independent of CHX treatment. Coomassie-stained protein gel and western blots against native proteins are shown. T, total protein.

(D) CHX inhibits Pab1 and Ssz1 entry into large aggregates, but not into small aggregates. Cell lysate was progressively fractionated at 8,000 g (pellet, P8), 20,000 g (P20), then 100,000 g (P100), and pellets and residual supernatant (S) were western blotted against Pab1 and Ssz1; intensity as proportion of total was quantified in two biological replicates (Figure S6), and a representative blot is shown.

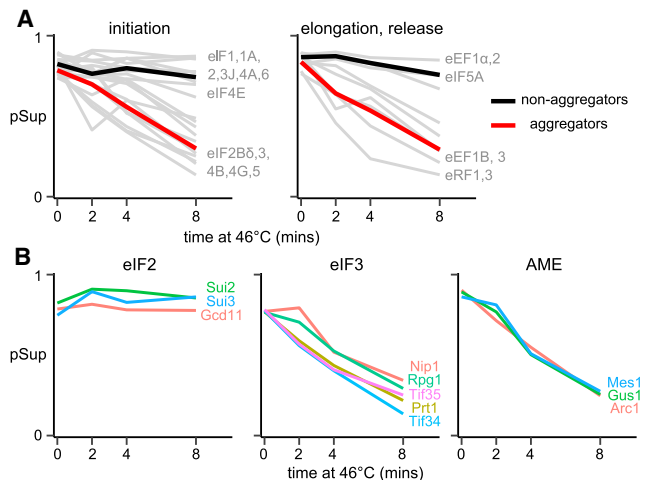


Figure 4. Stable Translation-Related Complexes Aggregate Coherently

Proportion in supernatant (pSup) is plotted against time of heat shock at 46°C; each panel shows one or more complexes and each line a protein component.

(A) pSup of all well-detected translation factors. Mean is shown for aggregators and non-aggregators in each plot.

(B) Aggregation of translation initiation factors 2 and 3 and of the multi-tRNA-synthetase complex.

(C) Aggregation of chaperone complexes involved in co-translational folding.

To examine proteome-scale trends, we compared groups of genes identified as reliably soluble, heat aggregators, or superaggregators in the 46°C heat-shock data set. Immediately after heat shock, aggregators and superaggregators synthesized from pre-shock amino acids are depleted from the supernatant compared to reliable soluble proteins (Figure 6D). After 20 min recovery at 30°C, the differences between these populations are smaller though still significant, and after 60 min of recovery, the distributions are indistinguishable, indicating complete disaggregation (Figure 6D). The post-shock ratios of aggregators and superaggregators are indistinguishable from those of reliably soluble proteins, indicating approximately the same level of new synthesis. At the same time, proteins whose ribosome occupancy increases at least 20-fold during heat shock (Gerashchenko and Gladyshev, 2014) show a substantial increase in new protein synthesis (Figure 6D). New synthesis post shock correlates well with ribosome occupancy during shock (Figure S2D).

In summary, the data show virtually complete disaggregation of endogenous aggregated proteins during recovery without elevated levels of degradative turnover.

DISCUSSION

The standard model of heat stress holds that heat causes protein damage and misfolding, disrupting function and causing exposure of natively buried hydrophobic residues, which triggers protein aggregation (Vabulas et al., 2010). This model was shaped by, and explains well, a wide array of observations, particularly the behavior of endogenous nascent polypeptides. A more recent regulatory interpretation holds that evolutionarily conserved heat-induced aggregation of some proteins into specific subcellular locations reflects a mechanism for attenuating translation (Grousl et al., 2009; Farny et al., 2009; Cherkasov et al., 2013) and protecting the cell during stress (Miller et al., 2015b).

Our study provides multiple lines of evidence indicating that many phenomena that correlate tightly for nascent polypeptides and exogenous unstable reporter constructs—phenomena such as heat-induced aggregation, loss of function, formation of sub-

cellular foci, and degradation—are in many cases completely separable and thus causally unrelated for endogenous mature eukaryotic proteins under acute stress. The standard misfolding model incompletely describes the behavior of most mature proteins during heat shock.

To illustrate, consider the aggressive yet fully reversible thermally induced aggregation of nuclear proteins, exemplified by Ett1 and Gbp2, in light of recent studies on nuclear quality control. The ubiquitin ligase San1 targets nuclear misfolded proteins for degradation (Gardner et al., 2005; Fredrickson et al., 2013). GFP constructs engineered with stretches of hydrophobic residues that promote formation of fluorescent nuclear foci and pelletable aggregates undergo San1-mediated degradation detectable within 1 hr (Fredrickson et al., 2013). Our expectation was that endogenous nuclear proteins that aggregate should be similarly degraded. However, despite aggressive aggregation of Ett1 and Gbp2 in the nucleus, they are restored to solubility without degradation.

The organized deposition of aggregated proteins into particular subcellular sites, such as stress granules, may provide fitness benefits to organisms during stress (Miller et al., 2015b). Stress granules may facilitate preferential translation of certain mRNAs during stress (Kedersha and Anderson, 2002). By providing a view into how proteins reversibly form large assemblies during stress, without necessary restriction to granular structures or particular sites, our study reveals a separate layer of phenomena that is rich with exciting functional possibilities. We hypothesize that the heat-induced aggregation of mature proteins reflects the action of a vast, fast-acting regulatory system based on massive molecular assembly and disassembly. This system couples rapid protein-autonomous stress-responsive assembling elements with slower-acting disassembling machines.

Such a system invokes transient interactions beyond quaternary structure, termed quinary organization (McConkey, 1982). Molecular mechanisms and components of quinary regulation may include multivalent interactions (Li et al., 2012), low-complexity sequences (Kato et al., 2012), and phase-separation phenomena, including protein and protein/RNA liquids (Weber and Brangwynne, 2012) and hydrogels (Kato et al., 2012). Our studies do not offer a mechanistic picture of aggregation or new evidence for particular physical states of quinary assemblies but do identify targets for study.

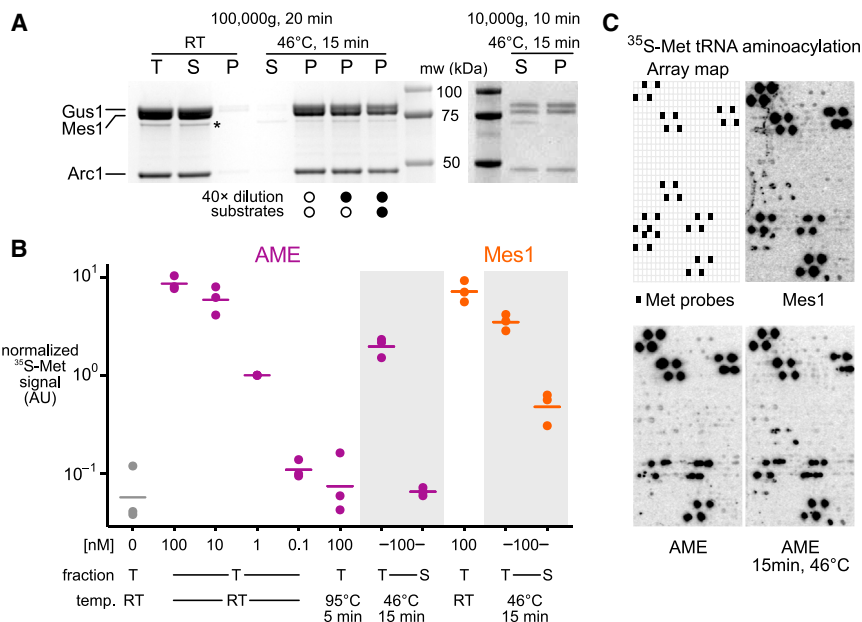


Figure 5. The Yeast Multisynthetase Complex Forms Active Aggregates in Response to Heat Shock In Vitro

(A) Recombinant purified AME complex is soluble before heat treatment and fully aggregated after (stained SDS PAGE; T, total; S, supernatant; P, pellet). A minor soluble degradation product is starred. Three heat-treated samples were incubated at room temperature (RT) for 1 hr (undiluted) or incubated for 1 hr at 30°C after 40 × dilution and after addition of substrates as indicated (see Experimental Procedures). (Right) Stoichiometry in aggregates revealed by lower-speed centrifugation. mw, molecular weight marker.

(B) Activity measured by aminoacylation of total yeast tRNA with ^{35}S -labeled methionine in a filter-binding assay. Three replicates are shown, with signal normalized by 1 nM AME RT levels. Lines indicate means.

(C) Fidelity measured by aminoacylation of tRNA-microarray-immobilized tRNAs with ^{35}S -labeled methionine. Each cell contains probes complementary to a single tRNA species, with tRNA-Met probes arrayed as indicated.

Because heat stress necessarily involves an influx of thermal energy, it would be efficient for aggregation to result from evolved, thermally induced conformational changes that promote quininary interactions. Such processes could be all but indistinguishable from misfolding at the molecular level (Sengupta and Garrity, 2013). The fundamental distinction is in fitness: misfolding is deleterious, whereas evolved quininary regulation is beneficial, suggesting testable and opposing predictions about the fitness consequences of blocking aggregation. We also anticipate that, as in the case of the aminoacyl-tRNA synthetases, evolved quininary interactions will be domain specific, organized, and rapidly reversible without degradation, unlike the behavior of misfolded proteins.

Our data suggest several mechanisms for focusing translation on stress-induced transcripts (Figure 7). Translation initiation on most yeast mRNAs depends upon initiation factors (eIFs) and auxiliary proteins (such as the RNA helicase Ded1). We find that these factors partition into two major classes, the heat-resistant factors (including eIF-1, 1A, 2) and heat-sensitive factors (including eIF-2B, 3, 4G, 5, Ded1). Shirokikh and Spirin (2008) demonstrated assembly of a normal AUG-associated translation initiation complex on uncapped mRNA in vitro in the absence of eIF-2B/3/4A/4B/4G/4E if a poly(A) leader sequence is present. This poly(A)-mediated cap-independent initiation mechanism may explain the cap-independent translation of heat-shock mRNAs (Rhoads and Lamphear, 1995; Barnes et al., 1995; Gerstel et al., 1992), which often possess unstructured, A-rich 5' UTRs (Holmgren et al., 1981) with reduced dependence on RNA unwinding (Lindquist and Petersen, 1990). We hypothesize that stress-sensitive aggregation of initiation and unwinding factors inhibits translation on most non-stress-relevant mRNAs.

The enzyme components of the AME complex, the aminoacyl-tRNA synthetases Mes1 and Gus1, have secondary transcriptional and translational activities in the nucleus and mitochondria, respectively, and are excluded from these compartments

by complexing with Arc1 (Frechin et al., 2014). We hypothesize that autonomous heat-sensitive self-assembly of AME complexes discovered here confines active AME components to the cytosol, suppressing secondary activities in other compartments and focusing aminoacylation activity in the cytosol, where it is needed during stress (Figure 7).

Molecular chaperones may act as regulatory disassembly factors quite separate from their role in protein folding and misfolding. For example, chaperone-mediated dissolution of AME assemblies would permit return of Gus1 and Mes1 to duty in other cellular compartments. Chaperone-mediated restoration of helicases and cap-dependent initiation factors to solubility would derepress translation of most mRNAs, titrating translational activity away from stress-induced messages and thus closing a feedback loop (Figure 7). Consistent with this, deletion of the disaggregase Hsp104 delays both heat-shock granule dissolution and reassembly of polysomes after heat shock (Cherkasov et al., 2013). Which factors (chaperones or other proteins) disassemble which assemblies, and whether and how specificity is achieved, can be addressed in large part using the methods that we have introduced here.

A similar autoregulatory mechanism has been proposed as a way to link protein quality control and translation through assembly of stress granules (Cherkasov et al., 2013). Our study suggests that neither misfolding nor stress-granule formation need be involved; indeed, heat stress/aggregation/chaperones seem likely to be a special case of a broader class of signal/assembly/disassemblase regulatory systems, each involving stress-specific quininary interactions. It seems likely that certain proteins will form assemblies under a wide range of stress conditions (e.g., translation initiation factors) but by stress-specific mechanisms, such as binding sites revealed by phosphorylation, pH-driven self-association, and thermally induced local unfolding. Stress-triggered formation of massive but unanchored assemblies of undamaged proteins, when reversible by stress-induced

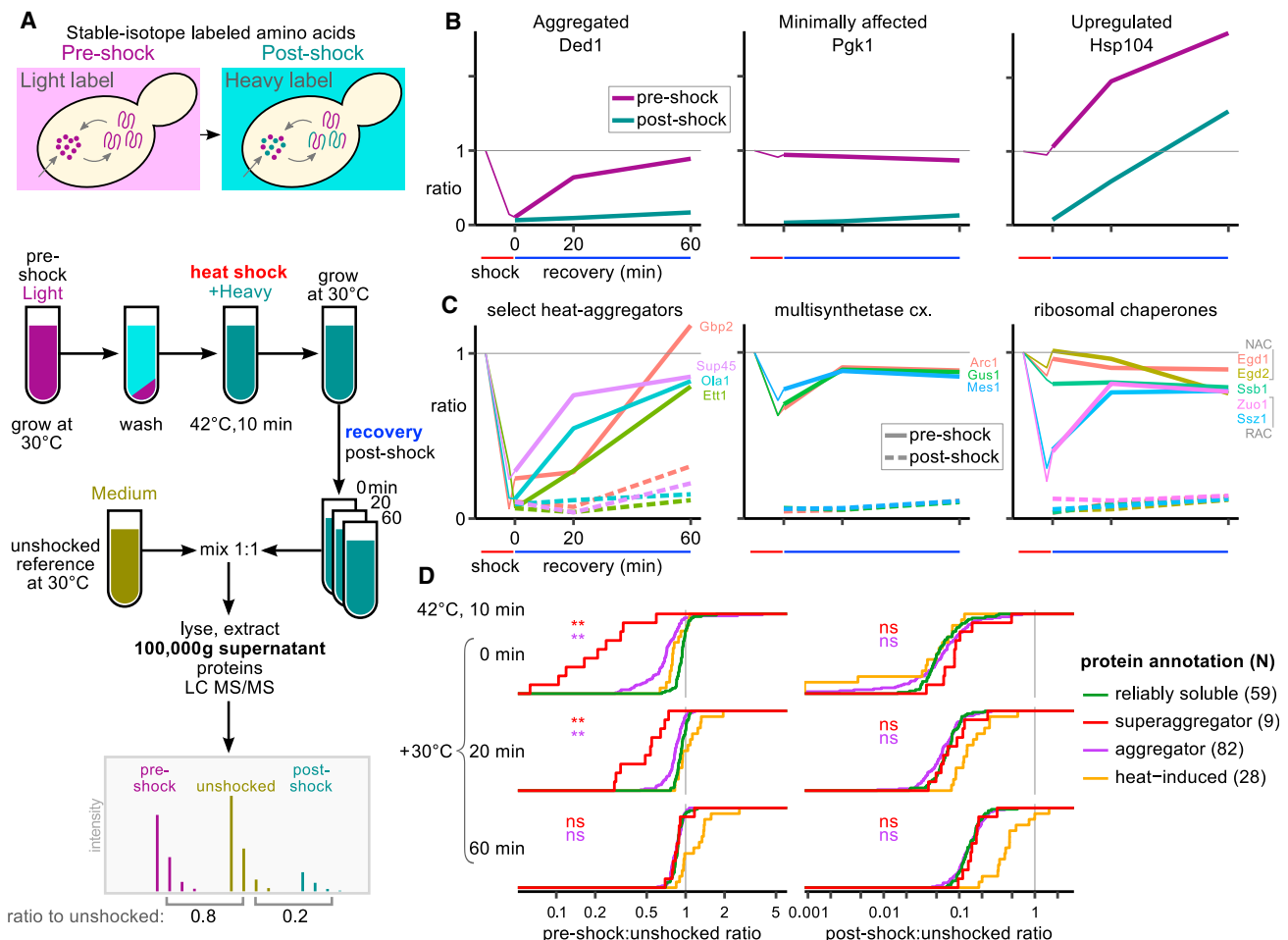


Figure 6. Heat-Aggregated Proteins Disaggregate during Recovery

(A) Schematic experimental design for SILAC media-shift measurement of soluble protein dynamics during recovery from heat shock.

(B) SILAC ratios measure aggregation or synthesis of example proteins Ded1, Pgk1, and Hsp104. Thin lines show pSup after 42°C, 8 min. heat shock from Figure 1.

(C) Select groups of heat-aggregating proteins during recovery after heat shock (others in Figure S4B).

(D) Heat-aggregated proteins disaggregate during recovery, while many proteins change minimally and known heat-induced proteins are synthesized. Cumulative distributions of the normalized ratio in the supernatant are plotted for reliably soluble proteins, superaggregators, other heat aggregators (annotated in the 46°C time course), and proteins whose ribosome occupancy increases at least 20-fold during 42°C, 20 min heat shock (Gerashchenko and Gladyshev, 2014). Wilcoxon rank sum test was used to compare the distributions of reliably soluble proteins to superaggregators and other aggregators, respectively, at each time point (**p < 0.001; ns, not significant).

disassembly activity, allows for a fast-acting autoregulatory response.

EXPERIMENTAL PROCEDURES

Full details are available in the [Supplemental Experimental Procedures](#).

Yeast Strains and Media

The yeast strains used in this study are listed in [Table S6](#). Unless otherwise stated, S288c-derived *S. cerevisiae* were grown in SC-complete at 30°C to mid-exponential phase.

Fractionation and Mass Spectrometry Measurement

Yeast were heat treated, flash frozen, and lysed. Protein from total lysate, 100,000 g × 20 min supernatant, and pellet fractions was chloroform-

methanol extracted, separately digested with trypsin using a FASP protocol (Wiśniewski et al., 2009), labeled by reductive dimethylation (Boersema et al., 2009), and mixed. Mixed samples were fractionated by anion exchange, and fractions were submitted for LC-MS/MS analysis on an Orbitrap Velos Pro (Thermo Fisher).

SILAC Recovery Assay

Yeast strains auxotrophic for arginine and lysine (RK) were grown with light (rep. 2, heavy) isotope-labeled RK at 30°C to mid-exponential phase, transferred to heavy (rep. 2, light) isotope-labeled RK, heat shocked for 10 min at 42°C, and allowed to recover at 30°C. Cells were harvested at specified times, mixed evenly with unheated cells grown in medium-isotope-labeled RK, and flash frozen. Mixed samples were lysed and fractionated, and only the supernatant fraction was chloroform-methanol extracted, trypsin digested, and submitted for LC-MS/MS.

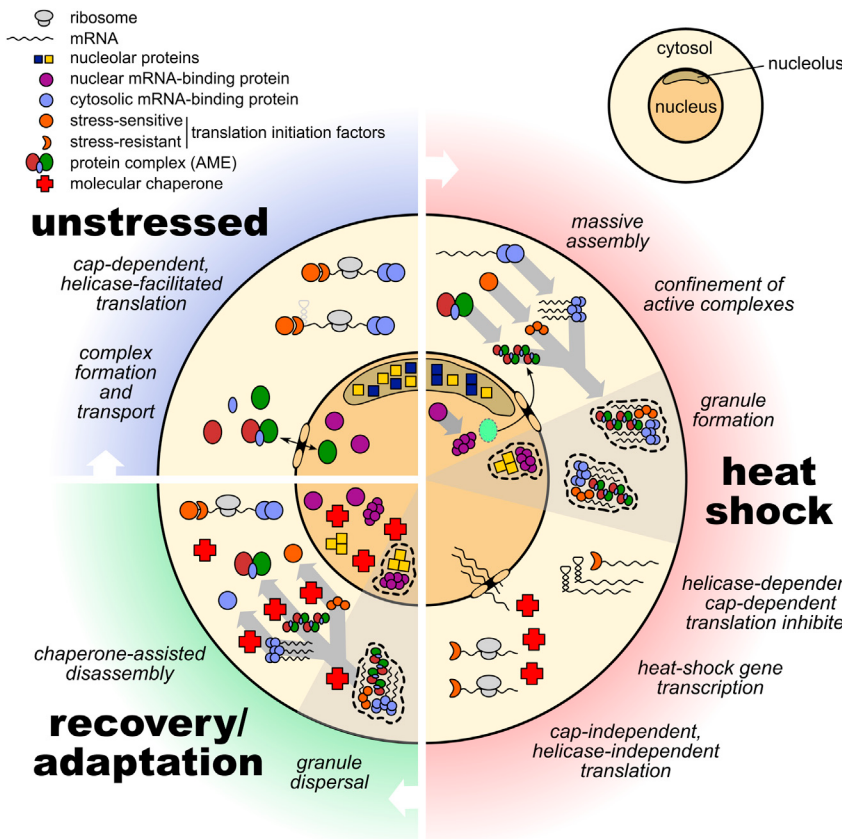


Figure 7. Mechanisms for Enhancing Cellular Remodeling by Massive Assembly during Heat Stress

request) were transformed into BY4741 and BY4742 according to standard lithium acetate protocol (Gietz and Schiestl, 2007) and selected. Two-color diploid yeast strains were constructed by crossing single-color labeled strains by standard methods.

Spinning-Disk Confocal Fluorescence Microscopy

Diploid yeast strains were imaged alive on an Olympus DSU spinning-disk confocal microscope using a 100× oil immersion objective and FITC/Cy2 and DsRed filter sets for Clover and mRuby2, respectively.

Purification of Multisynthetase Complex

Recombinant 6 × His-tagged Arc1, Gus1, and Mes1 were overexpressed, separately, in *E. coli* strain BL21 (DE3) and purified.

Aminoacylation Assay

Filter-based aminoacylation reactions and aminoacylation reactions for microarray analysis were performed as previously described (Netzer et al., 2009; Wiltrout et al., 2012).

Data Access

Raw mass spectrometry data are available on Chorus (<https://chorusproject.org>, project 753, experiments 1751 and 1752); processed data and analysis scripts are available on Dryad (<http://dx.doi.org/10.5061/dryad.hn16c>). Interactive data visualizations related to Figures 1 and 6 may be found at <http://drummondlab.org/endogenous-aggregates>.

SUPPLEMENTAL INFORMATION

Supplemental Information includes Supplemental Experimental Procedures, seven figures, and six tables and can be found with this article online at <http://dx.doi.org/10.1016/j.cell.2015.08.041>.

AUTHOR CONTRIBUTIONS

D.A.D., M.F.D., and E.W.J.W. designed the mass spectrometry experiments. E.W.J.W. and B.A.B. prepared samples for mass spectrometry, and B.A.B. obtained mass spectra. A.M.F., E.M.A., E.W.J.W., and D.A.D. designed and implemented data analysis. M.F.D., J.L.K.-S., A.E.R., and C.D.K. constructed yeast strains. J.L.K.-S. performed *in vivo* microscopy. E.W.J.W. ran western blots. E.V.P., P.R.L., J.A.R., A.E.R., and J.L.K.-S. purified proteins. E.V.P., M.H.S., P.R.L., J.A.R., T.P., and D.A.D. designed and performed multisynthetase experiments. D.A.D. and E.W.J.W. wrote the manuscript with the assistance and approval of all authors.

ACKNOWLEDGMENTS

We thank members of the Drummond lab for critical comments on the manuscript. This work was funded by grants from the Alfred P. Sloan Foundation to D.A.D. and E.M.A., the National Institutes of Health (GM105816 via the Protein Translation Research Network, and GM096193), and the Pew Charitable Trusts. D.A.D. is a Pew Scholar in the Biomedical Sciences. Imaging was performed at the University of Chicago Integrated Light Microscopy Facility; we

Data Analysis for Mass Spectrometry

Mass spectrometry runs were analyzed with MaxQuant (Cox et al., 2011), and reported peptide intensities were further analyzed using a statistical model. In brief, three intensities per peptide detection event—light, medium, and heavy—are noisy proxies for abundance in total, supernatant, and pellet, respectively. A Bayesian model, accounting for supernatant-to-total ratios, pellet-to-total ratios, variability in sample mixing, and measurement error, reports the proportion in supernatant for each detected protein.

In the SILAC recovery assay, we report median ratios of MaxQuant-estimated intensities, correcting for deviations from even mixing by fixing the median ratio to 1 for proteins reliably in the supernatant (section S1.5).

We define a protein as heat aggregating if it is (1) well-detected, i.e., two or more unique peptides reported at each time point; (2) moves consistently from supernatant to pellet, i.e., the rank correlation of pSup with time is at least 0.8; (3) moves substantially, i.e., pSup across the time course declines by at least 0.3. Superaggregating proteins are defined as the subset of heat aggregators for which pSup declines more than the most extreme HSG component at 2 min at 46°C (Tif4632, ΔpSup = 0.40).

Gene ontology (GO) enrichment analyses were performed using the topGO package (Alexa et al., 2006).

Protein Gel Electrophoresis and Western Blotting

SDS-PAGE was performed according to standard methods. Proteins were transferred to nitrocellulose membranes, detected with antibodies against Pab1 (EnCor; #MCA-1G1) or Ssz1 (Hundley et al., 2002), and visualized by chemiluminescence.

Generation of Diploid Yeast Strains

Plasmids pJLS033 and pJLS035 were constructed for C-terminal Clover and mRuby2 labeling at the native locus. Clover/mRuby2 KanMX cassette PCR fragments generated by unique primer pairs (sequences provided upon

thank V. Bindokas and C. Labno for their help. We thank B. Glick and K. Day for assistance with image processing, E. Craig for the generous gift of the Ssz1 antibody, Y. Gilad and B. Engelmann for use of computing resources, J. Piccirilli and B. Weissman for scintillation counting assistance, and T. Sosnick for assistance with absorbance and scattering measurements. Some computations were run on the Odyssey cluster supported by the FAS Division of Science, Research Computing Group at Harvard University.

Received: April 1, 2015

Revised: June 19, 2015

Accepted: August 5, 2015

Published: September 10, 2015

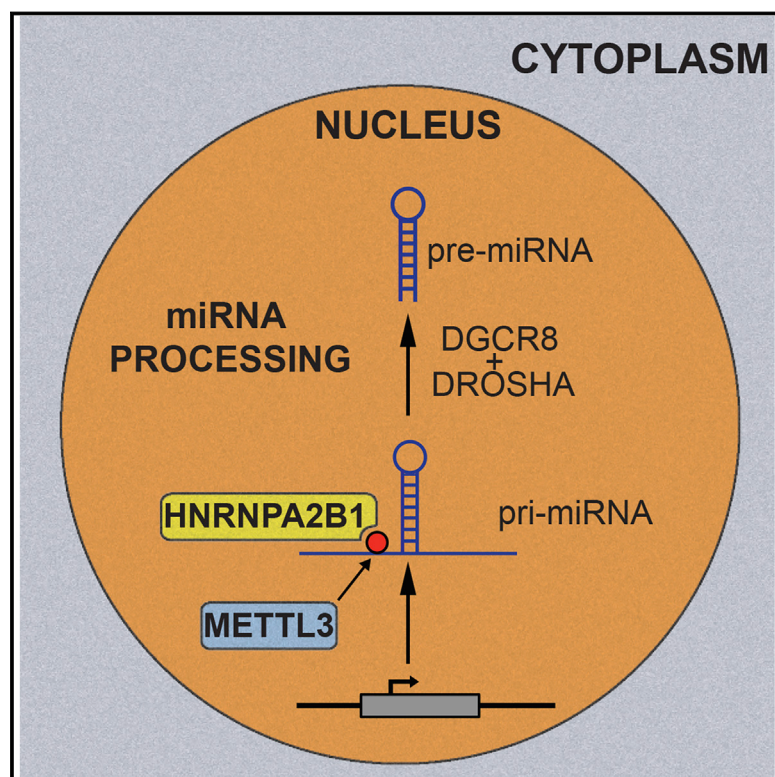
REFERENCES

- Aguilaniu, H., Gustafsson, L., Rigoulet, M., and Nyström, T. (2003). Asymmetric inheritance of oxidatively damaged proteins during cytokinesis. *Science* 299, 1751–1753.
- Alexa, A., Rahnenführer, J., and Lengauer, T. (2006). Improved scoring of functional groups from gene expression data by decorrelating GO graph structure. *Bioinformatics* 22, 1600–1607.
- Baler, R., Welch, W.J., and Voellmy, R. (1992). Heat shock gene regulation by nascent polypeptides and denatured proteins: hsp70 as a potential autoregulatory factor. *J. Cell Biol.* 117, 1151–1159.
- Barnes, C.A., MacKenzie, M.M., Johnston, G.C., and Singer, R.A. (1995). Efficient translation of an SSA1-derived heat-shock mRNA in yeast cells limited for cap-binding protein and eIF-4F. *Mol. Gen. Genet.* 246, 619–627.
- Boersema, P.J., Rajmakers, R., Lemeer, S., Mohammed, S., and Heck, A.J.R. (2009). Multiplex peptide stable isotope dimethyl labeling for quantitative proteomics. *Nat. Protoc.* 4, 484–494.
- Buchan, J.R., Nissan, T., and Parker, R. (2010). Analyzing P-bodies and stress granules in *Saccharomyces cerevisiae*. *Methods Enzymol.* 470, 619–640.
- Buchan, J.R., Yoon, J.-H., and Parker, R. (2011). Stress-specific composition, assembly and kinetics of stress granules in *Saccharomyces cerevisiae*. *J. Cell Sci.* 124, 228–239.
- Buchan, J.R., Kolaitis, R.-M., Taylor, J.P., and Parker, R. (2013). Eukaryotic stress granules are cleared by autophagy and Cdc48/VCP function. *Cell* 153, 1461–1474.
- Cherkasov, V., Hofmann, S., Druffel-Augustin, S., Mogk, A., Tyedmers, J., Stoecklin, G., and Bukau, B. (2013). Coordination of translational control and protein homeostasis during severe heat stress. *Curr. Biol.* 23, 2452–2462.
- Cherry, J.M., Hong, E.L., Amundsen, C., Balakrishnan, R., Binkley, G., Chan, E.T., Christie, K.R., Costanzo, M.C., Dwight, S.S., Engel, S.R., et al. (2012). *Saccharomyces Genome Database*: the genomics resource of budding yeast. *Nucleic Acids Res.* 40, D700–D705.
- Cox, J., Neuhauser, N., Michalski, A., Scheltema, R.A., Olsen, J.V., and Mann, M. (2011). Andromeda: a peptide search engine integrated into the MaxQuant environment. *J. Proteome Res.* 10, 1794–1805.
- Farny, N.G., Kedersha, N.L., and Silver, P.A. (2009). Metazoan stress granule assembly is mediated by P-eIF2 α -dependent and -independent mechanisms. *RNA* 15, 1814–1821.
- Firczuk, H., Kannambath, S., Pahle, J., Claydon, A., Beynon, R., Duncan, J., Westerhoff, H., Mendes, P., and McCarthy, J.E. (2013). An *in vivo* control map for the eukaryotic mRNA translation machinery. *Mol. Syst. Biol.* 9, 635.
- Frechin, M., Enkler, L., Tetaud, E., Laporte, D., Senger, B., Blancard, C., Hammann, P., Bader, G., Clauder-Münster, S., Steinmetz, L.M., et al. (2014). Expression of nuclear and mitochondrial genes encoding ATP synthase is synchronized by disassembly of a multisynthetase complex. *Mol. Cell* 56, 763–776.
- Fredrickson, E.K., Gallagher, P.S., Clowes Candadai, S.V., and Gardner, R.G. (2013). Substrate recognition in nuclear protein quality control degradation is governed by exposed hydrophobicity that correlates with aggregation and insolubility. *J. Biol. Chem.* 288, 6130–6139.
- Gardner, R.G., Nelson, Z.W., and Gottschling, D.E. (2005). Degradation-mediated protein quality control in the nucleus. *Cell* 120, 803–815.
- Gerashchenko, M.V., and Gladyshev, V.N. (2014). Translation inhibitors cause abnormalities in ribosome profiling experiments. *Nucleic Acids Res.* 42, e134.
- Gerstel, B., Tuite, M.F., and McCarthy, J.E.G. (1992). The effects of 5'-capping, 3'-polyadenylation and leader composition upon the translation and stability of mRNA in a cell-free extract derived from the yeast *Saccharomyces cerevisiae*. *Mol. Microbiol.* 6, 2339–2348.
- Gietz, R.D., and Schiestl, R.H. (2007). High-efficiency yeast transformation using the LiAc/SS carrier DNA/PEG method. *Nat. Protoc.* 2, 31–34.
- Glover, J.R., and Lindquist, S. (1998). Hsp104, Hsp70, and Hsp40: a novel chaperone system that rescues previously aggregated proteins. *Cell* 94, 73–82.
- Grousl, T., Ivanov, P., Frydlávová, I., Vasicová, P., Janda, F., Vojtová, J., Malinská, K., Malcová, I., Nováková, L., Janosková, D., et al. (2009). Robust heat shock induces eIF2 α -phosphorylation-independent assembly of stress granules containing eIF3 and 40S ribosomal subunits in budding yeast, *Saccharomyces cerevisiae*. *J. Cell Sci.* 122, 2078–2088.
- Grousl, T., Ivanov, P., Malcová, I., Pompach, P., Frydlávová, I., Slaba, R., Senohrabková, L., Nováková, L., and Hasek, J. (2013). Heat shock-induced accumulation of translation elongation and termination factors precedes assembly of stress granules in *S. cerevisiae*. *PLoS ONE* 8, e57083.
- Heck, J.W., Cheung, S.K., and Hampton, R.Y. (2010). Cytoplasmic protein quality control degradation mediated by parallel actions of the E3 ubiquitin ligases Ubr1 and San1. *Proc. Natl. Acad. Sci. USA* 107, 1106–1111.
- Holmgren, R., Corces, V., Morimoto, R., Blackman, R., and Meselson, M. (1981). Sequence homologies in the 5' regions of four *Drosophila* heat-shock genes. *Proc. Natl. Acad. Sci. USA* 78, 3775–3778.
- Hundley, H., Eisenman, H., Walter, W., Evans, T., Hotokezaka, Y., Wiedmann, M., and Craig, E. (2002). The *in vivo* function of the ribosome-associated Hsp70, Ssz1, does not require its putative peptide-binding domain. *Proc. Natl. Acad. Sci. USA* 99, 4203–4208.
- Jacobson, T., Navarrete, C., Sharma, S.K., Sideri, T.C., Ibstedt, S., Priya, S., Grant, C.M., Christen, P., Goloubinoff, P., and Tamás, M.J. (2012). Arsenite interferes with protein folding and triggers formation of protein aggregates in yeast. *J. Cell Sci.* 125, 5073–5083.
- Kato, M., Han, T.W., Xie, S., Shi, K., Du, X., Wu, L.C., Mirzaei, H., Goldsmith, E.J., Longgood, J., Pei, J., et al. (2012). Cell-free formation of RNA granules: low complexity sequence domains form dynamic fibers within hydrogels. *Cell* 149, 753–767.
- Kedersha, N., and Anderson, P. (2002). Stress granules: sites of mRNA triage that regulate mRNA stability and translatability. *Biochem. Soc. Trans.* 30, 963–969.
- Lam, A.J., St-Pierre, F., Gong, Y., Marshall, J.D., Cranfill, P.J., Baird, M.A., McKeown, M.R., Wiedemann, J., Davidson, M.W., Schnitzer, M.J., et al. (2012). Improving FRET dynamic range with bright green and red fluorescent proteins. *Nat. Methods* 9, 1005–1012.
- Li, P., Banjade, S., Cheng, H.C., Kim, S., Chen, B., Guo, L., Llaguno, M., Hollingsworth, J.V., King, D.S., Banani, S.F., et al. (2012). Phase transitions in the assembly of multivalent signalling proteins. *Nature* 483, 336–340.
- Lindquist, S. (1986). The heat-shock response. *Annu. Rev. Biochem.* 55, 1151–1191.
- Lindquist, S., and Petersen, R. (1990). Selective translation and degradation of heat-shock messenger RNAs in *Drosophila*. *Enzyme* 44, 147–166.
- Liu, B., Larsson, L., Caballero, A., Hao, X., Oling, D., Grantham, J., and Nyström, T. (2010). The polarisome is required for segregation and retrograde transport of protein aggregates. *Cell* 140, 257–267.
- Martínez-Alonso, M., González-Montalbán, N., García-Fruitós, E., and Villa-verde, A. (2009). Learning about protein solubility from bacterial inclusion bodies. *Microb. Cell Fact.* 8, 4.
- McConkey, E.H. (1982). Molecular evolution, intracellular organization, and the quininary structure of proteins. *Proc. Natl. Acad. Sci. USA* 79, 3236–3240.

- Medicherla, B., and Goldberg, A.L. (2008). Heat shock and oxygen radicals stimulate ubiquitin-dependent degradation mainly of newly synthesized proteins. *J. Cell Biol.* 182, 663–673.
- Miller, S.B., Ho, C.-T., Winkler, J., Khokhrina, M., Neuner, A., Mohamed, M.Y., Guilbride, D.L., Richter, K., Lisby, M., Schiebel, E., et al. (2015a). Compartment-specific aggregases direct distinct nuclear and cytoplasmic aggregate deposition. *EMBO J.* 34, 778–797.
- Miller, S.B.M., Mogk, A., and Bukau, B. (2015b). Spatially organized aggregation of misfolded proteins as cellular stress defense strategy. *J. Mol. Biol.* 427, 1564–1574.
- Mogk, A., Tomoyasu, T., Goloubinoff, P., Rüdiger, S., Röder, D., Langen, H., and Bukau, B. (1999). Identification of thermolabile *Escherichia coli* proteins: prevention and reversion of aggregation by DnaK and ClpB. *EMBO J.* 18, 6934–6949.
- Netzer, N., Goodenbour, J.M., David, A., Dittmar, K.A., Jones, R.B., Schneider, J.R., Boone, D., Eves, E.M., Rosner, M.R., Gibbs, J.S., et al. (2009). Innate immune and chemically triggered oxidative stress modifies translational fidelity. *Nature* 462, 522–526.
- Nover, L., Scharf, K.D., and Neumann, D. (1983). Formation of cytoplasmic heat shock granules in tomato cell cultures and leaves. *Mol. Cell. Biol.* 3, 1648–1655.
- Parsell, D.A., Kowal, A.S., Singer, M.A., and Lindquist, S. (1994). Protein disaggregation mediated by heat-shock protein Hsp104. *Nature* 372, 475–478.
- Preissler, S., and Deuerling, E. (2012). Ribosome-associated chaperones as key players in proteostasis. *Trends Biochem. Sci.* 37, 274–283.
- Pu, S., Wong, J., Turner, B., Cho, E., and Wodak, S.J. (2009). Up-to-date catalogues of yeast protein complexes. *Nucleic Acids Res.* 37, 825–831.
- Rhoads, R., and Lamphear, B. (1995). Cap-independent translation of heat shock messenger RNAs. *Curr. Top. Microbiol. Immunol.* 203, 131–153.
- Samanfar, B., Tan, H., Shostak, K., Chalabian, F., Wu, Z., Alamgir, M., Sunba, N., Burnside, D., Omidi, K., Hooshyar, M., et al. (2014). A global investigation of gene deletion strains that affect premature stop codon bypass in yeast, *Saccharomyces cerevisiae*. *Mol. Biosyst.* 10, 916–924.
- Sengupta, P., and Garrity, P. (2013). Sensing temperature. *Curr. Biol.* 23, R304–R307.
- Shirokikh, N.E., and Spirin, A.S. (2008). Poly(A) leader of eukaryotic mRNA bypasses the dependence of translation on initiation factors. *Proc. Natl. Acad. Sci. USA* 105, 10738–10743.
- Vabulas, R.M., Raychaudhuri, S., Hayer-Hartl, M., and Hartl, F.U. (2010). Protein folding in the cytoplasm and the heat shock response. *Cold Spring Harb. Perspect. Biol.* 2, a004390.
- Verghese, J., Abrams, J., Wang, Y., and Morano, K.A. (2012). Biology of the heat shock response and protein chaperones: budding yeast (*Saccharomyces cerevisiae*) as a model system. *Microbiol. Mol. Biol. Rev.* 76, 115–158.
- Weber, S.C., and Brangwynne, C.P. (2012). Getting RNA and protein in phase. *Cell* 149, 1188–1191.
- Wiltrot, E., Goodenbour, J.M., Fréchin, M., and Pan, T. (2012). Misacylation of tRNA with methionine in *Saccharomyces cerevisiae*. *Nucleic Acids Res.* 40, 10494–10506.
- Wiśniewski, J.R., Zougman, A., Nagaraj, N., and Mann, M. (2009). Universal sample preparation method for proteome analysis. *Nat. Methods* 6, 359–362.
- Zhou, C., Slaughter, B.D., Unruh, J.R., Guo, F., Yu, Z., Mickey, K., Narkar, A., Ross, R.T., McClain, M., and Li, R. (2014). Organelle-based aggregation and retention of damaged proteins in asymmetrically dividing cells. *Cell* 159, 530–542.

HNRNPA2B1 Is a Mediator of m⁶A-Dependent Nuclear RNA Processing Events

Graphical Abstract



Authors

Claudio R. Alarcón, Hani Goodarzi,
Hyeseung Lee, Xuhang Liu, Saeed
Tavazoie, Sohail F. Tavazoie

Correspondence

stavazoie@mail.rockefeller.edu

In Brief

The RNA-binding protein HNRNPA2B1 is a nuclear “reader” of the m⁶A mark, acting as an adaptor that recruits the Microprocessor complex to a subset of precursor miRNAs, facilitating their processing into mature miRNAs.

Highlights

- HNRNPA2B1 binds m⁶A-containing sites and the RGAC motif in nuclear transcripts
- HNRNPA2B1 mediates m⁶A-dependent primary microRNA processing events
- Modulation of HNRNPA2B1 and METTL3 causes similar changes to alternative splicing

Accession Numbers

GSE70061

HNRNPA2B1 Is a Mediator of m⁶A-Dependent Nuclear RNA Processing Events

Claudio R. Alarcón,¹ Hani Goodarzi,¹ Hyeseung Lee,¹ Xuhang Liu,¹ Saeed Tavazoie,² and Sohail F. Tavazoie^{1,*}

¹Laboratory of Systems Cancer Biology, Rockefeller University, New York, NY 10065, USA

²Department of Biochemistry and Molecular Biophysics and Department of Systems Biology, Columbia University, New York, NY 10032, USA

*Correspondence: stavazoie@mail.rockefeller.edu

<http://dx.doi.org/10.1016/j.cell.2015.08.011>

SUMMARY

*N*⁶-methyladenosine (m⁶A) is the most abundant internal modification of messenger RNA. While the presence of m⁶A on transcripts can impact nuclear RNA fates, a reader of this mark that mediates processing of nuclear transcripts has not been identified. We find that the RNA-binding protein HNRNPA2B1 binds m⁶A-bearing RNAs in vivo and in vitro and its biochemical footprint matches the m⁶A consensus motif. HNRNPA2B1 directly binds a set of nuclear transcripts and elicits similar alternative splicing effects as the m⁶A writer METTL3. Moreover, HNRNPA2B1 binds to m⁶A marks in a subset of primary miRNA transcripts, interacts with the microRNA Microprocessor complex protein DGCR8, and promotes primary miRNA processing. Also, HNRNPA2B1 loss and METTL3 depletion cause similar processing defects for these pri-miRNA precursors. We propose HNRNPA2B1 to be a nuclear reader of the m⁶A mark and to mediate, in part, this mark's effects on primary microRNA processing and alternative splicing.

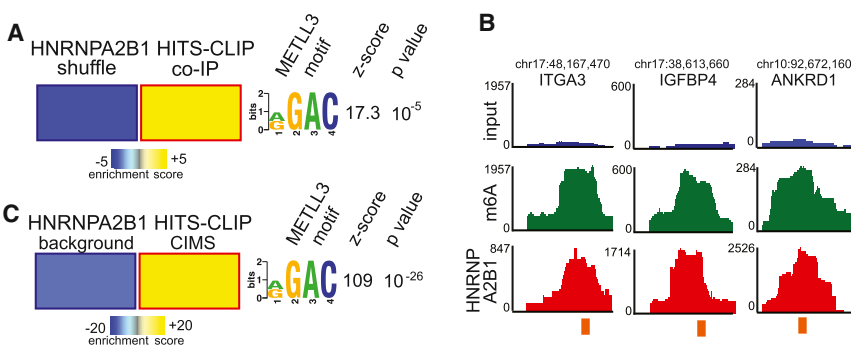
INTRODUCTION

Nucleotide modifications can expand the information content of nucleic acids. Methylation of cytosines on promoter DNA, for example, can alter the transcriptional output of genes. RNA can also be modified by a myriad of marks and mRNA modifications, including, among others, N⁶-methyladenosine, 5-methylcytosine, 2' O-methylation of ribose, and pseudouridylation (Jaffrey, 2014). The functional roles of the majority of these chemical modifications are unknown. The most common internal modification of eukaryotic messenger RNA is methylation of the N⁶ nitrogen on adenosine referred to as N⁶-methyladenosine (m⁶A). Each transcript contains one to three m⁶A marks on average, which are located in specific positions in introns, exons, and UTRs. Methylation of specific positions is non-stoichiometric—with only a fraction of transcripts containing this mark at specific sites. While this important modification was discovered over four decades ago, the transcriptome-wide mapping of this mark using next-generation sequencing analysis has recently revived interest in the biological role(s)

of m⁶A (Dominissini et al., 2012; Meyer et al., 2012; Wang et al., 2014a).

Methyltransferase like 3 (METTL3) was the first methyltransferase implicated in placing m⁶A on RNA (Dominissini et al., 2012; Meyer et al., 2012; Wei and Moss, 1974). METTL14, which exists in complex with METTL3, has also been shown to exhibit m⁶A methyltransferase activity (Liu et al., 2014). Fat mass and obesity-associated protein (FTO) was recently identified as an enzyme that can remove this mark (Jia et al., 2011). Classical experiments suggested a role for m⁶A in the nuclear processing of viral and non-viral transcripts (Carroll et al., 1990; Katz et al., 2015; Liu et al., 2015; Stoltzfus and Dane, 1982). More recent molecular studies have demonstrated m⁶A to exhibit both a nuclear role in splicing (Dominissini et al., 2012) and a cytoplasmic role in the regulation of RNA stability (Batista et al., 2014; Wang et al., 2014a). We have recently found that m⁶A plays an additional role in the nucleus in controlling microRNA biogenesis. M⁶A was found to be enriched in primary microRNA transcripts. Reducing m⁶A levels by depleting the m⁶A writer METTL3 reduced the levels of the majority of expressed microRNAs (Alarcón et al., 2015). This effect occurred in the nucleus since METTL3/m⁶A depletion reduced the association of the DGCR8-containing microRNA processing complex with primary microRNAs and caused unprocessed primary microRNA precursors to accumulate in the nucleus. These findings are consistent with a model wherein the m⁶A RNA mark is recognized and bound by nuclear reader protein(s), which recruit the Microprocessor complex to pri-miRNA containing transcripts—resulting in their processing. Recently the YTH domain family 2 (YTHDF2) protein was identified as a “reader” of m⁶A and found to regulate the stability of m⁶A-bearing transcripts in the cytoplasm (Wang et al., 2014a). The proposed role of m⁶A in the control of alternative splicing and our recent findings regarding its impact on primary microRNA processing (Alarcón et al., 2015) suggest the existence of nuclear reader(s) of m⁶A that bind this mark and mediate nuclear processing events that are mechanistically distinct from RNA stability regulatory events that could occur in the cytoplasm.

We herein identify HNRNPA2B1 as a nuclear reader of m⁶A. HNRNPA2B1 binds to RGm⁶AC containing sites on nuclear RNAs in vivo and in vitro. HNRNPA2B1 regulates the alternative splicing of exons in a set of transcripts in a similar manner as METTL3, the m⁶A “writer.” The global impact of HNRNPA2B1 depletion on alternative splicing is highly correlated with the global effect of METTL3 depletion on alternative splicing. HNRNPA2B1 depletion also impairs the nuclear processing of



(B) RNA-seq read density at exemplary loci where HNRNPA2B1 and m⁶A peaks intersect. Shown are the input nuclear RNA (blue), m⁶A-seq (green), and HNRNPA2B1 HITS-CLIP (red) reads. The orange bar denotes the sequence match to the RGAC motif.

(C) FIRE analysis of the enrichment of the RGAC motif in HNRNPA2B1 footprints. Sequences within 5 nt of HNRNPA2B1 cross-linking-induced deletions generated by HITS-CLIP protocol were significantly enriched for the RGAC motif when compared to background deletions. The motif, p value, and Z score are also shown.

a subset of microRNAs whose maturation is dependent on METTL3 activity. Moreover, HNRNPA2B1 interacts with the DGCR8 protein, a component of the pri-miRNA Microprocessor complex, and facilitates the processing of pri-miRNAs. Our findings implicate HNRNPA2B1 as a nuclear reader and effector of the m⁶A mark.

RESULTS

HNRNPA2B1 Binds to m⁶A-Bearing Sites in the Transcriptome

The presence of the m⁶A mark has been historically associated with the processing of nuclear transcripts. Our previous identification of m⁶A as a regulatory mark that promotes the processing of pri-miRNA transcripts—a process that occurs in the nucleus—also suggested the existence of one or more nuclear readers of this mark that mediate its downstream effector functions. Several approaches that combine UV cross-linking of RNA-binding proteins with immunoprecipitation and deep sequencing of bound RNAs have proven powerful at mapping the sites of interaction between RNA-binding proteins and their target RNAs (Hafner et al., 2010; König et al., 2010; Ule et al., 2005). Our laboratories have in the past few years conducted a number of such high-throughput sequencing of RNA isolated by cross-linking immunoprecipitation (HITS-CLIP; Zhang and Darnell, 2011) studies to map the genome-wide binding of a variety of RNA-binding proteins. Our analysis of the direct binding sites of one such RNA-binding protein, HNRNPA2B1 (Goodarzi et al., 2012), suggested that it might act as a reader of the m⁶A mark. HNRNPA2B1 is a member of the hnRNP family of RNA-binding proteins that are known to associate with pre-mRNAs in the nucleus. The m⁶A mark is known to occur within the RGAC motif, with R representing a purine (Schibler et al., 1977). To test the possibility that HNRNPA2B1 also recognizes this motif, we assessed the abundance of this sequence among the HNRNPA2B1 HITS-CLIP peaks relative to randomly generated sequence counterparts with similar dinucleotide frequencies (Giannopoulou and Elemento, 2011). Indeed, using the FIRE analysis pipeline (Elemento et al., 2007), we observed a highly

Figure 1. HNRNPA2B1 Recognizes m⁶A Methylation Sequences

(A) FIRE algorithm, in non-discovery mode, was used to assess enrichment of the RGAC motif among the HNRNPA2B1 HITS-CLIP peaks, obtained from MDA-MB-231 cells, relative to randomly generated sequences with similar dinucleotide frequencies. The figure shows a significant enrichment of the m⁶A motif (RGAC) in HNRNPA2B1 binding sites, where yellow indicates over-representation and blue represents under-representation. The magnitude of the representation is as per the heatmap scale shown at the bottom. The associated Z score and p value are also provided.

significant enrichment of the RGAC element in HNRNPA2B1 binding sites (Figure 1A).

We next overlapped the m⁶A peaks from an RNA-seq analysis of m⁶A-immunoprecipitated nuclear RNA (m⁶A-seq; Alarcón et al., 2015) with HNRNPA2B1 binding peaks obtained from HITS-CLIP of endogenous nuclear HNRNPA2B1 performed for this study in MDA-MB-231 breast cancer cells. We noted a significant number of cases wherein the HNRNPA2B1 peaks overlapped with m⁶A peaks (Figures 1B and S1A; p value < 1e-3), consistent with an enrichment of m⁶A at HNRNPA2B1 binding sites. Of the 1,912 human genes bound by HNRNPA2B1 and containing m⁶A peaks, 426 contained RGAC instances overlapping both an HNRNPA2B1 HITS-CLIP peak and an m⁶A-seq peak (FDR < 10%). Conducting this analysis on HITS-CLIP data we had previously generated for MBNL1 and TARBP2 revealed zero such cases of overlap for these RNA-binding proteins.

The enrichment of the RGAC motif in HNRNPA2B1 binding sites may be due to general proximity of the RGAC motif to the HNRNPA2B1 binding sites rather than due to direct interactions with the RGAC motif. The RNA-binding protein hnRNP, for example, has been shown to bind near—rather than directly to—the RGAC motif (Liu et al., 2015). Thus, to study the specificity of overlap between the HNRNPA2B1 footprint and the m⁶A consensus motif at nucleotide resolution, we took advantage of cross-linking-induced deletions that are a hallmark of HITS-CLIP experiments and that provide a nucleotide-level map of physical points of interaction (Zhang and Darnell, 2011). For this, we limited our search to the cross-linking-induced deletions that mark the sites of direct interactions between HNRNPA2B1 and its target RNAs (CIMS; Zhang and Darnell, 2011). We also defined a set of control sequences consisting of deletion-containing reads that represent the background occurrence of deletion events during HITS-CLIP sample preparation (i.e., these reads were not part of a peak or cluster; Figure S1). We then used FIRE to re-evaluate the abundance of the RGAC motif in HNRNPA2B1 footprints (i.e., cross-linking-induced deletion sites along with 5 nt flanking sequences on either side). We observed a highly significant enrichment of RGAC motifs at these cross-linking-induced

deletions (p value $< 1e-26$, Z score = 109; **Figure 1C**). A similar analysis applied to two other RNA-binding proteins for which comparable HITS-CLIP data were available revealed HNRNPA2B1 to be unique among this group in exhibiting a significant enrichment for proximal binding to the RGAC motif (**Figures 1C** and **S1C**). Importantly, 6.8% of the nuclear HNRNPA2B1 cross-linking-induced deletions overlapped with an m⁶A peak, whereas only 0.34% of the background deletions overlapped with m⁶A sites (20-fold enrichment, **Figure S1D**). These findings strongly support a role for HNRNPA2B1 in directly binding to a subset of m⁶A consensus sequences within the transcriptome.

METTL3 and HNRNPA2B1 Regulate Common Alternative Splicing Events

The m⁶A mark has been associated with Carroll et al. (1990), Katz et al. (2015), and Stoltzfus and Dane (1982) and causally implicated in pre-mRNA processing (Dominissini et al., 2012). Depletion of METTL3 has also been shown to impact alternative splicing (Dominissini et al., 2012). We hypothesized that HNRNPA2B1, by acting downstream of m⁶A placement by METTL3, may impact alternative splicing in a similar manner as METTL3. If this were the case, depleting HNRNPA2B1 should result in similar alterations in alternative splicing patterns as depletion of METTL3. To test this, we conducted high-throughput RNA sequencing (RNA-seq) on nuclear RNA from cells depleted of METTL3 and those depleted of HNRNPA2B1. We then employed MISO, a probabilistic framework (Katz et al., 2010), to quantify the relative expression of alternatively spliced exons in METTL3 and HNRNPA2B1 knockdown cells as well as controls. The differences in MISO-calculated Ψ (psi, percent-spliced in) values between each of the knockdown samples and the control samples were used as a measure of modulations in alternative splicing events upon depletion of each of these factors. Consistent with a role for HNRNPA2B1 in mediating alternative splicing effects downstream of METTL3/m⁶A, we observed that the global impact on alternative splicing was highly correlated in cells depleted for each of these genes. This effect was observed in skipped exons ($\rho = 0.335$; $p < 1e-200$, **Figure 2A**), retained introns ($\rho = 0.373$; $p < 1e-140$, **Figure 2B**), alternative first exons ($\rho = 0.378$; $p < 1e-300$, **Figure 2C**), and alternative last exons ($\rho = 0.299$; $p < 1e-170$; **Figure 2D**). The effects on alternative splicing in the context of HNRNPA2B1 and METTL3 depletion were seen in two independent cell lines (**Figures 2E**, **2F**, and **S2**). These findings reveal that HNRNPA2B1 depletion has similar genome-wide consequences on alternative splicing as METTL3 depletion. These observations, along with our findings that HNRNPA2B1 binds m⁶A sites, support a model whereby HNRNPA2B1 mediates, in part, the alternative splicing effects of METTL3 and the m⁶A mark.

HNRNPA2B1 Promotes Processing of METTL3-Dependent microRNAs and Interacts with the Microprocessor Machinery

We next asked whether HNRNPA2B1 governs the processing of pri-miRNAs that are dependent on METTL3/m⁶A for their processing. For this, we performed global microRNA profiling

in HEK293 cells depleted of HNRNPA2B1. HNRNPA2B1 knockdown caused a reduction in the levels of a large number of microRNAs (**Figures 3A** and **S3**). This reduction could also be visualized as a left shift in the population-level expression of miRNAs (**Figure 3B**; $p < 1e-3$). The reduction in mature microRNA expression mirrored what was previously observed upon METTL3 depletion (Alarcón et al., 2015).

We next investigated the overlap between the set of miRNAs impacted by HNRNPA2B1 depletion and those impacted by METTL3 depletion. Importantly, 95% (58 out of 61) of the miRNAs that decreased in their expression by more than 50% upon HNRNPA2B1 depletion were also affected, with similar intensity, upon depletion of METTL3 ($p < 1e-24$, **Figure 3C** and **Table S1**). The fraction of miRNAs affected by HNRNPA2B1 depletion was roughly half of the total miRNAs regulated by METTL3—indicating that HNRNPA2B1 regulates a major subset, but not all, of the m⁶A-dependent miRNAs.

In order to validate these findings using an independent approach, we performed quantitative PCR (qPCR) for specific miRNAs in the setting of HNRNPA2B1 knockdown using additional cell lines. Consistent with the findings described above, HNRNPA2B1 depletion caused a significant reduction in the expression levels of the mature forms of a number of m⁶A-regulated miRNAs in MDA-MB-231 cells (**Figure 4A**), as well as HEK293 cells (**Figure S4**). Moreover, the expression levels of these miRNAs were also dependent on METTL3, as their levels were similarly significantly reduced upon METTL3 depletion in both cell lines (**Figures 4B** and **S4**).

We next asked whether HNRNPA2B1 binds to pri-miRNA sites and whether it regulates the processing of METTL3/m⁶A-dependent microRNAs. To answer these questions, we identified m⁶A peaks in pri-miRNA transcripts from m⁶A-seq data and searched for co-occurrence with HNRNPA2B1 binding sites. Consistent with a direct role for HNRNPA2B1 in regulating the processing of these pri-miRNA transcripts, we noted overlaps between m⁶A peaks and HNRNPA2B1 binding sites detected by HITS-CLIP (**Figure 4C**). Importantly, of the 61 miRNAs affected by HNRNPA2B1 depletion, 53 contained m⁶A-seq tags, and 52 of those exhibited overlapping HNRNPA2B1 HITS-CLIP tags ($p = 3e-9$, **Figure 4D**). These findings are consistent with recognition of the m⁶A mark by HNRNPA2B1 at miRNA loci.

If HNRNPA2B1 mediates its effects in the nucleus prior to the processing of pri-miRNAs to pre-miRNAs, then its depletion should result in the accumulation of pri-miRNA transcripts within the nucleus. Consistent with this, depletion of HNRNPA2B1 resulted in the accumulation of specific pri-miRNAs in the nucleus, phenocopying the effect of METTL3 depletion (**Figure 5A**). HNRNPA2B1 thus positively regulates the nuclear processing of a set of pri-miRNAs. The processing of these pri-miRNAs is dependent on METTL3, the m⁶A writer, and HNRNPA2B1, a putative reader of this mark. These findings are consistent with a model wherein METTL3 and HNRNPA2B1 proteins comprise a pathway that controls the processing of a set of miRNA precursors.

A reader of m⁶A should serve as a bridge between this mark and effector proteins or adaptor proteins that would ultimately interact with effectors. The effector involved in pri-miRNA

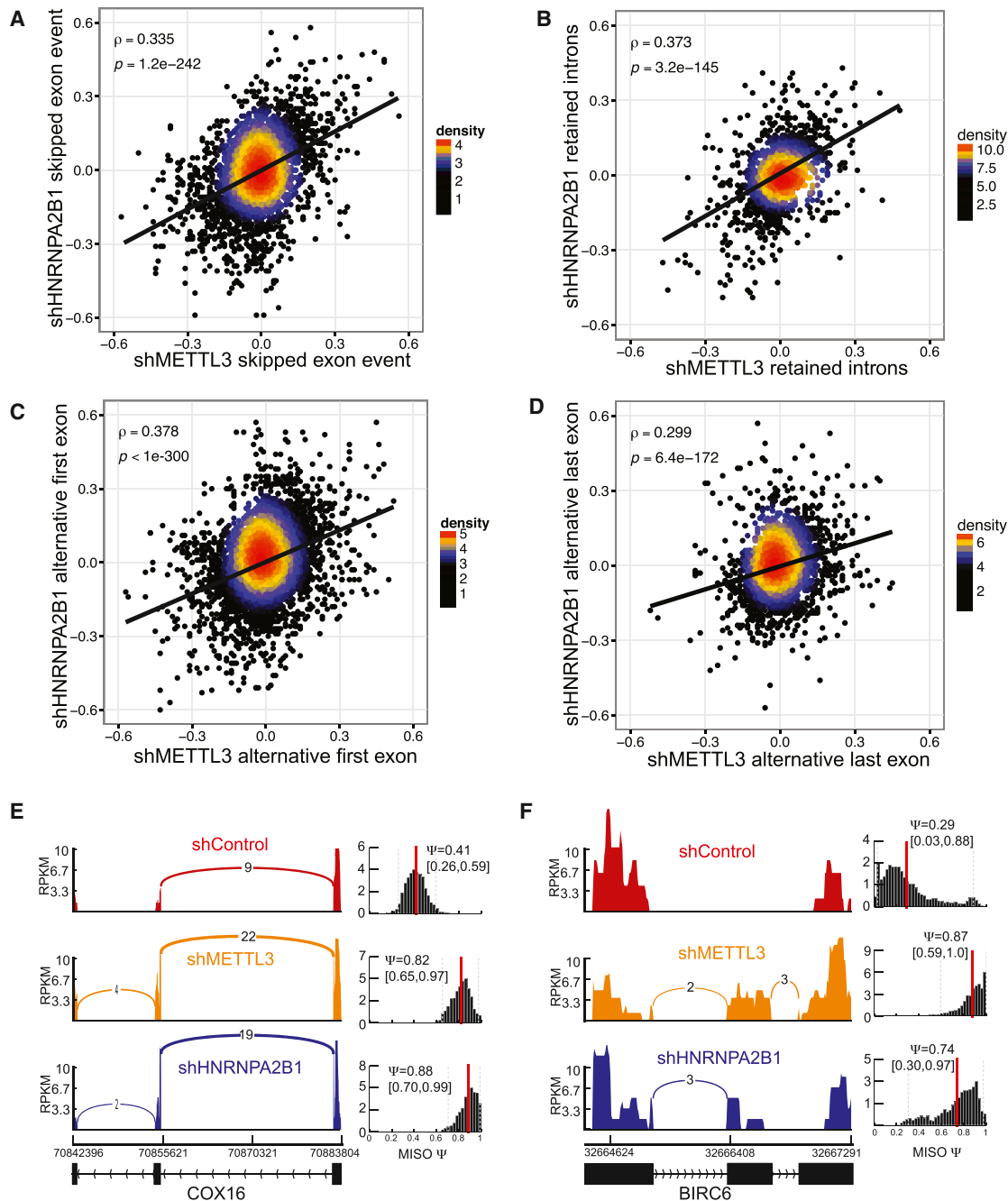


Figure 2. Depletion of HNRNPA2B1 and METTL3 Similarly Affect RNA Splicing

(A–D) Correlation between differential percent spliced in (Ψ) in annotated alternative splicing events following HNRNPA2B1 and METTL3 depletion. Annotated skipped exons (A), retained introns (B), alternative first exons (C), and alternative last exons (D) were quantified in HNRNPA2B1 and METTL3 knockdown MDA-MB-231 cells, respectively (relative to control cells). Spearman correlation was then used to assess the similarity in splicing modulations following depletion of METTL3 ($m^6\text{A}$ writer) and HNRNPA2B1 ($m^6\text{A}$ reader).

(E) Exemplary sashimi plots (Katz et al., 2015) showing concerted alternative splicing changes that occurred in MDA-MB-231 cells depleted of METTL3 or HNRNPA2B1.

(F) Exemplary of sashimi plots as in (E) but using an independent cell line, HeLa. Shown is the normalized coverage at each exon, along with the estimated Ψ value (percent spliced in). For example, in this case, 29% of transcripts were estimated to contain the skipped exon in the control sample, while this estimate was increased to 87% and 74% for METTL3 and HNRNPA2B1 depleted cells, respectively.

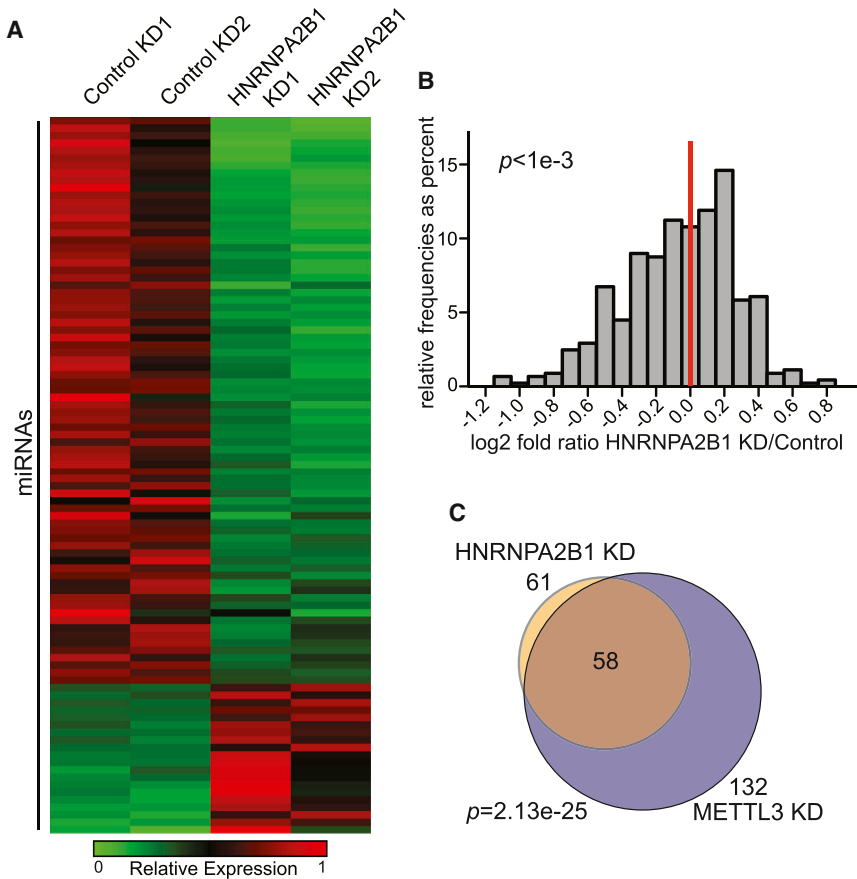


Figure 3. Depletion of HNRNPA2B1 Impacts miRNA Production

(A) Heatmap depicting the miRNAs affected at least by 50% by 2 independent shRNAs targeting HNRNPA2B1 in HEK293 cells. Red represents higher expression and green represents lower expression levels.

(B) Histogram of the fold change (\log_2) observed in miRNA expression, as obtained by genome-wide miRNA expression profiling shown in (A). The ratio of the average level for the two independent shRNAs over the average of the two controls is shown. The p value of the two-sample Kolmogorov-Smirnov test is indicated.

(C) Venn diagram depicting the intersection of miRNAs that were reduced by greater than 50% upon HNRNPA2B1 or METTL3 depletion. 132 miRNAs were downregulated by more than 50% upon METTL3 depletion, and 61 miRNAs were downregulated by 50% upon HNRNPA2B1 depletion. The extent of miRNAs detected by microarray in both experiments was 329. The p value was calculated based on the hypergeometric distribution.

processing is the Microprocessor complex, which is composed of the proteins DGCR8 and DROSHA. DGCR8 is an RNA-binding protein that recognizes the junction between the stem region and the flanking single-stranded RNA of the pri-miRNA hairpin. Hairpin recognition and binding allow for recruitment of the ribonuclease type III DROSHA, which cleaves the double-stranded RNA to release the pre-miRNA molecule (Denli et al., 2004; Gregory et al., 2004; Han et al., 2004, 2006; Landthaler et al., 2004). We had previously proposed the existence of one or more readers that could mediate the interaction between the m⁶A mark present in pri-miRNA regions and the Microprocessor to facilitate the recognition of the pri-miRNA among the large landscape of secondary structures that populate the transcriptome (Alarcón et al., 2015). Since HNRNPA2B1 recognizes m⁶A sequences and its depletion causes similar miRNA processing defects as METTL3 depletion, we investigated if it could link the m⁶A mark and the Microprocessor. Consistent with a direct role for HNRNPA2B1 in the regulation of pri-miRNA processing, immunoprecipitation of endogenous DGCR8 co-precipitated HNRNPA2B1, while reciprocal immunoprecipitation also revealed this interaction (Figures 5B and 5C). Importantly, this interaction persisted despite ribonuclease treatment, suggesting that the interaction between these two proteins is mediated by protein-protein interactions (Figures 5B and 5C). If HNRNPA2B1 recruits DGCR8 to a subset of pri-miRNA loci, then HNRNPA2B1 depletion should reduce the interaction of DGCR8 with pri-

miRNA substrates. Consistent with this, HNRNPA2B1 depletion reduced the binding of endogenous DGCR8 with HNRNPA2B1-dependent pri-miRNA substrates (Figure 5D). HNRNPA2B1 thus recognizes m⁶A sequences, interacts with the Microprocessor, and facilitates the processing of a set of METTL3-dependent pri-miRNAs. These collective findings are consistent with its proposed role as a reader of the m⁶A mark.

HNRNPA2B1 Binds Methylated RNA

We next sought biochemical evidence for the *in vivo* interaction of HNRNPA2B1 with methylated RNA. MDA-MB-231 cells were UV cross-linked, their nuclear fractions were isolated, and endogenous HNRNPA2B1 was immunoprecipitated with a specific antibody. Upon HNRNPA2B1 immunoprecipitation and SDS-PAGE, immunoblotting with the m⁶A antibody revealed HNRNPA2B1 to interact with methylated RNA (Figure 6A). Importantly, ribonuclease treatment diminished the m⁶A signal of high molecular weight corresponding to long RNAs associated with HNRNPA2B1 but did not affect the m⁶A signal at the molecular weight of HNRNPA2B1 (37 kilodaltons)—suggesting that HNRNPA2B1 directly associates with m⁶A methylated RNA and protects its RNA target sites from ribonuclease degradation (Figure 6A). The direct association between HNRNPA2B1 and m⁶A appears to be specific, since similar direct protection of m⁶A-containing RNA by another hnRNP RNA-binding protein was not observed (Figure S5A). If the methylated RNA that is bound by HNRNPA2B1 contains m⁶A, then depleting cells of the m⁶A writer METTL3 should reduce the HNRNPA2B1-bound m⁶A signal detected by western blot. Consistent with HNRNPA2B1 binding to cellular m⁶A, the m⁶A signal bound by endogenous HNRNPA2B1 recovered from METTL3-depleted

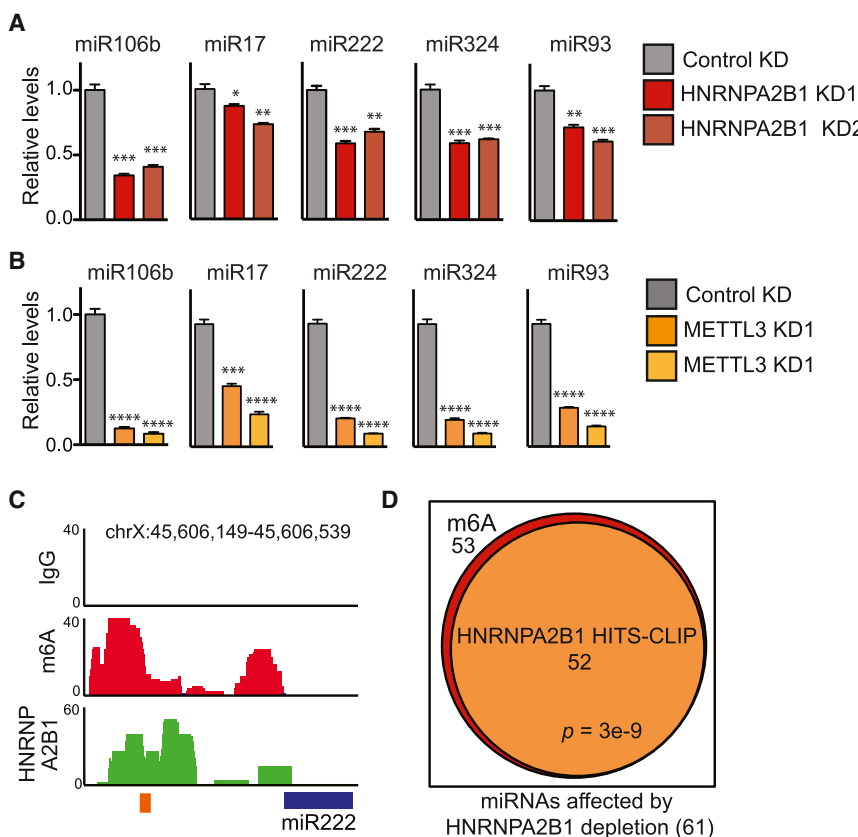


Figure 4. HNRNPA2B1 Binds to m⁶A-Methylated Pri-miRNA Sequences

(A) qRT-PCR quantification of exemplary miRNAs that were modulated by HNRNPA2B1 depletion in MDA-MB-231 cells. Stable cell lines expressing shControl vector or two independent shRNAs targeting HNRNPA2B1 were generated, and total RNA was extracted and quantified. ***p < 1e-3; **p < 1e-2; *p < 5e-2.

(B) Quantification of the expression levels of miRNAs shown in (A) when METTL3 was depleted in MDA-MB-231 cells by two independent shRNAs, as measured by qRT-PCR. p values as in (A). ****p < 5e-4; ***p < 1e-3. Error bars indicate SEM.

(C) Genome tracks depicting sequencing read coverage from m⁶A-seq (red) and HNRNPA2B1 HITS-CLIP (green) within an exemplary pri-miRNA obtained from MDA-MB-231 cells. The upper track represents the reads from the IgG immunoprecipitated control sample. The blue box indicates the position of the pre-miRNA, and the orange box indicates the position of the RGAC motif. The chromosomal location of the sequence depicted in the figure is shown at the top of the panel.

(D) Venn diagram showing the overlap between m⁶A-seq tags and HNRNPA2B1-HITS-CLIP tags within pri-miRNA regions of miRNAs affected by HNRNPA2B1 depletion. The p value was calculated based on the hypergeometric distribution.

cells was reduced relative to control cells (Figure 6B). Interestingly, Dominissini et al. (2012) used mass spectrometry to identify candidate proteins that bound m⁶A-modified RNA but not unmethylated RNA. Although not functionally studied, HNRNPA2B1 was among the set of proteins identified that preferentially bound m⁶A-modified RNA. Taken together, our findings reveal that endogenous HNRNPA2B1 directly interacts with m⁶A-modified RNA in vivo.

We next studied the interaction between HNRNPA2B1 and methylated RNA in vitro. Purified full-length HNRNPA2B1 exhibited some preference for binding methylated RNA probes relative to unmethylated ones as shown by gel shift assays (Figures S5B and S5C). The probes used for these assays correspond to sequences obtained from endogenous pri-miRNAs regions that contained m⁶A-seq tags, as well as endogenous HNRNPA2B1 binding sites (HITS-CLIP tags) (Figures S5D and S5E). Importantly, this preference was not observed using a different hnRNP protein (Figure S5F). We then generated a series of constructs containing GST-tagged individual domains. In isolation and under the conditions used in this study, only RRM1 exhibited a modest preference for m⁶A-containing RNA (Figure S5G); however, we cannot exclude the possibility that in vivo and in the context of full-length protein, additional protein domains could mediate or facilitate recognition and binding of the m⁶A mark. These results suggest that HNRNPA2B1 can preferentially associate with m⁶A-containing RNA in vitro and that the RRM1 motif could, in part, mediate this preference.

DISCUSSION

Our findings reveal that the HNRNPA2B1 RNA-binding protein binds the m⁶A consensus motif and also directly binds the m⁶A mark in vivo and in vitro. Loss-of-function experiments with HNRNPA2B1 and METTL3 resulted in similar effects on global alternative splicing patterns. HNRNPA2B1 was found to exhibit preferential in vitro binding to m⁶A-modified RNA substrates used in this study over unmodified substrates. Additionally, HNRNPA2B1 interacts with the Microprocessor protein DGCR8, enhances binding of DGCR8 to pri-miRNA transcripts, and positively regulates pri-miRNA processing in a similar manner as METTL3, the m⁶A writer. Moreover, we have identified a set of miRNAs whose processing is dependent on both METTL3 and HNRNPA2B1. These observations as a whole are consistent with a model wherein HNRNPA2B1 acts as a reader of the m⁶A mark in the nucleus and mediates, in part, the effects of m⁶A/METTL3 on microRNA processing (Figure 7).

YTHDF2 was recently identified as a cytoplasmic “reader” protein of the m⁶A mark. YTHDF2 was found to regulate the degradation of specific mRNAs by localizing them to processing bodies. The historical association of the m⁶A mark with pre-mRNA processing (Carroll et al., 1990; Finkel and Groner, 1983; Katz et al., 2015; Stoltzfus and Dane, 1982) and the more recent molecular studies linking m⁶A or components of the m⁶A-methylation machinery with splicing (Dominissini et al., 2012; Granadino et al., 1990; Horiuchi et al., 2013; Little

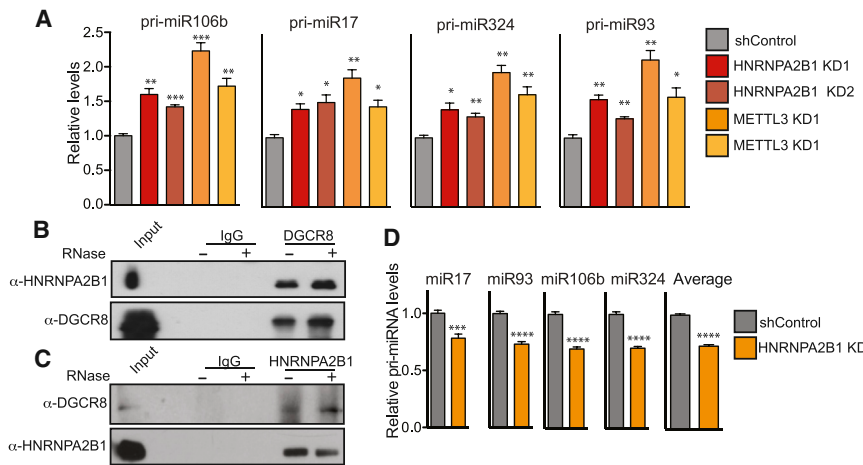


Figure 5. HNRNPA2B1 Regulates miRNA Processing and Interacts with the Microprocessor

(A) Pri-miRNA expression levels for the miRNAs shown in Figures 4B and 4C upon HNRNPA2B1 and METTL3 depletion as measured by qRT-PCR. All experiments were performed in biological triplicates. ***p < 1e-3; **p < 1e-2; *p < 5e-2.

(B) In vivo interaction between DGCR8 and HNRNPA2B1. HEK293 cells were chemically cross-linked before antibody-mediated immunoprecipitation of endogenous DGCR8. After immunoprecipitation, samples were washed and incubated with RNase as indicated. Western blots for HNRNPA2B1 and DGCR8 are shown.

(C) Same as (B), but the reciprocal immunoprecipitation was performed. In this case, endogenous HNRNPA2B1 was immunoprecipitated and its interaction with DGCR8 was detected by western blot under similar conditions.

(D) Quantification of DGCR8-bound pri-miRNAs. Endogenous DGCR8 was immunoprecipitated after UV-cross-linking and pri-miRNAs bound to it were extracted and quantified by qRT-PCR. The bar graph shows the qRT-PCR quantification of a panel of HNRNPA2B1-target miRNAs for which expression was shown to be reduced upon HNRNPA2B1 depletion. ***p < 5e-4; **p < 1e-3. Error bars indicate SEM.

et al., 2000; Liu et al., 2014; Ortega et al., 2003; Ping et al., 2014; Schwartz et al., 2014; Wang et al., 2014b; Zhao et al., 2014) suggested the existence of a nuclear factor that could recognize this modification. Moreover, our recent work implicating m⁶A/METTL3 in the processing of pri-miRNAs—an event occurring in the nucleus—also supported the existence of a nuclear “reader” and effector of this mark (Alarcón et al., 2015). The role of HNRNPA2B1 in m⁶A-dependent nuclear pri-miRNA processing and alternative splicing events, its direct binding to m⁶A and the RGAC motif in vivo, and its in vitro preference for specific m⁶A-modified substrates relative to unmodified substrates support a role for this RNA-binding protein as a nuclear “reader” and effector of this mark.

A natural question that arises is why there would exist distinct readers of m⁶A that act within the nucleus or the cytoplasm. The fates of RNA molecules within the nucleus and cytoplasm are fundamentally distinct. Within the nucleus, nascent transcripts are internally processed to yield mature messages lacking introns. Similarly, primary microRNA transcripts are processed within the nucleus to yield shorter pre-miRNA forms—the precursors for mature miRNAs. Within the cytoplasm, mRNAs can be localized to distinct compartments, translated, stabilized, or destabilized. The divergent processes that transcripts participate in within the nucleus or cytoplasm are mediated by distinct protein complexes, such as the microRNA and splicing machineries in the nucleus or the deadenylation complex in the cytoplasm. The existence of distinct nuclear and cytoplasmic readers that bind m⁶A but have additional protein-protein interaction domains would allow for each reader to interact with specific downstream effector proteins to mediate requisite events in the nucleus and cytoplasm. Consistent with this, YTHDF2 and HNRNPA2B1 contain distinct protein domains in addition to their RNA-binding domains—P/Q/N-rich domain for YTHDF2 and RGG and M9 domains for HNRNPA2B1. These domains likely mediate interactions with specific cytoplasmic and nuclear effector proteins, respectively, or could form binding sites for adaptor proteins that recruit these machineries. In the case of

HNRNPA2B1, its interaction with the Microprocessor represents an example of such selectivity. YTHDF2, on the other hand, has been shown to co-localize with components of the processing bodies in the cytoplasm (Wang et al., 2014a).

A long-standing question regarding m⁶A has been the molecular basis for the localization of m⁶A marks to specific infrequent (roughly one modification per 1,000 bases) sites in transcripts (Rottman et al., 1994). The basis for this specificity is unknown, given that the m⁶A consensus motif is short and therefore inherently non-specific. It has been proposed that local structural elements might contain the requisite contextual information that enables m⁶A marks to be deposited (Rottman et al., 1994). Indeed, the methylation site in arguably the best-studied m⁶A-containing transcript (prolactin) falls in a predicted stem-loop/bulge structure (Rottman et al., 1994). Moreover, similar stem-loop/bulge structures were predicted for multiple m⁶A consensus sites found in Rous sarcoma virus (RSV) RNA (Csepanyi et al., 1990; Kane and Beemon, 1985). With respect to “writing” of this mark, METTL3 has been shown to methylate single-stranded RNA substrates in vitro to a similar degree as structured substrates (Liu et al., 2014). While others and we have identified many m⁶A marks to also occur in regions that are not predicted to form structures, these historical findings suggest the presence of at least some m⁶A marks in structured contexts. Future in vivo RNA structural mapping studies aimed at establishing the fraction of structured versus unstructured sites that contain the m⁶A mark could provide important insights (Ding et al., 2014; Rouskin et al., 2014).

Another question that arises is whether the structured context within which m⁶A occurs is important for its “reading” by proteins such as HNRNPA2B1. While this question is beyond the scope of the current work and will require future genome-wide in vivo structural analyses, we speculate that HNRNPA2B1 could potentially bind to m⁶A at both unstructured/linear sites, as well as in structured sites given its multiple RRM domains. At linear sites, the RRM1 domain could potentially bind m⁶A-containing locations in linear RNA. At structured sites, the RRM1 domain

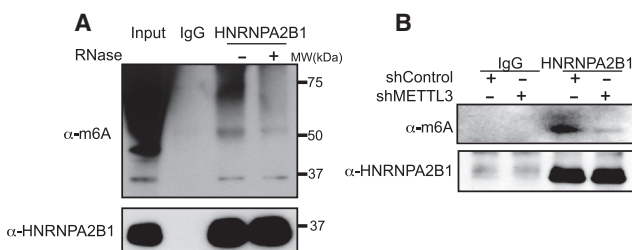


Figure 6. HNRNPA2B1 Binds m⁶A Methylation RNA

(A) Immunoprecipitation of endogenous HNRNPA2B1 from MDA-MB-231 cells. Cells were UV-cross-linked before immunoprecipitation, and samples were treated with RNase-A or left untreated as indicated after the immunoprecipitation. Western blotting was performed using the indicated antibodies. (B) Immunoprecipitation of endogenous HNRNPA2B1 and associated RNA from control cells or cells depleted of METTL3. Cells were UV-cross-linked prior to immunoprecipitation, and western blotting was done using the antibodies depicted in the figure.

could bind to an m⁶A in a single-stranded loop of a stem-loop structure while the RRM2 domain could bind to a single-stranded bulge irrespective of m⁶A-modification. Conversely, the RRM1 domain could bind an m⁶A in the bulge of a stem loop while the RRM2 domain could bind to a loop irrespective of its m⁶A modification. This speculative model is consistent with previously characterized transcriptome-wide binding of HNRNPA2B1 to AU-rich structural elements, which are less thermodynamically stable structures (Goodarzi et al., 2012). Another possibility is that the presence of the m⁶A mark in double-stranded RNA could increase its open-conformation probability, thereby facilitating RRM1 binding to the m⁶A-bearing strand (Roost et al., 2015). Thus, the presence of multiple RRM motifs in HNRNPA2B1 could enable it to bind cooperatively to two distinct sites such as a loop and a stem or a loop and a bulge within a stem loop. Future structural and molecular studies are needed to shed light on the details and dynamics of the events that follow m⁶A placement at linear and structured sites.

While we have implicated HNRNPA2B1 as a downstream mediator of the effects of the m⁶A mark/METTL3 in the nucleus, it is important to note that this protein may have multiple modes of RNA binding/recognition that are independent of the m⁶A modification. In fact, HNRNPA2B1 has been implicated in several aspects of RNA biology (He and Smith, 2009; Villarroya-Beltri et al., 2013), some of which might be independent of regulation by m⁶A. Additionally, our findings do not exclude the possibility that there exist additional “readers” of this mark within the nucleus that could mediate similar processing effects at other miRNA, exonic, or intronic loci or to mediate other aspects of RNA processing or localization. In fact, we have found that roughly half of the m⁶A-regulated miRNAs studied by us were dependent on HNRNPA2B1. This finding suggests the existence of additional nuclear “readers” of this mark that mediate miRNA processing, as well as other nuclear processing events. It would be quite interesting to determine whether other RNA-binding proteins of the hnRNP A/B family that share similar RRM domains recognize the m⁶A modification and mediate, in part, its effects on nuclear processing events.

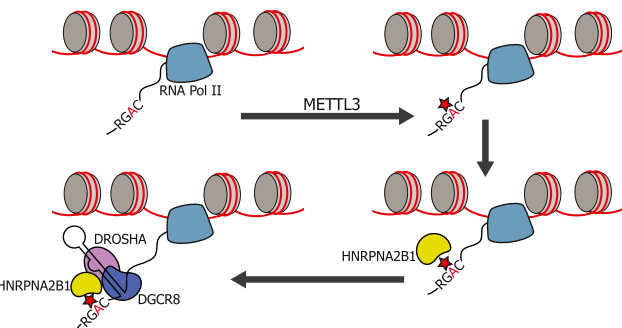


Figure 7. HNRNPA2B1 Is a Mediator of the m⁶A Mark

Schematic representation of the nuclear role of HNRNPA2B1 in pri-miRNA processing. HNRNPA2B1 is shown as a reader of the m⁶A methylation mark. Pri-miRNA processing is depicted in the model. The red star represents m⁶A mark on RNA, and the yellow shape represents the HNRNPA2B1 RNA-binding protein.

Our findings have identified HNRNPA2B1 as a nuclear “reader,” a downstream effector of the m⁶A mark and an adaptor for the Microprocessor complex. Future proteomic and biochemical studies are needed to elucidate the molecular networks and mechanisms by which this reader mediates other nuclear processing events downstream of the m⁶A mark.

EXPERIMENTAL PROCEDURES

Tissue Culture

MDA-MB-231, HeLa, and HEK293T cell lines were purchased from ATCC. All cells were cultured *in vitro* in DMEM supplemented with 10% fetal bovine serum (FBS), 1% penicillin-streptomycin, 2 mM L-Glutamine, 1 mM sodium pyruvate, and 2.5 μ g/ml fungizone. All experiments were conducted with cells from passage 2 to 5.

Stable Cell Lines

Generation of lentivirus-mediated knockdowns was performed as described previously (Tavazoie et al., 2008). Commercially available shRNAs purchased from Sigma were co-transfected with lentivirus packaging plasmids in HEK293T cells to generate lentivirus. Two shRNAs targeting HNRNPA2B1 (TRCN000001058, TRCN0000010582), two shRNAs specific for METTL3 (TRCN0000034715, TRCN0000034717), and a control shRNA (SHC002) were used for experiments. We generated stable fresh knockdown cell lines after 2 or 3 passages in order to avoid compensatory mechanisms of loss of knockdown.

qRT-PCR

Mature and pri-miRNAs were quantified by Taqman microRNA and Pri-miRNA assays. RNU44, U6 snRNA, GAPDH, and GusB were used as endogenous controls. Quantitative miRNAs expression data were obtained using the ABI Prism 7900HT Fast Real-Time PCR System, and data were analyzed by Relative Quantification (RQ) Manager software.

Small RNA Isolation

mirVana (Applied Biosystems) and Total RNA Purification Kit (Norgen Biotek) were used to extract total RNA from cells according to the manufacturer’s instructions.

RNA Sequencing

Samples were lysed using LB1 buffer (50 mM HEPES-KOH [pH 7.5], 140 mM NaCl, 1 mM EDTA, 10% glycerol, 0.5% Triton X-100, and protease inhibitors). RNA was extracted from the nuclear fraction using the Total RNA Purification

Kit (Norgen Biotek). RNA was subjected to RiboZero treatment (Epicenter), barcoded using ScriptSeq V2 kit (Epicenter), and sent for sequencing.

microRNA Expression Profiling

The RNA extracted from two independent stable knockdowns of HNRNPA2B1 and two control cells expressing a control hairpin were labeled and hybridized on miRNA microarrays by LC sciences. Of all the probes included in the array, those corresponding to 329 miRNAs revealed a signal above background in at least two of the samples and were also expressed in the microarray previously performed using METTL3 depleted cells.

ACCESSION NUMBERS

High-throughput sequencing data were deposited at GEO under the accession number GEO: GSE70061.

SUPPLEMENTAL INFORMATION

Supplemental Information includes Supplemental Experimental Procedures, five figures, and one table and can be found with this article online at <http://dx.doi.org/10.1016/j.cell.2015.08.011>.

ACKNOWLEDGMENTS

We are grateful to Alexander Nguyen for insightful comments and technical advice. We thank C. Zhao and C. Lai of the Rockefeller Genomics Resource Center for expert assistance with next-generation RNA sequencing. C.R.A. is the recipient of the Robert S. Bennett Postdoctoral Fellowship and is supported by the Debra and Leon Black Challenge Grant. H.G. is currently the recipient of a Ruth L. Kirschstein National Research Service Award from the NIH (T32CA009673-36A1). S.F.T. is a Department of Defense Era of Hope Scholar and a Department of Defense Breast Cancer Collaborative Scholars and Innovators Award recipient. S.T. was supported by the National Human Genome Research Institute (R01 HG003219).

Received: December 15, 2014

Revised: March 10, 2015

Accepted: July 8, 2015

Published: August 27, 2015

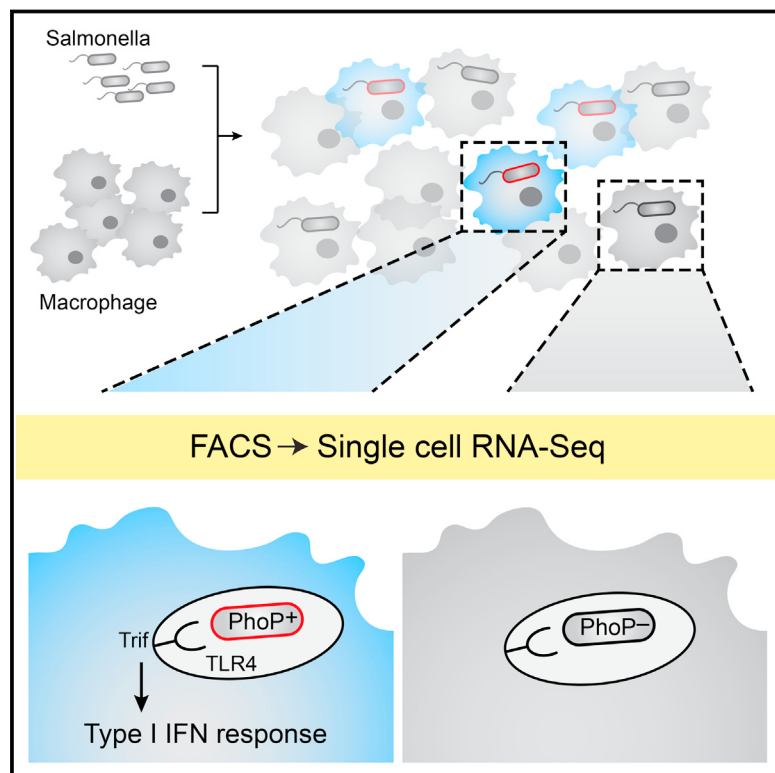
REFERENCES

- Alarcón, C.R., Lee, H., Goodarzi, H., Halberg, N., and Tavazoie, S.F. (2015). N6-methyladenosine marks primary microRNAs for processing. *Nature* 519, 482–485.
- Batista, P.J., Molinie, B., Wang, J., Qu, K., Zhang, J., Li, L., Bouley, D.M., Lujan, E., Haddad, B., Daneshvar, K., et al. (2014). m(6)A RNA modification controls cell fate transition in mammalian embryonic stem cells. *Cell Stem Cell* 15, 707–719.
- Carroll, S.M., Narayan, P., and Rottman, F.M. (1990). N6-methyladenosine residues in an intron-specific region of prolactin pre-mRNA. *Mol. Cell. Biol.* 10, 4456–4465.
- Csepány, T., Lin, A., Baldick, C.J., Jr., and Beemon, K. (1990). Sequence specificity of mRNA N6-adenosine methyltransferase. *J. Biol. Chem.* 265, 20117–20122.
- Denli, A.M., Tops, B.B., Plasterk, R.H., Ketten, R.F., and Hannon, G.J. (2004). Processing of primary microRNAs by the Microprocessor complex. *Nature* 432, 231–235.
- Ding, Y., Tang, Y., Kwok, C.K., Zhang, Y., Bevilacqua, P.C., and Assmann, S.M. (2014). In vivo genome-wide profiling of RNA secondary structure reveals novel regulatory features. *Nature* 505, 696–700.
- Dominissini, D., Moshitch-Moshkovitz, S., Schwartz, S., Salmon-Divon, M., Ungar, L., Osenberg, S., Cesarkas, K., Jacob-Hirsch, J., Amariglio, N., Kupiec, M., et al. (2012). Topology of the human and mouse m6A RNA methylomes revealed by m6A-seq. *Nature* 485, 201–206.
- Elemento, O., Slonim, N., and Tavazoie, S. (2007). A universal framework for regulatory element discovery across all genomes and data types. *Mol. Cell* 28, 337–350.
- Finkel, D., and Groner, Y. (1983). Methylation of adenosine residues (m6A) in pre-mRNA are important for formation of late simian virus 40 mRNAs. *Virology* 131, 409–425.
- Giannopoulou, E.G., and Elemento, O. (2011). An integrated ChIP-seq analysis platform with customizable workflows. *BMC Bioinformatics* 12, 277.
- Goodarzi, H., Najafabadi, H.S., Oikonomou, P., Greco, T.M., Fish, L., Salavati, R., Cristea, I.M., and Tavazoie, S. (2012). Systematic discovery of structural elements governing stability of mammalian messenger RNAs. *Nature* 485, 264–268.
- Granadino, B., Campuzano, S., and Sánchez, L. (1990). The *Drosophila melanogaster* fl(2)d gene is needed for the female-specific splicing of Sex-lethal RNA. *EMBO J.* 9, 2597–2602.
- Gregory, R.I., Yan, K.P., Amuthan, G., Chendrimada, T., Doratotaj, B., Cooch, N., and Shiekhattar, R. (2004). The Microprocessor complex mediates the genesis of microRNAs. *Nature* 432, 235–240.
- Hafner, M., Landthaler, M., Burger, L., Khorshid, M., Hausser, J., Berninger, P., Rothbächer, A., Ascano, M., Jungkamp, A.C., Munschauer, M., et al. (2010). PAR-CLIP—a method to identify transcriptome-wide the binding sites of RNA binding proteins. *J. Vis. Exp.* (41), 2034.
- Han, J., Lee, Y., Yeom, K.H., Kim, Y.K., Jin, H., and Kim, V.N. (2004). The Drosha-DGCR8 complex in primary microRNA processing. *Genes Dev.* 18, 3016–3027.
- Han, J., Lee, Y., Yeom, K.H., Nam, J.W., Heo, I., Rhee, J.K., Sohn, S.Y., Cho, Y., Zhang, B.T., and Kim, V.N. (2006). Molecular basis for the recognition of primary microRNAs by the Drosha-DGCR8 complex. *Cell* 125, 887–901.
- He, Y., and Smith, R. (2009). Nuclear functions of heterogeneous nuclear ribonucleoproteins A/B. *Cell. Mol. Life Sci.* 66, 1239–1256.
- Horiuchi, K., Kawamura, T., Iwanari, H., Ohashi, R., Naito, M., Kodama, T., and Hamakubo, T. (2013). Identification of Wilms' tumor 1-associated protein complex and its role in alternative splicing and the cell cycle. *J. Biol. Chem.* 288, 33292–33302.
- Jaffrey, S.R. (2014). An expanding universe of mRNA modifications. *Nat. Struct. Mol. Biol.* 21, 945–946.
- Jia, G., Fu, Y., Zhao, X., Dai, Q., Zheng, G., Yang, Y., Yi, C., Lindahl, T., Pan, T., Yang, Y.G., et al. (2011). N6-methyladenosine in nuclear RNA is a major substrate of the obesity-associated FTO. *Nat. Chem. Biol.* 7, 885–887.
- Kane, S.E., and Beemon, K. (1985). Precise localization of m6A in Rous sarcoma virus RNA reveals clustering of methylation sites: implications for RNA processing. *Mol. Cell. Biol.* 5, 2298–2306.
- Katz, Y., Wang, E.T., Airolidi, E.M., and Burge, C.B. (2010). Analysis and design of RNA sequencing experiments for identifying isoform regulation. *Nat. Methods* 7, 1009–1015.
- Katz, Y., Wang, E.T., Silterra, J., Schwartz, S., Wong, B., Thorvaldsdóttir, H., Robinson, J.T., Mesirov, J.P., Airolidi, E.M., and Burge, C.B. (2015). Quantitative visualization of alternative exon expression from RNA-seq data. *Bioinformatics* 31, 2400–2402.
- König, J., Zarnack, K., Rot, G., Curk, T., Kayikci, M., Zupan, B., Turner, D.J., Luscombe, N.M., and Ule, J. (2010). iCLIP reveals the function of hnRNP particles in splicing at individual nucleotide resolution. *Nat. Struct. Mol. Biol.* 17, 909–915.
- Landthaler, M., Yalcin, A., and Tuschl, T. (2004). The human DiGeorge syndrome critical region gene 8 and its *D. melanogaster* homolog are required for miRNA biogenesis. *Curr. Biol.* 14, 2162–2167.
- Little, N.A., Hastie, N.D., and Davies, R.C. (2000). Identification of WTAP, a novel Wilms' tumour 1-associated protein. *Hum. Mol. Genet.* 9, 2231–2239.
- Liu, J., Yue, Y., Han, D., Wang, X., Fu, Y., Zhang, L., Jia, G., Yu, M., Lu, Z., Deng, X., et al. (2014). A METTL3-METTL14 complex mediates mammalian nuclear RNA N6-adenosine methylation. *Nat. Chem. Biol.* 10, 93–95.

- Liu, N., Dai, Q., Zheng, G., He, C., Parisien, M., and Pan, T. (2015). N(6)-methyladenosine-dependent RNA structural switches regulate RNA-protein interactions. *Nature* **518**, 560–564.
- Meyer, K.D., Saletoye, Y., Zumbo, P., Elemento, O., Mason, C.E., and Jaffrey, S.R. (2012). Comprehensive analysis of mRNA methylation reveals enrichment in 3' UTRs and near stop codons. *Cell* **149**, 1635–1646.
- Ortega, A., Niksic, M., Bach, A., Wilm, M., Sánchez, L., Hastie, N., and Valcárcel, J. (2003). Biochemical function of female-lethal (2)D/Wilms' tumor suppressor-1-associated proteins in alternative pre-mRNA splicing. *J. Biol. Chem.* **278**, 3040–3047.
- Ping, X.L., Sun, B.F., Wang, L., Xiao, W., Yang, X., Wang, W.J., Adhikari, S., Shi, Y., Lv, Y., Chen, Y.S., et al. (2014). Mammalian WTAP is a regulatory subunit of the RNA N6-methyladenosine methyltransferase. *Cell Res.* **24**, 177–189.
- Roost, C., Lynch, S.R., Batista, P.J., Qu, K., Chang, H.Y., and Kool, E.T. (2015). Structure and thermodynamics of N6-methyladenosine in RNA: a spring-loaded base modification. *J. Am. Chem. Soc.* **137**, 2107–2115.
- Rottman, F.M., Bokar, J.A., Narayan, P., Shambrough, M.E., and Ludwiczak, R. (1994). N6-adenosine methylation in mRNA: substrate specificity and enzyme complexity. *Biochimie* **76**, 1109–1114.
- Rouskin, S., Zubradt, M., Washietl, S., Kellis, M., and Weissman, J.S. (2014). Genome-wide probing of RNA structure reveals active unfolding of mRNA structures in vivo. *Nature* **505**, 701–705.
- Schibler, U., Kelley, D.E., and Perry, R.P. (1977). Comparison of methylated sequences in messenger RNA and heterogeneous nuclear RNA from mouse L cells. *J. Mol. Biol.* **115**, 695–714.
- Schwartz, S., Mumbach, M.R., Jovanovic, M., Wang, T., Maciag, K., Bushkin, G.G., Mertins, P., Ter-Ovanesyan, D., Habib, N., Cacchiarelli, D., et al. (2014). Perturbation of m6A writers reveals two distinct classes of mRNA methylation at internal and 5' sites. *Cell Rep.* **8**, 284–296.
- Stoltzfus, C.M., and Dane, R.W. (1982). Accumulation of spliced avian retrovirus mRNA is inhibited in S-adenosylmethionine-depleted chicken embryo fibroblasts. *J. Virol.* **42**, 918–931.
- Tavazoie, S.F., Alarcón, C., Oskarsson, T., Padua, D., Wang, Q., Bos, P.D., Gerald, W.L., and Massagué, J. (2008). Endogenous human microRNAs that suppress breast cancer metastasis. *Nature* **451**, 147–152.
- Ule, J., Jensen, K., Mele, A., and Darnell, R.B. (2005). CLIP: a method for identifying protein-RNA interaction sites in living cells. *Methods* **37**, 376–386.
- Villarroya-Beltri, C., Gutiérrez-Vázquez, C., Sánchez-Cabo, F., Pérez-Hernández, D., Vázquez, J., Martín-Cofreces, N., Martínez-Herrera, D.J., Pascual-Montano, A., Mittelbrunn, M., and Sánchez-Madrid, F. (2013). Sumoylated hnRNPA2B1 controls the sorting of miRNAs into exosomes through binding to specific motifs. *Nat. Commun.* **4**, 2980.
- Wang, X., Lu, Z., Gomez, A., Hon, G.C., Yue, Y., Han, D., Fu, Y., Parisien, M., Dai, Q., Jia, G., et al. (2014a). N6-methyladenosine-dependent regulation of messenger RNA stability. *Nature* **505**, 117–120.
- Wang, Y., Li, Y., Toth, J.I., Petroski, M.D., Zhang, Z., and Zhao, J.C. (2014b). N6-methyladenosine modification destabilizes developmental regulators in embryonic stem cells. *Nat. Cell Biol.* **16**, 191–198.
- Wei, C.M., and Moss, B. (1974). Methylation of newly synthesized viral messenger RNA by an enzyme in vaccinia virus. *Proc. Natl. Acad. Sci. USA* **71**, 3014–3018.
- Zhang, C., and Darnell, R.B. (2011). Mapping in vivo protein-RNA interactions at single-nucleotide resolution from HITS-CLIP data. *Nat. Biotechnol.* **29**, 607–614.
- Zhao, X., Yang, Y., Sun, B.F., Shi, Y., Yang, X., Xiao, W., Hao, Y.J., Ping, X.L., Chen, Y.S., Wang, W.J., et al. (2014). FTO-dependent demethylation of N6-methyladenosine regulates mRNA splicing and is required for adipogenesis. *Cell Res.* **24**, 1403–1419.

Pathogen Cell-to-Cell Variability Drives Heterogeneity in Host Immune Responses

Graphical Abstract



Highlights

- Single-cell RNA-seq reveals heterogeneity of host-pathogen encounters
- PhoP-mediated LPS modifications occur in only a subset of bacteria during infection
- Intracellular recognition of modified LPS induces heterogeneous type I IFN response
- Heterogeneity is a key feature of pathogen population during infection

Authors

Roi Avraham, Nathan Haseley, Douglas Brown, ..., Ramnik J. Xavier, Aviv Regev, Deborah T. Hung

Correspondence

hung@molbio.mgh.harvard.edu

In Brief

Functional heterogeneity in the response of host cells to infection is driven by cell-to-cell transcriptional variations in the population of infecting pathogens.

Accession Numbers

GSE66528
GSE65529
GSE65530
GSE65531

Pathogen Cell-to-Cell Variability Drives Heterogeneity in Host Immune Responses

Roi Avraham,^{1,9} Nathan Haseley,^{1,2,9} Douglas Brown,¹ Cristina Penaranda,³ Humberto B. Jijon,^{4,5} John J. Trombetta,¹ Rahul Satija,^{1,10,11} Alex K. Shalek,^{1,12,13} Ramnik J. Xavier,^{1,4,6} Aviv Regev,^{1,7} and Deborah T. Hung^{1,3,4,8,*}

¹Broad Institute of MIT and Harvard, Cambridge, MA 02142, USA

²Department of Health, Sciences, and Technology, Massachusetts Institute of Technology, Boston, MA 02139, USA

³Department of Molecular Biology, Massachusetts General Hospital, Boston, MA 02114, USA

⁴Center for Computational and Integrative Biology, Massachusetts General Hospital, Boston, MA 02114, USA

⁵Division of Gastroenterology, Department of Medicine, University of Calgary, Calgary, AB T2N 1N4, Canada

⁶Gastrointestinal Unit, Center for the Study of Inflammatory Bowel Disease, Massachusetts General Hospital, Harvard Medical School, Boston, MA 02114, USA

⁷Howard Hughes Medical Institute, Department of Biology, Massachusetts Institute of Technology, Cambridge, MA 02139, USA

⁸Department of Microbiology and Immunobiology, Harvard Medical School, Boston, MA 02115, USA

⁹Co-first author

¹⁰Present address: New York Genome Center, New York, NY 10003, USA

¹¹Present address: Department of Biology, New York University, New York, NY 10003, USA

¹²Present address: Institute for Medical Engineering and Science and Department of Chemistry, Massachusetts Institute of Technology, Cambridge, MA 02139, USA

¹³Present address: Ragon Institute of MGH, MIT and Harvard, Cambridge, MA 02139, USA

*Correspondence: hung@molbio.mgh.harvard.edu

<http://dx.doi.org/10.1016/j.cell.2015.08.027>

SUMMARY

Encounters between immune cells and invading bacteria ultimately determine the course of infection. These interactions are usually measured in populations of cells, masking cell-to-cell variation that may be important for infection outcome. To characterize the gene expression variation that underlies distinct infection outcomes and monitor infection phenotypes, we developed an experimental system that combines single-cell RNA-seq with fluorescent markers. Probing the responses of individual macrophages to invading *Salmonella*, we find that variation between individual infected host cells is determined by the heterogeneous activity of bacterial factors in individual infecting bacteria. We illustrate how variable PhoPQ activity in the population of invading bacteria drives variable host type I IFN responses by modifying LPS in a subset of bacteria. This work demonstrates a causative link between host and bacterial variability, with cell-to-cell variation between different bacteria being sufficient to drive radically different host immune responses. This co-variation has implications for host-pathogen dynamics in vivo.

INTRODUCTION

Interactions between a pathogen and its host involve both a complex virulence program executed by pathogens and activation of

an orchestrated defense response by the host (Schwan et al., 2000). Genomic approaches—profiling the host, the pathogen, or both—have been employed in recent years to uncover substantial molecular details about host and bacterial factors that underlie infection outcomes (Eriksson et al., 2003). However, to date, these genomic studies have been typically based on averaging cellular behaviors across populations (Helaine et al., 2010), whereas the heterogeneous, stochastic, and dynamic nature of both host and pathogens suggests that descriptions of average behavior may fail to accurately characterize their interactions (Jaitin et al., 2014). For example, studies using flow cytometry and microscopy indeed indicate that disparate *Salmonella*-macrophage encounters give rise to diverse subpopulations with dramatically different individual outcomes (Claudi et al., 2014). Recent advances in single-cell expression analysis provide an attractive approach to probe subpopulations and cell-to-cell variability (Shalek et al., 2014).

One of the best-studied cellular models of the host-pathogen interaction is infection of macrophages with the enteric pathogen *Salmonella enterica* serovar *typhimurium* (*S. typhimurium*). *S. typhimurium* is a facultative, intracellular *Enterobacteriaceae* that causes a range of enteric diseases in mammalian hosts. It has evolved to evade host defenses by sensing the transition from extracellular to intravacuolar environments, triggering a global modulation of gene expression that activates diverse virulence strategies, including alterations of pathogen-associated molecular patterns (PAMPs) and secretion of compounds to alter macrophage response (Galán and Collmer, 1999). In a single population, both in vitro and in vivo, *S. typhimurium* has been shown to display significant cell-to-cell variation in attributes such as growth rate, expression of virulence factors, and sensitivity to antibiotics (Claudi et al., 2014). Using receptors that recognize PAMPs (e.g., lipopolysaccharides [LPS] by Toll-like

receptor 4 [Tlr4]), macrophage detection of invading bacteria results in a transcriptional response that leads to the production of inflammatory cytokines and a variety of effector defense mechanisms (Rosenberger et al., 2000). Like *S. typhimurium*, macrophages and other innate immune cells have been observed to display extensive cell-to-cell variation upon exposure to even homogeneous ligands (Shalek et al., 2014). Recent studies using single-cell RNA sequencing (RNA-seq) have found subsets of dendritic cells with differential responses to LPS stimulation both *in vitro* (Shalek et al., 2014) and *in vivo* (Jaitin et al., 2014).

The heterogeneous, stochastic, and dynamic nature of both macrophage and *Salmonella* populations suggests that their interaction is likely to result in a variety of subpopulations with different, complex phenotypes (Helaine et al., 2010). Indeed, infection of macrophages with *Salmonella* generates well-documented diverse outcomes: some macrophages engulf the bacteria, while others remain uninfected (McIntrye et al., 1967); some macrophages lyse the ingested bacteria, while others are permissive to intracellular bacterial survival (McIntrye et al., 1967); and some macrophages will undergo cell death with bacterial release (Monack et al., 1996), while others survive and allow bacteria to multiply or persist intracellularly (Helaine et al., 2010). Despite long-standing observations of these diverse outcomes, we currently lack an understanding of the underlying molecular mechanisms in either the host or pathogen.

How macrophages integrate signals from bacterial PAMPs to determine cell fate and how bacteria regulate different virulence strategies to optimize pathogenicity in the host environment are fundamental to understanding infection biology and finding novel treatment options for infectious disease. Understanding the basis and significance of heterogeneity could inform strategies that result in a more beneficial outcome to the host. The discovery that distinct subpopulations of immune cells vary in their transcriptional responses to uniform PAMPs (Shalek et al., 2014) suggests that there may be some variability in the intrinsic state of the host cells that accounts for their differential response. Adding complexity, infection with live bacteria, which have diverse regulatory states themselves, might result in an even wider range of transcriptional interactions with implications for infection outcome.

Here, we set out to test whether and how distinct infection outcomes are reflected in the transcriptional status of individual host cells, to decipher the mechanistic underpinnings of this variation in both the host and bacteria and to examine the relationship of this variation to infection outcomes *in vivo*.

RESULTS

Heterogeneous Outcomes of *Salmonella*-Macrophage Encounters

To quantitatively characterize outcomes of individual *S. typhimurium*-macrophage interactions, we developed a fluorescent system using GFP-expressing bacteria stained with the red dye pHrodo (Experimental Procedures), which binds to the cell wall of bacteria and increases in fluorescence in the low pH environment of macrophage lysosomes. In the early stages after *S. typhimurium* challenge, there are three possible outcomes (Figures 1A and S1A): (1) no infection, (2) infection

with intracellular survival of a bacterium, and (3) infection resulting in an intracellular dead bacterium. While live bacteria display both red and green fluorescence, dead bacteria fluoresce only red due to degradation of GFP. Exposed, but uninfected, macrophages do not fluoresce (Figure 1A). Importantly, using the GFP and pHrodo reporters, we can distinguish cells that had been initially infected but cleared the infecting bacterium (pHrodo⁺, GFP⁺) from those that had never been infected (pHrodo⁻, GFP⁻). We used this system to follow mouse bone-marrow-derived macrophages (BMMs) exposed to pHrodo-stained, GFP-expressing *S. typhimurium* at an MOI of 1:1 for 24 hr. Importantly, we used a low MOI to ensure that infected macrophages are generally infected with only one bacterium.

Microscopy and fluorescence-activated cell sorting (FACS) revealed diverse phenotypes, including uninfected cells and cells infected with single or multiple and live (yellow) or dead (red) bacteria, as has been previously described (McIntrye et al., 1967) (Figures 1B and 1C). This variability is neither simply a transient phenomenon nor a mere outcome of the specific MOI chosen, since it is sustained throughout the 24-hr time course (Figure S1B) and with increasing MOIs (Figure S1C). To better quantify bacterial burden in single cells, we sorted macrophages according to fluorescence phenotype and enumerated the number of intracellular bacteria by plating for colony-forming units (CFUs) (Experimental Procedures). As expected, no viable bacteria were recovered from uninfected or pHrodo⁺, GFP⁻ (dead bacteria) infected cells. GFP⁺, pHrodo⁺ cells contained a range of bacteria (Figure 1D), which correlated with GFP intensity (Figures S1D and S1E) and showed reduction in bacterial burden during the 24-hr time course, similar to other studies using primary cells infected at low MOIs (Monack et al., 1996; Schwan et al., 2000). Thus, individual host cells may vary widely in their ability to phagocytose bacteria and/or restrict bacterial growth after uptake.

Single-Cell RNA-Seq of Exposed Macrophages Accurately Distinguishes Transcriptional Changes Associated with Extracellular and Intracellular Bacterial Detection

To determine if cell-to-cell transcriptional variation in host cells may underlie some of these different outcomes, we used FACS to sort single macrophages based on fluorescence and generated single-cell RNA-seq libraries from individually sorted cells, as well as a time course of sorted populations of 150 cells (using SMART-seq; Trombetta et al., 2014; Experimental Procedures). To ensure that cell sorting and library construction methods did not significantly alter the measured cellular response, we also analyzed a time course of bulk RNA-seq libraries from entire exposed populations (5×10^5 cells) using Illumina's Tru-seq library construction method (Experimental Procedures). We found good agreement in expression patterns (Figures S1F and S1G) and differentially expressed genes (Figures S1H and S1I) among all three datasets, despite lower sensitivity from single cells, particularly for low abundance transcripts, as previously reported (Shalek et al., 2014).

Single-cell profiles clearly distinguished cells with different phenotypic states. We used a list of 535 genes that are upregulated in exposed macrophages in our single-cell libraries (DEseq

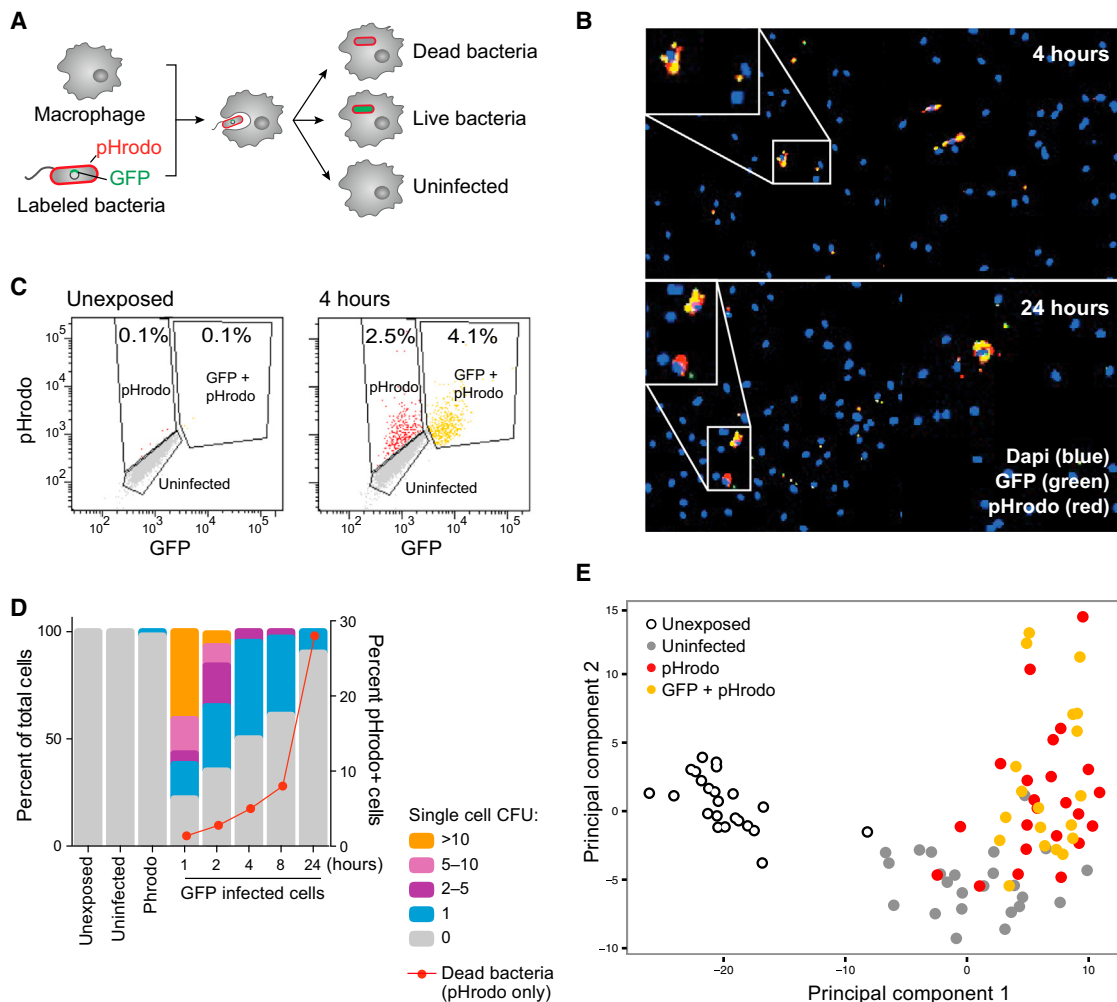


Figure 1. Heterogeneous Outcomes of BMM-Salmonella Encounters Are Captured by Single-Cell Expression Analysis

(A) Schematic representation of the experimental model, using BMMs infected with pHrodo-labeled, GFP-expressing *S. typhimurium*.
(B) Representative images of mouse BMMs exposed to *S. typhimurium* reveal heterogeneity in infection phenotype, including uninfected macrophages and infected macrophages containing live (yellow) or dead (red) bacteria at early (4 hr; top) and late (24 hr; bottom) time points.
(C) FACS analysis of fluorescently labeled populations (unexposed, left; exposed for 4 hr, right).
(D) CFUs enumerated from individual fluorescently labeled macrophages. Unexposed, uninfected, and pHrodo⁺, GFP⁻ cells had no or minimal surviving bacteria. GFP⁺ cells contain different numbers of cells over time (left y axis). The red line indicates the percentage of pHrodo-only infected cells, demonstrating the increase in the number of dead bacteria over time (right y axis).
(E) Single macrophages have distinct transcriptional responses depending on infection phenotype. 96 single cells from (C) were analyzed by RNA-seq and principle component analysis. The first two principal components (PC1 and PC2, 5% and 3% of the total variation, respectively; Table S1B) are shown.

See also Figure S1 and Table S1.

$p < 0.05$ and fold change >2 ; Experimental Procedures; Table S1B) to perform principal component analysis (PCA) on the single-cell expression data. PCA clearly distinguished both between exposed/unexposed macrophages (mostly on PC1) and between infected and uninfected macrophages (mostly on PC2) (Figures 1E and S1J). Taken together, the ability to distinguish these different phenotypes suggests that some pathways respond primarily to extracellular cues of bacterial presence, while others respond to intracellular cues.

To better understand these distinct responses, we calculated a metric we term the “intracellular-to-extracellular-response ra-

tio,” which reflects the magnitude of induction accounted for by bacterial infection verses extracellular bacterial exposure (Figure 2A; Experimental Procedures). We then classified genes based on their mode of response: cluster I contains genes that respond primarily to extracellular cues of bacterial presence, and cluster II contains genes that respond primarily to intracellular cues. Supporting our classification, many cluster I genes (responding to bacterial exposure, i.e., PC1 above) are known to be associated with the classic LPS response (e.g., Tnf and NF κ B) and many cluster II genes (responding to intracellular bacteria, i.e., PC2 above) are known to be associated with

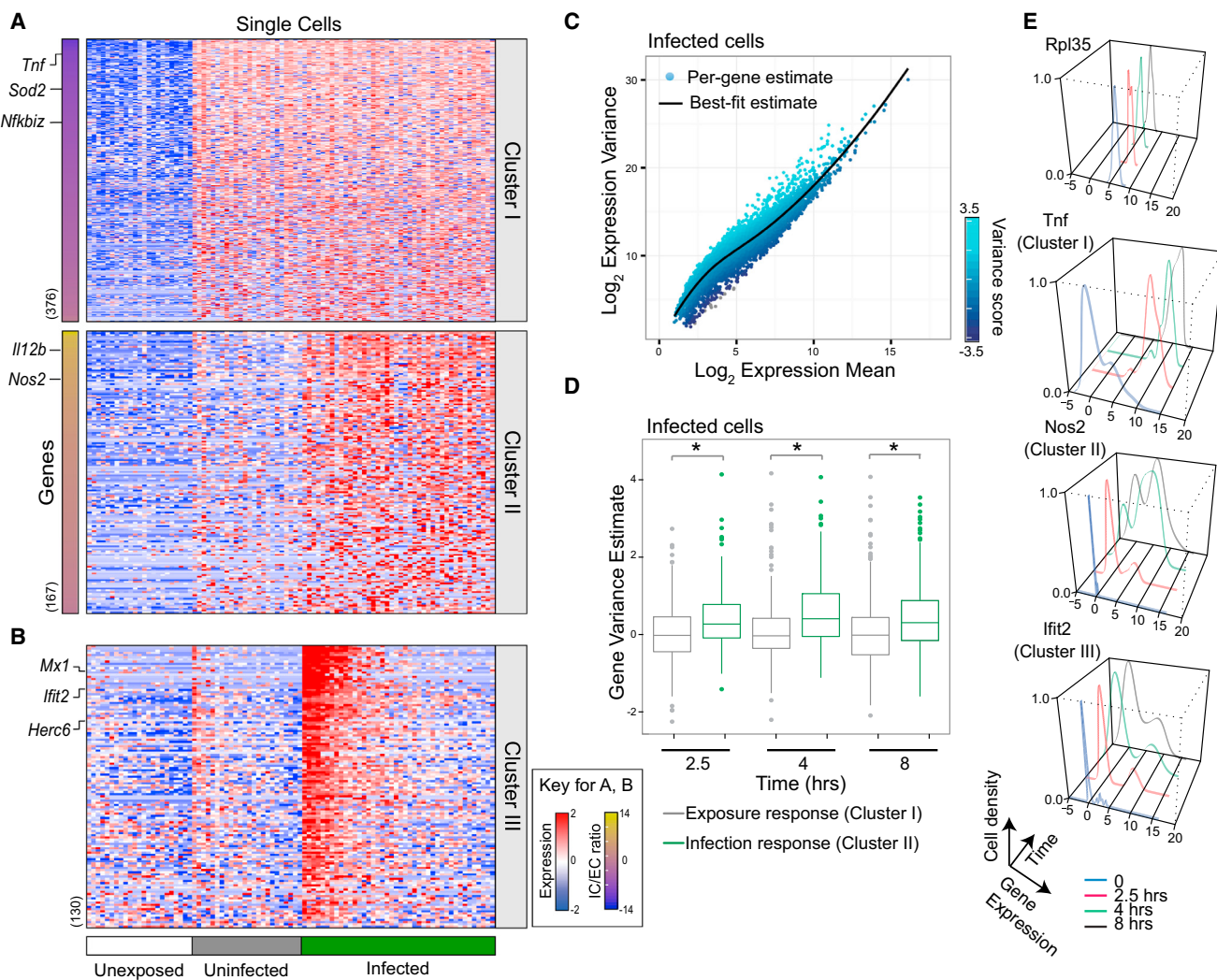


Figure 2. Single-Cell Expression Profiling Reveals Macrophage Subpopulations in Infected Cells

(A) Expression levels of genes (rows) in single BMMs (columns) were measured using single-cell RNA-seq after exposure to *S. typhimurium* and grouped by their infection phenotype (unexposed [white, n = 23], uninfected [gray, n = 24], and infected [green, n = 42]). Genes are categorized into two clusters as described. The number of genes in each cluster is denoted next to the heatmap. Genes are arranged by the extracellular or intracellular ratio (IC/EC ratio; left bars indicate the distribution of scores for each cluster; Table S2A).

(B) Analysis of gene correlations across single cells revealed a cluster of bimodally expressed genes in infected cells (cluster III). Cells in (A) and (B) are sorted according to average expression of cluster III.

(C) Highly variable genes in infected cells are enriched for immune response pathways (Table S2C). Localized regression was used to estimate the mean/variance relationship for genes in infected macrophages. Genes were assigned a variance score based on their distance from the fitted relationship (solid line).

(D) Box plots of variance scores for either exposure (cluster I) or infection response genes (cluster II), at three time points following infection, are shown. Infection response genes have reproducibly higher variance than exposure response genes ($p < 0.01$ by Wilcoxon rank-sum test; Table S2D).

(E) Representative examples of single-cell gene expression distributions in infected cells from clusters I, II, and III.

See also Figure S2 and Table S2.

antibacterial defense (e.g., Nos2 and II12b). While cluster I was relatively stable across different time points, many genes in cluster II were also found to be induced in uninfected cells at later time points (Figure S2A). At these early time points (8 hr), we did not detect differences between pHrodo⁺,GFP⁺ and pHrodo⁺,GFP⁻ infected cells, so these groups were merged for further analysis. While it also will be interesting to study possible differences between these infected populations at later time points

(12–24 hr), in this work we focused on analyzing the variation between single-infected cells, as discussed below, for a third cluster (cluster III).

Bimodal Induction of Type I IFN Response Genes in Infected Macrophages

It has been previously suggested that immune networks may be structured to produce subpopulations of cells with distinct

physiologies (Jin et al., 2014). Thus, we searched for additional clusters of genes that co-vary across multiple time points using weighted gene correlation network analysis (**Experimental Procedures**). We identified three gene clusters (clusters III, IV, and V) that met these criteria (Figures 2B, S2B, and S2C). Cluster III was particularly interesting as it was significantly enriched for the type I interferon (IFN) response (Table S2B), which has previously been shown to play a role in non-canonical inflammasome activation in response to infection with *S. typhimurium* (Rathinam et al., 2012). Cluster III is induced in approximately one-third of infected macrophages beginning at 4 hr post-exposure and continues to show bimodal expression at 8 hr, suggesting that this induction is not a transient phenomenon (Figure S2C). Notably, this cluster is also induced in uninfected cells at 8 hr. This may not be surprising given that interferon is a secreted soluble factor that may result in a non-cell-autonomous induction of this cluster later in uninfected cells (Honda and Taniguchi, 2006). Cluster IV is enriched for cell-cycle genes, is bimodal in unexposed cells, and decreases in expression upon exposure. It does not differentiate between uninfected, pHrodo⁺,GFP⁻, or pHrodo⁺,GFP⁺ cells at any time point (Mann-Whitney test, $p > 0.05$). Cluster V is highly expressed in all unexposed cells and has reduced expression in some cells upon exposure (becomes bimodal).

We verified representative expression patterns in cluster II and III genes using single-molecule RNA fluorescence *in situ* hybridization (FISH). Using pHrodo to identify infected cells, we confirmed both the induction of cluster II in all infected cells (e.g., Il1b, Il12b, and Nos2) and the bimodal induction of cluster III (e.g., Irf7 and Ifit2) in infected cells (Figure S2D). This method also allowed us to directly verify that the expression of cluster III was not correlated with GFP fluorescence, indicating that the heterogeneity we observe is not merely due to differences in bacterial burden (Figure S2E). It is important to note that single-cell analysis was required to identify the induction of cluster III between infected and uninfected cells. Analyzing sorted populations (Figure S2F) failed to identify these genes as they are not highly induced when averaged over all cells.

Infected Macrophages Display High Cell-to-Cell Variation in Genes from Immune Response Pathways

Motivated by the high variation of the type I IFN response between infected cells, we next examined whether immune responsive pathways in general show high variation between infected cells. We developed a scoring system based on localized linear regression to estimate each gene's variance in a manner that is largely independent of mean expression (**Experimental Procedures**; Figure 2C). We then tested each pathway (as annotated in MSigDB) for its enrichment of variable genes using gene set enrichment analysis (GSEA) (**Experimental Procedures**) and identified those pathways that are consistently variable across multiple time points post-exposure in infected macrophages. As expected from previous reports (Shalek et al., 2013), many pathways associated with housekeeping functions, such as ribosome function and oxidative phosphorylation, show consistently low variation. On the other hand, many pathways involved in the immune response, including Toll-like receptor signaling,

cytokine-cytokine receptor interactions and Rig-I receptor signaling, show consistently high variance for up to at least 8 hr after bacterial infection (Table S2C). Furthermore, at all time points evaluated, genes induced primarily by the intracellular bacterial signals of infection (cluster II) were more variable than those induced by extracellular exposure cues in infected macrophages (cluster I; Figures 2D and 2E). This difference suggests that within a seemingly homogenous population of infected cells there exists extensive cell-to-cell variation in the response to infection. This variation is characteristic of responses to intracellular cues of infection more than those to extracellular cues, possibly due to variability in intracellular bacterial state, bacterial burden, or bacterial clearance.

Intracellular Tlr4 Signaling through Trif and Irf3 Determines the Activation of the Type I IFN Response in Infected Cells

It has been previously suggested that LPS accounts for all the transcriptional responses to bacterial exposure, including intracellular bacterial detection (Rosenberger et al., 2000). LPS is detected by Tlr4, which signals through two different adaptor proteins Myd88 or Trif, depending on whether LPS is sensed at the cell membrane or at a phagosome, respectively (Kagan et al., 2008). Specifically, induction of the type I IFN response was shown to be mediated by Trif through the interferon regulatory factors Irf3 and Irf7 (Fitzgerald et al., 2003). We hypothesized that the differential activation of cluster III in infected cells may depend on key components of Tlr4/LPS signaling. Thus, we measured the transcriptional response of wild-type (WT), *Tlr4*^{-/-}, *Trif*^{-/-}, and *Myd88*^{-/-} immortalized BMMs (iBMMs) (**Experimental Procedures**) to infection with *S. typhimurium* at the single-cell level by monitoring an expression signature of 96 genes representative of clusters I, II, and III using qRT-PCR (Figure S3A; Table S2D; **Experimental Procedures**). Compared to WT cells, we found ablated activation of all three clusters in *Tlr4*^{-/-} cells (Figure 3A), suggesting that LPS and Tlr4 sensing dominate the transcriptional responses to infection, as previously suggested (Rosenberger et al., 2000). Next, to analyze the transcriptional response to infection of *Myd88*^{-/-} and *Trif*^{-/-} cells, we defined a “Trif-Myd88 ratio” to assess the dependence of each gene's expression on Trif versus Myd88 (Figure 3A; **Experimental Procedures**). We found that regulation is partitioned in cluster I and cluster II, with some genes being regulated by Myd88 and some by Trif. Cluster III, on the other hand, is regulated almost entirely through Trif (Figure 3A). Interestingly, Myd88 knockout upregulated this cluster in both infected and uninfected cells, which may indicate Myd88-dependent negative feedback inhibition of cluster III induction.

Next, we infected BMMs from WT, *Irf3*^{-/-}, and *Irf7*^{-/-} mice and found that knockout of Irf3 exclusively ablates the activity of cluster III in infected cells, while Irf7 knockout enhances its activation (Figure 3B). This suggests that while Trif has a role in the induction of all clusters, its activation of Irf3 is specific to cluster III and occurs in only a subset of infected cells. Based on these results, we tested two known inhibitors of the type I IFN response, BX795 (a TBK1 inhibitor; Lee et al., 2013) and BI2536 (a PLK inhibitor; Chevrier et al., 2011), and found that

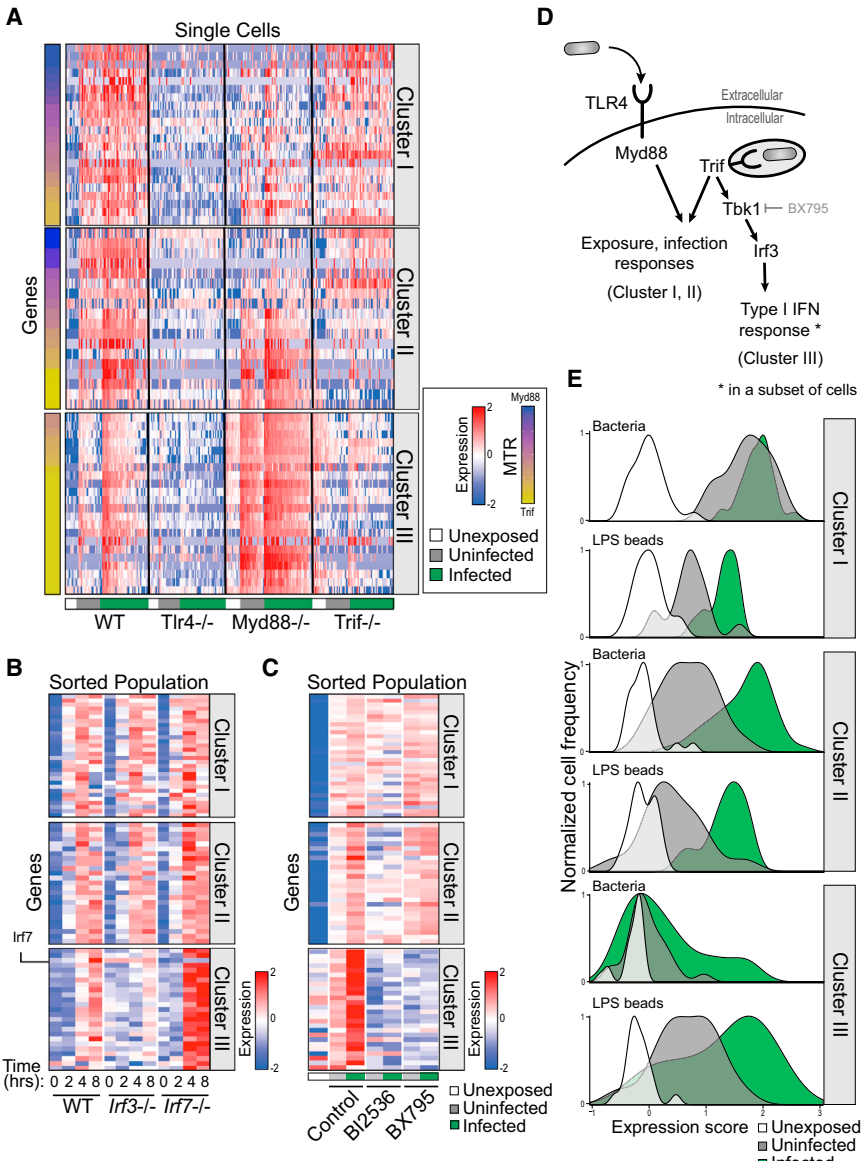


Figure 3. Analysis of Macrophage Pathways Regulating the Bimodal Induction of the Type I IFN Response

(A) Induction of cluster III is solely dependent on Trif signaling. iBMMs from WT, *Tlr4*–/–, *Myd88*–/–, or *Trif*–/– mice were infected with *S. typhimurium*, and expression of single cells was analyzed. Genes are arranged by a score summarizing their Myd88 or Trif dependence (MTR, left bars indicate the distribution of scores for each cluster; Table S3A).

(B) BMMs from *Irf3*–/– and *Irf7*–/– mice were infected with pHrodo-stained, GFP-labeled *S. typhimurium*. Decreased induction of representative genes from cluster III was evident in *Irf3*–/– cells, compared to increased induction in *Irf7*–/– cells (Table S3B).

(C) BMMs were infected with pHrodo-labeled, GFP-labeled *S. typhimurium*, in the presence of BI2536 and BX795. While BI2536 inhibited mostly cluster III genes but also genes from clusters I and II, BX795 specifically inhibited only the induction of cluster III genes (Table S3C).

(D) Schematic representation of the gene regulatory networks that control the response of macrophages to *S. typhimurium* infection. The induction of the type I IFN response is due to activation of Tbk1 and Irf3 in only a subset of infected cells. (E) Plots summarize the expression of each gene cluster in BMMs infected with live bacteria (top) or with LPS-coated beads (bottom) using a weighted average of scaled expression values (x axis) versus the frequency of single cells (y axis). In contrast to the bimodal activation of the type I IFN response in cells infected with live bacteria, there were a much higher proportion of cells that activated cluster III among the cells that had taken up LPS-coated beads.

See also Figure S3 and Table S3.

while BI2536 inhibited genes from all three clusters, BX795 specifically inhibited only cluster III genes (Figure 3C).

Overall, these data are consistent with a model in which single-cell transcriptional responses of macrophages to *S. typhimurium* exposure include a homogenous inflammatory response to bacterial exposure (cluster I) and a more variable antibacterial response to intracellular invasion (cluster II). Both responses are mediated by a combination of Myd88 and Trif activity. A third response also occurs in a fraction of infected cells, involving intracellular LPS detection by Tlr4, which signals through Trif and Irf3 and results in a bimodal type I IFN response (Figure 3D).

Live Bacteria, but Not LPS-Coated Beads, Elicit a Variable Type I IFN Response in Infected Cells

To study the molecular mechanisms that lead to activation of the type I IFN response in only a subset of infected macro-

phages, we explored this variation over time and in different infection models. A recent study showed that in dendritic cells exposed to LPS, the type I IFN response is initially bimodally expressed

and then uniformly induced over the entire population by 4 hr due to paracrine signaling (Shalek et al., 2014). In contrast, we have observed that the type I IFN response in macrophages infected with bacteria had sustained bimodal expression during the entire time course (8 hr). While we also observe additional non-cell-autonomous effects of type I IFN activation at late time points in uninfected cells (reminiscent of the induction pattern seen in dendritic cells exposed to LPS), these additional effects do not eliminate the bimodal response in cells infected with live bacteria. This discrepancy between a transient and sustained bimodal type I IFN response might be due to a difference between stimulation with soluble LPS versus LPS associated with an intact, infecting bacterium, other additional components of an intracellular bacterium, or a difference between host-cell types. To examine these possibilities, we compared transcriptional responses between

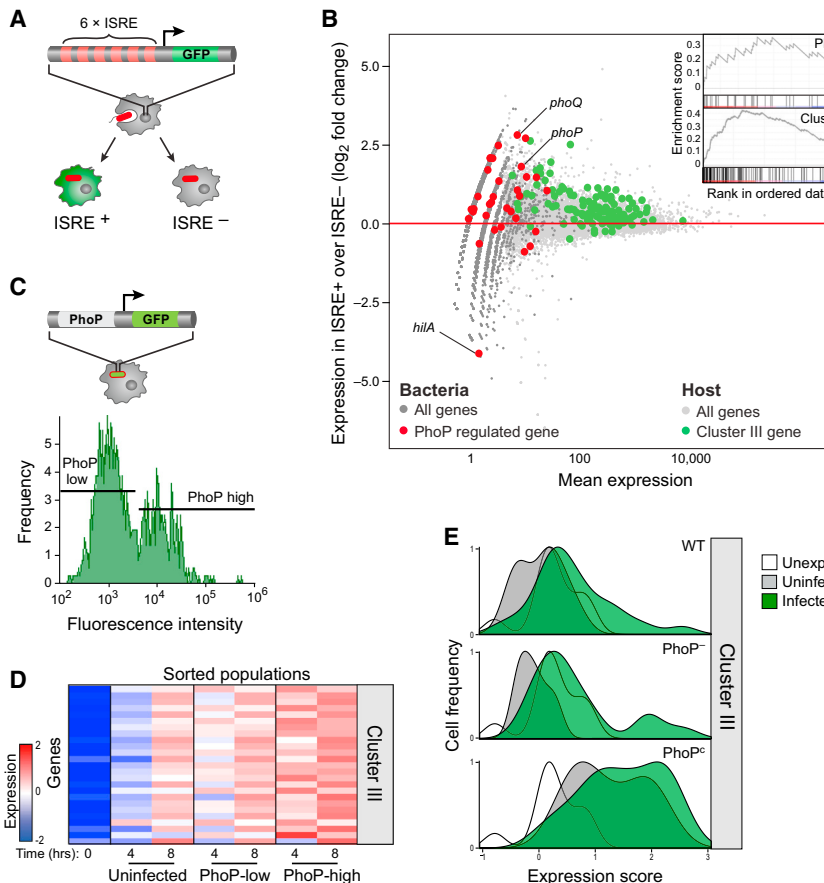


Figure 4. Heterogeneity of the Invading Bacterial Populations Shapes a Heterogeneous Host Type I IFN Response

(A) Schematic of iBMMs with a transcriptional reporter (6XISRE-GFP) of the activity of the type I IFN response.

(B) An MA plot of the induction levels of host and bacterial transcripts in ISRE-positive over ISRE-negative cells (y axis) versus the average absolute read counts (x axis) is shown. Infected ISRE-positive cells expressing high levels of cluster III genes (green dots) are infected with bacteria expressing higher levels of PhoP-regulated genes (red dots) compared with ISRE-negative cells. Inset indicates the enrichment of PhoPQ-regulated genes and cluster III (GSEA analysis, $p = 0.007$ and $p < 0.001$, respectively).

(C) Schematic of *S. typhimurium* with a transcriptional reporter of PhoP activity (*phoP*-GFP, top). PhoP displayed bimodal activity in infected macrophages, as analyzed by FACS (bottom, infected cells were identified by pHrodo).

(D) Cells infected with bacteria expressing high *phoP*-GFP show higher expression of cluster III genes compared to cells infected with bacteria expressing low *phoP*-GFP.

(E) Plots summarize the expression of the type I IFN response in BMMs infected with WT, PhoP^- , or PhoP^c strains of *S. typhimurium* with a weighted-average-based score (x axis) and display it versus the frequency of single cells (y axis). Infection with PhoP^c results in induction of the type I IFN response in almost all infected cells, compared to cells infected with WT or PhoP^- strains (Table S4).

See also Figure S4 and Table S4.

macrophages exposed to live *S. typhimurium* and macrophages exposed to fluorescently labeled latex beads coated with LPS extracted from *S. typhimurium* (Experimental Procedures). Macrophages exposed to LPS-coated beads indeed activated clusters I, II, and III (Figure S3B). To compare between different subpopulations after treatment with LPS-coated beads or live bacteria, we summarized the expression of each cluster with a single “eigen-gene” and calculated the density of these values across single cells (Experimental Procedures). Interestingly, compared to cells infected with bacteria, a much higher proportion of cells activated cluster III among the cells that had taken up LPS-coated beads (Figures 3E and S3C). This difference in activation was not the result of different levels of LPS exposure, since there was a uniform, but reduced, induction of clusters I and II in cells exposed to LPS-coated beads compared to live bacteria (Figure 3E). This result suggests that there may be a bacterial factor that varies (e.g., displays bimodal behavior) among individual invading bacteria that accounts for the heterogeneous expression of the type I IFN response upon bacterial uptake. However, on isolated LPS-coated beads, this factor’s heterogeneity is less pronounced. We also observe a stronger non-cell-autonomous effect in uninfected cells exposed to LPS-coated beads that may be due to the release of more interferon from infected cells.

The Variation in the Type I IFN Response Is Driven by Bimodal Activity of the Bacterial PhoPQ Two-Component System in Infecting Bacteria

Based on the hypothesis that the bimodal induction of the type I IFN response may be due to heterogeneity in the infecting bacteria, we sought to identify bacterial factors that may influence type I IFN expression. In the nucleus, Irf3 binds to the IFN-stimulated response element (ISRE; Honda and Taniguchi, 2006), a process that can be monitored at the single-cell level using a fluorescent reporter and FACS. We used iBMMs stably transduced with an ISRE fused to GFP as a reporter of the type I IFN response in individual cells (iBMM-ISRE; Figure 4A; Experimental Procedures). We infected iBMM-ISRE with RFP-expressing bacteria, sorted ISRE-positive and ISRE-negative infected populations, and used RNA-seq to simultaneously profile host and bacterial transcripts in each population (Experimental Procedures). We confirmed that indeed, the type I IFN response is more strongly induced in sorted ISRE-positive cells compared to sorted ISRE-negative cells (induction > 1.5 -fold, $p_{\text{FWER}} < 0.05$ GSEA; Figure 4B). Comparing the expression of bacterial pathways in these two populations, we found that targets of the bacterial transcription factor PhoP were significantly upregulated in ISRE-positive cells compared to ISRE-negative cells ($p_{\text{FWER}} < 0.05$, GSEA analysis; Figures 4B and S4A). In fact, both *phoP* and the associated *phoQ* gene were in the top 50

differentially expressed bacterial genes between these two populations, while *hilA*, a gene known to be repressed by PhoP, was among the most downregulated (Figure 4B). PhoP is the response regulator of a two-component system (with its cognate sensor kinase PhoQ) that is activated after a *Salmonella* bacterium is taken up by macrophages and induces the expression of genes important for intramacrophage survival (Groisman, 2001). We therefore hypothesized that variation in PhoP activity may underlie the variation in the type I IFN response.

To test this hypothesis, we first assessed the variation in PhoP activity among intracellular bacteria using an engineered reporter with a PhoP-sensitive promoter upstream of GFP (*phoP-GFP*). We infected BMMs with pHrodo-labeled *S. typhimurium* carrying the *phoP-GFP* reporter. Consistent with our hypothesis, we found that PhoP indeed had bimodal activity in the population of infected cells (Figure 4C). We then sorted GFP-high and GFP-low macrophage populations and confirmed the difference in the expression levels of *phoP* between GFP-high- and GFP-low-infected cells by quantitative PCR (Figure S4B). We found increased expression of the type I IFN response in the PhoP-high-, compared to PhoP-low-, infected cells (over a 5-fold increase at 4 hr and over a 3-fold increase at 8 hr, $p < 0.05$ at both time points by a bootstrap analysis; Figures 4D and S4C). Importantly, this difference in type I IFN expression was not observed when using a constitutive GFP reporter (Figure S4D), implying that the host cell is not responding primarily to differences in bacterial burden but to unique properties of PhoP-low and PhoP-high bacteria. No significant difference was observed in the expression of cluster I or cluster II between PhoP-high- and PhoP-low-infected cells (Figure S4E). Together, these results demonstrate a correlation between PhoPQ activity and the host type I IFN response.

To establish whether PhoP activity functionally determines type I IFN expression in the host cell, we infected macrophages with a *phoP*-null mutant (PhoP⁻) and a strain with a single mutation in the *phoQ* gene that renders it constitutively active (PhoP^c) (Miller and Mekalanos, 1990). Analyzing sorted infected populations, we found that cells infected with PhoP^c bacteria induce the type I IFN response more strongly than WT infected cells, while cells infected with PhoP⁻ bacteria induce a weaker response (Figure S4F). Interestingly, at the single-cell level, we found that infection with PhoP^c, like stimulation with LPS-coated beads, increased the fraction of cells inducing the type I IFN response (Figure 4E). PhoP^c exposure also elicited a type I IFN response in more uninfected cells than did WT or PhoP⁻ exposure, again implicating non-cell-autonomous effects. Similar proportions of PhoP⁻ and WT-infected cells induced the type I IFN response. Notably, no differences in the induction of clusters I or II were observed between the *phoP* mutants (Figures S4F and S4G). These results indicate that the type I IFN response is both correlated with and functionally the result of the activity of PhoPQ.

Intracellular Recognition of PhoPQ-Mediated LPS Modifications Results in Induction of the Type I IFN Response

PhoPQ is a global regulator of *S. typhimurium* virulence, involved in numerous cellular processes, including activation of type III secretion and cell-wall alterations (Groisman, 2001). To test

which of these processes might impact host type I IFN expression, we treated BMMs with supernatants or heat-killed bacteria from PhoP^c and PhoP⁻ cultures. Culture supernatants failed to elicit a differential type I IFN response, excluding the involvement of factors secreted by PhoP-regulated type III secretion systems (Figure S5A, bottom). Treatment with heat-killed cultures elicited a differential type I IFN response, corresponding to infection with live mutants (Figure S5A, top). This result would be consistent with cell-wall alterations playing a role in type I IFN induction.

These results, together with reports implicating PhoPQ as regulator of LPS modification (Guo et al., 1997), led us to hypothesize that PhoPQ may exert its influence on the type I IFN response through LPS modifications. To test this hypothesis, we extracted LPS from WT, PhoP⁻, and PhoP^c strains and used them to stimulate BMMs. We used a standard limulus amebocyte lysate (LAL) test to normalize LPS concentrations from the different extractions (Experimental Procedures). Similar to infection with live bacteria, LPS from PhoP^c induced higher levels of type I IFN-responsive genes compared to WT (over a 9-fold increase at 2 hr post-exposure, $p < 0.05$ by bootstrap analysis), while LPS from PhoP⁻ induced lower levels (over a 4-fold decrease at 2 hr post-exposure and over a 40-fold decrease at 4 hr post-exposure, $p < 0.05$ at each time point by bootstrap analysis; Figures 5A and S5B). Notably, stimulation of cells with commercially available LPS from *S. typhimurium* resulted in induction levels similar to LPS from WT (Figure S5C), validating our extraction method and quantifications of LPS. These results demonstrate that PhoPQ's modification of LPS is responsible for the induction of the type I IFN response.

Next, we sought to test whether variations in LPS on the surface of individual bacteria are sufficient to drive a bimodal type I IFN response. As it is not currently technically possible to query LPS modifications at the single-cell level, we simulated a heterogeneous population of "bacteria" by coating red fluorescent beads with LPS from the PhoP⁻ strain and green fluorescent beads with LPS from the PhoP^c strain. We then treated macrophages with an equal mixture of red and green LPS-coated beads, sorted macrophages according to the color of beads they had taken up, and examined induction of genes at the single-cell level. We used a low MOI treatment to preclude the uptake of more than one bead in a given cell. We observed no difference in the induction of cluster I and cluster II between cells that took up beads with LPS from PhoP⁻ or PhoP^c strains (Figure 5B, inset). In contrast, there was a clear shift in cluster III induction, with induction of this cluster in a larger proportion of cells taking up beads coated with PhoP^c LPS (74%) than in cells taking up beads coated with PhoP⁻ LPS (26%) (Figure 5B; $p = 0.003$ using a two-population proportion z test). Similar to exposure to live bacterial strains, a non-cell-autonomous effect was also evident in uninfected cells exposed to beads coated with PhoP^c LPS (Figure S5D). As controls, induction levels of green or red beads coated with LPS extracted from WT *S. typhimurium* were similar, no induction was observed using beads not coated with LPS, and comparable results were obtained in bead-color swap experiments (Figure S5D). Additionally, no significant expression changes were noted between our brightest and dimmest cells infected with beads coated with WT LPS (demonstrating that differences in LPS burden

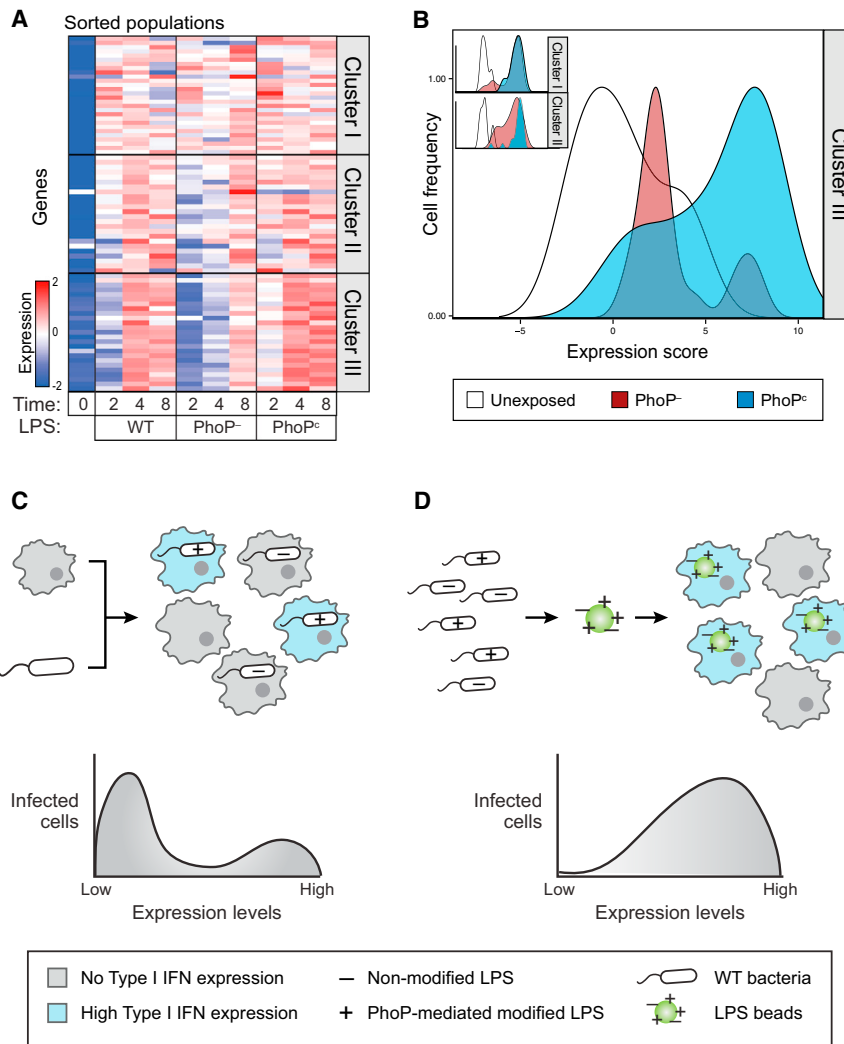


Figure 5. Cell-to-Cell Variation in LPS Modifications Mediated by PhoPQ Determines the Bimodal Induction of the Type I IFN Response

(A) Cells stimulated with LPS from the PhoP^c strain induce higher levels of type I IFN responsive genes compared to cells stimulated with LPS from the WT strain. Cells stimulated with LPS from the PhoP⁻ strain showed less induction of this cluster (Table S5A).

(B) BMMs were stimulated with a mixture of red and green fluorescent beads coated with LPS extracted from PhoP^c and PhoP⁻, respectively. Induction of the type I IFN response is evident in a larger proportion of cells taking up beads coated with PhoP^c LPS (blue) than in cells taking up beads coated with LPS from the PhoP⁻ strain (red). 74% of PhoP^c, compared to 26% of PhoP⁻, induce more than the highest unexposed cells (white); $p = 0.003$ using a two-population proportion z test (Table S5B).

(C and D) Schematic representation of the differences in the responses of BMMs to infection with live bacteria and to stimulation with LPS-coated beads. Live bacteria are more heterogeneous than LPS-coated beads.

See also Figure S5 and Table S5.

cannot explain our results; Figure S5E). These results indicate that the bimodal type I IFN response within a population of infected cells can be recapitulated by infecting with LPS-coated beads from PhoP⁻ and PhoP^c mutant strains. Thus, differences in the induction of the type I IFN response are determined not only by the internal state of the host cells or non-cell-autonomous effects between host cells but also as a direct result of the state of the infecting bacterium. Specifically, the extent of PhoPQ-regulated LPS modification of the invading bacterium accounts for the differences among individual intracellular “bacteria,” and this drives different host responses (Figures 5C and 5D).

LPS Modifications Mediated by PhoPQ Impact the In Vivo Type I IFN Response and Infection Outcome

To confirm bimodal induction of the type I IFN response of infected macrophages that had been naturally differentiated in vivo, we collected all cells from the peritoneal cavity of mice (Experimental Procedures) and immediately infected them with GFP-labeled *S. typhimurium*. After 2 hr, we sorted infected resi-

dent macrophages (Figure S6A) and analyzed the induction of clusters I, II, and III. We found similar expression patterns for all three clusters to those we observed in infected BMMs. Importantly, we found bimodal induction of the type I IFN response (Figure 6A), indicating that this pattern of response to infection is generalizable to macrophages from different tissues.

To determine the physiological importance of the relationship between bacterial PhoPQ, LPS variation, and the host type I IFN response, we next sought to demonstrate the same correlation in mice using LPS stimulation. We injected mice intraperitoneally (i.p.) with sub-lethal, normalized doses of LPS extracted from WT, PhoP⁻, and PhoP^c strains (Experimental Procedures). After 2 hr, we isolated peritoneal macrophages from treated mice (Figure S6A) and analyzed the in vivo induction of clusters I, II, and III. Notably, LPS from the PhoP^c strain induced higher levels of cluster III, while LPS from the PhoP⁻ strain had the opposite effect, thereby mirroring the in vitro infection results (Figure 6B). Minimal differences in clusters I and II were observed in vivo, similar to what was observed in vitro. Additionally, we confirmed the *Irf3* dependence of cluster III by performing this same experiment in *Irf3*^{-/-} mice (Figure 6B). These results demonstrate a relationship between modified LPS and type I IFN expression in mice and suggest that PhoPQ is an important regulator of the type I IFN response in vivo.

Ifnar1^{-/-} mice were previously shown to have prolonged survival after *S. typhimurium* challenge, demonstrating an important role for the type I IFN response in determining infection

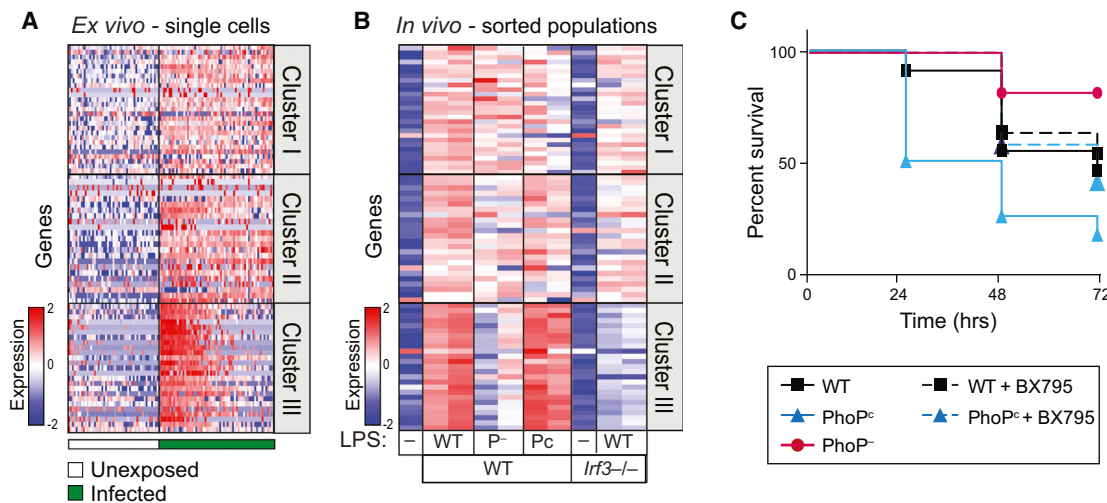


Figure 6. LPS Modifications Mediated by PhoPQ Impact In Vivo Infection Outcomes

(A) Like BMMs, peritoneal macrophages, when infected ex vivo with GFP-labeled *S. typhimurium*, show bimodal induction of cluster III. (Table S6A). (B) Activation of the type I IFN response in vivo was enhanced after stimulation with LPS extracted from PhoP^c and reduced after stimulation with LPS extracted from the PhoP⁻ strain, compared to LPS extracted from WT *S. typhimurium*. As a control, no induction of the type I IFN response was measured in *Irf3*^{-/-} mice (Table S6B). (C) Mice challenged with LPS extracted from PhoP^c (blue, n = 12) showed reduced survival compared to mice challenged with WT LPS (black, n = 11). Inhibition of the type I IFN response by co-administration of BX795 improved survival from PhoP^c challenge, restoring it to WT levels (dotted blue, n = 12). Mice challenged with LPS extracted from PhoP⁻ (red, n = 11) showed enhanced survival compared to WT. See also Figure S6 and Table S6.

outcome (Robinson et al., 2012). We thus sought to test whether bacterial PhoPQ activity, through its activation of the type I IFN response, has an impact on infection outcome similar to ablating signaling downstream of Ifnar. Because PhoP⁻ and PhoP^c strains are both avirulent in mice (Miller and Mekalanos, 1990), we turned to a mouse model of LPS-induced septic shock. Septic shock, a systemic response to severe bacterial infection, is considered an important determinant of infection outcome, as it is often associated with high mortality (Morrison and Ryan, 1987). We induced septic shock in mice using high doses of LPS extracted from WT, PhoP⁻, or PhoP^c *Salmonella* strains and monitored survival. Mice injected with normalized amounts of PhoP^c LPS had significantly higher mortality rates than mice injected with WT LPS (Figure 6C; p = 0.003, log rank test). Meanwhile, mice challenged with PhoP⁻ LPS had higher survival rates compared to WT LPS challenged mice (p = 0.003, log rank test). We then co-administered LPS extracted from PhoP^c with the small molecule BX795, which we had previously shown to be a specific inhibitor of the type I IFN response (Figure 3C) and found significantly improved survival rates of the PhoP^c LPS challenged mice (p = 0.031, log rank test). We further verified that these effects were mirrored in the transcriptional responses of peritoneal macrophages. The co-administration of the BX795 inhibitor, together with LPS extracted from a PhoP^c strain, abrogated the induction of type I IFN response, reducing it to levels similar to mice challenged with WT LPS (Figure S6B). These results demonstrate that the extent of LPS modification by PhoPQ and its interaction with the cognate host type I IFN response are important determinants of infection outcome in vivo.

DISCUSSION

A General Approach to Characterize the Transcriptional Underpinnings of Phenotypic Heterogeneity in Host-Pathogen Encounters

Heterogeneity between individual cells is a common feature of dynamic cellular processes, including signaling, transcription, and cell fate (Elowitz et al., 2002). Phenotypic heterogeneity has similarly long been observed as an important feature of infection, resulting from individual cellular encounters that involve highly dynamic, adaptable cells and bacteria. However, to date, tools for probing the variation in host-pathogen interactions have been limited and studies of host-pathogen interactions have relied on bulk, population-level measurements. Thus, the specific mechanisms underlying this heterogeneity remain largely unknown and demonstrations of its effects in vivo are still incomplete. Here, we present a generalizable approach to identify and characterize transcriptional heterogeneity in subpopulations that may underlie phenotypic variation of infection by directly probing individual macrophage-bacteria encounters. We use microscopy to map infection phenotypes to transcriptional states as determined by single-cell RNA-seq, resulting in a high-resolution view of host-pathogen interactions.

Heterogeneity of Pathogen Populations as a Mechanism to Shape the Host Immune Response

We revealed specific genetic pathways that show unexpectedly large amounts of variation between what otherwise appears to be identically infected cells. One such pathway is the type I IFN response, which was only fully induced in a fraction of

infected macrophages. Upon further investigation, we found that the level of type I IFN induction in infected macrophages is determined by the level of PhoPQ activity in the invading bacterium (Figures 4D and 4E).

Heterogeneity of transcriptional responses has been reported and traditionally ascribed to stochastic variation or intrinsic state of the cell. For example, a recent publication suggests that the induction of the antiviral response in dendritic cells in response to bacterial LPS stimulation is dependent on the existence of a relatively small fraction of “precocious” cells that initiate the response that eventually spreads through the population via paracrine responses (Shalek et al., 2014). Our work highlights the fact that immune activation also depends on the state of the invading pathogen. This demonstrates an alternative source of host heterogeneity, whereby intrinsic variation in bacterial populations shapes the host immune response. The *in vivo* experiments indicate functional consequences during infection of the variable factors identified and point to heterogeneity as a feature of pathogen populations that impacts infection.

Studies of the Immune Response in the Context of Heterogeneous Bacterial Ligands

Different types of LPS have been shown to produce dramatically different host responses, with diversity in LPS structures having been described between bacterial populations exposed to different environments (Paciello et al., 2013), different bacterial mutants (Guo et al., 1997), and different LPS variants, resulting from different isolation procedures (Gutschow et al., 2013). We now show that heterogeneity also exists within a single population of wild-type bacteria. While this alone may not be altogether surprising, we demonstrate that this variability has functional consequence.

There is accumulating evidence that cell-to-cell variation exists in the expression of numerous bacterial factors in addition to LPS, including other PAMPs and virulence factors. For example, bacteria in the same culture can be in either a motile (flagella-positive) or a non-motile (flagella-negative) state (Cummings et al., 2006) or contain very different levels of effector proteins (Schlumberger et al., 2005). Importantly, immunological studies of such molecules have often implicitly neglected pathogen variability by relying on measurements of host-cell response to what is assumed to be a homogenous ligand, ignoring the reality that such ligands actually result from a heterogeneous, diverse population. In this study, we show that coating beads with LPS isolated from a pooled, heterogeneous population of bacteria artificially limits heterogeneity by mixing modified and unmodified LPS stemming from different individual bacteria onto the same bead. This system thus fails to recapitulate the diversity of actual pathogens and the diversity of the cognate host response. The heterogeneity of the host response can be restored by reinstating the heterogeneity in the chemical stimulus (coating two sets of beads with LPS isolated from two different bacterial mutants (phoP^- and phoP^c), followed by mixing of the two sets of beads [Figure 5D]).

Importantly, although we show that bacterial heterogeneity in PhoPQ-mediated LPS modification has a significant effect in mediating the host type I IFN response, this is by no means the only determining factor and is not solely responsible for the het-

erogeneity we observe. It is well known that the type I IFN response can be induced by non-cell-autonomous effects, such as paracrine signaling, given that interferon is a soluble secreted molecule (Honda and Taniguchi, 2006). Indeed, we also observe induction of this cluster in uninfected cells at later time points during infection (Figure S2C). We also observe this paracrine signaling in a larger fraction of uninfected cells treated with PhoP^c LPS, probably due to the fact that a larger fraction of infected cells are inducing the type I response.

We also observe the induction of the type I IFN response in a small population of cells infected with the PhoP^- strain (Figure 4E). This demonstrates that infection with PhoP mutant strains does not perfectly mirror the naturally occurring low and high PhoP populations that we observe during WT infection, as genetically altering the strains cannot provide the fine-tuned regulation and variation that occurs in WT bacteria. It is a relatively common phenomenon that genetic knockout does not abolish an activity for a protein that is revealed by overexpression (Kitano, 2004); in fact, it has been demonstrated before that the PhoP^- strain does not always show the opposite phenotype of the phoP^c strain (Strandberg et al., 2012). This is generally indicative of redundant pathways and suggests that PhoPQ does not fully account for the variability observed in the host response. Other complementary bacterial pathways are also known to control LPS modifications, and it is likely that some of these also play a similar role in modulating type I IFN response. For example, one such possible candidate is the bacterial PmrAB two-component system (Perez and Groisman, 2007), and understanding the role of such additional regulators merits further investigation.

Possible Advantages of Bimodal Expression of Bacterial Factors within a Population in the Course of *In Vivo* Infection

It has been previously reported that while virulence factors allow growth and survival of the pathogen within the host, their activity elicits changes that seem both beneficial and detrimental to the bacteria (Ackermann et al., 2008). For example, while PhoPQ activation plays a key role in permitting intracellular survival by making *Salmonella* more resistant to environmental stressors, it is also associated with decreased transcytosis by epithelial cells and decreased replication rates (Groisman, 2001). This suggests that the utility of these factors may be highly dependent on environmental context. In changing environments, bistability or diversification of bacterial populations has been shown to be beneficial (Kussell and Leibler, 2005).

Recently, it has been shown that cooperation between virulent and avirulent subpopulations is essential for *S. enterica* pathogenicity (Diard et al., 2013). The effects of this cooperation were demonstrated using co-infection with genetically distinct mutant strains. Our work suggests that this strategy need not be restricted to mixed genetic subpopulations, but could occur between isogenic subpopulations during WT infection. For example, one could imagine a beneficial cooperation in which a population with high PhoPQ activity could induce a more robust immune response, as has previously shown to be helpful in overcoming the commensal microflora (Lupp et al., 2007), paying a metabolic cost that benefits a population with low

PhoPQ activity. In support of this, it is interesting that both the PhoP⁻ mutant and the PhoP^c mutant, that are unable to diversify PhoP activity, are attenuated (Miller and Mekalanos, 1990). Thus, in order to succeed in the complex host environments encountered throughout infection, *Salmonella* could tune the variation of factors, such as PhoPQ, to create distinct subpopulations that ensure that some pathogen subsets prevail in infection.

To conclude, this work establishes a mechanism by which transcriptional heterogeneity can have functional consequences for host-pathogen interactions, in this case through differences in pathogen detection. The ability of immune cells to respond to differences between individual pathogens implies that pathogen heterogeneity is a key feature of pathogen populations that impacts host response. This work suggests that further investigation of the role of bacterial heterogeneity as a mechanism to drive different host responses and the extent to which this strategy is employed by diverse pathogens is warranted to fully uncover its role in bacterial pathogenesis and, ultimately, in determining infection outcome.

EXPERIMENTAL PROCEDURES

Mice, Cell Lines, and Bacterial Strains

C57BL/6 WT mice were obtained from Jackson Laboratory. All animals were housed and maintained in a conventional pathogen-free facility at the Massachusetts General Hospital. All experiments were performed in accordance to the guidelines outlined by the MGH Committee on Animal Care. WT, *Tlr4*^{-/-}, *Trif*^{-/-}, and *Myd88*^{-/-} iBMMs were obtained from BEI Resources. *Irf3*^{-/-} and *Irf7*^{-/-} BMMs were a generous gift from Dr. Nir Hacohen (Broad Institute).

All *S. Typhimurium* strains used in this study were derived from the wild-type strain ATCC14028s or SL1344. The following 14028 mutant strains were a generous gift from Dr. Sam Miller (University of Washington): PhoP^c with pho-24 and PhoP⁻ with phoP::Tn10d-Cam (Miller and Mekalanos, 1990).

Cultures of *S. typhimurium* labeled with GFP (pFPV25.1; Addgene) were grown in Luria-Bertani (LB) medium at 37°C, washed in PBS, and incubated for 1 hr with pHrodo dye (Life Technologies). BMMs were infected at an MOI of 1:1. 30 min later, cells were washed with media containing 15 µg/ml gentamicin to remove *S. typhimurium* that were not internalized.

Single-Cell Sorting and Transcript Quantification

At the indicated time points, single cells were sorted by FACS and processed using the SMARTer whole transcriptome amplification protocol (Clontech). cDNA products were then converted to Illumina sequencing libraries using Nextera XT (Illumina). Samples were sequenced on an Illumina HiSeq-2500.

A mouse transcriptome was generated using Ensembl gene annotations and the December 2011 (GRCm38/mm10) build of the mouse genome. Alignment was done using RSEM (v.1.2.3). Transcript abundance was estimated using transcripts per million (TPM).

Bacterial reads were aligned to a composite mouse-*salmonella* transcriptome built by combining the mouse transcriptome above with the NCBI build of the SL1344 genome (NC_017718.1). Alignment of bacterial reads was done using BWA 0.7.10-r789, and an in-house script was used for transcript enumeration.

Differential expression analysis was done using DEseq (v.1.10.1), treating each cell in a given condition as replicate. Genes were considered differentially expressed only if they had a false discovery rate of less than or equal to 0.05 and an average fold change of at least 2-fold.

Heatmaps and Density Plots

To generate heatmaps, gene TPM values were transformed into log space ($\log_2(\text{expression} + 1)$) and scaled (by gene) to mean 0 and unit SD prior to plotting. Rows and columns were ordered as described in each figure legend.

For density plots summarizing the behavior of a gene cluster, PCA (biomarker) or a weighted average approach taking into account overall library quality (RNA-seq) was used to generate a single estimate per cell. Density estimates of these summary values were plotted and given the same maximum height for easy visualization.

Mouse LPS Stimulation

In vivo experiments were performed in C57BL/6J mice injected intraperitoneally with a sub-lethal (20 µg per mouse) or lethal (700 µg per mouse) dose of LPS extracted from WT, PhoP⁻, or PhoP^c *Salmonella* strains, and survival of mice was followed for 5 days.

Additional computational analyses and experiments performed using RNA-seq for simultaneous detection of host and intracellular bacterial transcripts, RNA-flowFISH (Panomics), knockout mice, and bacterial mutants are described in the [Supplemental Experimental Procedures](#).

ACCESSION NUMBERS

The accession numbers for the gene expression data reported in this paper are deposited in GEO: GSE66528, GSE65529, GSE65530, and GSE65531.

SUPPLEMENTAL INFORMATION

Supplemental Information includes Supplemental Experimental Procedures, six figures, and six tables and can be found with this article online at <http://dx.doi.org/10.1016/j.cell.2015.08.027>.

AUTHOR CONTRIBUTIONS

R.A. and D.T.H. conceived of and designed the study. R.A., N.H., D.B., C.P., and H.B.J. performed the experiments. N.H. performed computational analysis. R.A., N.H., and D.T.H. wrote the manuscript with extensive input from all authors.

ACKNOWLEDGMENTS

We thank Alan Grossman, Dan Kahne, Jon Kagan, Nir Hacohen, Itai Yanai, and Amy Barczak for discussions and comments. We thank Eduardo Villablanca for advice with in vivo experiments. We thank Ken Livak for help with Biomark experiments. We thank Leslie Gafney for help with graphical illustrations and figures. This work was supported by NIH grants (HG002295 to N.H.; DK043351 and U19AI109725 to R.J.X.; and F32 HD075541-02 to R.S.) and the NHGRI Center of Excellence in Genome Science (CEGS) Center of Cell Circuits (P50 HG006193) (to A.R.). A.R. was supported by the Klarman Cell Observatory. A.R. is a member of the Scientific Advisory Board of Thermo Fisher Scientific and Syros Pharmaceutical and is a consultant for Driver Group.

Received: January 30, 2015

Revised: May 8, 2015

Accepted: July 8, 2015

Published: September 3, 2015

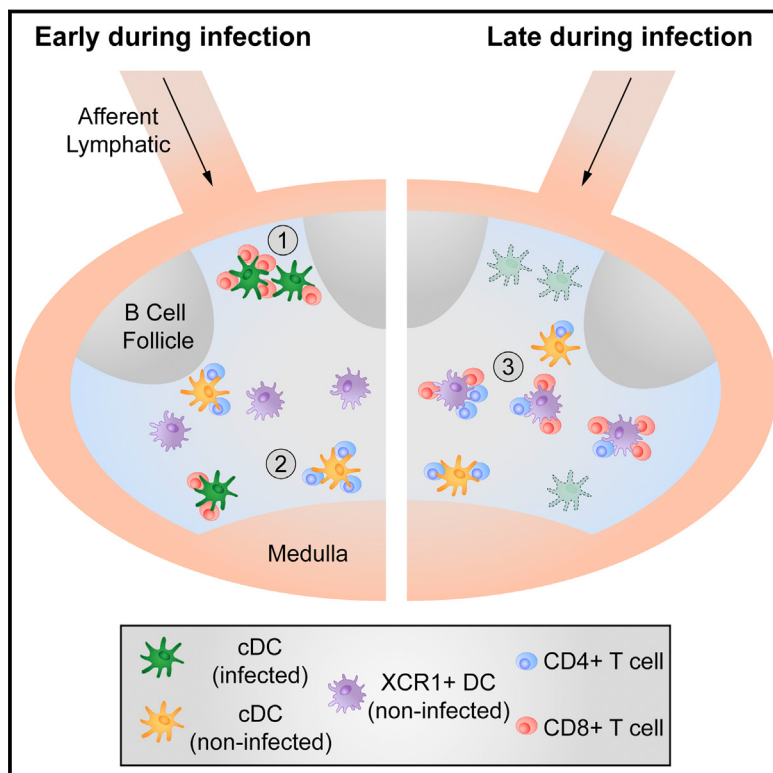
REFERENCES

- Ackermann, M., Stecher, B., Freed, N.E., Songhet, P., Hardt, W.D., and Doeblei, M. (2008). Self-destructive cooperation mediated by phenotypic noise. *Nature* **454**, 987–990.
- Chevrier, N., Mertins, P., Artyomov, M.N., Shalek, A.K., Iannaccone, M., Caccio, M.F., Gat-Viks, I., Tonti, E., DeGrace, M.M., Clouser, K.R., et al. (2011). Systematic discovery of TLR signaling components delineates viral-sensing circuits. *Cell* **147**, 853–867.
- Claudi, B., Spröte, P., Chirkova, A., Personnic, N., Zankl, J., Schürmann, N., Schmidt, A., and Bumann, D. (2014). Phenotypic variation of *Salmonella* in host tissues delays eradication by antimicrobial chemotherapy. *Cell* **158**, 722–733.
- Cummings, L.A., Wilkerson, W.D., Bergsbaken, T., and Cookson, B.T. (2006). In vivo, fliC expression by *Salmonella enterica* serovar *Typhimurium* is

- heterogeneous, regulated by ClpX, and anatomically restricted. *Mol. Microbiol.* 61, 795–809.
- Diard, M., Garcia, V., Maier, L., Remus-Emsermann, M.N., Regoes, R.R., Ackermann, M., and Hardt, W.D. (2013). Stabilization of cooperative virulence by the expression of an avirulent phenotype. *Nature* 494, 353–356.
- Elowitz, M.B., Levine, A.J., Siggia, E.D., and Swain, P.S. (2002). Stochastic gene expression in a single cell. *Science* 297, 1183–1186.
- Eriksson, S., Lucchini, S., Thompson, A., Rhen, M., and Hinton, J.C. (2003). Unravelling the biology of macrophage infection by gene expression profiling of intracellular *Salmonella enterica*. *Mol. Microbiol.* 47, 103–118.
- Fitzgerald, K.A., Rowe, D.C., Barnes, B.J., Caffrey, D.R., Visintin, A., Latz, E., Monks, B., Pitha, P.M., and Golenbock, D.T. (2003). LPS-TLR4 signaling to IRF-3/7 and NF- κ B involves the toll adapters TRAM and TRIF. *J. Exp. Med.* 198, 1043–1055.
- Galán, J.E., and Collmer, A. (1999). Type III secretion machines: bacterial devices for protein delivery into host cells. *Science* 284, 1322–1328.
- Groisman, E.A. (2001). The pleiotropic two-component regulatory system PhoP-PhoQ. *J. Bacteriol.* 183, 1835–1842.
- Guo, L., Lim, K.B., Gunn, J.S., Bainbridge, B., Darveau, R.P., Hackett, M., and Miller, S.I. (1997). Regulation of lipid A modifications by *Salmonella typhimurium* virulence genes phoP-phoQ. *Science* 276, 250–253.
- Gutschow, M.V., Hughey, J.J., Ruggero, N.A., Bajar, B.T., Valle, S.D., and Covert, M.W. (2013). Single-cell and population NF- κ B dynamic responses depend on lipopolysaccharide preparation. *PLoS ONE* 8, e53222.
- Helaine, S., Thompson, J.A., Watson, K.G., Liu, M., Boyle, C., and Holden, D.W. (2010). Dynamics of intracellular bacterial replication at the single cell level. *Proc. Natl. Acad. Sci. USA* 107, 3746–3751.
- Honda, K., and Taniguchi, T. (2006). IRFs: master regulators of signalling by Toll-like receptors and cytosolic pattern-recognition receptors. *Nat. Rev. Immunol.* 6, 644–658.
- Jaitin, D.A., Kenigsberg, E., Keren-Shaul, H., Elefant, N., Paul, F., Zaretsky, I., Mildner, A., Cohen, N., Jung, S., Tanay, A., and Amit, I. (2014). Massively parallel single-cell RNA-seq for marker-free decomposition of tissues into cell types. *Science* 343, 776–779.
- Jin, S.Q., Li, Y.Y., Pan, R.G., and Zou, X.F. (2014). Characterizing and controlling the inflammatory network during influenza A virus infection. *Sci. Rep.* 4.
- Kagan, J.C., Su, T., Horng, T., Chow, A., Akira, S., and Medzhitov, R. (2008). TRAM couples endocytosis of Toll-like receptor 4 to the induction of interferon-beta. *Nat. Immunol.* 9, 361–368.
- Kitano, H. (2004). Biological robustness. *Nat. Rev. Genet.* 5, 826–837.
- Kussell, E., and Leibler, S. (2005). Phenotypic diversity, population growth, and information in fluctuating environments. *Science* 309, 2075–2078.
- Lee, M.N., Roy, M., Ong, S.E., Mertins, P., Villani, A.C., Li, W., Dotiwala, F., Sen, J., Doench, J.G., Orzalli, M.H., et al. (2013). Identification of regulators of the innate immune response to cytosolic DNA and retroviral infection by an integrative approach. *Nat. Immunol.* 14, 179–185.
- Lupp, C., Robertson, M.L., Wickham, M.E., Sekirov, I., Champion, O.L., Gaynor, E.C., and Finlay, B.B. (2007). Host-mediated inflammation disrupts the intestinal microbiota and promotes the overgrowth of Enterobacteriaceae. *Cell Host Microbe* 2, 204.
- McIntrye, J., Rowley, D., and Jenkin, C.R. (1967). The functional heterogeneity of macrophages at the single cell level. *Aust. J. Exp. Biol. Med. Sci.* 45, 675–680.
- Miller, S.I., and Mekalanos, J.J. (1990). Constitutive expression of the phoP regulon attenuates *Salmonella* virulence and survival within macrophages. *J. Bacteriol.* 172, 2485–2490.
- Monack, D.M., Raupach, B., Hromockyj, A.E., and Falkow, S. (1996). *Salmonella typhimurium* invasion induces apoptosis in infected macrophages. *Proc. Natl. Acad. Sci. USA* 93, 9833–9838.
- Morrison, D.C., and Ryan, J.L. (1987). Endotoxins and disease mechanisms. *Annu. Rev. Med.* 38, 417–432.
- Paciello, I., Silipo, A., Lembo-Fazio, L., Curcurù, L., Zumsteg, A., Noël, G., Ciancarella, V., Sturiale, L., Molinaro, A., and Bernardini, M.L. (2013). Intracellular *Shigella* remodels its LPS to dampen the innate immune recognition and evade inflammasome activation. *Proc. Natl. Acad. Sci. USA* 110, E4345–E4354.
- Perez, J.C., and Groisman, E.A. (2007). Acid pH activation of the PmrA/PmrB two-component regulatory system of *Salmonella enterica*. *Mol. Microbiol.* 63, 283–293.
- Rathinam, V.A., Vanaja, S.K., Waggoner, L., Sokolovska, A., Becker, C., Stuart, L.M., Leong, J.M., and Fitzgerald, K.A. (2012). TRIF licenses caspase-11-dependent NLRP3 inflammasome activation by gram-negative bacteria. *Cell* 150, 606–619.
- Robinson, N., McComb, S., Mulligan, R., Dudani, R., Krishnan, L., and Sad, S. (2012). Type I interferon induces necroptosis in macrophages during infection with *Salmonella enterica* serovar Typhimurium. *Nat. Immunol.* 13, 954–962.
- Rosenberger, C.M., Scott, M.G., Gold, M.R., Hancock, R.E., and Finlay, B.B. (2000). *Salmonella typhimurium* infection and lipopolysaccharide stimulation induce similar changes in macrophage gene expression. *J. Immunol.* 164, 5894–5904.
- Schlumberger, M.C., Müller, A.J., Ehrbar, K., Winn, B., Duss, I., Stecher, B., and Hardt, W.D. (2005). Real-time imaging of type III secretion: *Salmonella* SipA injection into host cells. *Proc. Natl. Acad. Sci. USA* 102, 12548–12553.
- Schwan, W.R., Huang, X.Z., Hu, L., and Kopecko, D.J. (2000). Differential bacterial survival, replication, and apoptosis-inducing ability of *Salmonella* serovars within human and murine macrophages. *Infect. Immun.* 68, 1005–1013.
- Shalek, A.K., Satija, R., Adiconis, X., Gertner, R.S., Gaublomme, J.T., Raychowdhury, R., Schwartz, S., Yosef, N., Malboeuf, C., Lu, D., et al. (2013). Single-cell transcriptomics reveals bimodality in expression and splicing in immune cells. *Nature* 498, 236–240.
- Shalek, A.K., Satija, R., Shuga, J., Trombetta, J.J., Gennert, D., Lu, D., Chen, P., Gertner, R.S., Gaublomme, J.T., Yosef, N., et al. (2014). Single-cell RNA-seq reveals dynamic paracrine control of cellular variation. *Nature* 510, 363–369.
- Strandberg, K.L., Richards, S.M., and Gunn, J.S. (2012). Cathelicidin antimicrobial peptide expression is not induced or required for bacterial clearance during *salmonella enterica* infection of human monocyte-derived macrophages. *Infect. Immun.* 80, 3930–3938.
- Trombetta, J.J., Gennert, D., Lu, D., Satija, R., Shalek, A.K., and Regev, A. (2014). Preparation of single-cell RNA-seq libraries for next generation sequencing. *Curr. Protoc. Mol. Biol.* 107, 4.22.1–4.22.17.

Robust Anti-viral Immunity Requires Multiple Distinct T Cell-Dendritic Cell Interactions

Graphical Abstract



Authors

Sarah Eickhoff, Anna Brewitz, Michael Y. Gerner, ..., Tsuneyasu Kaisho, Ronald Nathan Germain, Wolfgang Kastenmüller

Correspondence

rgermain@nih.gov (R.N.G.),
wkastenm@uni-bonn.de (W.K.)

In Brief

During the course of a viral infection, CD4⁺ and CD8⁺ T lymphocyte activation is initially separated spatially, but a subset of dendritic cells acts as a platform to orchestrate their communication to optimize CD8⁺ T cell expansion and memory function.

Highlights

- Initial activation of CD4⁺ and CD8⁺ T lymphocytes is spatially separated
- Later during infection, XCR1⁺ DCs present antigen to both lymphocyte subsets
- XCR1⁺ DCs are a critical platform for delivery of CD4⁺ T cell help to CTL
- Absence of XCR1⁺ DCs leads to aberrant memory CD8⁺ T cell differentiation

Robust Anti-viral Immunity Requires Multiple Distinct T Cell-Dendritic Cell Interactions

Sarah Eickhoff,^{1,6} Anna Brewitz,^{1,6} Michael Y. Gerner,² Frederick Klauschen,³ Karl Komander,¹ Hiroaki Hemmi,^{4,5,8} Natalio Garbi,¹ Tsuneyasu Kaisho,^{4,5,8} Ronald Nathan Germain,^{2,7,*} and Wolfgang Kastenmüller^{1,7,*}

¹Institute for Experimental Immunology, University of Bonn, 53105 Bonn, Germany

²Lymphocyte Biology Section, Laboratory of Systems Biology, National Institute of Allergy and Infectious Diseases, National Institutes of Health, Bethesda, MD 20892, USA

³Institute of Pathology, Charité University Hospital Berlin, 10117 Berlin, Germany

⁴Laboratory for Immune Regulation, World Premier International Immunology Frontier Research Center, Osaka University, Suita, Osaka 565-0871, Japan

⁵Laboratory for Inflammatory Regulation, RIKEN Center for Integrative Medical Sciences (IMS-RCAI), Yokohama, Kanagawa 230-0045, Japan

⁶Co-first author

⁷Co-senior author

⁸Present address: Department of Immunology, Institute of Advanced Medicine, Wakayama Medical University, Wakayama, Wakayama 641-8509, Japan

*Correspondence: rgermain@nih.gov (R.N.G.), wkastenm@uni-bonn.de (W.K.)

<http://dx.doi.org/10.1016/j.cell.2015.08.004>

SUMMARY

Host defense against viruses and intracellular parasites depends on effector CD8⁺ T cells, whose optimal clonal expansion, differentiation, and memory properties require signals from CD4⁺ T cells. Here, we addressed the role of dendritic cell (DC) subsets in initial activation of the two T cell types and their co-operation. Surprisingly, initial priming of CD4⁺ and CD8⁺ T cells was spatially segregated within the lymph node and occurred on different DCs with temporally distinct patterns of antigen presentation via MHC I versus MHC II molecules. DCs that co-present antigen via both MHC molecules were detected at a later stage; these XCR1⁺ DCs are the critical platform involved in CD4⁺ T cell augmentation of CD8⁺ T cell responses. These findings delineate the complex choreography of cellular interactions underlying effective cell-mediated anti-viral responses, with implications for basic DC subset biology, as well as for translational application to the development of vaccines that evoke optimal T cell immunity.

INTRODUCTION

The induction of an adaptive immune response requires the interaction of several lymphoid and myeloid cell types. For the generation of cytotoxic T lymphocytes (CTL), initial activation of naïve CD8⁺ T cells occurs via antigen-presenting cells (APC) that engage the antigen-specific T cell receptor (TCR) and other stimulatory surface receptors of these lymphocytes (Curtsinger and Mescher, 2010). The critical MHC I molecules involved in TCR recognition by CD8⁺ T cells can be loaded with antigenic

determinants by a direct antigen-presentation pathway involving cytosolic proteins or by a cross-presentation pathway, which is fueled by extracellular proteins (Kurts et al., 2010). The latter is believed to play an essential role for pathogens that do not directly infect professional APC.

A second conventional T cell, the CD4⁺ helper T cell, is activated via antigen-presenting MHC II molecules. In distinction to the ligands involved in activation of CD8⁺ T cells, antigenic peptides presented by MHC II molecules are typically derived from extracellular proteins or intracellular proteins that are recycled from the cell surface (Germain, 1994). These CD4⁺ T cells provide crucial soluble and membrane-associated signals to antigen-specific B lymphocytes, leading to effective adaptive humoral immunity (Crotty, 2014). As with B cells and humoral responses, CD4⁺ T cells also provide molecular “help” to CTL, optimizing cellular immune responses by enhancing CD8⁺ T cell clonal expansion, differentiation, and survival (Castellino and Germain, 2006).

Although the functional parallel is clear, a conceptual problem in comparing CD4⁺ T cell help for humoral versus cellular responses in mouse models is that the interaction between CD4⁺ and CD8⁺ T cells cannot be direct, based on TCR engagement, as mouse CD8⁺ T cells do not express the necessary MHC II molecules to provide ligands for the CD4⁺ T cell TCR. This paradox was resolved by experiments showing that dendritic cells (DCs) serve as a platform to mediate communication between CD4⁺ and CD8⁺ T cells (Mitchison and O’Malley, 1987; Ridge et al., 1998). Both T cell subsets must interact with the same DC in an antigen- and TCR-dependent manner, meaning that the “platform” DC must present antigen to CD4⁺ and CD8⁺ T cells via both the MHC II and MHC I pathways, respectively (Bennett et al., 1997; Cassell and Forman, 1988).

Given that naïve lymphocytes specific for a given foreign antigen are rare, it has been argued that the likelihood of a (simultaneous, random) three-cell encounter is too low to be effective at driving the responses in question (Bevan, 2004).

This argument has been weakened by experiments showing that (1) a DC that had interacted with a CD4⁺ T cell could help a CD8⁺ T cell even after the CD4⁺ T cell was removed, removing the need for contemporaneous three-cell clustering (Ridge et al., 1998) and (2) DC-CD4⁺ T cell interactions lead to the production of the chemokines CCL3/4 that attract CD8⁺ T cells via CCR5 to the licensed DC optimizing rare cell contacts (Castellino et al., 2006).

The same intravital imaging methods that revealed such chemokine-mediated guidance also showed that, upon encounter with antigen-laden DCs, T cells arrest and initiate long-term interactions lasting for several hours (16–20 hr) (Bousso and Robey, 2003; Miller et al., 2002; Stoll et al., 2002). This means that both CD4⁺ and CD8⁺ T cells would be substantially delayed in finding a common DC even with chemokine guidance. Furthermore, the past decade has seen an increasingly detailed parsing of dendritic cells into distinct subsets with specific localizations within secondary lymphoid tissues (Gerner et al., 2012; Kisselkell et al., 2005), as well as the emergence of strong evidence for preferential presentation of antigen via MHC I and MHC II by different DC types (den Haan et al., 2000; Dudziak et al., 2007; Schnorrer et al., 2006). Together, the dynamic considerations and the complexity of DC biology raise the crucial issue of when, where, and on which DC do CD4⁺ and CD8⁺ T cells become activated and communicate.

In light of these unresolved questions, the present study aimed to elucidate the spatial and temporal events that occur during CD4⁺ T cell augmentation of CD8⁺ T cells responses (“help”) and to reveal the location and identity of the DC subset(s) that serve(s) as the communication platform for CD4⁺ and CD8⁺ T cells. Surprisingly, we found that early post-infection, antigen-specific activation of CD4⁺ and CD8⁺ T cells is spatially separated and mediated via non-infected and infected DC, respectively. XCR1⁺ (CD8^{α+}) DCs, which have been described to play a central role in CD8⁺ T cell priming, appeared to be dispensable for this initial activation of CD8⁺ T cells. After the triggering of both T cell subsets, CD4⁺ and CD8⁺ T cells translocated to a specific area in the paracortex, where they interacted with a third, non-infected XCR1⁺ DCs population, defining the platform for delivery of help. These findings delineate the complex choreography of cellular interactions underlying effective cell-mediated anti-viral responses with parallels to the spatio-temporal events involved in delivery of CD4⁺ T cell help during humoral immune responses.

RESULTS

Direct Priming of CD8⁺ T Cells Does Not Require XCR1⁺ DC

To understand how CD8⁺ T cells and CD4⁺ T cells interact with DCs during the induction of robust cell-mediated immune responses, we used a model system of vaccinia virus (VV) infection that supports both direct and cross-presentation pathways and elicits a CD4⁺ help-dependent CD8⁺ T cell response (Norbury et al., 2001; Wiesel et al., 2010). To allow for a time-resolved analysis of the cellular events, we initially carried out our experiments with the replication-deficient variant MVA (modified vaccinia virus Ankara). This attenuated virus produces

a single round of infection with full expression of early and late viral antigens (Drexler et al., 2004). 4 hr after intravenous (i.v.) infection of mice with MVA-GFP, we could detect infected DCs based on GFP expression. Phenotypic analysis of infected DCs revealed a comparable infection rate among CD8^{α+} and CD11b⁺ DCs in the spleen (Figure 1A). After infection with a recombinant virus that also expresses the ovalbumin-derived SIINFEKL determinant (MVA-NP-S-GFP), the infected DCs also presented virally expressed antigens via MHC I as quantified by antibody staining with clone 25.D1, which recognizes SIINFEKL bound to the mouse MHC I molecule H-2Kb. To test whether such directly infected DC could drive CD8⁺ T cell proliferation, we infected Kbm1 animals (Kbm1 is a mutant Kb unable to bind SIINFEKL) with MVA-OVA and MVA-OVA-Kb, respectively. In this experimental set-up, only MVA-OVA-Kb-infected DCs were able to present antigen and promote proliferation of OT-I cells (CD8⁺ ovalbumin-specific, TCR transgenic T cells), whereas non-infected or MVA-OVA-infected DC were unable to stimulate OT-I cell proliferation in culture (Figure 1B). This demonstrates that directly infected DCs present viral antigens and induce proliferation of antigen-specific CD8⁺ T cells ex vivo. In vivo, we could detect direct interactions between MVA-OVA-GFP-infected DCs and transferred OT-I lymphocytes shortly after infection using intravital two-photon microscopy (IVM) and analysis of stained lymph node (LN) sections (Movie S1 and Figure 1C). Arrested T cells were typically seen at the subcapsular sinus (SCS) and formed clusters in the interfollicular area and the cortical ridge as previously reported (Hickman et al., 2008; Kastenmüller et al., 2013). Because both DC and macrophages populate the area in which we see clusters of OT-I cells early after infection, we depleted macrophages using clodronate liposomes or used additional DC-specific reporter animals (Figures S1A–S1C) and analyzed clusters shortly after MVA-OVA-GFP infection. These data also indicated that DCs are the predominant cellular targets of early antigen recognition by the OT-I cells.

To elucidate whether different infected DC subsets have a differential capacity to stimulate OT-I cells, we infected mice i.v., sorted splenic CD11b⁺ or CD8^{α+} DCs 8 hr later, and co-cultured the sorted cells with CFSE-labeled OT-I cells. At 72 hr post-co-culture, we consistently observed similar proliferation of OT-I cells after co-incubation with either DC subset (Figures 1D and S1D). CD8^{α+} DCs substantially overlap with the XCR1⁺ DC subpopulation (Becker et al., 2014). Therefore, to further test whether CD8^{α+} DCs are required for activation of OT-I cells in vivo, we transferred OT-I cells into wild-type (WT) or XCR1-DTR animals (Yamazaki et al., 2013), treated them with *Diphtheria* toxin (DTX) to deplete the XCR1⁺ DCs, infected the animals with MVA-OVA in the footpad (f.p.), and then analyzed the expression of the early activation markers CD69 and CD25 on OT-I cells in the draining lymph node (dLN) 12 hr later. We found that the early activation of OT-I cells was unaltered in the absence of XCR1⁺ DCs (Figures 1E and 1F). In contrast, we found a small but consistent reduction in the early activation of OT-II cells (CD4⁺) also specific for OVA but presented by MHC II molecules (Figures 1E and 1F). In summary, we conclude that MVA infects various DC subsets in vivo that express and present antigens to CD8⁺ T cells leading to activation and T cell

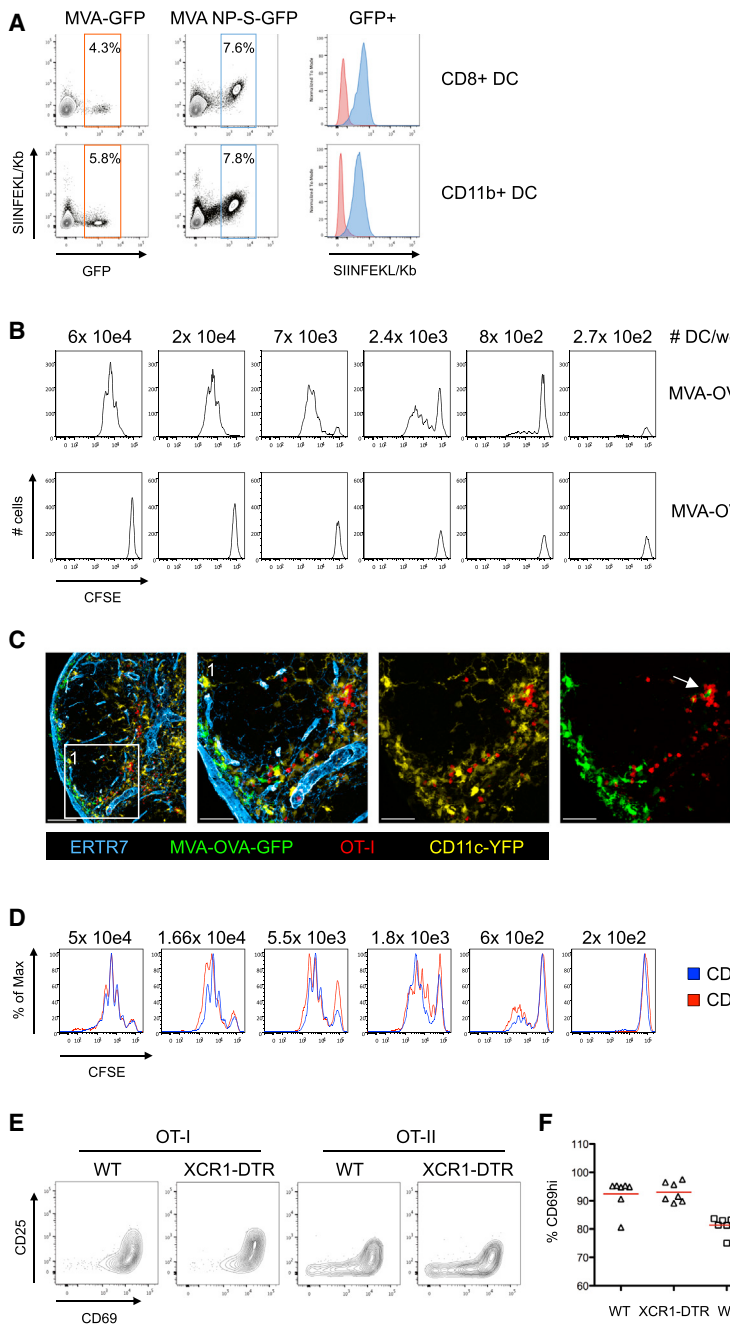


Figure 1. Direct Priming of CD8⁺ T Cells Does Not Require XCR1⁺ DCs

(A) Analysis of splenic DC after i.v. infection with MVA-GFP or MVA-NP-SIINFEKL-GFP (8 hr p.i.).

(B) Analysis of OT-I proliferation after ex vivo co-incubation with isolated splenic DC from Kbm1 mice infected with MVA-OVA or MVA-OVA-Kb (8 hr p.i.).

(C) Immunofluorescent (IF) images of a dLN showing clustering/interaction between transferred OT-I cells and infected (GFP-expressing) DC (MVA-OVA-GFP; f.p.; 8 hr p.i.).

(D) Analysis of OT-I proliferation after co-incubation with DC subsets sorted ex vivo (MVA-OVA; i.v.; 8 hr p.i.).

(E and F) Activation marker (CD25/CD69) upregulation on transferred OT-I and OT-II cells in the popliteal LN 12 hr after f.p. infection (MVA-OVA). Representative plots (E) and analysis (F) are shown comparing DTX-treated WT and XCR1-DTR animals.

Data are representative of three ($n = 3$) (A–D) and two ($n = 4$) (E and F) independent experiments. (E) Red bars indicate mean values. (C) Scale bars, 100/50 μ m. See also Figure S1 and Movie S1.

observed the migratory behavior of the transferred T cells *in situ* using IVM. As expected, we could readily detect arrested OT-I cells clustering around infected DCs. Surprisingly, however, OT-II cells did not co-arrest with their CD8⁺ T cell counterparts (Movie S2 and Figure 2A). Instead, they migrated similarly to polyclonal CD4⁺ control T cells at around 10 μ m/min (Figure 2B). Later after infection (8–12 hr), we were unable to detect OT-I/OT-II co-clusters using IVM (data not shown), although kinetic experiments with isolated cells recovered from these animals revealed that the majority of the OT-II cells were activated (CD69^{hi}) (Figure 2C) and therefore were likely to have engaged antigen-rich APC by this time point. These findings suggested that OT-II cells might be activated in deeper areas of the LN that are not typically visualized using IVM. Therefore, we analyzed frozen LN sections to identify

proliferation. For this initial activation, XCR1⁺(CD8 α ⁺)-expressing DCs appear to be dispensable.

Early Activation of CD4⁺ and CD8⁺ T Cells Occurs on Spatially Distinct DCs

Having established that antigen-specific CD8⁺ T cells are initially activated by infected DCs, we wished to clarify whether CD4⁺ T cells can provide cognate help via such infected, CD8⁺ T cell-engaged DCs. To this end, we transferred OT-I and OT-II cells into mice, infected the animals with MVA-OVA, and

the location OT-I and OT-II cell co-clusters. In line with our IVM data, we found that OT-II cells did not accumulate and cluster in the SCS area in contrast to OT-I cells (Figure 2D), which were found in proximity to MVA-infected (GFP-expressing) cells. OT-II cells did not cocluster substantially with OT-I, showing only random colocalization with OT-I at frequencies similar to OVA antigen-unspecific polyclonal CD4⁺ T cells (Figures S2A and S2B). To further assess this spatial separation of CD4⁺ and CD8⁺ T cells during initial antigen-dependent priming after viral infection, we analyzed spleen sections at similar time points.

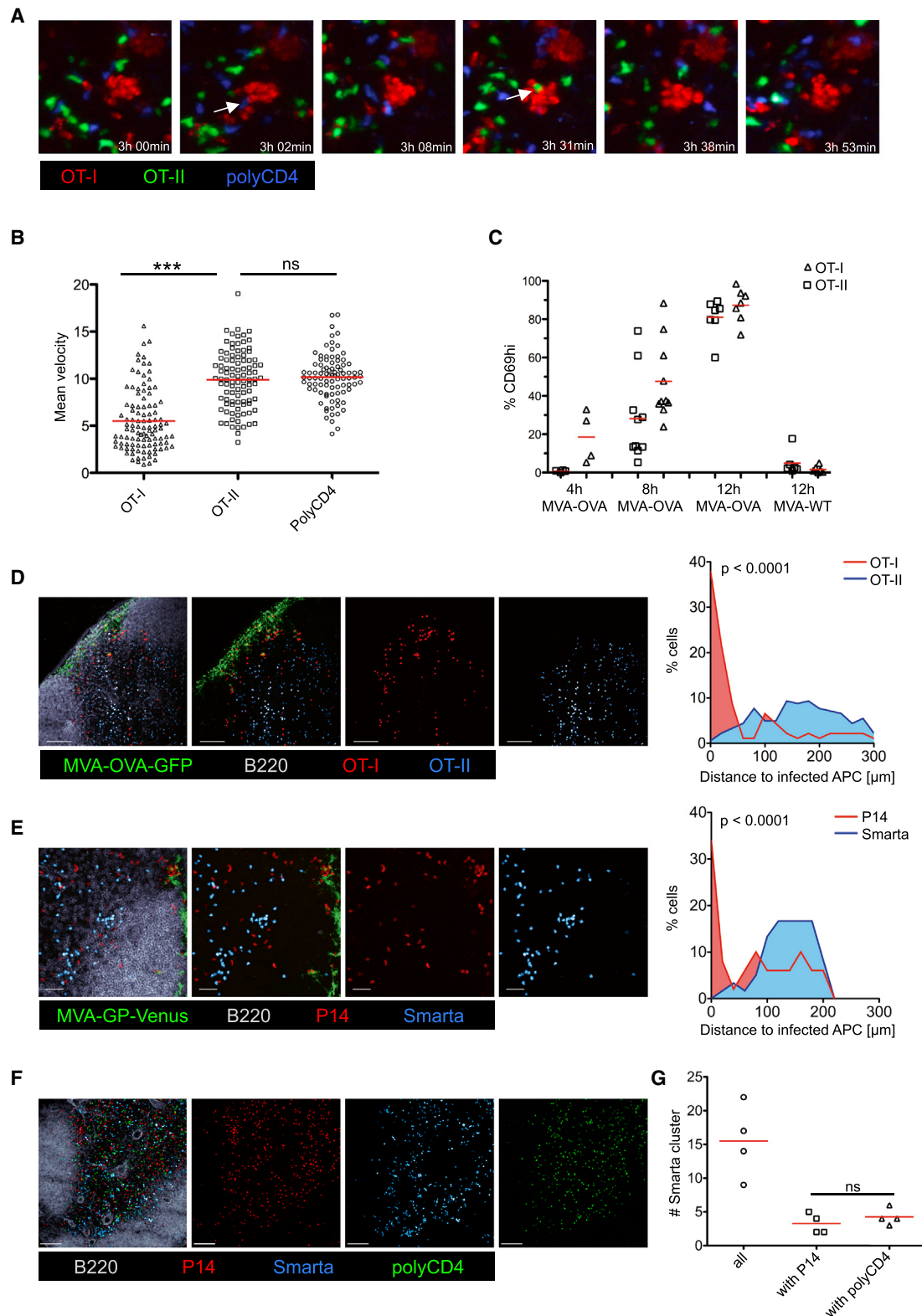


Figure 2. Priming of CD4⁺ and CD8⁺ T Cells Occurs on Spatially Distinct DCs

(A) Images from IVM of the popliteal LN 3–4 hr after MVA-OVA f.p. infection. OT-I, OT-II, and control cells (polyclonal CD4⁺ T cells) were transferred 24 hr prior to infection. White arrows indicate brief interaction between clustered OT-I and OT-II or control cells (see also Movie S2).

(legend continued on next page)

Again, we found a segregation of antigen-specific CD4⁺ and CD8⁺ T cells. OT-I cells were localized at the marginal zone in proximity to infected APC (Figures S2C and S2D). In contrast, OT-II cells remained in the white pulp, where they clustered and were activated by non-infected (GFP-negative) APC (Figures S2C and S2D).

To determine whether the segregation of OT-I and OT-II cells during activation is a phenomenon related to their particular TCRs, we generated MVA-GP-Venus and analyzed a different TCR transgenic T cell pair specific for the lymphocytic choriomeningitis virus (LCMV) glycoprotein (GP) (Smart/CD4⁺, P14/CD8⁺). Similar to our previous results, we found accumulation of antigen-specific CD8⁺ T cells (P14) around MVA-GP-Venus-infected DC while antigen-specific CD4⁺ T cells (Smart) accumulated in the paracortex (Figures 2E and S2E). Smart cells formed homogenous clusters in the paracortex of dLN that were only randomly intermixed with P14 cells, similar to non-specific control cells (Figures 2F and 2G). To further evaluate whether the observed separated activation of antigen-specific CD4⁺ versus CD8⁺ T cells is a more general feature of initial activation, we examined two additional experimental systems. As a first approach, we used recombinant adenovirus infections and found that OT-I cells translocated to the SCS and IFA to interact with directly infected APC, whereas OT-II cells remained in the paracortex where they were activated in an antigen-specific manner (Figures S2F–S2I). Second, we immunized mice with soluble OVA protein and LPS as adjuvant. Again, we found that activation of OT-I and OT-II cells is predominantly separated (Figures S2J–S2M and Movie S3). In summary, we conclude that the initial activation of antigen-specific CD4⁺ and CD8⁺ T cells is segregated and involves distinct DC in different locations within the lymph node or spleen.

Identification of DCs that Present Viral Antigen via both MHC I and MHC II Later after Infection

These findings were surprising in light of previous reports demonstrating that CD4⁺ help for CD8⁺ T cells occurs on a single DC co-presenting MHC I and MHC II antigens (Bennett et al., 1997; Cassell and Forman, 1988) and our prior studies showing how chemokines guide T cells to DCs co-presenting MHC I and MHC II ligands (Castellino et al., 2006). One way to reconcile the present observations with these prior findings is to postulate that the licensing and/or the delivery of help occurs later during the course of infection. To examine this possibility, we transferred OT-I, OT-II, and polyclonal CD4⁺ T cells into mice that had been infected for 30 hr and analyzed the location of these transferred cells in LN sections 8 hr after transfer (Figure 3A). With this experimental setup, we could readily detect OT-I and OT-II cell co-clusters, while polyclonal CD4⁺ T cells showed

an unbiased distribution (Figure 3B). When systematically comparing cellular positioning in the LN early (10 hr) versus late (38 hr) after infection, we found marked differences for OT-I cells and modest differences for OT-II cells (Figure 3C). This reflects the predominant activation of OT-I at the SCS/IFA early after infection (10 hr) versus the presence of antigen-bearing DCs in the paracortex at later time points (38 hr). These paracortical DCs were able to present antigen to and activate both OT-I and OT-II T cells, as indicated by the OT-I and OT-II T cells expressing activation markers in co-clusters surrounding such DCs (Figure 3D). Thus, later during infection, a common DC, positioned in the peripheral paracortex, presents antigen able to productively engage the TCR of both CD4⁺ and CD8⁺ T cells. Use of two experimental approaches to block DC migration (site removal, lymph vessel obliteration) revealed that migratory DCs were not required for the formation of OT-I/OT-II cell co-clusters during the late phase of infection (Figures S3A and S3B). Additionally, Batf3 KO animals that lack migratory CD103⁺ DCs but only a fraction of LN resident CD8α⁺ (XCR1⁺) DCs (Edelson et al., 2010) showed mixed OT-I/OT-II cell co-clusters, confirming that CD103⁺ migratory DCs were dispensable for the formation of such clusters (Figure S3B). It is important to note that the presence of clusters consisting of three different cell types (OT-I/OT-II/DC) does not necessarily mean that those ternary interactions occur or are necessary for delivery of help under physiological conditions, as in these experiments an artificially high number of precursor T cells was used to facilitate detection of the co-presenting DCs.

Non-infected Cross-presenting XCR1⁺ DCs Are the Information-Transmission Platform for CD4⁺ and CD8⁺ T Cells

Given that XCR1⁺ DCs were dispensable for early CD4⁺ and CD8⁺ T cell activation (Figure 1) but play a central role in immunogenic CTL priming (Shortman and Heath, 2010), we hypothesized that these DCs might be involved in the CD4⁺ and CD8⁺ T cell co-clustering we observed above. To investigate this hypothesis, we first attempted to identify which DC subset presents antigen to OT-I cells at a late stage of infection. CD11b⁺ and CD8α⁺ DCs were sorted 30 hr after infection and co-cultured with CFSE-labeled OT-I cells. In contrast to the results obtained early (8 hr) after infection (Figure 1D), at this later time point, exclusively CD8α⁺ (XCR1⁺) DCs induced OT-I cell proliferation (Figures 4A, S4A, and S4B). To test whether this is due to the known propensity of this DC subset to cross-present antigen, we infected C57BL/6 and Kbm1 mice with MVA-OVA-Kb, sorted the CD8α⁺ DC subset 30 hr later, and co-incubated these DCs with CFSE-labeled OT-I cells (Figure 4B). If direct antigen presentation was still occurring, directly infected Kbm1 DCs should

(B) Analysis of the mean velocity of transferred T cells using the data shown in Movie S2.

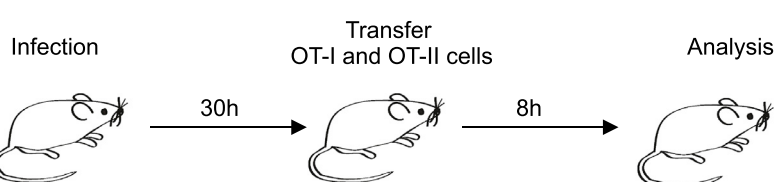
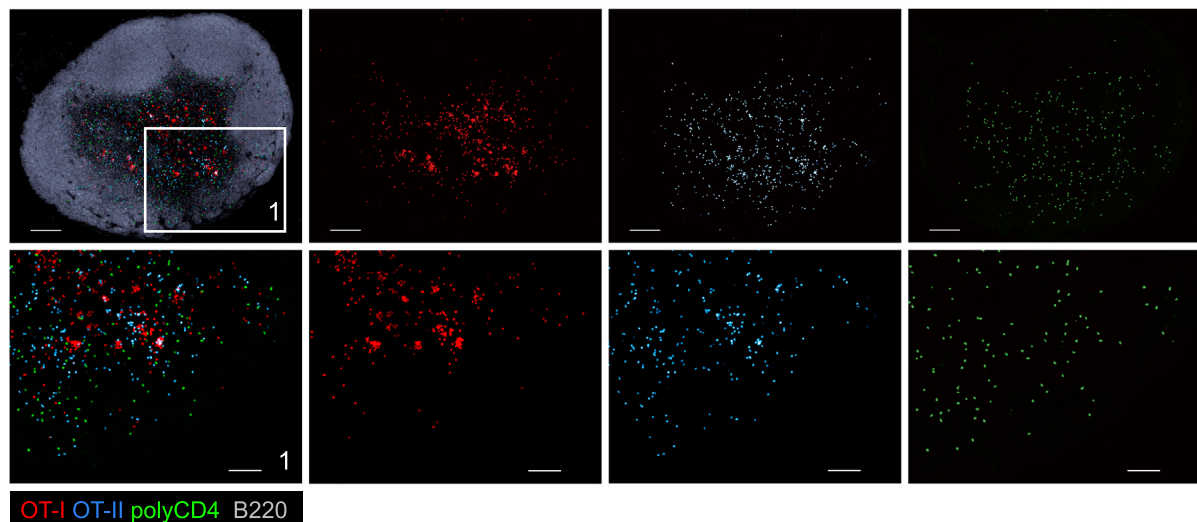
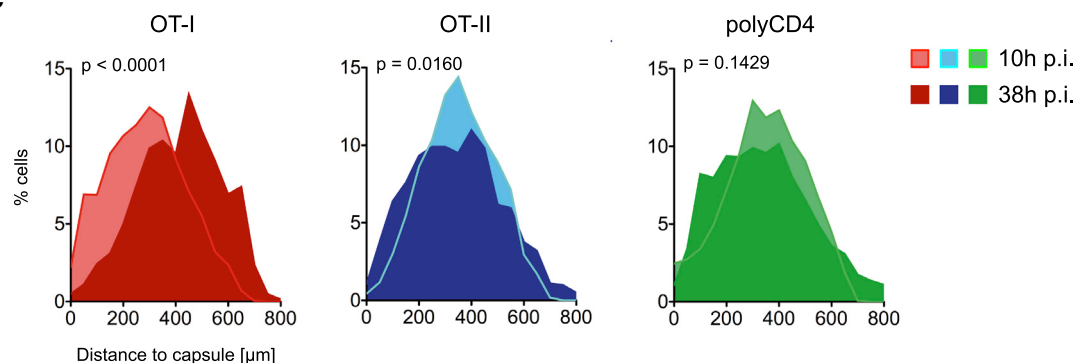
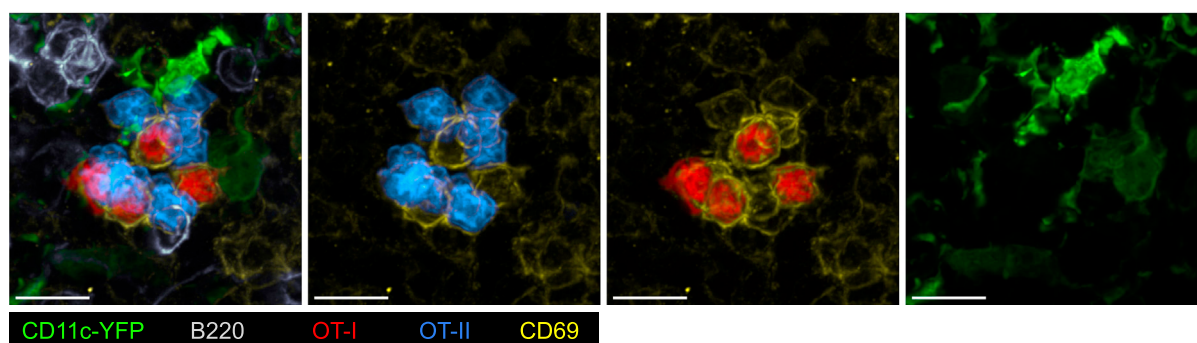
(C) Analysis of CD69 upregulation on transferred OT-I and OT-II cells in the dLN at different time points after f.p. infection (MVA-OVA/MVA WT).

(D–F) IF images of a dLN showing the localization of (D) transferred OT-I and OT-II cells (MVA-OVA-GFP), (E) transferred P14 and Smarta cells (MVA-GP-Venus); and (F) transferred P14, Smarta, and polyclonal CD4⁺ T cells (MVA-GP) 10 hr p.i. Histograms show distance of transferred cells from infected APC.

(G) Quantification of cluster abundance from four experiments as in (F).

Data are representative of at least two independent experiments (A and B, n = 10), (C and G, n = 4–8; pooled data) (D–F, n = 10). (B, C, and G) Red bars indicate mean values. ***p ≤ 0.001; ns, non-significant. Scale bars (D–F), 100 μm.

See also Figure S2 and Movie S2.

A**B****C****D**

(legend on next page)

still be able to drive OT-I cell proliferation due to virally driven Kb expression (Figure 1B). However, this was not the case, supporting the notion that, later during infection, at least when using replication-incompetent viruses, cross-presentation becomes the dominant pathway for MHCI loading with viral antigens.

We then examined whether XCR1⁺ DCs also served as the platform that communicates with both antigen-specific CD4⁺ and CD8⁺ T cells in vivo. We infected XCR1-DTR-Venus mice, treated them with DTX or PBS, and transferred OT-I and OT-II cells into these animals 30 hr post-infection and DTX treatment. XCR1⁺ DCs were detected in the middle of mixed OT-I/OT-II cell co-clusters in PBS-treated animals 8 hr after T cell transfer (Figure 4C). The XCR1⁺ DCs were not broadly distributed throughout the LN as in the steady state (Figure S4C) but rather formed aggregates that were intermixed with the co-clustered T cells (Figures 4C and S4D). DTX depletion of XCR1⁺ DCs led to a loss of mixed OT-I/OT-II cell co-clusters, while leaving distinct OT-II and separate, rare OT-I cell clusters (Figures 4C–4E). We next quantified the requirement for XCR1⁺ DCs in the stimulation of OT-I and OT-II cells at this late phase post-infection. 12 hr after T cell transfer, we harvested the dLN and analyzed OT-I and OT-II cells for CD69 expression using flow cytometry. In the absence of XCR1⁺ DCs, the fraction of activated OT-I cells dropped from 80% in WT to 15% in XCR1-DTR mice (Figure 4F). The activation of OT-II cells was modestly reduced from 60% to 40% if XCR1⁺ DCs were absent. Together, these data indicate that cross-presenting XCR1⁺ DCs serve as a platform for interaction (simultaneously or sequentially) with both antigen-specific CD4⁺ and CD8⁺ T cells at late times after infection.

XCR1⁺ DCs Are Also Critical for Communication between CD4⁺ and CD8⁺ T Cells during Productive VV Infection

We next examined whether these findings applied to events following infection with replication-competent VV that does not require antigen cross-presentation for T cell priming due to ongoing infection of DCs (Xu et al., 2010). First, we addressed whether initial CD4⁺ and CD8⁺ T cell priming is also spatially separated during VV infection. To this end, we transferred OT-I and OT-II cells into WT animals and infected them with VV-OVA. IVM 10 hr p.i. confirmed the near-absolute separation of arrested OT-I and OT-II cells, with the former forming clusters near the LN capsule and the latter in deeper areas of the LN (Figure 5A and Movie S4). Similar to MVA-OVA infection, VV-OVA infection induced the accumulation of OT-I cells at the SCS, where they interacted with infected DC (Figures 5B, S5A, and S5B) (Hickman et al., 2011). In contrast, OT-II cells remained in the paracortical areas of the LN and did not co-cluster with OT-I (Figures 5B, S5C, and S5D).

Next, we addressed whether late co-clustering of CD8⁺ and CD4⁺ T cells occurs after VV infection. Naive OT-I and OT-II cells

were transferred into WT mice 30 hr post-infection, and the dLN were examined by fluorescent microscopy 8 hr later. Central sagittal sections showed that mixed T cell clusters consisted of activated (CD69⁺) cells in the peripheral paracortex rather than in the deep paracortical central region (Figures 5C and S5E). Using VV-infected XCR1-DTR-Venus mice as recipients, we found that mixed OT-I/OT-II cell co-clusters were organized around XCR1⁺ DCs at this later time-point (Figure S5F). Depletion of XCR1⁺ DCs led to a loss of mixed OT-I/OT-II cell clusters, confirming that XCR1⁺ DCs are the predominant population involved in co-presentation of MHCI and MHCI determinants at this later stage, making them likely platforms for the delivery of help (Figures 5D–5F). In the absence of XCR1⁺ DCs, OT-II cell clusters were still present in the paracortex, typically in proximity to the medullary area. OT-I cell clusters were also present albeit in lower frequency and, importantly, were separated from OT-II cells (Figures 5E and 5F). Persistent OT-I clusters in the absence of XCR1⁺ DCs reflect ongoing VV replication and continued infection of LN resident DCs. Such clusters were largely absent after infection with the replication-deficient in MVA (Figures 3C and 3D), most likely due to the absence of infected DCs at this time point.

Localization of Endogenous Activated CD8⁺ T Cells during VV Infection

We next turned to an assessment of whether endogenous T cells are activated at similar anatomical sites as transferred TCR transgenic cells and whether both CD4⁺ and CD8⁺ T cells similarly seek out XCR1⁺ DCs later during infection. Labeled OT-I cells were transferred to WT recipients and the mice infected with VV-OVA. 8 hr later, we examined whether activated (CD69^{hi}) endogenous T cells were part of activated OT-I cell clusters. CD69^{hi} non-transgenic cells were found in close proximity to activated OT-I cells, arguing for an activation of endogenous cells by the same DC (Figure 6A). To analyze the location of activated T cells later during infection when CD69 expression is downregulated, we employed IFN γ (YFP) reporter animals. As expected, YFP-positive cells were not seen on fixed LN sections from naive mice (Figure S6A). In contrast, at 38 hr p.i., we found YFP-positive cells in the dLN that consisted of CD4⁺, CD8⁺, and double-negative (CD3⁺) T cells, as well as NK cells (Figures 6B and 6C). CD8⁺ T cells showed an increased cellular volume (Figure 6D) and the highest YFP expression (Figure 6E) as measured by forward scatter signal and the mean fluorescent intensity (MFI).

Using immunofluorescent analysis of LN sections from IFN γ reporter animals 40 hr after infection (VV-OVA), we detected YFP⁺ cells at the SCS and in the paracortex. To examine whether the YFP⁺ cells represent recently activated T cells, we blocked the entry of newly arriving naive T cells to the dLN using CD62L antibodies 14 hr post-infection. Under this condition,

Figure 3. CD4⁺ and CD8⁺ T Cells Co-cluster Later during Infection

- (A) Schematic of the experimental setup to reveal antigen-bearing cells later in the course of infection (MVA-OVA).
 - (B) IF images of the dLN showing the localization of OT-I, OT-II, and control cells (polyclonal CD4 T cells).
 - (C) Histograms showing cellular localization 10 hr (see Figure 2) or 38 hr p.i. (see experimental setup shown in A).
 - (D) IF image of the dLN showing a mixed OT-I/OT-II cell cluster and activation status (CD69).
- Data are representative of 10 (B and D, n = 20) or three (C, n = 3) independent experiments. Scale bars, (B) 200 μ m/100 μ m and (D) 10 μ m. See also Figure S3.

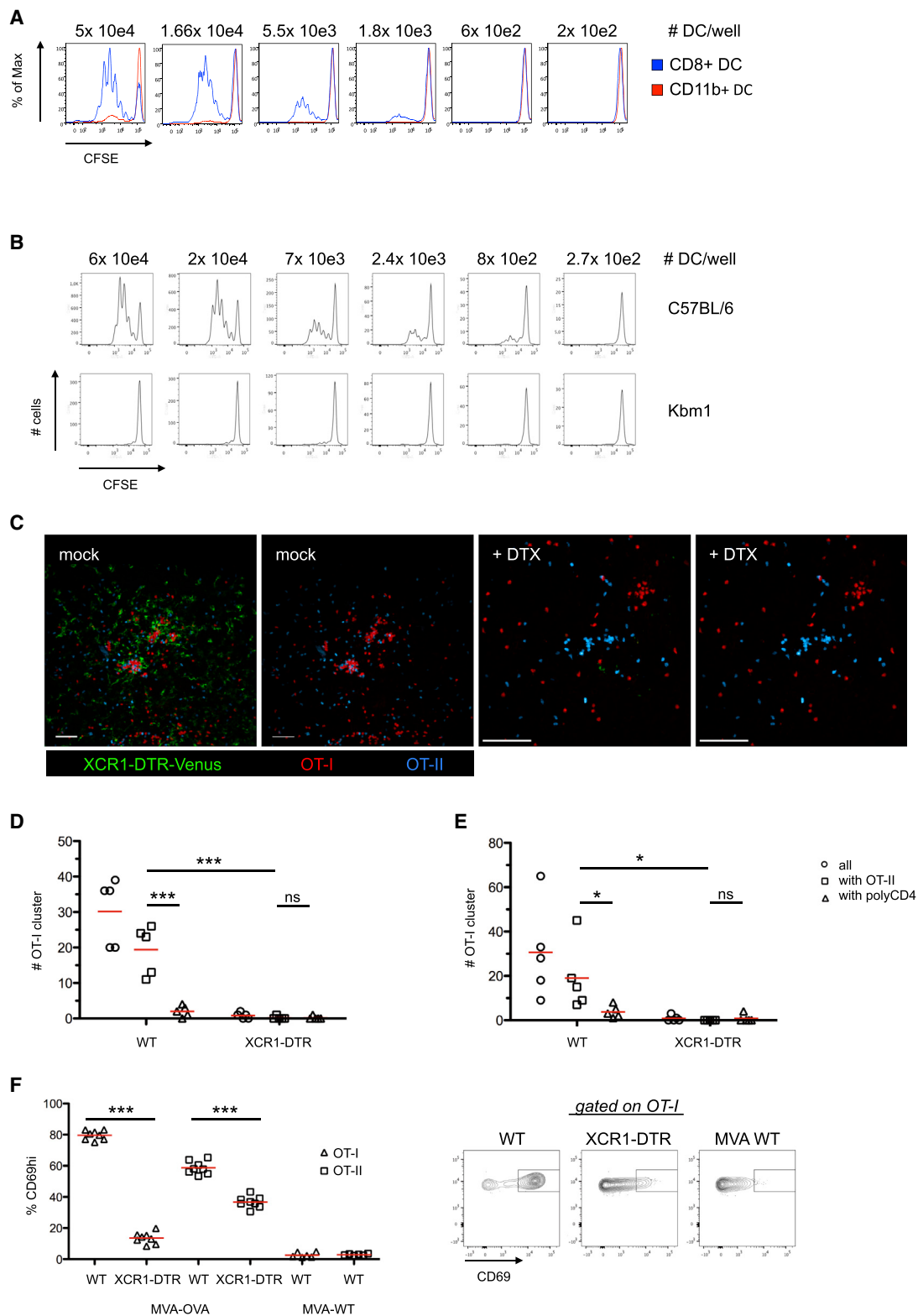


Figure 4. Non-infected Cross-presenting XCR1⁺ DCs Are the Information-Transmission Platform for CD4⁺ and CD8⁺ T Cells

(A) Proliferation of CFSE-labeled OT-I cells after ex vivo coincubation with sorted splenic DC subsets (MVA-OVA; i.v.; 30 hr p.i.).

(B) Proliferation of CFSE-labeled OT-I cells after ex vivo coincubation with isolated splenic DC from WT or Kbm1 mice (MVA-OVA-Kb; i.v.; 30 hr p.i.).

(legend continued on next page)

we found bright YFP⁺ CD8⁺ cells in the paracortex (Figure S6B). Dim YFP⁺ cells positioned in the paracortex were CD4⁺, CD8⁺, or double negative (Figure S6C). In contrast, YFP⁺ NK cells were also dim but positioned at the SCS area rather than the paracortex (Figures S6B and S6D). Even at a 100-fold higher dose of VV-OVA (10⁸), we did not observe cytokine-mediated activation of endogenous CD44⁺ CD8⁺ T cells, arguing that the identified enlarged, paracortical YFP⁺ CD8⁺ T cells reflect previously activated antigen-specific T cells (Figure S6E). To determine whether the location of such endogenous activated CD8⁺ T cells corresponds to areas of the dLN in which we expect CD4⁺ T cell help to be delivered, we transferred OT-I cells as described in Figure 3A. Endogenous YFP⁺ bright cells in the paracortex were CD69 negative or low and typically adjacent to clustered, transferred OT-I cells (Figure 6F). Examination of the distance between bright YFP⁺ cells in the paracortex and the transferred activated OT-I cells revealed that the majority of those cells were closer than 20 μm (Figure 6G). These several observations are consistent with the view that the sequential model in which initial T cell priming occurs on distinct DC subsets in different LN regions—and subsequently, information exchange occurs on XCR1⁺ DCs as platform that co-presents antigen via both MHC I and MHC II molecules—applies not just to TCR transgenic models, but to polyclonal anti-viral responses as well.

VV-Specific T Cells Activated in the Absence of XCR1⁺ DCs Are “Helpless”

If the XCR1⁺ DC platform is dispensable for early CTL activation but important for later differentiation and survival of the activated CTL, XCR1⁺ DC depletion should negatively impact proliferation, effector differentiation, and memory CTL function, equivalent to the situation of CTL priming in the absence of CD4⁺ T cell help (Wiesel and Oxenius, 2012). To test this prediction, we first analyzed the CD8⁺ T cell immune response on day (d)8 after VV infection in the presence or absence of CD4⁺ T cells. We found a significant reduction in the total number of antigen-specific CD8⁺ T cells in the spleen on d8 after infection (Figure 7A). A similar level of reduction in the immunodominant (B8R) CD8⁺ T cell response was also seen after depletion of XCR1⁺ DCs (Figure 7B). Combined CD4⁺ T cell and XCR1⁺ DC depletion showed no additional reduction as compared to CD4⁺ T cell depletion alone, arguing that help is delivered via XCR1⁺ DCs (Figure 7C). To see whether the observed reduction of the B8R-specific CD8⁺ T cell response upon XCR1⁺ DC depletion reflected the lack of help delivered via this DC population and not an unrelated function independent of antigen presentation to CD4⁺ T cells, we analyzed mixed BM (bone marrow) chimeric mice. MHCII KO × XCR1-DTR BM chimeric mice (50/50) were generated and infected with VV-OVA 8 weeks after reconstitution (Figures S7A and S7B). In these animals, application of DTX results in a 50% depletion of XCR1⁺ DCs with the remaining XCR1⁺ DCs lacking

expression of MHCII. Such MHCII-deficient DCs cannot serve as a platform for delivery of help (Figure 7D). The depletion of XCR1⁺ MHCII⁺ DCs led to a significant reduction in the anti-viral B8R-specific CD8⁺ T cell response on d8 post-priming (Figure 7E).

We further examined whether the absence of XCR1⁺ DCs impacts CD8⁺ T cell differentiation to an effector or memory state (Janssen et al., 2003; Shedlock and Shen, 2003; Sun and Bevan, 2003). We found a striking shift toward terminally differentiated effector cells (CD127⁻/KLRG1⁺) and a relative loss of memory precursors (CD127⁺/KLRG1⁻) if XCR1⁺ DCs were depleted (Figure 7F), along with a significant reduction in the capacity of the activated CD8⁺ T cells to produce IL-2 (Figure 7G). A similar loss in IL-2 producing cells was also observed when starting the depletion after infection (Figures S7C–S7E). In contrast, the capacity of antigen-specific CD8⁺ T cells to produce IFNγ appeared to be unaltered when comparing these conditions (Figure S7F). Next, we analyzed the memory response in mice that were previously infected with VV-OVA in the presence or absence of XCR1⁺ DCs. Interestingly, we detected only a small but significant reduction in the total numbers of B8R multimer-specific CD8⁺ T cell in the memory phase if XCR1⁺ DCs were absent during priming (Figure S7G). However, analysis of memory subsets on d60 post-prime showed a significant increase in KLRG1⁺ B8R multimer-specific memory T cells if XCR1⁺ DCs were depleted during priming (Figures 7H and 7I). This memory subset was characterized by prominent CD127 expression typically seen in classical central memory T cells (CD127^{hi}/KLRG1⁻). The antigen-specific CD8⁺ memory T cells had a full capacity to produce IFNγ if XCR1⁺ DCs were absent during priming (Figure 7J). Yet, these memory CD8⁺ T cells had a profound defect in IL-2 production (Figure 7K), which was characterized by a reduction of polyfunctional T cells (IFNγ⁺ TNFα⁺ IL-2⁺) (Figure 7K) and a reduced amount of IL-2 production on a single-cell level as measured by the MFI (Figure S7H). Finally, to test the capacity of the memory cells generated in the absence or presence of XCR1⁺ DCs to undergo optimal secondary expansion, we rechallenged such mice with *L. monocytogenes* expressing the B8R peptide (Lm-B8R). 5 days after challenge, we found that mice that lacked XCR1⁺ DCs during the priming with VV-OVA failed to mount a robust recall response against LM-B8R (Figure 7L), providing a physiological relevance of XCR1⁺ DCs as a critical platform for delivery of cognate helper signals from CD4⁺ T cells.

DISCUSSION

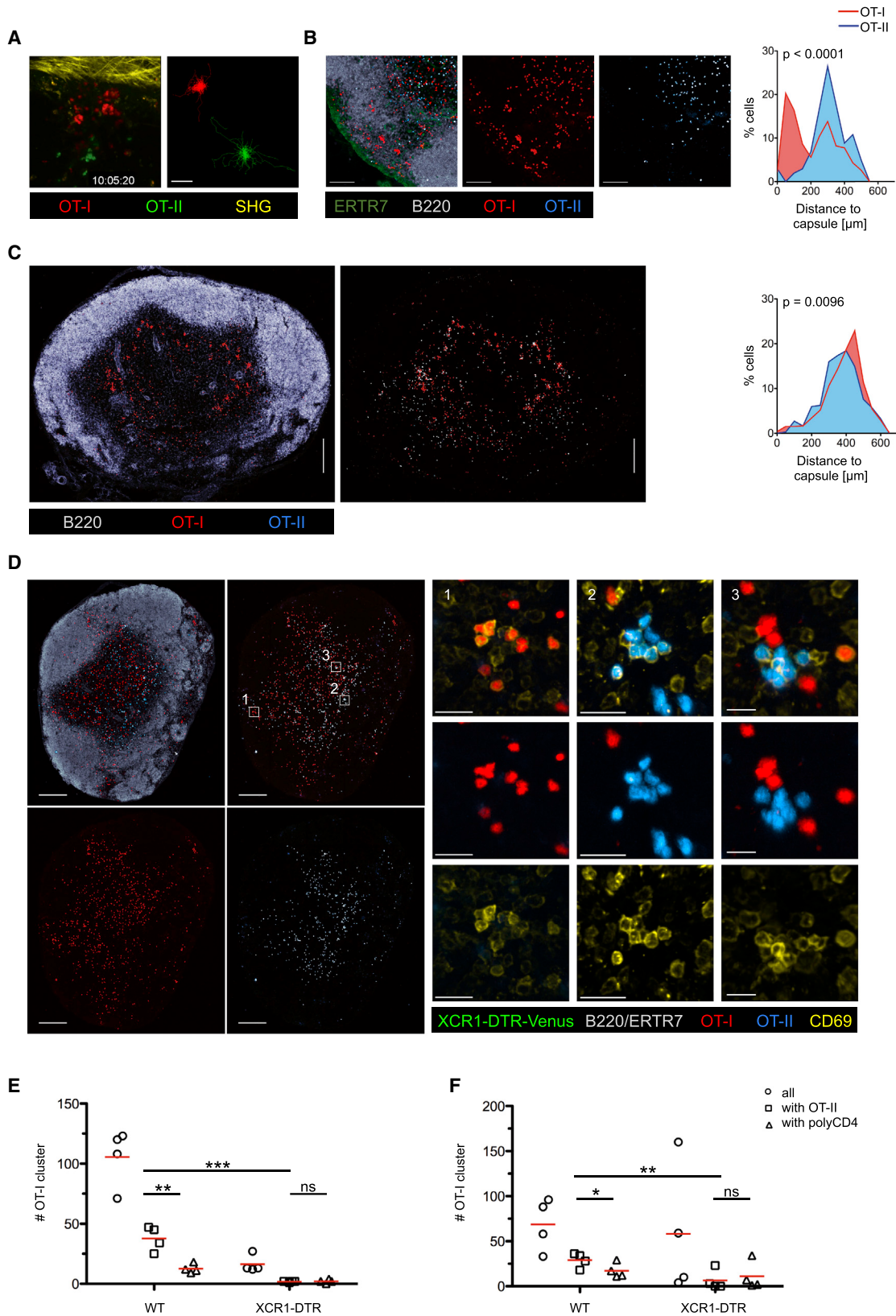
Here, we report the spatio-temporal dynamics of CD4⁺ and CD8⁺ T cells early after viral infection and the role of distinct DC subpopulations in both activation of and communication between CD4⁺ and CD8⁺ T cells during this crucial phase of the adaptive immune response. Our data reveal a complex

(C) Images of dLN using the experimental setup as in Figure 3A. XCR1-DTR-Venus mice were treated with PBS or DTX.

(D and E) T cell cluster abundance in the presence or absence of XCR1⁺ DC using a (D) semi-automated or (E) fully automated analysis.

(F) Analysis and representative plots of CD69 expression on OT-I/OT-II cells that were transferred 28 hr post-infection (MVA-OVA/MVA WT; f.p.) and analyzed 12 hr later in the dLN. Data are representative of three independent experiments (n = 8). (D–F) Red bars indicate mean values. ***p ≤ 0.001, *p ≤ 0.05; ns, non-significant. (C) Scale bars, 50 μm.

See also Figure S4.



(legend on next page)

choreography during the initiation of cell-mediated immunity, the specific features of which help clarify what seem to be contradictory observations in the literature. We find that (1) initial activation of CD4⁺ and CD8⁺ T cells is spatially separated and involves distinct DC; (2) CD8⁺ T cells are first activated by infected DC and CD4⁺ T cells by non-infected DC; (3) later during infection a third DC population (XCR1⁺ DCs) presents antigen to both CD4⁺ and CD8⁺ T cells; and (4) these XCR1⁺ DCs are a platform for communication between CD4⁺ and CD8⁺ T cells, shaping the differentiation of the latter and modulating memory programming even in situations in which cross-presentation per se is not required.

The finding that early CD4⁺ and CD8⁺ T cell activation post-infection is separated and orchestrated at distinct anatomical localizations was surprising. This feature may have been missed in previous studies because of an exclusive focus on the dynamic behavior of CD8⁺ T cells (Hickman et al., 2008, 2011; Kastenmüller et al., 2013) or the use of peptide-pulsed DC when co-analysis of both CD4⁺ and CD8⁺ behavior was studied (Beuneu et al., 2006; Castellino et al., 2006). Several reports previously showed a propensity of distinct DC subsets to present via either MHC I or MHC II molecules when using protein antigens (den Haan et al., 2000; Dudziak et al., 2007; Schnorrer et al., 2006). Factors that regulate such differential antigen-presentation among DC subsets have been described (Dudziak et al., 2007; Vander Lugt et al., 2014), and numerous viral immune evasion proteins that interfere with antigen-presentation have been identified (Alcami and Koszinowski, 2000). However, the profound spatial segregation of CD4⁺ versus CD8⁺ T cell activation early after infection requires additional investigation to more fully understand the basis for this phenomenon and its relevance to the acute and memory phases of immunity. Given the preferential localization of DC subsets within subregions of the LN (Gerner et al., 2012; Kissenfennig et al., 2005), these new findings suggest a complex combination of intrinsic DC biology and pathogen-associated effects on antigen presentation and localization of DC subsets will greatly affect the nature of the ensuing cell-mediated response.

It is unknown how many naive CD8⁺ T cells actually require signals derived from CD4⁺ T cells to mount a robust and functional memory CD8⁺ T cell response. In any given naive mouse repertoire of a few hundred CD8⁺ T cells specific for a foreign antigen, it might just be (the proliferative progeny of) a few initially activated T cells that receive functional “help” from CD4⁺ T cells. This quantitative issue places some limits on the interpretation of our results. Because we cannot directly visualize the specific subset of “helped” CD8⁺ T cells as they receive the necessary

molecular signals, we cannot formally exclude the possibility that the relevant memory CD8⁺ T cell pool is formed by the offspring of a few T cells that do not correspond to the bulk behavior of the cells we quantify. Specifically, it is possible that a minor, but biologically relevant population of naive CD8⁺ T cells encounters a cross-presenting (helped) XCR1⁺ DC first rather than undergoing initial activation on a directly infected non-licensed DC as in our proposed model.

Nonetheless, several lines of reasoning support the notion that CD4⁺ T cell help is primarily delivered to activated rather than naive CD8⁺ T cells. First, although CCR5 expression can occur in a TCR-independent manner, optimal upregulation of this chemokine receptor occurs upon antigen activation, giving the T cells the capacity to follow chemokine signals to the licensed DCs (Castellino et al., 2006). Second, naive T cells interact for many hours with DCs that present high-potency foreign antigens. During this period (defined as phase II by Mempel et al. [2004]), the DC-engaged CD8⁺ T cells would not be able to search for the optimal (licensed) DCs. After these long-lasting interactions, activated T cells enter a third phase that is characterized by short interactions with DCs (Mempel et al., 2004). To date, the biological relevance of this third phase has remained elusive. Our model assigns it a potential specific biological function, namely the search for licensed DCs. Third, besides CD8⁺ T cells, CD4⁺ T cells also require pre-activation in order to express the molecules that are required to deliver help, in particular CD40 ligand (Bennett et al., 1998; Ridge et al., 1998; Schoenberger et al., 1998). Finally, our new model reveals a close similarity between the cellular events that occur during CD4⁺ help for B cells and for CD8⁺ T cells. B cells and CD8⁺ T cells are activated separately from CD4⁺ T cell helpers at different anatomical locations before they come together for signal exchange (McHeyzer-Williams et al., 2006).

Besides the implication that pre-activated rather than naive lymphocytes deliver/receive help, LN-resident XCR1⁺ DCs have been identified as the critical platform on which such signals are transmitted. Interestingly, migratory DCs seemed dispensable for initial CD8⁺ T cell activation or for provision of help. Vaccinia virus particles directly disseminate to the dLN after local intradermal infection of the skin (Lin et al., 2013), in contrast to *Herpes simplex* virus that requires migratory DCs to shuttle antigen to the dLN (Bedoui et al., 2009). With the latter virus, migratory DCs are required to hand off antigen to LN-resident DCs (Allan et al., 2006). This hand-off is in line with our work showing the crucial requirement of LN-resident XCR1⁺ DCs rather than migratory DCs to act as a critical platform to provide help to CD8⁺ T cells.

Figure 5. XCR1⁺ DCs Are the Information Transfer Platform for CD4⁺ and CD8⁺ T Cells during VV Infection

- (A) IF image and translated tracks from IVM of the popliteal LN 10–11 hr after VV-OVA infection (f.p.). See also Movie S3.
 - (B) IF images of a dLN showing the localization and cluster formation of transferred OT-I and OT-II cells (VV-OVA; f.p.; 10 hr p.i.). Histogram shows distance of OT-I and OT-II from capsule.
 - (C and D) IF images of the dLN of a XCR-DTR-Venus mice treated with PBS (C) or DTX (D) showing the localization of labeled OT-I and OT-II cells following the experimental set-up shown in Figure 3A using VV-OVA. Histogram shows distance of OT-I and OT-II from capsule.
 - (E and F) T cell cluster abundance in the presence or absence of XCR1⁺ DCs using a (E) semi-automated or (F) fully automated analysis. Data are representative of three independent experiments ($n = 4$). (E and F) Red bars indicate mean values. *** $p \leq 0.001$, ** $p \leq 0.01$, and * $p \leq 0.05$; ns, non-significant. Scale bars, (A) 50 μ m, (B) 100 μ m, (C) 200 μ m, and (D) 200 μ m/20 μ m.
- See also Figure S5 and Movie S4.

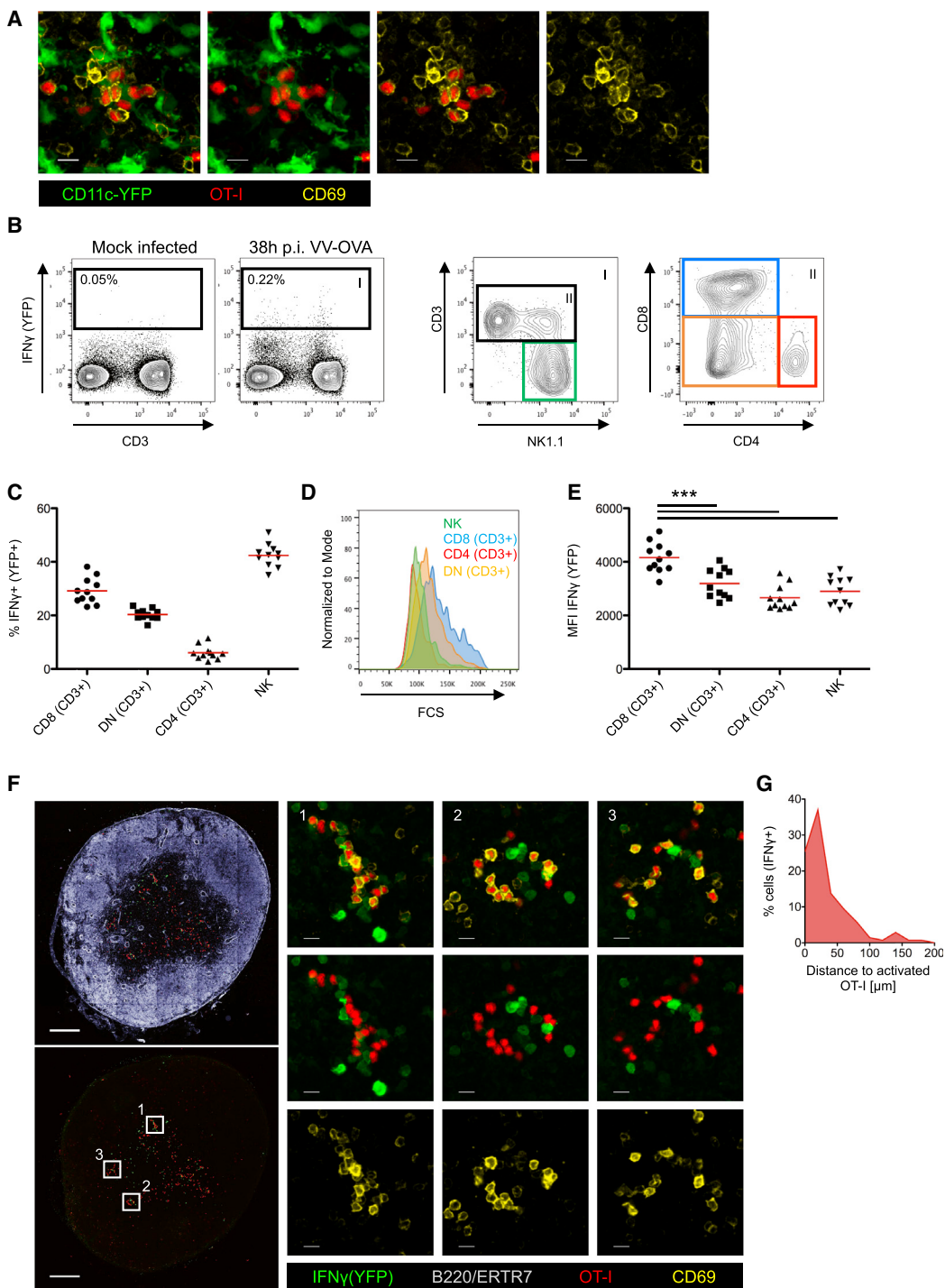


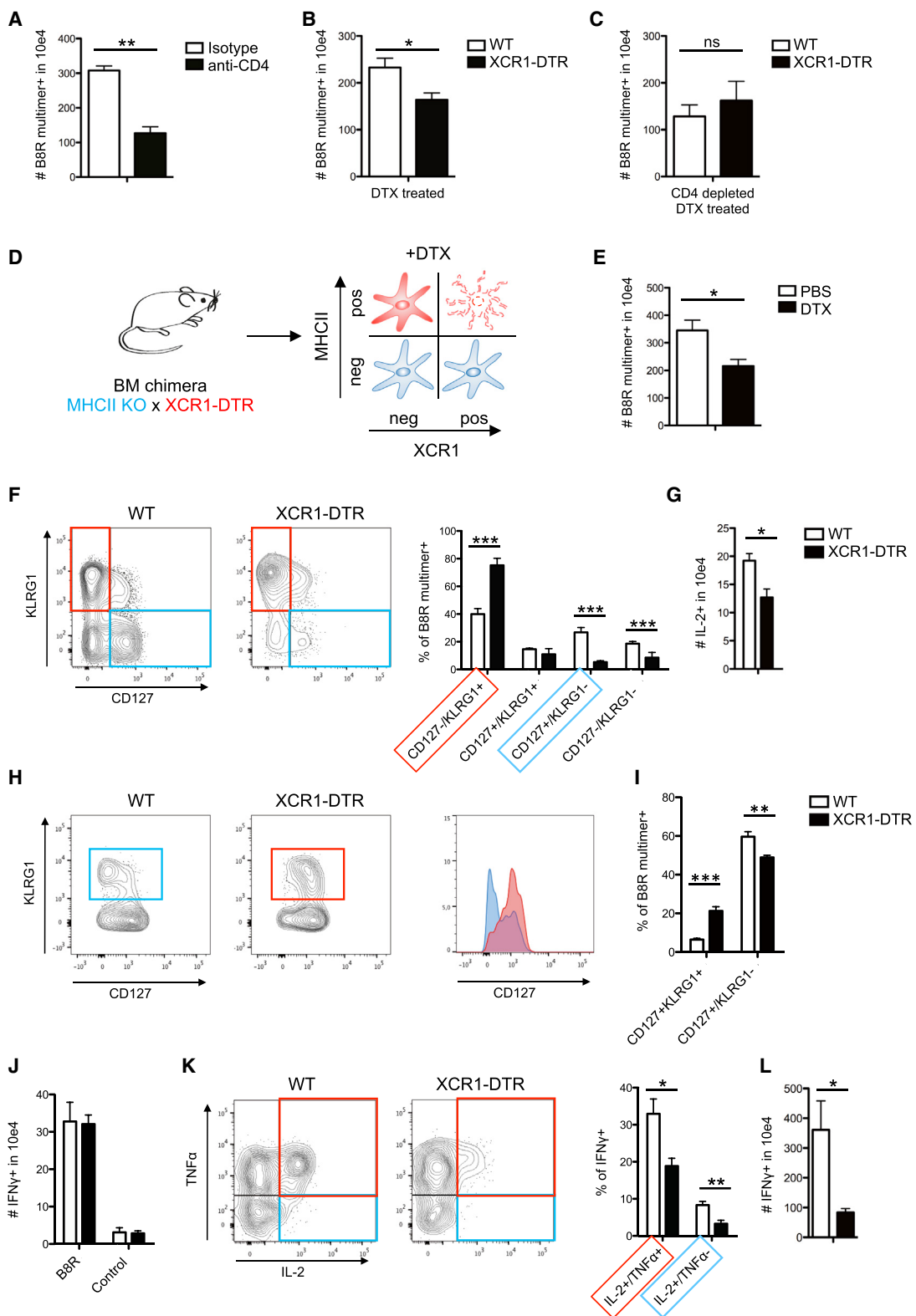
Figure 6. Localization of Endogenous Activated CD8⁺ T Cells during VV Infection

(A) IF Images of a LN showing co-localization of transferred OT-I cells and endogenous (non-OT-I) CD69^{hi} cells (VV-OVA; f.p.; 10 hr p.i.).

(B–E) Analysis of IFN γ (YFP⁺) reporter animals (VV-OVA; 36 hr p.i.). (B) Graphs show the gating strategy, (C) the cellular distribution, (D) the size distribution, and (E) the mean fluorescence intensity (MFI) of the YFP signal of IFN γ (YFP⁺) cells.

(F) IF images showing the localization of YFP-expressing cells 36 hr after infection of IFN γ (YFP⁺) reporter animals (VV-OVA; f.p.). OT-I cells were transferred 8 hr before analysis.

(G) Histogram shows the distance between IFN γ (YFP⁺) cells and activated (CD69^{hi}) OT-I cells. Data are representative of at least two independent experiments. (C), (E), and (G) show pooled data (C and E, n = 11) (G, n = 4). (C and E) Red bars indicate mean values. ***p ≤ 0.001. Scale bar, (A) 10 μ m and (F) 200 μ m/10 μ m. See also Figure S6.

**Figure 7. VV-Specific T Cells Activated in the Absence of XCR1⁺ DC Are “Helpless”**

(A–C) Analysis of the total numbers of B8R multimer-specific splenic CD8⁺ T cells 8 days after VV-OVA infection (i.p.). Comparison of (A) isotype versus CD4 depleted mice, (B) WT versus XCR1-DTR mice treated with DTX, and (C) WT versus XCR1-DTR mice treated with DTX and anti-CD4 antibody.

(legend continued on next page)

The XCR1⁺ DC subset has primarily received attention due to its capacity to cross-present antigens (Shortman and Heath, 2010). Our experiments have uncovered an important additional function by using a model that does not require cross-presentation for CD8⁺ T cell priming (Xu et al., 2010). In this situation, the absence of XCR1⁺ DCs had a small effect on the primary immune response, compared to the absence of CD4⁺ T cell help. However, we found a profound role of XCR1⁺ DCs on the differentiation of CD8⁺ T cells and the functionality of the resulting memory T cells, which largely lacked the ability to produce the IL-2 needed for an optimal recall response (Feau et al., 2011). This function of XCR1⁺ DCs is optimized by signals from CD4⁺ helper T cells, which is consistent with the equivalent reduction of the CD8⁺ T cell response after depletion of XCR1⁺ DCs or of CD4⁺ T cells (Figures 7A–7C).

The observations reported here provide a new level of understanding of the complex cell-cell interactions that underlie effective cell-mediated immune responses. Two distinct conventional T cell subsets (CD4⁺ and CD8⁺ $\alpha\beta$ T cells) and a variety of different DC subtypes (CD11b⁺, XCR1⁺, and possibly others) operate in a staged, dynamic process to provide both early effectors and memory cells that later support host defense upon re-infection. In the context of previous findings on the contribution of chemokine signaling to optimization of communication involving T cell subsets and DCs (Castellino et al., 2006; Hickman et al., 2011; Hugues et al., 2007) and evidence for phased changes in T cell migratory dynamics after viral infection (Mempel et al., 2004), we are now able to draw an increasing complete picture of how this limb of the adaptive immune system operates to enable rare cells to generate robust acute and memory responses. The new evidence for distinct roles of DC subsets in primary activation of CD4⁺ versus CD8⁺ T cells and as a platform for their communication also provides guidance for how to best direct vaccine components to drive specific aspects of immunity.

EXPERIMENTAL PROCEDURES

Animals

Mice were purchased from Jackson or Janvier Labs or maintained at in-house facilities. All mice were maintained in specific pathogen-free conditions at an Association for Assessment and Accreditation of Laboratory Animal Care-accredited animal facility. All procedures were approved by the NIAID Animal Care and Use Committee (NIH) and the North Rhine-Westphalia State Environment Agency (LUA NRW), respectively. For details on mouse strains, see Supplemental Information.

Viruses, Bacteria, and Infections

10^7 – 10^8 IU recombinant MVA, 10^6 – 10^7 PFU VV-OVA, 2×10^7 PFU Ad-OVA-GFP or 5×10^3 CFU LM-B8R were diluted in PBS and injected in the footpad (fotchuck [Kamala, 2007]), i.v. or i.p.

(D) Schematic of DC composition in BM chimeric animals (MHCI KO x XCR1-DTR → WT).

(E) Antiviral CD8⁺ immune response is shown comparing DTX versus PBS-treated BM chimeric animals on d8 (VV-OVA i.p.).

(F and G) Analysis of B8R-specific immune responses d8 p.i. (VV-OVA i.p.), comparing WT versus XCR1-DTR animals treated with DTX, showing (F) the phenotype of B8R multimer-specific CD8⁺ T cells and (G) the number of IL-2-producing CD8⁺ T cells after peptide (B8R) stimulation for 5 hr.

(H–L) Analysis of the immune response 60 p.i. (VV-OVA i.p.), comparing WT versus XCR1-DTR animals treated with DTX. (H) Phenotype and (I) relative frequency of B8R multimer-specific memory subsets. (J) Absolute numbers of IFN γ -producing CD8⁺ T cells, (K) relative frequency of polyfunctional CD8⁺ T cells (gated on IFN γ ⁺) after peptide (B8R) stimulation. (L) Recall response d5 after Lm-B8R challenge. Graph shows total numbers of IFN γ -producing CD8⁺ T cells after peptide (B8R) stimulation. Data are representative of three or two (L) independent experiments ($n = 4$). The graphs show mean +SEM., ** $p \leq 0.001$, ** $p \leq 0.01$, and * $p \leq 0.05$; ns, non-significant.

See also Figure S7.

Adoptive T Cell Transfer

OT-I, OT-II, P14, Smarta, or polyclonal control CD4⁺ T cells were purified using a MACS CD4- or CD8-negative selection kit (Miltenyi) combined with biotinylated anti-CD44 (IM7, BD Biosciences). $2\text{--}4 \times 10^6$ cells were transferred i.v.

In Vitro Proliferation Assay

OT-I cells were isolated and labeled with CFSE 5 μM (Invitrogen), followed by an ex vivo 72 hr co-incubation with isolated splenic DCs or LN-derived DCs.

Isolation of DC and Cell Sorting

Spleens or LNs were harvested and digested with Collagenase D/DNase for 30 min followed by a DC enrichment step using MACS CD11c-positive selection kit (Miltenyi) and sorting based on CD11c, MHCII, CD8, and CD11b staining using a FACSaria (BD Biosciences) cell sorter. Cellular purity was >95%.

Flow Cytometry

For analysis, LN and spleens were harvested and single-cell suspensions were generated. For details on antibodies, see Supplemental Information.

Immunofluorescence Staining

PLP-fixed, frozen tissues were cut, stained, mounted, and acquired on a 710 confocal microscope (Carl Zeiss Microimaging). For details on antibodies, see Supplemental Information.

Intravital Two-Photon Imaging

Mice were anesthetized, popliteal LNs were exposed, and intravital microscopy was performed using a protocol modified from a previous report (Kastenmüller et al., 2013). Raw imaging data were processed and analyzed with Imaris (Bitplane). For details, see Supplemental Information.

Analysis of Imaging Data

Images were systematically analyzed using a semi-automated (Imaris/Bitplane) and a fully automated approach. For details, see Supplemental Information.

Statistical Analysis

Student's t test (two-tailed) and Mann-Whitney test were used for the statistical analysis of differences between two groups with normal and non-normal distribution.

SUPPLEMENTAL INFORMATION

Supplemental Information includes Supplemental Experimental Procedures, seven figures, and four movies and can be found with this article online at <http://dx.doi.org/10.1016/j.cell.2015.08.004>.

AUTHOR CONTRIBUTIONS

S.E. and A.B. planned and performed experiments and analyzed data; M.Y.G., K.K., and H.H. analyzed data and designed experiments; F.K. developed analysis software and analyzed imaging data; and T.K. and N.G. were involved in study design. R.N.G. and W.K. conceptually designed the study, analyzed the data, and wrote the manuscript.

ACKNOWLEDGMENTS

We would like to thank S. Ebbinghaus and S. Rathmann for technical assistance; C. Kurts for scientific discussions and critically reading the manuscript; G. Sutter for help with generation of recombinant (rec.) MVA's; J. Bennink, R.M. Kedl, P. Knolle, and D.H. Busch for kindly providing VV-OVA, LM-B8R, AdOVA, and MHCI multimers, respectively. This research was supported by the Intramural Research Program, NIAID, and NIH. W.K. and N.G. are members of the DFG Excellence Cluster ImmunoSensation in Bonn, Germany and are supported by grant SFB670/SFB704. W.K. is supported by NRW-Rückkehrerprogramm of the German state of Northrhine-Westfalia. T.K. was supported by the Kishimoto Foundation, grants from The Ministry of Education, Culture, Sports, Science and Technology of Japan (MEXT), and Japan Society for the Promotion of Science. F.K. was supported by the Human Frontier Science Program (HFSP RGY007/2011) and the Einstein Foundation Berlin.

Received: January 19, 2015

Revised: June 7, 2015

Accepted: July 23, 2015

Published: August 18, 2015

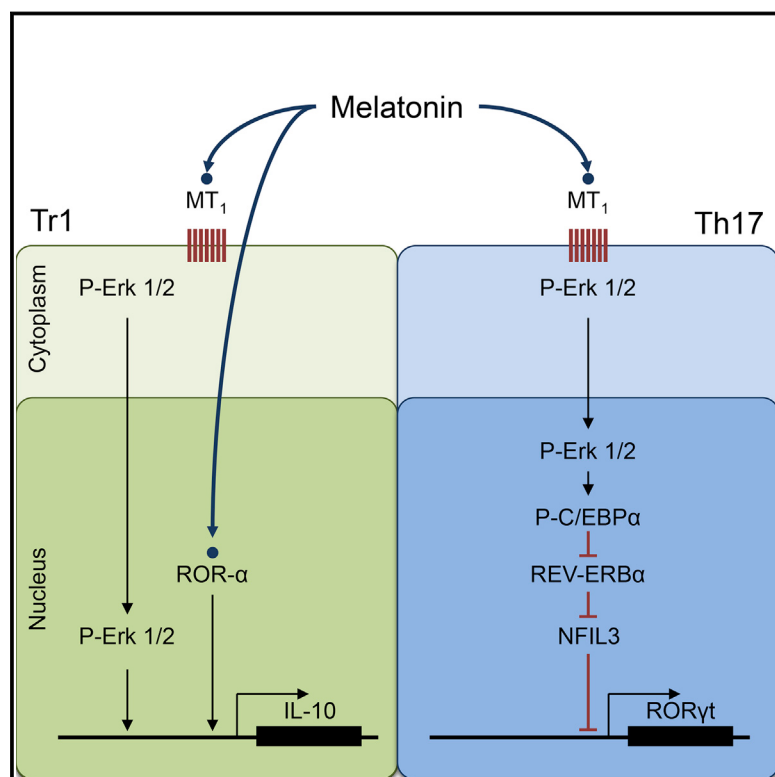
REFERENCES

- Alcami, A., and Koszinowski, U.H. (2000). Viral mechanisms of immune evasion. *Trends Microbiol.* 8, 410–418.
- Allan, R.S., Waithman, J., Bedoui, S., Jones, C.M., Villadangos, J.A., Zhan, Y., Lew, A.M., Shortman, K., Heath, W.R., and Carbone, F.R. (2006). Migratory dendritic cells transfer antigen to a lymph node-resident dendritic cell population for efficient CTL priming. *Immunity* 25, 153–162.
- Becker, M., Gütter, S., Bachem, A., Hartung, E., Mora, A., Jäkel, A., Hutloff, A., Henn, V., Mages, H.W., Gurka, S., and Krocze, R.A. (2014). Ontogenetic, Phenotypic, and Functional Characterization of XCR1(+) Dendritic Cells Leads to a Consistent Classification of Intestinal Dendritic Cells Based on the Expression of XCR1 and SIRP α . *Front. Immunol.* 5, 326.
- Bedoui, S., Whitney, P.G., Waithman, J., Eidsmo, L., Wakim, L., Caminschi, I., Allan, R.S., Wojtasik, M., Shortman, K., Carbone, F.R., et al. (2009). Cross-presentation of viral and self antigens by skin-derived CD103+ dendritic cells. *Nat. Immunol.* 10, 488–495.
- Bennett, S.R., Carbone, F.R., Karamalis, F., Miller, J.F., and Heath, W.R. (1997). Induction of a CD8+ cytotoxic T lymphocyte response by cross-priming requires cognate CD4+ T cell help. *J. Exp. Med.* 186, 65–70.
- Bennett, S.R., Carbone, F.R., Karamalis, F., Flavell, R.A., Miller, J.F., and Heath, W.R. (1998). Help for cytotoxic-T-cell responses is mediated by CD40 signalling. *Nature* 393, 478–480.
- Beuneu, H., Garcia, Z., and Bousso, P. (2006). Cutting edge: cognate CD4 help promotes recruitment of antigen-specific CD8 T cells around dendritic cells. *J. Immunol.* 177, 1406–1410.
- Bevan, M.J. (2004). Helping the CD8(+) T-cell response. *Nat. Rev. Immunol.* 4, 595–602.
- Bousso, P., and Robey, E. (2003). Dynamics of CD8+ T cell priming by dendritic cells in intact lymph nodes. *Nat. Immunol.* 4, 579–585.
- Cassell, D., and Forman, J. (1988). Linked recognition of helper and cytotoxic antigenic determinants for the generation of cytotoxic T lymphocytes. *Ann. NY Acad. Sci.* 532, 51–60.
- Castellino, F., and Germain, R.N. (2006). Cooperation between CD4+ and CD8+ T cells: when, where, and how. *Annu. Rev. Immunol.* 24, 519–540.
- Castellino, F., Huang, A.Y., Altan-Bonnet, G., Stoll, S., Scheinecker, C., and Germain, R.N. (2006). Chemokines enhance immunity by guiding naïve CD8+ T cells to sites of CD4+ T cell-dendritic cell interaction. *Nature* 440, 890–895.
- Crotty, S. (2014). T follicular helper cell differentiation, function, and roles in disease. *Immunity* 41, 529–542.
- Curtsinger, J.M., and Mescher, M.F. (2010). Inflammatory cytokines as a third signal for T cell activation. *Curr. Opin. Immunol.* 22, 333–340.
- den Haan, J.M., Lehar, S.M., and Bevan, M.J. (2000). CD8(+) but not CD8(-) dendritic cells cross-prime cytotoxic T cells in vivo. *J. Exp. Med.* 192, 1685–1696.
- Drexler, I., Staib, C., and Sutter, G. (2004). Modified vaccinia virus Ankara as antigen delivery system: how can we best use its potential? *Curr. Opin. Biotechnol.* 15, 506–512.
- Dudziak, D., Kamphorst, A.O., Heidkamp, G.F., Buchholz, V.R., Trumpfheller, C., Yamazaki, S., Cheong, C., Liu, K., Lee, H.-W., Park, C.G., et al. (2007). Differential antigen processing by dendritic cell subsets in vivo. *Science* 315, 107–111.
- Edelson, B.T., Kc, W., Juang, R., Kohyama, M., Benoit, L.A., Klekotka, P.A., Moon, C., Albring, J.C., Ise, W., Michael, D.G., et al. (2010). Peripheral CD103+ dendritic cells form a unified subset developmentally related to CD8alpha+ conventional dendritic cells. *J. Exp. Med.* 207, 823–836.
- Feau, S., Arens, R., Togher, S., and Schoenberger, S.P. (2011). Autocrine IL-2 is required for secondary population expansion of CD8(+) memory T cells. *Nat. Immunol.* 12, 908–913.
- Germain, R.N. (1994). MHC-dependent antigen processing and peptide presentation: providing ligands for T lymphocyte activation. *Cell* 76, 287–299.
- Gerner, M.Y., Kastenmüller, W., Ifrim, I., Kabat, J., and Germain, R.N. (2012). Histo-cytometry: a method for highly multiplex quantitative tissue imaging analysis applied to dendritic cell subset microanatomy in lymph nodes. *Immunity* 37, 364–376.
- Hickman, H.D., Takeda, K., Skon, C.N., Murray, F.R., Hensley, S.E., Loomis, J., Barber, G.N., Bennink, J.R., and Yewdell, J.W. (2008). Direct priming of anti-viral CD8+ T cells in the peripheral interfollicular region of lymph nodes. *Nat. Immunol.* 9, 155–165.
- Hickman, H.D., Li, L., Reynoso, G.V., Rubin, E.J., Skon, C.N., Mays, J.W., Gibbs, J., Schwartz, O., Bennink, J.R., and Yewdell, J.W. (2011). Chemokines control naïve CD8+ T cell selection of optimal lymph node antigen presenting cells. *J. Exp. Med.* 208, 2511–2524.
- Hugues, S., Scholer, A., Boissonnas, A., Nussbaum, A., Combadière, C., Amigorena, S., and Fétter, L. (2007). Dynamic imaging of chemokine-dependent CD8+ T cell help for CD8+ T cell responses. *Nat. Immunol.* 8, 921–930.
- Janssen, E.M., Lemmens, E.E., Wolfe, T., Christen, U., von Herrath, M.G., and Schoenberger, S.P. (2003). CD4+ T cells are required for secondary expansion and memory in CD8+ T lymphocytes. *Nature* 421, 852–856.
- Kamala, T. (2007). Hock immunization: a humane alternative to mouse footpad injections. *J. Immunol. Methods* 328, 204–214.
- Kastenmüller, W., Brandes, M., Wang, Z., Herz, J., Egen, J.G., and Germain, R.N. (2013). Peripheral prepositioning and local CXCL9 chemokine-mediated guidance orchestrate rapid memory CD8+ T cell responses in the lymph node. *Immunity* 38, 502–513.
- Kissenpennig, A., Henri, S., Dubois, B., Laplace-Builhé, C., Perrin, P., Romani, N., Tripp, C.H., Douillard, P., Leserman, L., Kaiserlian, D., et al. (2005). Dynamics and function of Langerhans cells in vivo: dermal dendritic cells colonize lymph node areas distinct from slower migrating Langerhans cells. *Immunity* 22, 643–654.
- Kurts, C., Robinson, B.W., and Knolle, P.A. (2010). Cross-priming in health and disease. *Nat. Rev. Immunol.* 10, 403–414.
- Lin, L.C., Flesch, I.E., and Tscharke, D.C. (2013). Immunodomination during peripheral vaccinia virus infection. *PLoS Pathog.* 9, e1003329.
- McHeyzer-Williams, L.J., Malherbe, L.P., and McHeyzer-Williams, M.G. (2006). Checkpoints in memory B-cell evolution. *Immunol. Rev.* 211, 255–268.
- Mempel, T.R., Henrickson, S.E., and Von Andrian, U.H. (2004). T-cell priming by dendritic cells in lymph nodes occurs in three distinct phases. *Nature* 427, 154–159.
- Miller, M.J., Wei, S.H., Parker, I., and Cahalan, M.D. (2002). Two-photon imaging of lymphocyte motility and antigen response in intact lymph node. *Science* 296, 1869–1873.

- Mitchison, N.A., and O'Malley, C. (1987). Three-cell-type clusters of T cells with antigen-presenting cells best explain the epitope linkage and noncognate requirements of the *in vivo* cytolytic response. *Eur. J. Immunol.* 17, 1579–1583.
- Norbury, C.C., Princiotta, M.F., Bacik, I., Brutkiewicz, R.R., Wood, P., Elliott, T., Bennink, J.R., and Yewdell, J.W. (2001). Multiple antigen-specific processing pathways for activating naive CD8+ T cells *in vivo*. *J. Immunol.* 166, 4355–4362.
- Ridge, J.P., Di Rosa, F., and Matzinger, P. (1998). A conditioned dendritic cell can be a temporal bridge between a CD4+ T-helper and a T-killer cell. *Nature* 393, 474–478.
- Schnorrer, P., Behrens, G.M., Wilson, N.S., Pooley, J.L., Smith, C.M., El-Sukkari, D., Davey, G., Kupresanin, F., Li, M., Maraskovsky, E., et al. (2006). The dominant role of CD8+ dendritic cells in cross-presentation is not dictated by antigen capture. *Proc. Natl. Acad. Sci. USA* 103, 10729–10734.
- Schoenberger, S.P.S., Toes, R.E.R., van der Voort, E.I.E., Offringa, R., and Melief, C.J.C. (1998). T-cell help for cytotoxic T lymphocytes is mediated by CD40-CD40L interactions. *Nature* 393, 480–483.
- Shedlock, D.J., and Shen, H. (2003). Requirement for CD4 T cell help in generating functional CD8 T cell memory. *Science* 300, 337–339.
- Shortman, K., and Heath, W.R. (2010). The CD8+ dendritic cell subset. *Immunol. Rev.* 234, 18–31.
- Stoll, S., Delon, J., Brotz, T.M., and Germain, R.N. (2002). Dynamic imaging of T cell-dendritic cell interactions in lymph nodes. *Science* 296, 1873–1876.
- Sun, J.C., and Bevan, M.J. (2003). Defective CD8 T cell memory following acute infection without CD4 T cell help. *Science* 300, 339–342.
- Vander Lugt, B., Khan, A.A., Hackney, J.A., Agrawal, S., Lesch, J., Zhou, M., Lee, W.P., Park, S., Xu, M., DeVoss, J., et al. (2014). Transcriptional programming of dendritic cells for enhanced MHC class II antigen presentation. *Nat. Immunol.* 15, 161–167.
- Wiesel, M., and Oxenius, A. (2012). From crucial to negligible: functional CD8+ T-cell responses and their dependence on CD4+ T-cell help. *Eur. J. Immunol.* 42, 1080–1088.
- Wiesel, M., Joller, N., Ehrlert, A.K., Crouse, J., Spörri, R., Bachmann, M.F., and Oxenius, A. (2010). Th cells act via two synergistic pathways to promote anti-viral CD8+ T cell responses. *J. Immunol.* 185, 5188–5197.
- Xu, R.H., Remakus, S., Ma, X., Roscoe, F., and Sigal, L.J. (2010). Direct presentation is sufficient for an efficient anti-viral CD8+ T cell response. *PLoS Pathog.* 6, e1000768.
- Yamazaki, C., Sugiyama, M., Ohta, T., Hemmi, H., Hamada, E., Sasaki, I., Fukuda, Y., Yano, T., Nobuoka, M., Hirashima, T., et al. (2013). Critical roles of a dendritic cell subset expressing a chemokine receptor, XCR1. *J. Immunol.* 190, 6071–6082.

Melatonin Contributes to the Seasonality of Multiple Sclerosis Relapses

Graphical Abstract



Authors

Mauricio F. Farez, Ivan D. Mascanfroni,
Santiago P. Méndez-Huergo, ...,
Gabriel A. Rabinovich,
Francisco J. Quintana, Jorge Correale

Correspondence

mfarez@fleni.org.ar (M.F.F.),
fquintana@rics.bwh.harvard.edu (F.J.Q.)

In Brief

Melatonin affects the differentiation and function of effector and regulatory T cells in vitro and in vivo, representing an environmental cue that contributes to the seasonality of multiple sclerosis relapses and a potential target for therapeutic intervention in immune-mediated diseases.

Highlights

- Melatonin levels negatively correlate with multiple sclerosis relapses in humans
- Melatonin treatment ameliorates pathology in a mouse model of multiple sclerosis
- Melatonin blocks ROR- γ t expression and Th17 differentiation
- Melatonin boosts Tr1 development via Erk1/2 and ROR- α

Melatonin Contributes to the Seasonality of Multiple Sclerosis Relapses

Mauricio F. Farez,^{1,*} Ivan D. Mascanfroni,² Santiago P. Méndez-Huergo,³ Ada Yeste,² Gopal Murugaiyan,² Lucien P. Garo,² María E. Balbuena Aguirre,^{1,4} Bonny Patel,² María C. Ysraelit,¹ Chen Zhu,^{2,5} Vijay K. Kuchroo,^{2,5} Gabriel A. Rabinovich,^{3,6} Francisco J. Quintana,^{2,7,*} and Jorge Correale^{1,7}

¹Center for Research on Neuroimmunological Diseases (CIEN), Raúl Carrea Institute for Neurological Research (FLENI), Buenos Aires 1428, Argentina

²Ann Romney Center for Neurologic Diseases, Brigham and Women's Hospital, Harvard Medical School, Boston, MA 02115, USA

³Laboratorio de Inmunopatología, Instituto de Biología y Medicina Experimental, Consejo Nacional de Investigaciones Científicas y Técnicas (IBYME-CONICET), Buenos Aires 1428, Argentina

⁴Department of Neurology, Hospital de Clínicas José de San Martín, Buenos Aires 1428, Argentina

⁵Evergrande Center for Immunologic Diseases, Brigham and Women's Hospital, Harvard Medical School, Boston, MA 02115, USA

⁶Facultad de Ciencias Exactas y Naturales, Universidad de Buenos Aires, Buenos Aires 1428, Argentina

⁷Co-senior author

*Correspondence: mfarez@fleni.org.ar (M.F.F.), fquintana@rics.bwh.harvard.edu (F.J.Q.)

<http://dx.doi.org/10.1016/j.cell.2015.08.025>

SUMMARY

Seasonal changes in disease activity have been observed in multiple sclerosis, an autoimmune disorder that affects the CNS. These epidemiological observations suggest that environmental factors influence the disease course. Here, we report that melatonin levels, whose production is modulated by seasonal variations in night length, negatively correlate with multiple sclerosis activity in humans. Treatment with melatonin ameliorates disease in an experimental model of multiple sclerosis and directly interferes with the differentiation of human and mouse T cells. Melatonin induces the expression of the repressor transcription factor Nfil3, blocking the differentiation of pathogenic Th17 cells and boosts the generation of protective Tr1 cells via Erk1/2 and the transactivation of the IL-10 promoter by ROR- α . These results suggest that melatonin is another example of how environmental-driven cues can impact T cell differentiation and have implications for autoimmune disorders such as multiple sclerosis.

INTRODUCTION

Multiple sclerosis (MS) is an immune-mediated disease of the CNS that is thought to result from the destruction of myelin by autoreactive T cells. CD4 $^{+}$ T cells characterized by the production of IFN- γ (Th1 cells) or IL-17 (Th17 cells) are considered important contributors to MS immunopathogenesis (Miossec et al., 2009; Sospedra and Martin, 2005; Steinman, 2014). FoxP3 $^{+}$ regulatory T cells (Tregs) and IL-10-secreting type 1 regulatory T cells (Tr1) regulate the activity of effector T cells, accordingly, deficits in Tregs and Tr1 cells have been described in MS (Astier et al., 2006; Sakaguchi et al., 2010; Viglietta et al., 2004). Thus, the balance between effector and regulatory

T cells controls MS disease activity (Miossec et al., 2009; Sospedra and Martin, 2005; Steinman, 2014).

Genetic polymorphisms have been associated with MS risk and/or pathogenesis (Beecham et al., 2013; Sawcer et al., 2011). However, environmental factors such as infections (Ascherio et al., 2001; Correale and Farez, 2007; Correale et al., 2006), sodium intake (Farez et al., 2014), smoking (Hernán et al., 2005), and vitamin D levels (Ascherio et al., 2014) are also known to affect MS development and course. Lower levels of vitamin D, for example, are associated with higher relapse rates (Runia et al., 2012; Simpson et al., 2010). As a result of the regulation of its synthesis by sun exposure, a significant seasonal fluctuation on vitamin D levels is observed in most locations, with a peak in spring-summer and a nadir in autumn and winter (Rosecrans and Dohnal, 2014). Thus, based on the reported anti-inflammatory effects of vitamin D (Correale et al., 2009) (Ascherio et al., 2010), MS relapse occurrence is predicted to peak during autumn and winter. However, several studies, including a meta-analysis (Jin et al., 2000) and a recent multicentric study (Sleiman et al., 2014) found that MS disease activity is higher in spring and summer, suggesting that additional factors play a role in MS relapse seasonality.

Here, we report that melatonin levels, which peak in autumn-winter, show an inverse correlation with clinical disease activity in MS patients. Moreover, melatonin limits the development of experimental autoimmune encephalitis (EAE) and controls Th17 and Tr1 cell differentiation. Thus, seasonal changes in melatonin levels may contribute to the decreased disease activity observed in autumn and winter through a mechanism mediated, at least partially, by the regulation of effector and regulatory T cells.

RESULTS

Melatonin Levels Are Negatively Correlated with MS Clinical Relapses

We first established the seasonality of MS relapses in our cohort of 139 relapsing remitting MS patients (Table 1). Using a Poisson

Table 1. Baseline and Clinical Characteristics of the Study Population

	All Participants (n = 139)
Age (years, mean ± SD)	38.6 ± 10.9
F:M (n)	87:52
Disease duration (years, median, range)	6 (1–20)
EDSS (median, range)	1 (0–4)
Treatment (n)	
None	2
Interferon	64
Glatiramer acetate	34
Natalizumab	2
Fingolimod	26
Other	11
6-SM levels (ng/mg creatinine, mean ± SEM)	
Summer	19.8 ± 1.5
Fall	21.8 ± 1.6
Winter	24.7 ± 0.6
Spring	19.2 ± 1.7
Vitamin D levels (ng/ml)	
Summer	27.8 ± 0.8
Fall	25.2 ± 0.1
Winter	21.7 ± 3.2
Spring	21.7 ± 3.3

regression model, we detected a 32% reduction in the number of relapses occurring during fall and winter (incidence rate-ratio [IRR] 0.682, 95% confidence interval [CI] 0.49–0.95, p = 0.02). Hence, the MS patient cohort used in this study shows the seasonality of MS relapses previously described for other cohorts (Jin et al., 2000; Spelman et al., 2014).

Melatonin production is stimulated by darkness and follows a seasonal pattern with higher levels during fall and winter (Brzezinski, 1997). Melatonin impacts several biological processes, including the circadian clock and the immune response (Brzezinski, 1997). Thus, we investigated the relationship between melatonin and MS disease activity by measuring 6-sulfatoxymelatonin (6-SM) levels in relapsing-remitting MS patients. Since 6-SM is the main melatonin metabolite, its levels in first morning urine are strongly correlated with nighttime melatonin secretion, supporting its use in epidemiological studies (Graham et al., 1998; McMullan et al., 2013). In agreement with previous reports (Morera and Abreu, 2007; Ueno-Towatari et al., 2007), we detected increased melatonin secretion during fall and winter, with lower levels during spring and summer (Figure 1A; Table 1). Moreover, we found a significant negative correlation between 6-SM levels and MS exacerbation rates (p < 0.01 Spearman's correlation). This was further confirmed in an age and gender-adjusted Poisson regression model, with a 3% reduction in the number of relapses for each 6-SM unit increase (IRR 0.97, 95% CI 0.95–0.99, p = 0.007). Finally, to test whether the relationship between melatonin levels and exacerbation rate

was synchronous, we lagged the occurrence of relapses for 1 (IRR 1.01, 95% CI 0.97–1.05; p = 0.7), 2 (IRR 1.03, 95% CI 0.99–1.07; p = 0.1), and 3 months (IRR 1.03, 95% CI 0.99–1.07; p = 0.7), with no evidence of a lagged effect in relapse occurrence.

We also assessed vitamin D levels and, as previously reported for healthy controls and MS patients in our region (Correale et al., 2009; Fassi et al., 2003), overall levels were low throughout the year with higher levels during summer but no significant correlation with MS relapses (Figure 1B). Finally, we did not detect a correlation between MS relapses and additional environmental factors such as reported upper respiratory tract infections and UV incidence, as determined by national registries and NASA satellites, respectively (Figures 1C and 1D). Thus, higher melatonin levels during fall and winter are associated with a reduction in clinical relapses.

Melatonin Ameliorates Experimental Autoimmune Encephalitis

Based on our epidemiological findings, we studied the effects of melatonin on CNS inflammation using the EAE model of MS. Naive C57BL/6 wild-type mice were immunized with MOG_{35–55} and treated daily with melatonin (5 mg/kg, intraperitoneally) or vehicle. Melatonin administration ameliorated EAE clinical symptoms (Figures 2A and S1A; Table S1). The amelioration of EAE was associated with a decreased number and frequency of Th17 cells in spleen, lymph nodes, and CNS; this decrease was also detected in IL-17⁺ IFN γ ⁺ and IL-17⁺ GM-CSF⁺ CD4⁺ T cells that have been associated to the pathogenesis of EAE (Codarri et al., 2011; El-Behi et al., 2011; Lee et al., 2012) (Figures 2C and 2D). We also detected a concomitant increase in IL-10 secreting CD4⁺ T cells; no significant changes were detected in the number or frequency of other T cell subsets, B cells, $\gamma\delta$ T cells, or innate lymphoid cells (ILCs) (Figures 2B and S1B–S1D).

To further characterize the effects of melatonin on the encephalitogenic T cell response, we analyzed the recall response to MOG_{35–55}. Splenocytes from melatonin-treated mice showed a diminished proliferative response to MOG_{35–55}, reduced IL-17 concomitant with increased IL-10 production, however, no significant effects were detected on IFN- γ production (Figures 2E and 2F). Thus, melatonin arrests the encephalitogenic Th17 cell response.

To investigate if melatonin acts directly on T cells or whether it controls the T cell response indirectly through its effects on antigen presenting cells, we co-incubated sorted CD4⁺ T cells from melatonin-treated or control mice with treatment-switched dendritic cells (DCs). When compared to controls isolated from vehicle-treated mice, CD4⁺ T cells from melatonin-treated mice co-incubated with splenic DCs isolated from control mice showed decreased proliferation and IL-17 secretion, concomitant with increased IL-10 production, (Figures 2G and 2H). Conversely, we did not detect significant differences when we used DCs isolated from melatonin or vehicle-treated mice to activate CD4⁺ T cells from control-treated mice.

In support for a direct effect of melatonin on T cells, melatonin suppressed the in vitro activation of naive 2D2⁺ transgenic T cells with MOG_{35–55} and DCs (Figures 2I and S1E) or with antibodies

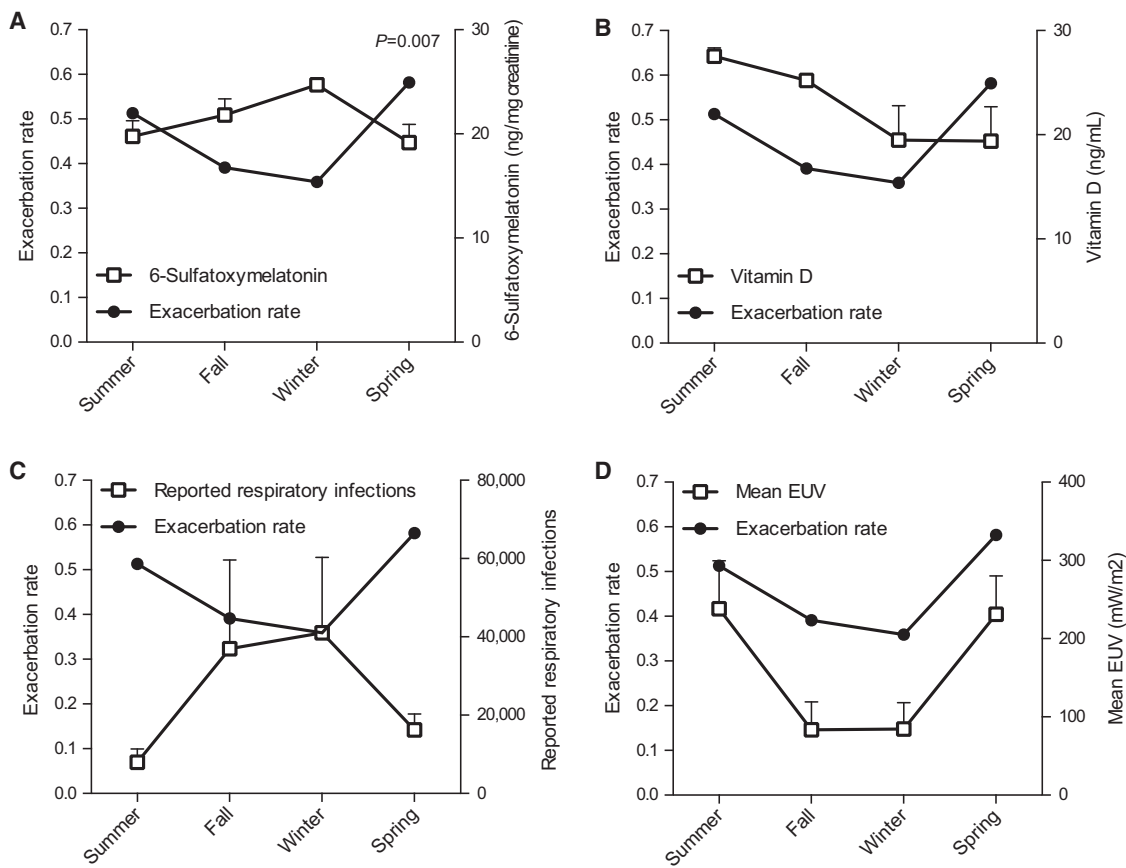


Figure 1. Melatonin Levels Show an Inverse Correlation with MS Clinical Relapses

(A) Exacerbation rate for each season was estimated for the duration of the follow-up and depicted in the primary axis. 6-sulfatoxymelatonin levels measured in first morning urine in each season is depicted as mean \pm SEM in secondary axis. p value corresponds to Poisson regression model.

(B–D) Lack of correlation between exacerbation rate and vitamin D (B), reported respiratory infections (C), and UV radiation in Buenos Aires city (D). See also Table 1.

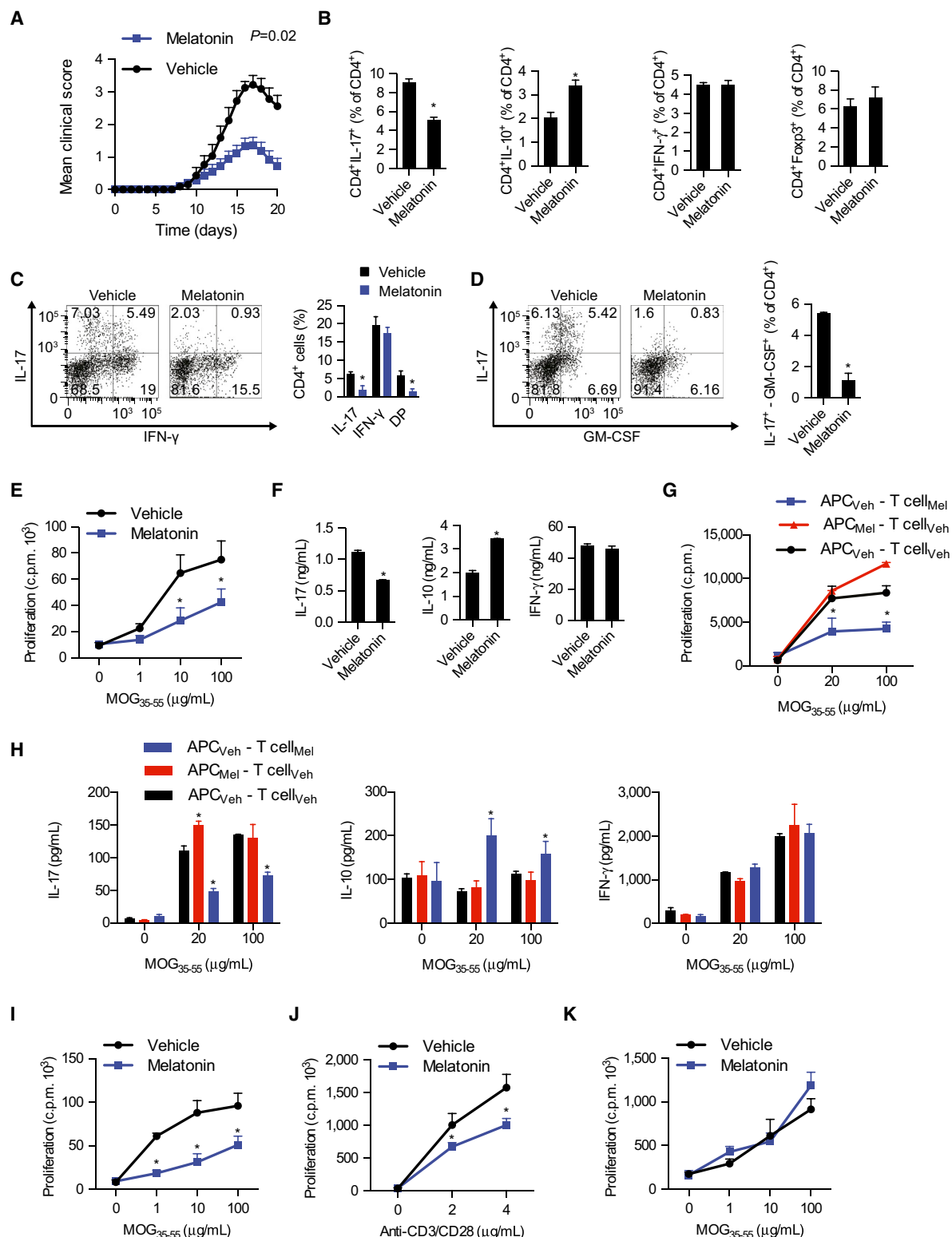
to CD3 and CD28 in the absence of DCs (Figure 2J). Pretreatment of DCs with melatonin did not affect their ability to activate 2D2⁺ T cells in the presence of MOG_{35–55} (Figure 2K). Melatonin did not increase apoptosis in CD4⁺ T cells stimulated with antibodies against CD3 and CD28, as indicated by the analysis of annexin V and propidium iodide staining by flow cytometry or the expression of Bcl-xL levels (Figures S1F and S1G). IL-10 blockade, however, abrogated the suppressive effects of melatonin on T cell proliferation (Figure S1H).

Melatonin Affects Human T Cell Differentiation

We then studied the effects of melatonin on human CD4⁺ T cells. In addition, we also analyzed the effects of agomelatine, which activates melatonin-dependent signaling (Hickie and Rogers, 2011). Based on the effects of melatonin administration on T cells during EAE, we focused our studies on human Th17 and Tr1 cells. Melatonin and agomelatine reduced the production of IL-17, RORC, and IL17A expression by human CD4⁺ T cells activated under Th17 polarizing conditions (Figures 3A–3C and S2), no effect was detected on the differentiation of human Th1 cells (Figures 3D–3F). Concomitantly, melatonin and

agomelatine increased IL10 expression. Indeed, melatonin and agomelatine also increased IL-10 production by human CD4⁺ T cells activated under Tr1 polarizing conditions (Figures 3G and 3H).

To further investigate the role of melatonin on the immune response in MS, we analyzed the correlation between serum melatonin levels and IL17 and IL10 expression in peripheral CD4⁺ T cells of 26 RRMS patients (Table S2). Using an age- and gender-adjusted linear regression model, we detected a negative correlation between melatonin in serum and IL17 expression in peripheral CD4⁺ T cells ($p = 0.012$): higher serum melatonin levels were associated to lower IL17 expression (Table S3). Conversely, linear regression analysis identified a positive correlation between higher IL10 expression in peripheral CD4⁺ T cells and melatonin in serum ($p = 0.003$). We did not detect a significant correlation between melatonin levels and the expression of RORC, NR1D1, or NFIL3 in CD4⁺ T cells (Table S3). Thus, melatonin modulates the differentiation of human Th17 and Tr1 cells in vitro, and endogenous melatonin levels are associated to the expression levels of IL17 and IL10 in peripheral CD4⁺ T cells in RRMS patients.

**Figure 2. Melatonin Administration Ameliorates EAE**

(A) EAE development in C57BL/6 treated with vehicle (0.01% DMSO) or melatonin (5 mg/kg). Data are representative of three independent experiments (means and SEM) ($n \geq 20$ mice/group). p value corresponds for the effect of treatment in a repeated-measures mixed effect model.

(legend continued on next page)

Melatonin Interferes with Th17 Generation

Together with Th1 cells, Th17 cells promote the development of EAE and are thought to contribute to MS pathogenesis (Korn et al., 2009). Based on the suppressive effects of melatonin on EAE and IL-17 production by CD4⁺ T cells, we studied the effects of melatonin on murine Th17 cell differentiation. Melatonin interfered with the differentiation of Th17 cells in vitro as indicated by the expression of rorc, IL-17, and the IL-23 receptor necessary for the differentiation of Th17 cells into fully pathogenic cells; no effects were detected on the differentiation of FoxP3⁺ iTregs, Th1, or Th2 cells. (Figures 4A, 4B, and S3) (Lee et al., 2012). Melatonin also increased the expression of IL-10, associated to non-pathogenic Th17 cells (Lee et al., 2012; McGeachy et al., 2007) (Figures 4A and 4B).

IFN γ and IL-2 have been shown to limit Th17 cell differentiation (Korn et al., 2009). However, in our studies Th17 cells were differentiated in the presence of IFN γ -blocking antibodies, and IL-2 blocking antibodies failed to abrogate the suppression of Th17 differentiation by melatonin (Figure S4A and S4B). Thus, melatonin suppresses Th17 cell differentiation through a mechanism independent of IFN γ or IL-2.

Physiological concentrations of melatonin result in the activation of signaling pathways controlled by membrane and nuclear receptors (Brzezinski, 1997). The melatonin membrane receptor MTNR1A is expressed by a variety of tissues including cells of the immune system (Jockers et al., 2008; Pozo et al., 1997). In addition, melatonin binds to the nuclear retinoid-related orphan receptor alpha (ROR- α), which is also expressed by immune cells (Pozo et al., 2004) and plays a role in Th17 development (Yang et al., 2008). We detected the expression of both MTNR1A and ROR- α on Th17 cells (Figures S4C and S4D). To study the role of MTNR1A signaling on the effects of melatonin on Th17 cells, we used the MTNR1A-specific agonists agomelatine and ramelteon (Karim et al., 2006) (Figure S4E). Similar to our observations with melatonin, MTNR1A activation by agomelatine or ramelteon suppressed the differentiation of Th17 cells (Figures 4C, 4D, S4F, and S4G). Conversely, melatonin failed to suppress the differentiation of MTNR1A-deficient (MTNR1A KO) Th17 cells (Figures 4E and 4F). Thus, MTNR1A mediates the suppressive effects of melatonin on Th17 cell differentiation.

Melatonin Suppresses Th17 Cell Differentiation via Erk1/2 and C/EBP α Activation

REV-ERB α (encoded by nr1d1) is a component of the circadian clock that promotes Th17 differentiation by limiting the expression of NFIL3, a direct inhibitor of rorc transcription (Yu et al., 2013). Melatonin regulates the activity of both circadian and seasonal clocks (Pévet, 2003). Indeed, melatonin levels show a circadian inverse correlation with nr1d1 expression, suggesting that melatonin affects REV-ERB α expression (Kojetin and Burris, 2014). Thus, we investigated whether melatonin acts on REV-ERB α to suppress Th17 cell differentiation.

Using reverse protein arrays (Farez et al., 2009) we analyzed signaling pathways triggered by melatonin in T cells and detected an MTNR1A-dependent increase in the activation of Erk1/2 (Figures 4G, 4H, S4H, and S4I). Of note, Erk1/2 inhibition has been previously shown to enhance Th17 cell differentiation (Tan and Lam, 2010) and Erk1/2 phosphorylation has been linked to the reduced expression of REV-ERB proteins (Castellano et al., 2014; Kojetin and Burris, 2014), but the mechanism involved and its relevance for T cells has not been characterized yet. Through a bioinformatic analysis of the nr1d1 promoter, we identified a binding site for the CAAT/enhancer-binding protein α (C/EBP α), a leucine zipper transcription factor involved in the regulation of cellular differentiation (Lekstrom-Himes and Xanthopoulos, 1998). C/EBP α is a downstream target of Erk1/2 activated by phosphorylation (Johnson, 2005). Thus, we analyzed whether Erk1/2 regulates the transcriptional activity of the nr1d1 promoter in a C/EBP α -dependent manner.

Th17 cell differentiation in the presence of melatonin led to C/EBP α phosphorylation and the recruitment of C/EBP α to the nr1d1 promoter (Figures 4I and 4J). C/EBP α phosphorylation and recruitment to the nr1d1 promoter were suppressed in MTNR1A KO T cells and in the presence of the Erk1/2 inhibitor UO216 (Figures 4I and 4J). Hence, melatonin triggers the recruitment of C/EBP α to the nr1d1 promoter in an MTNR1A- and Erk1/2-dependent manner.

To analyze the effects of C/EBP α on the transcriptional activity of the nr1d1 promoter, we used a reporter construct in which the nr1d1 promoter controls luciferase expression. Treatment of nr1d1 reporter-transfected HEK293 cells with melatonin or agomelatine resulted in decreased luciferase activity and similar

(B) Flow cytometry analysis of IL-17⁺, IL10⁺, IFN- γ ⁺, and FoxP3⁺ CD4⁺ cells from the spleen of vehicle- or melatonin-treated mice at day 7 after disease induction. At least four mice were analyzed per group and data are presented as mean \pm SEM. *p < 0.05 of unpaired t test.

(C and D) Flow cytometry analysis of IL-17⁺, IFN- γ ⁺, IL-17⁺-IFN- γ ⁺ (DP), and IL-17⁺-GM-CSF⁺ CD4⁺ T cells from the CNS of control- or melatonin-treated mice at the clinical peak of EAE. *p < 0.05 of unpaired t test.

(E) Proliferative responses of CD4⁺ T cells to MOG_{35–55} of vehicle- or melatonin-treated mice. At least three mice were analyzed per group and data are presented as mean \pm SEM. *p < 0.05 of one-way ANOVA.

(F) Cytokine secretion by proliferating CD4⁺ T cells from vehicle and melatonin-treated. Data are representative of three independent experiments (means and SEM). *p < 0.05 of unpaired t test.

(G and H) Proliferative responses (G) and cytokine profile (H) of CD4⁺ T cells in co-culture with dendritic cells derived from melatonin-treated or untreated mice. Data are representative of three independent experiments (means and SEM). *p < 0.05 of one-way ANOVA.

(I) Proliferative responses of melatonin-treated 2D2 CD4⁺ T cells to MOG_{35–55} in the presence of dendritic cells. Data are representative of three independent experiments (means and SEM). *p < 0.05 of one-way ANOVA.

(J) Proliferative responses of melatonin-treated 2D2 CD4⁺ T cells to MOG_{35–55} stimulated only with anti-CD3 and anti-CD28. Data are representative of three independent experiments (means and SEM). *p < 0.05 of one-way ANOVA.

(K) Proliferative responses of treated 2D2 CD4⁺ T cells to MOG_{35–55} stimulated melatonin-treated DCs. Data are representative of three independent experiments (means and SEM).

See also Figure S1 and Table S2.

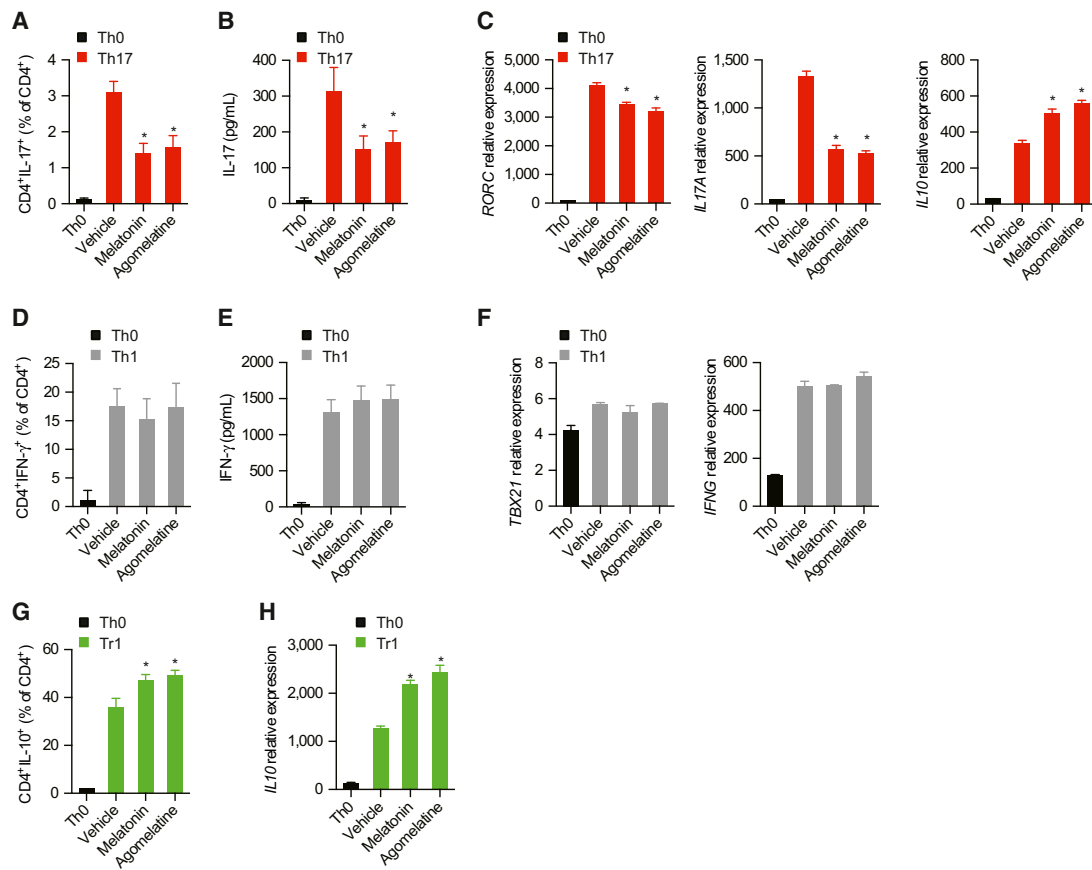


Figure 3. Melatonin Interferes with Human Th17 Cell Differentiation and Boosts Tr1 Generation

(A) Flow cytometry analysis of IL-17 expression in human Th17-differentiated CD4⁺ T cells (IL-1 β , IL-6, and TGF- β 1) in the presence or absence of melatonin (500 ng/ml) and agomelatine (500 ng/ml). Data are representative of three independent experiments (means and SEM). *p < 0.05 of one-way ANOVA.

(B) Cytokine quantification by ELISA of IL-17 in human Th17-differentiated CD4⁺ T cells in the presence or absence of melatonin (500 ng/ml) and agomelatine (500 ng/ml). Data are representative of three independent experiments (means and SEM). *p < 0.05 of one-way ANOVA.

(C) RT-PCR analysis of Th17 cells cultured as in (A). Data are representative of three independent experiments (means and SEM) *p < 0.05 of one-way ANOVA.

(D) Flow cytometry analysis of IFN- γ expression in human Th1-differentiated CD4⁺ T cells (IL-12) in the presence or absence of melatonin (500 ng/ml) and agomelatine (500 ng/ml). Data are representative of three independent experiments (means and SEM).

(E) Cytokine quantification by ELISA of IFN- γ in human Th1-differentiated CD4⁺ T cells in the presence or absence of melatonin (500 ng/ml) and agomelatine (500 ng/ml). Data are representative of three independent experiments (means and SEM). *p < 0.05 of one-way ANOVA.

(F) RT-PCR analysis of Th1 cells cultured as in (D). Data are representative of three independent experiments (means and SEM). *p < 0.05 of one-way ANOVA.

(G) Flow cytometry analysis of IL-10 expression in human Tr1-differentiated CD4⁺ T cell in the presence or absence of melatonin (500 ng/ml) and agomelatine (500 ng/ml). Data are representative of three independent experiments (means and SEM). *p < 0.05 of one-way ANOVA.

(H) RT-PCR analysis of Tr1 cells cultured as in (F). Data are representative of three independent experiments (means and SEM). *p < 0.05 of one-way ANOVA.

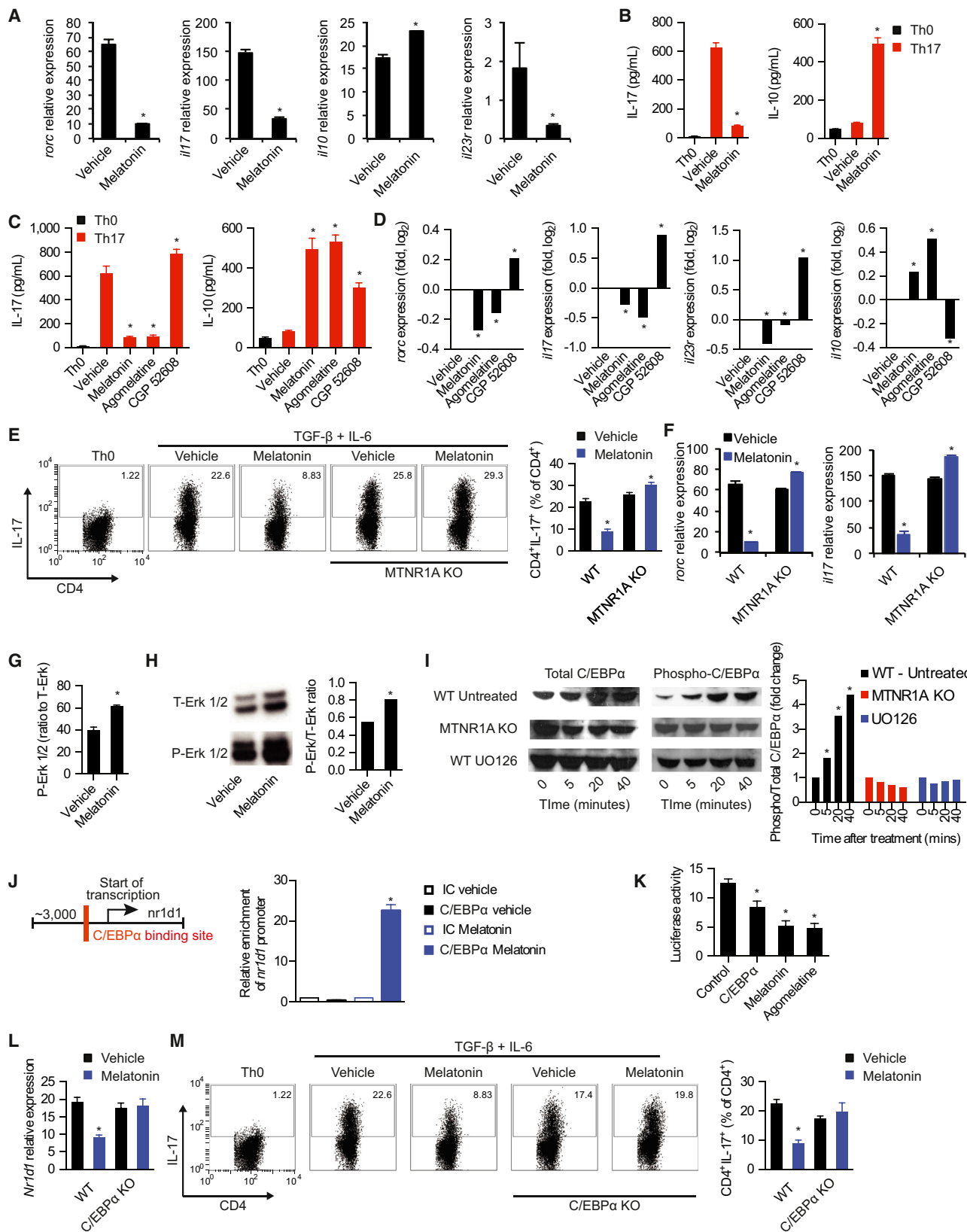
See also Figure S2.

effects were achieved by C/EBP α overexpression (Figure 4K). Finally, to investigate the role of C/EBP α on the suppression of Th17 cell differentiation by melatonin we used C/EBP α -deficient T cells (Yang et al., 2005). C/EBP α -deficiency abrogated the decrease in nr1d1 expression and the suppression of Th17 differentiation induced by melatonin (Figures 4L and 4M). Thus, melatonin suppresses the differentiation of Th17 cells through a mechanism mediated by MTNR1A, Erk1/2, and C/EBP α .

Melatonin Inhibits ROR- γ t and ROR- α Expression in Th17 Cells by Inducing Nfil3

Nfil3 limits Th17 cell differentiation by suppressing the expression of ROR- γ t (Yu et al., 2013). REV-ERB α inhibits nfil3 expres-

sion (Yu et al., 2013). Thus, we hypothesized that the decrease in nr1d1 expression induced by melatonin results in the Nfil3-dependent inhibition of rorc expression (Figure 5A). We detected nr1d1 expression in Th17 cells, but not in Th0 or Tr1 cells (Figure 5B). Melatonin suppressed nr1d1 expression during Th17 cell differentiation, resulting in a concomitant increase in the expression of the ROR- γ t repressor Nfil3 (Figures 5C and 5D). In agreement with our results on Th17 cell differentiation, the regulation of REV-ERB α and Nfil3 expression by melatonin was mediated by its membrane receptor MTNR1A and Erk1/2 (Figures 5C–5G). The relevance of the regulation of REV-ERB α expression for the modulation of Th17 cell differentiation by melatonin was confirmed in nr1d1 overexpression experiments



(legend on next page)

and by the use of REV-ERB α -deficient T cells. Nr1d1 overexpression and REV-ERB α deficiency abrogated the effects of melatonin on Th17 cell differentiation (Figures 5H–5K). Hence, MTNR1A-dependent signaling triggered by melatonin suppresses Th17 cell differentiation through the regulation of REV-ERB α expression.

ROR- α promotes Th17 cell differentiation (Yang et al., 2008). Accordingly, ROR- α activation by the specific agonist CGP 52608 boosted Th17 cell differentiation (Figures 4C and 4D). ROR- α is directly activated by melatonin (Brzezinski, 1997). Indeed, melatonin boosted the differentiation of MTNR1A-deficient Th17 cells (Figure 4E), suggesting that melatonin-triggered MTNR1A signaling interferes with the promotion of Th17 cell differentiation by ROR- α . Based on the inhibitory effects of NFIL3 on ROR- γt expression and Th17 cell differentiation (Yu et al., 2013), we studied whether NFIL3 also inhibits ROR- α expression.

A bioinformatics analysis identified NFIL3 binding sites in the rora and rorc promoters. Accordingly, we detected the recruitment of NFIL3 to the rora and rorc promoters in CD4 $^+$ T cells activated under Th17 polarizing conditions in the presence of melatonin, concomitant with a reduced expression of both ROR- α and ROR- γt (Figures 5L and 5M). We then investigated the relevance of the regulation of NFIL3 expression for the modulation of Th17 cell differentiation. Overexpression of NFIL3 (Figures 5N and 5O) and NFIL3-deficiency (Figures 5P and 5Q) abrogated the suppressive effects of melatonin on Th17 cell differentiation. Thus, the regulation of NFIL3 expression by melatonin mediates its inhibitory effects on the differentiation of Th17 cells in vitro. To evaluate the role of MTNR1A and NFIL3 on the suppression of Th17 cell differentiation by melatonin in vivo, we used RAG-1-deficient mice reconstituted with wild-type, MTNR1A-, REV-ERB α -, or NFIL3-deficient CD4 $^+$ T cells and immunized with MOG_{35–55} in CFA. In agreement with our in vitro observations, the suppression of Th17 cell differentiation by melatonin in vivo was abrogated by MTNR1A-, REV-ERB α -, and NFIL3-deficiency

(Figures 5R and S5). Indeed, we detected increased Th17 cell differentiation in response to treatment of mice reconstituted with MTNR1A-, REV-ERB α -, or NFIL3-deficient T cells, most likely reflecting the unopposed agonistic activity of melatonin on ROR- α and its promoting effects on the differentiation of Th17 cells. Taken together, these data suggest that melatonin interferes with Th17 cell differentiation via the inhibition of ROR- γt and ROR- α expression through an NFIL3-dependent mechanism.

Melatonin Boosts Tr1 Cell Differentiation via Erk1/2 and ROR- α

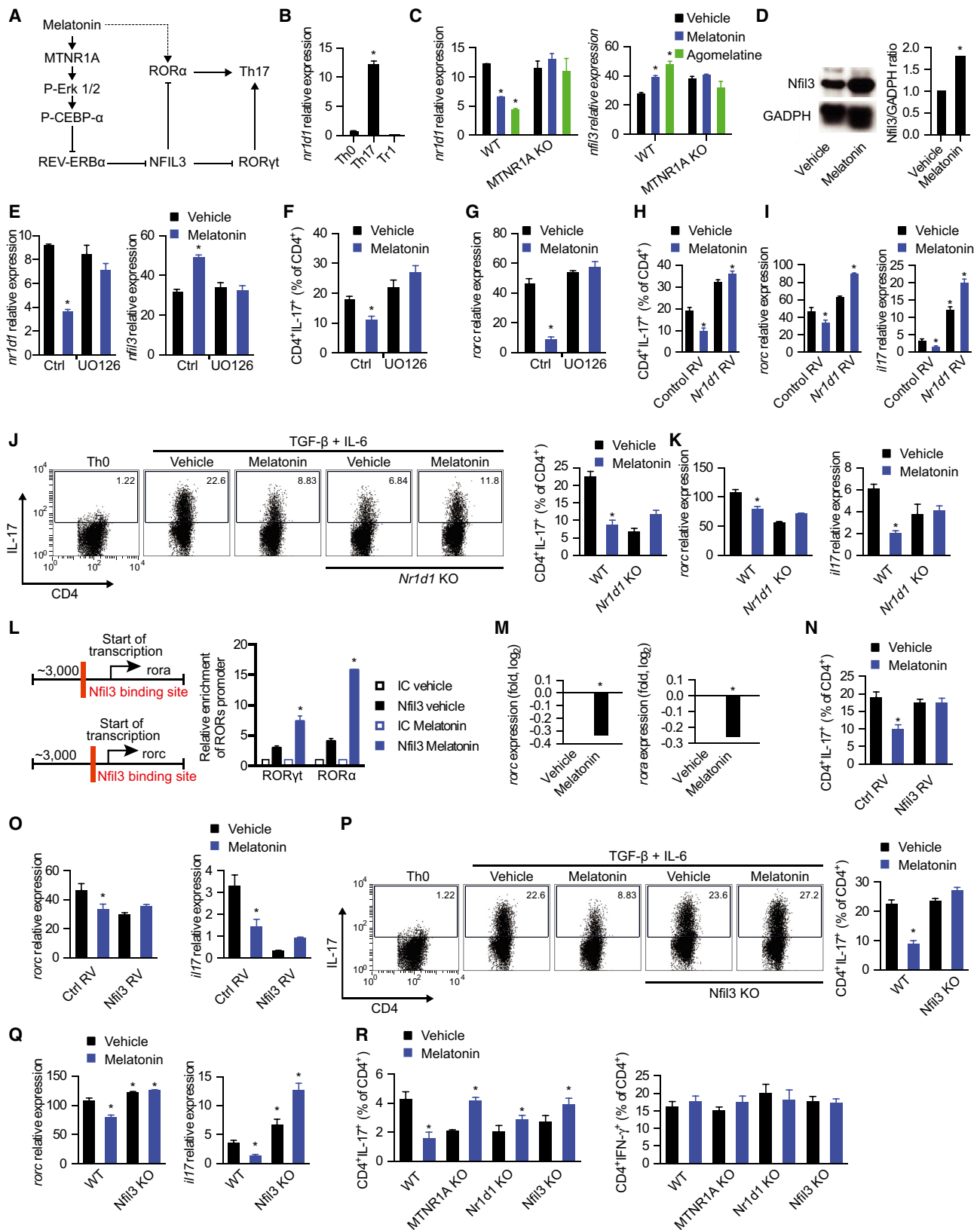
CD4 $^+$ IL-10-producing Tr1 cells play an important role in the regulation of the immune response (Pot et al., 2011; Roncarolo et al., 2006). The amelioration of EAE by melatonin administration was associated with an increase in IL-10-producing T cells (Figure 2). Thus, we investigated the effects of melatonin on the activation of naive CD4 $^+$ T cells under Tr1 polarizing conditions. We found that melatonin boosted the expression of IL-10 and the Tr1-associated molecules il21, ahr, and cmaf (Apetoh et al., 2010) (Figure 6A). In addition, melatonin boosted the suppressive activity of Tr1 cells in vitro (Figure 6B).

We then investigated the mechanisms underlying the effects of melatonin on Tr1 regulatory cells. We detected the expression of both MTNR1A and ROR- α by Tr1 cells (Figures S4C and S4D). Indeed, both agomelatine and CGP 52608, specific agonist for MTNR1A and ROR- α , respectively, boosted Tr1 cell differentiation (Figures 6C and 6D). In agreement with these results, MTNR1A deficiency or inhibition of MTNR1A-activated Erk1/2 by UO126 interfered with the boost in Tr1 differentiation by melatonin (Figures 6E and 6F). Of note, Erk1/2 activation is reported to promote cmaf-dependent IL-10 production by CD4 $^+$ T cells (Saraiwa et al., 2009). In addition, ROR- α deficiency suppressed the differentiation of Tr1 cells induced by IL-27 and its boost by melatonin (Figure 6G).

Figure 4. Melatonin Interferes with Th17 Cell Differentiation via the Erk1/2-C/EBP α Pathway

- (A) CD4 $^+$ naive T cells were differentiated into Th17 cells by the addition of TGF- β , IL-6 (0 hr), and IL-23 (48 hr) in the presence or absence of melatonin (2 ng/ml) and analyzed by RT-PCR after 72 hr. Displayed image is representative of five experiments. *p < 0.05 of unpaired t test.
- (B) Cytokine secretion analysis of IL-17 and IL-10 after 72 hr of culture as in (A). Data are representative of three independent experiments (means and SEM). *p < 0.05 of unpaired t test.
- (C) Cytokine secretion in Th17-differentiated CD4 $^+$ T cells in the presence or absence of melatonin (2 ng/ml), agomelatine (20 ng/ml, MTNR1A ligand), and CGP 52608 (20 ng/ml, ROR- α ligand). Data are representative of three independent experiments (means and SEM). *p < 0.05 of one-way ANOVA.
- (D) RT-PCR analysis of Th17 cells cultured as in (C). Data are representative of three independent experiments (means and SEM). *p < 0.05 of one-way ANOVA.
- (E) Flow cytometry analysis of IL-17 expression as in (A), in wild-type mice and MTNR1A-deficient mice. Data are representative of three independent experiments (means and SEM). *p < 0.05 of unpaired t test.
- (F) RT-PCR analysis of wild-type and MTNR1A-deficient mice cultured as in (E). Data are representative of three independent experiments (means and SEM). *p < 0.05 of unpaired t test.
- (G) Signal transduction profiling using reverse protein arrays. Data are representative of two independent experiments (means and SEM). *p < 0.05 of unpaired t test.
- (H) Immunoblot analysis of T-Erk1/2 and P-Erk1/2. Data are representative of two independent experiments (means and SEM).
- (I) Immunoblot analysis of T-C/EBP α and P-C/EBP α . Data are representative of two independent experiments (means and SEM).
- (J) Putative binding sites of C/EBP α in nr1d1 (left); chromatin immunoprecipitation with anti-C/EBP α (right). Data are representative of three independent experiments (means and SEM) *p < 0.05 of one-way ANOVA.
- (K) Luciferase activity of HEK293 cells transfected with a luciferase reporter construct for the nr1d1 promoter. Data are representative of three independent experiments (means and SEM). *p < 0.05 of unpaired t test.
- (L) Flow cytometry analysis of IL-17 expression as in (A) in wild-type mice and C/EBP α -deficient mice. Data are representative of two independent experiments (means and SEM). *p < 0.05 of one-way ANOVA.
- (M) Flow cytometry analysis of IL-17 expression as in (A) in wild-type mice and C/EBP α -deficient mice. Data are representative of three independent experiments (means and SEM). *p < 0.05 of unpaired t test.

See also Figures S3 and S4.



(legend on next page)

ROR- α exerts its biological effects by binding to ROR response elements (ROREs) in target genes (Jetten, 2009). A bioinformatic analysis identified ROR- α binding sites in the *il10* promoter (Figure 6H), suggesting that melatonin may increase the recruitment of ROR- α to the *il10* promoter and consequently, *il10* transcription. In agreement with this hypothesis, we detected increased binding of ROR- α to the *il10* promoter following T cell activation under Tr1 polarizing conditions in the presence of melatonin (Figure 6H). Moreover, ROR- α transactivated the *il10* promoter in reporter assays and synergized with the aryl hydrocarbon receptor (AhR) and c-Maf to boost their ability to promote *il10* expression (Apetoh et al., 2010; Gandhi et al., 2010) (Figure 6I). Taken together, these data suggest that melatonin boosts Tr1 cell differentiation through its effects on MTNR1A and ROR- α (Figure 6J).

DISCUSSION

Strong epidemiological evidence supports the role of vitamin D in reducing MS relapses (Ascherio et al., 2012). Strikingly, vitamin D levels are higher during spring and summer, when relapse occurrence in MS patients peaks. Thus, the observation of a lower occurrence of relapses in seasons characterized by lower vitamin D levels represents a “seasonal paradox”: relapses should be less frequent in spring and summer when vitamin D levels are higher, yet the opposite is found in most studies (Jin et al., 2000; Spelman et al., 2014), with a few exceptions (Løken-Amsrud et al., 2012). Our data may solve this paradox by identifying melatonin, whose levels are regulated

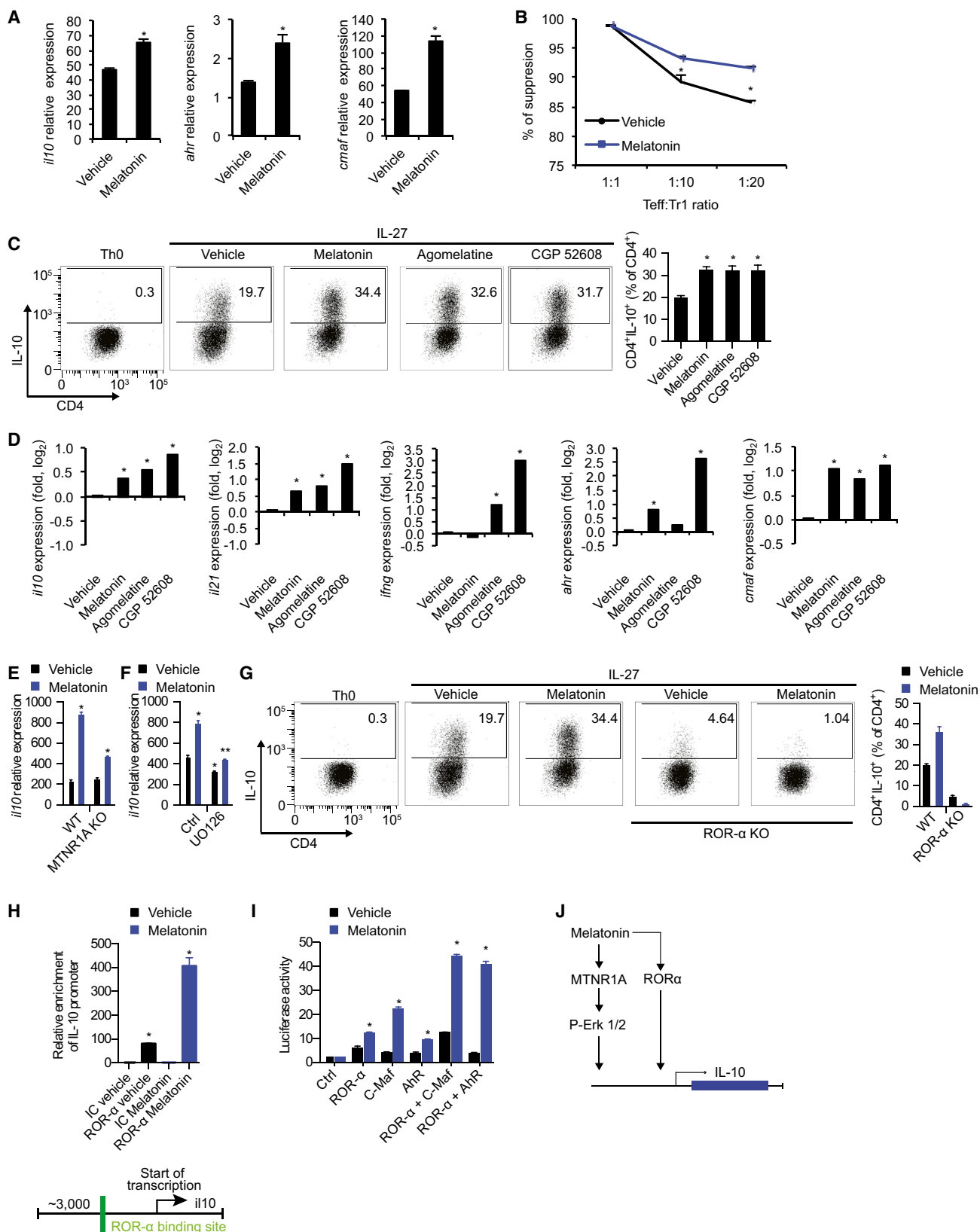
by seasonal fluctuations in day length, as an additional regulator of the immune response in MS. Note that night shift work, which is associated with lower overall melatonin levels (Schernhammer et al., 2004), increases the risk of developing MS (Hedström et al., 2011). These findings suggest that melatonin may also be an MS risk factor; the relationship between melatonin levels and the risk of developing MS is the focus of ongoing investigations. Finally, the interplay between melatonin and other seasonal environmental factors known to impact MS such as vitamin D in different geographic locations remains to be further elucidated.

The rise in the past 50 years in the incidence of autoimmune disorders has reached an epidemic proportion and cannot be accounted by genetic risk only. Thus, increasing attention is being paid to environmental factors and their impact in the immune response and T cell differentiation in particular. For example: several compounds present in household products can activate the aryl hydrocarbon receptor and impact both Th17 and regulatory cell differentiation (Quintana et al., 2008); sodium in westernized diet and processed foods can also enhance Th17 cell differentiation (Wu et al., 2013); the composition of commensal microbiota impacts T cell differentiation and response (Lathrop et al., 2011); and the lack of sun exposure and dietary habits can diminish vitamin D levels and affect regulatory cell function (Correale et al., 2009). Each of these environmental factors trigger different signaling pathways and the characterization of the complex interaction between them can shed light on the impact of the environment on the immune system.

Figure 5. Melatonin Interferes with Th17 Cell Differentiation by Limiting NFIL3 Expression

- (A) Schematic diagram of the proposed mechanisms mediating the effects of melatonin on Th17 cell differentiation.
- (B) RT-PCR analysis of *nr1d1* expression in CD4 $^{+}$ T cells activated under Th0, Th17, and Tr1 polarizing conditions for 3 days. Data are representative of three independent experiments (means and SEM). *p < 0.05 of unpaired t test.
- (C) RT-PCR analysis of *nr1d1* (left) and *nfil3* (right) expression in CD4 $^{+}$ T cells activated under Th17 polarizing conditions for 3 days treated with vehicle, melatonin (2 ng/ml), or agomelatine (20 ng/ml). Data are representative of three independent experiments (means and SEM). *p < 0.05 of unpaired t test. *NFIL3* expression was further confirmed by western blot.
- (D) Immunoblot analysis of *Nfil3*. Data are representative of two independent experiments (means and SEM).
- (E) RT-PCR analysis of *nfil3* expression in CD4 $^{+}$ T cells activated under Th17 polarizing conditions for 3 days in the presence of melatonin (2 ng/ml) and/or UO126. Data are representative of five independent experiments (means and SEM). *p < 0.05 of one-way ANOVA.
- (F and G) Flow cytometry analysis of IL-17 expression (F) and *rorc* expression (G) in CD4 $^{+}$ T cells activated under Th17 polarizing conditions in the presence of melatonin (2 ng/ml) and/or UO126. Data are representative of three independent experiments (means and SEM). *p < 0.05 of one-way ANOVA.
- (H and I) Flow cytometry analysis of IL-17 expression (H) and *rorc* and *il17* expression (I) in CD4 $^{+}$ T cells activated under Th17 polarizing conditions in the presence of melatonin (2 ng/ml), following infecting with a control or an *nr1d1*-encoding retrovirus. Data are representative of three independent experiments (means and SEM). *p < 0.05 of one-way ANOVA.
- (J and K) Flow cytometry analysis of IL-17 expression (J) and *rorc* and *il17* expression (K) in wild-type and REV-ERB α -deficient CD4 $^{+}$ T cells activated under Th17 polarizing conditions in the presence of melatonin (2 ng/ml). Data are representative of three independent experiments (means and SEM). *p < 0.05 of one-way ANOVA.
- (L) Putative binding sites of *Nfil3* in *rorc* and *rora* (left). ChIP analysis of the interaction of *NFIL3* with its putative binding sites in CD4 $^{+}$ T cells activated under Th17 polarizing conditions (right). Data are representative of three independent experiments (means and SEM). *p < 0.05 of one-way ANOVA.
- (M) RT-PCR analysis of *rorc* and *rora* expression in CD4 $^{+}$ T cells activated under Th17 polarizing conditions in the presence of melatonin (2 ng/ml). Data are representative of three independent experiments (means and SEM). *p < 0.05 of unpaired t test.
- (N and O) Flow cytometry analysis of IL-17 expression (N) and *rorc* and *il17* expression (O) in CD4 $^{+}$ T cells activated under Th17 polarizing conditions in the presence of melatonin (2 ng/ml) and transduced with a control or *nfil3*-encoding retrovirus. Data are representative of three independent experiments (means and SEM). *p < 0.05 of one-way ANOVA.
- (P and Q) Flow cytometry analysis of IL-17 expression (P) and *rorc* and *il17* expression (Q) in wild-type mice and *NFIL3*-deficient in CD4 $^{+}$ T cells activated under Th17 polarizing conditions in the presence of melatonin (2 ng/ml). Data are representative of three independent experiments (means and SEM). *p < 0.05 of one-way ANOVA.
- (R) Flow cytometry analysis of IL-17 and IFN- γ expression in CD4 $^{+}$ T cells from RAG-1-deficient mice reconstituted with wild-type, MTNR1A- REV-ERB α , or *NFIL3*-deficient CD4 $^{+}$ T cells, immunized with MOG_{35–55} in CFA and treated with vehicle or melatonin (5 mg/kg). *p < 0.05 of unpaired t test.

See also Figure S5.



(legend on next page)

Pro-inflammatory Th17 cells are thought to contribute to the pathogenesis of EAE and MS (Miossec et al., 2009). Th17 cell differentiation is regulated by ROR- α and ROR- γ t and therapies targeting Th17 cells are currently being tested in MS and other autoimmune diseases with preliminary encouraging results (Baeten and Kuchroo, 2013). Melatonin, despite having the potential to activate ROR- α , suppresses the generation of Th17 cells via its membrane receptor in a NFIL3-dependent fashion. Interestingly, it has been recently shown that the circadian clock suppresses Th17 development during nighttime through a similar NFIL3-dependent mechanism (Yu et al., 2013). Our work suggests that, in addition to Th17 cells, Tr1 cells are also regulated by melatonin during nighttime in an Erk1/2- and ROR- α -dependent manner. Based on the high evolutionary conservation of melatonin production by the pineal gland and its regulation by daylight (Macchi and Bruce, 2004), it is likely that the circadian and seasonal effects of melatonin on the immune response play an important role that resulted in its positive selection during evolution.

Tr1 cells are characterized by the production of IL-10 (Pot et al., 2011; Roncarolo et al., 2006). AhR, c-Maf, and Erk1/2 have been shown to regulate Tr1 cell development and IL-10 expression (Apetoh et al., 2010; Gandhi et al., 2010). Our work shows that melatonin promotes Tr1 cell differentiation by activating Erk1/2 signaling, which has been previously described to control IL-10 expression in T cells and DCs (Saraiva and O'Garra, 2010). We also identified ROR- α as a mediator of the effects of melatonin in Tr1 cells. Thus, these data suggest that melatonin utilizes multiple pathways to boost Tr1 cell differentiation.

The interplay between pro-inflammatory and regulatory cells controls the development of autoimmune diseases such as MS. Here, we report that melatonin, whose levels show seasonal variability, control the balance between pathogenic and regulatory T cells. However, in MS patients, melatonin is likely to act on several cell types to affect disease activity. Indeed, NFIL3 has been shown to play a role in human inflammatory bowel disease and autoimmune colitis through its activity on innate immune cells (Kobayashi et al., 2014). Thus, future studies should

investigate the effects of melatonin on innate immune cells in MS patients and also its role in inflammatory bowel disease and other immune-mediated disorders. Finally, although our data identify melatonin-dependent signaling as a potential target for therapeutic immunomodulation, the pathways involved are complex and likely cross-regulated. Thus, extreme caution should be exercised to evaluate the translational potential of these findings.

EXPERIMENTAL PROCEDURES

Patients

Consecutive patients with relapsing-remitting MS according to McDonald criteria (Polman et al., 2011) were recruited from the MS clinic at the Raúl Carrera Institute for Neurological Research (FLEN) between September of 2011 and November of 2012. Study protocol was approved by the Institutional Ethics Committee, and all subjects signed an informed consent form. See [Supplemental Experimental Procedures](#) for detailed information.

Animals and EAE

EAE was induced as follows: mice were immunized with 100 μ g MOG_{35–55} and 500 μ g mycobacterium tuberculosis extract H37Ra (Difco). Mice were also injected intraperitoneally with 200 ng pertussis toxin on days 0 and 2. Melatonin (5 mg/kg) or vehicle (0.01% DMSO) was administered daily at 7:00 p.m.

Flow Cytometry Staining and Acquisition

For intracellular cytokine staining, cells were stimulated for 4 hr at 37°C with phorbol 12-myristate 13-acetate (50 ng/ml; Sigma), ionomycin (1 μ g/ml; Sigma), and monensin (GolgiStop; 1 μ g/ml; BD Biosciences). After being stained for surface markers, cells were fixed and made permeable according to the manufacturer's instructions (BD Biosciences). All antibodies against cytokines were from Biolegend. All experiments were started at the same time (8:00–9:00 a.m.). Data were collected with a LSR II or FACSaria (BD Biosciences), then were analyzed with FlowJo software (Treestar).

Measurement of Cytokines

Secreted cytokines were measured in tissue culture supernatants after 72–96 hr by ELISA as previously described (Farez et al., 2009).

qRT-PCR

RNA was extracted with RNAeasy columns (QIAGEN), then cDNA was prepared according to the manufacturer's instructions (Applied Biosystems)

Figure 6. Melatonin Boosts Tr1 Cell Differentiation

- (A) RT-PCR analysis of il10, ahr, and maf expression in Tr1-differentiated CD4 $^{+}$ T cells in the presence or absence of melatonin (2 ng/ml). Data are representative of three independent experiments (means and SEM). *p < 0.05 of one-way ANOVA.
- (B) In vitro suppression assay, treated or untreated differentiated Tr1 cells as in A, were co-cultured after 72 hr with CD4 $^{+}$ T cells previously labeled with CSFE, and proliferation cycles (CSFE dilution) were measured after 48 hr by flow cytometry. Data are representative of two independent experiments (means and SEM). *p < 0.05 of one-way ANOVA.
- (C) Flow cytometry analysis of IL-10 expression in Tr1-differentiated CD4 $^{+}$ T cells in the presence or absence of melatonin (2 ng/ml), agomelatine (20 ng/ml, MTNR1A ligand), and CGP 52608 (20 ng/ml, ROR- α ligand). Data are representative of three independent experiments (means and SEM). *p < 0.05 of one-way ANOVA.
- (D) RT-PCR analysis of Tr1 cells cultured as in (C). Data are representative of three independent experiments (means and SEM). *p < 0.05 of one-way ANOVA.
- (E) RT-PCR analysis of il10 expression as in (C), in wild-type mice and MTNR1A-deficient mice. Data are representative of three independent experiments (means and SEM). *p < 0.05 of one-way ANOVA.
- (F) RT-PCR expression of il10 in melatonin-treated Tr1 cells with or without the addition of UO126. Data are representative of five independent experiments (means and SEM). *p < 0.05 of unpaired t test versus vehicle and signaling inhibitor control condition. **p < 0.05 versus vehicle of UO126-treated condition.
- (G) Flow cytometry analysis of IL-10 expression as in (C), in wild-type mice and ROR- α -deficient mice.
- (H) ROR- α putative binding site present in the il10 promoter (lower panel) and chromatin immunoprecipitation with anti-ROR- α (upper panel). Data are representative of three independent experiments (means and SEM). *p < 0.05 of unpaired t test.
- (I) Luciferase activity of HEK293 cells transfected with a luciferase reporter construct for the il10 promoter. Data are representative of three independent experiments (means and SEM). *p < 0.05 of unpaired t test.
- (J) Schematic diagram depicting the effects of melatonin in Tr1 cells.

and was used as template for real-time PCR. All primers and probes were provided by Applied Biosystems and were used on the ViiA 7 Real-Time PCR System (Applied Biosystems). Expression was normalized to the expression of the housekeeping gene Gapdh.

Immunoblot Analysis

For immunoblot analysis, cells were lysed with radio-immunoprecipitation buffer supplemented with protease inhibitor "cocktail" (Sigma-Aldrich). Total lysates of the different T cell subsets (40 µg) were resolved by electrophoresis through 4%-12% Bis-Tris Nupage gels (Invitrogen) and were transferred onto PVDF membranes (Millipore). The following primary antibodies were used: anti-ROR- α (Abcam), anti-MTNR1A (Santa Cruz), anti-total and phospho-Erk1/2 (Cell Signaling), anti-total C/EBP α (Cell Signaling), anti-phospho C/EBP α (Cell Signaling), anti-Nfil3 (Santa Cruz), and anti-GADPH (Abcam). Blots were developed with SuperSignal West Femto Maximum Sensitivity Substrate as suggested by the manufacturer (Pierce).

Statistical Analysis

A Poisson regression model was used to assess the impact of season 6-SM levels and the number of clinical relapses, generating an incidence rate ratio (IRR) and corresponding 95% confidence intervals (CI). A repeated-measures mixed model was used to assess the effect of treatment and its interaction with time in EAE experiments. A linear regression model was used to analyze the relationship between serum melatonin levels and IL-17 or IL-10 gene expression. Differences between two or more conditions were analyzed with Student's t test, Mann-Whitney test, one-way ANOVA, or Wilcoxon rank-sum test when appropriate. p values <0.05 were considered significant. Unless otherwise specified, all data are presented as mean \pm SEM. All statistical analyses were performed using Stata v12 (Statacorp).

SUPPLEMENTAL INFORMATION

Supplemental Information includes Supplemental Experimental Procedures, five figures, and three tables and can be found with this article online at <http://dx.doi.org/10.1016/j.cell.2015.08.025>.

AUTHOR CONTRIBUTIONS

M.F.F. performed epidemiologic analyses and in vitro and in vivo experiments, analyzed data, and wrote the manuscript. I.D.M. and S.P.M. performed in vitro and in vivo experiments with a comparable contribution. A.Y. performed in vitro and in vivo experiments. M.E.B. participated in human sample recollection, data analysis, and interpretation. L.G. and M.G. performed human in vitro experiments. B.P. performed bioinformatics analysis. M.C.Y. participated in human sample recollection, data analysis, and interpretation. C.Z. provided knockout mice. V.K.K. and G.A.R. edited the manuscript and participated in data interpretation. M.F.F., F.J.Q., and J.C. interpreted data, conceived and supervised the study, and edited the manuscript.

ACKNOWLEDGMENTS

This study was supported by the Allende Foundation and the MSIF Du-Pré grant (to M.F.F.), a grant from Biogen Idec and Novartis Argentina (to M.F.F. and J.C.) and Merck Serono Argentina (to J.C.), AI093903 and NS087867 from the NIH, RG4111A1 and JF2161-A-5 from the National Multiple Sclerosis Society, and PA0069 from the International Progressive MS Alliance to F.J.Q. We would like to thank Drs. Lora Hooper, Bart Staels, Vincent Laudent, Mitch Lazar, and Daniel Tenen for generously providing reagents used in these studies. We would also like to thank Jessica Kenison-White for technical assistance with mice colonies.

Received: December 4, 2014

Revised: May 4, 2015

Accepted: July 8, 2015

Published: September 10, 2015

REFERENCES

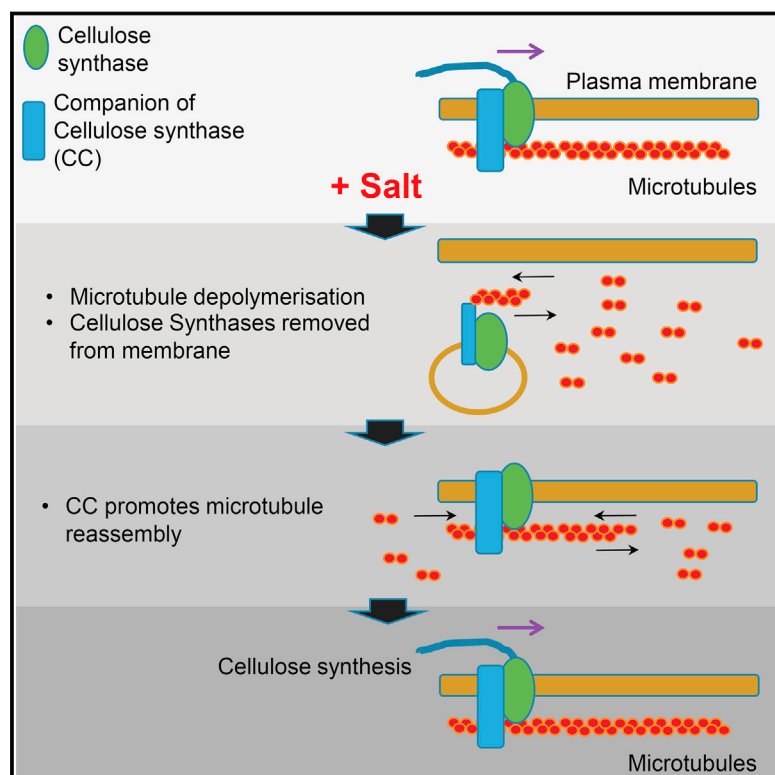
- Apetoh, L., Quintana, F.J., Pot, C., Joller, N., Xiao, S., Kumar, D., Burns, E.J., Sherr, D.H., Weiner, H.L., and Kuchroo, V.K. (2010). The aryl hydrocarbon receptor interacts with c-Maf to promote the differentiation of type 1 regulatory T cells induced by IL-27. *Nat. Immunol.* **11**, 854–861.
- Ascherio, A., Munger, K.L., Lennette, E.T., Spiegelman, D., Hernán, M.A., Olek, M.J., Hankinson, S.E., and Hunter, D.J. (2001). Epstein-Barr virus antibodies and risk of multiple sclerosis: a prospective study. *JAMA* **286**, 3083–3088.
- Ascherio, A., Munger, K.L., and Simon, K.C. (2010). Vitamin D and multiple sclerosis. *Lancet Neurol.* **9**, 599–612.
- Ascherio, A., Munger, K.L., and Lünemann, J.D. (2012). The initiation and prevention of multiple sclerosis. *Nat. Rev. Neurol.* **8**, 602–612.
- Ascherio, A., Munger, K.L., White, R., Köchert, K., Simon, K.C., Polman, C.H., Freedman, M.S., Hartung, H.-P., Miller, D.H., Montalbán, X., et al. (2014). Vitamin D as an early predictor of multiple sclerosis activity and progression. *JAMA Neurol.* **71**, 306–314.
- Astier, A.L., Meiffren, G., Freeman, S., and Hafler, D.A. (2006). Alterations in CD46-mediated Tr1 regulatory T cells in patients with multiple sclerosis. *J. Clin. Invest.* **116**, 3252–3257.
- Baeten, D.L., and Kuchroo, V.K. (2013). How Cytokine networks fuel inflammation: Interleukin-17 and a tale of two autoimmune diseases. *Nat. Med.* **19**, 824–825.
- Beecham, A.H., Patsopoulos, N.A., Xifara, D.K., Davis, M.F., Kemppinen, A., Cotsapas, C., Shah, T.S., Spencer, C., Booth, D., Goris, A., et al.; International Multiple Sclerosis Genetics Consortium (IMSGC); Wellcome Trust Case Control Consortium 2 (WTCCC2); International IBD Genetics Consortium (IIBDGC) (2013). Analysis of immune-related loci identifies 48 new susceptibility variants for multiple sclerosis. *Nat. Genet.* **45**, 1353–1360.
- Brzezinski, A. (1997). Melatonin in humans. *N. Engl. J. Med.* **336**, 186–195.
- Castellano, I., Ercole, E., and Palumbo, A. (2014). Nitric oxide affects ERK signaling through down-regulation of MAP kinase phosphatase levels during larval development of the ascidian *Ciona intestinalis*. *PLoS ONE* **9**, e102907.
- Codarri, L., Gyülvészi, G., Tosevski, V., Hesske, L., Fontana, A., Magnenat, L., Suter, T., and Becher, B. (2011). ROR γ t drives production of the cytokine GM-CSF in helper T cells, which is essential for the effector phase of autoimmune neuroinflammation. *Nat. Immunol.* **12**, 560–567.
- Correale, J., and Farez, M. (2007). Association between parasite infection and immune responses in multiple sclerosis. *Ann. Neurol.* **61**, 97–108.
- Correale, J., Fiol, M., and Gilmore, W. (2006). The risk of relapses in multiple sclerosis during systemic infections. *Neurology* **67**, 652–659.
- Correale, J., Ysraelit, M.C., and Gaitán, M.I. (2009). Immunomodulatory effects of Vitamin D in multiple sclerosis. *Brain* **132**, 1146–1160.
- El-Behi, M., Ceric, B., Dai, H., Yan, Y., Cullimore, M., Safavi, F., Zhang, G.-X., Dittel, B.N., and Rostami, A. (2011). The encephalitogenicity of T(H)17 cells is dependent on IL-1- and IL-23-induced production of the cytokine GM-CSF. *Nat. Immunol.* **12**, 568–575.
- Farez, M.F., Quintana, F.J., Gandhi, R., Izquierdo, G., Lucas, M., and Weiner, H.L. (2009). Toll-like receptor 2 and poly(ADP-ribose) polymerase 1 promote central nervous system neuroinflammation in progressive EAE. *Nat. Immunol.* **10**, 958–964.
- Farez, M.F., Fiol, M.P., Gaitan, M.I., Quintana, F.J., and Correale, J. (2014). Sodium intake is associated with increased disease activity in multiple sclerosis. *J. Neurol. Neurosurg. Psychiatry*. Published online August 28, 2014. <http://dx.doi.org/10.1136/jnnp-2014-307928>.
- Fassi, J., Russo Picasso, M.F., Furci, A., Sorroche, P., Jáuregui, R., and Plantalech, L. (2003). [Seasonal variations in 25-hydroxyvitamin D in young and elderly populations in Buenos Aires City]. *Medicina (B. Aires)* **63**, 215–220.
- Gandhi, R., Kumar, D., Burns, E.J., Nadeau, M., Dake, B., Laroni, A., Kozoriz, D., Weiner, H.L., and Quintana, F.J. (2010). Activation of the aryl hydrocarbon receptor induces human type 1 regulatory T cell-like and Foxp3(+) regulatory T cells. *Nat. Immunol.* **11**, 846–853.

- Graham, C., Cook, M.R., Kavet, R., Sastre, A., and Smith, D.K. (1998). Prediction of nocturnal plasma melatonin from morning urinary measures. *J. Pineal Res.* 24, 230–238.
- Hedström, A.K., Åkerstedt, T., Hillert, J., Olsson, T., and Alfredsson, L. (2011). Shift work at young age is associated with increased risk for multiple sclerosis. *Ann. Neurol.* 70, 733–741.
- Hernán, M.A., Jick, S.S., Logroscino, G., Olek, M.J., Ascherio, A., and Jick, H. (2005). Cigarette smoking and the progression of multiple sclerosis. *Brain* 128, 1461–1465.
- Hickie, I.B., and Rogers, N.L. (2011). Novel melatonin-based therapies: potential advances in the treatment of major depression. *Lancet* 378, 621–631.
- Jetten, A.M. (2009). Retinoid-related orphan receptors (RORs): critical roles in development, immunity, circadian rhythm, and cellular metabolism. *Nucl. Recept. Signal.* 7, e003.
- Jin, Y., de Pedro-Cuesta, J., Söderström, M., Stawiarsz, L., and Link, H. (2000). Seasonal patterns in optic neuritis and multiple sclerosis: a meta-analysis. *J. Neurol. Sci.* 181, 56–64.
- Jockers, R., Maurice, P., Boutin, J.A., and Delagrange, P. (2008). Melatonin receptors, heterodimerization, signal transduction and binding sites: what's new? *Br. J. Pharmacol.* 154, 1182–1195.
- Johnson, P.F. (2005). Molecular stop signs: regulation of cell-cycle arrest by C/EBP transcription factors. *J. Cell Sci.* 118, 2545–2555.
- Karim, A., Tolbert, D., and Cao, C. (2006). Disposition kinetics and tolerance of escalating single doses of ramelteon, a high-affinity MT1 and MT2 melatonin receptor agonist indicated for treatment of insomnia. *J. Clin. Pharmacol.* 46, 140–148.
- Kobayashi, T., Steinbach, E.C., Russo, S.M., Matsuoka, K., Nochi, T., Mahershak, N., Borst, L.B., Hostager, B., Garcia-Martinez, J.V., Rothman, P.B., et al. (2014). NFIL3-deficient mice develop microbiota-dependent, IL-12/23-driven spontaneous colitis. *J. Immunol.* 192, 1918–1927.
- Kojetin, D.J., and Burris, T.P. (2014). REV-ERB and ROR nuclear receptors as drug targets. *Nat. Rev. Drug Discov.* 13, 197–216.
- Korn, T., Bettelli, E., Oukka, M., and Kuchroo, V.K. (2009). IL-17 and Th17 Cells. *Annu. Rev. Immunol.* 27, 485–517.
- Lathrop, S.K., Bloom, S.M., Rao, S.M., Nutsch, K., Lio, C.-W., Santacruz, N., Peterson, D.A., Stappenbeck, T.S., and Hsieh, C.-S. (2011). Peripheral education of the immune system by colonic commensal microbiota. *Nature* 478, 250–254.
- Lee, Y., Awasthi, A., Yosef, N., Quintana, F.J., Xiao, S., Peters, A., Wu, C., Kleinewietfeld, M., Kunder, S., Hafler, D.A., et al. (2012). Induction and molecular signature of pathogenic TH17 cells. *Nat. Immunol.* 13, 991–999.
- Lekstrom-Himes, J., and Xanthopoulos, K.G. (1998). Biological role of the CCAAT/enhancer-binding protein family of transcription factors. *J. Biol. Chem.* 273, 28545–28548.
- Løken-Amsrud, K.I., Holmøy, T., Bakke, S.J., Beiske, A.G., Bjerve, K.S., Bjørnarå, B.T., Hovdal, H., Lilleås, F., Midgard, R., Pedersen, T., et al. (2012). Vitamin D and disease activity in multiple sclerosis before and during interferon-β treatment. *Neurology* 79, 267–273.
- Macchi, M.M., and Bruce, J.N. (2004). Human pineal physiology and functional significance of melatonin. *Front. Neuroendocrinol.* 25, 177–195.
- McGeachy, M.J., Bak-Jensen, K.S., Chen, Y., Tato, C.M., Blumenschein, W., McClanahan, T., and Cua, D.J. (2007). TGF-β and IL-6 drive the production of IL-17 and IL-10 by T cells and restrain T(H)-17 cell-mediated pathology. *Nat. Immunol.* 8, 1390–1397.
- McMullan, C.J., Schernhammer, E.S., Rimm, E.B., Hu, F.B., and Forman, J.P. (2013). Melatonin secretion and the incidence of type 2 diabetes. *JAMA* 309, 1388–1396.
- Miossec, P., Korn, T., and Kuchroo, V.K. (2009). Interleukin-17 and type 17 helper T cells. *N. Engl. J. Med.* 361, 888–898.
- Morera, A.L., and Abreu, P. (2007). Daytime/night-time and summer/winter melatonin and malondialdehyde rhythms: an inverse relationship. *J. Pineal Res.* 43, 313–314.
- Pévet, P. (2003). Melatonin: from seasonal to circadian signal. *J. Neuroendocrinol.* 15, 422–426.
- Polman, C.H., Reingold, S.C., Banwell, B., Clanet, M., Cohen, J.A., Filippi, M., Fujihara, K., Havrdova, E., Hutchinson, M., Kappos, L., et al. (2011). Diagnostic criteria for multiple sclerosis: 2010 revisions to the McDonald criteria. *Ann. Neurol.* 69, 292–302.
- Pot, C., Apetoh, L., Awasthi, A., and Kuchroo, V.K. (2011). Induction of regulatory Tr1 cells and inhibition of T(H)17 cells by IL-27. *Semin. Immunol.* 23, 438–445.
- Pozo, D., Delgado, M., Fernandez-Santos, J.M., Calvo, J.R., Gomariz, R.P., Martin-Lacave, I., Ortiz, G.G., and Guerrero, J.M. (1997). Expression of the Mel1a-melatonin receptor mRNA in T and B subsets of lymphocytes from rat thymus and spleen. *FASEB J.* 11, 466–473.
- Pozo, D., García-Mauriño, S., Guerrero, J.M., and Calvo, J.R. (2004). mRNA expression of nuclear receptor RZR/RORalpha, melatonin membrane receptor MT, and hydroxindole-O-methyltransferase in different populations of human immune cells. *J. Pineal Res.* 37, 48–54.
- Quintana, F.J., Basso, A.S., Iglesias, A.H., Korn, T., Farez, M.F., Bettelli, E., Caccamo, M., Oukka, M., and Weiner, H.L. (2008). Control of T(reg) and T(H)17 cell differentiation by the aryl hydrocarbon receptor. *Nature* 453, 65–71.
- Roncarolo, M.-G., Gregori, S., Battaglia, M., Bacchetta, R., Fleischhauer, K., and Levings, M.K. (2006). Interleukin-10-secreting type 1 regulatory T cells in rodents and humans. *Immunol. Rev.* 212, 28–50.
- Rosecrans, R., and Dohnal, J.C. (2014). Seasonal vitamin D changes and the impact on health risk assessment. *Clin. Biochem.* 47, 670–672.
- Runia, T.F., Hop, W.C.J., de Rijke, Y.B., Buljevac, D., and Hintzen, R.Q. (2012). Lower serum vitamin D levels are associated with a higher relapse risk in multiple sclerosis. *Neurology* 79, 261–266.
- Sakaguchi, S., Miyara, M., Costantino, C.M., and Hafler, D.A. (2010). FOXP3+ regulatory T cells in the human immune system. *Nat. Rev. Immunol.* 10, 490–500.
- Saraiva, M., and O'Garra, A. (2010). The regulation of IL-10 production by immune cells. *Nat. Rev. Immunol.* 10, 170–181.
- Saraiva, M., Christensen, J.R., Veldhoen, M., Murphy, T.L., Murphy, K.M., and O'Garra, A. (2009). Interleukin-10 production by Th1 cells requires interleukin-12-induced STAT4 transcription factor and ERK MAP kinase activation by high antigen dose. *Immunity* 31, 209–219.
- Sawcer, S., Hellenthal, G., Pirinen, M., Spencer, C.C.A., Patsopoulos, N.A., Moutsianas, L., Dilthey, A., Su, Z., Freeman, C., Hunt, S.E., et al.; International Multiple Sclerosis Genetics Consortium; Wellcome Trust Case Control Consortium 2 (2011). Genetic risk and a primary role for cell-mediated immune mechanisms in multiple sclerosis. *Nature* 476, 214–219.
- Schernhammer, E.S., Rosner, B., Willett, W.C., Laden, F., Colditz, G.A., and Hankinson, S.E. (2004). Epidemiology of urinary melatonin in women and its relation to other hormones and night work. *Cancer Epidemiol. Biomarkers Prev.* 13, 936–943.
- Simpson, S., Jr., Taylor, B., Blizzard, L., Ponsonby, A.-L., Pittas, F., Tremlett, H., Dwyer, T., Gies, P., and van der Mei, I. (2010). Higher 25-hydroxyvitamin D is associated with lower relapse risk in multiple sclerosis. *Ann. Neurol.* 68, 193–203.
- Sospedra, M., and Martin, R. (2005). Immunology of multiple sclerosis. *Annu. Rev. Immunol.* 23, 683–747.
- Spelman, T., Gray, O., Trojano, M., Petersen, T., Izquierdo, G., Lugaresi, A., Hupperts, R., Bergamaschi, R., Duquette, P., Grammond, P., et al. (2014). Seasonal variation of relapse rate in multiple sclerosis is latitude dependent. *Ann. Neurol.* 76, 880–890.
- Steinman, L. (2014). Immunology of relapse and remission in multiple sclerosis. *Annu. Rev. Immunol.* 32, 257–281.
- Tan, A.H.M., and Lam, K.P. (2010). Pharmacologic inhibition of MEK-ERK signaling enhances Th17 differentiation. *J. Immunol.* 184, 1849–1857.
- Ueno-Towatari, T., Norimatsu, K., Blazejczyk, K., Tokura, H., and Morita, T. (2007). Seasonal variations of melatonin secretion in young females under

- natural and artificial light conditions in Fukuoka, Japan. *J. Physiol. Anthropol.* 26, 209–215.
- Viglietta, V., Baecher-Allan, C., Weiner, H.L., and Hafler, D.A. (2004). Loss of functional suppression by CD4+CD25+ regulatory T cells in patients with multiple sclerosis. *J. Exp. Med.* 199, 971–979.
- Wu, C., Yosef, N., Thalhamer, T., Zhu, C., Xiao, S., Kishi, Y., Regev, A., and Kuchroo, V.K. (2013). Induction of pathogenic TH17 cells by inducible salt-sensing kinase SGK1. *Nature* 496, 513–517.
- Yang, J., Croniger, C.M., Lekstrom-Himes, J., Zhang, P., Fenyus, M., Tenen, D.G., Darlington, G.J., and Hanson, R.W. (2005). Metabolic response of mice to a postnatal ablation of CCAAT/enhancer-binding protein alpha. *J. Biol. Chem.* 280, 38689–38699.
- Yang, X.O., Pappu, B.P., Nurieva, R., Akimzhanov, A., Kang, H.S., Chung, Y., Ma, L., Shah, B., Panopoulos, A.D., Schluns, K.S., et al. (2008). T helper 17 lineage differentiation is programmed by orphan nuclear receptors ROR α and ROR γ . *Immunity* 28, 29–39.
- Yu, X., Rollins, D., Ruhn, K.A., Stubblefield, J.J., Green, C.B., Kashiwada, M., Rothman, P.B., Takahashi, J.S., and Hooper, L.V. (2013). TH17 cell differentiation is regulated by the circadian clock. *Science* 342, 727–730.

A Mechanism for Sustained Cellulose Synthesis during Salt Stress

Graphical Abstract



Authors

Anne Endler, Christopher Kesten, René Schneider, ..., Anja Froehlich, Norma Funke, Staffan Persson

Correspondence

staffan.persson@unimelb.edu.au

In Brief

Plant biomass provides us with many essential products and an understanding for how it is synthesized is therefore important to support human activities. A central element to plant biomass is the cell wall; a cellular exoskeleton in which the glucan-based polymer cellulose is a prominent component. This paper identifies a protein family whose members are components of the cellulose synthesizing machinery in plants and reveals a mechanism for how plants maintain their biomass producing capacity during saline conditions.

Highlights

- Identification of two components (CC1 and 2) of the cellulose synthase complex
- The CCs directly interact with microtubules and promote their dynamics
- The CCs support microtubule and cellulose synthase activity during salt stress
- A mechanistic model for how plant biomass is sustained during salt stress

A Mechanism for Sustained Cellulose Synthesis during Salt Stress

Anne Endler,^{1,2,4} Christopher Kesten,^{1,3,4} René Schneider,¹ Yi Zhang,¹ Alexander Ivakov,¹ Anja Froehlich,¹ Norma Funke,¹ and Staffan Persson^{1,3,*}

¹Max-Planck-Institut of Molecular Plant Physiology, Am Mühlenberg 1, 14476 Potsdam-Golm, Germany

²Targenomix GmbH, Am Mühlenberg 11, 14476 Potsdam-Golm, Germany

³School of Biosciences, University of Melbourne, Parkville 3010 VIC, Australia

⁴Co-first author

*Correspondence: staffan.persson@unimelb.edu.au

<http://dx.doi.org/10.1016/j.cell.2015.08.028>

SUMMARY

Abiotic stress, such as salinity, drought, and cold, causes detrimental yield losses for all major plant crop species. Understanding mechanisms that improve plants' ability to produce biomass, which largely is constituted by the plant cell wall, is therefore of upmost importance for agricultural activities. Cellulose is a principal component of the cell wall and is synthesized by microtubule-guided cellulose synthase enzymes at the plasma membrane. Here, we identified two components of the cellulose synthase complex, which we call companion of cellulose synthase (CC) proteins. The cytoplasmic tails of these membrane proteins bind to microtubules and promote microtubule dynamics. This activity supports microtubule organization, cellulose synthase localization at the plasma membrane, and renders seedlings less sensitive to stress. Our findings offer a mechanistic model for how two molecular components, the CC proteins, sustain microtubule organization and cellulose synthase localization and thus aid plant biomass production during salt stress.

INTRODUCTION

Changes in environmental conditions impact on plant biomass production and on growth distributions (Qin et al., 2011). Abiotic stresses, including drought, heat, cold, and salinity, are estimated to be the causative factor for up to 50% of yield loss for various crop species (Boyer, 1982). However, mechanisms that link salt stress and the biomass producing capabilities of plants remain tenuous.

Plant biomass is largely made up of plant cell walls, which provide the major sustainable resource for many human products including feed, food, and fuel (Somerville et al., 2010). Cellulose contributes the main bulk of plant cell walls and is the most abundant biopolymer on Earth. Cellulose consists of β -1,4-linked glucan chains that form microfibrils by intra- and inter-molecular hydrogen bonds (McFarlane et al., 2014). These microfibrils provide the main cell wall tensile strength, are essential for plant

development, for directed cell growth, and thus for plant stature (McFarlane et al., 2014). Cellulose is synthesized by plasma membrane located cellulose synthase (CesA) complexes (CSCs) (McFarlane et al., 2014), which are typically arranged as hexameric rosettes (Mueller and Brown, 1980). Using fluorescently tagged CesA proteins, the complexes have been observed as motile foci in the plasma membrane of *Arabidopsis thaliana* interphase cells (Paredez et al., 2006), supporting a model in which plasma membrane-based CesA movement represents its enzymatic activity (Morgan et al., 2013).

Plants typically contain two different types of cell walls; a primary wall that surrounds all growing cells and a secondary wall that provides support to specialized cells (McFarlane et al., 2014). Mutant analyses and co-immunoprecipitation studies have shown that three distinct CesA subunits are necessary to form a functional complex (McFarlane et al., 2014). Consequently, the primary wall CSCs in *Arabidopsis* require CesA1-, CesA3-, and a CesA6-related activity to be functional (Persson et al., 2007; Desprez et al., 2007). The CSCs are assumed to be assembled in the endoplasmic reticulum (ER) or Golgi and are transported to the cell surface where they are inserted into the plasma membrane adjacent to cortical microtubules (Gutierrez et al., 2009). The CesAs may also be found in small post-Golgi-related compartments referred to as small CesA compartments (smaCCs) (Gutierrez et al., 2009), or microtubule-associated CesA compartments (MASCs) (Crowell et al., 2009), which are hypothesized to be involved in either exo- or endocytosis of the CSCs (Gutierrez et al., 2009; Crowell et al., 2009).

Cellulose microfibrils are typically transversely organized and can align with cortical microtubules that are tethered to the plasma membrane, in elongating plant interphase cells (Green, 1962; Ledbetter and Porter, 1963; Baskin, 2001). Consistent with these observations, *in vivo* studies using fluorescently dual-labeled CesAs and microtubules revealed that the CSCs can track along cortical microtubules (Paredez et al., 2006) via the protein cellulose synthase interacting1 (CSI1) (Gu et al., 2010). Perturbations of microtubule organization, furthermore, affect the mechanical properties of the cell wall (Zhong et al., 2002; Fujita et al., 2011; Uyttewaal et al., 2012).

Cortical microtubules have been suggested to function as sensors of environmental stress in plant interphase cells (Nick, 2013). Microtubules disassemble rapidly after exposure to salt

and other osmotic stresses (Komis et al., 2002). Under prolonged stress the microtubule array gradually re-emerges, possibly as an array adapted to stress conditions (Wang et al., 2007). One probable regulator of the stress-induced microtubule de-polymerization is the atypical microtubule-associated protein kinase PHS1 that may phosphorylate tubulin and thereby block microtubule polymerization (Naoi and Hashimoto, 2004; Fujita et al., 2013). In addition, degradation of the microtubule stabilizing protein SPIRAL1 (SPR1) by the 26S proteasome is important for salt stress tolerance (Wang et al., 2011). Given the close association between cortical microtubules and the CSCs, it may be expected that salt stress impacts on cell wall synthesis and that lesions in cellulose-related components can alter salt tolerance. Indeed, mutations in e.g., CesA1, KORRIGAN (an endoglucanase associated with cellulose synthesis), CesA8, and the CesA-related protein cellulose synthase like D5 (CSDL5) led to changes in drought and salt stress tolerance (Chen et al., 2005; Kang et al., 2008; Zhu et al., 2010).

Here, we identified two plant-specific proteins (companion of cellulose synthase 1 and 2 [CC1 and CC2]) that can interact with the CesA proteins and with microtubules. Mutations of the proteins led to salt-sensitive phenotypes and altered microtubule and CSC behavior in vivo. Furthermore, in vitro and in vivo analyses revealed that the cytosolic parts of the CC proteins, which interact with microtubules, promote microtubule formation and dynamics. Thus, we present a mechanism in which the CC proteins promote microtubule dynamics and CesA activity to support biomass production during salt stress.

RESULTS

The CC Proteins Maintain Plant Growth during Adverse Conditions

Genes that contribute to cellulose synthesis are typically transcriptionally coordinated with the CesA genes (Persson et al., 2005). We identified At1g45688 (CC1) encoding a plant-specific protein of unknown function as being co-expressed with CesA1, CesA3, and CesA6 (Figure S1A). T-DNA insertion mutants (*cc1-1* and *cc1-2*) in this gene did not cause phenotypic deviations from wild-type. CC1 is part of a gene family of four members in *Arabidopsis*. Sequence homology, phylogenetic estimates of the corresponding protein sequences and expression analyses revealed At5g42860 (CC2) as the closest CC1 homolog (Figures S1B–S1F), indicating that CC2 could compensate for the loss of CC1 in the *cc1* mutants. This encouraged us to establish *cc1cc2* double mutants; still, we did not observe any phenotypic deviations from wild-type for *cc1cc2* grown on MS media plates. However, CC1 expression may be induced by salt (150 mM NaCl) (*Arabidopsis* eFP browser <http://bar.utoronto.ca/efp/cgi-bin/efpWeb.cgi>) (Winter et al., 2007). We therefore tested if the *cc1*, *cc2*, and *cc1cc2* mutants were sensitive to saline conditions. Figures 1A–1C show that hypocotyls of etiolated *cc1cc2* displayed cell swelling and elongation defects 3 days after transfer to salt containing plates (75 and 100 mM NaCl). In contrast, no differences in hypocotyl growth were observed when seedlings were grown in the dark on media supplemented with 100 or 250 mM sorbitol (Figure S1G), which correspond to osmolarity of 50 and 125 mM NaCl, respectively. When

measuring cellulose levels in the salt-stressed seedlings, we found that the *cc1cc2* seedlings contained significantly lower levels of cellulose compared to the control (Figure 1D; 150 mM NaCl).

To test if agents known to affect cellulose synthesis impacted on *cc1cc2* seedling growth, we grew the mutant lines on MS media supplemented with isoxaben and dichlobenil (DCB; cellulose synthesis inhibitors) (McFarlane et al., 2014) and oryzalin (a microtubule depolymerizing agent) (Morejohn et al., 1987). Indeed, the *cc1cc2* seedlings displayed clear growth defects, including cell swelling and reduced hypocotyl elongation, when grown on plates containing these agents (Figures S1G–S1L). The cellulose content was, furthermore, significantly reduced (~30%) in *cc1cc2* as compared to wild-type seedlings when grown on MS media supplemented with 2 nM isoxaben (Table S1). Other cell wall components (i.e., uronic acids and neutral sugars) did not show changes during these conditions (Table S1). To assess whether other members of the protein family (i.e., At2g41990; CC3 and At4g35170; CC4) contributed to the seedling phenotypes, we generated all possible single, double, triple, and quadruple mutant combinations between T-DNA null mutants of the four family members (Figure S1M) and analyzed the phenotypes of the mutants under stress conditions. We found clear growth defects only if both CC1 and CC2 were mutated in the seedlings (Figures 1E, 1F, and S1H–S1L). Hence, CC1 and CC2 are important proteins for seedling growth and cellulose synthesis during adverse growth conditions.

The CC Proteins Are Members of the Cellulose Synthase Complex

To investigate the subcellular localization of CC1 and CC2, we generated functional N-terminally tagged GFP fusions under the control of a constitutively active ubiquitin 10 promoter (Grefen et al., 2010) (Figures 2A and B) or under the control of their native promoters that behaved identical to the ubiquitin 10 driven constructs (Figures S2A and S2B). Visualization of GFP-CC1 and GFP-CC2 in etiolated hypocotyl cells showed that they could be discerned as motile foci that moved bi-directionally with an average speed of 227 ± 75 nm/min (GFP-CC1) and 216 ± 70 nm/min (GFP-CC2) in the plasma membrane (Figures 2C–2E, S2C, S2D, and S2G). These data are similar to what has been reported for the CSC (Paredez et al., 2006), suggesting that the CCs may track together with the CSCs. To substantiate this, we produced dual-labeled GFP-CC1 (or GFP-CC2) and tdTomato (tdT)-CesA6 lines (Sampathkumar et al., 2013) and observed that the fluorescent red and green foci co-migrated (Figures 2D–2G and S2C–S2I; Movie S1), and we therefore named the proteins companion of cellulose synthase (CC)1 and CC2. In addition, we observed that GFP-CC1 or GFP-CC2 proteins tracked along cortical microtubules in GFP-CC1 (or GFP-CC2) and mCherry (mCh)-TUA5 dual-label lines (Figures S2J and S2K; Movie S2) similar to what has been described for fluorescently labeled CesA proteins (Paredez et al., 2006). These data further suggest that the CCs are associated with CSCs in the plasma membrane. To investigate if the proteins can interact directly with the CesA proteins, we tested the interactions in yeast with the split-ubiquitin MbYTH system using the CesA1, CesA3, and CesA6 as bait proteins and the CC1 as prey protein.

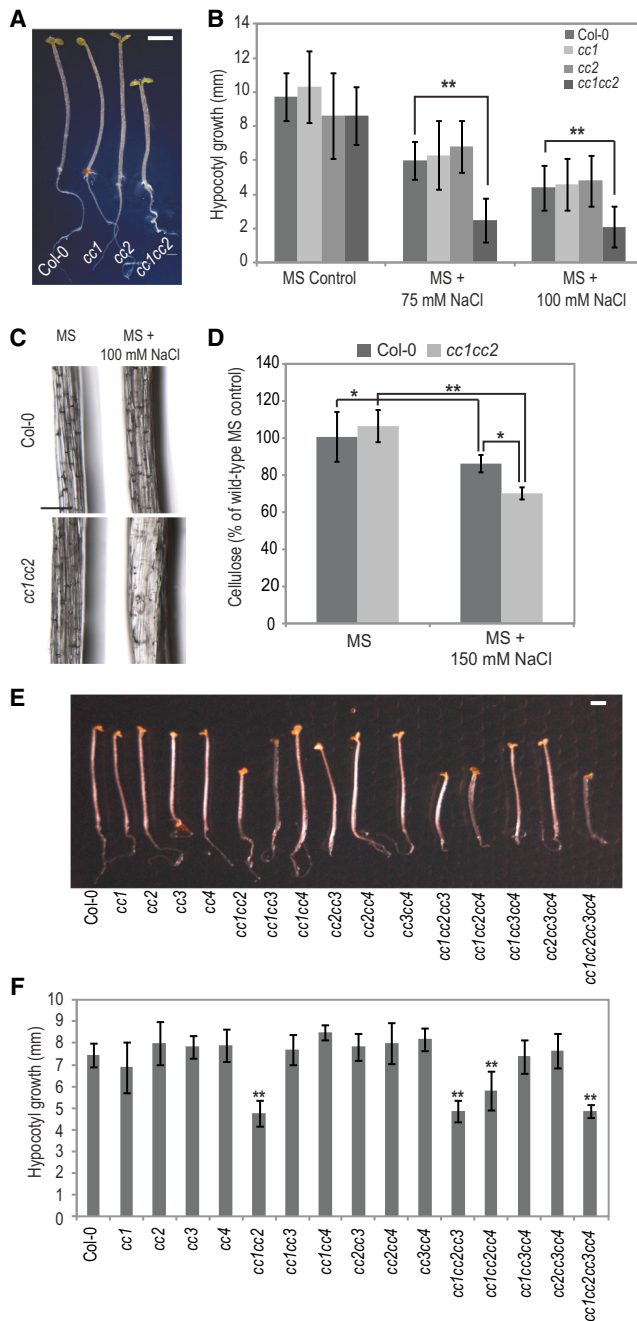


Figure 1. CC1 and CC2 Are Important for Seedling Stress Tolerance
(A) Seedlings germinated and grown for 2 days on MS plates and transferred to MS plates supplemented with 100 mM NaCl and grown for an additional 2 days in dark. Scale bar, 1 mm.

(B) Quantification of hypocotyl elongation of seedlings in (A). **p ≤ 0.001. Student's t test, values are mean, error bars are SD, n = 10 seedlings per biological replicate (rep). Three biological reps.

(C) Close-up of hypocotyl cells of seedlings grown as in (A) using differential interference contrast (DIC) microscopy. Scale bar, 200 μm.

(D) Cellulose levels in seedlings grown as in (E) but on media supplemented with 150 mM NaCl. Values are means expressed as % cellulose of wild-type seedlings grown on MS media. *p ≤ 0.005; **p ≤ 0.001. Student's t test, error bars are SD, n = 3 biological reps.

Yeast growth on selective media and positive β-galactosidase activity supported a direct interaction between the proteins (Figure 2H). These data were corroborated by reciprocal assays, i.e., using the CC1 as bait and the CesA proteins as prey (Figure 2H). Since CC1 can directly interact with the CesA proteins in yeast, and the CCs track together with the CSC in the plasma membrane, we propose that the CCs constitute members of the CSC.

CC1 Is Delivered Together with CesA to the Plasma Membrane, and the CC Proteins Are Localized to the trans-Golgi Network

To assess whether the CesA and the CC proteins are delivered together to the plasma membrane we studied the fluorescence recovery after photo-bleaching (FRAP) of the GFP-CC1 and tdT-CesA6 in dual-labeled etiolated hypocotyls. We tracked delivery of new CesA proteins to the plasma membrane and investigated whether these events coincided with the delivery of CC1 proteins. We observed co-delivery of the proteins to the plasma membrane in 60 of 114 events (53%). In the remaining 54 events, the GFP-CC1 was either delivered prior (21 events; 18%) or after (33 events; 29%) the tdT-CesA6 (six cells from six different seedlings). Hence, the majority of CC1 and CesA proteins are delivered together to the plasma membrane.

GFP-CC1 and GFP-CC2 also localized to cytoplasmic compartments (Figures 2I, 2J, and S2A), which did not show extensive overlap with the Golgi located CesAs (Figures 2I, S2L, and S2N). As the CC1- and CC2-labeled compartments resembled *trans*-Golgi network (TGN)/early endosome-related compartments, we crossed the GFP-CC1 or GFP-CC2 lines with lines expressing the TGN marker VHAa1 fused to RFP (Dettmer et al., 2006). Visualization of the fluorescent proteins in the dual-labeled progeny of this cross revealed substantial co-localization of the GFP and RFP channels (61.8% ± 2.3%), indicating that in addition to their plasma membrane localization, CC1 and CC2 are also localized to the TGN as defined by VHAa1-RFP (Figures 2J, S2M, and S2N).

CC1 Remains Associated with the CSC under Adverse Conditions

We next examined the behavior of GFP-CC1 in the presence of oryzalin or after treatment with isoxaben, which removes CesAs from the plasma membrane (Paredez et al., 2006). Treatment of dual-labeled GFP-CC1 and mCh-TUA5 etiolated hypocotyls with 20 μM oryzalin for 12-hr depolymerized the microtubules (Figure S3A). However, GFP-CC1 was not depleted from the plasma membrane, and time averages of time-lapse movies revealed that the GFP-CC1 foci were still motile along linear tracks (Figure S3A), similar to what has been reported for fluorescently tagged CesAs (Paredez et al., 2006). In addition, similar treatment (20 μM oryzalin for 12 hr) of dual-labeled GFP-CC1 (or

(E) Seedlings germinated and grown for 2 days on MS plates and transferred to MS plates supplemented with 100 mM NaCl and grown for an additional 4 days in dark. Scale bar, 1 mm.

(F) Quantification of hypocotyl elongation of seedlings in (E). **p ≤ 0.001. Student's t test, values are means, error bars are SD, n = 10 seedlings per biological rep. Three biological reps.

See also Figure S1 and Table S1.

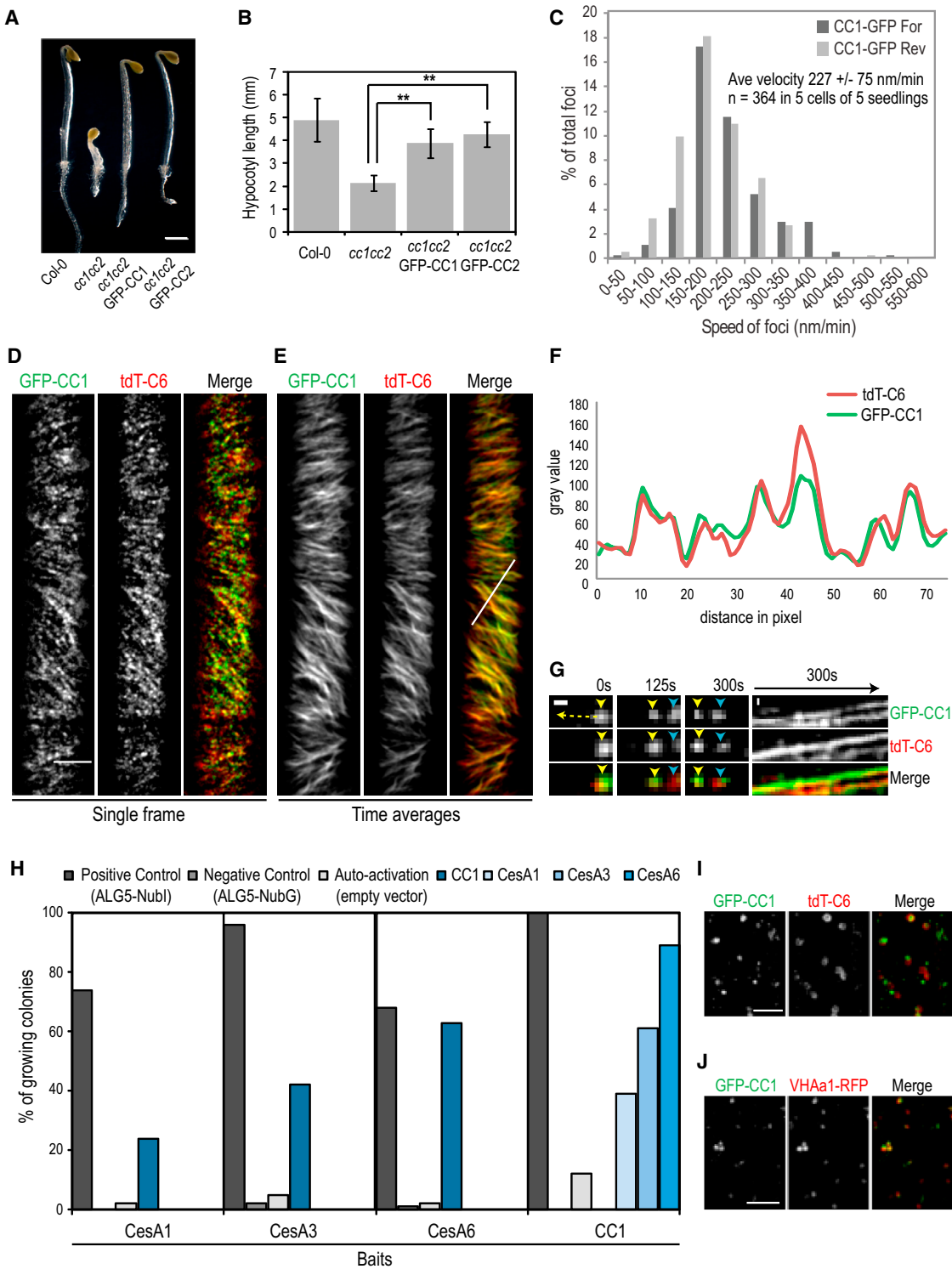


Figure 2. CC1 Co-migrates and Interacts with the Cellulose Synthase Complex

(A) Introduction of either GFP-CC1 or GFP-CC2 under the control of Ubiquitin10 promoter into *cc1cc2* double mutants restores etiolated hypocotyl growth when germinated and grown for four days on MS media supplemented with 1 nM isoxaben. Scale bar, 1 mm.

(B) Quantification of hypocotyls in (A). ** $p \leq 0.001$. Student's t test, values are means, error bars are SD, $n \geq 10$ seedlings per biological replicate (rep). Three biological reps.

(legend continued on next page)

GFP-CC2) and tdT-CesA6 seedlings revealed that CC1 and the CesAs still tracked together (Figures S3B–S3D). Isoxaben treatment depletes CSCs from the plasma membrane and lead to accumulation of CesAs in SmaCCs/MASCs tethered to the cell cortex (Paredez et al., 2006). Two hours isoxaben treatment (200 nM) depleted CesAs from the plasma membrane confirming that the treatment worked. Similarly, the GFP-CC1 signal also disappeared from the plasma membrane and accumulated in SmaCCs/MASCs together with the tdT-CesA6 fluorescence (Figures 3A and 3B).

To get a better understanding for how the CC proteins may influence cellulose synthesis during salt stress, we exposed dual-labeled GFP-CC1 and mCh-TUA5 seedlings to 200 mM NaCl for short time periods. After 6 hr of salt treatment, the GFP-CC1 signal located to small cytosolic bodies (CC bodies) that were reminiscent of SmaCCs/MASCs (Figure 3C). To confirm this, we exposed dual-labeled GFP-CC1 and tdT-CesA6 seedlings to the same treatment and observed co-localization of the GFP-CC1 and tdT-CesA6 signals (Pearson coefficient 0.58 ± 0.10; six cells from six seedlings in three experiments) (Figures 3C and 3D; Movie S3). These particles migrated as typical SmaCC/MASC compartments (Figure 3D) (Gutierrez et al., 2009), corroborating that the CC1 and CesA proteins re-locate to SmaCCs/MASCs after salt stress. Taken together, these data also support a robust interaction of the CCs and the CSC.

The CC Proteins Safeguard Microtubule and Cellulose Synthase Functions during Salt Stress

To assess the impact of salt stress on CesA and microtubule behavior in the absence of CC function, we generated YFP-CesA6 and mCh-TUA5 dual-labeled *cc1cc2* mutant plants. We imaged 3-day-old etiolated hypocotyls after 15, 30, and 45 min and 1, 2, 4, 8, 16, 28, 30, 34, and 50 hr of treatment with 200 mM NaCl. Similar to what has been described previously (Wang et al., 2007; Fujita et al., 2013), 200 mM NaCl abolished the cortical microtubule array after ~2 hr exposure in wild-type cells (Figures 4A and S4A). The microtubules then reassembled after ~8 hr and remained at the cortex as a stable array during subsequent observations (Figures 4A, 4B, and S4A). In contrast, the microtubule array disappeared very rapidly (~30 min) after salt exposure in the *cc1cc2* seedlings and reassembled already after 4 hr of salt exposure (Figures 4A, 4B, and S4A). However, in contrast to the wild-type cells, the microtubules in the *cc1cc2*

cells again gradually disappeared (~8 hr after salt exposure; Figures 4A, 4B, and S4A) and did not re-appear again during the course of the experiments (50 hr of treatment).

The salt treatment also affected the behavior of the CesAs. After ~30 min the CesA density in the plasma membrane decreased dramatically in the wild-type cells and led to an accumulation of CesA signal in SmaCCs/MASCs (Sampathkumar et al., 2013) (Figures 4A, S4B, and S4C). Surprisingly, the CesAs began to re-appear at the plasma membrane after ~8 hr of treatment, and the CesA patterns were indistinguishable from non-treated cells after 28 hr of salt treatment (Figures 4A, 4B, S4B, and S4C). In contrast, we observed a rapid disappearance of CesAs from the plasma membrane in the *cc1cc2* seedlings (~15 min after salt treatment; Figures 4A, 4B, S4B, and S4C). The depletion of the CesAs was not restored in the *cc1cc2* mutant during the course of the experiments (50 hr of treatment). Instead, the SmaCCs/MASCs that initially accumulated slowly vanished, and after 28 hr treatment only Golgi and/or other cytoplasmic compartment-located CesAs were observed (Figures 4A, 4B, and S4C). To corroborate these data, we also investigated the CesA (GFP-CesA3) behavior 2 days after transfer of seedlings to MS plates with intermediate salt concentrations (100 mM). While the CesAs appeared similar in density in *cc1cc2* cells as compared to controls, FRAP experiments revealed a substantial reduction in CesA delivery rates in the *cc1cc2* cells (Figure 4C). In addition, the CesAs migrated significantly slower in the *cc1cc2* mutant seedlings treated with 100 mM NaCl as compared to wild-type (mean speed in wild-type cells: 246 ± 70 and 218 ± 46 nm/min on MS and salt-containing MS media, respectively, mean speed in *cc1cc2* mutant cells: 221 ± 56 and 158 ± 53 nm/min on MS and salt-containing MS media, respectively; Student's t test; p < 2.7 E-108, between CesA speed in wild-type and *cc1cc2* on salt-containing MS media; n = six cells from three different seedlings). These data indicate an important function of the CC proteins in maintaining CesA function and microtubule stability during salt stress.

Mutations in the CC Proteins Lead to Impaired Microtubule Dynamics during Salt Stress

To investigate the impact of the CC proteins on microtubule behavior during salt stress, we analyzed microtubule dynamics using four parameters: growth, shrinkage, catastrophe, and rescue rates. As the microtubule arrays are behaving very

(C) GFP-CC1 fluorescent foci display bi-directional motility in the plasma membrane. Imaging of GFP-CC1 was done in 3-day-old etiolated seedlings in hypocotyl cells. Forward denotes the movement from left to right and reverse from right to left with regards to the major axes.

(D) GFP-CC1 and tdT-CesA6 (tdT-C6) co-localize at foci in the plasma membrane. Scale bar, 5 μm.

(E) Time-average projections of GFP-CC1 and tdT-C6 from (D) reveal co-migration of the fluorescent foci.

(F) Intensity plot of GFP-CC1 and tdT-C6 from transect in (E).

(G) Left: time frames of individual plasma membrane-located fluorescent GFP-CC1 and tdT-C6 foci reveal that they migrate as one foci first (yellow arrowhead at time 0 s). The foci split into two foci in both channels that maintain co-migration (time 125 and 300 s). Right: kymographs of 300-s movies of GFP-CC1 and tdT-C6 expressing cells from frames in left panel. Scale bar, 0.5 μm.

(H) Split-ubiquitin assays visualizing interaction of CesA and CC1 in yeast. The bars represent the percentage of yeast colonies grown after 4 days on selective medium at 30°C, growth indicates interaction of bait and prey proteins. Bait proteins were N-terminally fused to Cub (C-terminal part of ubiquitin), and prey proteins were fused with mutated N-terminal part of ubiquitin (NubG). In negative controls, baits are co-expressed with ALG5 (ER-protein) fused with NubG, in positive controls with ALG5 fused to wild-type N-terminal domain of ubiquitin (NubL), and in auto-activation controls with empty vector.

(I and J) Sub-cortical fluorescent compartments in hypocotyl cells expressing GFP-CC1 and tdT-C6 (I) or GFP-CC1 and VHAa1-RFP (J). For GFP-CC1 and VHAa1-RFP, 61.8% ± 2.3% of the signals co-localize; object-based co-localization was used based on the overlap approach (see Figure S2N). Scale bars, 5 μm. See also Figure S2 and Movies S1 and S2.

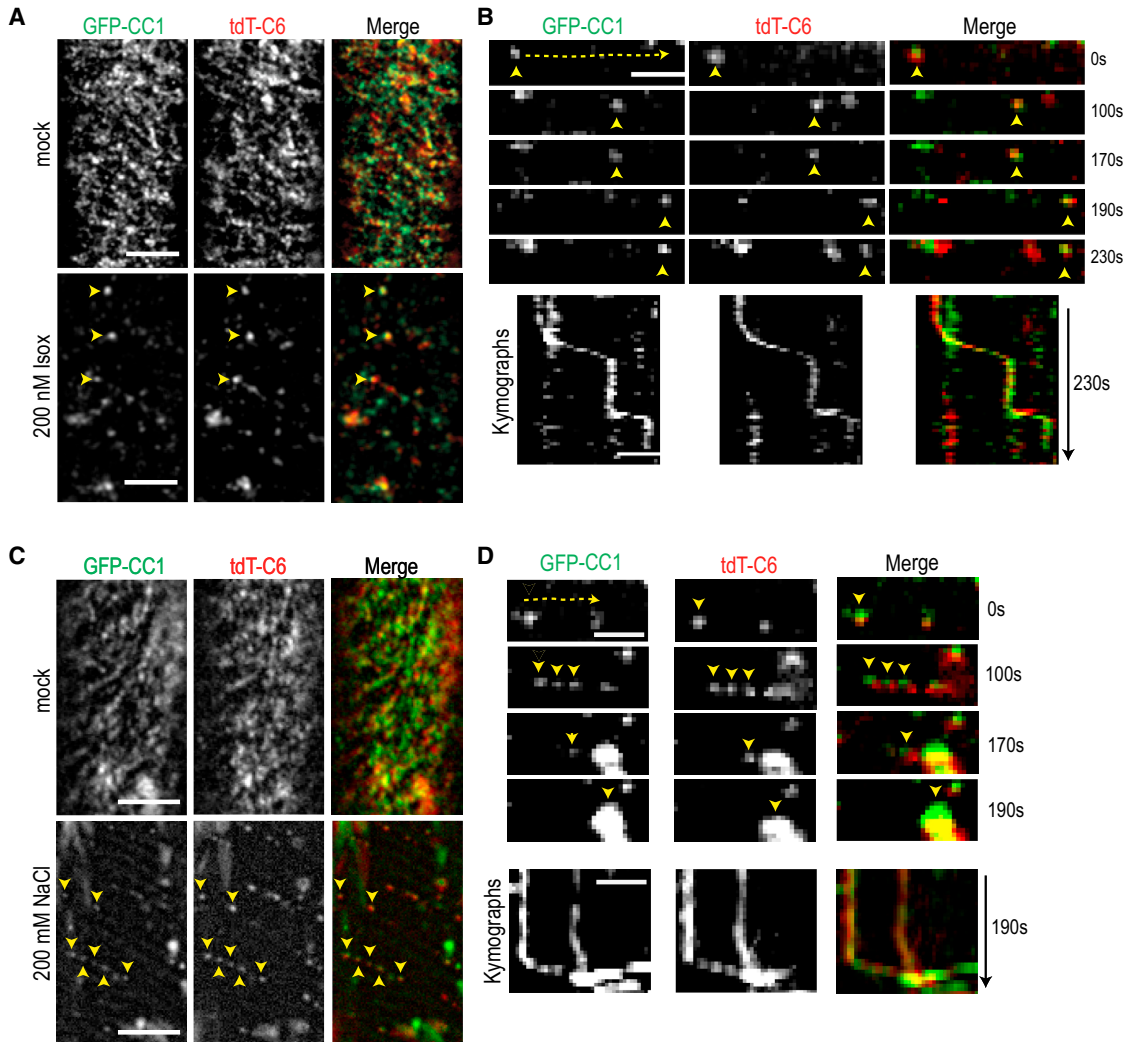


Figure 3. The CC Proteins Associate with smaCCs/MASCs after Exposure to Stress

(A) GFP-CC1 and tdTomato-CesA6 (tdT-C6) co-localize in small intracellular compartments (smaCCs/MASCs, indicated by arrowheads) after exposure to 200 nM isoxaben for 2 hr in 3-day-old etiolated seedlings. Scale bars, 5 μ m.

(B) Typical movement of smaCCs/MASCs observed in seedlings treated as in (A). GFP-CC1 and tdTomato-CesA6 (tdT-C6) co-localize in smaCCs/MASCs (arrowheads indicate smaCCs/MASCs, dotted line with arrow indicates movement of smaCCs/MASCs). First, the SmaCC/MASC is standing then moves fast (0–100 s), stands still (100–170 s), moves fast (170–190 s), and is static (190–230 s). The lower panel shows corresponding kymograph representing the movement of the smaCCs/MASCs along the dotted line over time (0–230 s). Scale bars, 2 μ m.

(C) GFP-CC1 and tdT-CesA6 (tdT-C6) co-localize in smaCCs/MASCs after exposure to 200 mM NaCl for 6 hr in 3-day-old etiolated seedlings. Arrowheads indicate smaCCs/MASCs. Scale bars, 5 μ m.

(D) Movement of smaCCs/MASCs observed in seedlings treated as in (C). GFP-CC1 and tdT-C6 co-localize in smaCCs/MASCs (indicated by arrowheads). Dotted line with arrow indicates movement of smaCCs/MASCs. Lower panel shows corresponding kymograph representing the movement of the smaCCs/MASCs along the dotted line over time. Scale bars, 2 μ m.

See also Figure S3 and Movie S3.

differently in the *cc1cc2* double mutant and wild-type cells after salt stress, we first estimated time points where the two arrays would be at comparable states. While the microtubule array in the *cc1cc2* mutant cells are becoming re-established ~2 hr after salt stress, the array in wild-type cells are typically re-established 6 hr after the stress (Figures 4B and S4A; ~16% microtubule cell coverage for both genotypes). We therefore chose to analyze the microtubule array dynamics at these time points. The microtu-

ble arrays behaved very similar in the wild-type and *cc1cc2* mutant cells under control conditions (Figures 4D–4G). However, the salt treatment caused significant changes in the behavior of the microtubule array in wild-type cells. In particular, catastrophe and rescue events were observed more frequently (Figures 4E and 4G), indicating that the microtubule array underwent substantial re-organization during the recovery phase after salt treatment. In contrast, catastrophe and rescue events were not

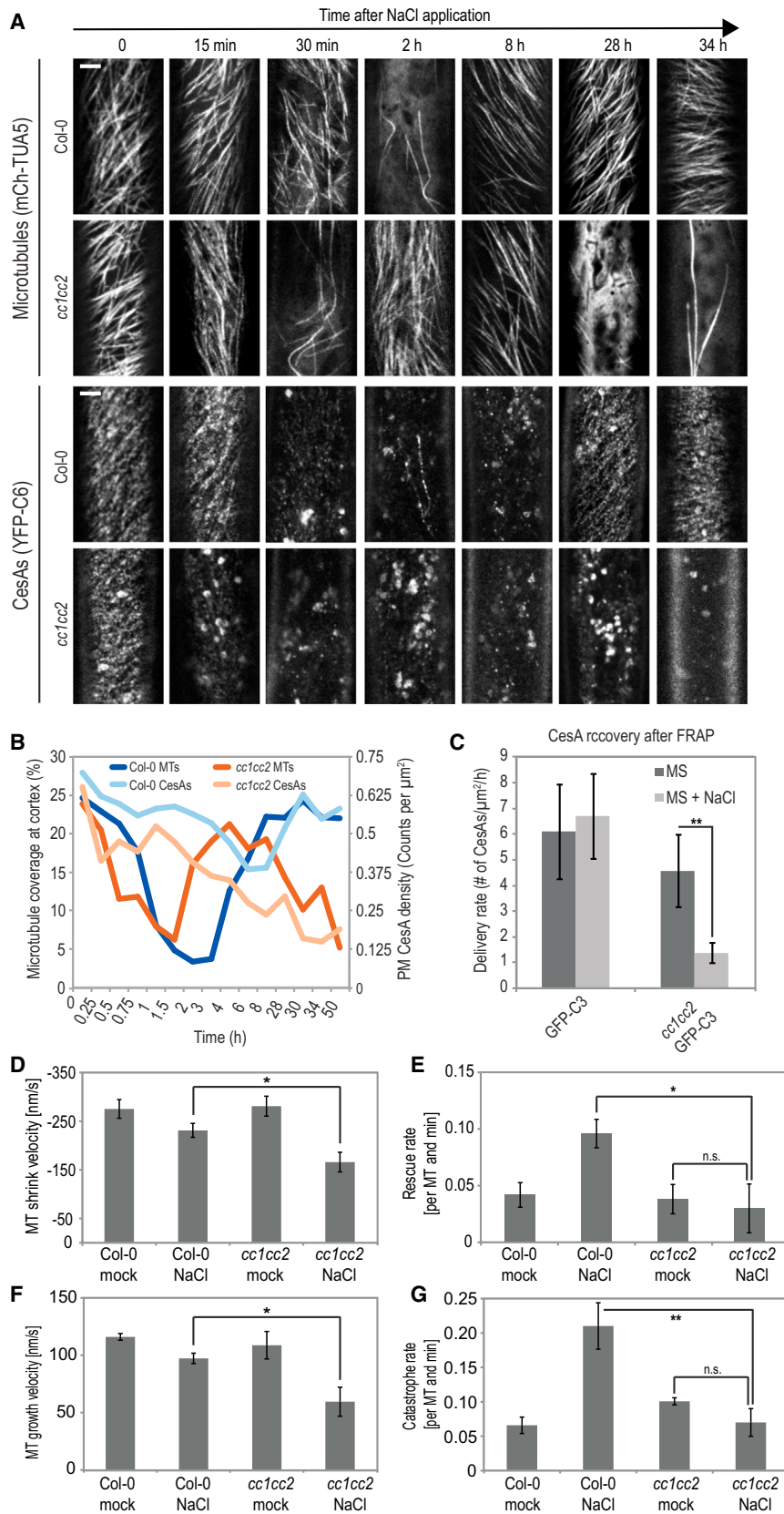


Figure 4. The CC Proteins Safeguard the Cortical Microtubule Array and CesA Activity during Salt Stress

(A) Typical microtubule and CesA coverage at the cell cortex and plasma membrane, respectively, in 3-day-old mCh-TUA5 and YFP-CesA6 expressing etiolated seedlings after exposure to 200 mM NaCl for times indicated. T = 0 indicates time just prior to salt exposure. Scale bar, 2.5 μ m.

(B) Quantification of microtubule and CesA coverage at the cell cortex and plasma membrane, respectively, from experiment exemplified in (A). Time indicates time after salt exposure. PM, plasma membrane. ANOVA analysis of microtubule coverage and CesA density support statistical significant differences between time and genotypes. See Figure S4 for error bars. n = 27 cells from three seedlings per time point and three biological replicates.

(C) FRAP of 4-day-old wild-type or *cc1cc2* hypocotyl cells expressing GFP-CesA3 (GFP-C3) exposed to 100 mM NaCl for 2 days. Graph displays re-population of the plasma membrane with fluorescent CesA foci (given as mean delivery rates of CesAs per area unit per hr) from five cells of five seedlings. **p \leq 0.001. Student's t test, error bars are SD.

(D–G) Microtubule dynamics in wild-type and *cc1cc2* mutant cells. The dynamics were estimated using a custom-made ImageJ macro (see *Supplemental Experimental Procedures*) and were done on cells 2 hr after salt stress (*cc1cc2* mutant cells) and 6 hr after salt stress (wild-type cells) in four cells from four different seedlings. These time points were chosen based on microtubule array re-establishment timing as indicated in (B) and in Figure S4A. **p \leq 0.001. Student's t test, error bars are SD. n.s., no significant difference. See also Figure S4.

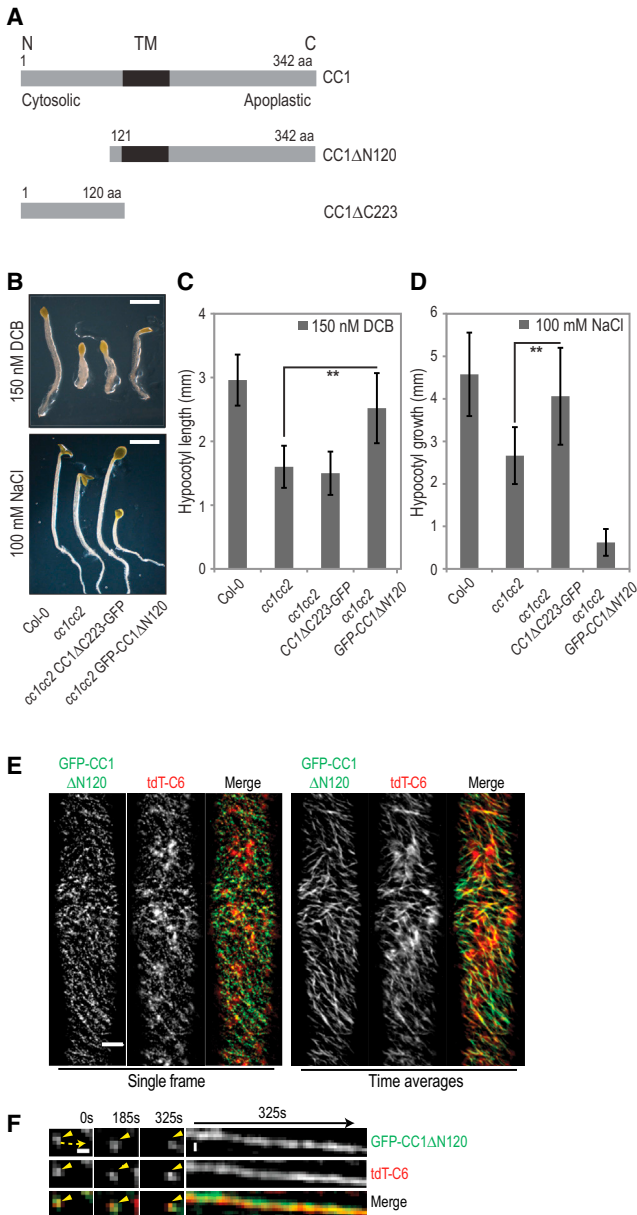


Figure 5. CC1 Truncations Restore Distinct Phenotypic Defects in cc1cc2 Mutant Seedlings

(A) Schematic outline of CC1 and truncations of the protein used in this paper. CC1 contains a predicted transmembrane domain (TM, black region). The N terminus is predicted to face the cytoplasm and the C terminus to the apoplast. Names of the truncations are indicated to the right of the schemes.

(B) GFP-CC1 Δ N120 and CC1 Δ C223-GFP are sufficient to restore cellulose-related defects and salt-induced microtubule defects, respectively, in cc1cc2 mutant seedlings. Wild-type (Col-0), cc1cc2 mutants, and cc1cc2 mutants that express CC1 Δ C223-GFP or GFP-CC1 Δ N120, respectively, were germinated and grown on MS plates supplemented with 150 nM of the cellulose synthesis inhibitor dichlobenil (DCB) for 5 days in the dark. The same lines were germinated and grown on MS media plates for 2 days. The seedlings were then transferred to MS plates supplemented with 100 mM NaCl and grown for an additional 3 days in the dark. Scale bars, 2 mm.

changed in the cc1cc2 mutant cells during the re-assembly phase after salt exposure as compared to control treatments (Figures 4E and 4G). These data indicate that the CC proteins are important for a dynamic microtubule array, and the ability of the microtubule arrays to re-organize itself is important to cope with salt stress.

The N and C Terminus of CC1 Have Distinct Cellular Functions

The CC proteins are plant-specific and lack clear homology to proteins of known function. The proteins are predicted to contain a transmembrane domain with their N-terminal domains facing the cytosol and the C-terminal parts in the apoplast (<http://aramemnon.uni-koeln.de/>) (Figure 5A). To characterize the N- and C-terminal regions of the CC proteins, we generated truncated CC1 proteins (Figure 5A) fused to GFP and transformed them into the cc1cc2 mutant plants. We found that the GFP-CC1 Δ N120 partially rescued the reduced and swollen cc1cc2 growth phenotype on MS media containing isoxaben and DCB (Figures 5B, 5C, and S5A). However, this construct was unable to restore cc1cc2 growth on MS media supplemented with oryzalin and NaCl (Figures 5B, 5D, and S5A). Hence, the C-terminal part of CC1 can restore defects in cc1cc2 related to cellulose synthesis inhibition. In contrast, the CC1 Δ C223-GFP construct completely restored seedling growth on MS media containing NaCl (Figures 5B and D), indicating a prominent role of the CC1 N terminus in salt-related growth defects of cc1cc2. However, the CC1 Δ C223-GFP was unable to restore growth on MS media supplemented with oryzalin, DCB, and isoxaben (Figures 5B, 5C, and S5A).

Interestingly, GFP-CC1 Δ N120 located to motile foci at the plasma membrane reminiscent to that of the CSCs (Figures 5E and 5F). Crosses between the GFP-CC1 Δ N120-expressing plants and plants expressing tdT-CesA6 confirmed that the GFP-CC1 Δ N120 tracked together with the CesA (Figures 5E, 5F, and S5B). These data show that CC1 Δ N120 is important for CesA-related functions and indicate that this part of the protein is responsible for the interaction of the CC1 with the CSC.

The N Terminus of the CC1 Interacts with Microtubules

Consistent with the topological prediction, the CC1 Δ C223-GFP showed mainly cytosolic localization. However, clear striated patterns of fluorescence could be distinguished at the cell cortex, reminiscent of microtubules (Figure 6A). We confirmed this by crossing the CC1 Δ C223-GFP line with a mCh-TUA5 expressing line (Figures 6A and 6B), suggesting that the N terminus of the

(C and D) Quantification of data in (B). **p ≤ 0.001. Student's t test, values are means, error bars are SD, n = 10 seedlings per biological replicate (rep). Three biological reps.

(E) GFP-CC1 Δ N120 and tdTCesA6 (tdT-C6) co-localize in the plasma membrane in 3-day-old etiolated hypocotyls cells. Left: one frame of a time series. Right: time average projections of time lapse movies of the fluorescent proteins. Scale bars, 5 μm.

(F) Left: time frames of individual plasma membrane-localized fluorescent GFP-CC1 Δ N120 and tdT-C6 foci. The proteins migrate as one foci. Right: kymographs of 325-s movies of GFP-CC1 Δ N120 and tdT-C6 expressing cells from which frames are presented in left panel. Scale bar, 0.5 μm. See also Figure S5.

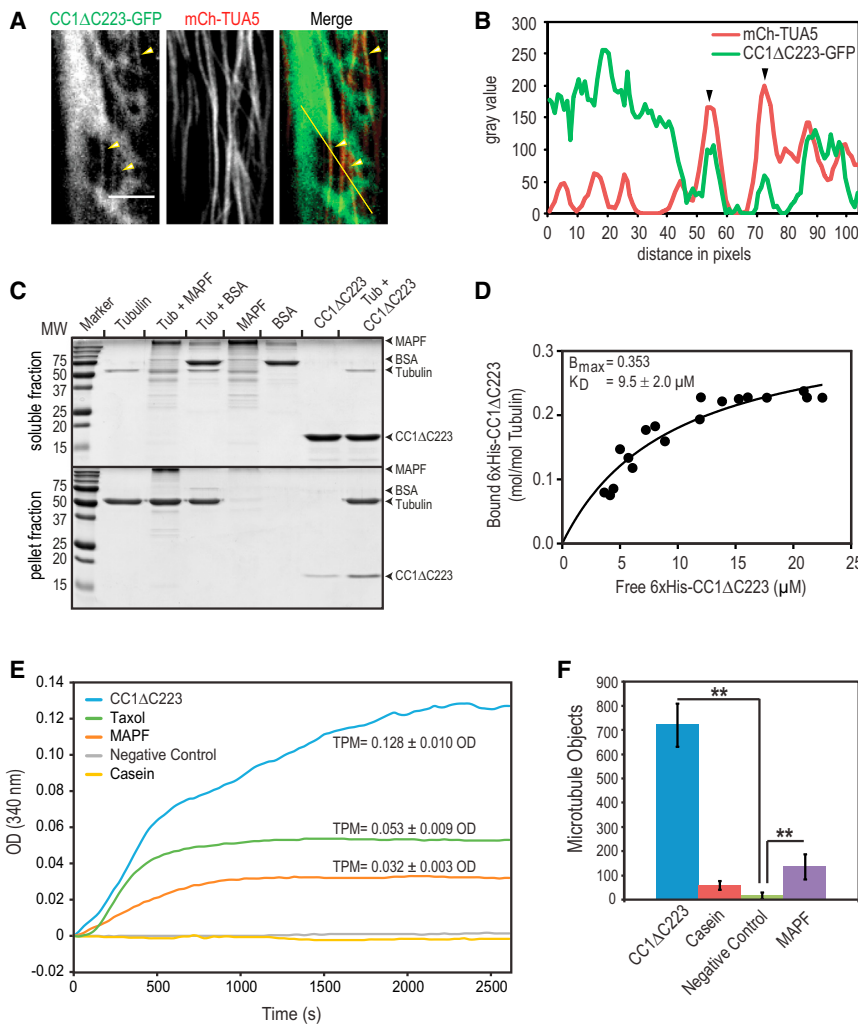


Figure 6. The CC1 N Terminus Binds to Microtubules In Vitro and In Vivo and Promotes Microtubule Formation

(A) CC1ΔC223-GFP is located largely to the cytosol, but also as striated patterns (yellow arrowheads) at the cell cortex that coincide with cortical microtubules in hypocotyl cells of 3-day-old etiolated seedlings expressing CC1ΔC223-GFP and mCh-TUA5. Scale bar, 5 μm.

(B) Intensity plot of the CC1ΔC223-GFP and mCh-TUA5 from transect in (A).

(C) Microtubule co-sedimentation assay of His-CC1ΔC223. His-CC1ΔC223 was enriched in the pellet fraction after centrifugation when Taxol-stabilized microtubules were present. Microtubule-associated protein fraction (MAPF) and BSA were used as positive and negative controls, respectively.

(D) A microtubule binding constant of His-CC1ΔC223 ($9.5 \pm 2.0 \mu M$) was determined by estimation of binding of His-CC1ΔC223 when microtubule levels were constant. K_D is indicated \pm SE, n = 3 technical replicates (reps).

(E) Microtubule turbidity assay. Tubulin was incubated with buffer (negative control), Casein (negative control), MAPF (positive control), Taxol (microtubule stabilizing agent) and His-CC1ΔC223 and microtubule formation measured at 340 nm. Curves are averages of three technical reps. Total polymer mass (TPM) is indicated \pm SD.

(F) In vitro microtubule formation assay using rhodamine-labeled tubulin together with buffer (negative control), Casein (negative control), microtubule-associated protein fraction (MAPF; positive control) and His-CC1ΔC223. Microtubules were counted as fluorescent objects in an area of $4,637 \mu M^2$ produced in the assay. **p \leq 0.001. Student's t test, values are means, error bars are SD, n = 3 technical reps.

See also Figure S6 and Movie S4.

CC1 can associate with microtubules in planta. These patterns were not seen in mCh-TUA5 transgenic plants expressing free-GFP (Figures S6A and S6B). To verify the putative association between the N terminus of CC1 and microtubules, we expressed and purified the CC1ΔC223 as a fusion protein with a 6× His tag from *Escherichia coli* (Figure S6C) and performed microtubule binding assays (Goode and Feinstein, 1994). In vitro polymerized and Taxol-stabilized microtubules were either mixed with CC1ΔC223, known microtubule-associated proteins (MAP; positive control) or BSA (negative control). The CC1ΔC223 interacted with microtubules as the protein co-sedimented with the microtubules after centrifugation. In the absence of microtubules, the CC1ΔC223 protein was mainly detected in the soluble fraction (Figure 6C). CC1ΔC223 lacking the His tag also co-sedimented with microtubules, indicating that the tag is not affecting CC1's affinity to the microtubules (Figure S6D). To estimate the affinity between CC1ΔC223 and the microtubules, we performed saturation binding assays in which we maintained a constant amount of stabilized microtubules, added an increasing amount of CC1ΔC223, and then precipitated the microtubules with ultracentrifugation. In this way, we estimated a dissociation constant

(K_D) of $9.6 \pm 2.0 \mu M$ (Figures 6D and S6E), which is ~10 times higher than that of CSI1 (Li et al., 2012) and ~20 times higher than that of MAP65 (Wicker-Planquart et al., 2004).

The N-Terminal Part of the CC1 Promotes Microtubule Formation In Vitro

The defects of microtubule re-assembly in the *cc1cc2* mutants after salt treatment suggested a role for the CC proteins in microtubule dynamics. To investigate this, we performed a microtubule turbidity assay based on the light-scattering properties of microtubules. Addition of CC1ΔC223 to the turbidity assays clearly promoted microtubule formation (Figure 6E). The resulting microtubule levels were enhanced ~4-fold in comparison to a MAP fraction and 2.4-fold to the microtubule stabilizing agent Taxol under the experimental conditions (Figure 6E). To confirm these data, we also performed microtubule formation assays using rhodamine-labeled tubulin and the *E. coli* produced CC1ΔC223 protein or controls (buffer only, casein, or a MAP fraction). Inclusion of CC1ΔC223 in the assay produced a considerable amount of fluorescent microtubule fragments (Figures 6F and S6F). The number of fluorescent fragments was

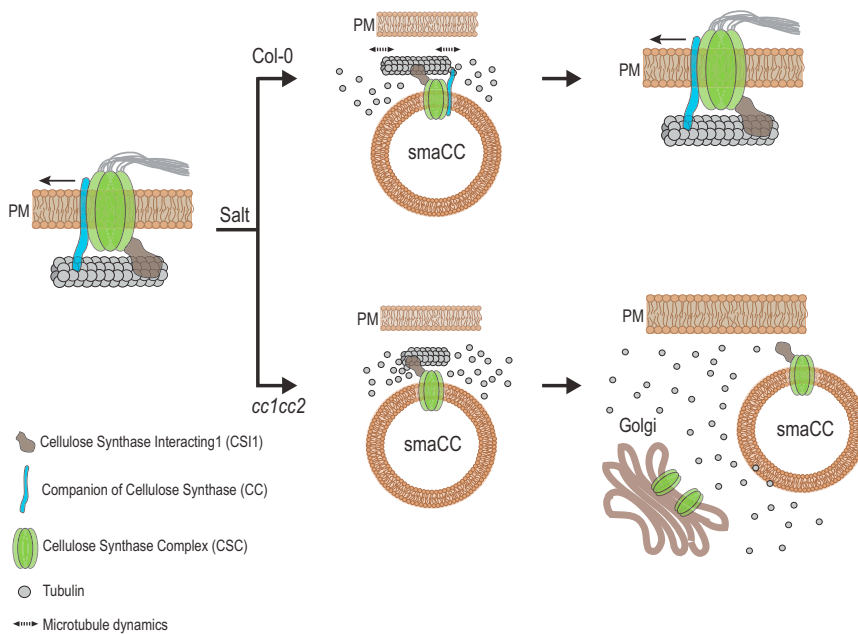


Figure 7. Schematic Model for CC Protein Function during Salt Stress

Under non-stressed conditions, the CSCs produce cellulose at the plasma membrane (PM) and are guided by CSI1 along cortical microtubules. After exposure to salt stress, microtubules are depolymerized and the CSCs displaced from the PM into smACCs/MASCs. The cytosolic N-terminal part of the CC proteins promotes microtubule dynamics, likely in concert with other microtubule-associated proteins, which lead to the establishment of a salt-tolerant microtubule array. The CSC pool re-populates the PM, possibly aided by the CesA-associated C-terminal domain of the CC proteins, and cellulose synthesis may be restored. In the absence of CC activity (*cc1cc2* mutants), a stress tolerant microtubule array is not produced, and the CSCs do not re-populate the PM.

significantly higher than what we observed in assays using the positive MAP fraction control (Figure 6F). To corroborate that these fragments were microtubules, we incubated the CC1ΔC223 assays on coverslips coated with immobilized kinesin1 proteins from *Drosophila melanogaster* (Nitzsche et al., 2010). Here, the kinesins move microtubule-related structures along the coverslip, and structures that are not microtubules would not be bound and transported by the kinesins. Indeed, the fluorescent fragments migrated across the slide (Movie S4) and are thus microtubule-related structures. Hence, the CC1ΔC223 promotes microtubule formation in vitro.

DISCUSSION

Abiotic and biotic stresses significantly impact on plant growth, and much effort is therefore invested into improving plant performance during adverse conditions. In this work, we outline a mechanism for how the major plant biomass producing enzyme complex, the CSC, can be sustained in its plasma membrane localization during salt stress via action through the identified CC protein family members.

While mutations that affect cell wall and cellulose synthesis impact on plant salt tolerance (Shi et al., 2003; Chen et al., 2005; Kang et al., 2008; Zhu et al., 2010), the underlying mechanisms are unresolved. Based on our findings, we propose a model in which the CesAs and CC proteins accumulate in cytoplasmic smACC/MASC-related compartments in response to salt (Figure 7). The cytoplasmic N termini of the CC proteins may here promote the re-assembly of the microtubule array. The C-terminal part of the CC proteins, on the other hand, aids in the recovery of the plasma membrane-based CesA pool (Figure 7). However, the dynamic behavior of the microtubule array that is aided by the N-terminal part of the CC protein is crucial for the recovery of the cell under salt stress as the C-terminal

part of CC1 was unable to restore growth of the *cc1cc2* mutant on salt-containing media. Hence, the salt stress-related growth phenotypes of *cc1cc2* are mainly due to defects of the microtubule array.

Salt stress results in both osmotic and ionic stress in plant cells (Munns and Tester, 2008), and it has been suggested that the ionic stress is the major factor that impacts on microtubule depolymerization (Wang et al., 2007). Consistent with this finding, osmotic stress using sorbitol did not cause any major growth defects of the *cc1cc2* seedlings, and it therefore appears likely that the CC proteins mainly function to sustain the microtubule array during ionic stress. Nevertheless, PHS1, a key component for the stress-induced de-polymerization of the microtubule array, promotes microtubule de-polymerization in response to osmotic stress (Fujita et al., 2013). Hence, the microtubule array appears to respond to both ionic and osmotic stress. PHS1 can phosphorylate Thr349 of α -tubulin to generate a polymerization incompetent tubulin isoform in response to sorbitol and salt treatments (Fujita et al., 2013). It is plausible that the CC proteins and PHS1 may have antagonistic effects following salt exposure. The effect of PHS1 would then be prominent in the *cc1cc2* mutant, consistent with the rapid depolymerization of microtubules in the *cc1cc2* mutants. The CC proteins could perhaps reduce the osmotic effects of PHS1, and it might therefore be possible that the proteins contribute both to osmotic and ionic stress responses of the microtubules. As the microtubule array becomes reassembled after ~8 hr of salt exposure (Wang et al., 2007), it appears that the PHS1 kinase activity drops after the initial microtubule de-polymerization events. Here, the CC proteins have an important function in the re-assembly and maintenance of the microtubule array and thus to cope with long-term saline conditions. In addition, SPR1, another microtubule-associated protein, antagonizes stress-induced microtubule de-polymerization (Wang et al., 2011). Under salt stress, SPR1 is rapidly degraded by the 26S proteasome, which is required for efficient microtubule disassembly (Wang et al., 2011). It is therefore plausible that the CC proteins function in concert with both PHS1 and SPR1 for microtubule functions

during salt stress. These relationships could perhaps also underpin the relatively faster re-assembly of the unstable microtubule array in the *cc1cc2* mutant cells after salt stress.

Microtubules are nucleated from ring-shaped complexes that contain γ -tubulins (Teixidó-Travesa et al., 2012) that coincide with existing microtubules (Nakamura et al., 2010). In addition, microtubule nucleation can occur via a mechanism that is independent of the γ -tubulin-ring complex during array recovery after stress (Lindeboom et al., 2013). While this mechanism is not known in plant cells, several microtubule plus end-binding proteins (Rogers et al., 2008; Rusan and Rogers, 2009), including transforming acidic coiled-coil family proteins and RanGTP-activated factors (Gruss and Vernos, 2004; Clarke and Zhang, 2008), have been suggested to support γ -tubulin-ring complex-independent microtubule nucleation in other organisms. Given that the CC1 N terminus promotes microtubule formation (Figures 6E and 6F), it is plausible that CC1 could contribute to γ -tubulin-ring complex independent microtubule nucleation during salt stress.

Our findings outline a mechanism in which components of the CSC can promote the cellulose-synthesizing capacity of the complex during salt stress. Hence, instead of simply migrating passively along cortical microtubules the CSC can, via the CC proteins, manipulate the microtubule behavior during stress to sustain its own activity.

EXPERIMENTAL PROCEDURES

A detailed description of the experimental procedure is enclosed in [Supplemental Experimental Procedures](#).

Plant Growth and Cell Wall Analysis

T-DNA insertion lines were obtained from the NASC (<http://arabidopsis.info/>), and fluorescent marker lines have been described previously. *Arabidopsis* plants and seedlings were grown as described by Sánchez-Rodríguez et al. (2012), and plates were supplemented with various inhibitors, salt, and sorbitol as indicated in figures and text. For salt treatments, seeds germinated on MS media were transferred to NaCl supplemented MS plates after 2 days. Four-day-old etiolated seedlings were used for cell wall extractions. Uronic acids, neutral sugars, and glucose residues for cellulose were determined as described in Sánchez-Rodríguez et al. (2012).

Spinning Disc Microscopy

Spinning disc microscopy was conducted on a Nikon Ti-E inverted microscope equipped with a CSU-X1 spinning disc head (Yokogawa), a CFI APO TIRF $\times 100$ N.A. 1.47 oil immersion objective, an Evolve charge-coupled device camera (Photometrics Technology) and a $\times 1.2$ lens between the spinning disc and camera.

Image Analysis

Co-localization analysis was performed using the JACoP plugin (Bolte and Cordelières, 2006) of ImageJ software package (Rasband, W.S. National Institute of Health). Cortical microtubule recovery after salt treatment was analyzed using a program based on MATLAB (MathWorks) applying the Sobel edge-detection algorithm on single images. To quantify CESAs recovery after salt treatment, the MaximumFinder feature of the ImageJ software package was used.

Heterologous Protein Expression and Microtubule Assays

CC1 Δ C223 was expressed in Rosetta (DE3) pLysS *E. coli* Cells (Merck Millipore). Microtubule binding assays of *CC1 Δ C223* were performed using the Microtubule Binding Protein Spin-down Assay Kit (Cytoskeleton) according to the manufacturer's instructions. Microtubule assembly rates were deter-

mined by measuring light scattering in a bulk phase turbidity assay (Gaskin et al., 1974). Microtubule properties after co-polymerization were visualized and tested using a microtubule gliding motility assay (Nitzsche et al., 2010).

SUPPLEMENTAL INFORMATION

Supplemental Information includes Supplemental Experimental Procedures, six figures, one table, and four movies and can be found with this article online at <http://dx.doi.org/10.1016/j.cell.2015.08.028>.

AUTHOR CONTRIBUTIONS

A.E., C.K., R.S., Y.Z., and S.P. designed the research. A.E., C.K., R.S., Y.Z., A.F., and N.F. performed the research. A.E., C.K., R.S., Y.Z., A.I., and S.P. analyzed data. A.E., C.K., and S.P. wrote the article. A.E. and C.K. share equal first authorship.

ACKNOWLEDGMENTS

D. melanogaster kinesin-1 heavy chain (DmKHC) was kindly provided by Prof. Stefan Diez, B CUBE, Dresden (Germany). Vector pETM11-SUMO3GFP was kindly provided by Dr. Hüseyin Besir, European Molecular Biology Laboratory, Heidelberg (Germany). We thank Drs. Clara Sanchez-Rodriguez and Heather McFarlane for useful comments, Dr. Martin Bringmann for help in cloning the truncated CC1 protein, and Drs. Luisa Trindade and Nasim Mansoori for aid with split-ubiquitin assays. Protein preparation was done in cooperation with Martina Leiderd and Anne Diehl (FMP Berlin Germany) with vector kindly provided by Patrick Loll (Drexel University Philadelphia, USA). The authors are grateful to the Max-Planck Gesellschaft for funding. C.K. was funded from an IMPRS fellowship via the MPG. Part of the research was funded through the DFG grant PE1642/6-1 and the ARC grant DP150103495.

Received: November 6, 2014

Revised: May 12, 2015

Accepted: July 23, 2015

Published: September 3, 2015

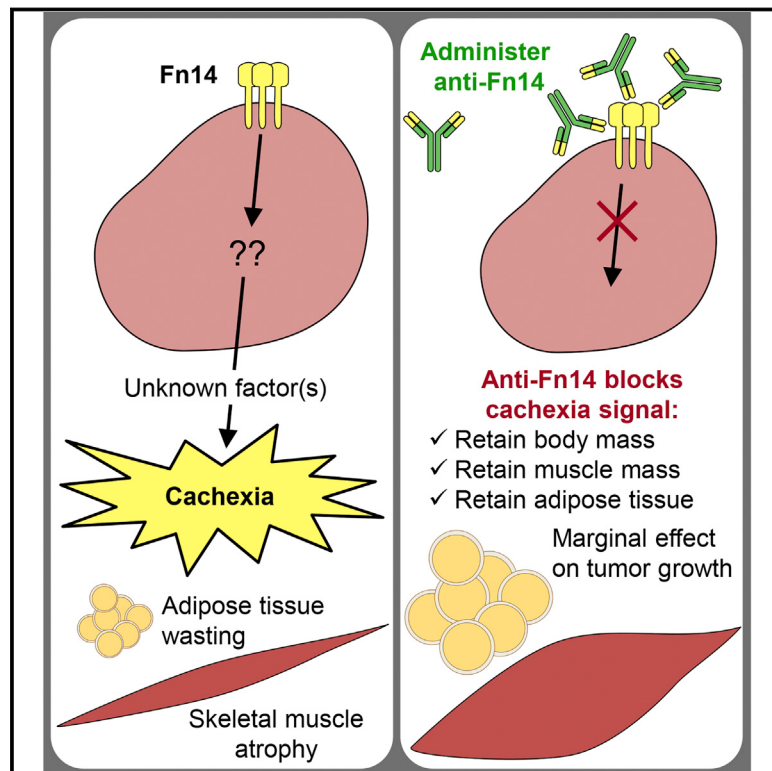
REFERENCES

- Baskin, T.I. (2001). On the alignment of cellulose microfibrils by cortical microtubules: a review and a model. *Protoplasma* 215, 150–171.
- Bolte, S., and Cordelières, F.P. (2006). A guided tour into subcellular colocalization analysis in light microscopy. *J. Microsc.* 224, 213–232.
- Boyer, J.S. (1982). Plant productivity and environment. *Science* 218, 443–448.
- Chen, Z., Hong, X., Zhang, H., Wang, Y., Li, X., Zhu, J.K., and Gong, Z. (2005). Disruption of the cellulose synthase gene, AtCesA8/IRX1, enhances drought and osmotic stress tolerance in *Arabidopsis*. *Plant J.* 43, 273–283.
- Clarke, P.R., and Zhang, C. (2008). Spatial and temporal coordination of mitosis by Ran GTPase. *Nat. Rev. Mol. Cell Biol.* 9, 464–477.
- Crowell, E.F., Bischoff, V., Desprez, T., Rolland, A., Stierhof, Y.D., Schumacher, K., Gonneau, M., Höfte, H., and Vernhettes, S. (2009). Pausing of Golgi bodies on microtubules regulates secretion of cellulose synthase complexes in *Arabidopsis*. *Plant Cell* 21, 1141–1154.
- Desprez, T., Juranić, M., Crowell, E.F., Jouy, H., Pochylova, Z., Parcy, F., Höfte, H., Gonneau, M., and Vernhettes, S. (2007). Organization of cellulose synthase complexes involved in primary cell wall synthesis in *Arabidopsis thaliana*. *Proc. Natl. Acad. Sci. USA* 104, 15572–15577.
- Dettmer, J., Hong-Hermesdorf, A., Stierhof, Y.D., and Schumacher, K. (2006). Vacuolar H⁺-ATPase activity is required for endocytic and secretory trafficking in *Arabidopsis*. *Plant Cell* 18, 715–730.
- Fujita, M., Himmelspach, R., Hocart, C.H., Williamson, R.E., Mansfield, S.D., and Wasteneys, G.O. (2011). Cortical microtubules optimize cell-wall crystallinity to drive unidirectional growth in *Arabidopsis*. *Plant J.* 66, 915–928.
- Fujita, S., Pytela, J., Hotta, T., Kato, T., Hamada, T., Akamatsu, R., Ishida, Y., Kutsuna, N., Hasezawa, S., Nomura, Y., et al. (2013). An atypical tubulin kinase

- mediates stress-induced microtubule depolymerization in *Arabidopsis*. *Curr. Biol.* 23, 1969–1978.
- Gaskin, F., Cantor, C.R., and Shelanski, M.L. (1974). Turbidimetric studies of the *in vitro* assembly and disassembly of porcine neurotubules. *J. Mol. Biol.* 89, 737–755.
- Goode, B.L., and Feinstein, S.C. (1994). Identification of a novel microtubule binding and assembly domain in the developmentally regulated inter-repeat region of tau. *J. Cell Biol.* 124, 769–782.
- Green, P.B. (1962). Mechanism for Plant Cellular Morphogenesis. *Science* 138, 1404–1405.
- Grefen, C., Donald, N., Hashimoto, K., Kudla, J., Schumacher, K., and Blatt, M.R. (2010). A ubiquitin-10 promoter-based vector set for fluorescent protein tagging facilitates temporal stability and native protein distribution in transient and stable expression studies. *Plant J.* 64, 355–365.
- Gruss, O.J., and Vernos, I. (2004). The mechanism of spindle assembly: functions of Ran and its target TPX2. *J. Cell Biol.* 166, 949–955.
- Gu, Y., Kaplinsky, N., Bringmann, M., Cobb, A., Carroll, A., Sampathkumar, A., Baskin, T.I., Persson, S., and Somerville, C.R. (2010). Identification of a cellulose synthase-associated protein required for cellulose biosynthesis. *Proc. Natl. Acad. Sci. USA* 107, 12866–12871.
- Gutierrez, R., Lindeboom, J.J., Paredez, A.R., Emons, A.M., and Ehrhardt, D.W. (2009). *Arabidopsis* cortical microtubules position cellulose synthase delivery to the plasma membrane and interact with cellulose synthase trafficking compartments. *Nat. Cell Biol.* 11, 797–806.
- Kang, J.S., Frank, J., Kang, C.H., Kajura, H., Vikram, M., Ueda, A., Kim, S., Bahk, J.D., Triplett, B., Fujiyama, K., et al. (2008). Salt tolerance of *Arabidopsis thaliana* requires maturation of N-glycosylated proteins in the Golgi apparatus. *Proc. Natl. Acad. Sci. USA* 105, 5933–5938.
- Komis, G., Apostolakos, P., and Galatis, B. (2002). Hyperosmotic stress induces formation of tubulin macrotubules in root-tip cells of *Triticum turgidum*: their probable involvement in protoplast volume control. *Plant Cell Physiol.* 43, 911–922.
- Ledbetter, M.C., and Porter, K.R. (1963). A “microtubule” in plant cell fine structure. *J. Cell Biol.* 19, 239–250.
- Li, S., Lei, L., Somerville, C.R., and Gu, Y. (2012). Cellulose synthase interactive protein 1 (CSI1) links microtubules and cellulose synthase complexes. *Proc. Natl. Acad. Sci. USA* 109, 185–190.
- Lindeboom, J.J., Lioutas, A., Deinum, E.E., Tindemans, S.H., Ehrhardt, D.W., Emons, A.M., Vos, J.W., and Mulder, B.M. (2013). Cortical microtubule arrays are initiated from a nonrandom prepattern driven by atypical microtubule initiation. *Plant Physiol.* 161, 1189–1201.
- McFarlane, H.E., Döring, A., and Persson, S. (2014). The cell biology of cellulose synthesis. *Annu. Rev. Plant Biol.* 65, 69–94.
- Morejohn, L.C., Bureau, T.E., Molé-Bajer, J., Bajer, A.S., and Fosket, D.E. (1987). Oryzalin, a dinitroaniline herbicide, binds to plant tubulin and inhibits microtubule polymerization *in vitro*. *Planta* 172, 252–264.
- Morgan, J.L., Strumillo, J., and Zimmer, J. (2013). Crystallographic snapshot of cellulose synthesis and membrane translocation. *Nature* 493, 181–186.
- Mueller, S.C., and Brown, R.M., Jr. (1980). Evidence for an intramembrane component associated with a cellulose microfibril-synthesizing complex in higher plants. *J. Cell Biol.* 84, 315–326.
- Munns, R., and Tester, M. (2008). Mechanisms of salinity tolerance. *Annu. Rev. Plant Biol.* 59, 651–681.
- Nakamura, M., Ehrhardt, D.W., and Hashimoto, T. (2010). Microtubule and katanin-dependent dynamics of microtubule nucleation complexes in the acentrosomal *Arabidopsis* cortical array. *Nat. Cell Biol.* 12, 1064–1070.
- Naoi, K., and Hashimoto, T. (2004). A semidominant mutation in an *Arabidopsis* mitogen-activated protein kinase phosphatase-like gene compromises cortical microtubule organization. *Plant Cell* 16, 1841–1853.
- Nick, P. (2013). Microtubules, signalling and abiotic stress. *Plant J.* 75, 309–323.
- Nitzsche, B., Bormuth, V., Bräuer, C., Howard, J., Ionov, L., Kerssemakers, J., Korten, T., Leduc, C., Ruhnow, F., and Diez, S. (2010). Studying kinesin motors by optical 3D-nanometry in gliding motility assays. *Methods Cell Biol.* 95, 247–271.
- Paredez, A.R., Somerville, C.R., and Ehrhardt, D.W. (2006). Visualization of cellulose synthase demonstrates functional association with microtubules. *Science* 312, 1491–1495.
- Persson, S., Wei, H., Milne, J., Page, G.P., and Somerville, C.R. (2005). Identification of genes required for cellulose synthesis by regression analysis of public microarray data sets. *Proc. Natl. Acad. Sci. USA* 102, 8633–8638.
- Persson, S., Paredez, A., Carroll, A., Palsdottir, H., Doblin, M., Poindexter, P., Khitrov, N., Auer, M., and Somerville, C.R. (2007). Genetic evidence for three unique components in primary cell-wall cellulose synthase complexes in *Arabidopsis*. *Proc. Natl. Acad. Sci. USA* 104, 15566–15571.
- Qin, F., Shinozaki, K., and Yamaguchi-Shinozaki, K. (2011). Achievements and challenges in understanding plant abiotic stress responses and tolerance. *Plant Cell Physiol.* 52, 1569–1582.
- Rogers, G.C., Rusan, N.M., Peifer, M., and Rogers, S.L. (2008). A multicomponent assembly pathway contributes to the formation of acentrosomal microtubule arrays in interphase *Drosophila* cells. *Mol. Biol. Cell* 19, 3163–3178.
- Rusan, N.M., and Rogers, G.C. (2009). Centrosome function: sometimes less is more. *Traffic* 10, 472–481.
- Sampathkumar, A., Gutierrez, R., McFarlane, H.E., Bringmann, M., Lindeboom, J.J., Emons, A.M., Samuels, L., Ketelaar, T., Ehrhardt, D.W., and Persson, S. (2013). Patterning and lifetime of plasma membrane-localized cellulose synthase is dependent on actin organization in *Arabidopsis* interphase cells. *Plant Physiol.* 162, 675–688.
- Sánchez-Rodríguez, C., Bauer, S., Hématy, K., Saxe, F., Ibáñez, A.B., Vodermaier, V., Konlechner, C., Sampathkumar, A., Rüggeberg, M., Aichinger, E., et al. (2012). Chitinase-like1/pom-pom1 and its homolog CTL2 are glucan-interacting proteins important for cellulose biosynthesis in *Arabidopsis*. *Plant Cell* 24, 589–607.
- Shi, H., Kim, Y., Guo, Y., Stevenson, B., and Zhu, J.K. (2003). The *Arabidopsis SOS5* locus encodes a putative cell surface adhesion protein and is required for normal cell expansion. *Plant Cell* 15, 19–32.
- Somerville, C., Youngs, H., Taylor, C., Davis, S.C., and Long, S.P. (2010). Feedstocks for lignocellulosic biofuels. *Science* 329, 790–792.
- Teixidó-Travesa, N., Roig, J., and Lüders, J. (2012). The where, when and how of microtubule nucleation – one ring to rule them all. *J. Cell Sci.* 125, 4445–4456.
- Uytewaal, M., Burian, A., Alim, K., Landrein, B., Borowska-Wykręt, D., Dedieu, A., Peaucelle, A., Ludynia, M., Traas, J., Boudaoud, A., et al. (2012). Mechanical stress acts via katanin to amplify differences in growth rate between adjacent cells in *Arabidopsis*. *Cell* 149, 439–451.
- Wang, C., Li, J., and Yuan, M. (2007). Salt tolerance requires cortical microtubule reorganization in *Arabidopsis*. *Plant Cell Physiol.* 48, 1534–1547.
- Wang, S., Kurepa, J., Hashimoto, T., and Smalle, J.A. (2011). Salt stress-induced disassembly of *Arabidopsis* cortical microtubule arrays involves 26S proteasome-dependent degradation of SPIRAL1. *Plant Cell* 23, 3412–3427.
- Wicker-Planquart, C., Stoppin-Mellet, V., Blanchoin, L., and Vantard, M. (2004). Interactions of tobacco microtubule-associated protein MAP65-1b with microtubules. *Plant J.* 39, 126–134.
- Winter, D., Vinegar, B., Nahal, H., Ammar, R., Wilson, G.V., and Provart, N.J. (2007). An “Electronic Fluorescent Pictograph” browser for exploring and analyzing large-scale biological data sets. *PLoS ONE* 2, e718.
- Zhong, R., Burk, D.H., Morrison, W.H., 3rd, and Ye, Z.H. (2002). A kinesin-like protein is essential for oriented deposition of cellulose microfibrils and cell wall strength. *Plant Cell* 14, 3101–3117.
- Zhu, J., Lee, B.H., Dellinger, M., Cui, X., Zhang, C., Wu, S., Nothnagel, E.A., and Zhu, J.K. (2010). A cellulose synthase-like protein is required for osmotic stress tolerance in *Arabidopsis*. *Plant J.* 63, 128–140.

Targeting of Fn14 Prevents Cancer-Induced Cachexia and Prolongs Survival

Graphical Abstract



Authors

Amelia J. Johnston, Kate T. Murphy, Laura Jenkinson, ..., Gordon S. Lynch, John Silke, Nicholas J. Hoogenraad

Correspondence

a.johnston@latrobe.edu.au (A.J.J.), n.hoogenraad@latrobe.edu.au (N.J.H.)

In Brief

Antibodies against the TWEAK receptor Fn14 prevent tumor-induced cachexia and extend lifespan by inhibiting weight loss and inflammation, although having only moderate effects on tumor growth.

Highlights

- Tumors expressing Fn14 cause cachexia in mice
- Fn14 antibodies extend lifespan by inhibiting tumor-induced cachexia
- Fn14- and TWEAK-deficient mice succumb to cancer cachexia
- Tumor Fn14 signaling, rather than host, is responsible for inducing cachexia

Targeting of Fn14 Prevents Cancer-Induced Cachexia and Prolongs Survival

Amelia J. Johnston,^{1,*} Kate T. Murphy,² Laura Jenkinson,¹ David Laine,¹ Kerstin Emmrich,¹ Pierre Faou,¹ Ross Weston,¹ Krishnath M. Jayatilleke,¹ Jessie Schloegel,¹ Gert Talbo,¹ Joanne L. Casey,¹ Vita Levina,¹ W. Wei-Lynn Wong,³ Helen Dillon,¹ Tushar Sahay,¹ Joan Hoogenraad,¹ Holly Anderton,^{1,4,5} Cathrine Hall,^{4,5} Pascal Schneider,⁶ Maria Tanzer,^{4,5} Michael Foley,¹ Andrew M. Scott,^{7,1} Paul Gregorevic,^{8,9} Spring Yingchun Liu,¹⁰ Linda C. Burkly,¹¹ Gordon S. Lynch,² John Silke,^{1,4,5} and Nicholas J. Hoogenraad^{1,*}

¹Department of Biochemistry and Genetics, La Trobe Institute for Molecular Science, La Trobe University, Melbourne, VIC 3086, Australia

²Basic and Clinical Myology Laboratory, Department of Physiology, The University of Melbourne, Melbourne, VIC 3010, Australia

³Institute of Experimental Immunology, University of Zürich, Zürich 8057, Switzerland

⁴The Walter and Eliza Hall Institute, Melbourne, VIC 3052, Australia

⁵Department of Medical Biology, The University of Melbourne, Melbourne, VIC 3050, Australia

⁶Department of Biochemistry, University of Lausanne, Epalinges 1066, Switzerland

⁷Olivia Newton-John Cancer Research Institute, Melbourne, VIC 3084, Australia

⁸Baker IDI Heart and Diabetes Institute, Melbourne, VIC 3004, Australia

⁹Department of Biochemistry and Molecular Biology, Monash University, Clayton, VIC 3800, Australia

¹⁰Broad Institute, MIT and Harvard, Cambridge, MA 02142, USA

¹¹Department of Immunology, Biogen Idec, 14 Cambridge Center, Cambridge, MA 02142, USA

*Correspondence: a.johnston@latrobe.edu.au (A.J.J.), n.hoogenraad@latrobe.edu.au (N.J.H.)

<http://dx.doi.org/10.1016/j.cell.2015.08.031>

SUMMARY

The cytokine TWEAK and its cognate receptor Fn14 are members of the TNF/TNFR superfamily and are upregulated in tumors. We found that Fn14, when expressed in tumors, causes cachexia and that antibodies against Fn14 dramatically extended lifespan by inhibiting tumor-induced weight loss although having only moderate inhibitory effects on tumor growth. Anti-Fn14 antibodies prevented tumor-induced inflammation and loss of fat and muscle mass. Fn14 signaling in the tumor, rather than host, is responsible for inducing this cachexia because tumors in Fn14- and TWEAK-deficient hosts developed cachexia that was comparable to that of wild-type mice. These results extend the role of Fn14 in wound repair and muscle development to involvement in the etiology of cachexia and indicate that Fn14 antibodies may be a promising approach to treat cachexia, thereby extending lifespan and improving quality of life for cancer patients.

INTRODUCTION

Fn14 (tumor necrosis factor receptor superfamily member 12A; TNFRSF12A) and its ligand TWEAK (TNFSF12) have been shown to play multiple roles in the process of wound repair and can promote angiogenesis, proliferation, migration, apoptosis, and inflammation (Burkly et al., 2011; Campbell et al., 2004; Vince and Silke, 2006; Winkles, 2008). Consistent with such a role, its expression is strongly induced by growth factors *in vivo* at sites of tissue injury and remodeling (Wiley et al., 2001; Winkles, 2008).

Fn14 expression is also increased in solid tumors (Culp et al., 2010; Wiley et al., 2001). Fn14 signaling therefore contributes to carcinogenesis, and targeting this pathway with monoclonal antibodies can inhibit tumor growth (Culp et al., 2010; Winkles, 2008).

Cachexia is a complex disease, best described as a metabolic disorder that includes progressive muscle wasting with or without the loss of fat stores. It frequently presents in the terminal stages of many chronic illnesses, including cancer (Tisdale, 2009), and may be present in 50%–80% of patients with solid tumors (Dewys et al., 1980; Walsh et al., 2000). Although cachexia reduces patient survival and response to chemotherapy and may account for ~25% of all cancer deaths (Warren, 1932), the molecular mechanisms are unknown, and there are no FDA approved drugs to treat it. Attempts to cure cachexia by increasing appetite or nutrition have proven unsuccessful in clinical trials. However, it has been suggested that interventions for cachexia could potentially be developed by targeting inflammatory processes that occur in concert with the wasting and metabolic imbalance that characterize cachexia (Muscaritoli et al., 2010).

Interleukin-1 (IL-1), IL-6, TNF, and interferon- γ are inflammatory cytokines that have been suggested to play a role in cachexia (Argilés et al., 2009; Tisdale, 2009). Glucocorticoids may also contribute to cachexia by upregulating tumor-derived factors such as lipid-mobilizing factor, which activates degradative pathways in adipose tissue leading to the breakdown of fat deposits and disrupted metabolic processes (Islam-Ali and Tisdale, 2001; Russell and Tisdale, 2005). Most recently, it has been shown that activation of the activin type-2 receptor ActRIIb by transforming growth factor β (TGF- β) family ligands drives a cachectic phenotype in mice and the degradation of contractile proteins through the ubiquitin-proteasome pathway. Recombinant decoy ActRIIb inhibited activation of this pathway and

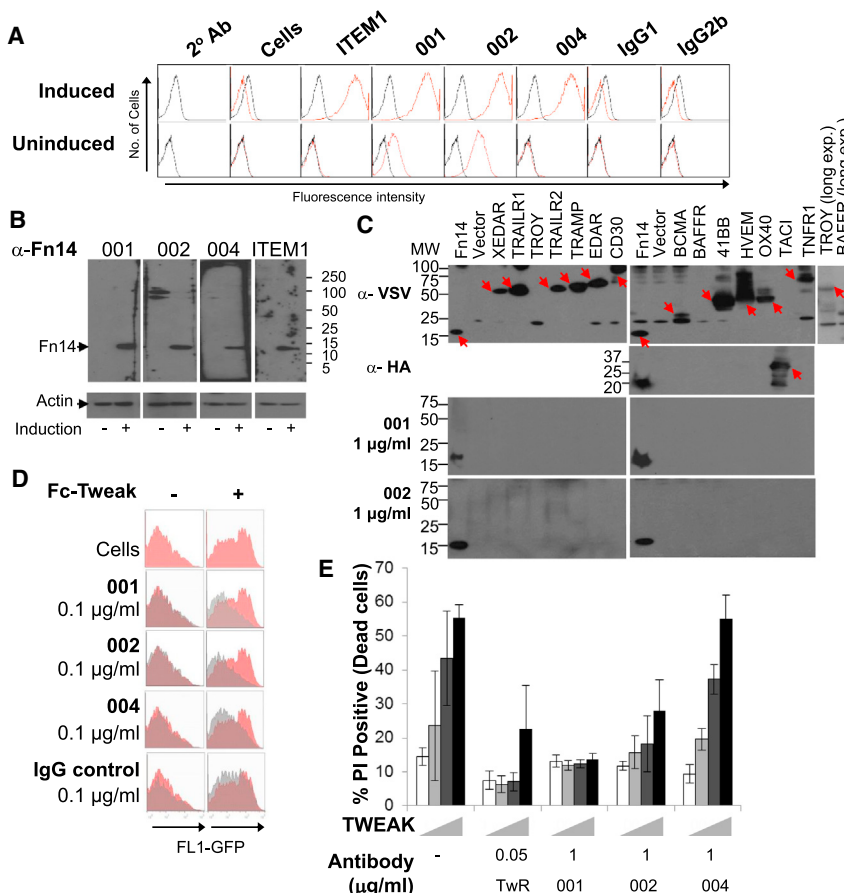


Figure 1. Fn14 Antibodies Antagonize TWEAK/Fn14 Signaling

(A) MEF H-Ras V12 cells expressing inducible hFn14 stained with indicated antibodies. Red: antibody staining; black: secondary antibody alone.

(B) Western blot of lysates from H-Ras V12 MEFs expressing inducible hFn14 ± induction probed with indicated Fn14 antibodies.

(C) Western blot of HEK293T cells transiently transfected with the indicated VSV or HA-tagged TNFSFR probed with indicated antibodies. Arrows indicate the expressed protein. Note 001 blot (right) was reprobed with anti-HA.

(D) GFP fluorescence of HEK293T NF-κB GFP reporter cells stimulated ± 100 ng/ml of Fc-TWEAK for 24 hr (pink), and cells co-incubated with the indicated antibodies (gray).

(E) Kym1 cell-death assay with increasing Fc-TWEAK dose and co-incubated with indicated antibodies for 24 hr, harvested, stained with PI, and percent PI-positive cells assessed determined by flow cytometry.

Data are means ± SEM ($n = 3$). See also Figure S1.

RESULTS

Monoclonal Antibodies against Fn14

To test the hypothesis that inhibition of Fn14 would limit tumor growth, we generated antagonist monoclonal antibodies against Fn14 by inoculating wild-type mice with recombinant human Fn14-Fc

and generated hybridomas as previously described (Galfrè and Milstein, 1981). Three monoclonal antibodies, 001, 002, and 004, were positive against a mouse embryonic fibroblast (MEF) cell line stably expressing inducible human Fn14 (hFn14; Figure 1A), as was a commercially available control anti-human Fn14, ITEM1 (Nakayama et al., 2003). ITEM1 and our three antibodies detected hFn14 specifically by western blot (Figure 1B). Human and mouse Fn14 are 92% identical in the extracellular domain, and two of the antibodies, 001 and 002, reacted against the uninduced MEF cell lines that express endogenous murine Fn14 (Figure 1A).

Because members of the TNF receptor superfamily (TNFRSF) share homology in their extra-cellular domains, these proteins are most likely to cross-react with Fn14 antibodies. However, several are only expressed in specific hematopoietic lineages, making it difficult to rule out cross-reactivity by screening cell lines. Therefore, VSV- or HA-tagged TNFRSF members were overexpressed in HEK293T cells and reacted with either a VSV, HA, 001, or 002 antibody. All TNFRSF receptors were expressed and detected by VSV or HA antibodies; however, only Fn14 was detected by 001 and 002 (Figure 1C).

TWEAK activates both canonical and non-canonical NF-κB signaling pathways (Salzmann et al., 2013; Varfolomeev et al., 2007, 2012; Vince et al., 2008). To address whether the Fn14 antibodies activated or blocked Fn14-dependent signaling, we

significantly increased survival and muscle mass of mice bearing cachexia-inducing tumors (Zhou et al., 2010). Unfortunately, however, decoy ActRIIb in clinical trials resulted in treatment-related bleeding issues in healthy adults and boys with Duchenne muscular dystrophy and were therefore stopped and have not been pursued for cachexia treatment.

Because of the demonstrated involvement of Fn14 signaling in tumor progression, we began our studies with the hypothesis that an antagonistic monoclonal antibody targeting Fn14 would inhibit tumor growth (Vince and Silke, 2006; Winkles, 2008). We developed and characterized three antagonist monoclonal antibodies against Fn14. Two of these antibodies showed variable ability to block tumor growth but were strikingly effective at preventing tumor-induced weight loss. We demonstrated that the tumor-induced loss of lean and fat mass is consistent with the development of cachexia. In addition, our Fn14 antibodies were able to prevent and reverse tumor-induced cachexia in different tumor models. We also demonstrated that the role of Fn14 in cachexia is independent of both host- and tumor-derived TWEAK. We further showed that although reported to be upregulated during atrophy, muscle-localized Fn14 is not actively involved in the loss of muscle mass, supporting the idea of an alternative role such as repair/regeneration. Our results support the hypothesis that inhibiting Fn14 signaling has therapeutic potential for cancer-induced cachexia.

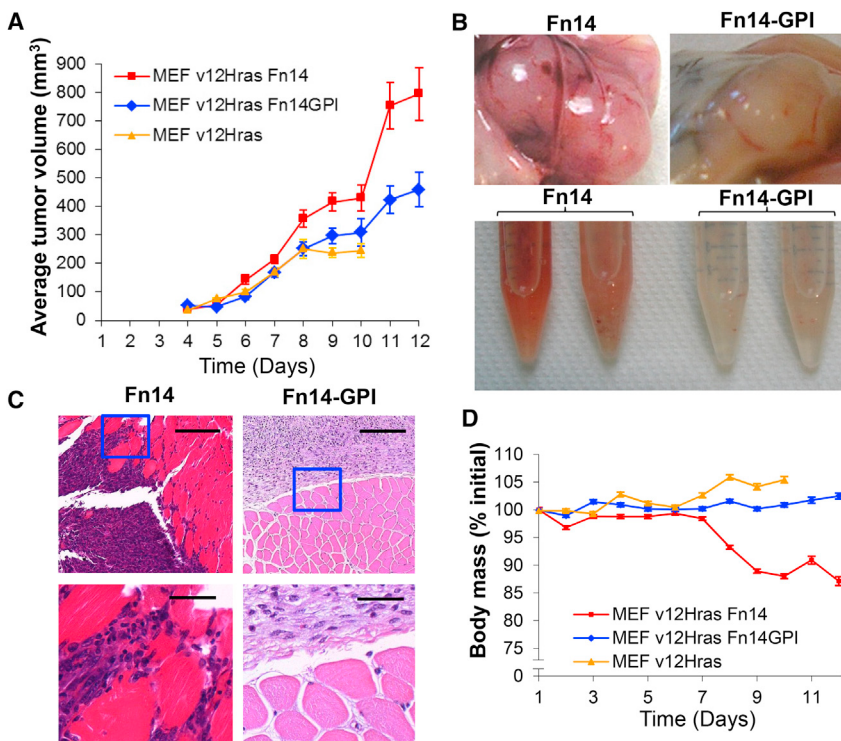


Figure 2. Ectopic Fn14 Expression in Tumors Causes Loss of Body Weight

(A) Female C57BL/6 mice injected with 5×10^6 tumor cells (day 1). Mean tumor volume \pm SEM of three independent experiments (Fn14, n = 26; Fn14-GPI, n = 20; H-Ras, n = 6).

(B) Representative images of in situ tumors from Fn14-expressing tumors (left) or Fn14-GPI-expressing tumors (right). Bottom image, disaggregated individual tumors from Fn14 (left) and Fn14-GPI (right).

(C) Fixed tumor sections stained with H&E. Left: Fn14-expressing tumor, and right: Fn14-GPI-expressing tumor taken on day 11. Images are 10 \times (upper, scale bar 160 μ m) and 40 \times magnification (lower, scale bar 40 μ m). Blue box represents area shown in 40 \times images.

(D) Body weight from mice in (A) standardized against starting weight. Data are means \pm SEM.

used a HEK293T cell line that expresses endogenous hFn14, stably transduced with a lentiviral NF- κ B reporter vector (Vince et al., 2008; Figure 1D). The antibodies were unable to stimulate NF- κ B, demonstrating that, in this assay, they are not Fn14 agonists (left column, Figure 1D). They did however block TWEAK/hFn14-induced NF- κ B (right column, Figure 1D). To functionally assess the ability of our antibodies to inhibit TWEAK/hFn14 signaling, we used Kym1 cells that are sensitive to cell death induced by TWEAK (Schneider et al., 1999; Vince et al., 2008). We co-incubated Kym1 cells \pm TWEAK (at 5, 50, or 200 ng/ml) and monoclonal antibodies at a concentration of 1 μ g/ml for 24 hr. Adherent and floating cells were harvested and stained with propidium iodide (PI), and the percentage of dead, PI-positive cells was determined by flow cytometry. Antibodies 001 and 002, but not 004, inhibited TWEAK-induced death of Kym1 cells (Figure 1E).

Consistent with results from the other assays, 001 and 002 bound both recombinant human and mouse Fn14 extracellular domains, whereas ITEM1 bound better to hFn14 than to mouse (Figure S1A). To define the epitope, we generated two “sub-domains” of the extracellular domain of Fn14 as peptides (Brown et al., 2006) and assessed antibody binding by quantitative ELISA. All antibodies bound efficiently and specifically to sub-domain 2 but not to sub-domain 1 (Figures S1B and S1C). These results demonstrate that IgG2b 001 and IgG1 002 antibodies bind specifically to an extracellular epitope present on both human and mouse Fn14 receptor.

Fn14-Expressing Tumors Cause Severe Weight Loss in Mice

To test our hypothesis that an Fn14 antibody could inhibit tumor growth, we generated an Fn14-expressing tumor cell

line and equivalent control cell lines to generate tumors in wild-type mice. MEFs derived from C57BL/6 embryos and transformed with an H-Ras V12 oncogene were infected with an hFn14-expressing lentivirus. As a control, we infected the same parental cell line with a lentivirus expressing only the extracellular domain of hFn14 fused to a GPI anchor. Both hFn14 and control cell lines formed tumors when injected into syngeneic C57BL/6 mice and initially grew at similar rates (Figure 2A). Post-mortem analysis of these mice revealed increased vascularity (Figure 2B) and tumor-invasive capacity (Figure 2C) in the hFn14-expressing tumors when compared with controls. Surprisingly, 8 days post-inoculation, mice bearing hFn14-expressing tumors, but not the control tumors, suffered rapid weight loss, and their overall health deteriorated quickly (Figure 2D). It was apparent the mice bearing Fn14 tumors were suffering from cachexia.

Fn14 Antibodies Block Fn14-Induced Cachexia in Mice

We next assessed the effect of anti-Fn14 therapy using the monoclonal antibody 001 against the weight loss seen in the mice bearing Fn14-expressing tumors. Mice were inoculated with MEF tumor cells expressing Fn14 or not and just prior to expected weight loss (day 6) were treated with 001 or an IgG2b isotype control. These hFn14-expressing tumors caused a rapid loss of body mass, and a single treatment with anti-Fn14, but not the control antibody, substantially prevented this loss (Figures 3A and S2A), even though tumor mass and volume were not significantly different between groups (Figure S2B). Fn14 tumors caused a decrease in mass of the tibialis anterior (TA) and plantaris muscles and a trend for lower muscle mass of extensor digitorum longus (EDL), soleus, gastrocnemius, and quadriceps (Figure 3B). There was no significant change in heart mass in Fn14 tumor-bearing mice (Figure 3C) but a significant decrease in subscapular fat mass (Figure 3D). The loss of muscle and fat mass in hFn14-expressing tumor mice was reduced by a single injection of anti-human Fn14 antibody (Figures 3B–3D).

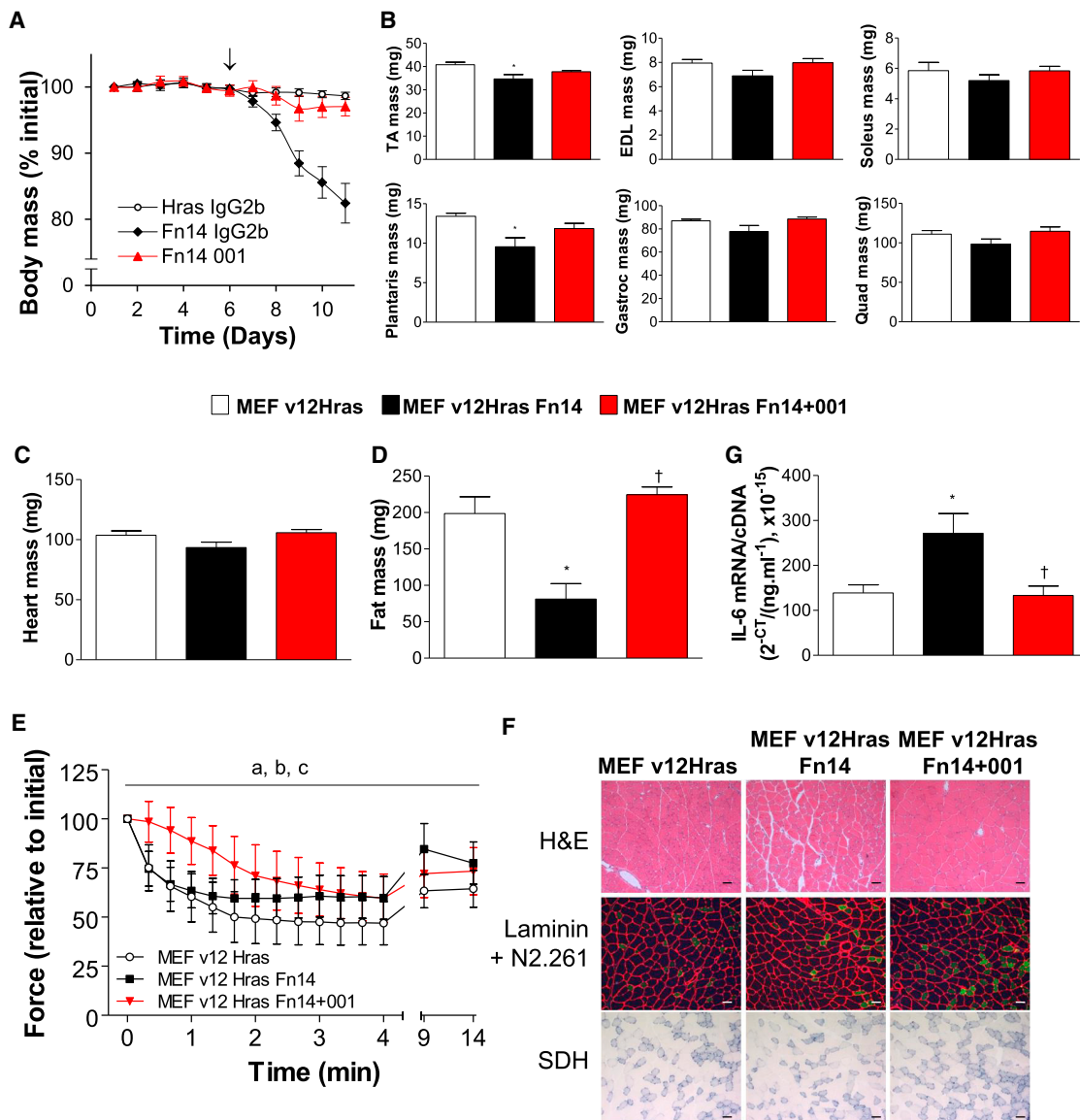


Figure 3. Anti-Fn14 Prevents Cachexia Caused by Fn14 Tumors

Female C57BL/6 mice inoculated with MEFs transduced with Fn14 (H-Ras V12 Fn14) or the parental MEF line (H-Ras V12) on day 1. Mice were treated with IgG2b control (H-Ras V12, H-Ras V12 Fn14, n = 8/group) or 001 (H-Ras V12 Fn14+001, n = 8) on day 6.

(A) Group body mass standardized against starting weight \pm SEM. Antibody treatment (↓; 5 mg/kg).

(B) Day 11, muscles were excised and weighed. TA: tibialis anterior, EDL: extensor digitorum longus, Gastroc: gastrocnemius, Quad: quadriceps.

(C) Heart and (D) subscapular fat were excised and weighed. Data are means \pm SEM (n = 8).

(E) Tetanic force production (expressed relative to initial maximum force) during and after 4 min of fatiguing intermittent stimulation in TA muscles in situ. Data are means \pm SEM (n = 8).

(F) Frozen TA muscle sections stained with H&E and reacted for anti-laminin (red), anti-myosin Ila (N2.261, green), and SDH activity (blue). Scale bar represents 100 μ m.

(G) Quantitation of IL-6 mRNA in TA muscles.

*p < 0.05 versus MEF v12 Hras; †p < 0.05 versus MEF v12 Hras Fn14. ^ap < 0.05 main effect MEF v12 Hras versus MEF v12 Hras Fn14, ^bp < 0.05 main effect MEF v12 Hras versus MEF v12 Hras Fn14+001, ^cp < 0.05 main effect MEF v12 Hras Fn14 versus MEF v12 Hras Fn14+001. Data are means \pm SEM (n = 8).

See also Figure S2.

In addition, the contractile properties of muscles in live mice were assessed on day 11, but there were no significant differences between groups in grip strength (data not shown), and in anesthetized mice there were no differences in peak twitch force (data not

shown), peak tetanic force, and specific (normalized) force of TA muscles in situ (Figure S2C). However, tetanic force over a range of stimulation frequencies (10–300 Hz) was lower in TA muscles from mice with hFn14 tumors than from mice bearing control

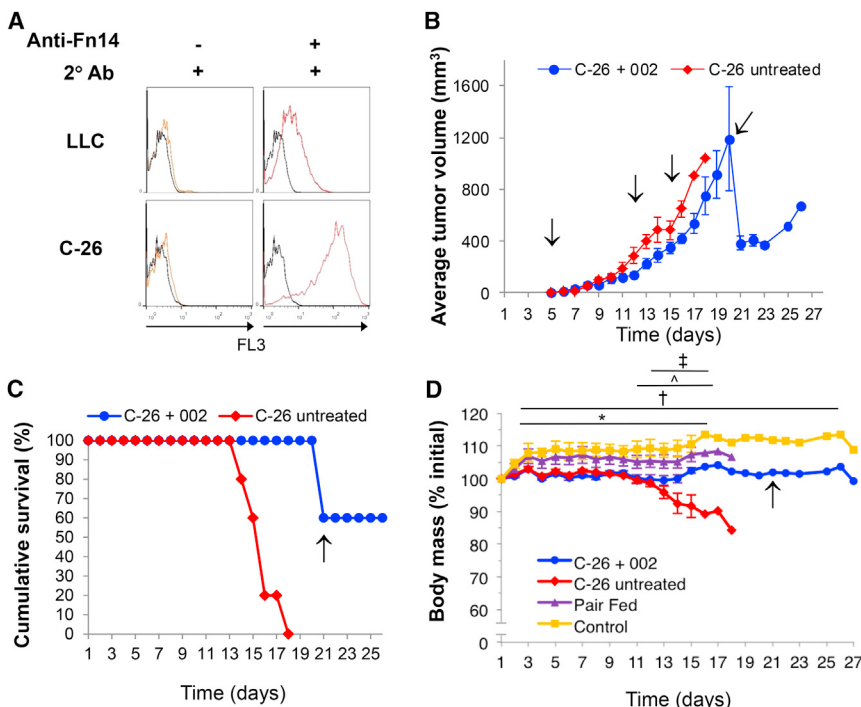


Figure 4. Fn14 Antibodies Prevent Tumor-Induced Weight Loss

(A) Flow cytometric analysis of mouse tumor cell lines LLC and C-26 adapted to low serum (0.5% FCS) and stained with anti-Fn14 (ITEM1). Black trace: unstained cells, orange trace: secondary stain only, red trace: anti-Fn14.

(B) Average tumor volume for CD2F1 male mice inoculated with 1×10^6 cells (s.c., day 1). Data are means \pm SEM. Antibody treatment (↓); 10 mg/kg. * $p < 0.05$ versus C-26.

(C) A Kaplan-Meier survival curve. $p < 0.01$ log-rank (Mantel-Cox) test.

(D) Group average mouse weight standardized to starting weight \pm SEM. * $p < 0.05$ control versus C-26; † $p < 0.05$ control versus C-26+002; ‡ $p < 0.05$ pair-fed versus C-26; ‡ $p < 0.05$ C-26 versus C-26+002.

Drop in average tumor volume of treated animals at day 21 in (B) coincides with culling of two mice due to ethical considerations (also noted by ↑ in C and D).

tumors, and this reduction in force was prevented by treatment with anti-Fn14 (Figure S2C, top panel). Anti-Fn14 also increased relative force production during and after a 4 min intermittent fatiguing stimulation protocol, indicating reduced muscle fatigability following anti-human Fn14 treatment (Figure 3E).

TA muscle sections were stained with hematoxylin and eosin (H&E), anti-laminin, and anti-myosin IIa to examine the effect of Fn14 tumor expression on muscle fiber architecture and cross-sectional area (Figure 3F). Tumors expressing hFn14 caused decreased muscle fiber cross-sectional area (Figure S2D), which was due to decreases in size of both type IIa and type IIx/b fibers (Figure S2E). A single injection of anti-Fn14 prevented the decrease in muscle fiber size (Figures 3F and S2D). Despite improvements in muscle fatigability, anti-Fn14 did not cause a shift in fiber-type proportions (Figures 3F and S2E) or muscle fiber oxidative capacity as assessed by succinate dehydrogenase (SDH) reaction intensity (Figures 3F and S2E). Assessment of mRNA levels of IL-6, an inflammatory marker of cachexia in TA muscle, also revealed that hFn14 tumors caused a significant increase in IL-6 expression in TA muscles compared to control tumors, and anti-Fn14 treatment blocked this increase (Figure 3G).

Fn14 Antibodies Increase Survival of Colon-26 Tumor-Bearing Mice

Given that tumor-expressed Fn14 had not been previously reported as a mediator of cachexia, it was important to assess whether this finding was more widely applicable. We therefore chose well-published mouse models of cachexia to further validate our findings. We assessed the level of Fn14 expression on two such tumor cell lines, Lewis lung carcinoma (LLC) and colon-26 (C-26), and demonstrated that they express low and high Fn14 levels, respectively (Figure 4A).

We chose to establish and utilize the C-26 tumor model to test the efficacy of anti-Fn14 given that the cell line expressed high levels of Fn14, and this

model generally displays more marked cachexia. Groups of five immunocompetent CD2F1 mice were inoculated with C-26 tumor cells, then treated or not with antibody 002 on days 5, 12, 15, and 20 post-inoculation. We chose monoclonal antibody 002 for this model given that it reacted slightly stronger than 001 to mouse Fn14 (Figure 1A). Antibody 002 is a different isotype than 001 and also has a subtly different Fn14 binding profile and ability to block Fn14 signaling compared to antibody 001. The tumors grew well, and although they displayed some inter-individual heterogeneity, growth was slightly slower in the treated compared to the untreated mice (Figure 4B). The survival of the treated mice was also extended dramatically (Figure 4C), and although the tumors in untreated and treated animals were comparable in size over the 18 days post-inoculation, untreated mice lost weight rapidly from day 11 onward, whereas treated mice maintained weight and condition during this period (Figure 4D). Maintenance of weight in a pair-fed control group showed that the loss in body mass in the untreated C-26 tumor mice was not due to differences in food intake (Figure 4D).

Fn14 Antibodies Block C-26 Tumor-Induced Cachexia

To more extensively characterize the weight loss and effect of anti-Fn14 treatment on C-26 tumor-bearing mice, we treated 10 mice with either anti-Fn14 002 or an isotype control IgG dosed on days 8, 12, and 16 post tumor inoculation and sacrificed them at day 22. The experiments presented in Figures 5 and 6 were performed in different labs with different sources of C-26 tumor cell lines than those presented in Figure 4, and as observed before, untreated C-26 tumor mice began to lose weight around 11 days post tumor inoculation. Although there was a slightly slower decline in weight using this alternative source of C-26 cells, anti-Fn14-treated mice again retained

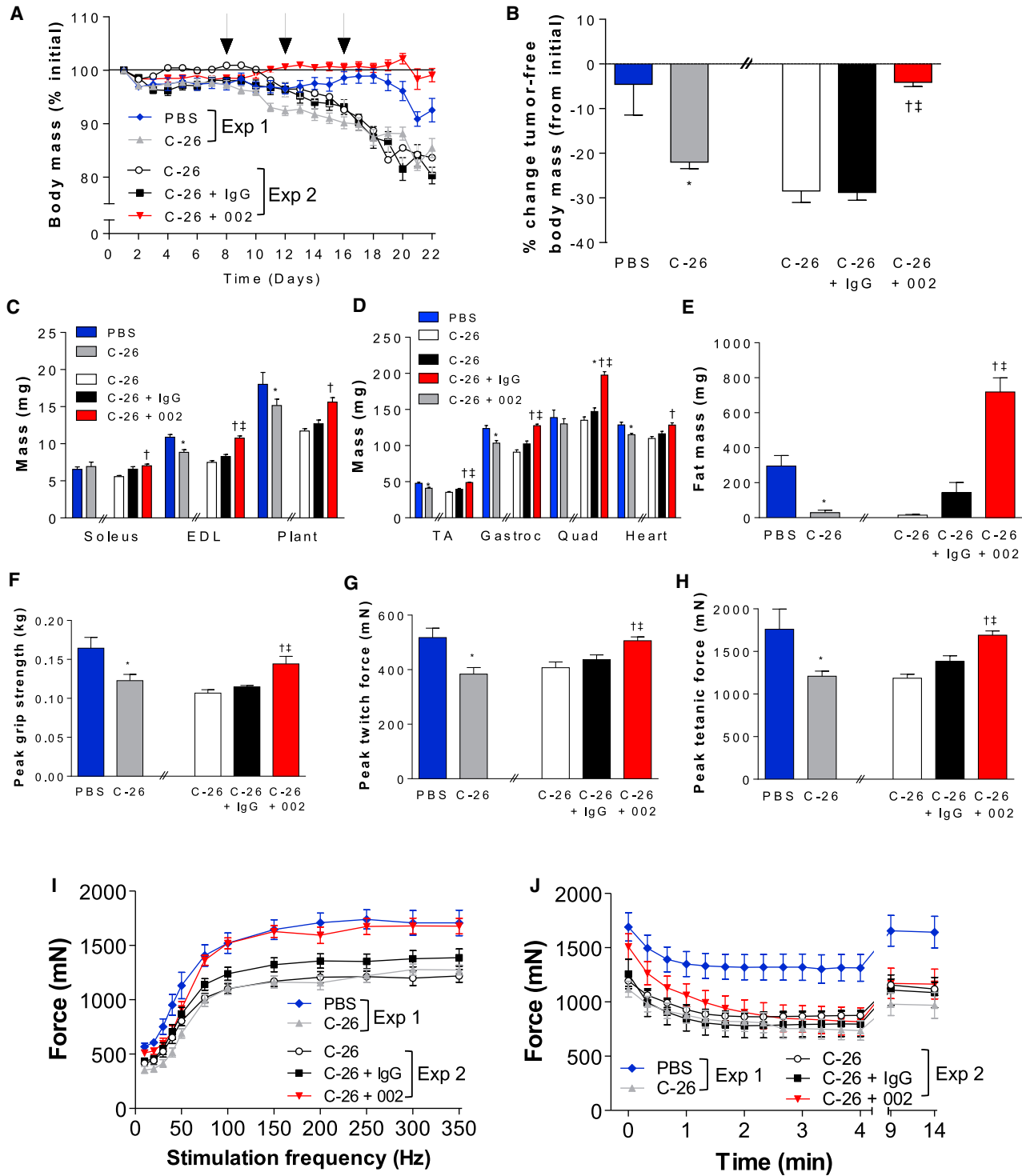


Figure 5. Fn14 Inhibition Attenuates Muscle Wasting and Weakness in C-26 Tumor-Bearing Mice

(A) Group average body weight standardized to starting weight \pm SEM of CD2F1 mice inoculated with PBS or 0.5×10^6 C-26 cells s.c. (day 1). Antibody injections (\downarrow ; 10 mg/kg). Relative body mass of C-26 from experiment 1 (gray, n = 23) significantly lower than PBS (blue, n = 14) from day 14 ($p < 0.05$). Body mass of C-26 from experiment 2 (white, n = 10) significantly lower than pair-fed 002-treated C-26 (red, n = 10) from day 16 ($p < 0.05$). Pair-fed IgG-treated C-26 (black, n = 10) body mass significantly lower than 002-treated C-26 from day 13 ($p < 0.05$).

(B) Day 22, tumors excised and weighed, and percent change in tumor-free body mass compared to pre-inoculation weight calculated. Data represent means \pm SEM. * $p < 0.05$ versus PBS; † $p < 0.05$ versus C-26 from experiment 2; ‡ $p < 0.05$ versus pair-fed IgG-treated C-26.

(legend continued on next page)

body weight (Figure 5A, Exp 1). We also assessed untreated C-26 tumor-bearing mice and a non-tumor group that were injected with PBS in place of C-26 cells and pair-fed against the C-26 group (blue and gray lines, respectively), and the data indicate reproducibility and that weight loss is unlikely due to food intake (Exp 2). Tumors in antibody-treated mice grew slower than in control mice, but weight loss was well advanced by day 17 when tumor size differences were negligible, indicating that the anti-tumor effect of the antibody was not the reason for the reduction in cachexia (Figures 5A and S3A). The preservation of weight in the anti-Fn14-treated mice was more apparent when the weights of the mice without tumors were measured (Figure 5B). Furthermore, the mass of several muscles in anti-Fn14-treated mice was significantly spared compared to control IgG-treated mice (Figures 5C and 5D). Heart and fat mass were also spared in anti-Fn14-treated mice (Figures 5D and 5E). Consistent with the preservation of muscle mass, peak grip strength in living mice at day 21 was increased in anti-Fn14-treated mice compared to control IgG-treated mice (Figure 5F). Peak twitch force (Figure 5G), peak tetanic force (Figure 5H), and tetanic force over a range of stimulation frequencies (Figure 5I) of TA muscles assessed in situ were also higher in anti-Fn14-treated animals compared to control-treated mice. After determining peak tetanic force, muscles were subjected to a 4 min intermittent stimulation protocol to induce muscle fatigue. Again, TA muscles of anti-Fn14-treated mice produced higher forces throughout most of the fatiguing stimulation protocol than control treated mice (Figure 5J).

These results demonstrated that the cachexia seen in C-26 tumor-bearing mice was caused by Fn14 and that those mice treated with anti-Fn14 antibody were not succumbing to cachexia. To investigate this at the cellular level, TA muscle sections were stained with H&E, revealing a larger fiber size in anti-Fn14-treated mice compared with the control treated mice (Figure 6A). Sections stained with anti-laminin confirmed the preservation of fiber size in anti-Fn14-treated mice (Figures 6B and S3B), and co-staining with a myosin IIa-specific antibody (N2.261) to identify type IIa and type IIx/b fibers revealed that the cross-sectional area of both fast, oxidative type IIa fibers and fast, glycolytic type IIx/b fibers was increased by anti-Fn14 treatment (Figures 6C and 6D). The proportion of type IIa and type IIx/b fibers was similar between treated and untreated

groups (Figure 6D), as was muscle fiber oxidative capacity as assessed by SDH (Figures 6C and S3C). These results show that protection of muscle mass and strength with anti-Fn14 treatment was due to the protection of individual muscle fibers and not a shift in muscle fiber-type composition.

Muscle atrophy has been shown to occur through activation of the ubiquitin proteasome and inhibition of the Akt/p70S6K pathway in muscle (Dogra et al., 2007). We therefore investigated the effect of anti-Fn14 treatment on the mRNA expression of the ubiquitin ligases MuRF-1 and atrogin-1 in the TA of these cachectic mice. Consistent with the increase in muscle mass and fiber size in anti-Fn14-treated mice, MuRF-1 and atrogin-1 mRNA expression was reduced in the TA muscles of anti-Fn14-treated tumor-bearing mice compared with untreated and IgG-treated mice (Figure 6E). In addition to loss of muscle, mRNA expression of the inflammatory cytokines IL-6 and TNF were significantly higher in TA muscles from C-26 control and control IgG-treated mice compared to anti-Fn14-treated mice, indicating that anti-Fn14 protects mice from muscle loss and also reduces the cachectic inflammatory phenotype (Figure 6F).

Not All Fn14 Antibodies Are Anti-cachectic

Given the complete blockade of cachexia onset and progression with the two antibodies we had tested, we next investigated whether any Fn14 antibody would be efficacious against the symptoms of cachexia. We assessed a third antagonistic antibody, 004, along with a commercially available antibody that has been reported to be a weak agonist, ITEM1. 004 is specific to human Fn14 and unlike either 001 or 002 did not cross-react with murine Fn14. Given that the MEF Fn14 tumor model expressed human Fn14, this was an ideal model to test for efficacy of this antibody. ITEM1, unlike 001, 002, or 004, did not antagonize or agonize TWEAK/Fn14 signaling in the NF- κ B reporter assay (Figures 1D and S4A). Human Fn14-expressing MEF tumors were established in mice, and a single dose of antibody was administered at day 7, just prior to noticeable weight loss (Figures S4B–S4D), or day 8, the first day of weight loss (Figures S4E and S4F), to randomized groups of mice. Consistent with the preceding experiments, 001 and 002 prevented weight loss induced by Fn14 tumors (Figures S4B, S4D, and S4E) and improved survival (Figures S4C and S4F). However, 004 and ITEM1 were unable to prevent Fn14 tumor-induced weight loss or improve survival. These results suggest that neither the ability

(C–E) Day 22, selected tissues were excised and weighed. (C) EDL: extensor digitorum longus, Plant: plantaris. (D) TA: tibialis anterior, Gastroc: gastrocnemius, Quad: quadriceps. (E) Epididymal fat. Data are means \pm SEM. *p < 0.05 versus PBS; †p < 0.05 versus C-26; ‡p < 0.05 versus pair-fed IgG-treated C-26.

(F) Day 21, whole-body strength was assessed using a grip-strength meter. Data are means \pm SEM. *p < 0.05 versus PBS; †p < 0.05 versus C-26 from experiment 2; ‡p < 0.05 versus pair-fed IgG-treated C-26.

(G and H) Day 22, (G) peak twitch force and (H) peak tetanic force of TA muscle were assessed in situ. Data are means \pm SEM. *p < 0.05 versus PBS; †p < 0.05 versus C-26 from experiment 2; ‡p < 0.05 versus pair-fed IgG-treated C-26.

(I) Day 22, tetanic force production at stimulation frequencies of 10–350 Hz assessed in TA muscles in situ. Data are means \pm SEM. Force from C-26 from experiment 1 (gray, n = 9) significantly lower than PBS (blue, n = 7) from 30 Hz (p < 0.05). Force from C-26 experiment 2 (white, n = 9) significantly lower than pair-fed 002-treated C-26 (red, n = 10) from 75 Hz (p < 0.05). Force from pair-fed IgG-treated C-26 (black, n = 9) significantly lower than 002-treated C-26 from 100–200 Hz (p < 0.05).

(J) Tetanic force production during and following 4 min fatiguing intermittent stimulation assessed in TA muscles in situ. Data are means \pm SEM. Force lower in C-26 from experiment 1 (gray, n = 8) compared to PBS (blue, n = 7, p < 0.001 group main effect). Force lower in C-26 from experiment 2 (white, n = 8) and pair-fed IgG-treated C-26 (black, n = 9) compared to pair-fed 002-treated C-26 (red, n = 10, p < 0.001 group main effect).

Exp 1 and Exp 2: experiments 1 and 2, respectively. In graphs in (B)–(F), double forward slash (//) denotes data obtained in two separate experiments. See also Figure S3.

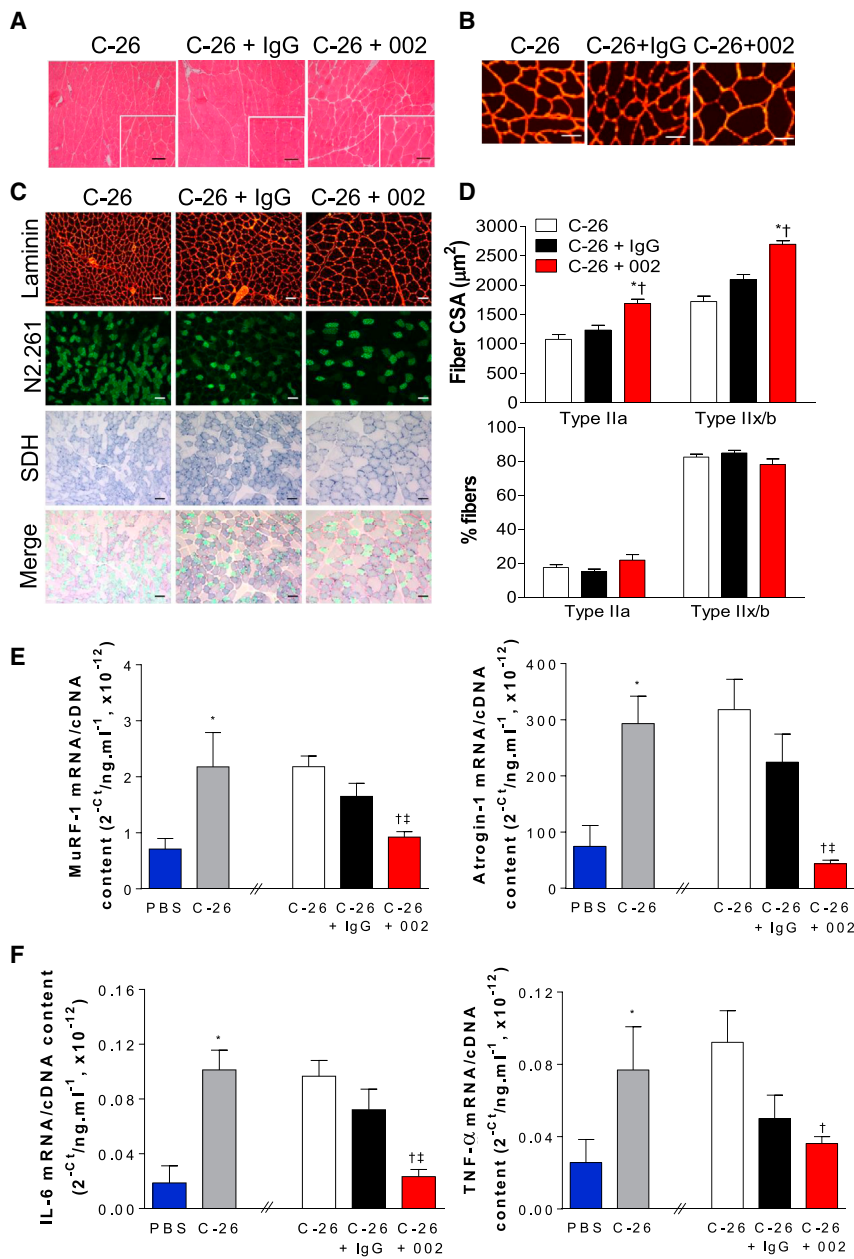


Figure 6. Fn14 Inhibition Induces Muscle Fiber Hypertrophy

CD2F1 mice were inoculated with 0.5×10^6 C-26 cells s.c. (day 1) and treated with indicated antibody (10 mg/kg; days 8, 12, and 16).

(A) Day 22, TA muscles excised and frozen for histological analysis. Representative images of muscle cross-sections stained with H&E and higher magnification inset are shown. Scale bar represents 100 μm .

(B) Muscle sections stained with anti-laminin (scale bar represents 100 μm). See also Figure S3B for quantification of muscle fiber cross-sectional area (CSA).

(C) Representative images of muscle sections and reacted for anti-laminin (red), anti-myosin Ila (N2.261, green, type Ila fibers), and SDH (blue, fiber oxidative capacity). Scale bar represents 100 μm .

(D) Laminin and N2.261 staining from (C) was used to quantify CSA (top) and relative proportion (bottom) of type Ila and type IIx/b fibers. Data are means \pm SEM. *p < 0.05 versus C-26; †p < 0.05 versus pair-fed IgG-treated C-26 (n = 8).

(E) MuRF-1 and atrogin-1 mRNA in TA muscles were quantitated. *p < 0.05 versus untreated PBS; †p < 0.05 versus untreated C-26 from experiment 2; ‡p < 0.05 versus pair-fed IgG-treated C-26 (n = 8–9). Data are means \pm SEM.

(F) Fn14 inhibition reduced expression of the pro-inflammatory cytokines IL-6 and TNF, and mRNA in TA muscles was quantitated. Mean \pm SEM. *p < 0.05 versus PBS; †p < 0.05 versus C-26; ‡p < 0.05 versus pair-fed IgG-treated C-26 (n = 8–9). Double forward slash (//) denotes data obtained in two separate experiments. See also Figure S3.

to bind human Fn14 nor antagonistic properties of an antibody to human Fn14 are sufficient to predict its ability to inhibit cachexia.

Host TWEAK and Fn14 Do Not Cause Cachexia

TWEAK/Fn14 signaling directly in muscle tissue has been reported to play a role not only in muscle development but also in muscle atrophy (Tajirihi et al., 2014). It was therefore important to determine whether Fn14 or TWEAK from the host tissue could be promoting the Fn14-dependent muscle loss seen in our MEF Fn14 cachexia model. In separate experiments, we established Fn14 tumors in *Fn14*^{-/-} or *Tweak*^{-/-} mice and compared these to tumors in wild-type mice. Mice were inoculated with Fn14 or Fn14-GPI tumor cells on day 1, and body weight and tumor

size were monitored (Figure 7). Body, tumor, muscle, and epididymal fat weight were assessed (Figures 7A–7C and S5), and there were no differences in the onset, severity, or timing of cachexia in either strain of knockout mice, suggesting that the signal for cachexia does not originate in host tissues but in the Fn14-expressing tumor cells.

Although these experiments were able to demonstrate that host TWEAK was not a player in cachexia, it was crucial to determine whether the tumor itself was a source of TWEAK involved in cachexia onset. We used the monoclonal TWEAK antibody MTW-1 for this purpose as it has been shown to effectively block the action of TWEAK in mice at reducing collagen-induced arthritis (Kamata et al., 2006). We confirmed in vitro that MTW-1, but not an isotype control antibody (Rat IgG1), blocked TWEAK-induced NF- κ B (Figure 7D). Wild-type mice bearing MEF Fn14 tumors were treated with MTW-1 or isotype control on day 7, and body weight was monitored over time. In contrast to the anti-Fn14 antibody treatment, MTW-1 (anti-TWEAK) had no effect on the rapid induction of cachexia by the Fn14 tumor (Figure 7E). Together, these results suggest that neither tumoral nor humoral sources

of TWEAK drive cachexia in this model and that the Fn14/TWEAK signaling pathway in muscle is not responsible for muscle atrophy.

Further Assessment of the Role of Muscle Fn14 in Atrophy

Given that the TWEAK/Fn14 pathway in muscle has been previously implicated in the induction of muscle atrophy pathways, yet our studies in knockout mice suggested no involvement, we next used a specific model whereby atrophy is induced in muscle by the expression of activin A, a soluble molecule well known for its involvement in binding the ActRIIb receptor on muscle cells and activating muscle atrophy pathways. We chose this model because recently, using next-gen sequencing, we found that muscle wasting induced by local transduction of mouse limb muscles with a recombinant adeno-associated virus-based vector expressing activin A (AAV:ActA) was associated with upregulation of Fn14 transcription. Abundance of Fn14 protein was increased approximately 10-fold in muscles administered the activin-expressing vector, compared with contralateral limb controls (Chen et al., 2014). Because local overexpression of activin A was proven to induce Fn14 expression in this muscle atrophy model, we asked whether induction of Fn14 was responsible for causing muscle wasting in activin A-overexpressing muscle or as a downstream consequence of atrophy pathway activation. To test this, we transduced the right TA muscle of C57BL/6 mice with an AAV vector expressing activin A and a control AAV vector in the left muscle. Mice were treated with Fn14 antibodies 001 or 002 or an IgG control antibody 4 days after administration of AAV vectors, for a total of six injections prior to assessment at the experimental endpoint 4 weeks later. Increased local expression of activin A caused muscle wasting as expected (Figures 7F and 7G); however, neither 001 nor 002 blocked activin A-induced muscle loss, indicating that although Fn14 is upregulated in muscle during activin A-induced muscle wasting, it does not cause loss of muscle mass.

Translation to Human Cancer

Given the dramatic pro-cachectic effects of Fn14-expressing tumors in mice, we were interested to see whether there were data that might indicate whether the same scenario pertains to human cancers. We examined the mRNA expression for a range of cancers in the GDAC (Genome Data Analysis Centre) Firehose at the Broad Institute. As with most databases, the presence of weight loss is unfortunately not annotated. However, for cancers where sufficient sample sizes exist, we were able to demonstrate a positive correlation for the expression of Fn14 with pro-inflammatory cytokines in human cancers (Figures S6 and S7). In breast, head and neck, lung, colorectal, and stomach cancer, IL-1 α , IL-1 β , IL-6, IL-8, and TNF (Figures S6 and S7) all correlate positively with Fn14 expression.

DISCUSSION

We developed antibodies to specifically block Fn14 signaling in order to test the hypothesis that they would reduce tumor growth and development. Our antibodies were specific and selected

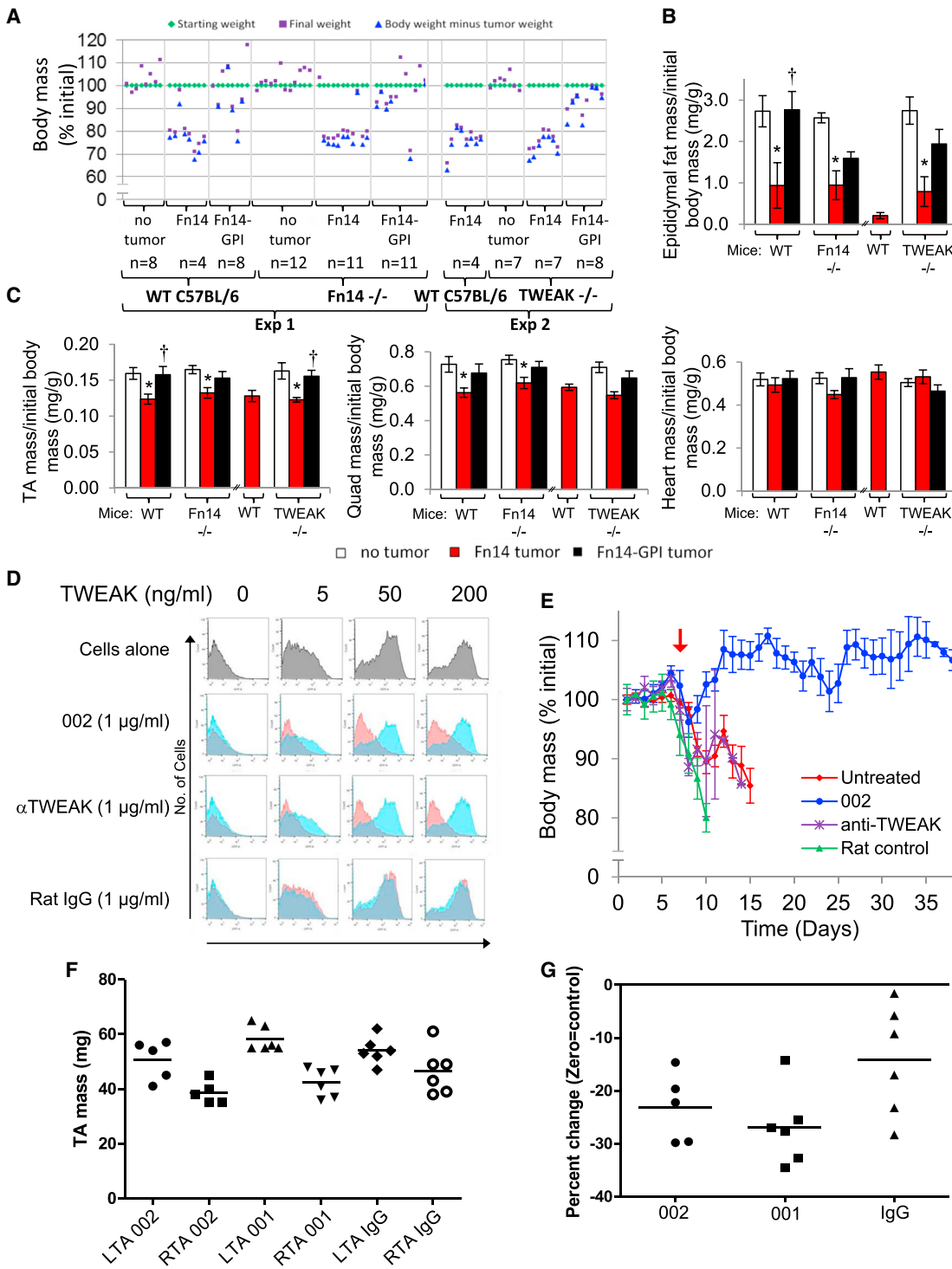
on the basis that they inhibited TWEAK/Fn14-induced NF- κ B signaling and cell death. We initiated studies *in vivo* on the basis that these antagonistic antibodies might impede tumor growth. Our antibodies, however, have incomplete and tumor-specific effects on tumor growth.

When we expressed Fn14 on tumors (MEF Fn14 model), it surprisingly induced severe weight loss and overall decline in health. Tumors can cause anorexia or suppress appetite (Macciò et al., 2012), but loss of weight in these mice was not due to a tumor effect on feeding because pair-fed controls retained body mass. Cachexia occurs in the presence of other illness, and cancer is one such example. The defining hallmark of cachexia is loss of lean muscle mass and, in some cases, loss of fat. The poor understanding of the signaling pathways that cause cachexia has meant that current cachexia therapies generally target the disease symptoms rather than the cause. For example, ghrelin, a peptide hormone originally isolated from the stomach that stimulates appetite, has been used in cachectic patients to combat loss of body mass (Macciò et al., 2012). However, this is ultimately ineffective because it does not address the cause of the disease.

We therefore investigated the possibility that signaling via Fn14 might contribute to cachexia. In our experiments, untreated and control-treated tumor-bearing mice lost significant muscle mass from all of the major skeletal muscles, and this loss was prevented by treatment with anti-Fn14. Furthermore, muscle function, along with fat stores, were also retained in the antibody-treated mice, and a decrease in inflammatory markers within target tissues was also observed. We were then able to extend these findings by reproducing the anti-cachectic ability of our Fn14-antibodies in the widely studied C-26 mouse model of cancer cachexia. Thus, targeting Fn14 on tumors presents a promising means for treatment of cancer cachexia. The finding that Fn14 is not only involved in wound healing (Winkles, 2008) but also causative of cancer cachexia is consistent with the concept that tumors resemble wounds that do not heal (Dvorak, 1986).

We had specifically chosen antibodies to Fn14 that could antagonize the action of TWEAK, in line with the hypothesis that Fn14-dependent cachexia is caused by an activation of signaling through Fn14. Although *in vitro* our antibodies can function as antagonists, we cannot rule out that *in vivo* these anti-cachectic antibodies are operating via Fc-dependent multi-merization pathways. *In vitro* studies showed the potential of cross-linked Fc domains to reveal agonistic activity (data not shown). This is a common and often desirable feature of antibodies and has been demonstrated for other Fn14 antibodies (Culp et al., 2010; Salzmann et al., 2013).

Combined with the ability of our Fn14 antibody to inhibit cachexia, these observations naturally led to the idea that TWEAK could be the factor that drives muscle wasting in these cancer-induced cachexia models, given that it is the only ligand reported for Fn14 to date. However, the MEF tumors induced cachexia to the same degree in both *Fn14*^{-/-} and *Tweak*^{-/-} mice, which is inconsistent with this hypothesis. Additionally, our data also demonstrated that TWEAK blockade (using a blocking TWEAK antibody) had no effect on the Fn14-induced cachexia, which raises the question of how Fn14 is inducing

**Figure 7. Host Fn14 and TWEAK Are Not Involved in Cachexia**

Wild-type, *Fn14*^{-/-} or *Tweak*^{-/-} mice were injected with MEF H-Ras V12 Fn14 or Fn14-GPI tumor cells (day 1).

(A) Starting and final weight and final body weight minus tumor mass, standardized to starting weight. Exp 1 and Exp 2: experiments 1 and 2, respectively. See also Figure S5.

(B and C) Group average (B) epididymal fat and (C) muscle (TA, quadriceps, and heart) standardized against starting body weight. In graphs, double forward slash (//) denotes data obtained in two separate experiments. *p < 0.05 versus non-tumor for that strain; †p < 0.05 versus Fn14 tumor for that strain. Data are means ± SEM.

(legend continued on next page)

cachexia in a ligand-independent fashion. Ligand-independent receptor multi-merization has been suggested for Fn14 by others as a possibility for pathway activation; however, this idea has stemmed from *in vitro* overexpression data (Brown et al., 2003; Han et al., 2003), and no *in vivo* physiological evidence exists to support this hypothesis. Although speculative, another possibility is the presence of a second unidentified ligand for Fn14. Although the mechanism remains unclear, there is no doubt that tumor-localized Fn14 induces cachexia in the models presented here, and antibody therapy ablates this condition.

In addition to its effects during tumorigenesis, Fn14 signaling (via the action of TWEAK) has been linked to inhibiting differentiation of myoblast to muscle (Dogra et al., 2006; Girgenrath et al., 2006) and promoting myoblast proliferation in the presence of TWEAK. *In vivo* studies using Fn14 or TWEAK knockout and TWEAK transgenic mice support the idea that regulating myogenesis and muscle repair are physiological functions of the TWEAK/Fn14 signaling axis (Tajirishi et al., 2014; Girgenrath et al., 2006; Mittal et al., 2010a, 2010b). Our data from both *Fn14*^{-/-} or *Tweak*^{-/-} mice, as well as a blocking TWEAK antibody, demonstrated that, at least in the models presented here, neither TWEAK nor Fn14 in muscle cells are involved in inducing muscle atrophy pathways directly. This raises the question of why Fn14 expression is increased in muscle during atrophy, and we speculate that this could be in a regenerative capacity. Supportive of such a hypothesis, Fn14 is required for the self-renewal of muscle progenitor cells, and Fn14 knockout mice display delayed muscle regeneration following injury (Girgenrath et al., 2006). In addition to our data generated from cancer-cachexia models, the model for activin A overexpression in muscle promotes upregulation of muscle Fn14 during muscle wasting. Fn14 antibody treatment did not prevent activin A-induced muscle loss, and in fact antibody treatment led to marginally smaller muscle mass than that in control-treated mice, again supporting the hypothesis of Fn14 functioning in a regenerative capacity.

Given that our data argues against the possibility that tumor-derived TWEAK is the causative factor in cancer cachexia and also against muscle atrophy being induced by signaling via localization of Fn14 in the muscle itself, this raises the question of the nature of the soluble factor produced by the tumor that relays the signal to distal tissues. Potential candidates for such signaling molecules could be activins or myostatin because cachexia induced by C-26 tumors was prevented by a decoy activin receptor (ActRII β) that inhibits activin/myostatin signaling. Interestingly, although muscle wasting caused by C-26 tumors was successfully prevented by the ActRII β decoy receptor, fat loss, another feature of cachexia, was unaffected (Zhou et al., 2010). In contrast, we have shown that anti-Fn14 treatment of C-26 cachectic animals prevented tumor-induced inflamma-

tion, fat loss, and reduction in muscle mass and function. Minimally we can conclude that if activin functions downstream of tumor Fn14 to induce cachexia, it is only one of the components produced by Fn14 tumors. Fn14 is therefore an attractive therapeutic target because it is not required for normal development and is generally absent in normal tissue yet increased in tumors.

Our data implicated tumor Fn14 as an inducer of cachexia in mice models, and therefore translation of these findings to humans was crucial. Cachectic mice lose weight very rapidly, whereas in human cancer patients, cachexia usually progresses slowly, with an average loss of 5% body mass over 12 months. In murine tumor models, the tumor can account for as much as 10% of the total mouse weight; in humans, tumor mass as a proportion of body weight rarely exceeds 1%. Mice also have a different metabolism than humans. Despite the need to be cautious when translating results from mouse models to humans, it is noteworthy that in our experiments similarly sized tumors caused very different cachectic effects. This demonstrates that cachexia is an active, independent process with the tumor directly driving the loss of muscle and fat.

Cancer cachexia has been estimated to be as high as 80% of all cancer cases (Wallengren et al., 2013), and cachexia has been attributed to a patient's inability to tolerate intensive treatment regimens (Argilés et al., 2009; Murphy and Lynch, 2009). Unfortunately, current databases are remarkably deficient concerning the presence of cachexia or its contribution to patient well-being and survival. Even so, our TCGA database analysis promisingly revealed positive correlations between many inflammatory cytokines implicated in cancer cachexia and Fn14 transcripts in patients. The typical lack of diagnosis of cachexia in patient cohorts means, however, that the data cannot directly address whether Fn14 expression plays a role in cachexia.

A therapy that directly targets cancer-associated cachexia is desperately needed. We have demonstrated that anti-Fn14 reagents present a tangible treatment and must now be tested for their efficacy in cancer patients presenting with hallmarks of cachexia. Prior to this, however, there is a pressing and urgent need to generate patient sample data that acknowledge and record central components to cachexia.

EXPERIMENTAL PROCEDURES

Monoclonal Antibody Generation—Immunization of Mice, Hybridoma Production, and Purification

Recombinant Fn14-Fc (Amgen) was used for immunizations. Female Balb/c mice were immunized intraperitoneally (i.p.) with 15 μ g of antigen emulsified in Complete Freund's adjuvant (Sigma). Incomplete Freund's adjuvant was used for subsequent boosts performed at 4 week intervals and final i.p. injection 3 days before spleen removal.

(D) Flow cytometric analysis of HEK293T NF- κ B GFP reporter assay. MTW-1 (anti-TWEAK), Rat IgG control, or antibody 002 (red) \pm 0–200 ng/ml Fc-TWEAK (gray and blue underlay).

(E) Standardized group body weight of C57BL/6 mice injected with MEF H-Ras V12 Fn14 tumor cells (day 1) and antibody treated (anti-TWEAK MTW-1, control IgG, or 002; day 7; 10 mg/kg; \downarrow). Data are means \pm SEM ($n = 8$).

(F) Absolute mass values for TA muscles injected with activin-expressing AAV vectors (right TA, RTA) or control vector (left TA, LTA); mice treated with 001, 002, or IgG control.

(G) Percentage change in TA muscle mass, injected with activin-expressing AAV vectors, compared with contralateral muscles receiving control vector.

Hybridoma fusions with SP20 cells were performed using ClonaCell-HY Hybridoma Kit (StemCell Technologies, Inc.). Selection and cloning steps were performed on methylcellulose-based semi-solid media in 96-well plates.

Antibody accumulated from hybridomas grown in serum-free conditioned medium and purified with Protein A Sepharose HiTrap MabSelect Xtra (GE Healthcare). Neutralized eluate from Protein A was concentrated and buffer exchanged with PBS using a vivaspin 20 column (Sartorius). All antibodies had endotoxin < 0.05 EU/mg, determined using Charles River Endosafe PTS.

Antibody Isotyping and Antibodies

Antibodies were isotype using the BD Cytometric Bead Array. ITEM1, IgG2b, IgG1, and TWEAK (MTW-1); rat IgG1 (Biolegend); anti-VSV (Sigma); anti-HA (made in-house); and AlexaFluor-647 secondary (Invitrogen) were used.

Generation of Constructs and Cell Lines

The 4-hydroxytamoxifen (4-OHT) inducible lentiviral vector previously described (Vince et al., 2007) was used to express human Fn14, or the Fn14 extracellular region fused to the TrailR3 GPI (Bossen et al., 2006), to create Fn14-GPI. Wild-type C57BL/6 MEFs were immortalized with a lentiviral SV40 Large T construct and transformed with a retroviral H-Ras V12 construct. This cell line was then transduced for expression of GEV16 and either Fn14 or Fn14-GPI. One hundred nanomolar 4-OHT was used for protein induction.

Transfections and Western Blotting

HEK293T cells were transiently transfected with DNA encoding TNFRSF members (Bossen et al., 2006) using Lipofectamine 2000. At 24 hr, cells were harvested and lysed in RIPA buffer. Inducible cell lines were grown to ~50% confluence, and Fn14 expression induced for 48 hr. Cells were harvested, washed, and resuspended in 20 mM Tris, pH 7.4, 10 µg/ml DNase1 and RNaseA. Genomic DNA from lysed cells was sheared (27G insulin syringe), samples centrifuged, supernatant collected, and further centrifuged. The pellet was resuspended in 1M Tris, 0.4% SDS, and proteins were separated by reducing SDS-PAGE and western blotted. HRP-conjugated secondary goat anti-mouse was used for detection.

Flow Cytometry

Cells (1×10^5) were incubated with antibody, washed, and stained with AlexaFluor-647-conjugated goat anti-mouse IgG, and flow cytometry was performed with a BD FACSCanto II. Data analysis was done with FlowJo. Fn14 expression was induced 24 hr prior.

HEK293T NF-κB GFP Assay

HEK293T cells containing a stably integrated lentiviral vector and an NF-κB promoter driving GFP (pTRH1 System Biosciences) were incubated for 24 hr ± Fc-TWEAK (5, 50, 100, or 200 ng/ml), ± antibodies. GFP fluorescence was measured by flow cytometry.

Kym1 Cell-Death Assay

Kym1 cell-death assays were performed as described (Vince et al., 2008). Briefly, 24 hr after TWEAK stimulation, live and dead cells were harvested, stained with PI, and analyzed by flow cytometry.

Tumor Cell Lines and Tumor Studies

Two independent sources of C-26 cells from Cell Line Services (Germany) (Figure 4) and a gift from Martha Belury (Ohio State University, Columbus, OH, USA) (Figures 5 and 6) were used; LLC were sourced from European Collection of Cell Cultures. Cells were cultured in 10% DMEM (MEF and LLC) or 10% RPMI (C-26). Mice were obtained from Animal Resources Centre (Canning Vale, Western Australia) or Monash Animal Services (Victoria), and all experiments were approved by the relevant Animal Ethics Committees from La Trobe University (AEC 13-52, 10-54, 11-37, and 10-19B), University of Melbourne (AEC 1112069), or the Alfred Medical Research and Education Precinct (AEC E/1289/2012/B). Tumor measurements were taken using digital calipers, and volume calculated ($\text{length} \times \text{width}^2/2$). Pair feeding was achieved by monitoring food intake of 'untreated' tumor group each 24 hr and providing the pair-fed group with that amount of food for the following 24 hr period. Mice received subcutaneous (s.c.) injection of PBS ± 5×10^5 – 5×10^6 cells

on experiment day 1 using an insulin syringe. Antibodies were administered by i.p. injection.

Grip-Strength Test

Whole-body strength was assessed on day 21 using a grip-strength meter (Columbus Instruments, Columbus, OH, USA) as described (Murphy et al., 2012).

Assessment of Functional Properties of TA Muscles

On day 22 (C-26 study) or day 11 (MEF study), mice were anesthetized with sodium pentobarbitone (i.p.; Nembutal; 60 mg/kg), and the contractile properties of the mouse TA muscle assessed (Murphy et al., 2010).

Skeletal Muscle Histology

Serial sections (5 µm) cut transversely through the TA muscle using a refrigerated (-20°C) cryostat (CTI Cryostat; IEC, Needham Heights, MA, USA). Sections were reacted with the following: laminin (Sigma-Aldrich) for mean myofiber cross-sectional area (CSA); SDH for oxidative enzyme activity; and N2.261 (developed by Dr Helen Blau, obtained from the Developmental Studies Hybridoma Bank) for percentage myosin Ila isoforms (Murphy et al., 2010). Digital images were obtained using an upright microscope (Axio Imager D1, Carl Zeiss, Göttingen, Germany), controlled and quantified by AxioVision AC software (Carl Zeiss).

Real-Time PCR Analyses

Total RNA was extracted from 10–20 mg TA muscle using a PureLink RNA Mini Kit (Invitrogen). RNA was transcribed into cDNA using the Invitrogen Super-Script VILO cDNA Synthesis Kit. Real-Time PCR with primers for MuRF-1, atrogin-1, IL-6, and TNF was performed (Murphy et al., 2010). Single-stranded DNA (ssDNA) content in each sample was determined using Quanti-iT Oli-Green ssDNA Assay Kit (Molecular Probes, Eugene, OR, USA). Gene expression was quantified by normalizing logarithmic cycle threshold (CT) value ($2^{-\text{CT}}$) to cDNA content of each sample to obtain the expression $2^{-\text{CT}}/\text{cDNA}$ content (ng.ml^{-1}).

Activin A Model of Muscle Atrophy

AAV vectors carrying activin A expression cassette, or control AAV, were injected at a dose of 1×10^9 vector genomes into TA muscles of ~8-week-old male isoflurane anaesthetized C57BL/6 mice, as described (Chen et al., 2014). Randomly assigned cohorts received a total of six antibody injections over 4 weeks beginning 4 days after AAV vector injection. TA muscles from both hindlimbs were excised at the experimental endpoint.

SUPPLEMENTAL INFORMATION

Supplemental Information includes Supplemental Experimental Procedures and seven figures and can be found with this article online at <http://dx.doi.org/10.1016/j.cell.2015.08.031>.

AUTHOR CONTRIBUTIONS

Monoclonal antibodies: D.L., A.J.J., L.J., V.L., K.E., T.S., H.D., J.H., G.T., P.F., N.J.H., and A.M.S. Design/creation of Fn14-expressing tumor model: W.W.-L.W., A.J.J., J. Silke, and L.J. Mouse experiments: L.J., A.J.J., D.L., K.M.J., R.W., H.A., P.F., and J.H. Constructs/cell lines: A.J.J., L.J., M.T., and P.S. Cachexia characterization/muscle function designed and conducted by G.S.L. and K.T.M. Activin A model experiments designed and conducted by P.G. Epitope mapping: M.F., J.L.C., K.E., J. Schloegel, P.F., and R.W. Flow cytometry: L.J. and D.L. and western blotting L.J. Fn14^{-/-} mice provided by L.C.B. Mouse genotyping: C.H. Human database analysis: S.Y.L. Manuscript preparation: L.J., L.C.B., P.S., P.G., and A.M.S. Project coordination, results interpretation, and manuscript writing: A.J.J., J. Silke, N.J.H., G.S.L., and K.T.M.

ACKNOWLEDGMENTS

We acknowledge financial support from the Cooperative Research Centre for Biomarker Translation and the NHMRC. We thank Timur Naim, Annabel Chee,

and Jennifer Trieu for expert technical assistance. We acknowledge the provision of the activin construct, AAV vectors, and technical assistance by Craig Harrison, Hongwei Qian, and Justin Chen. We also acknowledge Stephen Wilcox for MEF tumor cell line genome DNA sequencing. J. Silke is supported by NHMRC grants #541901 and 1058190. K.T.M. is supported by an NHMRC Career Development Fellowship. P.S. is supported by Swiss National Science Foundation grants. N.J.H., J. Silke, and A.M.S. are supported by an NHMRC Development Grant #1075504. L.C.B. is an employee and stockholder of Biogen, Inc.

Received: April 13, 2015

Revised: April 23, 2015

Accepted: August 13, 2015

Published: September 10, 2015

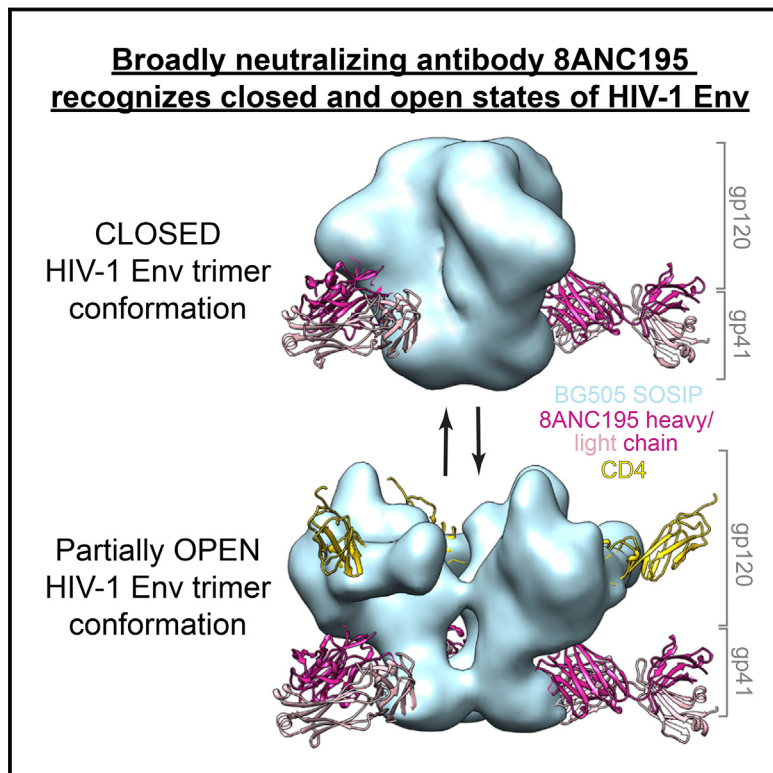
REFERENCES

- Argilés, J.M., Busquets, S., Toledo, M., and López-Soriano, F.J. (2009). The role of cytokines in cancer cachexia. *Curr. Opin. Support. Palliat. Care* 3, 263–268.
- Bossen, C., Ingold, K., Tardivel, A., Bodmer, J.L., Gaide, O., Hertig, S., Ambrose, C., Tschopp, J., and Schneider, P. (2006). Interactions of tumor necrosis factor (TNF) and TNF receptor family members in the mouse and human. *J. Biol. Chem.* 281, 13964–13971.
- Brown, S.A., Richards, C.M., Hanscom, H.N., Feng, S.L., and Winkles, J.A. (2003). The Fn14 cytoplasmic tail binds tumour-necrosis-factor-receptor-associated factors 1, 2, 3 and 5 and mediates nuclear factor- κ B activation. *Biochem. J.* 371, 395–403.
- Brown, S.A., Hanscom, H.N., Vu, H., Brew, S.A., and Winkles, J.A. (2006). TWEAK binding to the Fn14 cysteine-rich domain depends on charged residues located in both the A1 and D2 modules. *Biochem. J.* 397, 297–304.
- Burkly, L.C., Michaelson, J.S., and Zheng, T.S. (2011). TWEAK/Fn14 pathway: an immunological switch for shaping tissue responses. *Immunol. Rev.* 244, 99–114.
- Campbell, S., Michaelson, J., Burkly, L., and Puttermann, C. (2004). The role of TWEAK/Fn14 in the pathogenesis of inflammation and systemic autoimmunity. *Front. Biosci.* 9, 2273–2284.
- Chen, J.L., Walton, K.L., Winbanks, C.E., Murphy, K.T., Thomson, R.E., Makani, Y., Qian, H., Lynch, G.S., Harrison, C.A., and Gregorevic, P. (2014). Elevated expression of activins promotes muscle wasting and cachexia. *FASEB J.* 28, 1711–1723.
- Culp, P.A., Choi, D., Zhang, Y., Yin, J., Seto, P., Ybarra, S.E., Su, M., Sho, M., Steinle, R., Wong, M.H., et al. (2010). Antibodies to TWEAK receptor inhibit human tumor growth through dual mechanisms. *Clin. Cancer Res.* 16, 497–508.
- Dewys, W.D., Begg, C., Lavin, P.T., Band, P.R., Bennett, J.M., Bertino, J.R., Cohen, M.H., Douglass, H.O., Jr., Engstrom, P.F., Ezdinli, E.Z., et al.; Eastern Cooperative Oncology Group (1980). Prognostic effect of weight loss prior to chemotherapy in cancer patients. *Am. J. Med.* 69, 491–497.
- Dogra, C., Changotra, H., Wedhas, N., Qin, X., Wergedal, J.E., and Kumar, A. (2007). TNF-related weak inducer of apoptosis (TWEAK) is a potent skeletal muscle-wasting cytokine. *FASEB J.* 21, 1857–1869.
- Dogra, C., Changotra, H., Mohan, S., and Kumar, A. (2006). Tumor necrosis factor-like weak inducer of apoptosis inhibits skeletal myogenesis through sustained activation of nuclear factor- κ B and degradation of MyoD protein. *J. Biol. Chem.* 281, 10327–10336.
- Dvorak, H.F. (1986). Tumors: wounds that do not heal. Similarities between tumor stroma generation and wound healing. *N. Engl. J. Med.* 315, 1650–1659.
- Galfre, G., and Milstein, C. (1981). Preparation of monoclonal antibodies: strategies and procedures. *Methods Enzymol.* 73 (Pt B), 3–46.
- Girgenrath, M., Weng, S., Kostek, C.A., Browning, B., Wang, M., Brown, S.A., Winkles, J.A., Michaelson, J.S., Allaire, N., Schneider, P., et al. (2006). TWEAK, via its receptor Fn14, is a novel regulator of mesenchymal progenitor cells and skeletal muscle regeneration. *EMBO J.* 25, 5826–5839.
- Han, S., Yoon, K., Lee, K., Kim, K., Jang, H., Lee, N.K., Hwang, K., and Young Lee, S. (2003). TNF-related weak inducer of apoptosis receptor, a TNF receptor superfamily member, activates NF- κ B through TNF receptor-associated factors. *Biochem. Biophys. Res. Commun.* 305, 789–796.
- Islam-Ali, B.S., and Tisdale, M.J. (2001). Effect of a tumour-produced lipid-mobilizing factor on protein synthesis and degradation. *Br. J. Cancer* 84, 1648–1655.
- Kamata, K., Kamijo, S., Nakajima, A., Koyanagi, A., Kurosawa, H., Yagita, H., and Okumura, K. (2006). Involvement of TNF-like weak inducer of apoptosis in the pathogenesis of collagen-induced arthritis. *J. Immunol.* 177, 6433–6439.
- Macciò, A., Madeddu, C., and Mantovani, G. (2012). Current pharmacotherapy options for cancer anorexia and cachexia. *Expert Opin. Pharmacother.* 13, 2453–2472.
- Mittal, A., Bhatnagar, S., Kumar, A., Lach-Trifilieff, E., Wauters, S., Li, H., Makonchuk, D.Y., Glass, D.J., and Kumar, A. (2010a). The TWEAK-Fn14 system is a critical regulator of denervation-induced skeletal muscle atrophy in mice. *J. Cell Biol.* 188, 833–849.
- Mittal, A., Bhatnagar, S., Kumar, A., Paul, P.K., Kuang, S., and Kumar, A. (2010b). Genetic ablation of TWEAK augments regeneration and post-injury growth of skeletal muscle in mice. *Am. J. Pathol.* 177, 1732–1742.
- Murphy, K.T., Koopman, R., Naim, T., Leger, B., Trieu, J., Ibeabunjo, C., and Lynch, G.S. (2010). Antibody-directed myostatin inhibition in 21-mo-old mice reveals novel roles for myostatin signaling in skeletal muscle structure and function. *FASEB J.* 24, 4433–4442.
- Murphy, K.T., and Lynch, G.S. (2009). Update on emerging drugs for cancer cachexia. *Expert Opin. Emerg. Drugs* 14, 619–632.
- Murphy, K.T., Chee, A., Trieu, J., Naim, T., and Lynch, G.S. (2012). Importance of functional and metabolic impairments in the characterization of the C-26 murine model of cancer cachexia. *Dis. Model. Mech.* 5, 533–545.
- Muscaritoli, M., Anker, S.D., Argilés, J., Aversa, Z., Bauer, J.M., Biolo, G., Boirie, Y., Bosaeus, I., Cederholm, T., Costelli, P., et al. (2010). Consensus definition of sarcopenia, cachexia and pre-cachexia: joint document elaborated by Special Interest Groups (SIG) "cachexia-anorexia in chronic wasting diseases" and "nutrition in geriatrics". *Clin. Nutr.* 29, 154–159.
- Nakayama, M., Ishidoh, K., Kojima, Y., Harada, N., Kominami, E., Okumura, K., and Yagita, H. (2003). Fibroblast growth factor-inducible 14 mediates multiple pathways of TWEAK-induced cell death. *J. Immunol.* 170, 341–348.
- Russell, S.T., and Tisdale, M.J. (2005). The role of glucocorticoids in the induction of zinc-alpha2-glycoprotein expression in adipose tissue in cancer cachexia. *Br. J. Cancer* 92, 876–881.
- Salzmann, S., Seher, A., Trebing, J., Weisenberger, D., Rosenthal, A., Siegmund, D., and Wajant, H. (2013). Fibroblast growth factor inducible (Fn14)-specific antibodies concomitantly display signaling pathway-specific agonistic and antagonistic activity. *J. Biol. Chem.* 288, 13455–13466.
- Schneider, P., Schwenzer, R., Haas, E., Mühlbeck, F., Schubert, G., Scheurich, P., Tschoop, J., and Wajant, H. (1999). TWEAK can induce cell death via endogenous TNF and TNF receptor 1. *Eur. J. Immunol.* 29, 1785–1792.
- Tajirihi, M.M., Zheng, T.S., Burkly, L.C., and Kumar, A. (2014). The TWEAK-Fn14 pathway: a potent regulator of skeletal muscle biology in health and disease. *Cytokine Growth Factor Rev.* 25, 215–225.
- Tisdale, M.J. (2009). Mechanisms of cancer cachexia. *Physiol. Rev.* 89, 381–410.
- Varfolomeev, E., Blankenship, J.W., Wayson, S.M., Fedorova, A.V., Kayagaki, N., Garg, P., Zobel, K., Dynek, J.N., Elliott, L.O., Wallweber, H.J., et al. (2007). IAP antagonists induce autoubiquitination of c-IAPs, NF- κ B activation, and TNF α -dependent apoptosis. *Cell* 131, 669–681.
- Varfolomeev, E., Goncharov, T., Maeker, H., Zobel, K., Kömüves, L.G., Deshayes, K., and Vucic, D. (2012). Cellular inhibitors of apoptosis are global

- regulators of NF- κ B and MAPK activation by members of the TNF family of receptors. *Sci. Signal.* 5, ra22.
- Vince, J.E., and Silke, J. (2006). TWEAK shall inherit the earth. *Cell Death Differ.* 13, 1842–1844.
- Vince, J.E., Wong, W.W., Khan, N., Feltham, R., Chau, D., Ahmed, A.U., Benetatos, C.A., Chunduru, S.K., Condon, S.M., McKinlay, M., et al. (2007). IAP antagonists target cIAP1 to induce TNFalpha-dependent apoptosis. *Cell* 131, 682–693.
- Vince, J.E., Chau, D., Callus, B., Wong, W.W., Hawkins, C.J., Schneider, P., McKinlay, M., Benetatos, C.A., Condon, S.M., Chunduru, S.K., et al. (2008). TWEAK-Fn14 signaling induces lysosomal degradation of a cIAP1-TRAF2 complex to sensitize tumor cells to TNFalpha. *J. Cell Biol.* 182, 171–184.
- Wallengren, O., Lundholm, K., and Bosaeus, I. (2013). Diagnostic criteria of cancer cachexia: relation to quality of life, exercise capacity and survival in unselected palliative care patients. *Support. Care Cancer* 21, 1569–1577.
- Walsh, D., Donnelly, S., and Rybicki, L. (2000). The symptoms of advanced cancer: relationship to age, gender, and performance status in 1,000 patients. *Support. Care Cancer* 8, 175–179.
- Warren, S. (1932). The immediate cause of death in cancer. *Am. J. Med. Sci.* 184, 610–613.
- Wiley, S.R., Cassiano, L., Lofton, T., Davis-Smith, T., Winkles, J.A., Lindner, V., Liu, H., Daniel, T.O., Smith, C.A., and Fanslow, W.C. (2001). A novel TNF receptor family member binds TWEAK and is implicated in angiogenesis. *Immunity* 15, 837–846.
- Winkles, J.A. (2008). The TWEAK-Fn14 cytokine-receptor axis: discovery, biology and therapeutic targeting. *Nat. Rev. Drug Discov.* 7, 411–425.
- Zhou, X., Wang, J.L., Lu, J., Song, Y., Kwak, K.S., Jiao, Q., Rosenfeld, R., Chen, Q., Boone, T., Simonet, W.S., et al. (2010). Reversal of cancer cachexia and muscle wasting by ActRIIB antagonism leads to prolonged survival. *Cell* 142, 531–543.

Broadly Neutralizing Antibody 8ANC195 Recognizes Closed and Open States of HIV-1 Env

Graphical Abstract



Authors

Louise Scharf, Haoqing Wang, Han Gao,
Songye Chen, Alasdair W. McDowell,
Pamela J. Bjorkman

Correspondence

bjorkman@caltech.edu

In Brief

Broadly neutralizing antibodies against the HIV-1 envelope trimer are under consideration for therapeutic administration. Structural analysis of one such antibody, 8ANC195, uncovers a previously unseen conformation of the envelope protein and suggests that 8ANC195 binding partially closes the host receptor-bound open envelope trimer conformation.

Highlights

- 3.58 Å structure of 8ANC195-Env trimer defines the gp120-gp41 site of HIV vulnerability
- EM structure shows 8ANC195 binds Env trimer in CD4-bound partially open state
- 8ANC195 partially reverses CD4-induced open Env conformation
- Binding closed and open Env suggests neutralization of free and cell-bound virus

Accession Numbers

5CJX

Broadly Neutralizing Antibody 8ANC195 Recognizes Closed and Open States of HIV-1 Env

Louise Scharf,¹ Haoqing Wang,¹ Han Gao,¹ Songye Chen,¹ Alasdair W. McDowall,^{1,2} and Pamela J. Bjorkman^{1,*}

¹Division of Biology and Biological Engineering, California Institute of Technology, Pasadena, CA 91125, USA

²Howard Hughes Medical Institute, California Institute of Technology, Pasadena, CA 91125, USA

*Correspondence: bjorkman@caltech.edu

<http://dx.doi.org/10.1016/j.cell.2015.08.035>

SUMMARY

The HIV-1 envelope (Env) spike contains limited epitopes for broadly neutralizing antibodies (bNAbs); thus, most neutralizing antibodies are strain specific. The 8ANC195 epitope, defined by crystal and electron microscopy (EM) structures of bNAb 8ANC195 complexed with monomeric gp120 and trimeric Env, respectively, spans the gp120 and gp41 Env subunits. To investigate 8ANC195's gp41 epitope at higher resolution, we solved a 3.58 Å crystal structure of 8ANC195 complexed with fully glycosylated Env trimer, revealing 8ANC195 insertion into a glycan shield gap to contact gp120 and gp41 glycans and protein residues. To determine whether 8ANC195 recognizes the CD4-bound open Env conformation that leads to co-receptor binding and fusion, one of several known conformations of virion-associated Env, we solved EM structures of an Env/CD4/CD4-induced antibody/8ANC195 complex. 8ANC195 binding partially closed the CD4-bound trimer, confirming structural plasticity of Env by revealing a previously unseen conformation. 8ANC195's ability to bind different Env conformations suggests advantages for potential therapeutic applications.

INTRODUCTION

The envelope (Env) spike of HIV-1, a trimer of gp120-gp41 heterodimers, is the only target of neutralizing antibodies (Abs) and therefore the focus of vaccine design efforts. The discovery of highly potent broadly neutralizing antibodies (bNAbs) isolated from a subset of HIV-1-infected donors has brought new impetus to the idea of delivering bNAbs passively to protect against or treat HIV-1 infection. bNAbs have been shown to prevent and treat infection in mouse and macaque models (reviewed in West et al., 2014) and exhibited efficacy against HIV-1 in a human clinical trial (Caskey et al., 2015). Defining the epitopes and neutralization mechanisms of anti-HIV-1 bNAbs provides critical information for selecting combinations of bNAbs for passive delivery efforts and for design of immunogens to elicit similar Abs in a vaccine and can illuminate the complex process of viral entry.

Until recently, the HIV-1 Env spike was considered to have four defined bNAb epitopes: three on the gp120 subunit (the V1V2-glycan epitope at the apex of the Env trimer, the V3-loop region centered on the Asn₃₃₂_{gp120} oligomannose patch, and the binding site for the host receptor CD4) and the fourth involving the gp41 membrane-proximal external region (MPER) (reviewed in West et al., 2014). Within the last year, three Abs were discovered to target distinct regions of the gp120-gp41 interface. Two of the subunit-spanning bNAbs, PGT151 and 35O22, are trimer specific and do not bind to gp120 monomers (Blattner et al., 2014; Huang et al., 2014). The gp120-gp41-spanning bNAb 8ANC195 binds both to gp120 monomers and gp140 trimers (Scharf et al., 2014; Scheid et al., 2011).

8ANC195 was originally isolated in a screen that identified many CD4-binding site (CD4bs) Abs, but its epitope did not map as a conventional CD4bs bNAb (Scheid et al., 2011). We used computational analyses of neutralization data to predict that intact potential N-linked glycosylation sites at positions 234_{gp120} and 276_{gp120} are essential for the activity of 8ANC195, suggesting that the epitope was near, but not within, the CD4bs on gp120 (West et al., 2013). A 3.0 Å resolution crystal structure of 8ANC195 Fab and CD4 domains 1 and 2 (sCD4) bound to a gp120 core revealed extensive contacts with N-linked glycans attached to Asn₂₃₄_{gp120} and Asn₂₇₆_{gp120} and defined a site of Env vulnerability involving glycans and the gp120 inner domain that is not targeted by other bNAbs (Scharf et al., 2014). Finally, negative-stain single-particle electron microscopy (EM) reconstruction of a native-like soluble Env trimer (BG505 SOSIP.664, hereafter referred to as BG505 SOSIP [Sanders et al., 2013]) complexed with three 8ANC195 Fabs confirmed the binding site on gp120 and further suggested that 8ANC195 spanned the gp120-gp41 subunit interface to contact gp120 with its heavy chain (HC) and gp41 with its light chain (LC) (Scharf et al., 2014). These structural studies suggested that 8ANC195 did not inhibit HIV-1 infection by blocking the CD4bs on gp120 (indeed, the crystal structure demonstrated simultaneous binding of sCD4 and 8ANC195 Fab) but, rather, that recognition of both Env subunits by 8ANC195 could facilitate neutralization by preventing conformational changes required for gp41-mediated fusion of the host cell and viral membranes.

However, the precise nature of the 8ANC195 epitope on gp41 could not be elucidated due to the low resolution of the 8ANC195-BG505 SOSIP EM structure; nor was it known whether 8ANC195 would block or accommodate conformational changes in Env trimers upon CD4 binding. To address these

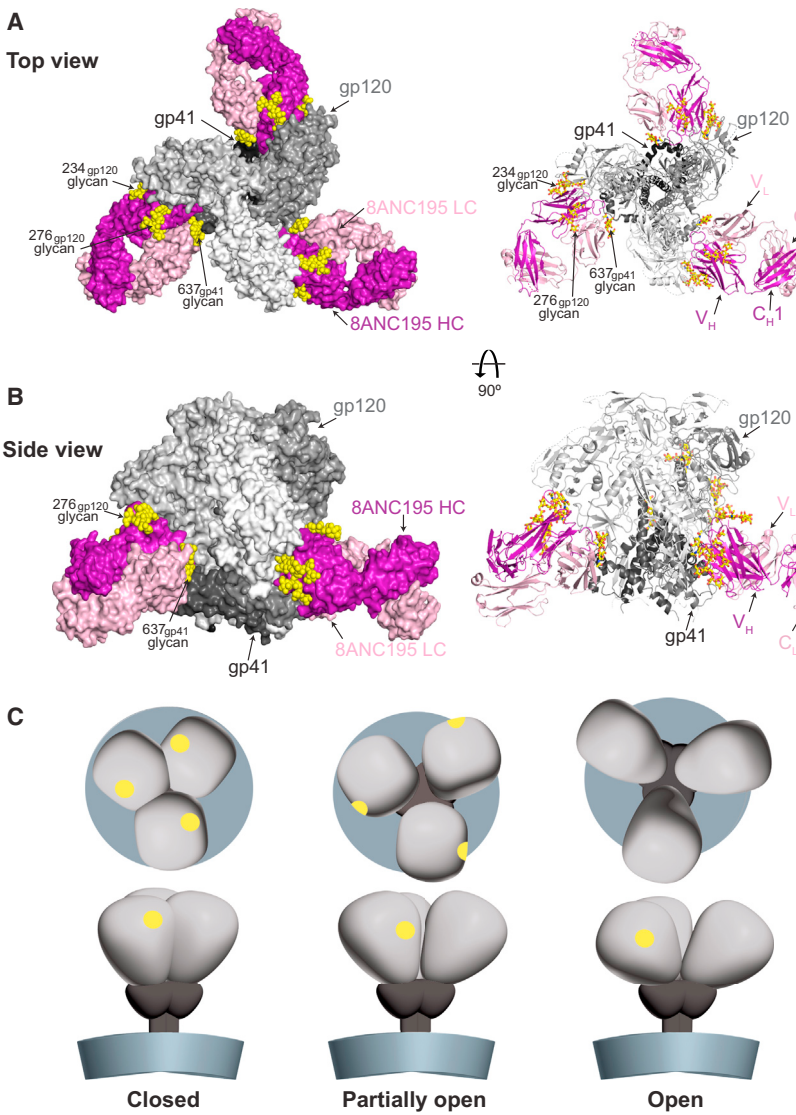


Figure 1. Overview of 8ANC195_{G52K5}-BG505 SOSIP Structure

8ANC195_{G52K5} Fabs are dark pink (HC) and light pink (LC), gp120 subunits are different shades of light gray, and gp41 subunits are different shades of dark gray. N-linked glycans at the Fab-trimer interface are yellow.

(A) 8ANC195_{G52K5}-Env structure seen from the top in space-filling (left) and ribbon diagram (right) representations.

(B) 8ANC195_{G52K5}-Env structure seen from the side in space-filling (left) and ribbon diagram (right) representations.

(C) Conformations of HIV-1 Env trimers shown schematically (adapted from figures in Liu et al., 2008) as seen from above (top) and the side (bottom) (CD4-binding site, yellow; remainder of gp120, light gray; gp41, dark gray; membrane, blue-gray). The closed structure was observed for unliganded virion-bound trimers (Liu et al., 2008) and structures involving liganded BG505 SOSIP trimers (Julien et al., 2013a; Lyumkis et al., 2013; Pancera et al., 2014). The partially open structure was observed for virion-bound trimers associated with b12 or A12 (Liu et al., 2008). Open structures were observed for trimers associated with CD4 or the Fab from the CD4-induced Ab 17b (Merk and Subramanian, 2013).

See also Figure S1 and Table S1.

conformational change on its target antigen benefits an anti-HIV-1 bNAb.

RESULTS

Characterization of Complete 8ANC195 Epitope in the Context of HIV-1 Env Trimer

To elucidate the complete 8ANC195 epitope on Env trimer at atomic resolution, we solved a 3.58 Å resolution crystal structure of a more potent 8ANC195 variant, γ52_{HCK5}LC (Scharf et al., 2014)

questions, we solved a crystal structure of an 8ANC195-BG505 SOSIP complex to define the 8ANC195 epitope at the gp120-gp41 interface at atomic resolution, allowing structural comparison of a subunit-spanning bNAb bound to a gp120 monomer and to a gp140 Env trimer. Furthermore, we used binding studies to show that 8ANC195 can recognize CD4-bound Env trimers; thus, the conformational changes induced by CD4 binding do not preclude 8ANC195 recognition of the gp120-gp41 interface. To visualize the conformational state of Env trimer bound to both CD4 and 8ANC195, we used three-dimensional (3D) EM reconstruction to demonstrate that 8ANC195 binding prevents the full opening of Env trimer that is associated with the conformational change induced by CD4 to allow subsequent co-receptor binding and fusion of host and viral membranes. These studies provide structural and biochemical evidence of a bNAb recognizing both the closed and open conformational states of HIV-1 Env and suggest that the ability to accommodate

(hereafter referred to as 8ANC195_{G52K5}), complexed with BG505 SOSIP (Figure 1 and Table S1). Trimers were expressed in kifunensine-treated HEK cells to yield protein containing Man₈₋₉GlcNAc₂ high-mannose N-glycans (Elbein et al., 1990) at all potential N-linked glycosylation sites (pseudoviruses containing only high-mannose glycans or mixtures of high-mannose and complex glycans were neutralized equivalently by 8ANC195_{G52K5}; Table S3). Crystallization trials were conducted with complexes of BG505 SOSIP, sCD4, and 8ANC195_{G52K5} Fab produced by first purifying BG505 SOSIP complexed with sCD4 by size exclusion chromatography (SEC) (Figures S1A and S1B), adding 8ANC195_{G52K5} Fab, and then repeating the SEC to purify the ternary complex (Figure S1C). Although the crystallization drops contained all three proteins, resulting crystals did not include sCD4 (Figure S1D), and electron density maps showed density only for one BG505 SOSIP and three 8ANC195_{G52K5} Fabs per asymmetric unit. When we docked

three copies of sCD4 in the appropriate location on BG505 SOSIP by aligning the gp120-sCD4 portion of the 8ANC195-gp120-sCD4 complex structure (PDB: 4P9H) with gp120 in the trimer portion of 8ANC195_{G52K5}-BG505 SOSIP structure and refined their all-atom occupancies, the occupancies of sCD4 atoms refined toward zero, confirming the absence of sub-stoichiometric amounts of sCD4 in the crystals.

The 8ANC195_{G52K5}-BG505 SOSIP structure revealed the variable heavy (V_H), variable light (V_L), and constant heavy and light (C_H and C_L) domains of three Fabs bound at the gp120-gp41 interface of an Env trimer (Figures 1A and 1B). The trimer is in the closed, prefusion state, similar to the conformation of BG505 SOSIP in previous crystal and EM structures (Julien et al., 2013a; Do Kwon et al., 2015; Lyumkis et al., 2013; Pancera et al., 2014) and as revealed for bNAb-bound BG505 SOSIP by hydrogen-deuterium exchange (Guttman et al., 2015), rather than the open conformation observed in EM structures of both virion-associated and soluble Env trimers, including sCD4 or the CD4-induced Ab 17b (Harris et al., 2011; Liu et al., 2008; Sanders et al., 2013; Tran et al., 2012) (Figure 1C). Since no Abs were bound to the apex of the trimer in our crystals, by contrast with previous crystal structures of BG505 SOSIP bound to PGT122 (Julien et al., 2013a) or PGT122 and 35O22 (Pancera et al., 2014), the V1/V2 loops of the trimer in the 8ANC195_{G52K5}-BG505 SOSIP structure are less ordered (Figure S1E). However, well-resolved regions of the trimer showed no major structural rearrangements compared with a previous structure of similar resolution (PDB: 4TVP) (Figure S1E). Trimers for previous crystal structures contained only high-mannose *N*-linked glycans that were treated with EndoH to truncate accessible *N*-linked glycans to a single *N*-acetyl glucosamine (NAG) (Julien et al., 2013a; Do Kwon et al., 2015; Pancera et al., 2014), whereas our trimer structure includes all potential *N*-linked glycans in an untruncated form. Nevertheless, we observed no major conformational changes compared with previous structures, with the exception of some disordering of the trimer apex, likely due to the lack of stabilization by crystal contacts or Fab binding to this region.

The placement of the 8ANC195_{G52K5} V_H domain relative to the gp120 subunit of gp140 was relatively close to that observed in the 8ANC195-gp120-sCD4 complex structure ($C\alpha$ rmsd of 2.1 Å; all V_H residues), with closest agreement at the 8ANC195_{G52K5}-gp120 interface (Figure S2A). The interactions with gp120 are reproduced in the context of the trimer, including contacts with protein residues in the gp120 inner domain and with *N*-linked glycans at Asn234_{gp120} and Asn276_{gp120} (Figures 2A, 2B, and 3 and Table S2). The Asn276_{gp120} glycan, normally complex type in native HIV-1 Envs (Binley et al., 2010; Go et al., 2011), is high mannose in the crystallized Env trimer. This gp120 glycan forms an interface with framework region residues in V_H domain strands A and B and the N-terminal portion of CDRH1 using only the core pentasaccharide common to both high-mannose and complex-type *N*-glycans (Scharf et al., 2014), which we suggested is an adaptation to recognize both complex-type and high-mannose glycans at a particular *N*-linked glycosylation site on Env (Mouquet et al., 2012; Scharf et al., 2014). The overall conformation of V_H is conserved ($C\alpha$ rmsd of 0.67 Å after aligning all V_H residues). However, there are rearrangements in the residues of the third complementarity determining region of the

HC (CDRH3) to accommodate and interact with gp41 (Figures 2B, 3, S2C, and S2D). Furthermore, V_L is shifted slightly from the position observed in the 8ANC195-gp120-sCD4 structure, also to accommodate and interact with gp41 (Figures 2B, 3, S2C, and S2D). Compared with the low-resolution EM reconstruction (Scharf et al., 2014), the 8ANC195_{G52K5}-BG505 SOSIP crystal structure shows a closer interaction of the Fab and trimer, confirming the Fab placement observed in the complex structure with gp120 (Figure S2E).

As described previously, 8ANC195 contacts a large epitope on gp120 alone (3,750 Å² of total buried surface area in gp120-8ANC195-sCD4 structure [Scharf et al., 2014]). The interface on gp120 is 3,835 Å² in the context of the trimer (Figures 2A and 2B and Table S2), and contacts with gp41 make the 8ANC195_{G52K5} epitope more extensive, adding 1,810 Å² total buried surface area between gp41 and the Fab (485 Å² between gp41 and HC; 1,325 Å² between gp41 and LC). 771 Å² of this interface is between the LC and the Asn637_{gp41} glycan, which is ordered to the branching mannose (MAN) residue in the core pentasaccharide (NAG-NAG-MAN) (Figures 2C and 3). The first CDR of the LC, CDRL1, stabilizes CDRH3 and interacts with residues near the kink in α 9_{gp41} (nomenclature for gp41 secondary structures as in Pancera et al., 2014) and residues 613_{gp41}-615_{gp41} in a loop N terminal to α 8_{gp41} that is positioned underneath the kink in α 9_{gp41} at Asn637_{gp41} (Figures 2C and 3). This interaction rationalizes our previous observation that a germline (gl) reversion that altered two residues and removed one from CDRL1 (T30S_{LC}, G30aΔ_{LC}, N31S_{LC}) drastically decreased the potency of 8ANC195 (Scharf et al., 2014), possibly because Gly30a_{LC} introduces a kink in CDRL1 that allows the mature Ab to engage and accommodate this region of gp41. The second LC CDR, CDRL2, mainly accommodates the Asn637_{gp41} glycan (Figure 2C). A conservative two-residue gl reversion in this loop (G51A_{LC}, A52S_{LC}) caused a large decrease in neutralization potency (Scharf et al., 2014), likely because the loop in the mature Ab containing Gly51_{LC}-Ala52_{LC} is more compact and flexible, allowing the LC to avoid clashes with the Asn637_{gp41} glycan. Thr30_{LC} is within hydrogen-bonding distance of Glu634_{gp41} and Ser615_{gp41} side chains and the backbone carbonyl oxygen of Tyr638_{LC}. Other LC residues in CDRL1 and CDRL2 in the vicinity of gp41 could participate in water-mediated H bonds (Asn31_{LC}, Trp32_{LC}, Arg50_{LC}, Gly51_{LC}, and Leu54_{LC}), but we cannot place water molecules at the current resolution.

To determine the functional importance of gp41 contacts by 8ANC195, we assessed the effects of alanine mutants of 8ANC195 HC and LC residues located in the vicinity of gp41 in the 8ANC195_{G52K5}-BG505 SOSIP structure (Table S3 and Figure 3). 8ANC195 IgG mutants W32A_{LC}, Y49A_{LC}, and Y91A_{LC} showed decreased neutralization potencies against HIV-1 strains YU2 and BG505, and W100aA_{HC} showed slightly decreased potency against YU2 (Table S3). These results are rationalized by the complex structure (Figure 3): Trp100a_{HC}, conserved in all 8ANC195-related HCs (Scharf et al., 2014), inserts its side chain into a hydrophobic pocket at the gp120-gp41 interface, suggesting that the loss of this interaction reduces the binding energy. The W32A_{LC} mutation resulted in a complete loss of neutralization potency against YU2 and BG505. Trp32_{LC} makes no direct contacts with gp41 but could

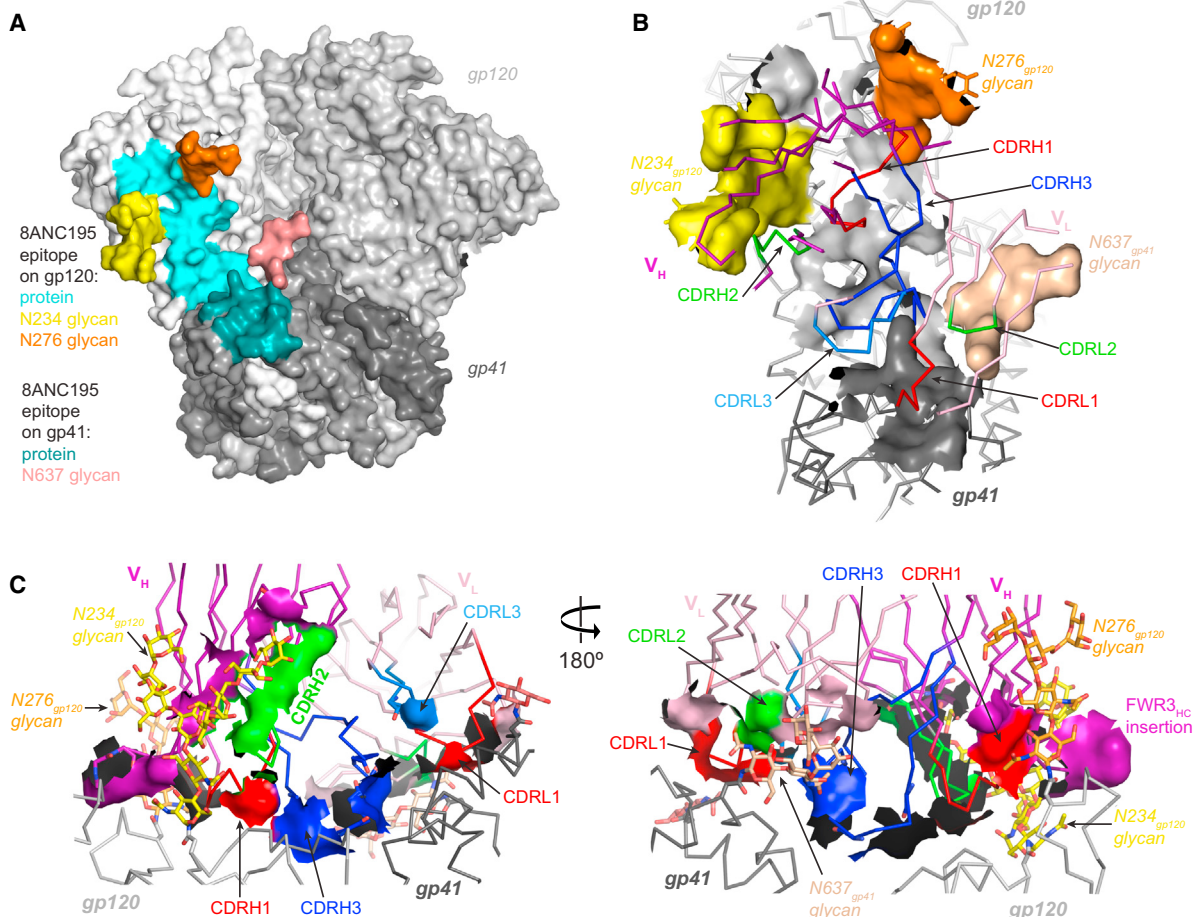


Figure 2. Interfaces in 8ANC195_{G52K5}-BG505 SOSIP Structure

(A) 8ANC195_{G52K5} epitope. BG505 SOSIP is shown in space-filling representation with the gp120 and gp41 portions of one protomer in white and medium gray, respectively (other two protomers are light gray). Glycan and protein portions of the 8ANC195_{G52K5} epitope are highlighted in the indicated colors on one protomer.

(B) Close-up of contact areas. Relevant portions of 8ANC195_{G52K5} are shown in wire representation with atoms within buried surface areas on BG505 SOSIP shown as colored surfaces.

(C) Details of interactions with glycans on gp120 and gp41. Buried surface areas on 8ANC195_{G52K5} are shown as colored surfaces. See also Figure S2 and Table S2.

engage in water-mediated H bonds with Glu634_{gp41}. In addition, it makes stacking interactions with His100f_{HC} side chain, likely stabilizing the complicated CDRH3 conformation involved in gp120 interactions (Scharf et al., 2014). The hydroxyl group of Tyr49_{LC} is within hydrogen-bonding distance of the branching mannose of the Asn637_{gp41} glycan, potentially allowing the Ab to accommodate this conserved glycan, and the ring portion of the side chain makes hydrophobic interactions with Leu100d_{HC}, potentially stabilizing the CDRH3 conformation. The hydroxyl group of Tyr91_{LC} forms H bonds with Gly100c_{HC} and Lys50_{LC}, again stabilizing the CDRH3 conformation.

Effects of N-Linked Glycans Attached to gp41 on Neutralization by 8ANC195

To further explore the roles of N-linked glycans within the 8ANC195 epitope on gp41, we evaluated the effects of

removing glycans attached to Asn611_{gp41}, Asn625_{gp41}, and Asn637_{gp41} (by one, two, or three Asn-Gln mutations) on YU2 pseudovirus neutralization by WT 8ANC195 and partially gl-reverted chimeric Abs.

Neutralization by 8ANC195 did not depend strongly upon the presence of glycans attached to Asn611_{gp41}, Asn625_{gp41}, or Asn637_{gp41} (Table S4). However, glycan recognition may play a more prominent role during maturation of 8ANC195 from its gl progenitor, as evidenced by neutralization behaviors of partial gl chimeric LCs. 8ANC195 containing a gl reversion that altered two residues and removed one from CRDL1 (T30S_{LC}, G30aΔ_{LC}, N31S_{LC}) (8ANC195 glCDRL1) exhibited >130-fold reduced neutralization potency against YU2 compared to the fully mature Ab, but its neutralization capacity was completely ablated if the Env target lacked glycosylation at Asn611_{gp41} or Asn625_{gp41}. These glycans may have partially stabilized Ab binding in

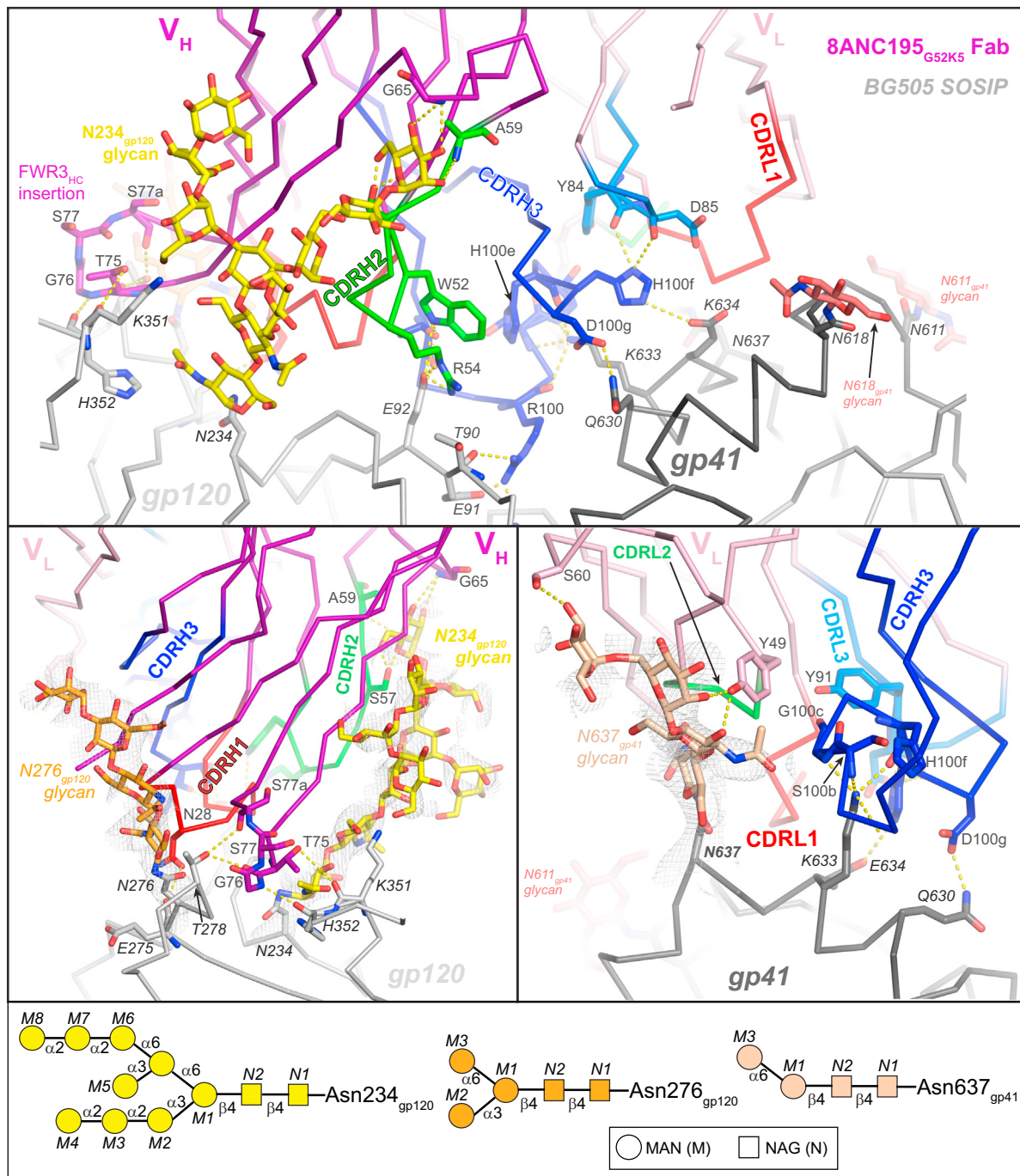


Figure 3. Contacts between 8ANC195_{G52K5} Fab and BG505 SOSIP Protein Residues and Glycans

Proteins are shown as C α traces with interface residues as sticks (oxygen, red; nitrogen, blue). CDRs and framework regions (FWRs) of 8ANC195_{G52K5} at the interface are highlighted and labeled. Putative H bonds are shown as yellow dots. Env glycans at the interface are yellow (Asn234_{gp120}), orange (Asn276_{gp120}), and tan (Asn637_{gp41}) and are enclosed in electron density from a 2F $_o$ -F $_c$ simulated annealing omit map contoured at 1.0 σ (gray mesh) in the lower structure panels. Schematic structures of the ordered portions of these N-linked glycans are shown at the bottom. See also Tables S3 and S4.

progenitors of the mature 8ANC195, which would have had shortened CDRL1 loops in addition to two amino acid substitutions. Conversely, glycosylation at Asn637_{gp41} may destabilize

binding of progenitor Abs since neutralization potency of 8ANC195 gICDR1 against YU2 was partially restored (16-fold) when the Asn637_{gp41} site was knocked out. The destabilizing

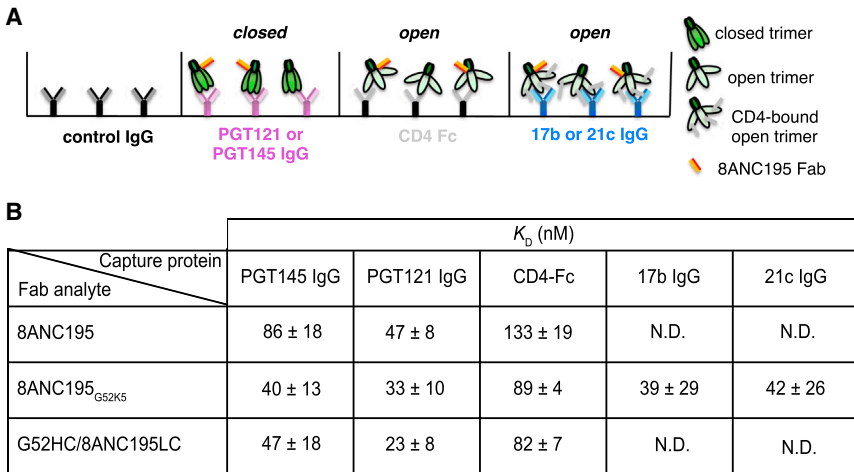


Figure 4. Effects of Env Trimer Conformational State on Binding Affinity of 8ANC195

(A) Schematic representation of coupled surfaces and injected analytes. A control IgG (mG053), an IgG recognizing closed trimers (PGT121 or PGT145), CD4-Fc (recognizing open trimers), and a CD4-induced Ab (17b or 21c) recognizing open CD4-bound trimers were immobilized on separate flow cells of a biosensor chip. BG505 SOSIP trimers were injected, resulting in binding to surfaces except for the control flow cell. 8ANC195, 8ANC195_{G52K5}, or a G52HC/8ANC195LC chimera Fab was then injected over the IgG-BG505 SOSIP complex.

(B) Summary of affinities (K_D values; reported as mean ± SD for three independent experiments) for combinations of capture proteins and analytes. Since PGT145 indirectly inhibited binding of 8ANC195 to BG505 SOSIP trimers and PGT121 enhanced 8ANC195 binding (Derking et al., 2015), our affinity measurements likely underestimated (PGT145-captured trimers) or overestimated (PGT121-captured trimers) the affinity of 8ANC195 for closed trimer. N.D., not determined.

See also Figure S3.

influence of Asn637_{gp41} glycosylation had a greater effect than stabilizing influences of Asn611_{gp41} and Asn625_{gp41} glycans, as the net effect in double or triple knockouts involving Asn637_{gp41} was only partial restoration of neutralizing activity. In the case of a target with an Asn611_{gp41}/Asn637_{gp41} double knockout, neutralization by 8ANC195 gICDR1 was improved by >30-fold and was brought to within the same order of magnitude as mature 8ANC195.

8ANC195 containing a conservative two-residue gl reversion in CDRL2 (G51A_{LC}, A52S_{LC}) (8ANC195 gICDR2) was ~16-fold reduced in neutralization potency compared to the mature Ab; its remaining potency was further diminished by 8.6-fold if the YU2 Env lacked glycosylation at Asn625_{gp41} but was partially restored (1.8-fold) if it lacked glycosylation at Asn637_{gp41}. The restorative effect of the knockout of Asn637_{gp41}-linked glycosylation was again dominant over effects of also removing Asn625_{gp41}-linked glycan in a double knockout. The knockout of Asn611_{gp41}-linked glycosylation had only a minor effect on neutralization by 8ANC195 gICDR2 but amplified the restorative effect of the Asn637_{gp41} knockout from 1.8-fold to >8-fold in the double and triple knockouts. The CDRL2 loop lies in apposition to the glycan attached to Asn637_{gp41} in the 8ANC195_{G52K5}-BG505 SOSIP crystal structure and ~15 Å from the Asn611_{gp41} glycosylation site (Figure 3). Given the closer proximity of CDRL2 to the Asn637_{gp41} glycan, interactions between the two might be influenced synergistically by a loss of glycosylation at Asn611_{gp41}. In the case of a chimeric Ab containing the mature 8ANC195 HC and a gl LC (8ANC195 mHC/glLC), which had a 19-fold reduced neutralization potency against YU2, a stabilizing effect of Asn611_{gp41} glycosylation and destabilizing effect of Asn637_{gp41} glycosylation were evident in several of the pairings.

These results are consistent with Asn637_{gp41} glycosylation interfering with neutralization of a partially immature 8ANC195, Asn625_{gp41} glycosylation enhancing neutralization,

and Asn611_{gp41} glycosylation having positive or detrimental effects depending on complex factors. Mature 8ANC195 may have evolved promiscuity toward recognition of viruses containing or lacking glycans at these positions. Such viruses may be present in a viral swarm containing many mutated viruses. The evolution of promiscuous recognition may have arisen through layers of redundancy in stabilizing interactions that are only revealed on partial reversion to the gl form. Thus, we speculate that mature 8ANC195 accommodates, rather than productively interacts with, at least some of the gp41 glycans.

8ANC195 Binds CD4-Bound Env Trimers

We previously showed that 8ANC195 and sCD4 can bind simultaneously to monomeric gp120 and that addition of sCD4 did not detectably alter the in vitro neutralization potency of 8ANC195 (Scharf et al., 2014). sCD4 binding has little to no effect on the structures of monomeric gp120 cores (Kwon et al., 2012) but results in rotation of gp120 protomers to create an open structure in virion-bound Env trimers and SOSIP gp140s, including BG505 SOSIP (Harris et al., 2011; Liu et al., 2008; Sanders et al., 2013; Tran et al., 2012) (Figure 1C). Although sCD4 does not preclude binding of 8ANC195 to gp120, changes between the closed and open states of trimeric Env at the gp120-gp41 interface could disrupt the 8ANC195 epitope on open Env trimers.

To determine whether 8ANC195 can bind sCD4-bound open Env trimers, we used SPR to evaluate binding to different trimer conformational states. For these experiments, we immobilized IgGs on a biosensor chip that captured BG505 SOSIP trimers with different bNAbs: PGT145 and PGT121, which bind to closed Env (Julien et al., 2013a; Pancera et al., 2014; Pugach et al., 2015); CD4-Fc (Capon et al., 1989), which should capture open trimers; and CD4-induced Abs 17b and 21c (Sullivan et al., 1998; Xiang et al., 2002), which should capture sCD4-bound open trimers (Figures 4A and S3). 17b Fab induces opening of some Env trimers in the absence of CD4 binding (Tran et al.,

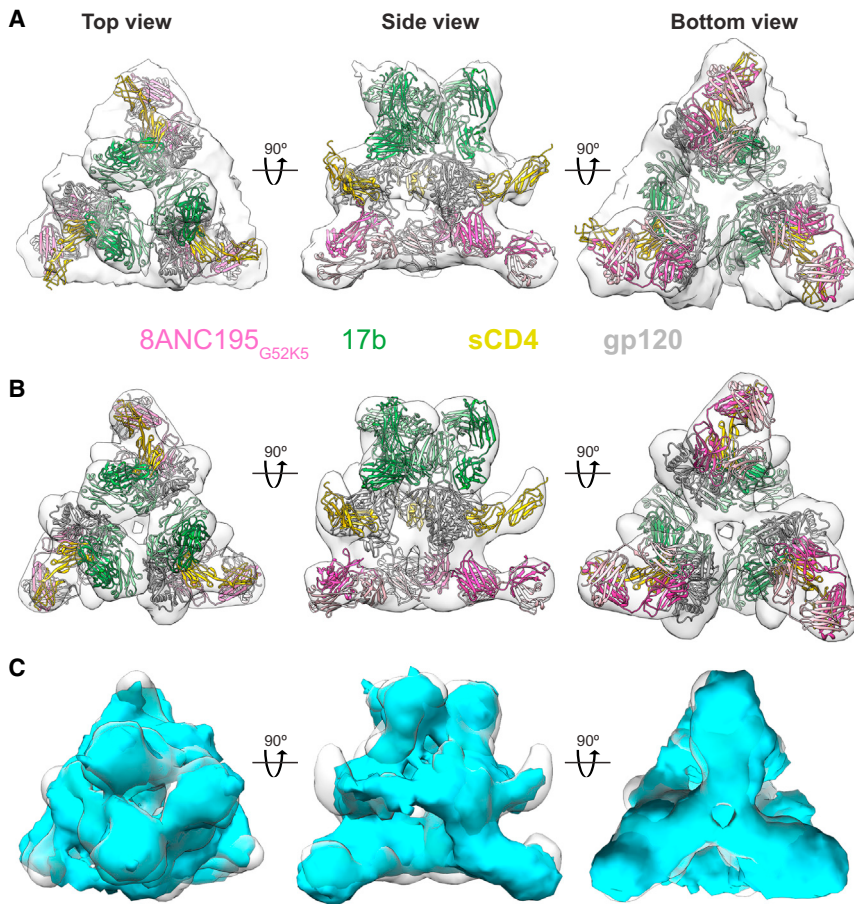


Figure 5. EM Reconstructions of BG505 SOSIP-sCD4-17b-8ANC195_{G52K5} Complex

The X-ray structures of a gp120-sCD4-17b complex (PDB: 1RZK) and 8ANC195 Fab (PDB: 4P9M) were fit to EM densities and are shown from the top, side, and bottom.

(A) ~23 Å resolution EM density derived from cryo-ET and sub-tomogram averaging.

(B) ~17 Å resolution EM density derived from negative-stain single-particle reconstruction.

(C) Superposition of densities from cryo-ET/sub-tomogram averaging (cyan) and negative-stain single-particle (light gray) reconstructions.

See also Figures S4 and S5.

8ANC195 Recognizes a Partially Open Env Trimer in the Presence of sCD4 and 17b

Having shown that it is possible for 8ANC195/8ANC195_{G52K5} to recognize CD4-bound BG505 SOSIP trimers, we sought to determine how this class of Ab accommodates conformational changes involved in transitioning from the closed to open trimeric state (Figure 1C). We prepared complexes of BG505 SOSIP trimers, sCD4, 17b Fab, and 8ANC195_{G52K5} Fab for EM structure determinations (Figures 5, 6, S4, and S5), reasoning that binding of 17b Fab to a CD4-bound open trimer would prevent a potential full reversion to a closed trimeric conformation since it is not possible to

2012), but 17b does not bind to BG505 SOSIP unless sCD4 is present (Sanders et al., 2013), and the 21c epitope includes portions of CD4 as well as gp120 (Diskin et al., 2010). Thus, both CD4-induced Abs will only bind to sCD4-BG505 SOSIP complexes.

8ANC195 and 8ANC195_{G52K5} Fabs were injected over the trimer-bound surface to determine their affinities for BG505 SOSIP in its closed and open states. 8ANC195, 8ANC195_{G52K5}, and a chimeric Fab differing from 8ANC195 only in the K100R_{HC} mutation (8ANC195_{G52K5} HC/8ANC195 LC) bound to closed trimer with slightly higher affinities than to CD4-Fc-bound open trimer (Figures 4B and S3). No decrease in affinity was observed for 8ANC195_{G52K5} binding to CD4-bound BG505 SOSIP captured by 17b or 21c, perhaps reflecting stabilization of the 8ANC195_{G52K5}-sCD4-BG505 SOSIP complex by the CD4-induced Abs.

We also attempted to determine a binding affinity for the interaction between 8ANC195 IgG-bound BG505 SOSIP trimers and sCD4. In reciprocal experiments to those described above, sCD4 was injected over 8ANC195-captured trimers. Only weak binding that could not be fit to a binding model was observed (Figure S3). Since sCD4 binds to unliganded BG505 SOSIP (Julien et al., 2013b) (Figures S1A and S1B), this result suggests that pre-binding of 8ANC195 to Env diminishes its ability to interact with CD4.

accommodate three 17b Fabs at the apex of a closed gp140 trimer (Figure 6A). To ensure that the trimers were in an open conformation when given the opportunity to bind 8ANC195_{G52K5}, we first purified BG505 SOSIP-sCD4-17b complexes by SEC, added 8ANC195_{G52K5} Fab, and then subjected the four-component mixture to SEC again, obtaining stable quaternary complexes, as confirmed by SDS-PAGE (Figure S4A).

In order to obtain a reference-free reconstruction of the BG505 SOSIP-sCD4-17b-8ANC195_{G52K5} complex that included no assumptions about trimer conformation or how many ligands were bound, we initially determined a ~23 Å structure by sub-tomogram averaging of cryoelectron tomography (cryo-ET) data obtained from 3D reconstruction of a tilt series of two-dimensional (2D) projection images (Figures 5A and S4). With no model or symmetry imposed, the sub-tomogram-averaged structure showed a 3-fold symmetric particle with densities for three 17b Fabs at the apex, three sCD4 molecules around the middle, and three 8ANC195_{G52K5} Fabs at the bottom. Since a co-crystal structure of gp120-sCD4-17b can be fit as a unit into EM structures of open CD4-bound Env trimers (Harris et al., 2011; Liu et al., 2008; Sanders et al., 2013), we first fit the density with gp120-sCD4-17b coordinates (PDB: 1RZK), resulting in a 3-fold symmetric distribution of gp120, sCD4, and 17b. We next fit 8ANC195 Fab (PDB: 4P9M) into three protruding densities at the predicted gp120-gp41-spanning epitope.

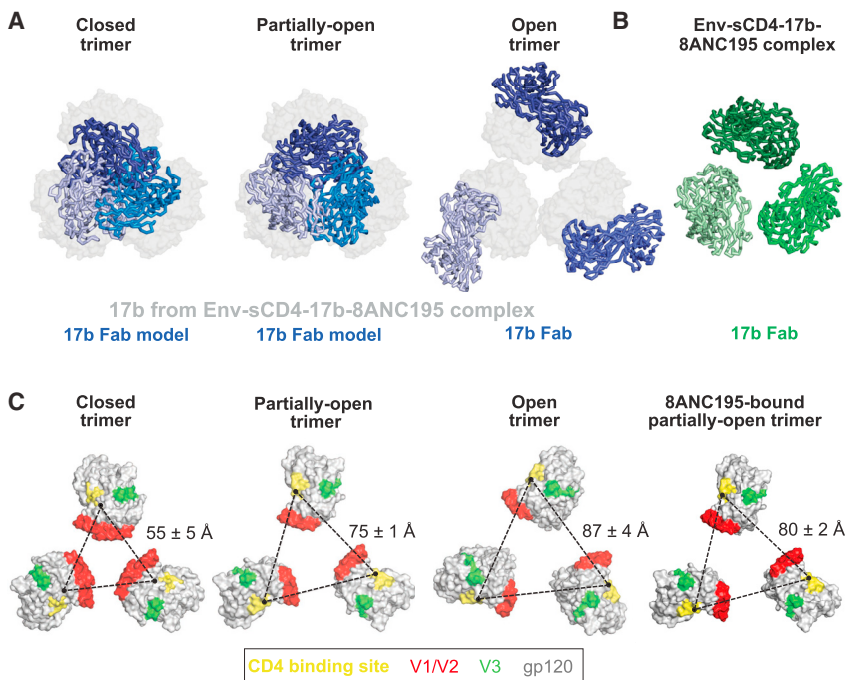


Figure 6. Comparison of Different Conformations of Env Trimers in BG505 SOSIP-sCD4-17b-8ANC195_{G52K5} and Other Env Trimer Complexes Illustrated by 17b and gp120 Positions

(A) Overlay of 17b Fabs from BG505 SOSIP-sCD4-17b-8ANC195_{G52K5} complex (gray space-filling representations) with 17b Fabs complexed with Env trimers in different conformational states (thick C α traces in shades of blue). 17b Fabs shown after superimposition of gp120s from trimers (trimers and other ligands not shown). (Left) 17b modeled onto 3DNN coordinates of a closed trimer. (Middle) 17b modeled onto 3DNL coordinates of a partly open trimer. (Right) 17b taken from 3DNO structure of a CD4- and 17b-bound open trimer. Note that three 17b Fabs cannot be accommodated without clashes when modeled onto the gp120s of closed and partly open trimer structures.

(B) C α trace of the three 17b Fabs from the BG505 SOSIP-sCD4-17b-8ANC195_{G52K5} complex.

(C) Positions of gp120s (gray space-filling representation with locations of CD4-binding site in yellow, V3 loop in green, and base of V1V2 domain in red) in Env trimers adopting the indicated conformations. The locations of Asp368_{gp120} are shown as a black dot for each trimer conformation, with the distance between the C α of this residue in adjacent protomers indicated. Distances are presented as the mean and SD for the analogous distance in representative structures in each conformation.

See also Figure S6 and Table S5.

To verify and extend the structural details, we next determined a negative-stain single-particle reconstruction of the BG505 SOSIP-sCD4-17b-8ANC195_{G52K5} complex at ~17 Å resolution (Figures 5B and S5). Potentially due to conditions during staining or drying of the grid or the low-sample concentrations necessary to obtain grids containing an optimal distribution of particles, not all complexes contained stoichiometric numbers of ligands. Therefore, we included a 3D classification procedure after reference-free 2D classification to sort particles containing the stoichiometric complex from sub-stoichiometric complexes, resulting in selection of approximately half of the initially selected particles from good 2D classes. The resulting reconstruction showed density for three copies each of 8ANC195_{G52K5}, 17b, and sCD4 bound to BG505 SOSIP, and we again fit the density using coordinates for gp120-sCD4-17b and 8ANC195 Fab structures (Figure 5B). The two reconstructions showed similar placements of three gp120s, three sCD4s, and six Fabs (Figures 5C). We used the higher-resolution single-particle reconstruction for subsequent analyses.

From comparisons with other Fab- and Fab-sCD4-Env structures, it is evident that the trimer in our BG505 SOSIP-sCD4-17b-8ANC195_{G52K5} structure is not in a closed conformation (Figure 6). As expected, given that the trimer is not closed, the placement of 8ANC195_{G52K5} in the EM structure is shifted somewhat from its placement in the 8ANC195_{G52K5}-BG505 SOSIP (closed trimer) crystal structure (Figure S6). To determine whether the trimer in the EM structure is fully open, we investigated the arrangement of 17b Fabs, noting that they are positioned differently in the BG505 SOSIP-sCD4-17b-

8ANC195_{G52K5} structure than in open trimer structures (Figures 6A and 6B) (Harris et al., 2011; Liu et al., 2008; Sanders et al., 2013; Tran et al., 2012), suggesting that the trimer in the BG505 SOSIP-sCD4-17b-8ANC195_{G52K5} complex is less open than in other sCD4-bound or 17b-bound structures. To more precisely describe the conformational state of the Env trimer in the BG505 SOSIP-sCD4-17b-8ANC195_{G52K5} complex, we measured distances between a CD4bs residue in each gp120 protomer of the trimer and compared them to the corresponding distances in structures of trimers in different conformational states (Figures 1C and 6C and Table S5). This comparison showed that the trimer in the BG505 SOSIP-sCD4-17b-8ANC195_{G52K5} structure adopts a previously unseen partially open state that is midway between a partially open state observed for Env bound to either b12 (a CD4bs Ab) or A12 VHH (a CD4bs llama Ab fragment) and the open state observed for the sCD4/17b-bound open trimer (Merk and Subramaniam, 2013). Thus, addition of 8ANC195_{G52K5} Fab to the BG505 SOSIP-sCD4-17b complex resulted in partial closure of the trimer, suggesting that stable 8ANC195_{G52K5} binding is incompatible with a fully open Env trimer conformation and would therefore block conformational changes leading to fusion between the viral and host membranes.

DISCUSSION

Here, we present an atomic resolution structure of 8ANC195_{G52K5} bound to BG505 SOSIP, a native-like soluble HIV-1 Env trimer in the closed, prefusion conformation. The

interface of 8ANC195_{G52K5} with Env trimer (5,645 Å² total buried surface area) is much larger than typical Ab-antigen complexes (Jones and Thornton, 1996), and 8ANC195 uses a large proportion of its accessible surface to engage its antigen, primarily using CDRs to contact protein portions and framework regions to contact glycan portions of the epitope. The structure solidifies previous evidence that the 8ANC195 epitope spans gp120 and gp41 (Scharf et al., 2014) and reveals details of extensive interactions with N-linked glycans on both gp120 and gp41. Rather than penetrating the glycan shield of HIV-1 Env with only a single loop, a strategy employed by Abs such as PG9 and PGT128 (McLellan et al., 2011; Pejchal et al., 2011), 8ANC195 inserts its entire variable region into a gap in the Env trimer glycan shield at the interface of gp120 and gp41. 8ANC195 makes productive interactions with gp120 glycans at Asn234_{gp120} and Asn276_{gp120}, since neutralization potency decreases when these glycosylation sites are knocked out (West et al., 2013). However, the mature Ab appears to accommodate, rather than productively contact, gp41 glycans, e.g., the Asn637_{gp41} glycan, since the neutralization potency of 8ANC195 is not affected when this glycan is removed despite the large contact area between the Asn637_{gp41} glycan and 8ANC195_{G52K5}.

In addition to recognizing both gp120 monomer and closed Env trimer, we also provide SPR and EM evidence that 8ANC195 can bind to Env trimers complexed with sCD4 and the CD4-induced Ab 17b. CD4 binding normally induces an open state of both virion-bound and soluble HIV-1 Env trimers involving rotation of gp120 subunits away from the center axis of the trimer (Harris et al., 2011; Liu et al., 2008; Sanders et al., 2013; Tran et al., 2012). However, despite recognizing an epitope that spans the gp120-gp41 interface, a region thought to undergo conformational changes upon CD4 binding to allow rotation of the gp120 subunits, 8ANC195 binds CD4-bound Env trimers with little to no decrease in affinity compared with closed, non-CD4-bound trimers. 17b, which binds at the apex of Env trimer, prevents reclosing of Env trimer that has opened upon CD4 binding because three 17b Fabs cannot be accommodated on a closed Env trimer (Figure 6A). Thus, our EM structure of a partially open BG505 SOSIP-sCD4-17b-8ANC195 complex suggests that 8ANC195 binding to fully open CD4-bound Env trimers results in a conformational change toward the closed state but that complete closure of the trimer is prevented by steric clashing of 17b Fabs. Alternatively, when Env trimer is bound to CD4, 8ANC195 could stabilize a partially open conformation in equilibrium with fully open CD4-bound Env. Taken together with our crystal structure showing a closed 8ANC195_{G52K5}-bound trimer despite pre-incubation of trimer with sCD4, the observation that the trimer in the BG505 SOSIP-sCD4-17b-8ANC195_{G52K5} complex is partially, rather than fully, open implies that 8ANC195 prefers binding to the closed trimer. This suggests that its mechanism of neutralization likely involves preventing the complete conformational change necessary for the trimer to bind co-receptor and/or expose the fusion peptide and fuse with the target cell membrane.

Although our results suggest that 8ANC195 preferentially recognizes closed Env trimers, its ability to also recognize other Env conformations suggests that 8ANC195 can neutralize virions regardless of Env conformational state, including virions with

constitutively open spikes such as those found on CD4-independent strains (White et al., 2010, 2011). It also suggests that, in addition to neutralizing free virions, 8ANC195 could neutralize virions already engaged by CD4 at a target cell membrane. This is a useful property of an HIV-1 bNAb since Abs with these properties could inhibit cell-to-cell spread of HIV-1, which is most effectively prevented by Abs that bind triggered Env conformations (Abela et al., 2012). Finally, recent evidence from single-molecule FRET studies (Munro et al., 2014) and molecular ruler measurements of virion-associated Env trimers (Galimidi et al., 2015) suggests that Env on free virions can exhibit transitions from the closed state to more open conformations; thus, recognition of Env states other than the closed state should be useful for neutralization of cell-bound as well as free virions.

The finding that the trimer in our BG505 SOSIP-sCD4-17b-8ANC195_{G52K5} complex structure was partially, rather than fully, open, as observed in previous CD4-, 17b-, and CD4/17b-bound trimer structures (Harris et al., 2011; Liu et al., 2008; Sanders et al., 2013; Tran et al., 2012), suggests that the trimer re-closed somewhat upon 8ANC195 binding. This result implies more structural plasticity of HIV-1 Env than previously assumed and prompts reevaluation of current models for target cell fusion by Env after CD4 engagement to address, for example, whether the partially closed CD4-bound structure revealed in this work can engage co-receptors. We hypothesize that, when 8ANC195 engages a CD4-bound (open) trimer, it partially recloses the trimer or captures and stabilizes a pre-existing conformation because the complex with a partially open trimer is more favorable for Ab binding. This reclosing of the trimer may result in dissociation of CD4, either due to steric constraints on partially open trimers or the relatively low affinity of sCD4 for trimer (~600 nM) (Julien et al., 2013b). In stabilized soluble Env trimers, 8ANC195 binding may result in complete re-closure of the trimer, as observed in our BG505 SOSIP-8ANC195_{G52K5} crystal structure. This model suggests that CD4 engagement of HIV-1 spike trimers does not lead to an immediate irreversible conformational change but, rather, that the conformational change is reversible as long as no major rearrangement of gp41 has occurred. Alternatively, the highly stabilized design of SOSIP trimers may be responsible for the apparent reversibility of CD4-induced conformational changes. However, single-molecule FRET experiments on HIV-1 virions showed that membrane-bound Env trimers sample three distinct conformational states in the absence of ligands and that ligands such as Abs and CD4 only changed the sizes of the populations occupying each state (Munro et al., 2014). The FRET study reported a sequence of conformational changes in unbound trimer involving transitions from closed to fully open, open to partially open, and then partially open to closed, supporting our hypothesis that membrane-bound Env trimers can re-close from a fully open state spontaneously, a process that may be assisted by an Ab that prefers to engage the closed state.

Combinations of bNAbs are being considered for treatment and prevention of HIV-1 infection by passive delivery methods because mixtures of active molecules (bNAbs or small molecule drugs) are required to prevent the appearance of escape mutants in a rapidly mutating virus such as HIV-1 (Horwitz et al., 2013; Klein et al., 2012). Two or more bNAbs targeting

different epitopes are favored because the virus is presumed unable to mutate several potentially conserved sites simultaneously. In addition to targeting an epitope distinct from other known bNAbs, 8ANC195 can accommodate different conformational states (including a CD4-bound state), making it an attractive candidate for use in combination therapies with bNAbs that (1) cannot tolerate such changes, (2) are unable to engage a CD4-bound open trimer, and/or (3) allow HIV-1 to spread through cell-to-cell transmission, as is the case for potent CD4-binding site Abs in the VRC01 family (Abela et al., 2012). 8ANC195 may also be a target for vaccine development since it targets conserved regions on Env such as gp41 and the Asn₂₇₆_{gp120} glycan.

EXPERIMENTAL PROCEDURES

Detailed methods are provided in the [Supplemental Experimental Procedures](#).

Protein Production and Purification

8ANC195, 8ANC195_{G52K5}, 17b, PGT145, mG053, 2G12, CD4-Fc (domains 1 and 2 of human CD4 fused to human IgG1 Fc), human IgG1 Fc, and partially gl-reverted IgGs and/or Fab's were produced by transient transfection and purified using affinity chromatography and SEC, as described in previous studies (Diskin et al., 2011; Scharf et al., 2014). sCD4 (domains 1 and 2; residues 1–186 of mature CD4) was produced in baculovirus-infected Hi5 insect cells and was purified using affinity chromatography and SEC, as described previously (Diskin et al., 2010; Scharf et al., 2014). Untagged BG505 SOSIP.664 was constructed, expressed, and purified as described (Sanders et al., 2013). In brief, HEK293-6E cells treated with 5 μM kifunensine (Sigma) were co-transfected with plasmids encoding BG505 SOSIP.664 and soluble furin, and trimers were purified from cell supernatants using a 2G12 immunoaffinity chromatography and SEC.

Crystallization

Samples for crystallography were produced by incubating BG505 SOSIP with a 3-fold molar excess of sCD4 and were purified by SEC. The resulting complex was incubated with a 3-fold molar excess of 8ANC195_{G52K5} Fab and purified by SEC. Crystals of 8ANC195_{G52K5} Fab-BG505 SOSIP (space group P2₁; $a = 117.74 \text{ \AA}$, $b = 195.22 \text{ \AA}$, $c = 119.09 \text{ \AA}$; $\beta = 101.6^\circ$) were obtained in 100 mM Tris (pH 8.0), 15% PEG 3,350, and 2% 1,4-dioxane at 20°C and frozen in liquid N₂ after cryoprotection.

Crystallographic Data Collection, Structure Determination, and Refinement

X-ray diffraction data were collected at the Argonne National Laboratory Advanced Photon Source (APS) beamline 23-ID-D using a Pilatus3 6M detector and were processed using XDS (Kabsch, 2010). The structure was solved by molecular replacement using a trimeric model of BG505 SOSIP (PDB: 4TPV) and three copies of 8ANC195 Fab (PDB: 4P9M). The model was refined to 3.58 Å using Phenix (Adams et al., 2010) and manual model building in Coot (Emsley and Cowtan, 2004). In the final model ($R_{\text{work}} = 24.1\%$; $R_{\text{free}} = 28.6\%$), 96%, 4%, and 0% of the residues were in the favored, allowed, and disallowed regions, respectively, of the Ramachandran plot.

SPR

Experiments were performed using a Biacore T200 (Biacore). Protein A coupled on a CM5 chip (Biacore) was used to immobilize capture proteins (PGT145 IgG, PGT121 IgG, CD4-Fc, 17b IgG, 21C IgG, or mG053 IgG control), followed by injection of human Fc to block remaining protein A binding sites. BG505 SOSIP was subsequently injected and washed with running buffer (HBS-EP+, GE Healthcare). 8ANC195, 8ANC195_{G52K5}, and mutant/chimeric Fab's were injected over flow cells at increasing concentrations (1.95 to 1,000 nM) at flow rates of 50 μl/min for 180 s and were allowed to dissociate for 600 s. Flow cells were regenerated with one pulse each of 10 mM glycine

(pH 2.5) and 1 M guanidine HCl at a flow rate of 90 μl/min. On/off rates ($k_{\text{on}}/k_{\text{off}}$) and binding constants (K_D) were calculated by kinetic analyses after subtraction of backgrounds using a 1:1 binding model with or without a bulk reflective index (RI) correction as appropriate (Biacore T200 Evaluation software).

Cryoelectron Tomography

Purified BG505 SOSIP-sCD4-17b-8ANC195_{G52K5} complexes were diluted to 60 μg/ml in TBS immediately before plunge freezing to avoid complex dissociation at low concentration. Quantifoil R2/2 NH2 copper finder grids were vitrified in liquid ethane using a Mark IV Vitrobot (FEI Company) and Tilt series (±60°, 1° angular increments) were collected on a FEI Tecnai G2 Polara transmission electron microscope equipped with 300 keV FEG, a Gatan energy filter, and a Gatan K2 Summit direct detector using the UCSF tomography software package (Zheng et al., 2007) under low-dose conditions (120 e⁻/Å² total for the tilt series at ~8 μm underfocus) at a nominal magnification of 41,000× so that each pixel represented 2.6 Å. Tomographic reconstructions and CTF corrections were calculated using IMOD (Kremer et al., 1996). Subtomogram averaging of 1,745 subvolumes was performed using PEET (Nicastro et al., 2006) without an external reference or applying C3 symmetry, resulting in a ~23 Å structure estimated by a 0.143 gold-standard Fourier shell correlation (FSC) calculated using IMOD (Kremer et al., 1996).

Negative-Stain Single-Particle EM

Purified BG505 SOSIP-sCD4-17b-8ANC195_{G52K5} complexes were diluted to 10 μg/ml in TBS immediately before adding 3 μl to a glow discharged ultrathin C film on holey carbon support film, 400 mesh, Cu grids (Ted Pella) followed by cross-linking using glutaraldehyde vapor and staining with uranyl acetate. Data were collected using a FEI Tecnai T12 transmission electron microscope operating at 120 keV equipped with a Gatan Ultrascan 2k × 2k CCD using a 0.5 s exposure time at a nominal magnification of 42,000× at 1 μm defocus, resulting in 2.5 Å per pixel. A total of 23,951 particles were picked using EMAN2.1 (Tang et al., 2007) and RELION (Scheres, 2012), and the CTF correction was done using EMAN2.1. Initial reference-free 2D class averaging was performed using RELION, and the particles were further sorted using 3D classification in RELION. Refinement was conducted using 80 Å low-pass-filtered structures calculated from models of 8ANC195-sCD4-17b docked onto gp120 cores of partially open (PDB: 3DNL) trimer and 7,174 particles with C3 symmetry applied. The resolution of the final reconstruction was ~17 Å calculated with RELION (Scheres, 2012) using a gold-standard FSC and a 0.143 cutoff, as recommended for resolution estimations for single-particle EM reconstructions (Scheres and Chen, 2012). Coordinates from crystal structures were fit into the sub-tomogram averaged or negative-stain single-particle EM structures using UCSF Chimera (Pettersen et al., 2004).

ACCESSION NUMBERS

SUPPLEMENTAL INFORMATION

补充信息包括补充实验程序、六个图例和五张表格，可以在本文的在线补充材料中找到，网址为 <http://dx.doi.org/10.1016/j.cell.2015.08.035>。

AUTHOR CONTRIBUTIONS

L.S. 准备了用于结构研究的样品并进行了分析；H.W.、L.S.、S.C. 和 A.W.M. 收集了 EM 数据；H.W. 和 L.S. 解决并分析了 EM 结构；H.G. 表达并纯化了蛋白；L.S.、H.W. 和 P.J.B. 分析了数据并撰写了手稿。

ACKNOWLEDGMENTS

This research was supported by the National Institute Of Allergy and Infectious Diseases of the National Institutes of Health Grant HIVRAD P01 AI100148 (P.J.B.) (the content is solely the responsibility of the authors and does not necessarily represent the official views of the National Institutes of Health), the Bill and Melinda Gates Foundation (Collaboration for AIDS Vaccine Discovery Grant 1040753 [P.J.B.]), the National Institutes of Health Grant 2 P50 GM082545-06 (P.J.B.), the American Cancer Society Grant PF-13-076-01-MPC (L.S.), and the Molecular Observatory at Caltech supported by the Gordon and Betty Moore Foundation. We thank the Gordon and Betty Moore and Beckman Foundations for gifts to Caltech that helped support electron microscopy; Grant Jensen for advice and support for EM; Jost Vielmetter and the Caltech Protein Expression Center for producing proteins and use of the Biacore T200; Priyanti Gnanapragasam and René Mares for performing neutralization assays; the beamline staff at the Advanced Photon Source GM/CA-CAT for use and support for beamline 23ID-D; Marta Murphy and Rachel Galimidi for assistance with figures; and Michel Nussenzweig, Johannes Scheid, and Anthony West for helpful discussions and critical reading of the manuscript.

Received: May 3, 2015

Revised: June 19, 2015

Accepted: July 28, 2015

Published: September 10, 2015

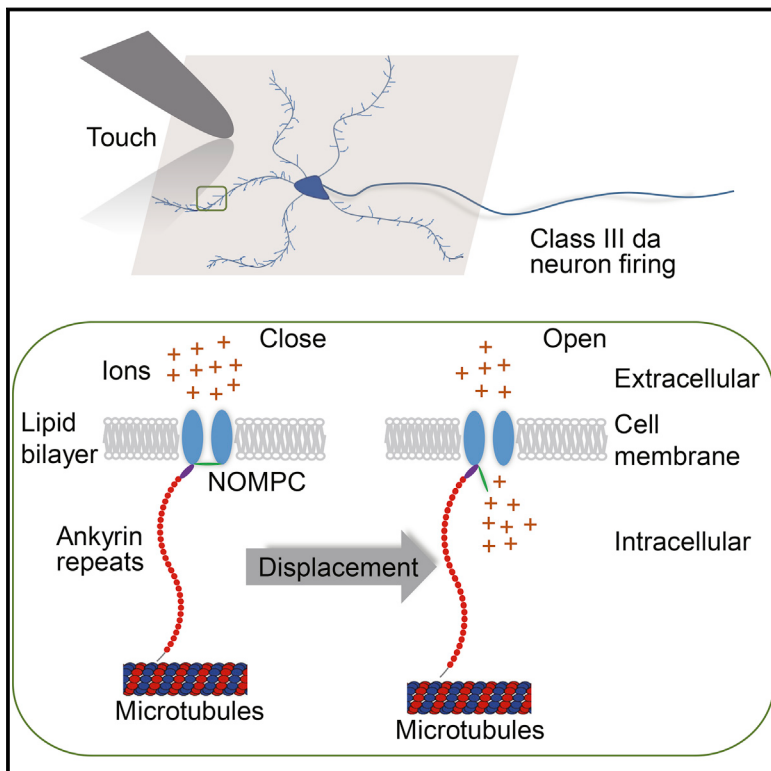
REFERENCES

- Abela, I.A., Berlinger, L., Schanz, M., Reynell, L., Günthard, H.F., Rusert, P., and Trkola, A. (2012). Cell-cell transmission enables HIV-1 to evade inhibition by potent CD4bs directed antibodies. *PLoS Pathog.* 8, e1002634.
- Adams, P.D., Afonine, P.V., Bunkóczki, G., Chen, V.B., Davis, I.W., Echols, N., Headd, J.J., Hung, L.W., Kapral, G.J., Grosse-Kunstleve, R.W., et al. (2010). PHENIX: a comprehensive Python-based system for macromolecular structure solution. *Acta Crystallogr. D Biol. Crystallogr.* 66, 213–221.
- Binley, J.M., Ban, Y.E., Crooks, E.T., Eggink, D., Osawa, K., Schief, W.R., and Sanders, R.W. (2010). Role of complex carbohydrates in human immunodeficiency virus type 1 infection and resistance to antibody neutralization. *J. Virol.* 84, 5637–5655.
- Blattner, C., Lee, J.H., Sliepen, K., Derking, R., Falkowska, E., de la Peña, A.T., Cupo, A., Julien, J.P., van Gils, M., Lee, P.S., et al. (2014). Structural delineation of a quaternary, cleavage-dependent epitope at the gp41-gp120 interface on intact HIV-1 Env trimers. *Immunity* 40, 669–680.
- Capon, D.J., Chamow, S.M., Mordenti, J., Marsters, S.A., Gregory, T., Mitsuya, H., Byrn, R.A., Lucas, C., Wurm, F.M., Groopman, J.E., et al. (1989). Designing CD4 immunoadhesins for AIDS therapy. *Nature* 337, 525–531.
- Caskey, M., Klein, F., Lorenzi, J.C., Seaman, M.S., West, A.P., Jr., Buckley, N., Kremer, G., Nogueira, L., Braunschweig, M., Scheid, J.F., et al. (2015). Viremia suppressed in HIV-1-infected humans by broadly neutralizing antibody 3BNC117. *Nature* 522, 487–491.
- Derking, R., Ozorowski, G., Sliepen, K., Yasmeen, A., Cupo, A., Torres, J.L., Julien, J.P., Lee, J.H., van Montfort, T., de Taeye, S.W., et al. (2015). Comprehensive antigenic map of a cleaved soluble HIV-1 envelope trimer. *PLoS Pathog.* 11, e1004767.
- Diskin, R., Marcovecchio, P.M., and Bjorkman, P.J. (2010). Structure of a clade C HIV-1 gp120 bound to CD4 and CD4-induced antibody reveals anti-CD4 polyreactivity. *Nat. Struct. Mol. Biol.* 17, 608–613.
- Diskin, R., Scheid, J.F., Marcovecchio, P.M., West, A.P., Jr., Klein, F., Gao, H., Gnanapragasam, P.N., Abadir, A., Seaman, M.S., Nussenzweig, M.C., and Bjorkman, P.J. (2011). Increasing the potency and breadth of an HIV antibody by using structure-based rational design. *Science* 334, 1289–1293.
- Elbein, A.D., Tropea, J.E., Mitchell, M., and Kaushal, G.P. (1990). Kifunensine, a potent inhibitor of the glycoprotein processing mannosidase I. *J. Biol. Chem.* 265, 15599–15605.
- Emsley, P., and Cowtan, K. (2004). Coot: model-building tools for molecular graphics. *Acta Crystallogr. D Biol. Crystallogr.* 60, 2126–2132.
- Galimidi, R.P., Klein, J.S., Politzer, M.S., Bai, S., Seaman, M.S., Nussenzweig, M.C., West, A.P., Jr., and Bjorkman, P.J. (2015). Intra-spike crosslinking overcomes antibody evasion by HIV-1. *Cell* 160, 433–446.
- Go, E.P., Hewawasam, G., Liao, H.X., Chen, H., Ping, L.H., Anderson, J.A., Hua, D.C., Haynes, B.F., and Desai, H. (2011). Characterization of glycosylation profiles of HIV-1 transmitted/founder envelopes by mass spectrometry. *J. Virol.* 85, 8270–8284.
- Guttman, M., Cupo, A., Julien, J.P., Sanders, R.W., Wilson, I.A., Moore, J.P., and Lee, K.K. (2015). Antibody potency relates to the ability to recognize the closed, pre-fusion form of HIV Env. *Nat. Commun.* 6, 6144.
- Harris, A., Borgnia, M.J., Shi, D., Bartesaghi, A., He, H., Pejchal, R., Kang, Y.K., Depetrini, R., Marozsan, A.J., Sanders, R.W., et al. (2011). Trimeric HIV-1 glycoprotein gp140 immunogens and native HIV-1 envelope glycoproteins display the same closed and open quaternary molecular architectures. *Proc. Natl. Acad. Sci. USA* 108, 11440–11445.
- Horwitz, J.A., Halper-Stromberg, A., Mouquet, H., Gitlin, A.D., Tretiakova, A., Eisenreich, T.R., Malbec, M., Gravemann, S., Billerbeck, E., Dorner, M., et al. (2013). HIV-1 suppression and durable control by combining single broadly neutralizing antibodies and antiretroviral drugs in humanized mice. *Proc. Natl. Acad. Sci. USA* 110, 16538–16543.
- Huang, J., Kang, B.H., Pancera, M., Lee, J.H., Tong, T., Feng, Y., Imamichi, H., Georgiev, I.S., Chuang, G.Y., Druz, A., et al. (2014). Broad and potent HIV-1 neutralization by a human antibody that binds the gp41-gp120 interface. *Nature* 515, 138–142.
- Jones, S., and Thornton, J.M. (1996). Principles of protein-protein interactions. *Proc. Natl. Acad. Sci. USA* 93, 13–20.
- Julien, J.P., Cupo, A., Sok, D., Stanfield, R.L., Lyumkis, D., Deller, M.C., Klasse, P.J., Burton, D.R., Sanders, R.W., Moore, J.P., et al. (2013a). Crystal structure of a soluble cleaved HIV-1 envelope trimer. *Science* 342, 1477–1483.
- Julien, J.P., Sok, D., Khayat, R., Lee, J.H., Doores, K.J., Walker, L.M., Ramos, A., Diwanji, D.C., Pejchal, R., Cupo, A., et al. (2013b). Broadly neutralizing antibody PGT121 allosterically modulates CD4 binding via recognition of the HIV-1 gp120 V3 base and multiple surrounding glycans. *PLoS Pathog.* 9, e1003342.
- Kabsch, W. (2010). Integration, scaling, space-group assignment and post-refinement. *Acta Crystallogr. D Biol. Crystallogr.* 66, 133–144.
- Klein, F., Halper-Stromberg, A., Horwitz, J.A., Gruell, H., Scheid, J.F., Bourne, S., Mouquet, H., Spatz, L.A., Diskin, R., Abadir, A., et al. (2012). HIV therapy by a combination of broadly neutralizing antibodies in humanized mice. *Nature* 492, 118–122.
- Kremer, J.R., Mastronarde, D.N., and McIntosh, J.R. (1996). Computer visualization of three-dimensional image data using IMOD. *J. Struct. Biol.* 116, 71–76.
- Kwon, Y.D., Finzi, A., Wu, X., Dogo-Isonagie, C., Lee, L.K., Moore, L.R., Schmidt, S.D., Stuckey, J., Yang, Y., Zhou, T., et al. (2012). Unliganded HIV-1 gp120 core structures assume the CD4-bound conformation with regulation by quaternary interactions and variable loops. *Proc. Natl. Acad. Sci. USA* 109, 5663–5668.
- Do Kwon, Y., Pancera, M., Acharya, P., Georgiev, I.S., Crooks, E.T., Gorman, J., Joyce, M.G., Guttman, M., Ma, X., Narpaia, S., et al. (2015). Crystal structure, conformational fixation and entry-related interactions of mature ligand-free HIV-1 Env. *Nat. Struct. Mol. Biol.* 22, 522–531.
- Liu, J., Bartesaghi, A., Borgnia, M.J., Sapiro, G., and Subramaniam, S. (2008). Molecular architecture of native HIV-1 gp120 trimers. *Nature* 455, 109–113.
- Lyumkis, D., Julien, J.P., de Val, N., Cupo, A., Potter, C.S., Klasse, P.J., Burton, D.R., Sanders, R.W., Moore, J.P., Carragher, B., et al. (2013). Cryo-EM structure of a fully glycosylated soluble cleaved HIV-1 envelope trimer. *Science* 342, 1484–1490.
- McLellan, J.S., Pancera, M., Carrico, C., Gorman, J., Julien, J.P., Khayat, R., Louder, R., Pejchal, R., Sastry, M., Dai, K., et al. (2011). Structure of HIV-1 gp120 V1/V2 domain with broadly neutralizing antibody PG9. *Nature* 480, 336–343.

- Merk, A., and Subramaniam, S. (2013). HIV-1 envelope glycoprotein structure. *Curr. Opin. Struct. Biol.* 23, 268–276.
- Mouquet, H., Scharf, L., Euler, Z., Liu, Y., Eden, C., Scheid, J.F., Halper-Stromberg, A., Gnanapragasam, P.N., Spencer, D.I., Seaman, M.S., et al. (2012). Complex-type N-glycan recognition by potent broadly neutralizing HIV antibodies. *Proc. Natl. Acad. Sci. USA* 109, E3268–E3277.
- Munro, J.B., Gorman, J., Ma, X., Zhou, Z., Arthos, J., Burton, D.R., Koff, W.C., Courter, J.R., Smith, A.B., 3rd, Kwong, P.D., et al. (2014). Conformational dynamics of single HIV-1 envelope trimers on the surface of native virions. *Science* 346, 759–763.
- Nicastro, D., Schwartz, C., Pierson, J., Gaudette, R., Porter, M.E., and McIntosh, J.R. (2006). The molecular architecture of axonemes revealed by cryo-electron tomography. *Science* 313, 944–948.
- Pancera, M., Zhou, T., Druz, A., Georgiev, I.S., Soto, C., Gorman, J., Huang, J., Acharya, P., Chuang, G.Y., Ofek, G., et al. (2014). Structure and immune recognition of trimeric pre-fusion HIV-1 Env. *Nature* 514, 455–461.
- Pejchal, R., Doores, K.J., Walker, L.M., Khayat, R., Huang, P.S., Wang, S.K., Stanfield, R.L., Julien, J.P., Ramos, A., Crispin, M., et al. (2011). A potent and broad neutralizing antibody recognizes and penetrates the HIV glycan shield. *Science* 334, 1097–1103.
- Pettersen, E.F., Goddard, T.D., Huang, C.C., Couch, G.S., Greenblatt, D.M., Meng, E.C., and Ferrin, T.E. (2004). UCSF Chimera—a visualization system for exploratory research and analysis. *J. Comput. Chem.* 25, 1605–1612.
- Pugach, P., Ozorowski, G., Cupo, A., Ringe, R., Yasmeen, A., de Val, N., Derking, R., Kim, H.J., Korzun, J., Golabek, M., et al. (2015). A native-like SOSIP.664 trimer based on an HIV-1 subtype B env gene. *J. Virol.* 89, 3380–3395.
- Sanders, R.W., Derking, R., Cupo, A., Julien, J.P., Yasmeen, A., de Val, N., Kim, H.J., Blattner, C., de la Peña, A.T., Korzun, J., et al. (2013). A next-generation cleaved, soluble HIV-1 Env trimer, BG505 SOSIP.664 gp140, expresses multiple epitopes for broadly neutralizing but not non-neutralizing antibodies. *PLoS Pathog.* 9, e1003618.
- Scharf, L., Scheid, J.F., Lee, J.H., West, A.P., Jr., Chen, C., Gao, H., Gnanapragasam, P.N., Mares, R., Seaman, M.S., Ward, A.B., et al. (2014). Antibody 8ANC195 reveals a site of broad vulnerability on the HIV-1 envelope spike. *Cell Rep.* 7, 785–795.
- Scheid, J.F., Mouquet, H., Ueberheide, B., Diskin, R., Klein, F., Oliveira, T.Y., Pietzsch, J., Fenyo, D., Abadir, A., Velinzon, K., et al. (2011). Sequence and structural convergence of broad and potent HIV antibodies that mimic CD4 binding. *Science* 333, 1633–1637.
- Scheres, S.H. (2012). RELION: implementation of a Bayesian approach to cryo-EM structure determination. *J. Struct. Biol.* 180, 519–530.
- Scheres, S.H., and Chen, S. (2012). Prevention of overfitting in cryo-EM structure determination. *Nat. Methods* 9, 853–854.
- Sullivan, N., Sun, Y., Sattentau, Q., Thali, M., Wu, D., Denisova, G., Gershoni, J., Robinson, J., Moore, J., and Sodroski, J. (1998). CD4-Induced conformational changes in the human immunodeficiency virus type 1 gp120 glycoprotein: consequences for virus entry and neutralization. *J. Virol.* 72, 4694–4703.
- Tang, G., Peng, L., Baldwin, P.R., Mann, D.S., Jiang, W., Rees, I., and Ludtke, S.J. (2007). EMAN2: an extensible image processing suite for electron microscopy. *J. Struct. Biol.* 157, 38–46.
- Tran, E.E., Borgnia, M.J., Kuybeda, O., Schauder, D.M., Bartesaghi, A., Frank, G.A., Sapiro, G., Milne, J.L., and Subramaniam, S. (2012). Structural mechanism of trimeric HIV-1 envelope glycoprotein activation. *PLoS Pathog.* 8, e1002797.
- West, A.P., Jr., Scharf, L., Horwitz, J., Klein, F., Nussenzweig, M.C., and Bjorkman, P.J. (2013). Computational analysis of anti-HIV-1 antibody neutralization panel data to identify potential functional epitope residues. *Proc. Natl. Acad. Sci. USA* 110, 10598–10603.
- West, A.P., Jr., Scharf, L., Scheid, J.F., Klein, F., Bjorkman, P.J., and Nussenzweig, M.C. (2014). Structural insights on the role of antibodies in HIV-1 vaccine and therapy. *Cell* 156, 633–648.
- White, T.A., Bartesaghi, A., Borgnia, M.J., Meyerson, J.R., de la Cruz, M.J., Bess, J.W., Nandwani, R., Hoxie, J.A., Lifson, J.D., Milne, J.L., and Subramaniam, S. (2010). Molecular architectures of trimeric SIV and HIV-1 envelope glycoproteins on intact viruses: strain-dependent variation in quaternary structure. *PLoS Pathog.* 6, e1001249.
- White, T.A., Bartesaghi, A., Borgnia, M.J., de la Cruz, M.J., Nandwani, R., Hoxie, J.A., Bess, J.W., Lifson, J.D., Milne, J.L., and Subramaniam, S. (2011). Three-dimensional structures of soluble CD4-bound states of trimeric simian immunodeficiency virus envelope glycoproteins determined by using cryo-electron tomography. *J. Virol.* 85, 12114–12123.
- Xiang, S.H., Doka, N., Choudhary, R.K., Sodroski, J., and Robinson, J.E. (2002). Characterization of CD4-induced epitopes on the HIV type 1 gp120 envelope glycoprotein recognized by neutralizing human monoclonal antibodies. *AIDS Res. Hum. Retroviruses* 18, 1207–1217.
- Zheng, S.Q., Keszthelyi, B., Branlund, E., Lyle, J.M., Braufeld, M.B., Sedat, J.W., and Agard, D.A. (2007). UCSF tomography: an integrated software suite for real-time electron microscopic tomographic data collection, alignment, and reconstruction. *J. Struct. Biol.* 157, 138–147.

Ankyrin Repeats Convey Force to Gate the NOMPC Mechanotransduction Channel

Graphical Abstract



Authors

Wei Zhang, Li E. Cheng,
Maike Kittelmann, ..., Martin C. Göpfert,
Lily Yeh Jan, Yuh Nung Jan

Correspondence

yuhnung.jan@ucsf.edu

In Brief

Study of mechanotransduction channel NOMPC reveals a tether mechanism of mechanogating in which the N-terminal ARs of NOMPC form a tether linking the channel and the microtubules that convey force exerted via cell deformation to gate the channel and activate touch-sensitive neurons.

Highlights

- ARs are essential for NOMPC mechanogating in vitro and in vivo
- Microtubule association is required for NOMPC mechanogating
- ARs are a main component of the filaments that tether NOMPC to microtubules
- Transferring the ARs to voltage-gated potassium channels confers mechanosensitivity

Ankyrin Repeats Convey Force to Gate the NOMPC Mechanotransduction Channel

Wei Zhang,^{1,3} Li E. Cheng,^{1,3} Maike Kittelmann,^{2,3,4} Jiefu Li,¹ Maja Petkovic,¹ Tong Cheng,¹ Peng Jin,¹ Zhenhao Guo,¹ Martin C. Göpfert,² Lily Yeh Jan,¹ and Yuh Nung Jan^{1,*}

¹Departments of Physiology, Biochemistry, and Biophysics, Howard Hughes Medical Institute, University of California, San Francisco, San Francisco, CA 94158, USA

²Department of Cellular Neurobiology, University of Göttingen, 37077 Göttingen, Germany

³Co-first author

⁴Present address: Plant Cell Biology, Oxford Brookes University, Gipsy Lane, Oxford OX3 0BP, UK

*Correspondence: yuhnung.jan@ucsf.edu

<http://dx.doi.org/10.1016/j.cell.2015.08.024>

SUMMARY

How metazoan mechanotransduction channels sense mechanical stimuli is not well understood. The NOMPC channel in the transient receptor potential (TRP) family, a mechanotransduction channel for *Drosophila* touch sensation and hearing, contains 29 Ankyrin repeats (ARs) that associate with microtubules. These ARs have been postulated to act as a tether that conveys force to the channel. Here, we report that these N-terminal ARs form a cytoplasmic domain essential for NOMPC mechanogating in vitro, mechanosensitivity of touch receptor neurons in vivo, and touch-induced behaviors of *Drosophila* larvae. Duplicating the ARs elongates the filaments that tether NOMPC to microtubules in mechanosensory neurons. Moreover, microtubule association is required for NOMPC mechanogating. Importantly, transferring the NOMPC ARs to mechanoinsensitive voltage-gated potassium channels confers mechanosensitivity to the chimeric channels. These experiments strongly support a tether mechanism of mechanogating for the NOMPC channel, providing insights into the basis of mechanosensitivity of mechanotransduction channels.

INTRODUCTION

Mechanotransduction channels convert mechanical stimuli into neuronal signals (Arnadóttir and Chalfie, 2010; Coste et al., 2012; Vollrath et al., 2007). Several models have been proposed regarding how the mechanical force triggers channel opening (Kung, 2005; Lumpkin and Caterina, 2007; Orr et al., 2006). In the membrane force model, the force exerted via lipids in the membrane gates the channel. Alternatively, the tether model posits that the channel is tethered to intra- and/or extracellular structures and the force that is exerted by these molecular tethers gates the channel (Gillespie and Walker, 2001; Orr et al., 2006). Those models are not mutually exclusive as the

cell membrane and tethers may act in concert in transmitting forces to the channel gate. While there is considerable evidence supporting the membrane force model for the bacterial MscL channel (Anishkin and Kung, 2013) and eukaryotic potassium channels (Brohawn et al., 2012, 2014a, 2014b; Lolicato et al., 2014), direct molecular evidence for the tether model has been lacking.

In the tether model, both rigid and elastic cellular components are required to couple stimulus-induced displacements to the membrane-bound channel (Lumpkin and Caterina, 2007). The rigid structures are thought to be composed of intracellular cytoskeletal elements and/or extracellular matrix components (Anishkin and Kung, 2013; Kung, 2005), and microtubules have been found to be essential for the mechanogating of TRPV1 channels on cells undergoing hypertonicity-induced shrinking (Prager-Khoutorsky et al., 2014). The molecular identities of the elastic components that transduce mechanical force to the channels and promote channel gating, however, remain unknown. Protein motifs that exhibit a certain level of elasticity have been suggested to function as gating springs that pull open the channels during mechanotransduction. The stomatin-related protein Mec-2 in the MEC channel complex of *Caenorhabditis elegans* touch receptors (Goodman et al., 2002; Hu et al., 2010), tip link proteins in vertebrate hair cells (Grillet et al., 2009; Morgan and Barr-Gillespie, 2013; Phillips et al., 2008), and Ankyrin repeats (ARs) domain of some TRP channels (Gaudet, 2008; Howard and Bechstedt, 2004; Jin et al., 2006; Sotomayor et al., 2005b) are all candidates for such elastic tethers. The Ankyrin domain of 33 residues is a structural motif implicated in protein-protein interactions (Gaudet, 2008; Jin et al., 2006; Lee et al., 2006; Yang et al., 1998). Domains with a large tandem array of ARs resemble a coil with elasticity (Gaudet, 2008), making them intriguing candidates.

Among all known TRP channels, the NOMPC channel has the largest number of ARs (Montell, 2004, 2005), which are important for NOMPC functions in larval locomotion (Cheng et al., 2010). NOMPC fulfills essentially all the criteria for a bona fide mechanotransduction channel and mediates touch sensation in *Drosophila* larvae (Arnadóttir and Chalfie, 2010; Yan et al., 2013). NOMPC is also involved in the hearing of *Drosophila* larvae and adults (Bechstedt and Howard, 2008; Effertz et al., 2011; Kamikouchi et al.,

2009; Lehnert et al., 2013; Liang et al., 2011; Zhang et al., 2013), collective behavior of adult flies (Ramdy et al., 2015), proprioception at adult leg joints (Chadha et al., 2015), and tension sensing in the hindgut of larvae (Zhang et al., 2014). NOMPC forms functional mechanotransduction channels in heterologous expression systems (Gong et al., 2013; Yan et al., 2013), thus facilitating structure-function studies of its mechanosensitivity (Zanini and Göpfert, 2013). These favorable features of NOMPC provide an opportunity to test the involvement of ARs, possibly functioning as a tether, in mechanotransduction.

In this study, we tested NOMPC mutants with various deletion or duplication of ARs and found that the integrity of 29 ARs is important for mechanogating of NOMPC in expression systems *in vitro* and in touch receptor neurons *in vivo*, since only NOMPC constructs with one or two complete sets of 29 ARs are mechanosensitive and effective in mediating touch-induced larval behavior. Having found that ARs associate with microtubules and doubling the ARs of NOMPC in mechanosensory campaniform sensilla results in lengthening of the membrane-microtubule connectors, we further showed that microtubule association is essential for NOMPC mechanosensitivity. To test whether ARs could confer mechanosensitivity, we transferred ARs from NOMPC to the voltage-gated potassium channel Kv1.2 and Kv2.1 that normally show little or no mechanosensitivity and found that the chimeric channels respond to mechanical force with dose-dependent activation beyond the level achievable with depolarization. These findings provide strong evidence for the ability of ARs to mediate mechanosensitivity by functioning as a tether linking the channel and the microtubules and thus provide a precedent for the tether mechanism of mechanogating.

RESULTS

The Ankyrin Repeats Are a Cytoplasmic Domain of NOMPC

To investigate the function of ARs in the N terminus of NOMPC, we first assessed its localization relative to the cell membrane. Topological modeling indicated that NOMPC bears either 6 or 7 trans-membrane segments (Figure S1). To elucidate the topology of NOMPC, we employed antibodies recognizing different regions of NOMPC protein for immunostaining of cells in either permeabilized or non-permeabilized conditions. Surface expression of NOMPC in transfected S2 cells was confirmed with an antibody against an extracellular epitope in the putative pore region of NOMPC (α NOMPC-EC; Figure 1A), which recognized NOMPC in the plasma membrane in the non-permeabilized condition (Figure 1B; Movie S1). We found that both the N terminus and the C terminus of NOMPC are on the cytoplasmic side of the membrane, since antibodies against the N terminus of NOMPC (α NOMPC-N-ter; Figure 1A) (Liang et al., 2011) or the C terminus of NOMPC (α NOMPC-C-ter; Figure 1A) (Cheng et al., 2010) immunostained permeabilized, but not non-permeabilized, cells (Figures 1B and 1C). These results suggest a topology of NOMPC with six trans-membrane helices and intracellular N and C termini (Figure 1A), which is typical of TRP channels (Venkatachalam and Montell, 2007).

AR Structure Is Essential for NOMPC Surface Expression

Immunostaining of NOMPC on the cell membrane with antibodies recognizing the extracellular domain of NOMPC (α NOMPC-EC) revealed that deleting all 29 ARs of NOMPC abolished surface expression (Figure 1E). To study the differential roles of ARs, we generated truncated NOMPC channels with different numbers of ARs. Δ 1-12 ARs, which contains a total of 17 ARs, was constructed to resemble the cold-sensitive TRPA1 channels that contain 14–18 ARs in their N terminus (Julius, 2013; Paulsen et al., 2015). Through molecular dynamics simulations using crystallographic structures, Sotomayor et al. (2005b) showed that proteins containing 12 and 17 ARs could both respond to small forces by changing the curvature of ARs (Sotomayor and Schulten, 2007). Δ 13-29ARs (which contains the first 12 ARs) was constructed to test if there is a difference between these two blocks of ARs. NOMPC channel surface expression was abolished when the last 17 ARs (Δ 13-29ARs-NOMPC) or the last 14 ARs (Δ 16-29ARs-NOMPC) were deleted (Figures 1F and 1G). In contrast, deleting the first 12 ARs led to greater surface expression of NOMPC (Δ 1-12ARs-NOMPC) and a higher open probability (Figures 1H, S2A, and S2B), whereas swapping the first 12 ARs and the last 17 ARs of NOMPC abolished surface expression (Figure 1I). Duplicating the ARs in NOMPC (29+29ARs-NOMPC) was compatible with surface expression (Figure 1J), as was the addition of 17 ARs inserted near the first trans-membrane segment (TM1) of NOMPC (29+17ARs-NOMPC) (Figure 1K). It appears that most of the ARs, especially those preceding the trans-membrane segments, are required for NOMPC protein folding, assembly, or membrane targeting. Furthermore, only those mutant and wild-type (WT) NOMPC proteins that displayed surface expression exhibited spontaneous channel activity (Figures 1D–1K).

The Integrity of ARs Is Required for Mechanotransduction by NOMPC Channels

The ARs of NOMPC have been proposed to mediate the gating of mechanotransduction channels (Howard and Bechstedt, 2004; Sotomayor et al., 2005a). To test this possibility, we recorded from outside-out patches excised from transfected S2 cells and stimulated the membrane patches that were held at a specific voltage level with brief negative pressure (50 mmHg) applied via a high speed pressure clamp.

Among those mutant NOMPC channels with membrane expression, only NOMPC with duplicated ARs (29+29ARs-NOMPC) exhibited mechanogating (Figures 2A and 2B). Whereas current amplitude normalized to patch membrane area as determined by membrane capacitance suggested the current mediated by wild-type NOMPC was larger than that mediated by NOMPC with duplicated ARs (Figure 2C, red bars), normalizing the mechanosensitive current amplitude by the level of surface expression revealed that the mechanosensitive current response of NOMPC with duplicated ARs was comparable to that of wild-type NOMPC (Figure 2C, black bars). In contrast, deforming the membrane with the same pressure did not evoke responses of mutant Δ 1-12ARs-NOMPC or 29+17ARs-NOMPC (Figures 2A–2C), even though both proteins exhibited surface expression and spontaneous channel activities. The spontaneous channel activities were likely

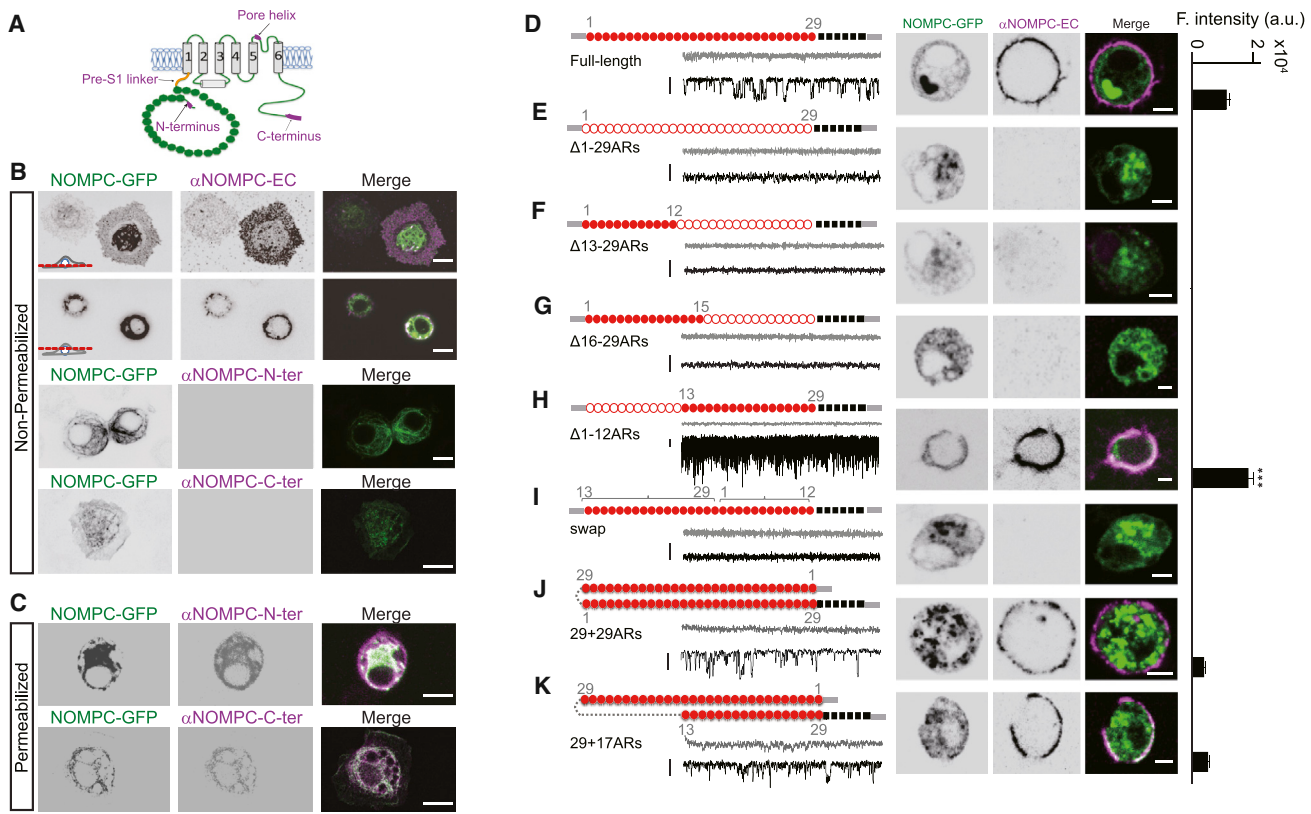


Figure 1. Ankyrin Repeats Are Essential for NOMPC Membrane Expression

- (A) A schematic topology of predicted architecture of a NOMPC channel subunit. Magenta tags indicate the epitopes recognized by antibodies used in this study.
- (B) Non-permeabilized staining of NOMPC protein with antibody against the pore helix (α NOMPC-EC), NOMPC N terminus (α NOMPC-N-ter) and NOMPC C terminus (α NOMPC-C-ter) (scale bar, 10 μ m).
- (C) Permeabilized staining of NOMPC protein (scale bar, 10 μ m).
- (D-K) Schematic molecular architectures, surface staining (scale bar, 5 μ m) and spontaneous channel activities (scale bar, 10 pA) of NOMPC channels with different number and arrangements of ARs. Filled red circles indicate an Ankyrin domain; empty red circles indicate a deleted Ankyrin domain; black bars indicate transmembrane segments; and numbers (gray) indicate the original order of the Ankyrin domain. Current traces were obtained at holding potential of 0 mV (gray) and -60 mV (black) (scale bar, 10 pA). Bar plots on the right represent fluorescence intensity (F. intensity) of surface NOMPC staining (a.u., n = 28, 10, 10, 11, 25, 12, 17, and 29). Paired t test between time full-length and Δ1-12ARs-NOMPC, ***p < 0.001.
- (D) Spontaneous channel activity and membrane expression of full-length NOMPC.
- (E) Deletion of all 29 ARs of NOMPC impaired spontaneous channel activity and membrane expression.
- (F) Deletion of 13-29 ARs of NOMPC impaired spontaneous channel activity and membrane expression.
- (G) Deletion of 16-29 ARs of NOMPC impaired spontaneous channel activity and membrane expression.
- (H) Deletion of 1-12 ARs of NOMPC increased spontaneous channel activity and membrane expression.
- (I) Swap of first 12 and last 17 ARs eliminated spontaneous channel activity and surface expression.
- (J) NOMPC with doubled ARs has normal membrane targeting.
- (K) NOMPC with extra 17 ARs has normal membrane targeting.
- All error bars denote \pm SEM. See also Figures S1 and S2 and Movie S1.

from NOMPC channels, since they showed similar single channel conductance (Figure S2B) and could be blocked with the same channel blocker Gd³⁺ (Figure S2C).

Similar results were obtained when the S2 cells were stimulated with a piezo-actuator and the responses were recorded at the whole-cell configuration (Figure 2D). The amplitude of these mechanogated currents depended on the strength of mechanical stimulation (Figures 2E and 2F). Notably, the Δ1-12ARs-NOMPC exhibited a larger open probability than wild-type NOMPC in the absence of mechanical stimulation (Figures S2A and S2B). Thus, the integrity of the structure of

29 ARs from NOMPC is essential for mechanogating, possibly by forming a full turn of a helix for force transduction (Howard and Bechstedt, 2004). The requirement of all 29 ARs for NOMPC mechanogating might also explain why the number of ARs (29) is conserved across NOMPC homologs in fly, nematodes, zebrafish, and frogs (Kang et al., 2010; Sidi et al., 2003).

ARs Are Required for NOMPC Channel Function In Vivo

Class III dendritic arborization (da) neurons in the *Drosophila* larval body wall rely on mechanotransduction by NOMPC to

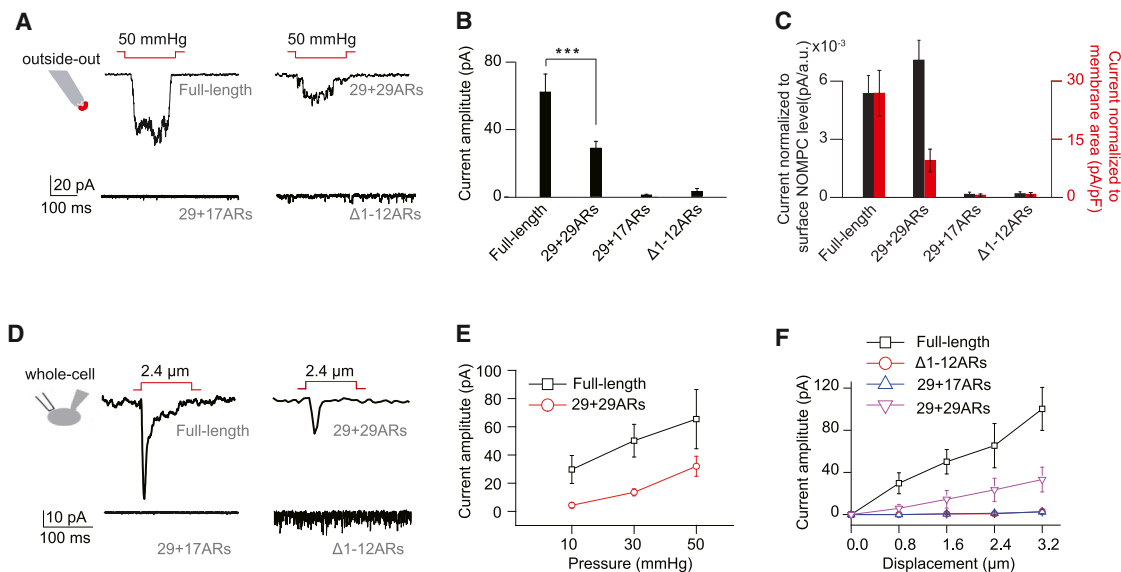


Figure 2. Integrity of Ankyrin Repeats Is Required for NOMPC Mechanogating

(A) Representative traces of mechanogated current from NOMPC channels with different number of ARs on an outside-out patch held at -60 mV.
 (B) Plots of mechanogated current amplitudes (absolute value) ($n = 12, 11, 8$ and 7). one-way analysis of variance followed by Tukey's comparison, *** $p < 0.001$.
 (C) Plots of mechanogated current amplitudes normalized to surface expression level (dark bars) and membrane capacitance (red bars) ($n = 12, 11, 8$ and 7). one-way analysis of variance followed by Tukey's comparison, *** $p < 0.001$.
 (D) Representative traces of mechanogated current triggered by piezo displacements from NOMPC channels with different number of ARs on a transfected cell held at -60 mV.
 (E and F) Dose-dependent curves of NOMPC mechanogated currents to pressure (E) ($n = 10$ and 7) and piezo displacements (F) ($n = 10, 6, 8$ and 7). All error bars denote \pm SEM.
 See also Figure S2.

sense gentle touch (Yan et al., 2013). Null mutations of *nompC* abolish touch-evoked response of these neurons. To study the functional role of NOMPC ARs in these mechanosensory neurons, we tested whether NOMPC channels with different numbers of ARs driven by a class III da neuron-specific Gal4 driver (19-12-Gal4) can functionally rescue touch sensitivity in the *nompC*-null mutant background. The GFP-tagged mutant NOMPC channels showed expression throughout the dendritic arborizations of the neurons, similar to that of wild-type NOMPC (Figure 3A). Non-permeabilized immunostaining of larval neurons revealed that both wild-type and 29+29ARs-NOMPC could be trafficked to the plasma membrane of dendrites. However, the expression level of 29+29ARs-NOMPC in class III da neurons was lower than that of wild-type NOMPC (Figures S3A and S3B), similar to what was observed in heterologous cells (Figures 1J). A single touch displacing the body wall by 20 μm triggered the firing of multiple action potentials of class III da neurons in wild-type, but not in *nompC* mutant, larvae (Figures 3B and 3C). Expression in class III da neurons of wild-type NOMPC or NOMPC with duplicated ARs (29+29ARs), but not of NOMPC with 29+17ARs, Δ1-29ARs, or Δ1-12ARs, rescued the mutant phenotype on touch-evoked response (Figures 3B and 3C). The partial rescue of NOMPC with 29+29ARs might be due to a lower expression level (Figures S3A and S3B). Together with our in vitro results shown in Figure 2, these findings illustrate that the integrity of the 29 ARs is essential for the mechanosensory function of NOMPC.

channels in vivo and the ability of class III da neurons to respond to gentle touch.

NOMPC-Mediated Larval Touch Sensation Requires ARs

Drosophila third-instar larvae show stereotyped behavioral responses to gentle touch that are mediated by the class III da neurons (Tsubouchi et al., 2012; Yan et al., 2013). Compared to the gentle touch response of wild-type controls, *nompC*-null mutant larvae displayed a greatly reduced touch response (Figure 3D). Expressing wild-type NOMPC, but not NOMPC channels with Δ1-29ARs, Δ1-12ARs, or 29+17ARs, in the class III da neurons of *nompC*-null mutants restored their touch sensitivity (Figure 3D). NOMPC channels with 29+29ARs could partially rescue touch sensation (Figure 3D), in accord with their lower capability of inducing mechanosensitive responses in S2 cells and class III da neurons (Figures 2E, 2F, and 3C). Thus, in addition to being essential for NOMPC mechanogating and mechanically evoked neuronal response of sensory neurons, NOMPC ARs are required for behavioral responses to touch stimuli.

ARs Are an Essential Component for Membrane-Microtubule Connectors

Mechanosensory campaniform sensilla in the *Drosophila* haltere bear filamentous connections between the plasma membrane and the microtubule cytoskeleton, known as membrane-microtubule connectors (MMCs). These MMCs have been suggested

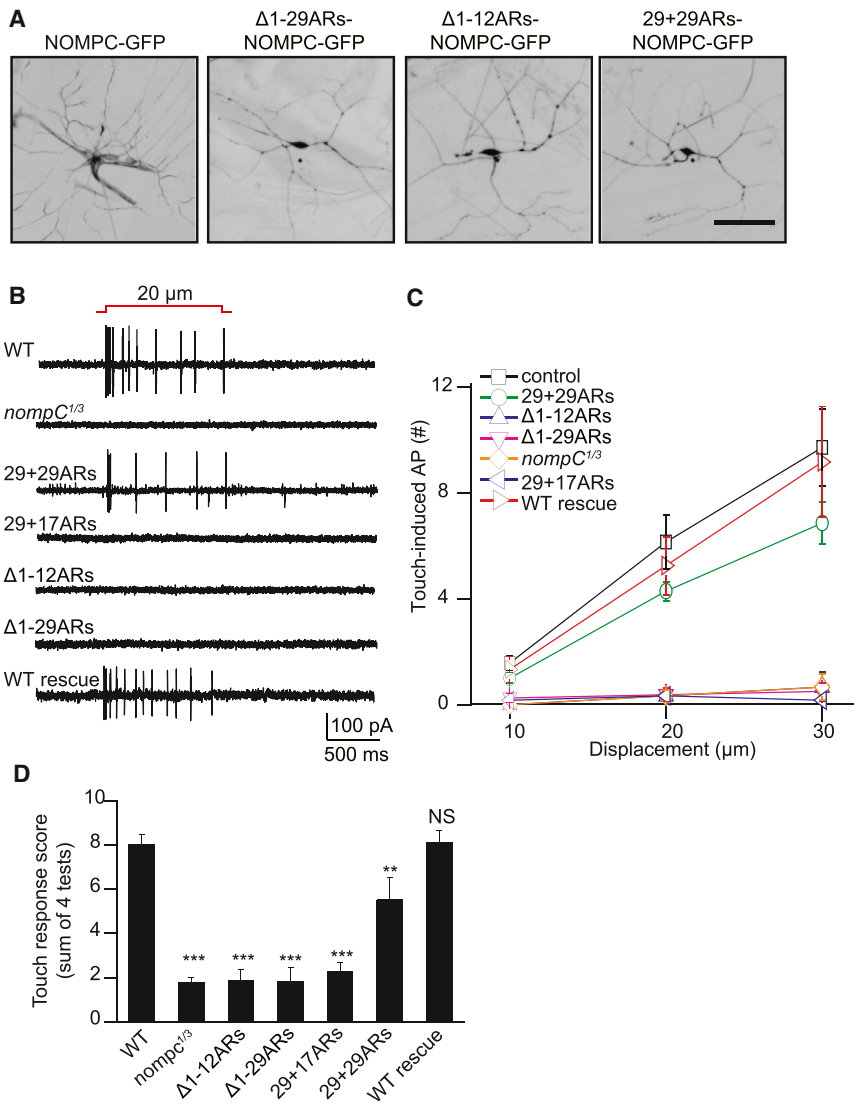


Figure 3. NOMPC Channel Functions In Vivo Require Ankyrin Repeats

(A) Wild-type and mutant NOMPC expression in class III da neurons of *nompC* null mutants (scale bar, 50 μm).

(B) Class III da neurons' response to mechanical stimulation, revealing functional rescue of *nompC* null phenotype by full-length NOMPC and 29+29ARs-NOMPC, but not other mutated NOMPC channels.

(C) Dose-dependent neuronal response to mechanical displacement of increasing distance on larval body wall.

(D) Rescue of the deficient touch response of *nompC* null mutant larvae by expressing full-length NOMPC or 29+29ARs-NOMPC, but not other mutated NOMPC channels in their class III da neurons with a class III da neurons specific Gal4 driver (19-12-Gal4). We used unpaired t test for comparison between two groups, and one-way analysis of variance followed by Tukey's comparison for analyses of three or four groups. ns, not significant. **p < 0.01, ***p < 0.001. All error bars denote ± SEM. Genotypes are as follows: control: *w¹¹⁸*, *nompC*: *nompC¹*/*nompC³*. WT rescue (full-length NOMPC): *nompC¹*/*nompC³*; 19-12-Gal4, UAS-NOMPC-GFP. Δ1-29ARs: *nompC¹*/*nompC³*; 19-12-Gal4/UAS-Δ1-29ARs-NOMPC-GFP. Δ1-12ARs: *nompC¹*/*nompC³*; 19-12-Gal4/UAS-Δ1-12ARs-NOMPC-GFP. 29+17ARs: *nompC¹*/*nompC³*; 19-12-Gal4, UAS-29+17ARs-NOMPC-GFP. 29+29ARs: *nompC¹*/*nompC³*; 19-12-Gal4, UAS-29+29ARs-NOMPC-GFP. All flies are in *w* background.

See also Figure S3.

MMCs (mean MMC length ± SD: 18 ± 5 nm [NOMPC^{29+29ARs}] versus 15 ± 5 nm [NOMPC⁺]) (Figures 4D and S4) and a larger spacing between the membrane and the microtubule (mean distance ± SD: 15 ± 4 nm [NOMPC^{29+29ARs}] versus 12 ± 4 nm [NOMPC⁺]) (Figure 4D).

to represent the ARs domain of NOMPC, tethering the channel to the microtubules (Liang et al., 2013). This raises the prospect that ARs might anchor to the microtubules and play a role in mechanical transduction (Zanini and Göpfert, 2013). Because of the favorable anatomy of campaniform sensilla in the *Drosophila* haltere, whose dendritic tips are packed with NOMPC and whose MMCs are arranged in a regular array that can be discerned with EM (Figure 4A), we used these sensory organs to test whether the ARs of NOMPC might be visualized as a tether. Consistent with previous observations (Liang et al., 2013), we found that MMCs were indeed present in wild-type flies ("NOMPC⁺") but virtually lost in *nompC¹*-null mutants ("NOMPC⁻") (Figures 4A–4C and S4). In *nompC¹* mutants, the MMCs were restored by expressing 29+29ARs-NOMPC in the receptors via *nompC*-GAL4, indicating that 29+29ARs-NOMPC integrates properly with its duplicated ARs domain binding microtubules (Figures 4A–4C and S4). Replacing wild-type NOMPC with 29+29ARs-NOMPC yielded significantly longer

A priori, we had not expected that replacing wild-type NOMPC with 29+29ARs-NOMPC would cause such ultrastructural effects; loss of NOMPC protein reportedly leaves the microtubule-membrane distance largely unaffected (Liang et al., 2013), suggesting that the MMCs adjust their tension to fit into this pre-set distance (Zanini and Göpfert, 2013). However, when we systematically analyzed the membrane-microtubule distance in NOMPC⁺ and NOMPC⁻ flies, we found that this distance was slightly, yet significantly, larger in *nompC*-null mutants (mean distance ± SD: 17 ± 5 nm [NOMPC⁻] versus 12 ± 4 nm [NOMPC⁺]) (Figure 4D). It thus appears that the MMCs pull together the membrane and the microtubules, explaining why changes in their spacing and in the MMC length can be discerned when NOMPC is replaced with 29+29ARs-NOMPC. In flies expressing 29+29ARs-NOMPC, the distribution of microtubule-membrane distances were significantly different from those observed in NOMPC⁺ and NOMPC⁻ flies (Figure 4D), assuming intermediate values.

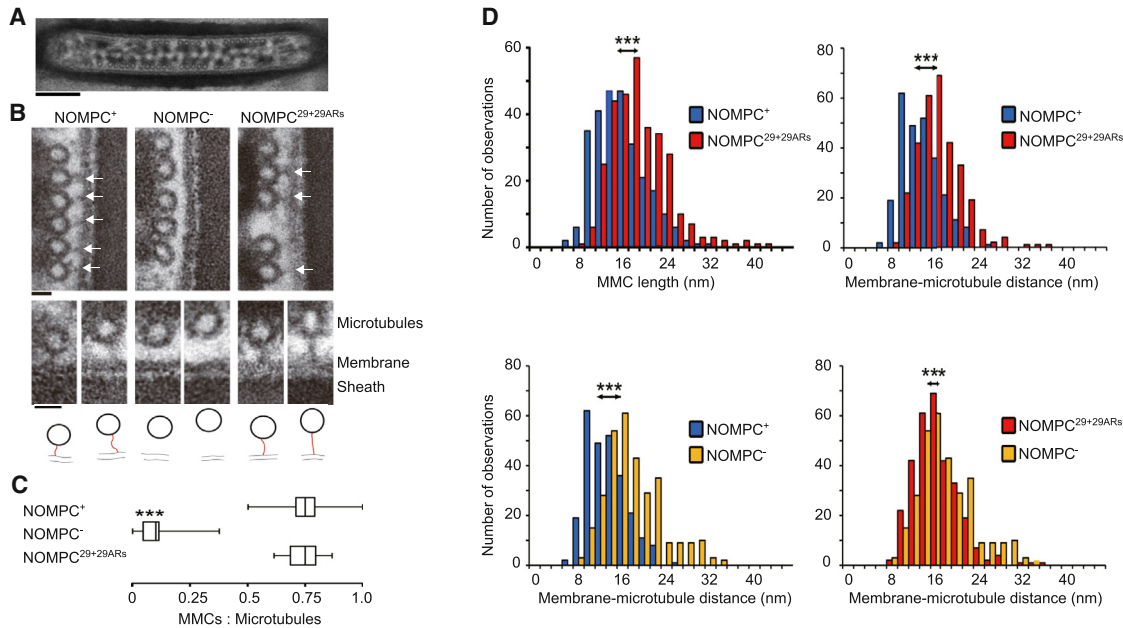


Figure 4. ARs Are the Essential Component of Membrane-Microtubule Connectors

(A) Overall structure the dendritic tip from haltere campaniform sensillium (scale bar, 200 nm).

(B) Cross-sections through the mechanosensitive dendritic tips of campaniform mechanoreceptors from the *Drosophila* haltere, depicting the extracellular sheath, the cell membrane, microtubules, and membrane-microtubule connectors (MMCs, arrows). MMCs are present in NOMPC⁺ wild-type flies (left) but lost in *nompC*⁻ null mutants (NOMPC⁻, middle). Expressing 29+29ARs-NOMPC in the null mutants via NOMPC-GAL4 restores the MMCs (NOMPC^{29+29ARs}, right) (scale bar, 20 nm). Lower panel: Close-ups of the MMCs (top) and respective MMC tracings (bottom). For each strain, examples with a small (left) and a large (right) microtubule-membrane distance are displayed (scale bar, 20 nm. Red lines highlight the MMCs structure).

(C) Relative abundance of MMCs in NOMPC⁺, NOMPC⁻, and NOMPC^{29+29ARs} flies, calculated as the fraction of microtubules that associate with MMCs. MMC abundances in NOMPC^{29+29ARs} flies resemble those in NOMPC⁺ flies ($p > 0.05$), and both differ significantly from the abundance in NOMPC⁻ flies that lack NOMPC protein ($p < 0.001$; two-tailed Mann-Whitney U-tests with Bonferroni correction; numbers of analyzed campaniform receptors: 31 (NOMPC⁺), 24 (NOMPC⁻), and 41 (NOMPC^{29+29ARs})).

(D) Upper left: length distribution of the MMCs in NOMPC⁺ ($n = 267$) and NOMPC^{29+29ARs} rescue flies, in which wild-type NOMPC is replaced with NOMPC^{29+29ARs} ($n = 307$). Upper right: respective distribution of the membrane-microtubule distance ($n = 261$ and 306, respectively). Lower left: membrane-microtubule distance in NOMPC⁺ ($n = 261$) compared with that of NOMPC⁻ flies ($n = 310$). Lower right: membrane-microtubule distance in NOMPC⁻ mutants compared with that of NOMPC^{29+29ARs} flies. ***Significant differences ($p < 0.001$; two-tailed Mann-Whitney U-tests with Bonferroni correction). Numbers of analyzed campaniform receptors as in (C). All error bars denote \pm SD.

See also Figure S4.

Microtubule Is Required for Mechanogating of NOMPC Channels

Heterologously expressed NOMPC proteins reportedly also associate with microtubules in cultured cells (Cheng et al., 2010). Double immune-labeling of NOMPC and microtubules revealed co-localization of NOMPC and microtubules in transfected S2 cells, especially in areas near the cell surface (Figure 5A). Staining of non-permeabilized cells with NOMPC antibody (α NOMPC-EC) further revealed that NOMPC channels on the plasma membrane co-localized with microtubules (Figure 5B). Furthermore, TIRF (total internal reflection fluorescence) microscopy imaging of the non-permeabilized staining is consistent with the notion that surface NOMPC channels interact with cortical microtubules in the vicinity of the membrane (Figures 5C and S5A). NOMPC expression in S2 cells did not alter the microtubule distribution (Figure S5B). To test whether NOMPC proteins bind to microtubules, we carried out the co-sedimentation assay. We found that wild-type NOMPC proteins from lysate of cells transfected with NOMPC associate with microtubules

(Figure 5D). Furthermore, affinity-purified NOMPC proteins (Figure S5C) also interacted strongly with microtubules (Figure 5D), indicating that NOMPC channels may bind to microtubules in cells.

In light of a recent report implicating interactions between TRPV1 channels and microtubules in osmotically induced cell shrinkage (Prager-Khoutorsky et al., 2014), we tested whether microtubules are required for mechanogating of NOMPC. Applying 100 nM of the microtubule-depolymerizing drug nocodazole (Vasquez et al., 1997) to the cytoplasmic side of the S2 cell membrane in inside-out patches drastically reduced the NOMPC current response to mechanical stimuli, shortly after the onset of nocodazole infusion (Figure 5E). Nocodazole also had a similar effect when tested in the cell-attached mode (Figures 5F and 5G). Nocodazole treatment had no effect on NOMPC expression levels in the plasma membrane as revealed by NOMPC surface staining (Figures S5D and S5E). Nocodazole specifically reduced the NOMPC mechanogated current without affecting the voltage gating of Kv1.2 and Kv2.1 channels (Figures

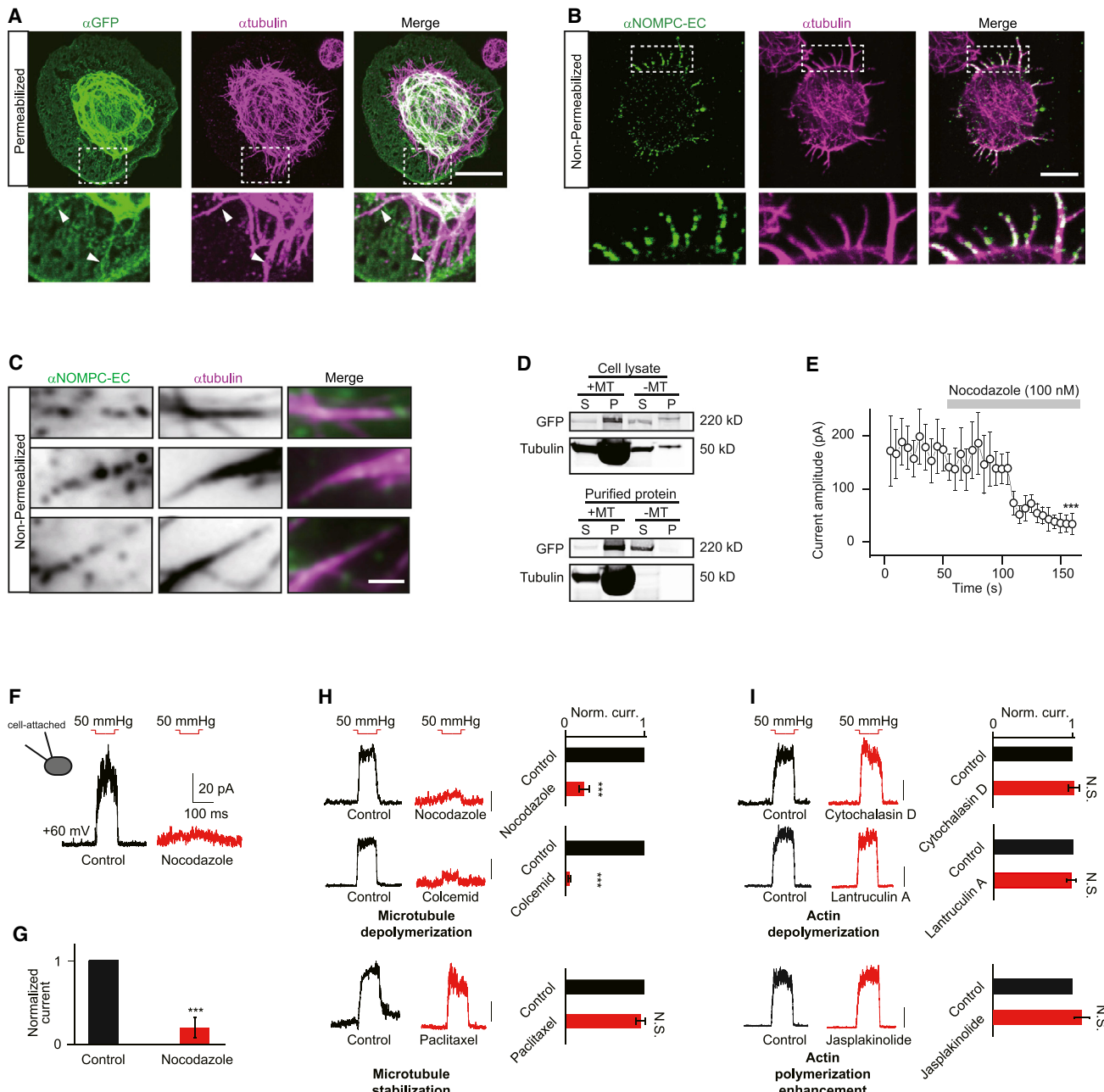


Figure 5. The NOMPC Channel's Association with Microtubules Is Important for Mechanogating

- (A) Staining of NOMPC and microtubules in NOMPC transfected S2 cells (scale bar, 5 μ m). A focal plane of 0.35 μ m was taken near the coverslip surface.
- (B) Staining of surface expressed NOMPC and microtubules in NOMPC transfected S2 cells (scale bar, 5 μ m). A focal plane of 0.35 μ m was taken near the coverslip surface.
- (C) TIRF microscopy showed interaction between membrane NOMPC and microtubules near the cell cortical area (scale bar, 1 μ m).
- (D) Co-sedimentation assay of NOMPC form cell lysate or affinity purification with tubulin (+MT, with tubulin; -MT, without tubulin; S, supernatant; P, pellet).
- (E) Time course of nocodazole blockage of NOMPC's mechanogated current (paired t test between time 0 and 150 s, ***p < 0.001, n = 6).
- (F and G) Nocodazole (100 nM) blockage of NOMPC's mechanogated current at cell-attached mode (**p < 0.001, paired t test, n = 6 and 6). Membrane patches were held at +60 mV.
- (H) An inside-out patch with NOMPC channels show mechanogated current (Norm. curr.: Normalized current) to negative pressure of 50 mmHg at +60 mV. This current was reduced by adding nocodazole (100 nM, n = 7) or colcemid (10 μ M, n = 6) but not paclitaxel (10 nM, n = 6) to the saline (scale bar, 50 pA. ***p < 0.001, N.S.: not significant, paired t test).
- (I) The mechanogated current of NOMPC to negative pressure of 50 mmHg at +60 mV was not effected by adding cytochalasin D (10 nM, n = 6), latrunculin A (1 μ M, n = 6) or jasplakinolide (100 nM, n = 7) to the saline (scale bar, 50 pA. N.S., not significant, paired t test).

See also Figure S5.

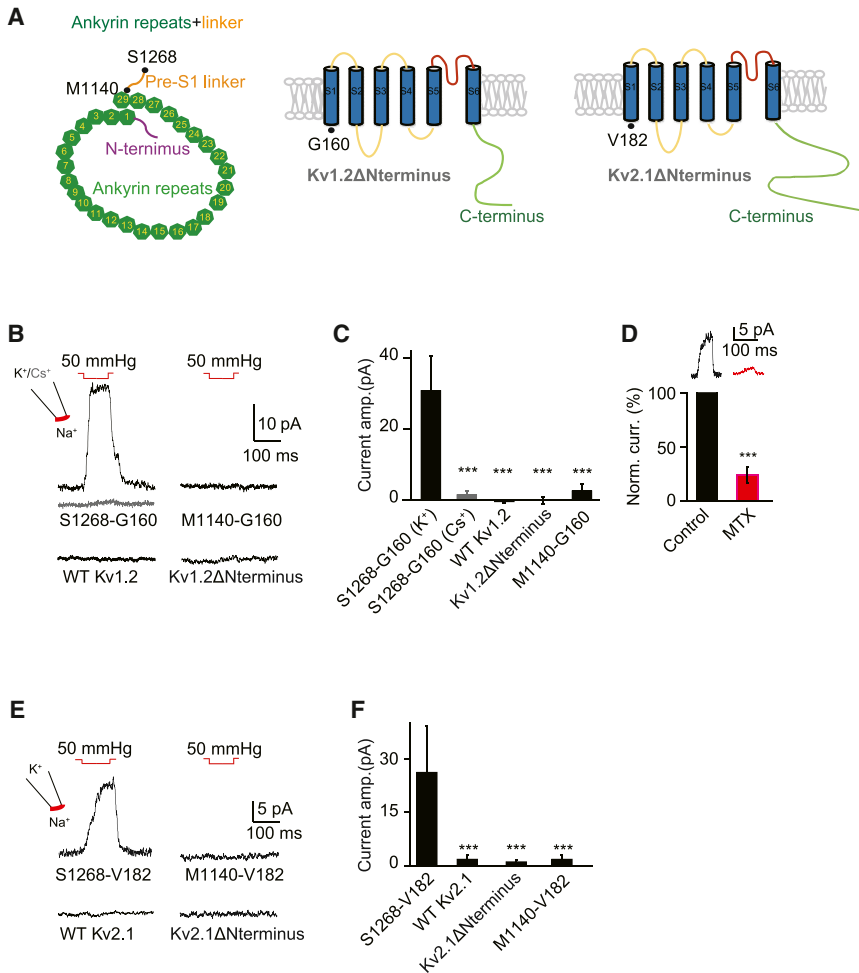


Figure 6. Ankyrin Repeats from NOMPC Confer Mechanosensitivity to Kv Channels

(A) Strategy of constructing chimeric channels between NOMPC and Kv1.2 or Kv2.1. Amino acids defining the borders of protein fragments are highlighted with black dots.

(B) Chimeric channel S1268-G160-Kv1.2 exhibited mechanogated current to membrane deformation caused by negative pressure, which was absent in Cs⁺ solution (gray trace), while full-length Kv1.2 (WT Kv1.2), Kv1.2 with truncated N terminus (Kv1.2 Δ Nterminus) and M1140-G160-Kv1.2 chimeric were not responsive to the same stimulus. Outside-out membrane patches were held at 60 mV.

(C) Plots of mechanogated current amplitudes ($n = 26, 8, 10, 7$ and 7). One-way analysis of variance followed by Tukey's comparison for analyses of multiple groups. *** $p < 0.001$.

(D) Mechanogated current was partially blocked with maurotoxin (MTX) (*** $p < 0.001$, paired t test, $n = 6$).

(E) Chimeric channel S1268-V182-Kv2.1 exhibited mechanogated current to membrane deformation caused by negative pressure, while full-length Kv2.1 (WT Kv2.1), Kv2.1 with truncated N terminus (Kv2.1 Δ Nterminus) and M1140-V182-Kv2.1 chimeric were not responsive to the same stimulus. Outside-out membrane patches were held at 60 mV.

(F) Plots of mechanogated current amplitudes ($n = 20, 7, 7$ and 7). One-way analysis of variance followed by Tukey's comparison for analyses of multiple groups. *** $p < 0.001$. All error bars denote \pm SEM.

See also Figure S6.

S5F–S5I). A chemically unrelated microtubule-depolymerizing drug colcemid had a similar effect on NOMPC channel gating, whereas enhancing microtubule polymerization with paclitaxel did not interfere with NOMPC activity (Figure 5H), further indicating that microtubules are essential for NOMPC mechanogating. In contrast, either stabilizing or disrupting the actin cytoskeleton had no effect on NOMPC mechanogating (Figure 5I). These findings indicate that NOMPC mechanosensitivity critically depends on the integrity of microtubules.

ARs Transferred from NOMPC to Kv Channels Confer Mechanosensitivity

Lastly, we tested if transferring the ARs from NOMPC to other ion channels could confer mechanosensitivity. We first chose as a recipient the mouse Kv1.2 voltage-gated potassium channel with a structure (Long et al., 2005) bearing architectural similarity with that of TRP channels (Kalia and Swartz, 2013). We constructed a chimeric protein by fusing the NOMPC N-terminal cytosolic domain, including the 29 ARs (M1-S1268 from NOMPC) with the Kv1.2 transmembrane (TM) domain and C terminus (G160-V499 from Kv1.2) (S1268-G160-Kv1.2 chimera) (Figure 6A). To test if mechanical stimuli gate this chimeric channel, we applied

50 mmHg pressure to outside-out patches obtained from transfected S2 cells. Mechanically evoked currents were detected in K⁺, but not Cs⁺, containing intracellular solutions, when the membrane potential was held at +60 mV (Figures 6B and 6C). By contrast, no mechanosensitive current was detectable in patches with wild-type Kv1.2 or Kv1.2 without its N-terminal cytosolic domain (Kv1.2 Δ Nterminus) (Figures 6B and 6C). Our experiments further revealed that the pre-S1 linker of NOMPC is important for mechanotransduction since a chimeric channel containing the NOMPC ARs, but not this linker (M1-M1120 from NOMPC) and the Kv1.2 TM domain and C terminus (G160-V499 from Kv1.2) (M1120-G160-Kv1.2 chimera), was not mechanosensitive (Figures 6B and 6C). To corroborate that the mechanosensitive current indeed originated from the S1268-G160-Kv1.2 chimera, we tested the specific Kv1.2 channel blocker maurotoxin (MTX) (Kharrat et al., 1997), which blocked the mechanosensitive current of the chimeric channel (Figure 6D), while having no effect on NOMPC channel activity (Figures S6A and S6B).

Kv1.2 was reported to be slightly mechanosensitive when stimulated with a piezo actuator (Hao et al., 2013), even though it was not mechanosensitive in our assay system (Figures 6B and 6C). To further validate that ARs are capable of conferring

mechanosensitivity, we constructed chimeric channels by transferring ARs from NOMPC to the trans-membrane domain and C terminus of another voltage-gated K⁺ channel Kv2.1 (Figure 6A), which was reported to show no mechanosensitivity (Hao et al., 2013). Again, the chimeric channel (S1268-V182-Kv2.1 chimera) exhibited mechanosensitivity similar to that of ARs-Kv1.2 chimeric channels, whereas wild-type Kv2.1, Kv2.1 lacking the N-terminal cytosolic domain (Kv2.1ΔNterminus), and a chimeric channel containing the NOMPC ARs, but not the linker and the Kv2.1 TM domain and C terminus (M1120-G182-Kv2.1 chimera), were not mechanosensitive (Figures 6E and 6F).

Chimeric Channels Share Similar Gating Mechanisms with NOMPC

Dose-dependent responses to mechanical stimuli and adaptation to prolonged mechanical stimulation are hallmarks of mechanosensitivity. Both chimeric channels showed dose-dependent responses when stimulated with different levels of pressure applied to the membrane, similar to that of NOMPC channels. The current amplitudes increased progressively with the pressure intensity (Figures 7A and S7A). The chimeric channels appeared to exhibit lower current amplitude to pressure as compared to wild-type NOMPC (Figures 2E, 7B, and S7B). Mechanosensitive currents from the S1268-G160-Kv1.2 chimera exhibited adaptation in response to maintained pressure stimulation (Figure 7C).

Next, we wanted to know whether the mechanosensitive currents of the chimeric channels depend on their interacting with microtubules. Similar to NOMPC channels, the chimeric channels exhibited microtubule interaction, which was more prominent than that of wild-type Kv channels (Figures 7E and S7C). The mechanogated current from ARs-Kv1.2 chimeric channels also depended on microtubule integrity, since disrupting microtubules with nocodazole largely abolished the mechanical response of the chimeric channels (Figure 7D), while leaving voltage-gating of wild-type Kv1.2 channels unaffected (Figures S5F and S5G). These experiments provide further support that ARs are part of a tether that links the channels with microtubules.

Without the Kv1.2 or Kv2.1 N terminus that includes the T1 tetramerization domain, the chimeric channels yielded smaller currents, and the voltage dependence of the normalized current (I/I_{max}) was shifted to the right for both Kv1.2 (Figures 7F–7H) and Kv2.1 (Figures 7I–7K). By applying a 50 mmHg pressure pulse to patches with ARs-Kv chimeric channels during each membrane depolarization step, we normalized the current at the plateau phase near the end of the depolarization, as well as the current during the pressure pulse to the current induced by depolarization to +100 mV (I_{max}) (Figures 7H and 7K). This revealed a synergistic action of voltage gating and mechanogating. Mechanical stimulation shifted the I-V curve of ARs-Kv channels to the left, while having no effect on wild-type Kv channels at any voltage tested, leaving the $V_{1/2}$ unchanged, which was 12.1 mV for Kv1.2 (Figure 7H) and 28 mV for Kv2.1 (Figure 7K). It thus appears that transferring the ARs of NOMPC confers mechanosensitivity to the chimeric channel containing the voltage sensor and the pore of Kv1.2 or Kv2.1, by allowing the chimeric channels to respond to mechanical force and activate to a greater extent than what could be achieved by depolarization.

DISCUSSION

In this study, we have provided evidence that ARs are essential for NOMPC mechanogating. We further show that mechanogating of NOMPC requires the integrity of microtubules associated to the plasma membrane, providing a precedent for a tethered mechanism for mechanotransduction channel activation. That the ARs of NOMPC can render voltage-gated potassium channels mechanosensitive highlights their functional sufficiency for mechanogating for those normally mechanoinsensitive channels.

The Components of MMCs

Documenting that duplicating the NOMPC ARs elongates the MMCs, our analysis supports previous indications (Liang et al., 2013) that the ARs are the main components of the MMCs. Based on our analysis, duplicating the ARs elongates the MMCs by ca. 20%, but does not duplicate their length. Possibly, the length increase is underestimated when being assayed only in a two-dimensional plane, and adjacent Ankyrins might also have moved closer together, which cannot be resolved by electron-microscopy. Alternatively, it seems likely that the MMC length is constrained by the membrane-microtubule distance, and that the MMCs are fit into this pre-set distance by adjusting their tension rather than their length. Measured membrane-microtubule distances are larger for NOMPC⁻ than for NOMPC⁺ flies, suggesting that the membrane and the microtubules are pulled together by the MMCs. Upon duplication of the ARs, the membrane-microtubule distance assumes intermediate values in between those of NOMPC⁻ and NOMPC⁺ flies, pointing to a reduced pull by—and a reduced stiffness of—the MMCs.

Hence, although the membrane-microtubule distance remains largely unaltered when NOMPC is lost (Liang et al., 2013), the slight change that shows up when large numbers of sensilla are analyzed explains why we detected the MMC elongation that arises when NOMPC is replaced by 29+29ARs-NOMPC.

The Regulation of NOMPC Gating by Other Cellular Components

Heterologous expression of NOMPC in S2 cells is sufficient to generate mechanosensitive channels. However, NOMPC channels and their homologs serve multiple functions in different mechanosensors (Chadha et al., 2015; Effertz et al., 2011; Kang et al., 2010; Lehnert et al., 2013; Ramdya et al., 2015; Sidi et al., 2003; Yan et al., 2013; Zhang et al., 2013, 2014), and their functions may be regulated differently in different cell types. It is conceivable that in different mechanosensors, NOMPC interacts with different sets of molecules that regulate channel opening in vivo, a possibility that warrants future investigation for better understanding of the mechanical gating machinery. Notably, Ankyrin domain is a motif for mediating protein-protein interactions in various biological processes, raising the possibility that other proteins bind to ARs to regulate NOMPC channel functions.

Our current findings support a tether model, in which NOMPC channels dock to intracellular cytoskeleton via their ARs that form the gating tethers. There are two different versions of the tether model: (1) an intracellular tether model and (2) a model involving both intracellular and extracellular tethers (Lumpkin

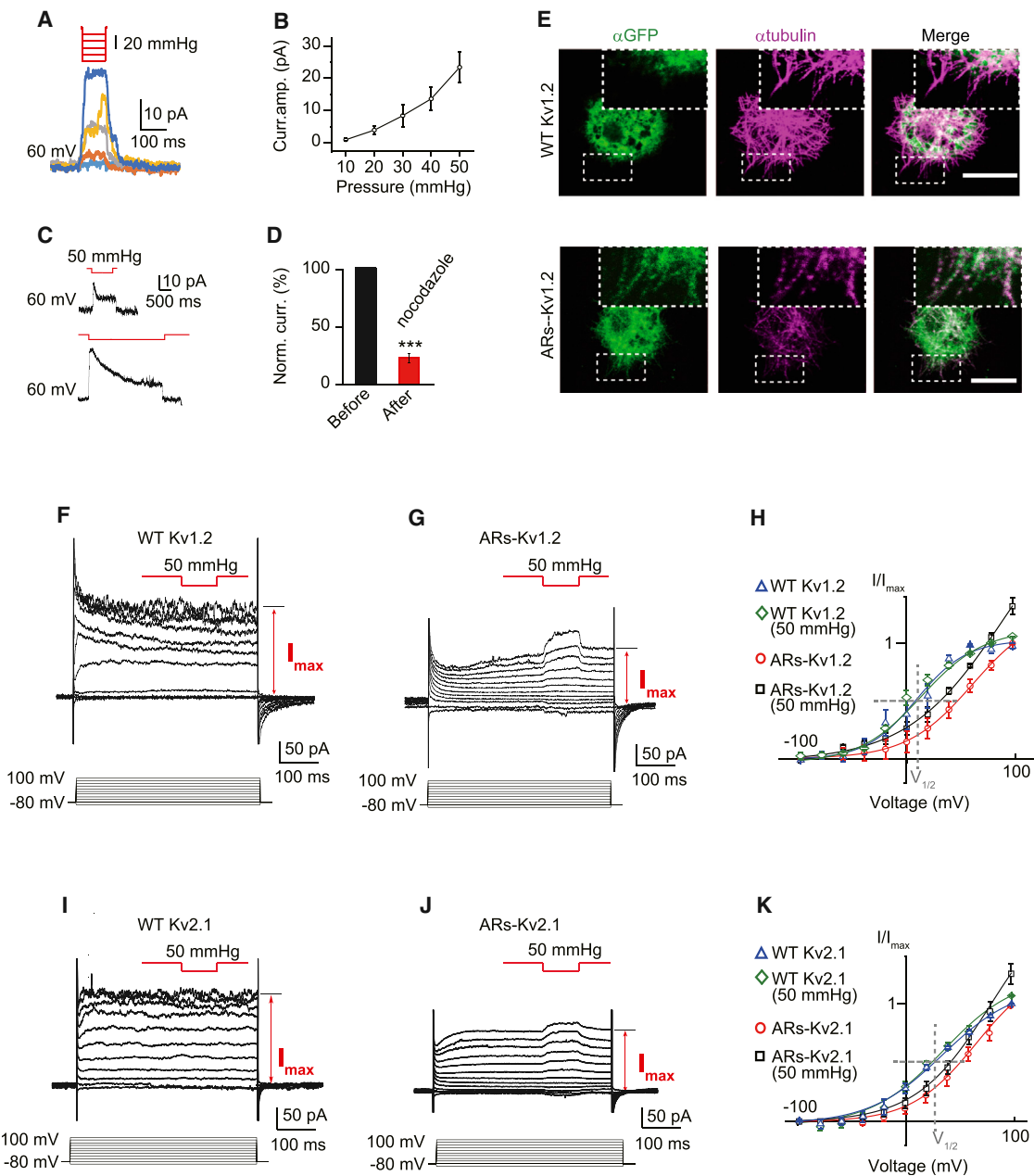


Figure 7. Biophysical Properties of Mechanosensitive Chimeric Channels

- (A) Mechanogated current amplitude of ARs-Kv1.2 (S1268-G160-Kv1.2) chimeric channel increased with higher pressure (pressure ranged from 10 mmHg to 50 mmHg with 10 mmHg increment).
- (B) Dose-dependent curve of mechanogated current of ARs-Kv1.2 to pressure ($n = 6$).
- (C) Mechanogated current from ARs-Kv1.2 chimeric channel showed adaptation to prolonged stimulation. Membrane patches were held at 60 mV.
- (D) Mechanogated current from ARs-Kv1.2 chimeric channel was blocked by nocodazole ($n = 6$, $***p < 0.001$).
- (E) Co-labeling of WT Kv1.2 channel and ARs-Kv1.2 chimeric channel with microtubules (scale bar, 5 μ m; boxes highlighting microtubule filaments).
- (F and G) Representative current traces of WT Kv1.2 (F) and ARs-Kv1.2 chimeric channel chimeric channels (G) with pressure application during depolarization.
- (H) I-V curves of WT Kv1.2 and ARs-Kv1.2 chimeric channel with or without mechanical stimulation, normalized to current without mechanical stimuli at +100 mV (gray dash lines highlighting the I-V relationship at $V_{1/2}$). Membrane patches were held at -80 mV ($n = 4$ for each condition).
- (I and J) Representative current traces of WT Kv2.1 (I) and ARs-Kv2.1 (S1268-V182-Kv2.1) chimeric channel (J) with pressure application during depolarization.
- (K) I-V curves of WT Kv2.1 and ARs-Kv2.1 chimeric channel with or without mechanical stimulation, normalized to current without mechanical stimuli at +100 mV (gray dash lines highlighting the I-V relationship at $V_{1/2}$). Membrane patches were held at -80 mV ($n = 4$ for WT Kv2.1 and 5 for chimeric channel). All error bars denote \pm SEM.

See also Figure S7.

and Caterina, 2007). In this study, we have provided strong evidence that ARs serve as an intracellular tether. It remains an open question whether there are any extracellular partners of NOMPC channels involved in their gating, either with direct or indirect interactions. NOMPA, a protein identified in the same genetic screen (Kernan et al., 1994) that also led to the discovery of NOMPC, is required for the normal development of chordotonal neurons in fly hearing organs (Boekhoff-Falk, 2005). Immunostaining of fly Johnston organs has shown that NOMPA localizes at the tip of chordotonal neurons and might play a role in docking the dendritic tips to their supporting cells (Chung et al., 2001). Further experiments would be needed to test whether NOMPC interacts with NOMPA or other proteins in the mechanosensory organs.

The Transformation of Mechanical Forces to Protein Dynamics

Our finding that ARs from NOMPC can gate chimeric Kv channels with their N termini replaced by these ARs, set the stage to create mechanotransduction channels/machineries by protein engineering. Compared to the chimeric channels, NOMPC is more susceptible to forces conveyed by ARs, raising the possibility that the trans-membrane domain of NOMPC is more amenable to mechanogating. We wish to emphasize that while our results strongly support the notion that ARs function as a tether for mechanogating of NOMPC, our results do not exclude the potential role of interactions between NOMPC protein and the membrane lipids nearby. Structural information of the NOMPC channel will be valuable for future investigation of force transmission and force-displacement conversion within a mechanotransduction channel protein, as well as the potential roles of the lipid molecules in the membrane near NOMPC.

EXPERIMENTAL PROCEDURES

Constructs of Mutated NOMPC Channels and Mechanogated Chimeric Channels

To generate NOMPC Ankyrin repeats deletion or elongation constructs, a PCR-based approach was used. The mutated NOMPC coding regions were cloned into pUAST vector for cell transfection and transgenic fly injections. To generate the synthetic mechanogated potassium channels, fragments of NOMPC Ankyrin repeats and Kv1.2/Kv2.1 trans-membrane domains were assembled into pAc5.1/V5-His A (Invitrogen) with C terminus GFP by following the Gibson Assembly Kit (NEB) protocol. See the [Supplemental Experimental Procedures](#) for construct sequences and primer information.

Immunostaining and Microscopy

For non-permeabilized staining, the transfected cells were incubated with primary antibody before fixation. For permeabilized staining, cells were fixed and incubated with PBST for 10 min. The cells were then blocked and stained with primary and secondary antibodies. Larval body wall neuron staining was performed as reported previously (Grueber et al., 2002). See the [Supplemental Experimental Procedures](#) for antibodies information and TIRF microscopy settings.

Biochemistry

The *Drosophila nompC* gene was expressed in and purified from a baculovirus transduction-based system with HEK293S GnTi⁻ cells. Cell lysate or the purified protein of interest was added to the polymerized microtubules or resuspension buffer alone as negative control. The mix was incubated at room

temperature for 20 min and spun for 10 min. The supernatant and pellet, resuspended in equal volume of the resuspension buffer, were collected and analyzed. See the [Supplemental Experimental Procedures](#) for cell culture, protein purification, and co-sedimentation details.

Electron Microscopy

Halteres and attached fragments of the thorax were fixed and then dehydrated in an ethanol series, including a block staining step. Infiltration was done for 2 days, raising the Durcupan concentration from 30% to 90%. 70-nm ultrathin sections were cut and transferred onto copper mesh grids. Micrographs were taken with a JEOL electron microscope with a GatanOrius 1200A camera. See the [Supplemental Experimental Procedures](#) for full transmission electron microscopy methods.

Electrophysiological Recordings

Drosophila S2 cells were cultured in Schneider's *Drosophila* medium, supplied with 5% fetal bovine serum at 25°C. An Effectene Kit (QIAGEN) was used to transfect cells, in accordance with the product's protocol. Recordings were carried out 1–2 days after transfection. Drugs were dissolved in the bath solution to the final concentration right before experiments. The drug-containing solution was perfused to the recording chamber. Larval electrophysiological recordings were carried out as previously described (Yan et al., 2013). See the [Supplemental Experimental Procedures](#) for sample preparation, recording solutions, drug concentrations, and electrophysiological recording configurations.

Mechanical Stimulation

A glass probe was driven by a piezo actuator to deliver mechanical stimulation. For larval body wall stimulation, the stimulation pipette was sealed and fire-polished to a diameter around 20 μm. For cultured S2 cells, the pipette was sealed and polished by microforge to a diameter around 1 μm. Negative pressure was applied to the membrane patches via a High Speed Pressure Clamp (HSPC; ALA Scientific). See the [Supplemental Experimental Procedures](#) for details on mechanical stimulation delivery.

SUPPLEMENTAL INFORMATION

Supplemental Information includes Supplemental Experimental Procedures, seven figures, and one movie and can be found with this article online at <http://dx.doi.org/10.1016/j.cell.2015.08.024>.

AUTHOR CONTRIBUTIONS

W.Z., L.E.C., and M.K. conducted most experiments. J.L. and T.C. made the chimeric constructs. M.P., P.J., and Z.G. helped on protein purification and biochemical assay. W.Z., M.K., M.C.G., L.Y.J., and Y.N.J. wrote the manuscript. All of the authors discussed the results and commented on the manuscript.

ACKNOWLEDGMENTS

We thank C. Zuker (Columbia University) for fly lines and J. Howard (Yale University) for a NOMPC antibody. We thank S.Q. Zhang and H.H. Yang for help on chimeric protein design, S. Yadav for assistance on antibody staining, D. Kamiyama and M. He for assistance on TIRF microscopy, and J. Trimmer for Kv2.1 clones. We thank S. Younger, S. Barbel, and M. Winkler for technical support and members of the Y.N.J. and M.C.G. labs for their discussion. This work was supported by DFG grants (SPP 1608 GO 1092/2-1, GO 1092/1-2, and SFB 889 A1) (to M.C.G.), a BRAINseed award (to Y.N.J., P.A., and L.Y.J.), and NIH grants (R37NS040929 and 5R01MH084234) (to Y.N.J.). L.Y.J. and Y.N.J. are investigators of the Howard Hughes Medical Institute.

Received: January 5, 2015

Revised: May 26, 2015

Accepted: July 13, 2015

Published: September 10, 2015

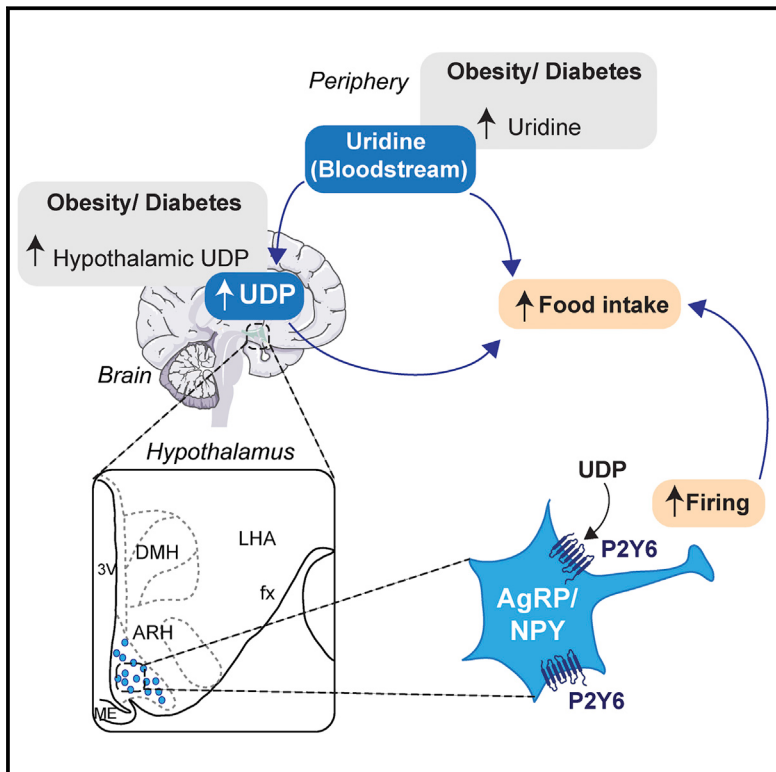
REFERENCES

- Anishkin, A., and Kung, C. (2013). Stiffened lipid platforms at molecular force foci. *Proc. Natl. Acad. Sci. USA* 110, 4886–4892.
- Arnadóttir, J., and Chalfie, M. (2010). Eukaryotic mechanosensitive channels. *Annu. Rev. Biophys.* 39, 111–137.
- Bechstedt, S., and Howard, J. (2008). Hearing mechanics: a fly in your ear. *Curr. Biol.* 18, R869–R870.
- Boekhoff-Falk, G. (2005). Hearing in *Drosophila*: development of Johnston's organ and emerging parallels to vertebrate ear development. *Dev. Dyn.* 232, 550–558.
- Brohawn, S.G., del Márquez, J., and MacKinnon, R. (2012). Crystal structure of the human K2P TRAAK, a lipid- and mechano-sensitive K⁺ ion channel. *Science* 335, 436–441.
- Brohawn, S.G., Campbell, E.B., and MacKinnon, R. (2014a). Physical mechanism for gating and mechanosensitivity of the human TRAAK K⁺ channel. *Nature* 516, 126–130.
- Brohawn, S.G., Su, Z., and MacKinnon, R. (2014b). Mechanosensitivity is mediated directly by the lipid membrane in TRAAK and TREK1 K⁺ channels. *Proc. Natl. Acad. Sci. USA* 111, 3614–3619.
- Chadha, A., Kaneko, M., and Cook, B. (2015). NOMPC-dependent mechanotransduction shapes the dendrite of proprioceptive neurons. *Neurosci. Lett.* 597, 111–116.
- Cheng, L.E., Song, W., Looger, L.L., Jan, L.Y., and Jan, Y.N. (2010). The role of the TRP channel NompC in *Drosophila* larval and adult locomotion. *Neuron* 67, 373–380.
- Chung, Y.D., Zhu, J., Han, Y., and Kernan, M.J. (2001). nompA encodes a PNS-specific, ZP domain protein required to connect mechanosensory dendrites to sensory structures. *Neuron* 29, 415–428.
- Coste, B., Xiao, B., Santos, J.S., Syeda, R., Grandl, J., Spencer, K.S., Kim, S.E., Schmidt, M., Mathur, J., Dubin, A.E., et al. (2012). Piezo proteins are pore-forming subunits of mechanically activated channels. *Nature* 483, 176–181.
- Effertz, T., Wiek, R., and Göpfert, M.C. (2011). NompC TRP channel is essential for *Drosophila* sound receptor function. *Curr. Biol.* 21, 592–597.
- Gaudet, R. (2008). A primer on ankyrin repeat function in TRP channels and beyond. *Mol. Biosyst.* 4, 372–379.
- Gillespie, P.G., and Walker, R.G. (2001). Molecular basis of mechanosensory transduction. *Nature* 413, 194–202.
- Gong, J., Wang, Q., and Wang, Z. (2013). NOMPC is likely a key component of *Drosophila* mechanotransduction channels. *Eur. J. Neurosci.* 38, 2057–2064.
- Goodman, M.B., Ernstson, G.G., Chelur, D.S., O'Hagan, R., Yao, C.A., and Chalfie, M. (2002). MEC-2 regulates *C. elegans* DEG/ENaC channels needed for mechanosensation. *Nature* 415, 1039–1042.
- Grillet, N., Kazmierczak, P., Xiong, W., Schwander, M., Reynolds, A., Sakaguchi, H., Tokita, J., Kachar, B., and Müller, U. (2009). The mechanotransduction machinery of hair cells. *Sci. Signal.* 2, pt5.
- Grueber, W.B., Jan, L.Y., and Jan, Y.N. (2002). Tiling of the *Drosophila* epidermis by multidendritic sensory neurons. *Development* 129, 2867–2878.
- Hao, J., Padilla, F., Dandonneau, M., Lavebratt, C., Lesage, F., Noël, J., and Delmas, P. (2013). Kv1.1 channels act as mechanical brake in the senses of touch and pain. *Neuron* 77, 899–914.
- Howard, J., and Bechstedt, S. (2004). Hypothesis: a helix of ankyrin repeats of the NOMPC-TRP ion channel is the gating spring of mechanoreceptors. *Curr. Biol.* 14, R224–R226.
- Hu, J., Chiang, L.Y., Koch, M., and Lewin, G.R. (2010). Evidence for a protein tether involved in somatic touch. *EMBO J.* 29, 855–867.
- Jin, X., Touhey, J., and Gaudet, R. (2006). Structure of the N-terminal ankyrin repeat domain of the TRPV2 ion channel. *J. Biol. Chem.* 281, 25006–25010.
- Julius, D. (2013). TRP channels and pain. *Annu. Rev. Cell Dev. Biol.* 29, 355–384.
- Kalia, J., and Swartz, K.J. (2013). Exploring structure-function relationships between TRP and Kv channels. *Sci. Rep.* 3, 1523.
- Kamikouchi, A., Inagaki, H.K., Effertz, T., Hendrich, O., Fiala, A., Göpfert, M.C., and Ito, K. (2009). The neural basis of *Drosophila* gravity-sensing and hearing. *Nature* 458, 165–171.
- Kang, L., Gao, J., Schäfer, W.R., Xie, Z., and Xu, X.Z. (2010). *C. elegans* TRP family protein TRP-4 is a pore-forming subunit of a native mechanotransduction channel. *Neuron* 67, 381–391.
- Kernan, M., Cowan, D., and Zuker, C. (1994). Genetic dissection of mechanosensory transduction: mechanoreception-defective mutations of *Drosophila*. *Neuron* 12, 1195–1206.
- Kharrat, R., Mansuelle, P., Sampieri, F., Crest, M., Oughideni, R., Van Rietschoten, J., Martin-Eauclaire, M.F., Rochat, H., and El Ayeb, M. (1997). Maurotoxin, a four disulfide bridge toxin from *Scorpio maurus* venom: purification, structure and action on potassium channels. *FEBS Lett.* 406, 284–290.
- Kung, C. (2005). A possible unifying principle for mechanosensation. *Nature* 436, 647–654.
- Lee, G., Abdi, K., Jiang, Y., Michaely, P., Bennett, V., and Marszalek, P.E. (2006). Nanospring behaviour of ankyrin repeats. *Nature* 440, 246–249.
- Lehnert, B.P., Baker, A.E., Gaudry, Q., Chiang, A.S., and Wilson, R.I. (2013). Distinct roles of TRP channels in auditory transduction and amplification in *Drosophila*. *Neuron* 77, 115–128.
- Liang, X., Madrid, J., Saleh, H.S., and Howard, J. (2011). NOMPC, a member of the TRP channel family, localizes to the tubular body and distal cilium of *Drosophila* campaniform and chordotonal receptor cells. *Cytoskeleton (Hoboken)* 68, 1–7.
- Liang, X., Madrid, J., Gärtner, R., Verbavatz, J.M., Schiklenk, C., Wilsch-Bräunner, M., Bogdanova, A., Stenger, F., Voigt, A., and Howard, J. (2013). A NOMPC-dependent membrane-microtubule connector is a candidate for the gating spring in fly mechanoreceptors. *Curr. Biol.* 23, 755–763.
- Lolicato, M., Riegelhaupt, P.M., Arrigoni, C., Clark, K.A., and Minor, D.L., Jr. (2014). Transmembrane helix straightening and buckling underlies activation of mechanosensitive and thermosensitive K(2P) channels. *Neuron* 84, 1198–1212.
- Long, S.B., Campbell, E.B., and Mackinnon, R. (2005). Crystal structure of a mammalian voltage-dependent Shaker family K⁺ channel. *Science* 309, 897–903.
- Lumpkin, E.A., and Caterina, M.J. (2007). Mechanisms of sensory transduction in the skin. *Nature* 445, 858–865.
- Montell, C. (2004). Molecular genetics of *Drosophila* TRP channels. *Novartis Found Symp.* 258, 3–12, discussion 12–17, 98–102, 263–106.
- Montell, C. (2005). *Drosophila* TRP channels. *Pflugers Arch.* 451, 19–28.
- Morgan, C.P., and Barr-Gillespie, P.G. (2013). Mechanotransduction: the elusive hair cell transduction channel revealed? *Curr. Biol.* 23, R887–R890.
- Orr, A.W., Helmke, B.P., Blackman, B.R., and Schwartz, M.A. (2006). Mechanisms of mechanotransduction. *Dev. Cell* 10, 11–20.
- Paulsen, C.E., Armache, J.P., Gao, Y., Cheng, Y., and Julius, D. (2015). Structure of the TRPA1 ion channel suggests regulatory mechanisms. *Nature* 520, 511–517.
- Phillips, K.R., Biswas, A., and Cyr, J.L. (2008). How hair cells hear: the molecular basis of hair-cell mechanotransduction. *Curr. Opin. Otolaryngol. Head Neck Surg.* 16, 445–451.
- Prager-Khoutorsky, M., Khoutorsky, A., and Bourque, C.W. (2014). Unique interwoven microtubule scaffold mediates osmosensory transduction via physical interaction with TRPV1. *Neuron* 83, 866–878.
- Ramdy, P., Lichocki, P., Cruchet, S., Frisch, L., Tse, W., Floreano, D., and Benton, R. (2015). Mechanosensory interactions drive collective behaviour in *Drosophila*. *Nature* 519, 233–236.
- Sidi, S., Friedrich, R.W., and Nicolson, T. (2003). NompC TRP channel required for vertebrate sensory hair cell mechanotransduction. *Science* 301, 96–99.
- Sotomayor, M., Corey, D.P., and Schulten, K. (2005a). In search of the hair-cell gating spring elastic properties of ankyrin and cadherin repeats. *Structure* 13, 669–682.

- Sotomayor, M., Corey, D.P., and Schulten, K. (2005b). Molecular dynamics study of mechanosensation proteins ankyrin and cadherin. *Biophys. J.* **88**, 288a–288a.
- Sotomayor, M., and Schulten, K. (2007). Single-molecule experiments in vitro and in silico. *Science* **316**, 1144–1148.
- Tsubouchi, A., Caldwell, J.C., and Tracey, W.D. (2012). Dendritic filopodia, Ripped Pocket, NOMPC, and NMDARs contribute to the sense of touch in *Drosophila* larvae. *Curr. Biol.* **22**, 2124–2134.
- Vasquez, R.J., Howell, B., Yvon, A.M., Wadsworth, P., and Cassimeris, L. (1997). Nanomolar concentrations of nocodazole alter microtubule dynamic instability in vivo and in vitro. *Mol. Biol. Cell* **8**, 973–985.
- Venkatachalam, K., and Montell, C. (2007). TRP channels. *Annu. Rev. Biochem.* **76**, 387–417.
- Vollrath, M.A., Kwan, K.Y., and Corey, D.P. (2007). The micromachinery of mechanotransduction in hair cells. *Annu. Rev. Neurosci.* **30**, 339–365.
- Yan, Z., Zhang, W., He, Y., Gorczyca, D., Xiang, Y., Cheng, L.E., Meltzer, S., Jan, L.Y., and Jan, Y.N. (2013). *Drosophila* NOMPC is a mechanotransduction channel subunit for gentle-touch sensation. *Nature* **493**, 221–225.
- Yang, Y., Nanduri, S., Sen, S., and Qin, J. (1998). The structural basis of ankyrin-like repeat function as revealed by the solution structure of myotrophin. *Structure* **6**, 619–626.
- Zanini, D., and Göpfert, M.C. (2013). Mechanosensation: tethered ion channels. *Curr. Biol.* **23**, R349–R351.
- Zhang, W., Yan, Z., Jan, L.Y., and Jan, Y.N. (2013). Sound response mediated by the TRP channels NOMPC, NANCHUNG, and INACTIVE in chordotonal organs of *Drosophila* larvae. *Proc. Natl. Acad. Sci. USA* **110**, 13612–13617.
- Zhang, W., Yan, Z., Li, B., Jan, L.Y., and Jan, Y.N. (2014). Identification of motor neurons and a mechanosensitive sensory neuron in the defecation circuitry of *Drosophila* larvae. *eLife* **3**. <http://dx.doi.org/10.7554/eLife.03293>.

Hypothalamic UDP Increases in Obesity and Promotes Feeding via P2Y6-Dependent Activation of AgRP Neurons

Graphical Abstract



Authors

Sophie M. Steculorum, Lars Paeger, Stephan Bremser, ..., Marco Idzko, Peter Kloppenburg, Jens C. Brüning

Correspondence

bruening@sf.mpg.de

In Brief

The UDP-selective P2Y6 receptor controls orexigenic AgRP neurons and food intake regulation. The pathway is deregulated in obesity, making P2Y6 a potential target for treatment.

Highlights

- P2Y6 are highly expressed in ARH neurons
- UDP activates orexigenic AgRP neurons through P2Y6-dependent signaling
- UDP activates feeding through activation of AgRP neurons
- Hypothalamic UDP synthesis increases in obesity through elevated circulating uridine supply

Hypothalamic UDP Increases in Obesity and Promotes Feeding via P2Y6-Dependent Activation of AgRP Neurons

Sophie M. Steculorum,^{1,2,3} Lars Paeger,^{3,4} Stephan Bremser,^{3,4} Nadine Evers,^{1,2,3} Yvonne Hinze,⁵ Marco Idrzko,⁶ Peter Kloppenburg,^{3,4} and Jens C. Brüning,^{1,2,3,7,*}

¹Max Planck Institute for Metabolism Research, Department of Neuronal Control of Metabolism, Gleueler Str. 50, 50931 Cologne, Germany

²Center for Endocrinology, Diabetes and Preventive Medicine (CEDP), University Hospital Cologne, 50924 Cologne, Germany

³Excellence Cluster on Cellular Stress Responses in Aging Associated Diseases (CECAD) and Center of Molecular Medicine Cologne (CMMC), University of Cologne, Joseph-Stelzmann-Str. 26, 50931 Cologne, Germany

⁴Biozentrum, Institute for Zoology, University of Cologne, Zülpicher Str. 47a, 50674 Cologne, Germany

⁵Max Planck Institute for Biology of Ageing, Cologne, Joseph-Stelzmann-Str. 9B 50931 Cologne, Germany

⁶Department of Pneumology, Freiburg University Medical Center, Albert-Ludwigs-University, Hugstetter Str. 49, 79106 Freiburg, Germany

⁷National Center for Diabetes Research (DZD), Ingolstädter Land Str. 1, 85764 Neuherberg, Germany

*Correspondence: bruening@sf.mpg.de

<http://dx.doi.org/10.1016/j.cell.2015.08.032>

SUMMARY

Activation of orexigenic AgRP-expressing neurons in the arcuate nucleus of the hypothalamus potently promotes feeding, thus defining new regulators of AgRP neuron activity could uncover potential novel targets for obesity treatment. Here, we demonstrate that AgRP neurons express the purinergic receptor 6 (P2Y6), which is activated by uridine-diphosphate (UDP). In vivo, UDP induces ERK phosphorylation and cFos expression in AgRP neurons and promotes action potential firing of these neurons in brain slice recordings. Consequently, central application of UDP promotes feeding, and this response is abrogated upon pharmacologic or genetic inhibition of P2Y6 as well as upon pharmacogenetic inhibition of AgRP neuron activity. In obese animals, hypothalamic UDP content is elevated as a consequence of increased circulating uridine concentrations. Collectively, these experiments reveal a potential regulatory pathway in obesity, where peripheral uridine increases hypothalamic UDP concentrations, which in turn can promote feeding via PY6-dependent activation of AgRP neurons.

INTRODUCTION

Facing the escalating burden of obesity and type 2 diabetes mellitus (T2DM) (Geiss et al., 2014; WHO, 2006), there is an urge to further define the regulatory principles underlying the control of body weight and glucose homeostasis and to define novel targets for therapeutic intervention. Research over the past decades revealed the critical importance of the central nervous system (CNS) and, more specifically, the hypothalamus in control of homeostatic processes governing energy balance and glycemic control (Schwartz et al., 2013; Sohn et al., 2013).

Here, particularly the arcuate nucleus of the hypothalamus (ARH) is of critical importance to coordinate food intake and glycemic control with the energy state of the organism (Sohn et al., 2013; Varela and Horvath, 2012). The ARH contains two main functionally antagonistic neuronal populations: the orexigenic neurons co-expressing neuropeptide Y (NPY) and agouti-related peptide (AgRP) and the anorexigenic neurons that produce proopiomelanocortin (POMC) (Sohn et al., 2013; Varela and Horvath, 2012). Thus, the melanocortin circuitry downstream of AgRP and POMC neurons orchestrates behavioral responses such as feeding and locomotor activity, as well as changes in peripheral glucose metabolism in rodents and in humans (Cone, 2005; Farooqi and O’Rahilly, 2008).

AgRP/NPY and POMC neurons express leptin and insulin receptors, and several studies previously highlighted the critical importance of insulin and leptin action specifically on AgRP/NPY and/or POMC neurons in their anorexigenic and glucoregulatory effects (Belgardt and Brüning, 2010; Könner and Brüning, 2012; Varela and Horvath, 2012; Vogt and Brüning, 2013). However, while leptin and insulin are indisputably critical regulators of AgRP/NPY and POMC neurons, the discovery that obesity and T2DM are associated with the onset of neuronal leptin and insulin resistance in these two neuronal populations limits pharmaceutical interventions targeting these hormonal pathways (Friedman, 2004; Könner and Brüning, 2012; Vogt and Brüning, 2013). Thus, defining alternative signaling pathways in control of the melanocortin circuitry will ultimately expand the panel of putative drugs targets for the treatment of obesity and T2DM.

Among all potential new regulators of the central control of feeding behavior and glucose homeostasis, the family of G-protein-coupled receptors (GPCRs) carries enormous therapeutic potential since, on one hand, they are well known to regulate virtually all core physiological functions and, on the other hand, they are attractive targets for pharmacological intervention due to their high-affinity binding and selectivity (Allen and Roth, 2011). Recently, Ren and coworkers discovered that Gpr17 is expressed on AgRP neurons and that Gpr17 downregulation secondary to AgRP-specific FoxO1 deletion is associated with

decreased body weight and food intake (Ren et al., 2012). Given the putative role of Gpr17 in feeding regulation, we thought of investigating whether related GPCRs could also be expressed on hypothalamic neurons, thereby controlling their function and associated behavioral outcomes. Gpr17 is structurally and phylogenetically related to the purinergic receptors family (P2), more specifically to P2Y receptors activated by uracil nucleotides (Daniele et al., 2011). Interestingly, members of the P2Y family, such as P2Y1 and P2Y14, have previously been associated with homeostatic processes such as food intake and insulin sensitivity (Burnstock et al., 2011; Kittner et al., 2006; Xu et al., 2012). Here, we find that, among uracil nucleotide-sensitive P2Y receptors with so far unknown function in the central control of energy and glucose homeostasis, P2Y6 is the highest expressed in the ARH. Therefore, we decided to directly focus on the putative role of P2Y6 in energy and glucose homeostasis. P2Y6 is a receptor for the nucleotide uridine-diphosphate (UDP), whose synthesis in the CNS depends on the salvage pathway, which is directly controlled by the peripheral supply of the precursor metabolite uridine (Cansev, 2006; Ipata, 2011).

We demonstrate that UDP activates AgRP neurons in a P2Y6-dependent fashion. In accordance with its stimulatory effect on AgRP neurons, centrally administered UDP displays orexigenic effects, which are abrogated upon pharmacologic or genetic inhibition of P2Y6 as well as upon pharmacogenetic inhibition of AgRP neurons. Moreover, hypothalamic UDP content is increased in obesity. Our experiments thus reveal a potential regulatory pathway in obesity, where elevated uridine supply from the periphery increases hypothalamic UDP content to activate AgRP neurons and ultimately promote positive energy balance.

RESULTS

P2Y6 Are Expressed in Neurons of Key Hypothalamic Feeding Regions

In order to identify potential novel GPCR-coupled regulators of energy homeostasis, we assessed the expression of P2Y receptors activated by uracil nucleotides, which have not previously been linked to energy and glucose homeostasis in hypothalamus as well as in microdissected ARH. These analyses revealed that, both in hypothalamus and in microdissected ARH, the expression level of *P2ry6*-mRNA was ten times higher as compared to the other studied P2Y members (Figures S1A and S1B). To further investigate whether P2Y6 is particularly enriched in the ARH, we next compared the expression levels of *P2ry6*-mRNA in different hypothalamic regions such as the ARH, the paraventricular nucleus of the hypothalamus (PVH), the ventromedial nucleus of the hypothalamus (VMH), the dorsomedial nucleus of the hypothalamus (DMH), and the lateral hypothalamic area (LHA). The greatest mRNA expression level of *P2ry6* was found in the ARH, where it is expressed \approx 25 to 40% higher than in other hypothalamic regions (Figure 1A). Since P2Y6 has been described as the receptor for uridine-diphosphate (UDP), we next analyzed whether the expression of P2Y6 occurs in the same regions where UDP is produced. A critical step in neuronal UDP synthesis relies on phosphorylation of uridine, which is mediated by uridine-cytidine kinases (UCK)-1 and -2 (Anderson and

Brockman, 1964). Expression analyses of *Uck1* and *Uck2* mRNA revealed an overall similar pattern to that of P2Y6 (Figures 1B and 1C).

Next, we aimed to verify P2Y6 expression in hypothalamic nuclei through the analyses of GFP immunohistochemistry in mice, which express GFP from the endogenous *P2ry6* locus (*P2Y6-EGFP* mice) (Bar et al., 2008). Consistent with the pattern of *P2ry6* mRNA expression, these immunohistochemical analyses revealed a very specific regional distribution of P2Y6-dependent GFP expression most prominently in the ARH and to a minor extent in the PVH, while the VMH, the DMH, and LHA exhibited only a minor proportion of cells positive for GFP expression (Figures 1D and S1C). We also compared the expression pattern of P2Y6-dependent GFP expression with that of the endogenous *P2ry6* mRNA available through the Allen Brain Atlas, which revealed a similar distribution of *P2ry6* expression in the hypothalamus (<http://mouse.brain-map.org/experiment/show?id=1800>). Collectively, these analyses revealed a predominant enrichment of P2Y6 expression in the ARH.

To further investigate which cell type in the ARH expresses P2Y6, we next performed co-immunohistochemical staining for GFP in *P2Y6-EGFP* mice and for antibodies directed to either CD11b (microglia) or GFAP (astrocytes) or using fluorescent Nissl staining NeuroTrace (neurons). There was no overlap between cells expressing GFAP or CD11b and those expressing GFP from the *P2ry6* locus (Figure 1E). In contrast, there was a clear overlap of immunoreactivity for P2Y6-dependent GFP expression in the NeuroTrace-positive neurons in the ARH (Figure 1E). Taken together, these experiments clearly indicate that the UDP receptor P2Y6 is highly expressed in neurons of the ARH.

The P2Y6 Agonist UDP Activates Neurons in the ARH

Having identified a restricted domain of P2Y6 expression in neurons of the ARH, we next investigated whether intracerebroventricular (icv) application of the P2Y6 agonist UDP modulates activation of ARH neurons. Following icv administration of either vehicle (i.e., saline) or 30 μ M UDP, quantitative assessment of cFos immunoreactive cells revealed a 2.5-fold increase in cFos immunoreactivity in the ARH (Figure 2A). Similarly, the VMH, DMH, and LHA exhibited a significant increase in cFos-immunoreactive cells following icv UDP application (Figure S2A). In contrast, cFos immunoreactivity in the PVH was only increased to a minor extent (Figure S2A). Since cFos activation can occur either directly in the respective brain area or indirectly via *trans*-synaptic activation of cells located in projecting areas of directly activated neurons, we sought to investigate the direct effect of UDP on its P2Y6. In the periphery, UDP action on P2Y6 can lead to tyrosine phosphorylation of MAP kinases ERK-1 and ERK-2 (pERK) (Bar et al., 2008). Using a hypothalamic cell line, we found that, indeed, UDP activated ERK-phosphorylation also in these cells (Figure S2B). Therefore, we used pERK as a direct readout of UDP action on P2Y6. Quantification of pERK immunoreactivity revealed that UDP significantly increased the number of pERK-positive cells in the ARH (Figure 2B). Taken together, these analyses revealed that P2Y6 are expressed on ARH neurons and that they are functional, as UDP directly activates signaling in these neurons.

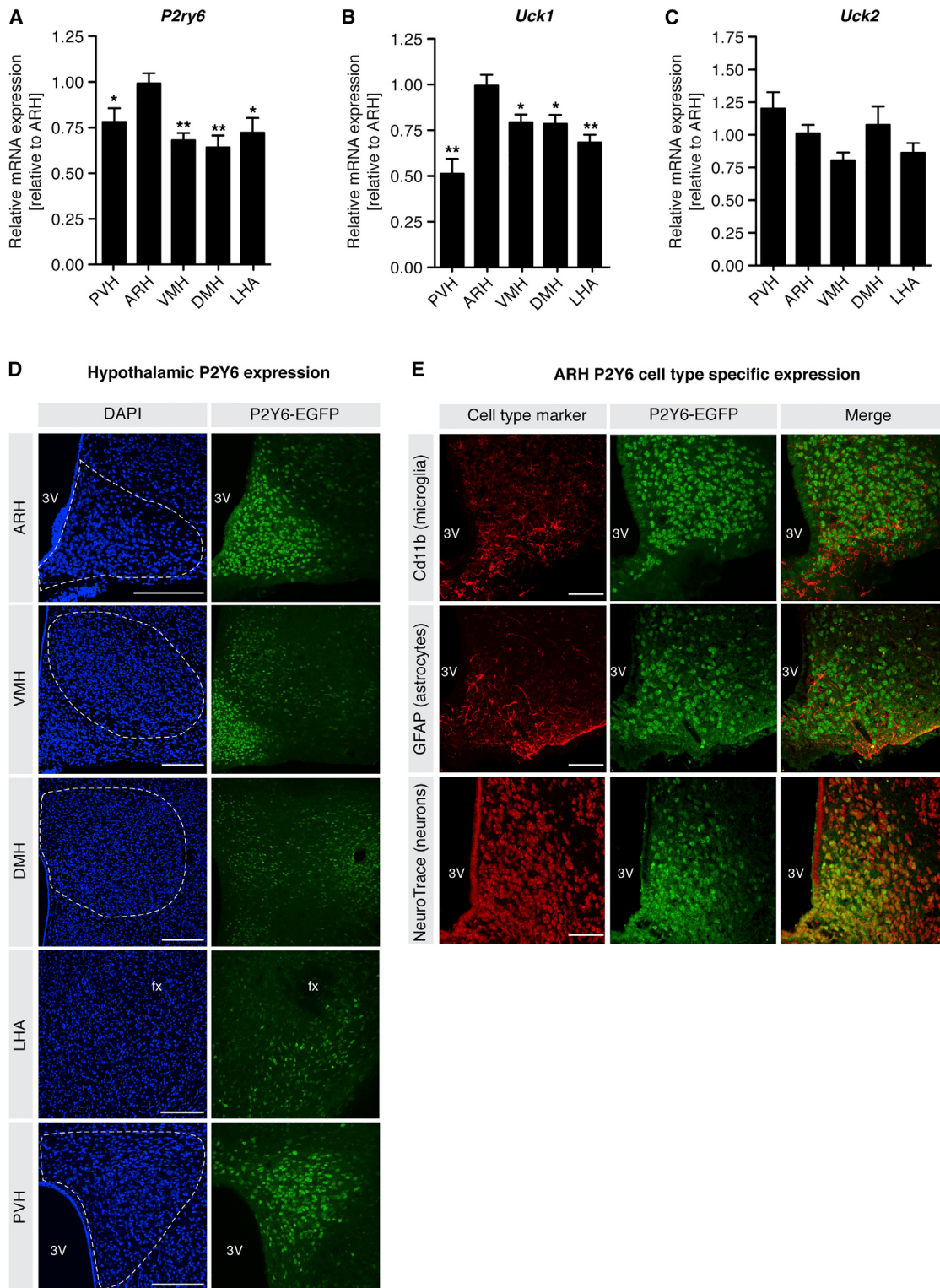


Figure 1. P2Y6 Is Highly Expressed in Neurons of the Arcuate Nucleus

(A–C) Quantitative real-time PCR analysis of (A) pyrimidinergic receptor P2Y₆, G protein coupled, 6 (*P2y6*) (n = 18–20 samples per region), (B) uridine-cytidine kinase 1 (*Uck1*) (n = 18–20 samples per region), and (C) uridine-cytidine kinase 2 (*Uck2*) (n = 17–19 samples per region) mRNA expression in key microdissected hypothalamic regions: the paraventricular nucleus of the hypothalamus (PVH), the arcuate nucleus of the hypothalamus (ARH), the ventromedial nucleus of the hypothalamus (VMH), the dorsomedial nucleus of the hypothalamus (DMH), and the lateral hypothalamic area (LHA).

(legend continued on next page)

UDP Activates AgRP/NPY-Expressing Neurons in the ARH

Given the expression of the UDP receptor P2Y6 in the ARH, as well as the clear activation of both cFos-expression and ERK phosphorylation in the ARH in response to icv UDP application, we next aimed to define the molecular identity of the P2Y6-expressing, UDP-responsive neurons in this region. Interestingly, UDP-induced pERK immunoreactive cells displayed a specific anatomical distribution mainly in the ventromedial region of the ARH (Figure 2B). Given that the ventromedial part of the ARH mainly contains AgRP/NPY-coexpressing neurons (Chronwall, 1985), we next directly investigated the specific effect of P2Y6/UDP on those neurons. For this purpose, we repeated the UDP-induced pERK experiments in mice, which express GFP under control of the NPY promotor (NPY-GFP mice). This analysis revealed that, indeed, the number of NPY-expressing neurons exhibiting pERK immunoreactivity doubled following icv UDP application, as compared to vehicle-treated controls (Figure 2C). Similar results were found using cFos as a readout for NPY neuron activation (Figure S2C). In contrast, UDP failed to significantly increase pERK immunoreactivity in GFP-expressing anorexigenic POMC neurons of POMC-GFP mice (Figure 2D). Collectively, these experiments indicate that UDP specifically evokes ERK phosphorylation immunoreactivity in orexigenic AgRP/NPY neurons, but not in POMC neurons.

Based on the restricted action of UDP on AgRP/NPY neurons in the ARH, we specifically focused on the role of UDP/P2Y6 on this neuronal population. We first investigated the expression of P2Y6 on AgRP/NPY neurons. To this end, we performed a co-immunohistochemistry for GFP expression on ARH sections of P2Y6-EGFP mice together with antisera directed against AgRP. This analysis revealed co-expression of P2Y6 and endogenous AgRP (Figures 3A and S3A). In addition, we performed co-staining of endogenous P2Y6 in transgenic mice that express the red tomato protein under control of the AgRP promoter through Cre-loxP-mediated recombination in AgRP^{tdTomato} mice (Figures 3B, S3B, and S3C). Using this approach, we also found that genetically marked AgRP neurons express endogenous P2Y6 receptors.

Next, we aimed to further directly support the notion that the P2Y6 agonist UDP can modulate the activity of AgRP-expressing neurons in the ARH. Therefore, we performed perforated patch-clamp recordings from AgRP^{tdTomato} neurons (Figures 3C–3F). Here, we also found that >60% of AgRP neurons are sensitive to UDP (Figure 3E), as application of 3 μM UDP resulted in an increased action potential frequency of these cells (Figures 3C–3F). In contrast, when we conducted similar recordings in brain slices of POMC-GFP mice, we found that only a small proportion of POMC neurons are responsive to UDP and that UDP does not significantly affect POMC neuron action potential firing on a population basis (Figures S3D and S3E). Collectively, these

experiments indicate that orexigenic AgRP/NPY-coexpressing neurons in the ARH not only express the UDP receptor P2Y6, but that they are also directly activated following UDP application both *in vitro* and *in vivo*.

UDP Promotes Feeding via P2Y6-Dependent Activation of AgRP Neurons

In light of the pivotal role of AgRP neuron activation in the stimulation of food intake, we investigated whether UDP was indeed capable of promoting an increase in feeding. Therefore, control mice were icv injected with increasing doses of UDP before the onset of the dark period, i.e., when spontaneous feeding occurs in mice. Indeed, central application of UDP acutely enhanced spontaneous food intake in a dose-dependent manner (Figure 4A). Importantly, the same dose of centrally applied UDP (30 μM), which evoked the strongest activation of neurons in the ARH, also elicited the strongest stimulatory effect on food intake by increasing food intake by 45% compared to animals subjected to vehicle injection (Figures 4A and S4A–S4C).

To directly assess whether the ability of centrally applied UDP to activate feeding depends on AgRP neuron activation, we investigated the effect of centrally administered UDP in mice, which allow for pharmacogenetic inhibition of AgRP neurons. To this end, we injected AgRP^{Cre} mice bilaterally into the ARH with an AAV, which co-expresses in a Cre-dependent manner the inhibitory DREADD channel hM4D and mCherry. Immunostaining for m-Cherry revealed successful bilateral targeting of the ARH in these mice (Figure 4B). While in Cre-negative control animals bilateral injection of the AAV and intraperitoneal CNO application had no effect on UDP's ability to increase food intake, UDP's food intake-stimulatory effect was completely abolished upon CNO-mediated inhibition of AgRP neurons of AAV-injected AgRP^{Cre} mice (Figure 4C). While AgRP neuron activity is required for UDP's orexigenic effect, mRNA expression levels of *AgRP*, *Npy*, or *Pomc* are not affected over time by icv UDP application (Figures S4D–S4F). Taken together, these experiments clearly revealed that centrally applied UDP enhances food intake and that this effect is abolished when activation of AgRP neurons is specifically inhibited.

To further elucidate the specific contribution of P2Y6-mediated signaling in UDP-dependent activation of food intake, we took both a pharmacological and a genetic approach. We first compared the orexigenic effect of centrally applied UDP in either the absence or presence of the well-characterized P2Y6 antagonist MRS 2578. Again, while UDP injection increased food intake by ≈50% also in these independent sets of experiments, this response was completely abrogated upon co-treatment with the P2Y6 antagonist (Figure 5A). Importantly, for this experiment, we used a dose of MRS 2578 that does not modulate food intake

(D) Representative microphotographs of GFP immunostaining (P2Y6-EGFP, green) and of corresponding nuclear counterstaining (DAPI, blue) in the ARH, the VMH, the DMH, the LHA, and the PVH of P2Y6-EGFP mice.

(E) Representative microphotographs of ARH co-immunostaining of P2Y6-EGFP (P2Y6-EGFP, green) and of: (top row) integrin αM (Cd11b, microglia, red), (middle row) glial fibrillary acidic protein (GFAP, astrocytes, red), and (bottom row) fluorescent Nissl staining (NeuroTrace, neurons, red).

Data are presented as mean ± SEM. Scale bars: D, 100 μm and E, 50 μm. V3, third ventricle. *p < 0.05 and **p < 0.01, as determined by one-way ANOVA followed by Newman-Keuls posthoc test. See also Figure S1.

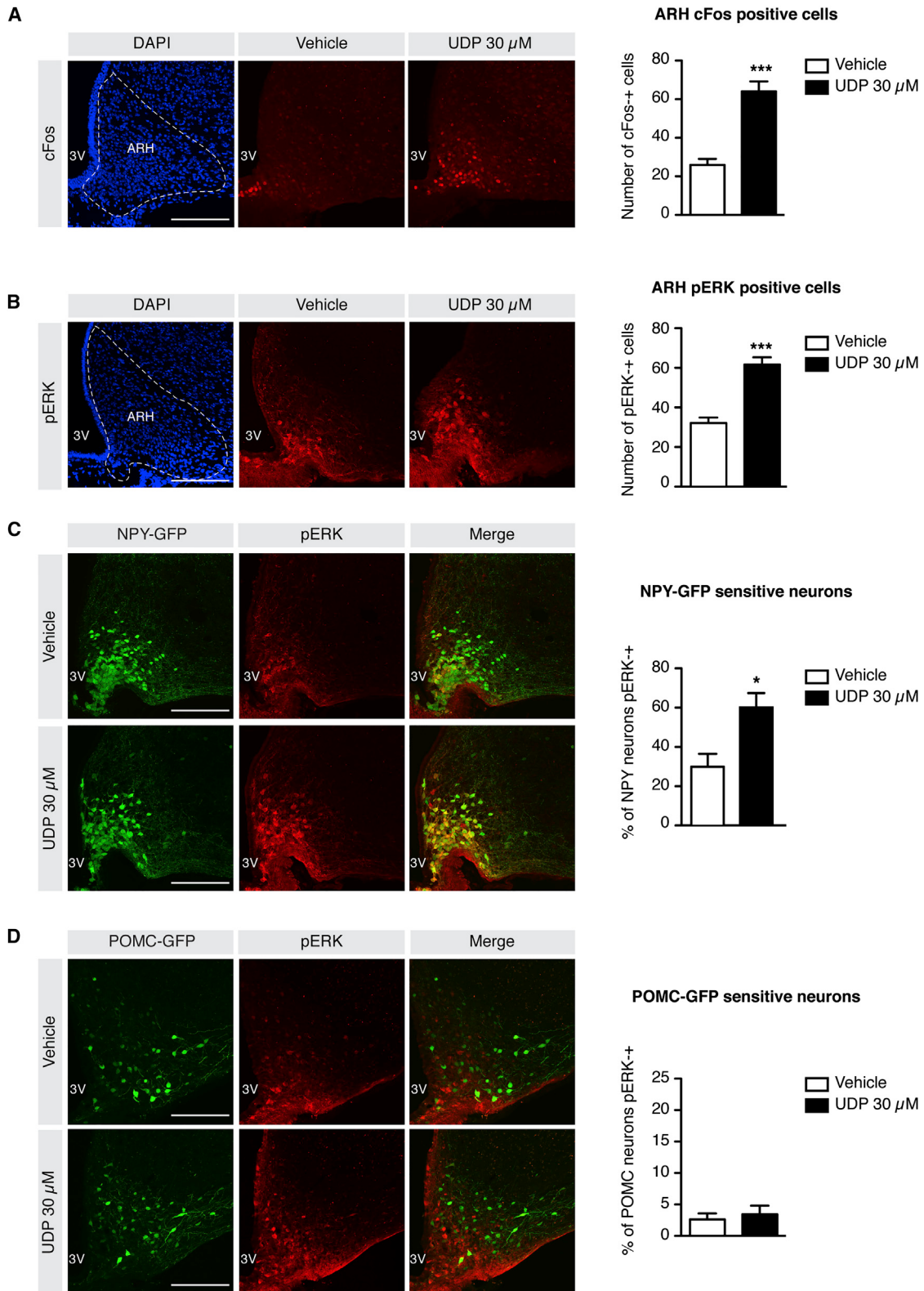


Figure 2. UDP Triggers pERK Activation in Orexigenic AgRP Neurons, but Not in Anorexigenic POMC Neurons

(A and B) Confocal images and quantification comparison of (A) cFos- and (B) pERK-immunoreactive cells in the arcuate nucleus (ARH) of mice after intra-cerebroventricular administration of vehicle (saline) or 30 μ M UDP ($n_{cFos} = 7$ versus 9; $n_{pERK} = 14$ versus 16).

(legend continued on next page)

by itself (Figure 5A). To investigate whether the inhibition of UDP-induced feeding by central administration of MRS 2578 might stem from unspecific side effects of the antagonist, we also tested the effect of MRS 2578 on the ability of centrally applied ghrelin to increase feeding. Here, icv application of 2 µg ghrelin increased feeding to a comparable extent as observed upon UDP injection (Figure 5B). However, co-application of the P2Y6 antagonist MRS 2578 had no effect on ghrelin's ability to increase food intake (Figure 5B). These findings clearly provided the first evidence that UDP's ability to increase feeding is specifically mediated via P2Y6-dependent signal transduction.

To further support this notion, we compared the ability of centrally applied UDP to increase food intake in control and in P2Y6-deficient mice ($P2Y6^{\Delta/\Delta}$). While UDP clearly increased feeding in control mice, it completely failed to increase food intake in litter mates lacking functional P2Y6 expression (Figure 5C). In contrast, P2Y6-deficient mice exhibited a comparable ability to increase food intake in response to central ghrelin application, as compared to their litter mate controls (Figure 5D). Collectively, both pharmacological and genetic inhibition of P2Y6 specifically abrogate the acute orexigenic action of centrally applied UDP, but not of ghrelin, clearly demonstrating that UDP specifically engages P2Y6 signaling to increase food intake.

Having defined that the food-intake-promoting activity of UDP is mediated through P2Y6-dependent signaling, we aimed to assess whether UDP's ability to increase AgRP neuron firing depends on functional P2Y6 signaling. To this end, we performed electrophysiological recordings from genetically identified AgRP neurons in $AgRP^{tdTomato}$ mice. MRS 2578 preincubation abrogated UDP's ability to increase action potential firing of all but a single recorded AgRP neuron (Figures 5E and 5F). Thus, not only UDP-induced activation of feeding, but also UDP-stimulated activation of AgRP neurons critically depends on functional P2Y6 signaling.

Hypothalamic UDP Concentrations Are Increased in Obesity

Having identified a regulatory role for UDP-evoked P2Y6-dependent signaling in control of AgRP neuron activity and feeding, we assessed whether P2Y6 expression or UDP concentrations might be altered in the hypothalamus in obesity. Therefore, we compared the hypothalamic mRNA expression of *P2ry6* in control mice and diet-induced obese animals as well as in control mice and mice carrying a mutation in the leptin receptor gene (*db/db* mice). This analysis revealed unaltered expression of *P2ry6* in the hypothalamus of diet-induced and genetically obese animals (Figures 6A and 6B). In contrast, ultra-performance liquid chromatography (UPLC)-based assessment of hypothalamic UDP concentrations revealed a significant increase in hypothalamic UDP content in both obese mouse models (Figures 6C and 6D). Moreover, hypothalamic UDP concentrations positively correlated both with body weight and markers of impaired

glucose homeostasis such as fasting glycemia and HOMA-IR in obese mice (Figures 6E and 6F). Collectively, these experiments revealed that, under conditions of obesity, hypothalamic concentrations of the P2Y6 ligand UDP are increased in the absence of alterations in *P2ry6* mRNA expression.

Circulating Uridine Concentrations Are Increased in Obesity and Can Promote Hypothalamic UDP Synthesis

Since we detected elevated hypothalamic UDP concentrations in both diet-induced and genetically determined obesity, we further investigated potential mechanisms underlying this phenomenon. Thus, we monitored the mRNA expression of key enzymes of UDP synthesis and conversion (Figure S5). However, there was no consistent alteration in hypothalamic mRNA expression for the key regulatory gene products in UDP synthesis or conversion detectable in the hypothalamus of high-fat-diet-fed or *db/db* mice (Figures 7A and 7B).

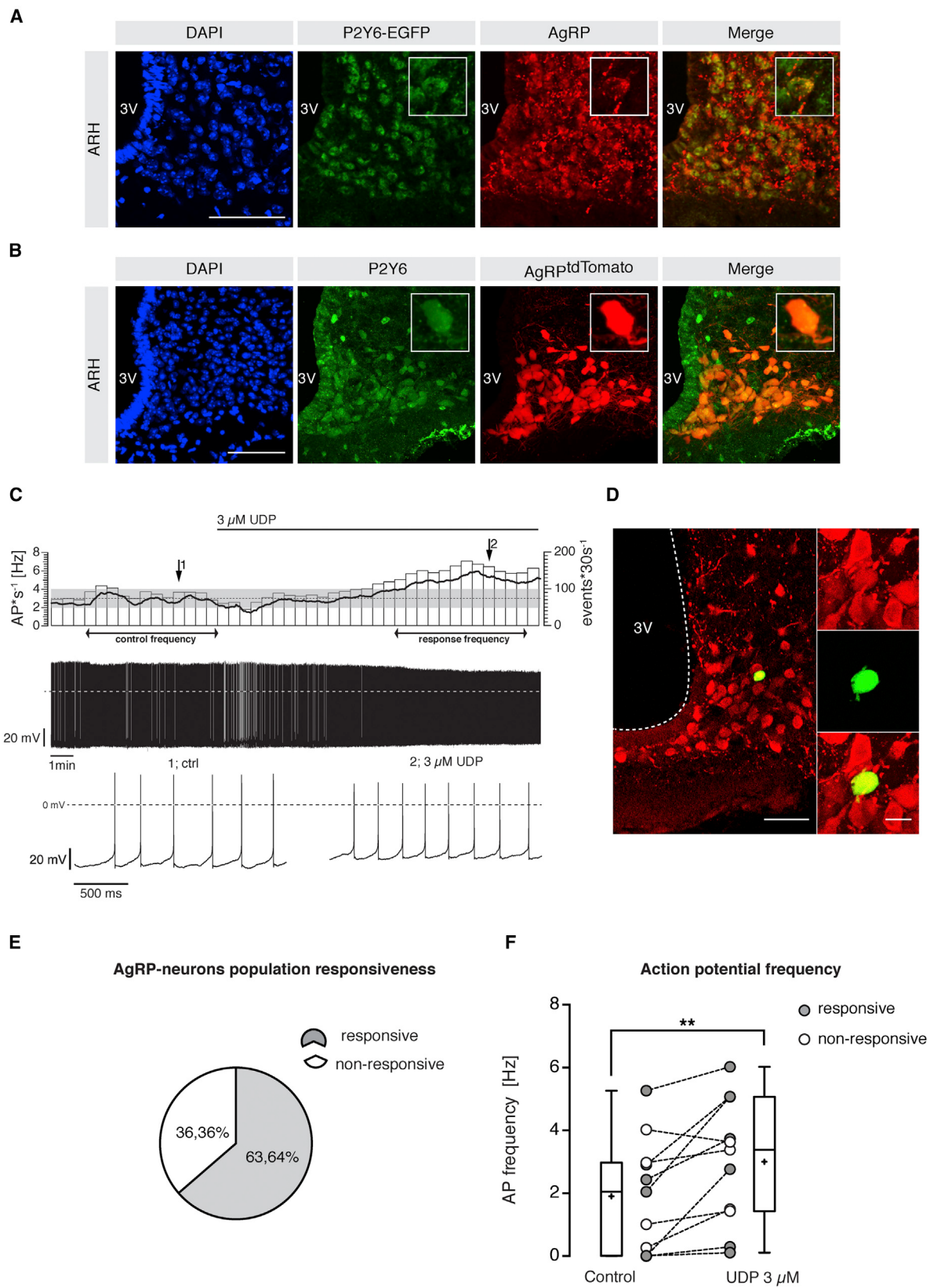
Neuronal UDP synthesis critically depends on the availability of uridine, which reaches the brain via transporter-mediated uptake (Cansev, 2006; Ipata, 2011). Therefore, we compared the expression of known transporters for pyrimidine and pyrimidine metabolites in the hypothalamus of control mice and diet-induced obese animals, as well as *db/db* mice. However, there was no consistent alteration in the mRNA expression of *Slc28a* and *Slc29a* family members in diet-induced or genetically determined obesity (Figures 7C and 7D).

In contrast, when we assessed circulating serum uridine concentrations, there was a significant increase in serum uridine concentrations in obese mice (Figure 7E). Moreover, we detected a positive correlation between serum uridine concentrations and hypothalamic UDP content in these animals (Figure 7F). Collectively, these data indicate that, in obesity, serum uridine concentrations increase and this subsequently may lead to increased hypothalamic UDP synthesis.

To directly address whether elevation of serum uridine concentrations—as observed in obesity—can lead to increased hypothalamic UDP synthesis, we next injected control animals intraperitoneally with uridine. The acute i.p. injection of 50 mg/kgBW uridine resulted in a rapid increase of serum uridine concentrations 60 min post injection and serum levels returned to baseline concentrations 90 min after injection (Figure 7G). This increase in circulating uridine concentrations resulted in subsequent elevation of hypothalamic UDP content as early as 90 min after peripheral application of uridine (Figure 7H). Finally, consistent with the notion that increased hypothalamic UDP concentrations can enhance feeding, animals injected intraperitoneally with uridine increased food intake significantly 4 hr after peripheral application of uridine (Figure 7I). Taken together, our experiments revealed that, in obesity, circulating uridine concentrations are increased, providing enhanced substrate availability for hypothalamic UDP synthesis and ultimately promoting feeding via UDP-induced P2Y6 signaling in the CNS (Figure S6).

(C and D) Confocal images and quantitative comparison of (C) NPY-GFP and (D) POMC-GFP expressing neurons pERK immunoreactive after intracerebroventricular administration of vehicle (saline) or 30 µM UDP ($n_{NPY-GFP} = 4$ versus 5; $n_{POMC-GFP} = 5$ versus 5). Scale bar, 100 µm. V3, third ventricle.

Data are presented as mean ± SEM. ** $p < 0.01$, *** $p < 0.001$, as determined by unpaired Student's t test. See also Figure S2.



(legend on next page)

DISCUSSION

Better defining the regulatory processes underlying the central control of food intake and metabolism is key to the development of novel drugs targeting the current obesity and diabetes epidemic (Geiss et al., 2014; WHO, 2006). Here, we have unraveled a pathway that regulates feeding behavior as we uncover an unappreciated role for the UDP-selective P2Y6 in control of AgRP neuron activity and their associated orexigenic effects. Moreover, we reveal that this UDP/P2Y6 pathway is activated in response to raising uridine supply from the periphery of the organism, as observed in obesity, where both circulating uridine concentrations and hypothalamic UDP content are increased (Figure S6). While currently little information is available on the physiological regulation of circulating uridine or hypothalamic UDP concentrations in relation to acute changes in energy state, some studies have recently described that circulating plasma uridine concentrations are increased in humans suffering from T2DM and correlate with the degree of insulin resistance also in rodents, consistent with the increase of circulating uridine in *db/db* mice reported here (Dudzinska et al., 2013; Hamada et al., 2007; Hawkins et al., 1997; Urasaki et al., 2014; Yamamoto et al., 2010). Given that AgRP neurons are not only critical for the control of feeding, but also for control of hepatic glucose production (Könner et al., 2007), altered uridine/UDP-mediated control of these cells may not only contribute to obesity development, but also to the pathogenesis of altered glucose homeostasis. Clearly, future studies on P2Y6-deficient mice will have to delineate the role of UDP/P2Y6-dependent signaling in the development of obesity and T2DM, as well as states of negative energy balance or weight loss.

Extracellular nucleotides act as signaling molecules to mediate a wide range of cellular and physiological responses by acting on cell-surface purinergic receptors (P2) (Abbracchio et al., 2009; Burnstock et al., 2011). A striking example of the importance of purinergic signaling was the discovery that ATP acts as a neurotransmitter regulating core functions, such as circadian rhythm, sensory processes, and nociception, as well as higher-order cognitive functions, including motivation, learning, and memory (Burnstock, 2006; Burnstock et al., 2011). Surprisingly, despite indisputable recognition of the critical importance of purine and pyrimidine signaling as a privileged

route for cell-to-cell communication in numerous physiological processes, very little is known about the role of purinergic signaling in the CNS-dependent control of energy and glucose homeostasis. Within the several members of the P2 family, we particularly focused on the P2 receptors activated by uracil nucleotides and derived sugar nucleotides based on their structural and phylogenetic similarity to Gpr17 (Daniele et al., 2011), which was recently identified as a novel FoxO1-dependent regulator of AgRP neuron activity (Ren et al., 2012). Among the uracil nucleotides and derivatives-binding members with unknown function in the CNS-dependent control of metabolism, P2Y6 stands out by its high expression levels in the ARH. As opposed to the hippocampus, where P2Y6 colocalizes with activated microglia (Koizumi et al., 2007), in the ARH of lean mice, we identify P2Y6 as being specifically expressed in neurons, providing evidence for a region-dependent, cell-type-specific expression pattern of P2Y6 in the CNS. Guided by the microglial expression of P2Y6, previous studies had mostly focused on the microglial role of P2Y6, where P2Y6 signaling was demonstrated to activate microglia and to promote phagocytosis (Koizumi et al., 2007). Here, we show that, in contrast, P2Y6 directly activates AgRP neurons in the ARH to potently promote feeding, while it only has minor effects on the activation of anorexigenic POMC neurons. This notion is consistent with the robust activation of feeding upon optogenetic or pharmacogenetic activation of AgRP neurons (Aponte et al., 2011; Krashes et al., 2011) and their previously defined crucial role for the maintenance of feeding, as evidenced by toxin-mediated ablation of these cells in adult mice (Gropp et al., 2005; Luquet et al., 2005).

Besides our demonstration that AgRP neurons express P2Y6 and that AgRP neuron activity is required to promote feeding in response to centrally applied UDP, we reveal that UDP triggers pERK phosphorylation and increased action potential firing in a substantial proportion of AgRP neurons. Excitatory effects of UDP have previously been described in cultured sympathetic neurons in which UDP-induced depolarization evoked noradrenaline release (Nörenberg et al., 2000; von Käggen et al., 1997). Accordingly, similar mechanisms may occur in AgRP neurons, where UDP induces increased firing of action potentials to subsequently release GABA and the characteristic orexigenic neuropeptides produced by these cells, i.e., NPY and AgRP. Recently, Krashes and coworkers described the differential functions of neuromediators released by AgRP neurons in controlling temporally distinct phases of eating behavior. Here, GABA and NPY are

Figure 3. AgRP Neurons Express P2Y6 Whose Activation by UDP Directly Increases Firing Rate

(A and B) Representative microphotographs of co-immunostaining of (A) P2Y6-EGFP (P2Y6-EGFP, green) and of AgRP (AgRP, red) and (B) P2Y6 (P2Y6, green) and AgRP^{tdTomato} (AgRP^{tdTomato}, red) in the arcuate nucleus of the hypothalamus (ARH).

(C) UDP effect on a single AgRP neuron. Action potential frequency (black line) and respective rate histogram (30 s bins, top), original recording (middle), and traces in higher resolution (bottom) of an AgRP neuron increasing firing frequency in response to the application of 3 μM UDP. Shaded gray background indicates ± 3 × SD and the dotted line the respective mean of the control calculated from 12 bins of 30 s each. Arrows beneath the bins indicate the bins used to calculate means and SD for control and effect, respectively. The increase in action potential frequency is larger than 3 × SD of the control, thus defining this neuron as a responsive neuron.

(D) Recorded neuron, identified by antibody staining against tdTomato (red) and a biocytin fill of the recorded neuron (green).

(E) Overall responsiveness to 3 μM UDP of the recorded AgRP neuron population ($n = 11$ in total: 4 non-responsive neurons versus 7 responsive).

(F) Quantification of action potential (AP) frequency ($n = 11$, responsive and non-responsive pooled). Gray circles mark single recordings responding with a significant increase in AP frequency; open circles are non-responsive neurons. All recordings have been conducted in synaptically isolated neurons. Scale bars: A and B, 50 μm and D, 40 μm and 10 μm in the magnifications, respectively. V3, third ventricle. Data are represented as boxplots generated according to the Tukey method (mean, “+”; median, horizontal line). ** $p < 0.01$, as determined by paired Student's *t* test, including all recorded 11 neurons. See also Figure S3.

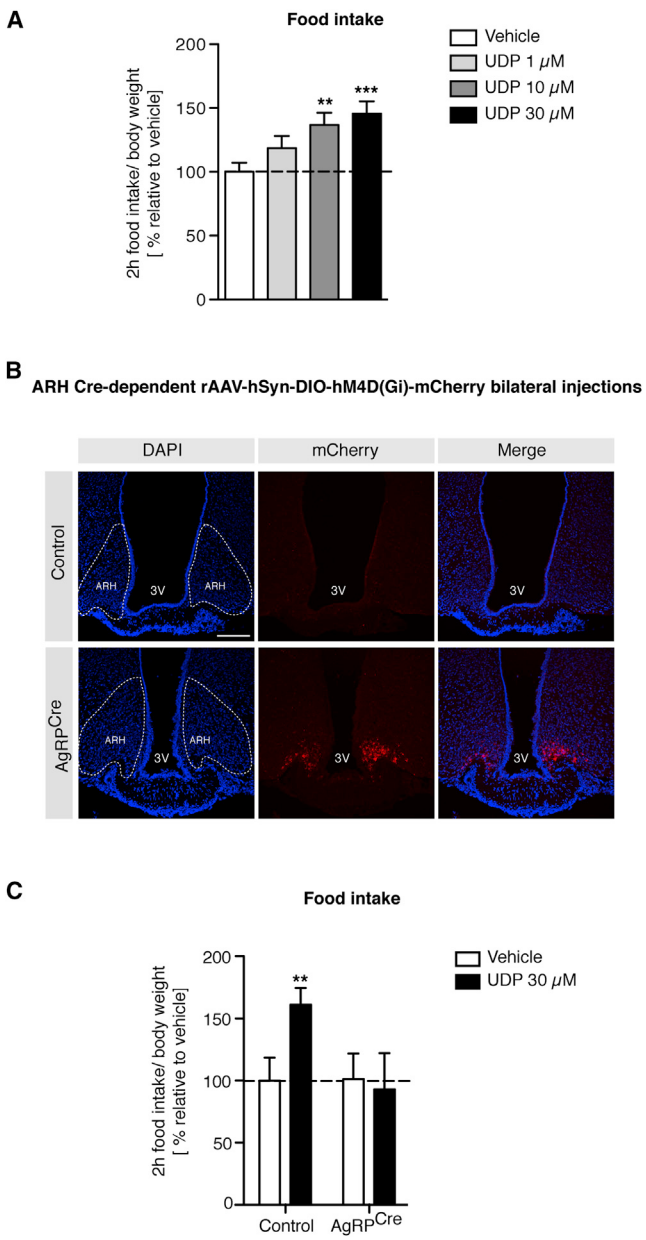


Figure 4. Central UDP Dose Dependently Increases Food Intake, and Its Orexigenic Effects Require AgRP Neuron Activity

(A) 2 hr food intake measurement (depicted as food intake to body weight) after intracerebroventricular (icv) administration of increasing doses of UDP (1 μ M, 10 μ M, and 30 μ M) or vehicle (saline) ($n = 26$ versus 13 versus 11 versus 14). (B) Representative microphotographs of mCherry immunostaining in control and AgRP^{Cre} mice injected bilaterally in the arcuate nucleus (ARH) with Cre-dependent rAAV-hSyn-DIO-hM4D(Gi)-mCherry (mCherry, red; DAPI counterstaining, blue). Scale bar, 100 μ m. V3, third ventricle.

(C) 2 hr food intake measurement in virus-injected AgRP^{Cre} mice or control wild-type litter mates. Mice received CNO injections (0.3 mg/kgBW) 15 min prior to icv administration of 30 μ M UDP or vehicle (saline) ($n = 6$ versus 8 versus 5 versus 5).

Data are presented as mean \pm SEM. ** $p < 0.01$, *** $p < 0.001$, as compared to vehicle as determined by one-way ANOVA followed by Newman-Keuls post-hoc test (A) or unpaired Student's t test (C). See also Figure S4.

promoting food intake in the short term, whereas AgRP is responsible for the long-term stimulation of eating (Krashes et al., 2013). This study and the specific short-term effect of UDP on food intake suggest that the orexigenic effect of UDP may depend on GABA- and/or NPY-mediated signals originating from AgRP/NPY co-expressing neurons rather than on AgRP. This notion is further substantiated through the notion that UDP acutely promotes feeding without obvious changes in the transcription of *Agrp* and *Npy* mRNAs. However, this assumption will have to be directly addressed in future studies.

In accordance with the ability of UDP to increase Ca^{2+} levels in neurons, it is well described that activation of P2Y6 by UDP leads to activation of various Ca^{2+} -dependent signaling pathways, including IP_3 accumulation and an increase in cytoplasmic free Ca^{2+} from intracellular Ca^{2+} stores (Brunschweiger and Müller, 2006). In addition, P2Y6 shares convergent signaling pathways with the receptor for ghrelin, which also exerts its orexigenic effects predominantly through the activation of AgRP neurons (Tschöp et al., 2000 and for review, Andrews, 2011). First, as for ghrelin (Steculorum et al., 2015), we found that UDP activates MAPK/ERK signaling in AgRP neurons both *in vitro* and *in vivo*. Second, several peripheral effects of P2Y6 directly rely on AMPK activation (Balasubramanian et al., 2013, 2014), and AMPK is a critical element in mediating the orexigenic effects of ghrelin through activation of AgRP/NPY neurons (Andrews, 2011). Moreover, consistent with a critical role for AMPK regulation in AgRP neuron activity, AgRP cell-specific AMPK-deficient mice develop a lean phenotype (Claret et al., 2007), further supporting the idea that the orexigenic effect of UDP may indeed be associated with a P2Y6-dependent activation of AMPK in these cells. Clearly, the downstream signaling pathway(s) of P2Y6 in AgRP/NPY neurons will have to be further characterized in detail.

Another key aspect of the results presented here is our demonstration that the orexigenic effect of UDP completely relies on functional P2Y6 signaling, as evidenced by pharmacologic and genetic inhibition of P2Y6 signaling. This rules out the possibility that UDP is used as a precursor metabolite by membrane-bound or soluble enzymes since P2Y6 is the exclusive receptor for UDP and not for its metabolites, such as UDP glucose or UTP, which, respectively, act through P2Y14 and P2Y2/P2Y4 (Brunschweiger and Müller, 2006). This point is of critical importance, as it was previously shown that UDP glucose, when co-injected icv with leukotrienes, increases food intake (Ren et al., 2012). Our experiments thus clearly identify specifically P2Y6 as a target for inhibiting the food-intake-promoting actions of increased hypothalamic UDP in obesity.

In addition to expression of P2Y6, we reveal that critical components of enzymatic machinery for the biosynthesis of UDP—UCK-1 and -2, which catalyze the phosphorylation of uridine to UMP and represent the rate-limiting step for the UDP production (Anderson and Brockman, 1964)—are highly expressed in the ARH. The exact nature of UDP-synthesizing and -releasing cells, as well as a potential autocrine versus paracrine mode of UDP action on P2Y6 expressed on AgRP neurons, still remains to be investigated. CNS UDP biosynthesis is critically dependent on uridine supply and therefore directly relies on uridine uptake from the periphery (Cansev, 2006; Ipata, 2011). Irrespective of

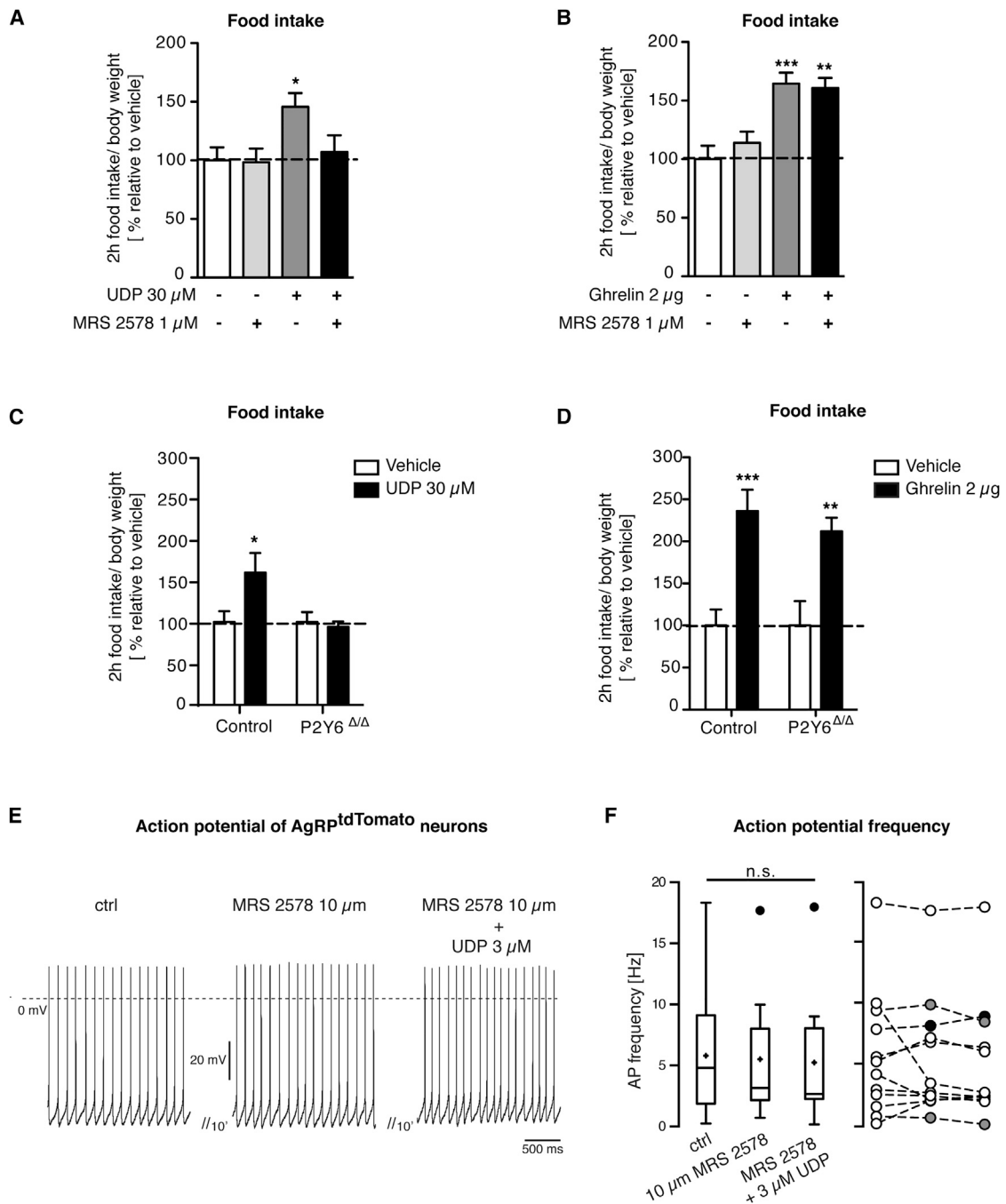


Figure 5. UDP Promotes Feeding and Activates AgRP Neurons via P2Y6-Dependent Signaling

(A–D) 2 hr food intake measurement after intracerebroventricular (icv) administration of (A) vehicle (0.1% DMSO), 1 μ M of the P2Y6-specific antagonist MRS 2578, 30 μ M UDP or co-icv of 30 μ M UDP, and 1 μ M MRS 2578 (n = 10 versus 11 versus 14 versus 12) or (B) vehicle (0.1% DMSO), 1 μ M MRS 2578, 2 μ g ghrelin or co-icv of 2 μ g ghrelin, and 1 μ M MRS 2578 (n = 13 versus 13 versus 14 versus 14). 2 hr food intake measurement after icv administration of (C) vehicle (saline) or 30 μ M UDP or (D) vehicle (saline) or 2 μ g ghrelin in P2Y6 $^{\Delta/\Delta}$ or control littermates (n_C = 10 versus 6 versus 9 versus 6, n_D = 9 versus 9 versus 5 versus 6).

(E) Original traces showing the action potential firing during the application of MRS 2578 and during the application of 3 μ M UDP in the presence of MRS 2578. (F) Quantification of action potential frequency (AP) (n = 12). One neuron significantly increased (black circle) and two decreased (gray circles) action potential frequency upon application of 3 μ M UDP in the presence of MRS 2578.

Data are presented as mean \pm SEM. *p < 0.05 (A–D) and as boxplots generated according to the Tukey method (mean, “+”; median, horizontal line) (F). *p < 0.05, **p < 0.01, ***p < 0.001, as compared to vehicle or control as determined by one-way ANOVA followed by Newman-Keuls posthoc test (A, B, F) or unpaired Student's t test (C and D).

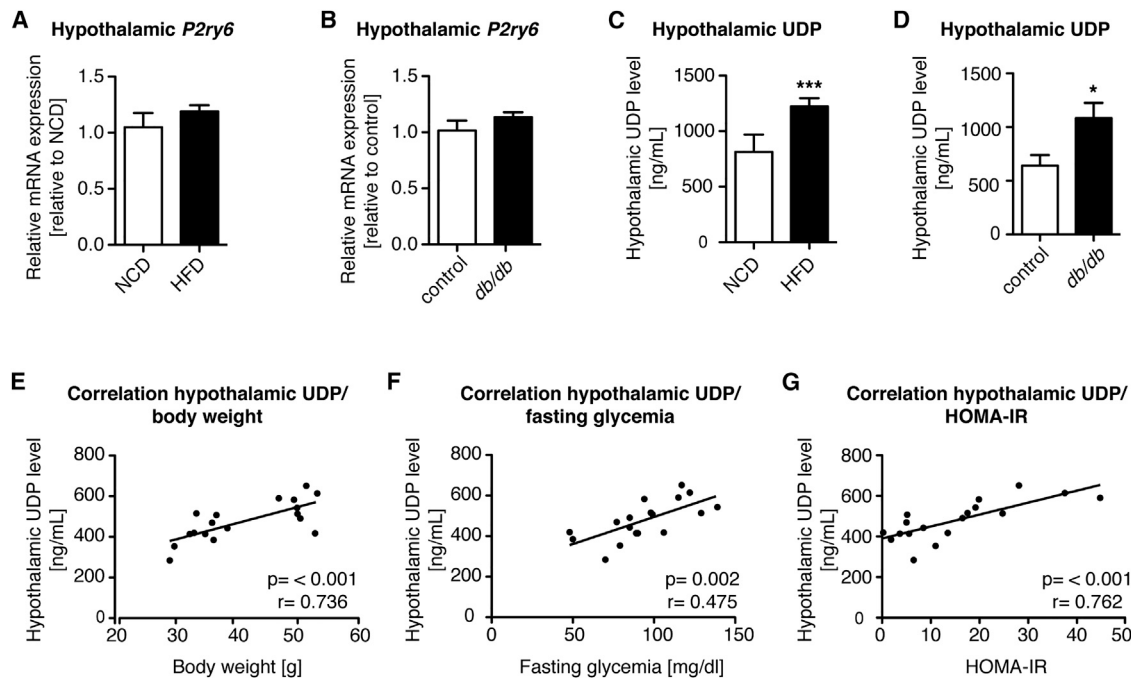


Figure 6. Hypothalamic UDP Content Is Increased in Dietary and Genetically Obese Mice

(A and B) Quantitative real-time PCR analysis of *pyrimidinergic receptor P2Y, G protein coupled, 6 (P2Y6)* in hypothalamus of (A) diet-induced obese animals fed a high-fat diet (HFD) or control animals receiving a normal chow diet (NCD) ($n = 7$ versus 8) and (B) *db/db* and their control littermates ($n = 5$ versus 7). (C–F) Hypothalamic contents of (C) HFD versus NCD mice ($n = 10$ versus 9) and (D) in *db/db* and control mice ($n = 7$ versus 7). Correlation of hypothalamic UDP and (E) body weight, (F) fasting glycemia, and (G) the homeostatic model assessment index of insulin resistance (HOMA-IR) in NCD and HFD mice ($n = 18$) (r , Pearson's r).

Data are presented as mean \pm SEM. ** $p < 0.01$, *** $p < 0.001$, as determined by unpaired Student's t test (A–D) or Pearson's correlation (E and F). See also Figure S5.

whether UCK-1 and UCK-2 expression in the ARH are restricted to neurons (autocrine regulation) or other cell types to promote paracrine UDP/P2Y6 signaling in AgRP neurons, our results clearly show that increased hypothalamic UDP concentrations, as observed in obese mice, and the hyperphagia secondary to elevated central UDP can be mimicked by peripheral application of uridine. Notably, insulin resistance in humans correlates with increased circulating uridine concentrations (Dudzinska et al., 2013; Hamada et al., 2007). While the predominant source of uridine in lean subjects is the liver (Dobolyi et al., 2011), future studies will have to unravel the mechanisms and tissues responsible for increased uridine synthesis in metabolic disorders.

In summary, the present study identifies the UDP/P2Y6 axis as a regulator of AgRP neuron activity and feeding behavior. This offers the unique opportunity to pursue agonists and antagonists for this GPCR as targets for the treatment of diseases associated with negative or positive energy balance.

EXPERIMENTAL PROCEDURES

Animal Care

All animal procedures were conducted in compliance with protocols approved by local government authorities (Bezirksregierung Köln, Cologne, Germany) and were in accordance with National Institutes of Health guidelines. Unless otherwise stated, animals were fed normal chow diet. Diet-induced obese mice were fed a high-fat diet containing 26.2% carbohydrates, 26.3% protein, and 34.9% fat (60% of calories from fat) or corresponding normal chow control

diet. C57Bl/6N were purchased from Charles Rivers. *db/db* mice and their control litter mates were purchased from The Jackson Laboratories. All experiments have been performed in adult mice.

Genetic Mouse Models

All mice used in this study were previously published and have been described in the respective paper: P2Y6-EGFP and P2Y6-deficient mice (Bar et al., 2008), NPY-GFP mice (B6.FVB-Tg(Npy-hrGFP)1Low/J) (van den Pol et al., 2009), POMC-GFP mice (C57BL/6J-Tg(Pomc-EGFP)1Low/J) (Cowley et al., 2001), AgRP-IRES-Cre mice (AgRP^{Cre}) (Tong et al., 2008), and tdTomato reporter mice (B6;129S6-Gt(ROSA) 26Sor^{tm1(CAG-tdTomato)Hze}/J) (Madisen et al., 2010).

Food Intake Measurement

For all food intake studies, mice received administration of the compound prior to the onset of the dark phase, and food intake measurement was performed during the dark phase using chow diet.

Intracerebroventricular Injections

Intracerebroventricular (icv) cannulations were performed as described elsewhere (Klöckener et al., 2011). Mice received icv administration of 2 μ L of each compounds.

AAVs Stereotaxic Injections and CNO Administration

Bilateral injections of AAVs into the ARH were performed as described elsewhere (Betley et al., 2013). rAAV5/hsyn-DIO-hM4D(Gi)-mCherry was obtained from the UNC Gene Therapy Vector Core. Animals received intraperitoneal injections of clozapine N-oxide (CNO, 0.3 mg/kgBW; Sigma) 15 min prior to icv administration of UDP, as described above.

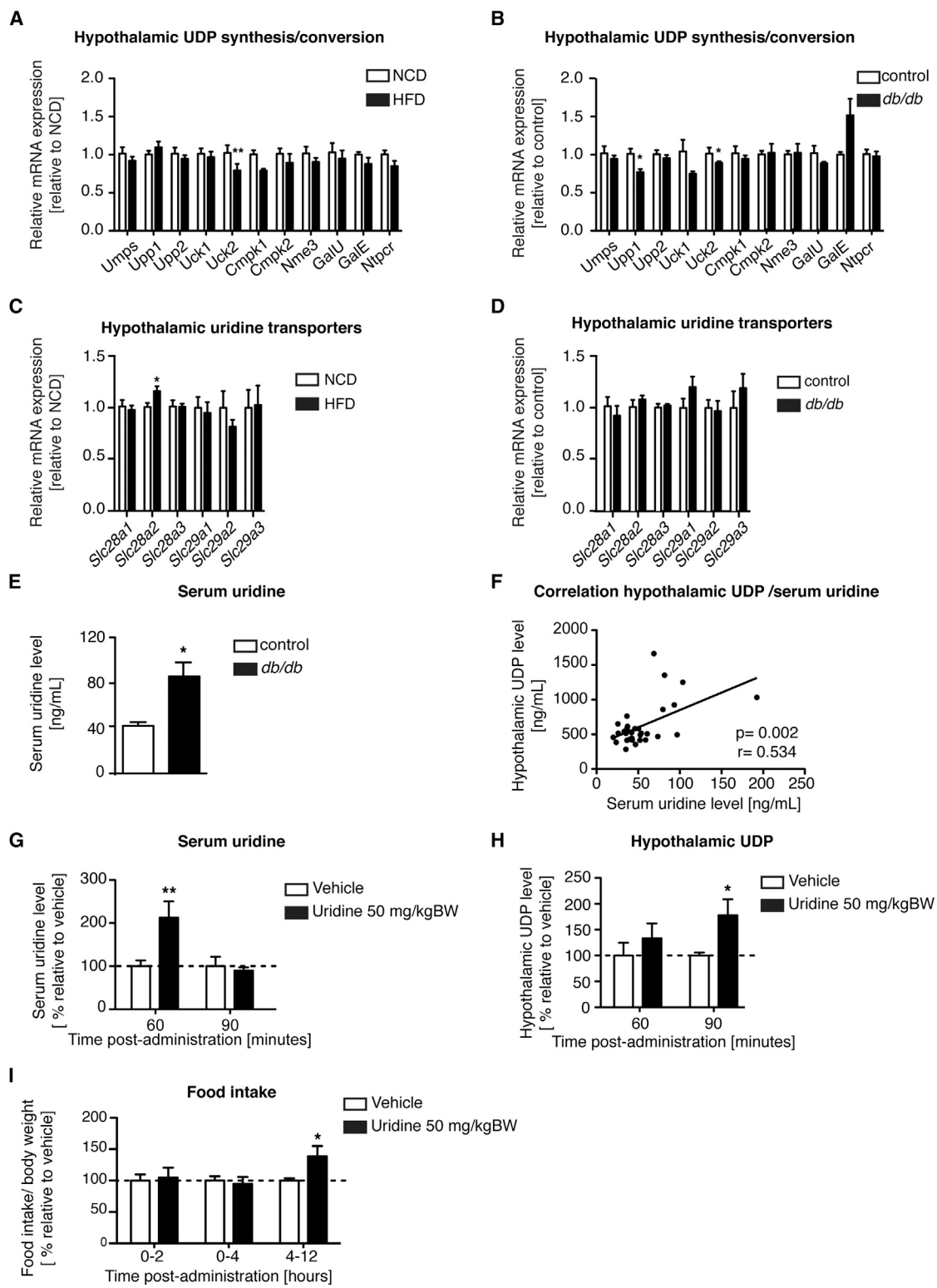


Figure 7. Hypothalamic UDP Is Increased in Obesity as a Consequence of Elevated Peripheral Uridine Supply

(A and B) Quantitative real-time PCR analysis of mRNA expression levels of enzymes involved in UDP synthesis and conversion in (A) diet-induced obese mice fed a high-fat diet (HFD) or a normal chow diet (NCD) ($n = 5$ versus 5) and (B) in db/db and their control litter mates ($n = 5$ versus 6).

(C and D) mRNA expression levels of transporters of uridine and uridine-associated nucleotides in (C) HFD and NCD mice ($n = 8$ versus 8) and in (D) db/db and their control litter mates ($n = 5$ versus 7).

(legend continued on next page)

Intraperitoneal Administration of Uridine

12-week-old C57Bl6/N male mice received 50 mg/kgBW of uridine (i.p.; 10 µl/g; Sigma) or vehicle (saline).

Ultra-Performance Liquid Chromatography

See the [Supplemental Experimental Procedures](#) for additional details.

Immunohistochemistry

Mice were perfused transcardially with 4% paraformaldehyde, and brains were processed as described previously ([Steculorum et al., 2015](#)). References and dilution used for each antibody are included in the [Supplemental Experimental Procedures](#). Pictures were acquired using a confocal Leica TCS SP-8-X microscope equipped with a 20× objective.

Electrophysiology

Perforated patch recordings were performed on brain slices from AgRP^{tdTomato} or POMC-GFP mice. For detailed information, see the [Supplemental Experimental Procedures](#).

Gene Expression Analysis, Cell Culture, Western Blot, and Analytical Procedures

For basic procedures, see the [Supplemental Experimental Procedures](#).

Statistics

All values were expressed as the means ± SEM. Statistical analyses were conducted using GraphPad PRISM (version 5.0a). Data sets with only two independent groups were analyzed for statistical significance using unpaired two-tailed Student's t test. Data sets comparing food intake in the same animal subjected to two different treatments were analyzed for statistical significance using paired two-tailed Student's t test. Data sets with more than two groups were analyzed using one-way analysis of variance (ANOVA) followed by Newman-Keuls posthoc test. For correlation analysis, the Pearson product-moment correlation (Pearson's r) was used and reported in the corresponding figure. All p values below 0.05 were considered significant. *p < 0.05, **p < 0.01, and ***p < 0.001.

SUPPLEMENTAL INFORMATION

Supplemental Information includes Supplemental Experimental Procedures and six figures and can be found with this article online at <http://dx.doi.org/10.1016/j.cell.2015.08.032>.

AUTHOR CONTRIBUTIONS

J.C.B. and S.M.S. conceived the project, designed the experiments, and wrote the manuscript. S.M.S. performed experiments and analyzed data. N.E. provided technical assistance. L.P., S.B., and P.K. performed and analyzed electrophysiological recordings. Y.H. conducted UPLC analysis, and M.I. provided the P2Y6-EGFP and P2Y6-deficient mice.

ACKNOWLEDGMENTS

We are grateful to Änne Lautenschläger and Helmut Wratil for outstanding technical assistance. We thank Joel Elmquist and Brad B. Lowell for providing the AgRP^{Cre} mice used in this study. This work was supported by a grant from the DFG (BR 1492/7-1) to J.C.B. and received funding by the DFG within the framework of the TRR134 and within the Excellence Initiative by German Federal and State Governments (CECAD). This work was funded (in part) by the Helmholtz Alliance ICEMED (Imaging and Curing Environmental Metabolic

Diseases) through the Initiative and Networking Fund of the Helmholtz Association. Moreover, the research leading to these results has received funding from the European Union Seventh Framework Programme (FP7/2007-2013) under grant agreement n° 266408. S.M.S. was funded by the Humboldt-Bayer program of the Alexander Von Humboldt foundation and received a grant from the Excellence Cluster on Cellular Stress Responses in Aging Associated Diseases (CECAD). Images from the illustration were used and adapted from Servier Medical Art.

Received: February 27, 2015

Revised: May 6, 2015

Accepted: August 12, 2015

Published: September 10, 2015

REFERENCES

- Abbracchio, M.P., Burnstock, G., Verkhratsky, A., and Zimmermann, H. (2009). Purinergic signalling in the nervous system: an overview. *Trends Neurosci.* 32, 19–29.
- Allen, J.A., and Roth, B.L. (2011). Strategies to discover unexpected targets for drugs active at G protein-coupled receptors. *Annu. Rev. Pharmacol. Toxicol.* 51, 117–144.
- Anderson, E.P., and Brockman, R.W. (1964). Feedback Inhibition of Uridine Kinase by Cytidine Triphosphate and Uridine Triphosphate. *Biochim. Biophys. Acta* 91, 380–386.
- Andrews, Z.B. (2011). Central mechanisms involved in the orexigenic actions of ghrelin. *Peptides* 32, 2248–2255.
- Aponte, Y., Atasoy, D., and Sternson, S.M. (2011). AGRP neurons are sufficient to orchestrate feeding behavior rapidly and without training. *Nat. Neurosci.* 14, 351–355.
- Balasubramanian, R., Maruoka, H., Jayasekara, P.S., Gao, Z.G., and Jacobson, K.A. (2013). AMP-activated protein kinase as regulator of P2Y(6) receptor-induced insulin secretion in mouse pancreatic β-cells. *Biochem. Pharmacol.* 85, 991–998.
- Balasubramanian, R., Robaye, B., Boeynaems, J.M., and Jacobson, K.A. (2014). Enhancement of glucose uptake in mouse skeletal muscle cells and adipocytes by P2Y6 receptor agonists. *PLoS ONE* 9, e116203.
- Bar, I., Guns, P.J., Metallo, J., Cammarata, D., Wilkin, F., Boeynaems, J.M., Bult, H., and Robaye, B. (2008). Knockout mice reveal a role for P2Y6 receptor in macrophages, endothelial cells, and vascular smooth muscle cells. *Mol. Pharmacol.* 74, 777–784.
- Belgardt, B.F., and Brüning, J.C. (2010). CNS leptin and insulin action in the control of energy homeostasis. *Ann. N Y Acad. Sci.* 1212, 97–113.
- Betley, J.N., Cao, Z.F., Ritola, K.D., and Sternson, S.M. (2013). Parallel, redundant circuit organization for homeostatic control of feeding behavior. *Cell* 155, 1337–1350.
- Brunschweiger, A., and Müller, C.E. (2006). P2 receptors activated by uracil nucleotides—an update. *Curr. Med. Chem.* 13, 289–312.
- Burnstock, G. (2006). Historical review: ATP as a neurotransmitter. *Trends Pharmacol. Sci.* 27, 166–176.
- Burnstock, G., Krügel, U., Abbracchio, M.P., and Illes, P. (2011). Purinergic signalling: from normal behaviour to pathological brain function. *Prog. Neurobiol.* 95, 229–274.
- Cansev, M. (2006). Uridine and cytidine in the brain: their transport and utilization. *Brain Res. Brain Res. Rev.* 52, 389–397.

(E) Serum uridine levels of control and *db/db* mice (n = 9 versus 10).

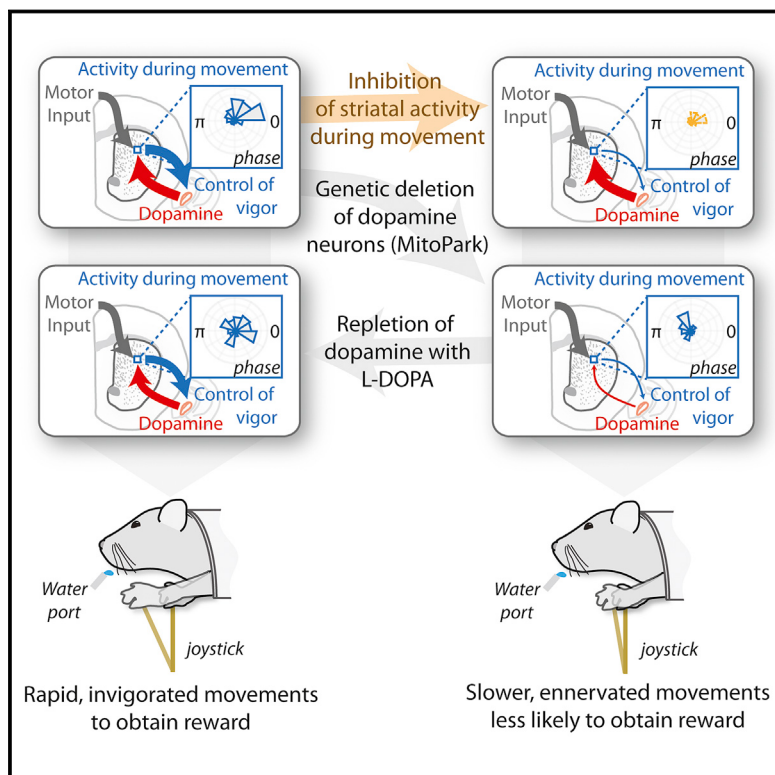
(F–I) (F) Correlation of hypothalamic UDP and serum uridine levels (n = 29) (r, Pearson's r). Effects of intraperitoneal injection of uridine (50 mg/kgBW) or vehicle (saline) in C57Bl6/N mice on (G) serum uridine (n = 4–5 per group) and on (H) hypothalamic UDP contents (n = 5 per group) 60 and 90 min post-injection as well on (I) food intake (n = 15 per group).

Data are presented as mean ± SEM. *p < 0.05, **p < 0.01, as determined by unpaired Student's t test (A–E and G–I) or Pearson's correlation (F). See also Figure S6.

- Chronwall, B.M. (1985). Anatomy and physiology of the neuroendocrine arcuate nucleus. *Peptides* 6 (Suppl 2), 1–11.
- Claret, M., Smith, M.A., Batterham, R.L., Selman, C., Choudhury, A.I., Fryer, L.G., Clements, M., Al-Qassab, H., Heffron, H., Xu, A.W., et al. (2007). AMPK is essential for energy homeostasis regulation and glucose sensing by POMC and AgRP neurons. *J. Clin. Invest.* 117, 2325–2336.
- Cone, R.D. (2005). Anatomy and regulation of the central melanocortin system. *Nat. Neurosci.* 8, 571–578.
- Cowley, M.A., Smart, J.L., Rubinstein, M., Cerdán, M.G., Diano, S., Horvath, T.L., Cone, R.D., and Low, M.J. (2001). Leptin activates anorexigenic POMC neurons through a neural network in the arcuate nucleus. *Nature* 411, 480–484.
- Daniele, S., Trincavelli, M.L., Gabelloni, P., Lecca, D., Rosa, P., Abbracchio, M.P., and Martini, C. (2011). Agonist-induced desensitization/resensitization of human G protein-coupled receptor 17: a functional cross-talk between purinergic and cysteinyl-leukotriene ligands. *J. Pharmacol. Exp. Ther.* 338, 559–567.
- Dobolyi, A., Juhász, G., Kovács, Z., and Kardos, J. (2011). Uridine function in the central nervous system. *Curr. Top. Med. Chem.* 11, 1058–1067.
- Dudzinska, W., Lubkowska, A., Jakubowska, K., Suska, M., and Skotnicka, E. (2013). Insulin resistance induced by maximal exercise correlates with a post-exercise increase in uridine concentration in the blood of healthy young men. *Physiol. Res.* 62, 163–170.
- Farooqi, I.S., and O'Rahilly, S. (2008). Mutations in ligands and receptors of the leptin-melanocortin pathway that lead to obesity. *Nat. Clin. Pract. Endocrinol. Metab.* 4, 569–577.
- Friedman, J.M. (2004). Modern science versus the stigma of obesity. *Nat. Med.* 10, 563–569.
- Geiss, L.S., Wang, J., Cheng, Y.J., Thompson, T.J., Barker, L., Li, Y., Albright, A.L., and Gregg, E.W. (2014). Prevalence and incidence trends for diagnosed diabetes among adults aged 20 to 79 years, United States, 1980–2012. *JAMA* 312, 1218–1226.
- Gropp, E., Shanabrough, M., Borok, E., Xu, A.W., Janoschek, R., Buch, T., Plum, L., Balthasar, N., Hampel, B., Waisman, A., et al. (2005). Agouti-related peptide-expressing neurons are mandatory for feeding. *Nat. Neurosci.* 8, 1289–1291.
- Hamada, T., Mizuta, E., Yanagihara, K., Kaetsu, Y., Sugihara, S., Sonoyama, K., Yamamoto, Y., Kato, M., Igawa, O., Shigemasa, C., et al. (2007). Plasma levels of uridine correlate with blood pressure and indicators of myogenic purine degradation and insulin resistance in hypertensive patients. *Circ.* J. 71, 354–356.
- Hawkins, M., Angelov, I., Liu, R., Barzilai, N., and Rossetti, L. (1997). The tissue concentration of UDP-N-acetylglucosamine modulates the stimulatory effect of insulin on skeletal muscle glucose uptake. *J. Biol. Chem.* 272, 4889–4895.
- Ipata, P.L. (2011). Origin, utilization, and recycling of nucleosides in the central nervous system. *Adv. Physiol. Educ.* 35, 342–346.
- Kittner, H., Franke, H., Harsch, J.I., El-Ashmawy, I.M., Seidel, B., Krügel, U., and Illes, P. (2006). Enhanced food intake after stimulation of hypothalamic P2Y1 receptors in rats: modulation of feeding behaviour by extracellular nucleotides. *Eur. J. Neurosci.* 24, 2049–2056.
- Klöckener, T., Hess, S., Belgardt, B.F., Paeger, L., Verhagen, L.A., Husch, A., Sohn, J.W., Hampel, B., Dhillon, H., Zigman, J.M., et al. (2011). High-fat feeding promotes obesity via insulin receptor/PI3K-dependent inhibition of SF-1 VMH neurons. *Nat. Neurosci.* 14, 911–918.
- Koizumi, S., Shigemoto-Mogami, Y., Nasu-Tada, K., Shinozaki, Y., Ohsawa, K., Tsuda, M., Joshi, B.V., Jacobson, K.A., Kohsaka, S., and Inoue, K. (2007). UDP acting at P2Y6 receptors is a mediator of microglial phagocytosis. *Nature* 446, 1091–1095.
- Könner, A.C., and Brüning, J.C. (2012). Selective insulin and leptin resistance in metabolic disorders. *Cell Metab.* 16, 144–152.
- Könner, A.C., Janoschek, R., Plum, L., Jordan, S.D., Rother, E., Ma, X., Xu, C., Enriori, P., Hampel, B., Barsh, G.S., et al. (2007). Insulin action in AgRP-expressing neurons is required for suppression of hepatic glucose production. *Cell Metab.* 5, 438–449.
- Krashes, M.J., Koda, S., Ye, C., Rogan, S.C., Adams, A.C., Cusher, D.S., Maratos-Flier, E., Roth, B.L., and Lowell, B.B. (2011). Rapid, reversible activation of AgRP neurons drives feeding behavior in mice. *J. Clin. Invest.* 121, 1424–1428.
- Krashes, M.J., Shah, B.P., Koda, S., and Lowell, B.B. (2013). Rapid versus delayed stimulation of feeding by the endogenously released AgRP neuron mediators GABA, NPY, and AgRP. *Cell Metab.* 18, 588–595.
- Luquet, S., Perez, F.A., Hnasko, T.S., and Palmiter, R.D. (2005). NPY/AgRP neurons are essential for feeding in adult mice but can be ablated in neonates. *Science* 310, 683–685.
- Madisen, L., Zwingman, T.A., Sunkin, S.M., Oh, S.W., Zariwala, H.A., Gu, H., Ng, L.L., Palmiter, R.D., Hawrylycz, M.J., Jones, A.R., et al. (2010). A robust and high-throughput Cre reporting and characterization system for the whole mouse brain. *Nat. Neurosci.* 13, 133–140.
- Nörenberg, W., von Kügelgen, I., Meyer, A., Illes, P., and Starke, K. (2000). M-type K⁺ currents in rat cultured thoracolumbar sympathetic neurones and their role in uracil nucleotide-evoked noradrenaline release. *Br. J. Pharmacol.* 129, 709–723.
- Ren, H., Orozco, I.J., Su, Y., Suyama, S., Gutiérrez-Juárez, R., Horvath, T.L., Wardlaw, S.L., Plum, L., Arancio, O., and Accili, D. (2012). FoxO1 target Gpr17 activates AgRP neurons to regulate food intake. *Cell* 149, 1314–1326.
- Schwartz, M.W., Seeley, R.J., Tschöp, M.H., Woods, S.C., Morton, G.J., Myers, M.G., and D'Alessio, D. (2013). Cooperation between brain and islet in glucose homeostasis and diabetes. *Nature* 503, 59–66.
- Sohn, J.W., Elmquist, J.K., and Williams, K.W. (2013). Neuronal circuits that regulate feeding behavior and metabolism. *Trends Neurosci.* 36, 504–512.
- Steculorum, S.M., Collden, G., Coupe, B., Crozier, S., Lockie, S., Andrews, Z.B., Jarosch, F., Klussmann, S., and Bouret, S.G. (2015). Neonatal ghrelin programs development of hypothalamic feeding circuits. *J. Clin. Invest.* 125, 846–858.
- Tong, Q., Ye, C.P., Jones, J.E., Elmquist, J.K., and Lowell, B.B. (2008). Synaptic release of GABA by AgRP neurons is required for normal regulation of energy balance. *Nat. Neurosci.* 11, 998–1000.
- Tschöp, M., Smiley, D.L., and Heiman, M.L. (2000). Ghrelin induces adiposity in rodents. *Nature* 407, 908–913.
- Urasaki, Y., Pizzorno, G., and Le, T.T. (2014). Uridine affects liver protein glycosylation, insulin signaling, and heme biosynthesis. *PLoS ONE* 9, e99728.
- van den Pol, A.N., Yao, Y., Fu, L.Y., Foo, K., Huang, H., Coppari, R., Lowell, B.B., and Broberger, C. (2009). Neuromedin B and gastrin-releasing peptide excite arcuate nucleus neuropeptide Y neurons in a novel transgenic mouse expressing strong Renilla green fluorescent protein in NPY neurons. *J. Neurosci.* 29, 4622–4639.
- Varela, L., and Horvath, T.L. (2012). Leptin and insulin pathways in POMC and AgRP neurons that modulate energy balance and glucose homeostasis. *EMBO Rep.* 13, 1079–1086.
- Vogt, M.C., and Brüning, J.C. (2013). CNS insulin signaling in the control of energy homeostasis and glucose metabolism - from embryo to old age. *Trends Endocrinol. Metab.* 24, 76–84.
- von Kügelgen, I., Nörenberg, W., Illes, P., Schobert, A., and Starke, K. (1997). Differences in the mode of stimulation of cultured rat sympathetic neurons between ATP and UDP. *Neuroscience* 78, 935–941.
- WHO (2006). Obesity and Overweight (Fact sheet 311), World Health Organization (<http://www.who.int/mediacentre/factsheets/fs311/en/index.html>).
- Xu, J., Morinaga, H., Oh, D., Li, P., Chen, A., Talukdar, S., Mamane, Y., Manconi, J.A., Nawrocki, A.R., Lazarowski, E., et al. (2012). GPR105 ablation prevents inflammation and improves insulin sensitivity in mice with diet-induced obesity. *J. Immunol.* 189, 1992–1999.
- Yamamoto, T., Inokuchi, T., Ka, T., Yamamoto, A., Takahashi, S., Tsutsumi, Z., Tamada, D., Okuda, C., and Moriwaki, Y. (2010). Relationship between plasma uridine and insulin resistance in patients with non-insulin-dependent diabetes mellitus. *Nucleosides Nucleotides Nucleic Acids* 29, 504–508.

Dopamine Is Required for the Neural Representation and Control of Movement Vigor

Graphical Abstract



Authors

Babita Panigrahi, Kathleen A. Martin,
Yi Li, ..., Brett D. Mensh, Alla Y. Karpova,
Joshua T. Dudman

Correspondence

dudmanj@janelia.hhmi.org

In Brief

Movement vigor, reduced in Parkinson's disease, is regulated by dopamine-dependent activity in the striatum.

Highlights

- A mouse model of Parkinson's disease produces a persistent reduction in effort
- The neural representation of movement vigor in striatum requires dopamine
- Acute suppression of striatal activity during execution enervates movement
- Dopamine repletion is sufficient to restore striatal activity and invigorate movement

Dopamine Is Required for the Neural Representation and Control of Movement Vigor

Babita Panigrahi,¹ Kathleen A. Martin,¹ Yi Li,¹ Austin R. Graves,¹ Alison Vollmer,¹ Lars Olson,² Brett D. Mensh,¹ Alla Y. Karpova,¹ and Joshua T. Dudman^{1,*}

¹Janelia Research Campus, Howard Hughes Medical Institute, Ashburn, VA 20147, USA

²Department of Neuroscience, Karolinska Institutet, 171 77 Stockholm, Sweden

*Correspondence: dudmanj@janelia.hhmi.org

<http://dx.doi.org/10.1016/j.cell.2015.08.014>

SUMMARY

Progressive depletion of midbrain dopamine neurons (PDD) is associated with deficits in the initiation, speed, and fluidity of voluntary movement. Models of basal ganglia function focus on initiation deficits; however, it is unclear how they account for deficits in the speed or amplitude of movement (vigor). Using an effort-based operant conditioning task for head-fixed mice, we discovered distinct functional classes of neurons in the dorsal striatum that represent movement vigor. Mice with PDD exhibited a progressive reduction in vigor, along with a selective impairment of its neural representation in striatum. Restoration of dopaminergic tone with a synthetic precursor ameliorated deficits in movement vigor and its neural representation, while suppression of striatal activity during movement was sufficient to reduce vigor. Thus, dopaminergic input to the dorsal striatum is indispensable for the emergence of striatal activity that mediates adaptive changes in movement vigor. These results suggest refined intervention strategies for Parkinson's disease.

The ability to generate and refine voluntary movements in order to achieve an intended outcome is a critical function of the nervous system. To achieve an intended purpose, one need not only select and initiate the appropriate action, but such decisions must be turned into actions that are correctly timed and sufficiently vigorous (e.g., pushing hard enough). The rapid and reliable execution of purposive movements belies the complex sequence of computations required for the selection/planning, initiation, and subsequent online control of execution (Wolpert and Ghahramani, 2000). These computations are performed in distributed, interacting circuits including the neocortex, basal ganglia, and cerebellum (Doya, 2000). The discovery that the progressive depletion of dopamine neurons (PDD) in the midbrain is the primary cause of Parkinson's disease (Ehringer and Hornykiewicz, 1960) demonstrated the critical role of the basal ganglia in the control of movement (Albin et al., 1989; DeLong, 1990). Many models of basal ganglia function focus on explaining action selection and initiation (Albin et al., 1989; Frank, 2011; Hikosaka et al., 2000; Mink, 1996). However,

disruption of basal ganglia activity, and specifically the loss of dopamine signaling, also profoundly affects the timing, velocity, and fluidity of movement execution (Berardelli et al., 2001; Buhusi and Meck, 2005; Turner and Desmurget, 2010). For example, acute inactivation or lesion of the basal ganglia output can affect the velocity of movements without altering their selection or initiation (Desmurget and Turner, 2010; Horak and Anderson, 1984). In further support of a broad role for the basal ganglia in movement control, the majority of the modulation of neural activity in the basal ganglia occurs after movement planning and initiation (Bar-Gad et al., 2003; Turner and Desmurget, 2010) and is correlated with multiple aspects of movement execution (Rueda-Orozco and Robbe, 2015). However, it has proven difficult to resolve the role of the basal ganglia in the online control of movement due to the sparseness and complexity of the neural representation of movement-related parameters (DeLong and Wichmann, 2009).

A reduction in the vigor of voluntary movement is one of the most profound effects of either acute or chronic disruption of dopamine signaling (Palmeter, 2008; Salamone and Correa, 2012). In studies of dopamine-depleted rodents, a reduction in the number or frequency of reward-seeking actions ("response vigor") has reliably been observed. In Parkinson's disease, reduced vigor generally manifests as both a slowing of movement (bradykinesia) and a reduction in the total amount of movement (akinesia)—deficits that can be ameliorated by pharmacological treatment (Berardelli et al., 2001). Behavioral studies in Parkinsonian patients have revealed that the reduced velocity of movement ("movement vigor") is a primary deficit rather than a result of compensation for coordination deficits (Baraduc et al., 2013; Mazzoni et al., 2007). The extent to which such deficits in movement vigor are present in dopamine-depleted rodents is unclear, although it has been proposed that dopamine acting in the dorsal striatum is necessary to "energize" or invigorate action (Niv, 2007; Wang et al., 2013). Nonetheless, the tight link between the state of dopaminergic signaling in the basal ganglia and the extent of bradykinesia suggests that comparing activity patterns between normal and dopamine-depleted states during purposive movements could aid in the identification of neural correlates critical for control of movement. However, whether or how PDD alters the neural representation of movement in the primary target of midbrain dopamine neurons—the striatum—has not been described.

Here, we use a mouse model of PDD (Ekstrand et al., 2007) to explore the role of the basal ganglia in controlling the vigor of

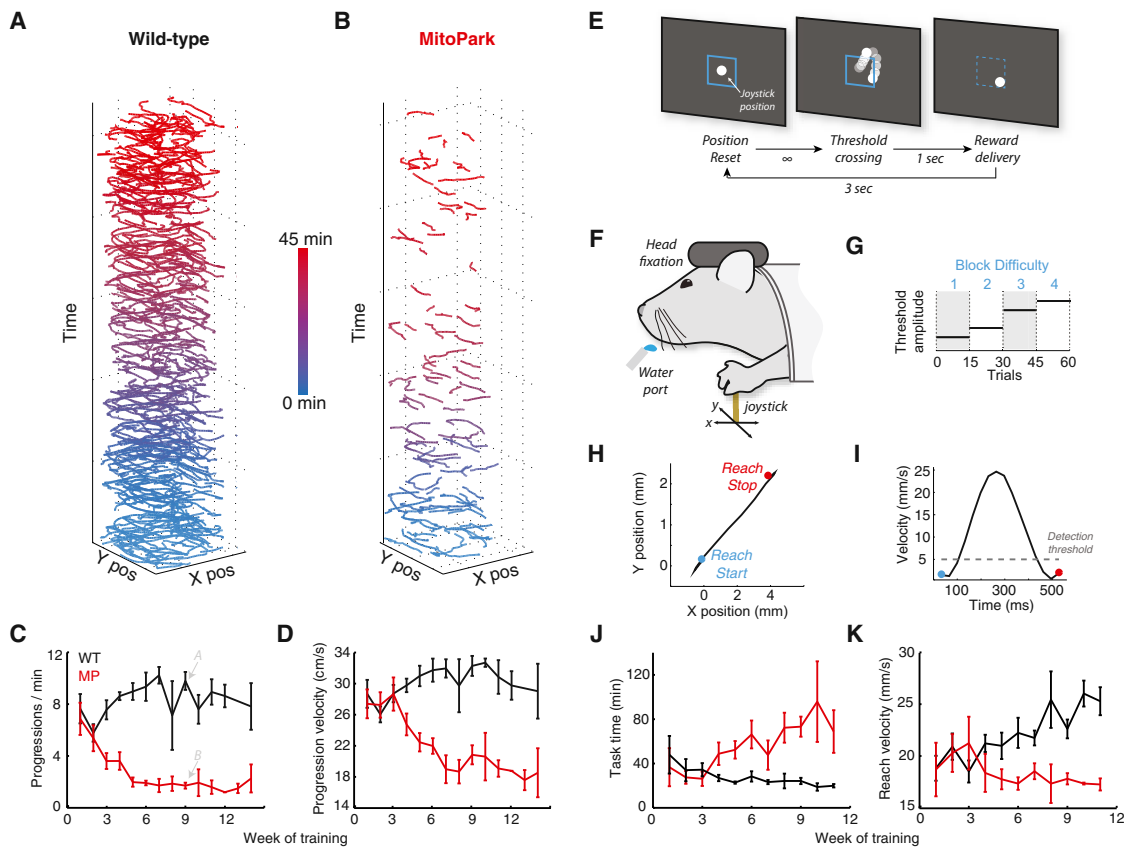


Figure 1. Bradykinesia Is Evident in Both Gross and Fine Motor Tasks

(A and B) Mouse position in the open field over 45 min. Discrete bouts of locomotion (“progressions”) were extracted and colored according to start time. Example session of WT (A) and MitoPark (B) mice after 9 weeks of behavioral monitoring (~20 weeks of age).

(C and D) Longitudinal plot of the number of progressions per minute (C) and peak velocity during the progression (D) as a function of the training session.

(E) Schematic representation of the effort-based head-fixed task. Upon the position reset, suprathreshold joystick displacement (white dot indicates joystick position, blue box indicates threshold) triggered water reward delivery.

(F) Mice were restrained in a head fixation system with an accessible joystick and lick port.

(G) The displacement threshold was altered every 15 trials (block).

(H and I) Individual reaches were extracted from continuous voltage measurements (H) by thresholding the velocity (I) to detect a reach (see [Supplemental Experimental Procedures](#)).

(J and K) Time to complete 105 trials (J) and peak velocity of reaching movements (K) plotted as a function of the number of weeks of training. Neural recordings commenced after at least 12 weeks of training (~22 weeks of age) for both WT and MitoPark mice. Error bars reflect the SEM.

See also [Figures S1](#) and [S2](#).

voluntary, purposive movement. The MitoPark model uses a selective genetic deletion of an essential mitochondrial transcription factor in midbrain dopamine neurons resulting in gradual post-natal cell death and progressive dysregulation of basal ganglia circuitry. MitoPark mice exhibit a progressive bradykinesia of locomotion that exacerbates over the course of months, in parallel with the emergence of akinesia described previously ([Galter et al., 2010; Li et al., 2013](#)). To explore the neural basis of this reduced movement vigor, we combined neural recordings from the dorsal striatum with an effort-based operant task that requires mice to adjust the vigor of a reaching movement to obtain reward efficiently. Our findings argue that the loss of the normal striatal representation of movement during execution is a circuit mechanism for reduced movement vigor following dopamine depletion. The parallel phenotypes in the MitoPark

model and Parkinson’s disease suggest that this could also be a circuit mechanism of bradykinesia in patients.

Bradykinesia in MitoPark Mice Is Evident in Both Gross and Fine Motor Tasks

Although bradykinesia is well characterized in Parkinson’s disease patients, it has not been examined in detail during PDD in animal models. We characterized the emergence of gross motor dysfunction in individual mice that were allowed to freely explore an open-field environment. Wild-type (WT) mice (10 weeks old) exhibited stable levels of total movement in the subsequent 15 weeks of behavioral testing ([Figure 1A](#)). By contrast, MitoPark mice displayed a stereotypical and progressive decline in the overall frequency of movement ([Figure 1B](#)), reaching a minimum of ~25 weeks postnatal (a point at which striatal dopamine levels

are <20% of WT levels) (Ekstrand et al., 2007; Galter et al., 2010). Concomitant with this decline in total movement, we observed a decline in the peak velocity of bouts of locomotion (“progressions”) in MitoPark mice (Figures 1C, 1D, and S1). The MitoPark cohort became significantly bradykinetic relative to WT littermates during the fourth week of testing ($p < 0.05$, ANOVA with Bonferroni correction) at an age (~14–15 weeks) when significant decreases in striatal dopamine levels are first detected (Ekstrand et al., 2007; Galter et al., 2010). Thus, bradykinesia is a dramatic phenotype in the MitoPark mouse and is tightly correlated with the loss of striatal dopamine.

The observed bradykinesia was accompanied by significant alterations to the trajectories of locomotion such that the tortuosity increased over the course of dopamine depletion in MitoPark mice (Figure S2). This could reflect variation in heading associated with repeated short bouts of slow locomotion, or could indicate that bradykinesia in locomotion was a consequence of a more pervasive deficit in coordination. In Parkinsonian patients, it has been shown that bradykinesia occurs without pervasive coordination deficits (Baraduc et al., 2013; Mazzoni et al., 2007). Thus, we next asked whether the reduced vigor that manifests in locomotion would also be apparent in fine control of limb movements. We placed mice in a head-fixed operant chamber in which a joystick was positioned within reach of the forelimbs (Figures 1E and 1F). In this task, mice were required to produce a forelimb movement (“reach”) with sufficient vigor to displace the joystick from a starting position past a threshold distance to obtain a water reward (Figures 1H and 1I). The joystick was spring loaded and thus, in the absence of any applied force, returned to a central position. The task was effort-based because the average power or the rate of energy expenditure during a displacement of the joystick was proportional to reach amplitude and velocity (see *Supplemental Experimental Procedures*). Trials were arranged in blocks of 15 trials with distinct amplitude thresholds required to trigger reward (levels 1–4; Figure 1G). Following a suprathreshold displacement of the joystick, a small liquid reward was delivered with a 1-s delay. The task was self-paced and trials were not terminated until a movement of sufficient amplitude was made, thereby requiring subjects to use the presence or absence of a delayed reward to infer the required displacement.

Mice were able to learn to complete blocks of all difficulties within a few weeks of training. Over the course of training, WT mice were able to rapidly adapt the vigor of their movements to the changing threshold requirements. Initially, MitoPark mice were also able to perform the task efficiently; however, as the degeneration of dopamine neurons progressed, performance was severely compromised (Figure 1J). By ~25 weeks of age, the performance of MitoPark mice was so severely compromised that completion of all blocks required more than 90 min compared with the 10–15 min required by WT mice of the same age and training.

The time to complete the task could reflect aberrant coordination, slowness of movement, or other deficits. Thus, we next analyzed the kinematics of discrete reaches (Figures 1H and 1I). WT mice showed an increasing peak reach velocity that correlated with improving task performance (Figure 1K). We then asked whether individual reaches in MitoPark mice were

bradykinetic by analogy to the slow velocity of locomotion bouts. Indeed, the peak velocity of reaches systematically declined in the MitoPark mice in parallel with the increasing time required to complete the task (Figure 1K).

To efficiently collect reward, we hypothesized that mice would expend relatively less effort in trials with smaller displacement requirements even without an explicit requirement to do so. To examine this prediction, we computed parameters of each reach as a function of the block in which the reach occurred. We analyzed the entire outward component of the movement such that a movement made well beyond the threshold would be recorded. Thus, large movements in blocks with low displacement thresholds were possible. Conversely, trials continued until a suprathreshold movement was recorded and subthreshold movements were possible and included in the block-wise analysis. We found that the average and peak velocity of forelimb movements were the parameters most strongly correlated with the threshold requirement. Reach velocity was used as a correlate of vigor in subsequent analyses (Figure S3). Consistent with efficient task performance, we found that in WT mice the peak velocity of a reach was well correlated with block difficulty (Figure 2A). Efficiency was also obtained by a progressive reduction in the total displacement of joystick trajectories in the hardest blocks (Figure 2B). Together, these changes led to an improvement in task performance such that the time to complete a block gradually became independent of block difficulty in WT mice ($\rho = -0.68$; $p < 0.05$; Figure S4). In summary, WT mice learn to make a fixed, small number of discrete reaches adapted to the threshold requirement of the trial.

If the loss of dopamine signaling plays an important role in adapting movement vigor, then PDD should manifest as a declining velocity of forelimb movements. Prior to significant differences in locomotion, MitoPark mice likewise completed the effort-based task comparably, or even better, than WT littermates. Concomitant with the emergence of deficits in locomotion, MitoPark mice began a progressive increase in time required to complete the task (Figure 1J) due to a disproportionate amount of time spent to complete the most difficult blocks ($\rho = 0.83$; $p < 0.001$; Figure S4). The behavioral deficit became apparent around an age (14–15 weeks) when striatal dopamine levels are first significantly reduced (Ekstrand et al., 2007; Galter et al., 2010). This is consistent with the notion that the performance deficit resulted from a failure of dopamine-depleted mice to complete movements of sufficient vigor to reliably collect reward. However, despite the decline in the peak velocity of reaches (Figure 1K), these velocities were still significantly tuned to block difficulty with a correlation similar to that of WT mice at all stages of dopamine depletion (Figures 2A and S3). This observation is consistent with a stable slope, but reduced average, movement vigor observed in Parkinsonian patients (Baraduc et al., 2013). Likewise, the increased total displacement (summed over all reaches) required to complete a block of trials requiring large, vigorous movements (Figure 2B) is akin to the selective increase in the number of attempts required to successfully perform large, rapid reaches in Parkinsonian patients (Mazzoni et al., 2007).

Studies in animal models of acute dopamine depletion have observed a reduced willingness of an animal to engage in

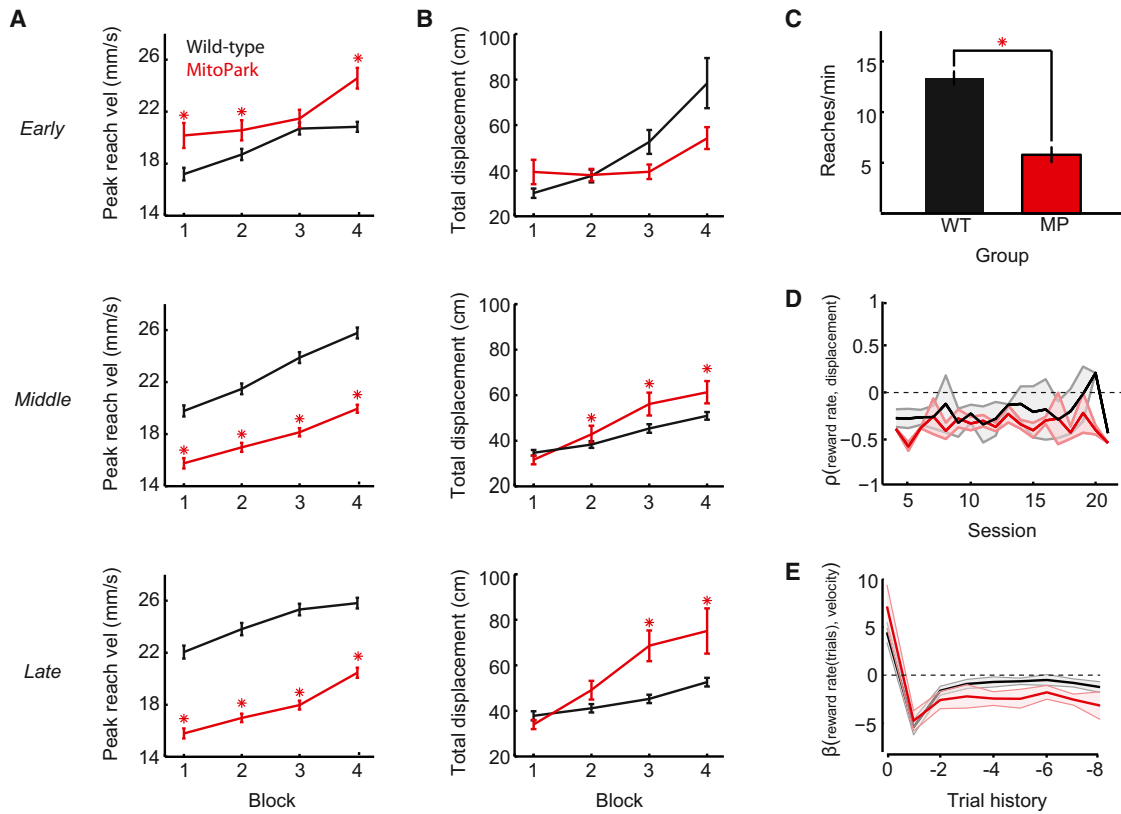


Figure 2. Dopamine Depletion Produces Akinesia and Bradykinesia but Spares Tuning to Task Demands

(A) Average peak reach velocity as a function of the block in which the movement occurred for sessions divided into Early (<4 weeks of training), Middle (4–8 weeks), and Late (9–13 weeks) phases of training.

(B) The total joystick displacement (path length) summed over all reaches for each block.

(C) Frequency of reaches during late-phase task performance.

(D) Correlation (ρ) between the time since previous reward (reward rate) and the total displacement per trial.

(E) Beta values obtained from a multiple regression of reach velocity as a function of reward rate for the previous eight trials. In all plots, data for WT mice are shown in black and MitoPark mice in red. Error bars reflect the SEM. Asterisks indicate significant differences (ANOVA, post hoc testing; $p < 0.05$). See also Figures S3, S4, and S5.

effortful, reward-seeking actions (Salamone and Correa, 2012). Behavioral studies in Parkinsonian patients have argued that bradykinesia is a consequence of an increased probability that a slow movement is made (Mazzoni et al., 2007) rather than an explicit unwillingness to perform effortful movements. This prompted us to examine whether the behavioral deficit in the MitoPark mice was secondary to a declining motivation to collect reward or disrupted adaptation of movement vigor.

We first note that although MitoPark mice with substantial dopamine depletion develop bradykinesia, it is due to a change in the mean velocity of forelimb movements rather than an inability to adapt the relative vigor of movement to block difficulty (Figure 2A). Moreover, MitoPark mice exhibited more total movement per trial in the hardest blocks relative to their WT counterparts (Figure 2B) suggesting intact motivation to pursue reward. Consistent with this observation, we found that there was a significant reduction in the frequency of forelimb movements (Figure 2C), but that this change was independent of block. The decrease in the average velocity of movement was likely not a consequence of aberrant motor control, because the tortuosity

of reach trajectories was not correlated with block (Figure S3). Finally, when we examined blocks of reduced difficulty that were added to the end of a session, we found that MitoPark mice completed the early and late blocks of equivalent difficulty at indistinguishable rates (Figure S5), suggesting that the increased time to complete the most difficult trials was not related to fatigue or decreasing motivation to collect water as the session progressed.

How does dopamine depletion result in bradykinesia? The intact tuning of reach velocity to trial block suggests that MitoPark mice are still able to detect changes in reward rate and adapt movement vigor. For example, the correlation between the instantaneous reward rate and total displacement was independent of PDD (Figure 2D). To efficiently solve the task, movement vigor should be adapted not only to the instantaneous reward rate, but also as a function of the history of reward (i.e., effort across trials with a consistent threshold should be consistent). We thus computed a multiple regression between the average velocity of movement and the instantaneous reward rate over recent trials (Figure 2E). While the initial derivative component was unaltered,

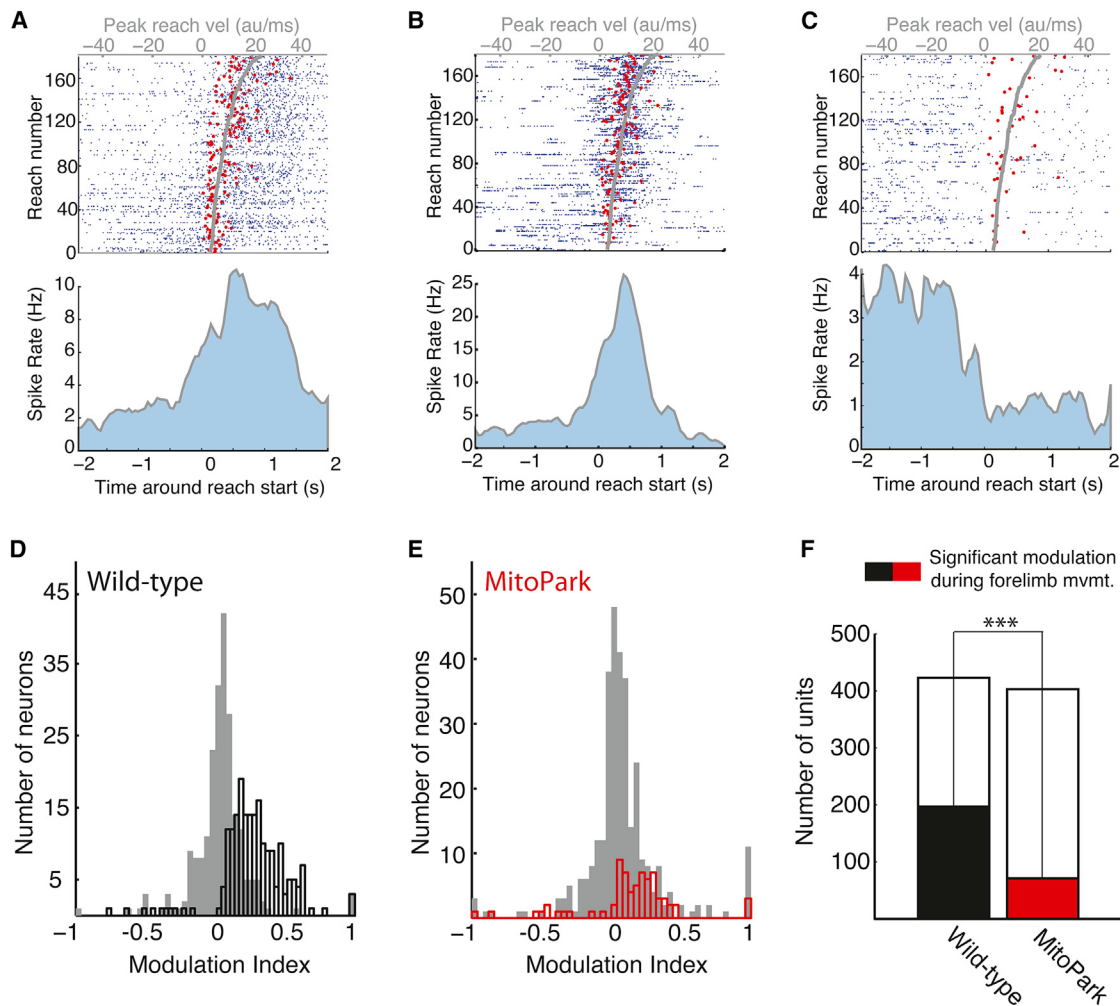


Figure 3. The Neural Representation of Forelimb Movements in the Dorsal Striatum Is Altered by PDD

(A–C) Peri-event raster plots and spike density functions for a set of simultaneously recorded units from the dorsal striatum of WT mouse exhibited sustained positive (A), transient positive (B), and negative (C) modulation of their firing rate during reaches. Upper panels show raster plots aligned to the onset of the reach and sorted by the peak velocity of the reach. Reach velocity is plotted in gray, scaled according to the top axis. Red dots indicate median spike time during each reach. Lower plots show the corresponding spike density function.

(D and E) Histogram of modulation index for all recorded units is shown for both WT (D) and MitoPark (E) cohorts.

(F) Population data showing number of units recorded in each cohort (open bars) and number of units significantly modulated ($p < 0.05$, rank-sum test) during forelimb movements (filled bars). A significantly greater proportion of WT neurons (47%) compared to MitoPark neurons (18%) were modulated by forelimb movements ($p < 0.001$, two sample proportion t test).

MitoPark behavior was characterized by sustained non-zero β values that extended for several trials of reward history. Thus, our data suggest that dopamine depletion does not impair the ability to detect changes in reward or even to transiently adapt movement vigor, but rather leads to a sustained drift toward lethargy independent of recent experience.

Neural Correlates of Movement Vigor in the Dorsal Striatum

It has been suggested that dysregulated neural activity in the dorsal striatum (Mazzoni et al., 2007; Niv et al., 2007), the major target of midbrain dopamine projections and the structure with most profoundly impaired dopamine levels in the MitoPark

mice (Galter et al., 2010), could underlie the impairment in movement vigor following PDD. To examine the striatal representation of forelimb movements and its sensitivity to PDD, we recorded activity in the dorsal striatum of WT and MitoPark mice at ≥ 20 weeks of age—a point at which MitoPark mice show profound behavioral deficits and have $<20\%$ the striatal dopamine concentration of WT mice. Using silicon probe electrode arrays that span ~ 1.5 mm of dorsal striatum, we were able to record the activity of a population of single units ($N = 423$) in WT mice performing the effort-based operant task. We observed single units with significant positive or negative modulation of firing rates throughout the duration of forelimb movements (Figures 3A–3C). The fraction of units with significant firing rate

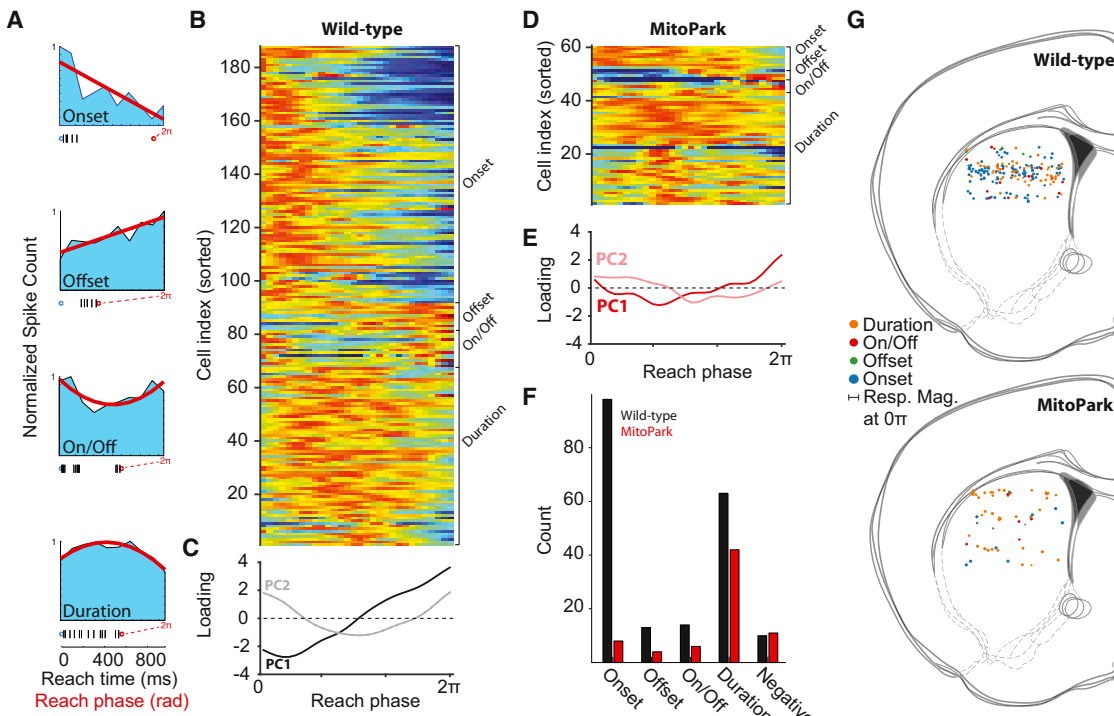


Figure 4. Dopamine Depletion Is Accompanied by a Reduction in Phasic Recruitment of Striatal Activity during Movement

All units with significantly more spikes during forelimb movements than an equivalent duration baseline period were used to compute peri-event phase histograms (PEPH). PEPHs were computed by linearly warping individual spike times onto the phase of forelimb movement.

(A) Example PEPHs for the classes with a significant linear component to a second-order polynomial fit (onset and offset) are shown in the upper two panels. Example PEPHs for the classes with a significant quadratic component to a second-order polynomial fit (on/off and duration) are shown in lower two panels. Example raster plot (prior to warping) from a single reach is shown below each example unit.

(B) Normalized PEPH for all positively modulated WT units ($n = 188$).

(C) The first two principal components (PC1, black; PC2, light black) are shown for the PEPH matrix from WT mice.

(D) Normalized PEPH for all positively modulated units recorded in MitoPark mice ($n = 61$).

(E) First two principal components (PC1, red; PC2, light red) are shown for PEPH matrix from MitoPark recordings.

(F) Bar plot showing number of units observed for each response class for WT (black) and MitoPark (red) recordings.

(G) For each positively modulated neuron, recording position was estimated from shank number (1–8) from which it was recorded and recording site depth. Color reflects functional class. Marker diameter reflects extent of modulation at 0π phase of reach. Coronal sections from a mouse brain atlas are presented as reference.

See also Figure S6.

modulation during forelimb movement was substantial in the motor cortex-recipient dorsal striatum of WT mice (47%; $n = 198$ out of 423, Figures 3D and 3F), but dropped dramatically in MitoPark mice (18%, $n = 71$ out of 403, $Z = 9.92$, $p < 0.001$, two sample proportion test, Figures 3E and 3F).

The multiple degrees of freedom available for movement lead to many spatiotemporal patterns of muscle contraction that produce movements of a given vigor (Wolpert and Ghahramani, 2000). For example, consider two movements of a similar amplitude and duration: for movements with a more rapid initial acceleration a larger, delayed deceleration would be required. Thus, a neural representation of vigor could be reflected in multiple phases of movement execution. This prompted us to examine the dynamics of the neural representation of movement vigor and its sensitivity to PDD. Due to the highly variable duration of reaching movements, we computed the phase of each spike as a function of the duration of individual reaches to produce a

peri-event phase histogram (PEPH) (Figure 4A). Across the population, the majority of the variance of the PEPH structure was captured by a linear and quadratic function of reach phase reflected by the first two principal components (Figures 4B and 4C); each PEPH was thus fit with a second-order polynomial and the slope and curvature terms extracted.

This analysis revealed four distinct functional classes defined by the phase of movement in which units were the most active: onset near the start of movement, offset near the end of movement, on/off near the start and end of movement, and duration units throughout movement (Figures 4A–4C). Negatively modulating cells were defined as those whose activity was suppressed during movement. We found that the distribution of response classes in WT mice was dominated by onset units characterized by a negative slope and little curvature in the PEPH and duration units characterized by a near zero slope and negative curvature (Figure 4A). Analogous response classes were observed in

MitoPark mice (Figures 4D and 4E); however, the population of modulated neurons in MitoPark mice revealed an absence of transient recruitment of striatal units around movement onset, indicative of a disproportionate loss of onset units ($n = 98$ cells in WT; $n = 8$ in MP, Figures 4F and 4G).

Bradykinesia that results from PDD is correlated with a change in the dynamics of striatal activity after initiation, especially during the earliest phase of a forelimb movement (i.e., prior to the peak velocity and amplitude of the reach). This suggests that striatal activity could play a causal role in determining movement vigor. Consistent with a role for striatal activity in determining movement vigor, we note that onset cells are most active at an early phase of movement ($0.46\pi \pm 0.26$ SD; Figure 4B)—well before the later phases of the reach where either velocity ($0.95\pi \pm 0.01$ SD) or amplitude (2π) is maximal. However, it is also possible that the disrupted neural representation of movement is, in part, a consequence of altered movements. To address this question, we first sought a more quantitative description of the reach trajectories themselves (Figures 5A–5D). We found that over the course of PDD, there was no significant change in the tortuosity of reaches (Figure 5A). This is consistent with a preserved control of coordination in MitoPark mice, similar to evidence for the unimpaired coordination in Parkinsonian patients (Baraduc et al., 2013; Mazzoni et al., 2007). We next examined aligned reach trajectories taken from recording sessions in the WT and MitoPark mice (Figure 5B). We found that the trajectories were highly similar with no change in off-axis movement, but a selective decrease in the amplitude and velocity of the movement along the major axis of the trajectory (Figure 5C) due to a redistribution of reach velocities within the same range of absolute velocities (Figure 5D). Thus, the disrupted neural representation of movement vigor was present despite the fact that MitoPark mice could and occasionally did make equivalently rapid movements to WT mice. Further, a disrupted neural representation of movement was present when controlling for reach velocity (Figure S6) and without a change in the maximal firing rate modulation (Figure S7).

If activity in dorsal striatal neurons is sufficient to control movement vigor, then on a given reach neural activity should predict vigor. Indeed, we observed a substantial fraction of units in which the maximum instantaneous firing rate during a reach correlated with the effort (amplitude and velocity) of the movement (Figures 5E–5H). We found that single unit firing rates were well correlated with several features of reaches (amplitude, velocity; Figure 5F) and substantially less with parameters that reflect the coordination of movement (tortuosity, direction). The correlation between neural activity and reach velocity was strongest for the current reach, with reduced correlation to either prior or subsequent reaches (Figure 5G). The correlation between neural activity and reach parameters was not independent: units with strong correlations to reach velocity also tended to be well correlated with the reach distance (path length; Figure 5H). Across the population of units in MitoPark mice, the mean magnitude of the correlation with velocity was, however, significantly reduced without a change in the correlation with distance (Figure 5H).

Neural correlates of reach velocity were most prevalent in the onset and duration classes (90% and 94% of cells, respectively), with the offset and onset/offset classes displaying more modest

correlations with movement vigor (54% and 43% of cells, respectively). A significant decrease in the fraction of duration cells in which maximum firing rates correlated with peak reach velocities was observed in MitoPark mice ($n = 63$ cells, 94% modulated in WT $n = 42$, 27% modulated in MitoPark, $Z = 4.934$, $p < 0.01$, two sample proportion test). Less pronounced differences between the WT and MitoPark groups were observed for the offset ($n = 13$ cells, 54% modulated in WT and $n = 4$ cells, 25% modulated in MitoPark), onset/offset ($n = 14$ cells, 43% modulated in WT, $n = 6$, 52% modulated in MitoPark), and duration ($n = 63$ cells, 54% modulated in WT, $n = 42$ cells, 52% modulated in MitoPark) classes (see also Figure 6).

Further consistent with a causal role, we found that activity prior to movement initiation was altered in MitoPark mice and that pre-movement activity of many individual neurons was predictive of the velocity of the upcoming reach (Figure S7). Thus, these data suggest a model in which the loss of onset cells and the impaired coding by duration cells combine to reduce the vigor of the currently executed movement, producing a persistent bias toward bradykinesia.

Dopamine Repletion Ameliorates the Neural Representation and Behavior

If the observed changes in the striatal population dynamics indeed represent a putative circuit mechanism of the bradykinetic phenotype in PDD, then not just the behavioral, but also the neural phenotype may be ameliorated by acute restoration of dopaminergic tone. Oral levodopa (LD) administration is the most widely used pharmacological dopamine replacement therapy for Parkinson's disease. In patients it produces a dramatic amelioration of both akinesia and bradykinesia (Berardelli et al., 2001) and in rats it can partially normalize striatal activity following acute depletion of dopamine (Hernandez et al., 2013). In MitoPark mice, we observed a progressively more pronounced effect of oral L-DOPA treatment (see Experimental Procedures) on voluntary movement in the open-field locomotion assay with PDD. At ~24 weeks of age (>12 weeks of training) L-DOPA treatment restored the amount of voluntary movement to near WT levels (Galster et al., 2010) and partially restored the velocity of progressions (Figures 6A and 6B). There were no significant effects of an equivalent course of L-DOPA treatment on WT behavior (Figures 6A and 6B).

To further test the link between movement vigor and neural dynamics in the basal ganglia, we assessed the effect of L-DOPA treatment on behavioral and neural phenotypes observed in MitoPark mice in our effort-based task. L-DOPA treatment lead to a dramatic improvement in performance by MitoPark mice, evidenced by a ~50% reduction in the mean time to complete trials (Figure 6C), despite unchanged total number of reaches made per trial (Figure 6D). The improvement in task performance was a consequence of an increased rate and velocity of forelimb movements (Figures 6E and 6F). The latter resulted from a restoration of the relatively symmetric distribution of reach velocities, reflected by a reduction in the skew (Figures 6G and S5). Importantly, L-DOPA treatment did not impair the tuning of reach velocity to block (Figure 6H).

Analysis of an additional 465 single units in MitoPark mice performing the effort-based task following L-DOPA administration

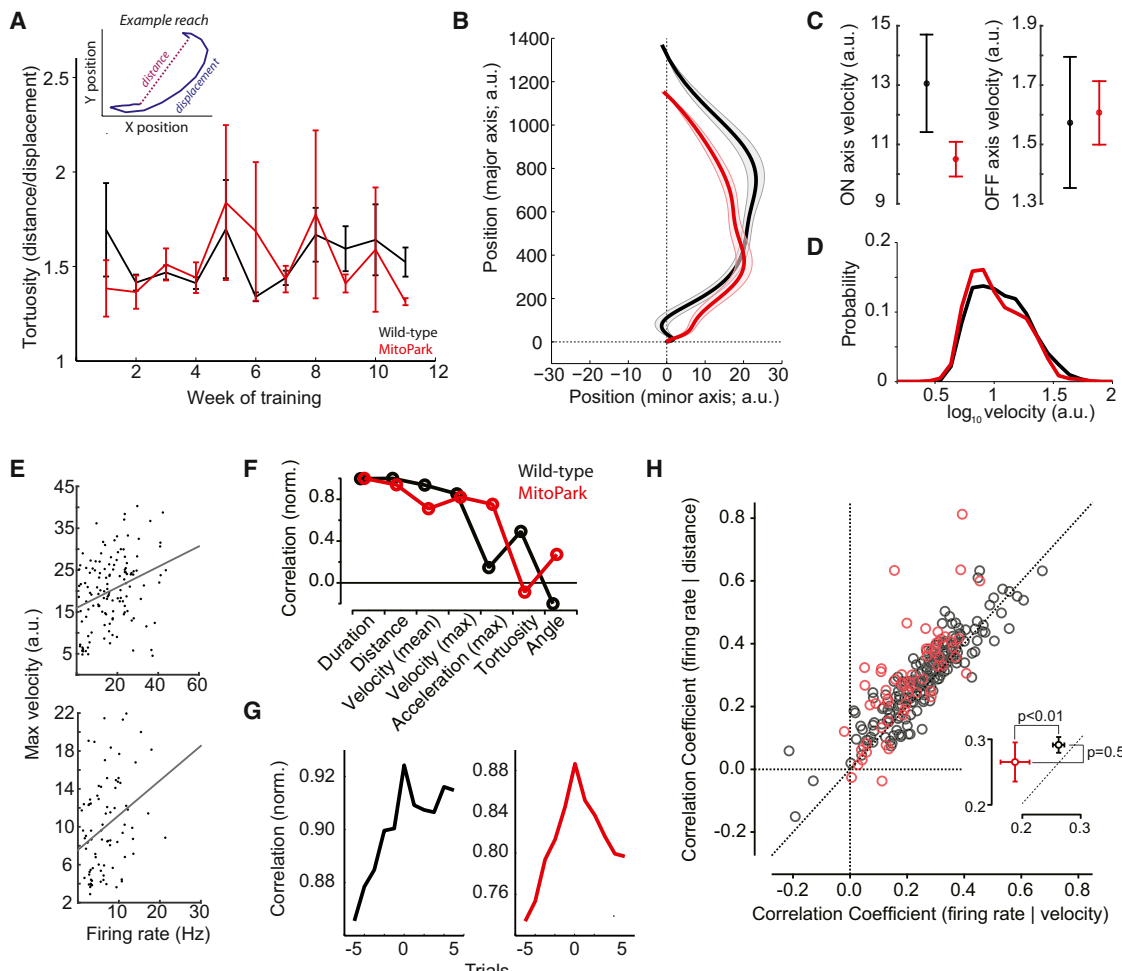


Figure 5. Striatal Representation of Movement Vigor Is Not Due to Trajectory Differences

- (A) Tortuosity (distance [path length] divided by displacement [endpoints]) of joystick trajectories (reaches) was not significantly different between WT and MitoPark mice at any stage of training.
- (B) Outward component of mean reach is shown for WT and MitoPark mice during electrophysiological recording sessions (see [Experimental Procedures](#)).
- (C) Dopamine depletion in MitoPark mice resulted in reduced amplitude and peak velocity of reaches along the major axis of motion (ON axis; left). There was no significant difference in velocity along orthogonal movement axis (OFF axis; right).
- (D) Histogram of log-transformed distribution of reach velocities for WT (black) and MitoPark (red) recording sessions.
- (E) Two example neurons that show significant trial-wise correlations between average firing rate and peak velocity of joystick movement. Both neurons are onset cells.
- (F) Normalized correlation coefficients were calculated between the firing rate and reach parameters for all cells significantly modulated during forelimb movement. Neural activity was best correlated with measures of movement vigor (duration, distance, and velocity).
- (G) Cross correlations between firing rate and reach velocity were computed over a range of -5 to +5 trials. In both WT and MitoPark mice, correlations were maximal for the current trial.
- (H) The firing of individual units during movement similarly correlated with both total distance of joystick movement and maximum velocity. Inset shows correlation coefficient across the WT ($n = 188$) and MitoPark ($n = 61$) neuron population. P-values are obtained using a rank-sum test. Error bars and shaded areas reflect the SEM.

See also [Figure S7](#).

revealed a significant increase of the proportion of cells that significantly modulated their firing rate during forelimb movements ([Figure 6I](#); $n = 127$ cells in LD-treated MitoPark mice, $n = 71$ in untreated MitoPark mice; $Z = 3.4$, $p < 0.001$, two sample proportion test). Although the proportions of onset/offset and offset cells within this population were restored to levels indistinguishable from those observed in WT mice, the effect on the

other functional classes was either partial or excessive ([Figure 6J](#)). For example, the proportion of onset cells did increase significantly ($n = 33$ cells in L-DOPA-treated MitoPark mice, $n = 8$ in untreated PD mice; $Z = 3.5$, $p < 0.001$, two sample proportion test), but did not reach the level of WT mice ($n = 33$ in L-DOPA-treated MitoPark mice, $n = 98$ in untreated WT mice, $Z = 6.8$, $p < 0.0001$, two-sample proportion test). Moreover,

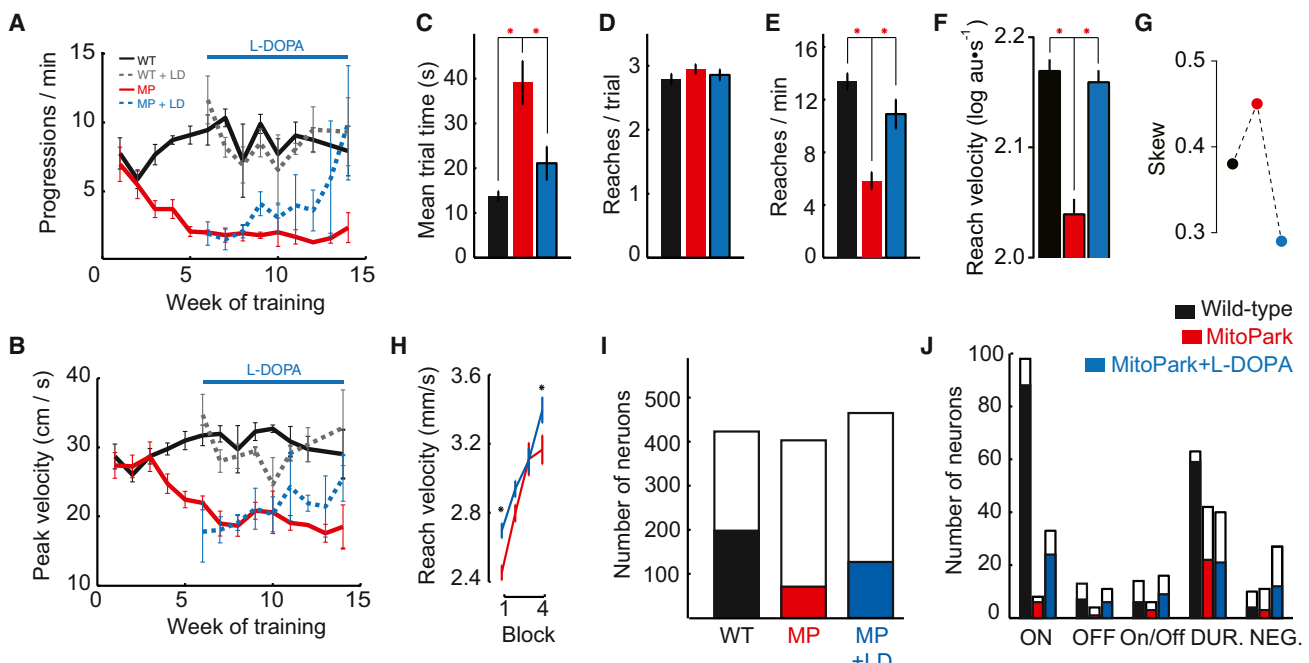


Figure 6. L-DOPA Ameliorates Akinesia, Bradykinesia, and the Neural Representation of Forelimb Movement

(A and B) Number of progressions per minute (A) and peak velocity during a progression (B) replotted from Figure 1 in solid lines. Overlaid are interleaved sessions following oral administration of L-DOPA (dashed lines).

(C–G) Summary data describing mean trial time (C), reaches per trial (D), reach frequency (E), reach velocity (F), and skew of reach velocities (G) for WT (black), MitoPark, and MitoPark following oral L-DOPA administration (blue).

(H) Average reach velocity as a function of block from paired sessions immediately prior to (red) and after (blue) L-DOPA administration.

(I) Number of single units isolated (“neurons”; open bars) and number of units with significant firing rate modulation during forelimb movements (filled bars) for WT (black), MitoPark (red) and MitoPark following L-DOPA administration (blue) groups.

(J) Distribution of units according to response type (see Experimental Procedures and Figure 4) (open bars) and fraction of those units with significant correlation to reach velocity (filled bars) for WT (black), MitoPark before (red) and after L-DOPA administration (blue). Error bars reflect the SEM.

See also Figure S6.

L-DOPA treatment had no significant effect on the proportion of duration cells. These results indicate that in just a few tens of trials, the deficit in the neural representation of forelimb movements in the dorsal striatum can be significantly ameliorated by acute restoration of dopaminergic tone.

Suppression of Striatal Activity during Movement Reduces Vigor

The observed tight link between the state of striatal dopaminergic signaling and movement vigor provides strong support for the notion that the basal ganglia is involved in the online control of movement. However, changes in neural activity in the basal ganglia that result from the altered dopaminergic state in MitoPark mice with and without L-DOPA treatment presumably are not restricted to movement execution (Figure S7) (Hernandez et al., 2013). Although the largest functional changes were found during movement, it remained uncertain whether a reduced recruitment of striatal activity during movement was sufficient to reduce movement vigor. We therefore asked whether acutely suppressing activity of striatal projection neurons selectively during movement would alter movement vigor. We trained an additional three mice expressing Archaerhodopsin-3 (Han et al., 2011) in direct pathway neurons of the striatum (Gong

et al., 2003) to perform the effort-based task. Once animals attained expert performance, we suppressed striatal activity on 19.2% \pm 2.8% of reaches (randomly selected) by delivering light through bilateral optical fibers implanted at the center of our recording target in dorsal striatum (Figure 7A). We ensured that the perturbation was done selectively during movement by triggering light delivery only after trial start and once the reach had crossed a threshold lower than the threshold of the easiest block (Figure 7B). We observed a systematic reduction in peak velocity of reaches in “light ON” trials for all mice ($p < 0.001$; paired t test), whereas reach amplitude and tortuosity were unaffected by the presence or absence of photostimulation ($p > 0.97$; Figure 7C). Acute suppression of striatal activity during movement execution is thus sufficient to selectively induce bradykinesia of forelimb movements similar to that produced by PDD.

DISCUSSION

The neural mechanisms for the precise control of movement remain poorly understood (Doya, 2000; Shenoy et al., 2013). The view that the basal ganglia are selectively engaged in the planning and selection of specific movements learned through reinforcement has been ascendant (DeLong and Wichmann,

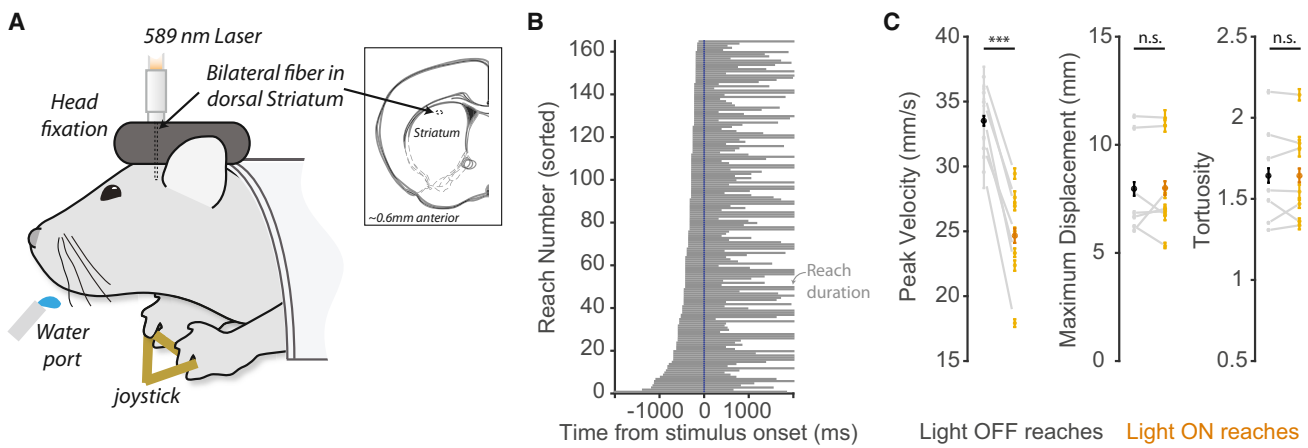


Figure 7. Suppression of Dorsal Striatal Activity during Movement Execution Is Sufficient to Reduce Vigor

(A) Schematic of the experimental design. Head-fixed mice expressing Archaerhodopsin-3/eGFP in projection neurons of the dorsal striatum were trained to perform the effort-based task (see [Experimental Procedures](#)). Optical fibers were implanted bilaterally with tips positioned in the area of neural recordings. A fiber-launched 589 nm laser was coupled to the chronically implanted fiber stub during seven behavioral sessions from three mice.

(B) Brief illumination (1 mW; 450 ms duration) was triggered during the first reach of a trial on a random set of interleaved trials (~20%). The distribution of stimulus onset latency is shown as a function of the duration of the concurrent reach (gray bars).

(C) Reach parameters were extracted and compared between reaches in which photo activation was present ("Light ON") and control reaches with no photo activation ("Light OFF"). Peak reach velocity, maximal displacement, and tortuosity of the reach are shown for all mice and all sessions. Asterisks indicate significant differences (paired t test; $p < 0.001$, not significant [n.s.] = $p > 0.05$).

2009) and focused substantial interest on the physiological correlates of reward processing and action initiation. Here, we provide evidence that the dynamics of activity in the dorsal striatum is critical for controlling the vigor of movements during execution (Turner and Desmurget, 2010). Single units in the dorsal striatum represent the velocity of forelimb movement, with the largest modulation of activity occurring early in movement execution. A profound disruption of the striatal representation of movement vigor is observed in PDD concomitant with the emergence of a dramatic behavioral deficit. The tight link between striatal dynamics and control of movement vigor is particularly apparent from our finding that amelioration of the behavioral phenotype by L-DOPA treatment is accompanied by a rapid amelioration of movement-related striatal activity. Finally, we show that acute manipulation of striatal activity during movement is sufficient to produce bradykinesia. Thus, the vigor of a currently executed movement is determined, at least in part, by striatal activity. Furthermore, dopamine depletion is associated with a dramatic alteration in striatal population activity recruited during effortful, purposive movement.

Here, we show that progressive depletion of midbrain dopamine neurons leads to a concomitant emergence of akinesia and bradykinesia. Bradykinesia in MitoPark mice does not appear to be secondary to altered control of movement, but rather reflects a reduced probability of committing vigorous actions even when it is required for efficient collection of reward. These results closely resemble recent observations in Parkinsonian patients (Baraduc et al., 2013; Mazzoni et al., 2007). Our observation of normal sensitivity to reward rate (Figures 2D and 2E) suggests that reward processing may be relatively spared in MitoPark mice. This could reflect the relative sparing of ventral tegmental dopamine neurons in MitoPark mice at the

stage of PDD examined (Ekstrand et al., 2007). Dopamine neurons are also not uniquely required for signaling reward information, as reward prediction signals have been observed in non-dopaminergic neurons in the basal ganglia (Bryden et al., 2011; Cohen et al., 2012; Fan et al., 2012; Pan et al., 2013; Stalnaker et al., 2012) and other brain areas (Schultz, 2006). There is good evidence, for example in the control of bird song, that multiple distinct neural states can produce equivalent movements (Leonardo, 2005). In this sense, it is likely that striatal activity provides one neural mechanism sufficient for invigorating action, but is not the only mechanism by which movement vigor can be altered. The intact single trial changes in movement vigor could reflect adaptive changes in movement elicited by circuits outside the dorsal striatum with access to information about reward, e.g., cerebellum (Doya, 2000; Stein and Aziz, 1999).

In mice with PDD described here, in primates with striatal inactivations (Muranishi et al., 2011), and in Parkinsonian patients (Mazzoni et al., 2007), changes in outcome fail to be incorporated into persistent changes in behavior. In the context of our task, we observed an intact adaptation of movement vigor on the trial subsequent to a change in reward rate, but a persistent drift toward reduced movement vigor on subsequent trials (Figure 2E). Acute optogenetic silencing and progressive dopamine depletion both indicate that robust movement-related activity in the dorsal striatum is necessary for executing vigorous voluntary movements. Dopamine repletion with a synthetic precursor produced rapid (minutes) amelioration of movement-related activity in the dorsal striatum and increased movement vigor. Thus, these data suggest a model in which intact dopamine signaling is required for the stable emergence of movement-related population activity in the striatum, and this population activity in turn mediates persistent changes in movement vigor. It is

important to note that while we have shown striatal activity prior to and during movement is sufficient to determine movement vigor, striatal activity at later phases of movement (e.g., duration cells) provides a reliable correlate of movement vigor that may be used for learned changes on subsequent trials. Tonic dopamine in the dorsal striatum has been proposed to be essential for regulating movement vigor (Mazzoni et al., 2007; Niv et al., 2007)—a model in which increased motivation to obtain reward is tied to the invigoration of the reward seeking actions. The progressive depletion of midbrain dopamine neurons and pharmacological repletion with L-DOPA are thought to modulate tonic dopamine levels consistent with such a model. However, there is evidence that MitoPark mice have severely compromised phasic dopamine release in addition to a reduction in tonic dopaminergic tone (Good et al., 2011). A further complication is our observation that, under stable motivation to seek reward, mice can flexibly increase and decrease movement vigor (Figure S5). Thus, the detailed circuit mechanisms by which dopamine signaling is required for persistent changes in the striatal representation of movement remain to be fully elucidated.

It is unknown whether the functional response classes reported here map onto specific neuron types. The rapid emergence of neural correlates of movement vigor following the acute restoration of dopaminergic tone suggests that these functional properties are acquired through learning rather than being determined by afferent or efferent connectivity. In our data, ~40% of neurons recorded in a region of dorsal striatum with substantial input from frontal/motor cortex (Pan et al., 2010) had significant modulation during forelimb movements. One possibility is that these 40% are predominantly direct pathway neurons. Consistent with such an interpretation, we show that acute suppression of direct pathway neurons during movement is sufficient to elicit bradykinesia (Figure 7). Alternatively, a recruitment of both direct and indirect pathway neurons is consistent with the recent observation that lever pressing recruits both pathways (the relationship to movement vigor was not studied) (Cui et al., 2013; Isomura et al., 2013). A balanced recruitment of direct and indirect pathway neurons could be important for selective invigoration of a specific movement without a concomitant invigoration of, or aberrant initiation of, competing behaviors, i.e., to prevent a generalized invigoration of behavior in this context (Niv et al., 2007). This latter alternative would be more consistent with previous functional models that propose the basal ganglia selects among competing motor programs (Mink, 1996). Developing molecular strategies to identify and manipulate specific functional classes of striatal neurons could prove critical for effective intervention against bradykinesia.

Whether lessons learned in a mouse model of PDD will be applicable to patients with Parkinson's disease remains an open question. One way to test the applicability of our findings is to extend functional imaging studies (Martinu et al., 2012) to determine if there is selective loss of phasic striatal activity during vigorous movements in Parkinson's patients. In dopamine-depleted mice, we observed an increase in striatal activity prior to movement (Figure S7) followed by an aberrant reduction in activity during early phases of movement execution. From these results, we predict that optimal intervention strategies in Parkinson's disease would be those that restore the relationship

between pre-movement activity and phasic activity during movement execution. Pharmacological restoration of dopaminergic tone was relatively effective, however it also appeared to aberrantly alter aspects of the neural representation of movement that could be problematic. Deep brain stimulation applied without respect to movement timing partially ameliorates bradykinesia in human subjects (Baraduc et al., 2013). We propose that a strategy combining open-loop deep brain stimulation with closed-loop changes in stimulation during movement execution could offer the potential for improved outcomes in subjects with severe bradykinesia.

EXPERIMENTAL PROCEDURES

Subjects

All experiments and procedures were approved by the Institutional Animal Care and Use Committee and were consistent with the standards set forth by the Association for Assessment and Accreditation of Laboratory Animal Care. The MitoPark model achieves cell type-specific deletion of dopamine neurons by crossing mice with a knock-in allele of cre-recombinase driven by the dopamine transporter (Slc6a3) with a knock-in floxed Tfam allele. Following recombination, deletion of TFAM produced progressive dopamine cell loss concurrent with motor dysfunction (Ekstrand et al., 2007). Six WT (DAT::cre^{+/-} × TFAM^{loxP/loxP}; three males, three females) mice and six MitoPark (MP; DAT::cre^{+/cre} × TFAM^{loxP/loxP}; three males, three females) mice were longitudinally followed for the duration of the study (~9–26 weeks). For optogenetic experiments (Figure 7), experimental subjects were three adult male mice generated by crossing Drd1a::cre mice with mice that drove Archaerhodopsin-3/eGFP expression following recombination mediated by cre recombinase. The surgical protocol was initiated between 9 and 11 weeks and performed as described previously (Osborne and Dudman, 2014).

Open-Field and L-DOPA Sensitivity

An open-field task characterized the gross motor phenotype of global movement over time. A total of 124 WT and 146 MitoPark open-field sessions lasting 45 min each were recorded longitudinally at regular intervals between 12–23 and 10–23 weeks of age in WT and MitoPark groups, respectively. A custom-developed circuit board with light-emitting diodes was connected to the headcap of the animal and custom software recorded movement with an overhead video camera. Details of the analysis are provided in the *Supplemental Experimental Procedures*.

Effort-Based Operant Task

In the head-fixed reaching task a total of 102 WT and 92 PD sessions were recorded longitudinally at regular intervals between 14–24 weeks and 12–22 weeks of age for the WT and PD groups, respectively. Mice were restricted to consume 1.5 ml of water per day obtained primarily in the task. Mice underwent three training sessions in the head-fixed rig prior to data acquisition to ensure task learning. Mice were placed in a darkened chamber with both paws positioned on a small metal handle (1.5 mm o.d.) attached to a joystick with two degrees of freedom. Movement was coupled to a variable resistor, whose voltage drop was recorded at 10 kHz, filtered, smoothed and down-sampled to 250 Hz resolution. Task details are described in the main text with additional specific details provided in the *Supplemental Experimental Procedures*.

Analysis of Movement Trajectories

Discrete trajectories, defined as a reach, were extracted by detecting periods of sustained movement with a speed >0.75 cm/s. Reaches were required to last at least 100 ms and were considered discrete reaches if there was a period of at least 100 ms of subthreshold velocity prior to the next reach. Reach initiation and termination were determined by inferring time points of zero-crossings in movement velocity (with a noise tolerance determined separately). In the absence of a zero crossing, a point of zero acceleration was used to determine end points. The analysis of reach trajectories followed a technique

described in detail previously (Gallivan and Chapman, 2014) and additional details can be found in the main text and in the **Supplemental Experimental Procedures**.

Electrophysiological Recordings

Extracellular electrophysiology was performed in the dorsal striatum of awake, behaving mice during the joystick task in WT, MitoPark, and LD-treated MitoPark groups. Sixty-four -channel silicon probe arrays (NeuroNexus; "Buzsaki64" site arrangement) were acutely implanted in the dorsal striatum (0 mm from bregma, −2.0 mm to −3.0 mm depth from surface) for two to four recording sessions over several days per animal. Recordings were performed at the end of behavioral training, after L-DOPA sensitivity was apparent in MitoPark mice and when task time plateaued in WT mice (19–26 weeks in MitoPark, 24–29 weeks in WT mice). Electrodes were prepared for recording by reducing the site impedance below 750 kOhm. Broadband continuous data (0.1 Hz–7.5 kHz) were recorded with simultaneous sampling of voltage from the joystick, the lick port, and digital signals from the behavior control system (30 kHz sample rate on all channels; Blackrock Microsystems). Probes were coated with fluorescent coating (Dil) for site localization during histology. Additional details about data analysis and spike sorting are provided in the **Supplemental Experimental Procedures**.

All analyses and figures for the manuscript were generated in MATLAB 2013a or later and Igor Pro Version 6.2+. All statistical tests were implemented using the Statistics Toolbox for MATLAB with a significance threshold of 0.05 unless otherwise indicated.

SUPPLEMENTAL INFORMATION

Supplemental Information includes Supplemental Experimental Procedures and seven figures and can be found with this article online at <http://dx.doi.org/10.1016/j.cell.2015.08.014>.

AUTHOR CONTRIBUTIONS

B.P., A.Y.K., A.V., and J.T.D. designed the study. B.P., K.A.M., and J.T.D. performed all experiments with assistance from Y.L. L.O. contributed the mouse lines. B.P., K.A.M., A.G., and J.T.D. analyzed the data. B.P., B.M., A.G., A.Y.K., and J.T.D. wrote the manuscript with input from all authors.

ACKNOWLEDGMENTS

We thank members of the A.Y.K. and J.T.D. labs for critical reading and feedback on the manuscript. J.T.D. and A.Y.K. are Group Leaders at Janelia Research Campus and this work was supported by the Howard Hughes Medical Institute (HHMI). B.P. was an HHMI Medical Fellow. L.O. is supported by the Swedish Research Council (ERC grant 322744) and Swedish Brain Power. L.O. is a co-owner of a company that owns commercial rights to the MitoPark mouse.

Received: January 7, 2015

Revised: April 24, 2015

Accepted: July 17, 2015

Published: September 10, 2015

REFERENCES

- Albin, R.L., Young, A.B., and Penney, J.B. (1989). The functional anatomy of basal ganglia disorders. *Trends Neurosci.* 12, 366–375.
- Bar-Gad, I., Morris, G., and Bergman, H. (2003). Information processing, dimensionality reduction and reinforcement learning in the basal ganglia. *Prog. Neurobiol.* 71, 439–473.
- Baraduc, P., Thobois, S., Gan, J., Broussolle, E., and Desmurget, M. (2013). A common optimization principle for motor execution in healthy subjects and parkinsonian patients. *J. Neurosci.* 33, 665–677.
- Berardelli, A., Rothwell, J.C., Thompson, P.D., and Hallett, M. (2001). Pathophysiology of bradykinesia in Parkinson's disease. *Brain* 124, 2131–2146.
- Bryden, D.W., Johnson, E.E., Diao, X., and Roesch, M.R. (2011). Impact of expected value on neural activity in rat substantia nigra pars reticulata. *Eur. J. Neurosci.* 33, 2308–2317.
- Buhusi, C.V., and Meck, W.H. (2005). What makes us tick? Functional and neural mechanisms of interval timing. *Nat. Rev. Neurosci.* 6, 755–765.
- Cohen, J.Y., Haesler, S., Vong, L., Lowell, B.B., and Uchida, N. (2012). Neuron-type-specific signals for reward and punishment in the ventral tegmental area. *Nature* 482, 85–88.
- Cui, G., Jun, S.B., Jin, X., Pham, M.D., Vogel, S.S., Lovinger, D.M., and Costa, R.M. (2013). Concurrent activation of striatal direct and indirect pathways during action initiation. *Nature* 494, 238–242.
- DeLong, M.R. (1990). Primate models of movement disorders of basal ganglia origin. *Trends Neurosci.* 13, 281–285.
- DeLong, M., and Wichmann, T. (2009). Update on models of basal ganglia function and dysfunction. *Parkinsonism Relat. Disord.* 15 (Suppl 3), S237–S240.
- Desmurget, M., and Turner, R.S. (2010). Motor sequences and the basal ganglia: kinematics, not habits. *J. Neurosci.* 30, 7685–7690.
- Doya, K. (2000). Complementary roles of basal ganglia and cerebellum in learning and motor control. *Curr. Opin. Neurobiol.* 10, 732–739.
- Ehringer, H., and Hornykiewicz, O. (1960). [Distribution of noradrenaline and dopamine (3-hydroxytyramine) in the human brain and their behavior in diseases of the extrapyramidal system]. *Klin. Wochenschr.* 38, 1236–1239.
- Ekstrand, M.I., Terzioglu, M., Galter, D., Zhu, S., Hofstetter, C., Lindqvist, E., Thams, S., Bergstrand, A., Hansson, F.S., Trifunovic, A., et al. (2007). Progressive parkinsonism in mice with respiratory-chain-deficient dopamine neurons. *Proc. Natl. Acad. Sci. USA* 104, 1325–1330.
- Fan, D., Rossi, M.A., and Yin, H.H. (2012). Mechanisms of action selection and timing in substantia nigra neurons. *J. Neurosci.* 32, 5534–5548.
- Frank, M.J. (2011). Computational models of motivated action selection in corticostriatal circuits. *Curr. Opin. Neurobiol.* 21, 381–386.
- Gallivan, J.P., and Chapman, C.S. (2014). Three-dimensional reach trajectories as a probe of real-time decision-making between multiple competing targets. *Front. Neurosci.* 8, 215.
- Galster, D., Pernold, K., Yoshitake, T., Lindqvist, E., Hoffer, B., Kehr, J., Larsson, N.G., and Olson, L. (2010). MitoPark mice mirror the slow progression of key symptoms and L-DOPA response in Parkinson's disease. *Genes Brain Behav.* 9, 173–181.
- Gong, S., Zheng, C., Doughty, M.L., Losos, K., Didkovsky, N., Schambra, U.B., Nowak, N.J., Joyner, A., Leblanc, G., Hatten, M.E., and Heintz, N. (2003). A gene expression atlas of the central nervous system based on bacterial artificial chromosomes. *Nature* 425, 917–925.
- Good, C.H., Hoffman, A.F., Hoffer, B.J., Chefer, V.I., Shippenberg, T.S., Backman, C.M., Larsson, N.G., Olson, L., Gellhaar, S., Galter, D., et al. (2011). Impaired nigrostriatal function precedes behavioral deficits in a genetic mitochondrial model of Parkinson's disease. *FASEB J.* 25, 1333–1344.
- Han, X., Chow, B.Y., Zhou, H., Klapoetke, N.C., Chuong, A., Rajimehr, R., Yang, A., Baratta, M.V., Winkle, J., Desimone, R., and Boyden, E.S. (2011). A high-light sensitivity optical neural silencer: development and application to optogenetic control of non-human primate cortex. *Front. Syst. Neurosci.* 5, 18.
- Hernandez, L.F., Kubota, Y., Hu, D., Howe, M.W., Lemaire, N., and Graybiel, A.M. (2013). Selective effects of dopamine depletion and L-DOPA therapy on learning-related firing dynamics of striatal neurons. *J. Neurosci.* 33, 4782–4795.
- Hikosaka, O., Takikawa, Y., and Kawagoe, R. (2000). Role of the basal ganglia in the control of purposive saccadic eye movements. *Physiol. Rev.* 80, 953–978.
- Horak, F.B., and Anderson, M.E. (1984). Influence of globus pallidus on arm movements in monkeys. I. Effects of kainic acid-induced lesions. *J. Neurophysiol.* 52, 290–304.

- Isomura, Y., Takekawa, T., Harukuni, R., Handa, T., Aizawa, H., Takada, M., and Fukai, T. (2013). Reward-modulated motor information in identified striatum neurons. *J. Neurosci.* 33, 10209–10220.
- Leonardo, A. (2005). Degenerate coding in neural systems. *J. Comp. Physiol. A Neuroethol. Sens. Neural Behav. Physiol.* 191, 995–1010.
- Li, X., Redus, L., Chen, C., Martinez, P.A., Strong, R., Li, S., and O'Connor, J.C. (2013). Cognitive dysfunction precedes the onset of motor symptoms in the MitoPark mouse model of Parkinson's disease. *PLoS ONE* 8, e71341.
- Martinu, K., Degroot, C., Madjar, C., Strafella, A.P., and Monchi, O. (2012). Levodopa influences striatal activity but does not affect cortical hyper-activity in Parkinson's disease. *Eur. J. Neurosci.* 35, 572–583.
- Mazzoni, P., Hristova, A., and Krakauer, J.W. (2007). Why don't we move faster? Parkinson's disease, movement vigor, and implicit motivation. *J. Neurosci.* 27, 7105–7116.
- Mink, J.W. (1996). The basal ganglia: focused selection and inhibition of competing motor programs. *Prog. Neurobiol.* 50, 381–425.
- Muranishi, M., Inokawa, H., Yamada, H., Ueda, Y., Matsumoto, N., Nakagawa, M., and Kimura, M. (2011). Inactivation of the putamen selectively impairs reward history-based action selection. *Exp. Brain Res.* 209, 235–246.
- Niv, Y. (2007). Cost, benefit, tonic, phasic: what do response rates tell us about dopamine and motivation? *Ann. N Y Acad. Sci.* 1104, 357–376.
- Niv, Y., Daw, N.D., Joel, D., and Dayan, P. (2007). Tonic dopamine: opportunity costs and the control of response vigor. *Psychopharmacology (Berl.)* 191, 507–520.
- Osborne, J.E., and Dudman, J.T. (2014). RIVETS: a mechanical system for *in vivo* and *in vitro* electrophysiology and imaging. *PLoS ONE* 9, e89007.
- Palmiter, R.D. (2008). Dopamine signaling in the dorsal striatum is essential for motivated behaviors: lessons from dopamine-deficient mice. *Ann. N Y Acad. Sci.* 1129, 35–46.
- Pan, W.X., Mao, T., and Dudman, J.T. (2010). Inputs to the dorsal striatum of the mouse reflect the parallel circuit architecture of the forebrain. *Front. Neuroanat.* 4, 147.
- Pan, W.X., Brown, J., and Dudman, J.T. (2013). Neural signals of extinction in the inhibitory microcircuit of the ventral midbrain. *Nat. Neurosci.* 16, 71–78.
- Rueda-Orozco, P.E., and Robbe, D. (2015). The striatum multiplexes contextual and kinematic information to constrain motor habits execution. *Nat. Neurosci.* 18, 453–460.
- Salamone, J.D., and Correa, M. (2012). The mysterious motivational functions of mesolimbic dopamine. *Neuron* 76, 470–485.
- Schultz, W. (2006). Behavioral theories and the neurophysiology of reward. *Annu. Rev. Psychol.* 57, 87–115.
- Shenoy, K.V., Sahani, M., and Churchland, M.M. (2013). Cortical control of arm movements: a dynamical systems perspective. *Annu. Rev. Neurosci.* 36, 337–359.
- Stalnaker, T.A., Calhoon, G.G., Ogawa, M., Roesch, M.R., and Schoenbaum, G. (2012). Reward prediction error signaling in posterior dorsomedial striatum is action specific. *J. Neurosci.* 32, 10296–10305.
- Stein, J.F., and Aziz, T.Z. (1999). Does imbalance between basal ganglia and cerebellar outputs cause movement disorders? *Curr. Opin. Neurol.* 12, 667–669.
- Turner, R.S., and Desmurget, M. (2010). Basal ganglia contributions to motor control: a vigorous tutor. *Curr. Opin. Neurobiol.* 20, 704–716.
- Wang, A.Y., Miura, K., and Uchida, N. (2013). The dorsomedial striatum encodes net expected return, critical for energizing performance vigor. *Nat. Neurosci.* 16, 639–647.
- Wolpert, D.M., and Ghahramani, Z. (2000). Computational principles of movement neuroscience. *Nat. Neurosci.* 3 (Suppl), 1212–1217.

Structural Insights into the Dynamic Process of β_2 -Adrenergic Receptor Signaling

Aashish Manglik, Tae Hun Kim, Matthieu Masureel, Christian Altenbach, Zhongyu Yang, Daniel Hilger, Michael T. Lerch, Tong Sun Kobilka, Foon Sun Thian, Wayne L. Hubbell, R. Scott Prosser, and Brian K. Kobilka*

*Correspondence: kobilka@stanford.edu

<http://dx.doi.org/10.1016/j.cell.2015.08.045>

(Cell 161, 1101–1111; May 14, 2015)

In the Introduction of the above article, we neglected to cite Chung et al. (2012), Liu et al. (2012), Kim et al. (2013), and Horst et al. (2013). These papers demonstrate how ^{19}F NMR has been applied to study the role of dynamics in GPCR function and provide a broad context for understanding the advance coming out of our combined application of ^{19}F NMR and DEER spectroscopy to uncover conformational changes during $\beta_2\text{AR}$ activation.

REFERENCES

- Chung, K.Y., Kim, T.H., Manglik, A., Alvares, R., Kobilka, B.K., and Prosser, R.S. (2012). Role of detergents in conformational exchange of a G protein-coupled receptor. *J. Biol. Chem.* 287, 36305–36311.
- Horst, R., Liu, J.J., Stevens, R.C., and Wüthrich, K. (2013). β_2 -adrenergic receptor activation by agonists studied with ^{19}F NMR spectroscopy. *Angew. Chem. Int. Ed. Engl.* 52, 10762–10765.
- Kim, T.H., Chung, K.Y., Manglik, A., Hansen, A.L., Dror, R.O., Mildorf, T.J., Shaw, D.E., Kobilka, B.K., and Prosser, R.S. (2013). The role of ligands on the equilibria between functional states of a G protein-coupled receptor. *J. Am. Chem. Soc.* 135, 9465–9474.
- Liu, J.J., Horst, R., Katritch, V., Stevens, R.C., and Wüthrich, K. (2012). Biased signaling pathways in β_2 -adrenergic receptor characterized by ^{19}F -NMR. *Science* 335, 1106–1110.

Timeline: Sending Out an SOS

Brian Plosky, Deputy Editor
Molecular Cell

X-rays cause mutations

1927



Proposal of the SOS model
for an inducible response to
DNA damage

1974

p53 is a key transcriptional
regulator in the mammalian
DNA damage response (DDR)

2003-2005

Sensing single-stranded
DNA activates the DDR
Single-stranded DNA is created
by resection of one strand at a
double-strand break or it is
exposed during replication stress
and can activate the DDR.



2009

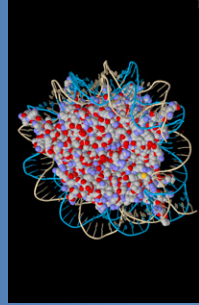
Coordination of nucleases
Nucleases that process DNA structures
such as stalled replication forks,
Holliday junctions, and interstrand
crosslinks work together as a complex.

1900

2000

End-resection control
determines repair pathway
choice at double-strand breaks
Resection of broken DNA ends
determines whether homologous
recombination or non-homologous
endjoining will be used for repair.

2007-2010



Histone H2AX phosphorylation
as platform for and indicator
of the DDR

1998

Damaged DNA can be
replicated by specialized
DNA polymerases

1999

Eukaryotic cell-cycle
checkpoints

1989

Cleavage of LexA regulates
the SOS response

1980-1981

Mechanisms for
excision repair and
recombination described

1964

Bacterial cells can recover
from UV exposure

1935

Timeline: Checkpoint Blockade

Joao Monteiro, Editor
Cell

